Transactions of the ASME®



**Transactions of the ASME, Journal of Heat Transfer** (ISSN 0022-1481) is published quarterly (Feb., May, Aug., Nov.) for $155 per year by The American Society of Mechanical Engineers, 345 East 47th Street, New York, NY 10017. Second class postage paid at New York, NY and additional mailing offices. POSTMASTER: Send address changes to The Journal of Heat Transfer, c/o THE AMERICAN SOCIETY OF MECHANICAL ENGINEERS, 22 Law Drive, Box 2300, Fairfield, NJ 07007-2300.
**CHANGES OF ADDRESS** must be received at Society headquarters seven weeks before they are to be *effective. Please send old label and new address.*
**PRICES:** To members, $29.00, annually; to nonmembers, $155.00.
Add $15.00 for postage to countries outside the United States and Canada.
**STATEMENT from By-Laws.** The Society shall not be responsible for statements or opinions advanced in papers or . . . printed in its publications (B7.1, para. 3).

**INDEXED** by Applied Mechanics Reviews and Engineering Information, Inc.

# Journal of Heat Transfer

Published Quarterly by The American Society of Mechanical Engineers

VOLUME 110 • NUMBER 4(A) • NOVEMBER 1988

## ANNOUNCEMENTS



## TECHNICAL PAPERS

## TECHNICAL NOTES

**J. V. Beck**
Heat Transfer Group,
Michigan State University,
Department of Mechanical Engineering,
East Lansing, MI

**H. A. McLain**

**M. A. Karnitz**

Energy Divison,
Oak Ridge National Laboratory,
Oak Ridge, TN

**J. A. Shonder**

**E. G. Segan**

Construction Engineering Research
Laboratory,
U.S. Army,
Champaign, IL

# Heat Losses From Underground Steam Pipelines

*A new transient solution describing the heat transfer around a single buried steam pipe was developed. The solution technique uses Green's functions and is particularly appropriate at distances greater than two or three pipe radii from the pipe. The solution models the pipe as a line heat source and considers a convective boundary condition at the soil surface. It was shown that for long time periods, the solution reduces to a steady-state expression that is believed to describe heat loss rates better than some current, commonly used steady-state relations. The solution was used with parameter estimation techniques to design an experimental procedure for determining buried steam pipe heat loss rates and depths from near-surface soil temperature measurements. Sensitivity coefficients derived from the solution were used to identify the linearly independent parameters and the optimum locations for the temperature measurements. An example of the use of this procedure is presented.*

## 1 Introduction

District and central heating systems have been applied extensively througout the United States. In many systems, heat is distributed to buildings from a central plant as steam flowing through buried pipelines. Frequently, the insulation around the buried pipes deteriorates and causes excessive heat loss. Because of increasing fuel costs and the high expense of replacing steam mains, a procedure for estimating heat loss to assist in determining the necessity or priority of pipeline replacement is of great interest. The basic objective of this paper is to present a simple method for estimating the relative heat loss from underground steam pipelines.

The paper presents a procedure for estimating heat loss from single underground steam pipelines using soil temperatures measured relatively near the ground surface. It has the advantage of using temperature values relatively easy to obtain compared with the method using deep ($>0.6$ m) subsurface values (Kusuda et al., 1983). The latter method often requires a relatively large ground-drilling device to position the temperature sensors.

The analytical justification for using shallow underground temperature measurements is presented. This method requires that the soil heat transfer coefficient $h$ be included in the analysis. The influence of this parameter on deep subsurface temperatures is not important and thus was not included in the analysis published by Kusuda et al. (1983). The transient nature of the in situ temperature measurements is also addressed in this paper. This analysis is limited to heat losses from a single underground pipe. For systems with condensate return, it should be noted that the condensate temperature is much lower than the supply steam temperature and, as a consequence, the condensate heat loss is much lower.

A number of investigators have proposed mathematical models for the steady-state temperature distribution around buried pipes with heat loss to the ground surface. These models are based on a solution of a two-dimensional heat conduction problem which, for constant thermal conductivity, involves Laplace's equation with appropriate boundary conditions. One of the earliest solutions is from Schofield (1941), who gave the temperature distribution around a line source inside a semi-infinite medium with an isothermal surface. He proposed a correction, called Schofield's added-thickness rule, for the convective heat loss at the ground surface. Eckert and Drake (1957) also discussed the case of a line source in a semi-infinite medium with an isothermal surface.

Several authors considered finite-diameter buried cylinders but provided numerical values for only the thermal resistance rather than the temperature distribution, which is required herein. Thiyagarajan and Yovanovich (1974) gave the thermal resistance for a constant heat flux at the pipe and an isothermal surface of the semi-infinite body. Schneider (1985) calculated the resistance for a convective boundary condition at the pipe as well as the ground surface.

The Green's function method is used herein to solve the transient heat transfer problem, and the significance of the transient solution is addressed. An example of using this solution to estimate buried steam pipe heat losses from shallow ($<0.3$ m) subsurface temperature measurements is given. In this procedure, the analytical solution was used together with parameter estimation theory to determine the optimum locations for the temperature measurements.

## 2 Heat Transfer Model

A transient heat conduction model is employed to describe the temperature distribution near the buried pipe. The physical model (Fig. 1) shows a steam pipe located a distance $D$ below the soil surface. The main quantity of interest is the heat flow per unit length of pipe, $Q$. Details regarding the temperature distribution near the pipe are not needed, because the temperature measurements are made "far" (two or three pipe radii) from the pipe (Thiyagarjan and Yovanovich, 1974). Hence, information regarding the heat transfer coefficient inside the pipe and the insulation of the pipe is not needed. At the soil surface are a time-varying absorbed solar heat flux of $q_{sol}(t)$ and the heat transfer to the ambient air at temperature $T_\infty(t)$; the heat transfer coefficient at the surface of the soil is denoted by $h$.

The temperature distribution in the soil around steam pipes, particularly near the soil–air surface, is transient with daily and yearly variations. It is pointed out herein that it is appropriate to use a steady-state solution, provided the correct

Contributed by the Heat Transfer Division for publication in the JOURNAL OF HEAT TRANSFER. Manuscript received by the Heat Transfer Division September 25, 1987. Keywords: Conduction, Measurement Techniques, Transient and Unsteady Heat Transfer.

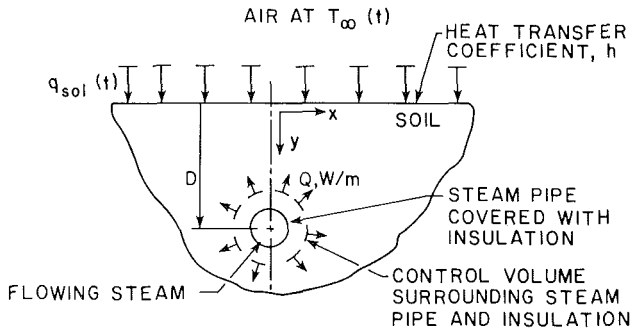


**Fig. 1 Diagram showing a steam pipe buried a depth *D* below soil surface**

one-dimensional transient temperatures are used. This point is important if near-surface soil temperature measurements are taken over several hours. To explain the problem more fully, a new transient analysis based on the use of Green's functions is presented.

The main assumptions for the heat transfer model are as follows: conduction is the dominant mode of heat flow in the soil; the soil thermal conductivity $k$, specific heat $c$, and density $\rho$ are constant; the ground surface heat transfer coefficient $h$ is constant with position and time; radiation from the heated soil surface can be incorporated into the convective heat transfer coefficient; the soil surface conditions are uniform with $x$ (Fig. 1); the depth $D$ of the pipe is "large" compared to the effective pipe radius; the temperatures are measured near the soil surface, not near the pipe; the heat flow $Q$ does not vary or varies only slowly with time and does not vary or varies only slightly along the pipe axis.

The soil thermal conductivity is assumed to be constant in this investigtion because the primary purpose of this procedure is to determine the regions of relatively large heat losses in buried steam networks. Although the conductivity is dependent on the soil composition and moisture content, the thermal diffusion equation used in this analysis typically smoothes the variations in this parameter. The justification of this assumption can be checked further by examining the temperature residuals—the differences between the measured and calculated temperatures. If the differences are small and random, then the assumption is adequate; and if not, the model may need improvement. Examination of the data published by Kusuda et al. (1983) revealed relatively small residuals. Moreover, in an independent test by the authors in the Oak Ridge, TN, area, transient soil temperatures obtained at depths from several centimeters to more than one meter were analyzed using sequential estimation theory (Beck and Arnold, 1977) to estimate the soil thermal diffusivity. The diffusivity value was found to be a constant, and the residuals using the diffusion model were very small.

The mathematical model is the two-dimensional transient heat conduction equation

$$\alpha\left[\frac{\partial^2 T}{\partial x^2}+\frac{\partial^2 T}{\partial y^2}\right]+\frac{\alpha}{k}\,g=\frac{\partial T}{\partial t} \tag{1}$$

The boundary condition at the soil surface, $y = 0$, is

$$-k\,\frac{\partial T}{\partial y}\,\Big|_{y=0}=h\left[T_\infty(t)-T(x,0,t)\right]+q_{sol}(t) \tag{2}$$

Both $T_\infty(t)$ and $q_{sol}(t)$ can have arbitrary time variations. For large values of $y$ (i.e., large soil depths), the temperature approaches a constant,

$$T(x,\infty,t)=T_0 \tag{3}$$

For large absolute values of the horizontal distance $x$, there is negligible effect of the steam pipe; thus, the heat flow is one-dimensional and there is no gradient in the $x$ direction

$$-k\,\frac{\partial T}{\partial x}=0,\ \text{for } x\to\infty \text{ and } x\to-\infty \tag{4}$$

The initial temperature distribution is unknown, but its value is not critical, because the time period continues indefinitely. One of the simplest assumptions is to choose the "initial time" to be when the one-dimensional temperature distribution is nearly equal to the deep depth value of $T_0$

$$T(x,y,0)=T_0 \tag{5}$$

In addition to the above, there is an energy source due to the buried steam pipe. Because the depth $D$ is assumed to be large compared to the pipe radius (two or three pipe radii away), the pipe can be simply modeled as a line source $g$

$$g=Q\delta(D-y')\delta(x') \tag{6}$$

where $\delta(z)$ is the Dirac delta function; it has the characteristics of having the integral over $x'$ and $y'$ of $\delta(D-y')\delta(x')$ equal to unity if it includes $\delta(D)\delta(0)$, or, otherwise, zero.

The general solution for equations (1)–(6) can be symbolically written, using Green's functions, in the form (Beck and Karnitz, 1986)

$$T(x,y,t)=T_0$$
$$+\frac{\alpha}{k}\int_{\tau=0}^{t} q_{sol}(\tau)\int_{x'=-\infty}^{\infty} G(x,y,t;x',0,\tau)\,dx'\,d\tau$$
$$+\frac{\alpha h}{k}\int_{\tau=0}^{t} T_\infty(\tau)\int_{x'=-\infty}^{\infty} G(x,y,t;x',0,\tau)\,dx'\,d\tau$$

## Nomenclature

$b$ = dimensionless quantity defined in equation (9*e*)
Bi = Biot number = $hD/k$
$c$ = specific heat
$D$ = depth of pipe
$E_1(\cdot)$ = expected value integral defined in equation (9*b*)
$g$ = volume energy source
$G(\cdot)$ = Green's function
$h$ = heat transfer coefficient
$k$ = thermal conductivity
$n$ = number of datum points
$Q$ = heat loss per unit length of pipe
$q_{sol}$ = solar heat flux
$r_1^+$ = dimensionless radius defined in equation (9*c*)
$r_2^+$ = dimensionless radius defined in equation (9*d*)
$S_{LS}$ = least squares sum function
$t$ = time
$T$ = temperature
$T_0$ = initial temperature
$T_1$ = undisturbed temperature at depth $y$
$T_\infty$ = ambient air temperature
$x$ = horizontal distance normal to pipe centerline
$x_0$ = correction for pipe centerline location
$y$ = depth below surface
$Y$ = measured temperature
$\alpha$ = thermal diffusivity = $k/\rho c$
$\beta$ = parameter
$\gamma$ = Euler's constant in equation (10)
$\delta(\cdot)$ = Dirac delta function
$\Delta_2$ = optimality criterion defined in equation (22)
$\rho$ = density
$\tau$ = dummy time variable

**Subscripts and Superscripts**

$i$ = datum point number
$k$ = iteration
$'$ = dummy variable

$$+\frac{\alpha}{k}\int_{\tau=0}^{t} Q\int_{x'=-\infty}^{\infty}\int_{y'=0}^{\infty} G(x, y, t; x', y', \tau) \times \delta(D-y')\partial(x')dx'dy'd\tau \tag{7}$$

The second and third terms on the right side of the equation represent the temperature distribution in the soil if no heat source is present. Because this distribution is independent of $x$, these terms can be represented by the function $T_1(y, t)$. Using the notation for Green's functions proposed by Beck (1984), equation (7) becomes

$$T(x, y, t) = T_0 + T_1(y, t) + \frac{\alpha Q}{k}\int_{\tau=0}^{t} G_{X00}(x, t; 0, \tau) G_{Y30}(y, t; D, \tau)d\tau \tag{8a}$$

where

$$G_{X00}(x, t; 0, \tau) = [4\alpha\pi(t-\tau)]^{-1/2}\exp\left[-\frac{x^2}{4\alpha(t-\tau)}\right] \tag{8b}$$

and

$$G_{Y30}(y, t; D, \tau) = [4\alpha\pi(t-\tau)]^{-1/2}\left\{\exp\left[-\frac{(y-D)^2}{4\alpha(t-\tau)}\right] + \exp\left[-\frac{(y+D)^2}{4\alpha(t-\tau)}\right]\right\} - \frac{h}{k}\exp\left[\frac{\alpha(t-\tau)h^2}{k^2} + \frac{h(y+D)}{k}\right] \times \operatorname{erfc}\left\{\frac{y+D}{[4\alpha(t-\tau)]^{1/2}} + \frac{h}{k}[\alpha(t-\tau)]^{1/2}\right\} \tag{8c}$$

Details of the integration of this relation are given by Beck and Karnitz (1986). For Biot numbers having values greater than 10, the range of interest, the integrated relation is

$$T(x, y, t) = T_0 + T_1(y, t) + \frac{Q}{4\pi k}\left\{E_1\left(\frac{r_1^{+2}}{4\alpha t/D^2}\right) - E_1\left(\frac{r_2^{+2}}{4\alpha t/D^2}\right) + 2\exp(b^{-1})E_1\left(\frac{r_2^{+2}}{4\alpha t/D^2} + b^{-1}\right)\right\} \tag{9a}$$

where $E_1$, $r_1^{+2}$, and $r_2^{+2}$ are defined by

$$E_1(z) = \int_z^{\infty} u^{-1}e^{-u}du \tag{9b}$$

$$r_1^{+2} = \left(\frac{x}{D}\right)^2 + \left(\frac{y}{D} - 1\right)^2 \tag{9c}$$

$$r_2^{+2} = \left(\frac{x}{D}\right)^2 + \left(\frac{y}{D} + 1\right)^2 \tag{9d}$$

$$b = \frac{2\left[\frac{y}{D} + 1\right]}{\mathrm{Bi}\left[\left(\frac{x}{D}\right)^2 + \left(\frac{y}{D} + 1\right)^2\right]} \tag{9e}$$

Equation (9) is the transient solution for the temperature at any $x$ and $y$ in the ground for the pipe located at $y = D$ and $x = 0$.

If the temperatures of the steam do not vary with time, the solution can be simplified by letting $t$ go to infinity, but $E_1(z)$ with $z \to 0$ goes to infinity. However, for the first two $E_1(\cdot)$ expressions in equation (9), one positive and one negative, this effect cancels. Using the relation (Abramowitz and Stegan, 1964)

$$E_1(z) = \gamma - \ln z + z - \ldots, \quad \gamma = 0.577216 \tag{10}$$

in equation (9) for small $z$ (i.e., large times $t$) gives the "steady-state" result of

$$T_s(x, y, t) = T_0 + T_1(y, t) + \frac{Q}{4\pi k}\left[\ln\frac{x^2 + (y+D)^2}{x^2 + (y-D)^2} + 2\exp(b^{-1})E_1(b^{-1})\right] \tag{11}$$

Furthermore, for Bi having values of at least 10, the value of $b^{-1}$ is at least 5. For such "large" values, $\exp(b^{-1})\,E_1(b^{-1})$ in equation (11) can be approximated by

$$\exp(b^{-1})E_1(b^{-1}) = b - b^2 + 2b^3 - 3b^4 \tag{12}$$

The term $\exp(b^{-1})\,E_1(b^{-1})$ in equation (11) is quite important, particularly so when measurements are taken near the ground surface, because the natural logarithm term goes to zero and it is the only contribution inside the brackets.

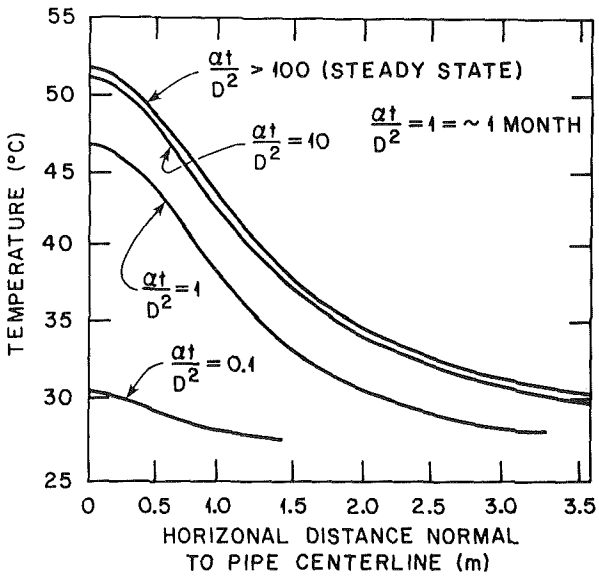


Fig. 2 Temperature at $y = 0.23$ m for $D = 1.22$ m, $Q = 385$ W/m, Bi = 10, $T_0 + T_1(y, t) = 27.2$°C

Plots of the above equations are instructive. The transient relation given by equation (9) is considered first, and the following values are used: $k = 1.3$ W/m−K, $a = 0.485 \times 10^{-6}$ m²/s, $y = 0.23$ m, $D = 1.22$ m, $Q = 385$ W/m, and $h = 10.65$ W/m²−K. For convenience, the sum of $T_0$ and $T_1(y, t)$ is considered to be the constant value of 27.2°C. Figure 2 shows a plot of equation (9) for these conditions; the temperature is plotted versus distance for fixed dimensionless times. Three observations are drawn from this figure. First, the transients are quite slow. If a pipeline is not used during an extended period, then the temperature can take as long as ten months to approach steady-state conditions after being reactivated. Second, the thermal effect can extend a considerable distance from the pipe; the distance to decrease to 50 percent of the maximum steady state value is about 1.2 m (about $D$), and the distance to reduce to 10 percent of the maximum is 3.6 m (about $3D$). Third, although the temperature changes considerably between $\alpha t/D^2 = 1$ and 10, the difference in the temperature at $x = 0$ and that at a moderate distance (such as $x = 1.2$ or 2.4 m) is nearly constant. In other words, the shape of the temperature curve is nearly constant for $\alpha t/D^2 > 1$ and for $x < 2D$.

For steady-state conditions, Fig. 3 shows a plot of equation

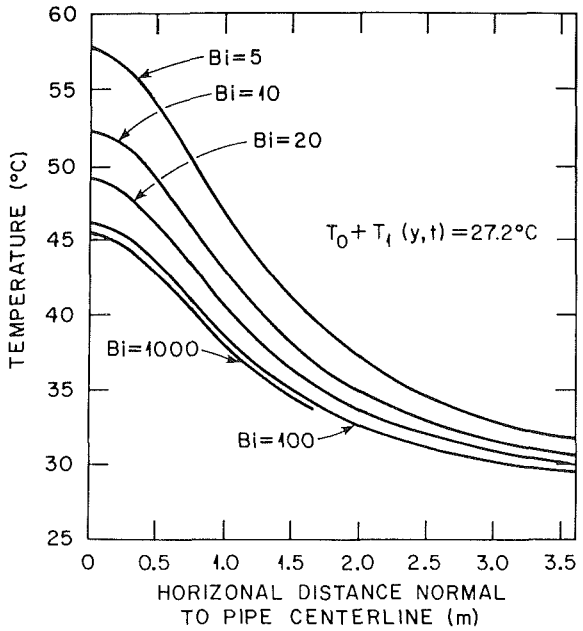


**Fig. 3 Steady-state temperatures at $y = 0.23$ m for $D = 1.22$ m and $Q = 385$ W/m**

(11) at the above conditions for different Bi values. Doubling the Bi value (doubling of the $h$ value) from 10 to 20, the expected range of interest, causes only a 2.8 K change at $x = 0$. This insensitivity of temperature changes to changes in Bi values suggests that the value of $h$ need not be precisely known when estimating $Q$.

For Bi greater than 10, an excellent approximation can be made to the steady-state solution, equation (11), by letting

$$\ln\frac{N}{x^2+(y-D)^2}=\ln\frac{x^2+(y+D)^2}{x^2+(y-D)^2}+2\exp(b^{-1})E_1(b^{-1}), \quad (13)$$

and solving for $N$. Using equation (12) to evaluate $\exp(b^{-1})E_1(b^{-1})$ and neglecting the higher order terms, it was shown by Beck and Karnitz (1986) that

$$T_s(x,y,t)=T_0+T_1(y,t)+\frac{Q}{4\pi k}\ln\frac{\left(\frac{x}{D}\right)^2+\left(\frac{y}{D}+1+\frac{2}{\mathrm{Bi}}\right)^2-\frac{4}{\mathrm{Bi}^2}}{\left(\frac{x}{D}\right)^2+\left(\frac{y}{D}-1\right)^2} \quad (14)$$

Equation (14) is an improvement on Schofield's added-thickness rule for buried line heat sources with convective heat transfer at the ground surface (Schofield, 1941). If the $-4/\mathrm{Bi}^2$ term is dropped, equation (14) becomes the Schofield relation.

## 3 Parameter Estimation Procedure

Parameter estimation theory has been under development for a number of years, and many papers and several books have been written on this subject (e.g., Beck and Arnold, 1977; Bard, 1974; Draper and Smith, 1966; Daniel and Wood, 1971). The method of least squares is used herein. Several important concepts related to the sensitivity coefficients and experimental design are noted. Beck and Arnold (1977) list eight standard statistical assumptions for the least-squares method to be appropriate. If the assumptions are not satisfied, another method may be more appropriate.

The least-squares criterion is that the sum $S_{LS}$

$$S_{LS}=\sum_{i=1}^{n}\left(Y_i-T_i\right)^2 \quad (15)$$

is minimized with respect to the parameters. At the minimum value of the sum, the first derivatives with respect to the unknown parameters are zero. The parameters of interest here are $Q$ and $D$ in equation (14), because both the buried pipe heat loss rate and depth are often unknown in field situations. The first derivatives of equation (15) for these parameters are

$$\frac{\partial S_{LS}}{\partial Q}=-2\sum_{i=1}^{n}\left[Y_i-T_i\right]\frac{\partial T_i}{\partial Q}=0$$

$$\frac{\partial S_{LS}}{\partial D}=-2\sum_{i=1}^{n}\left[Y_i-T_i\right]\frac{\partial T_i}{\partial D}=0 \quad (16)$$

Because the value of $T$ in equation (14) is a nonlinear function of $D$, equation (16) is a set of nonlinear equations.

These nonlinear equations can be solved using the Gauss linearization procedure (Beck and Arnold, 1977). This is an iteration procedure starting with initial estimates of $Q$ and $D$. At the $k$th iteration in this procedure, the value of $T_i$ in equation (16) is replaced with $T_i^{(k+1)}$ determined by the Taylor series approximation

$$T_i^{(k+1)}=T_i^{(k)}+\frac{\partial T_i^{(k)}}{\partial Q}\left[Q^{(k+1)}-Q^{(k)}\right]+\frac{\partial T_i^{(k)}}{\partial D}\left[D^{(k+1)}-D^{(k)}\right] \quad (17)$$

New values of $Q$ and $D$ for the $k+1$ iteration are then calculated by combining equations (16) and (17) and solving them simultaneously. The partial derivatives are evaluated in this calculation using the values of $Q$ and $D$ calculated in the preceding iteration. The iteration continues until the change in the values of $Q$ and $D$ between iterations become negligible. See Beck and Arnold (1977) for refinements of this procedure.

The partial derivatives in equations (16) and (17) are called "sensitivity coefficients," and examination of these coefficients can be effective in devising soil temperature experiments for estimating $Q$ and $D$.

In general, the sensitivity coefficients are desired to be (1) large and (2) uncorrelated. The physical units of the coefficient depend on the unit of the parameter; therefore, it is convenient to compare the values of the normalized coefficient, $\beta\,\partial T/\partial\beta$, where $\beta$ is the parameter. If $T$ has units of temperature, the value of the normalized coefficient has the unit of temperature and can be compared with the actual temperature rise in the experiment. If the value is on the order of the magnitude of the $T$ change, then the sensitivity coefficients are termed "large."

The term "uncorrelated" means that the sensitivity coefficients are not linearly dependent. For the temperature relation given by equation (14), there is a linear dependence between the parameters $Q$, $k$, and $h$, because it can be shown that

$$Q\frac{\partial T}{\partial Q}+h\frac{\partial T}{\partial h}+k\frac{\partial T}{\partial k}=0 \quad (18)$$

Because of equation (18), it is not possible to measure the values of all these parameters simultaneously from a set of temperature measurements.

In the other extreme case of estimating a single parameter, each of the above parameters can be estimated if the others are known, because no sensitivity coefficient is zero. The sensitivity coefficients for Bi = 10 are shown in Fig. 4(*a*) for measurements at the surface, and Fig. 4(*b*) shows values for $y/D = 0.1875$. In both figures, the $Q$ sensitivity coefficient curves have the largest magnitudes. Hence, $Q$ can be estimated with the greatest accuracy. The $D$ sensitivity coefficient has a relatively large amplitude near $x = 0$. The values start negative and then increase to small positive values. The $k$ sensitivity coefficient is very small near $y = 0$ and is much larger in amplitude for $y/D = 0.1875$ [Fig. 4(*b*)]. The $h$ sensitivity coefficients is relatively small and independent of the depth $y$;

**Table 1 Measured soil temperatures at Location 6 (measurement depth, 0.18 m)**

| Location, m | Temperature, °C |
|---|---|
| −1.83 | 30.6 |
| −1.22 | 21.5 |
| −0.61 | 33.2 |
| 0.00 | 34.9 |
| 0.61 | 35.2 |
| 1.22 | 32.7 |
| 1.83 | 30.5 |
| 15.00 | 26.2 |
| 15.00 | 25.7 |
| 15.00 | 25.2 |

hence, $h$ is difficult to estimate accurately from temperature measurements in this type of experiment. On the other hand, fixing $h$ at an inaccurate value while estimating the other parameters will not greatly affect the estimates.

The two parameters that can be estimated simultaneously most accurately are $Q$ and $D$. Note that the amplitudes of each sensitivity curve start large, but the shapes are quite different, with the $Q$ curve being always positive and the $D$ curve changing signs. The fact that the $Q$ curve starts positive and the $D$ curve starts negative is not significant. It is important that measurements be taken at $x = 0$ (location of maximum absolute values of $Q\partial T/\partial Q$ and $D\partial T/\partial D$) and also at some distance, when $D\partial T/\partial D$ is much smaller, to reduce the correlation between the $D$ and $Q$ sensitivity coefficients.

The parameter $k$ is of particular interest, in addition to $Q$ and $D$. If measurements are only taken at $y = 0$, both $Q$ and $k$ cannot be estimated because the $k$ sensitivity coefficient has such small amplitude [Fig. 4($a$)]. Also, measurements at $y/D = 0.1875$ [Fig. 4($b$)] are not sufficient because the $Q$ and $k$ sensitivity curves are nearly proportional.

The selection of the locations for measuring the subsurface soil temperatures can be determined using the sensitivity coefficients. For estimating $Q$ and $D$, the maximum sensitivity coefficients are located over the pipe centerline, $x = 0$. This is then expected to be one of the optimal locations.

For the remaining temperature measurements, three other location on each side of the pipe and on a line perpendicular to the pipe were selected in this example. Specifying that the spacing between the adjacent locations is equal, the optimal experimental criterion for two parameters is to maximize the relation (Beck and Arnold, 1977)

$$\Delta_2 = \left[\sum_{i=1}^{n}\left(\frac{\partial T_i}{\partial Q}\right)^2\right]\left[\sum_{i=1}^{n}\left(\frac{\partial T_i}{\partial D}\right)^2\right] - \left[\sum_{i=1}^{n}\left(\frac{\partial T_i}{\partial Q}\right)\left(\frac{\partial T_i}{\partial D}\right)\right]^2 \quad (19)$$

Figure 5 shows the values of the $\Delta_2$ function using Fig. 4($b$) sensitivity coefficient data for seven equally spaced measurement locations centered at $x = 0$. The maximum value of $\Delta_2$ is at about 1.5 m, which is the optimal location for the farthest temperature measurement for a pipe depth of 1.22 m and a measurement depth at 0.23 m. The $\Delta_2$ values decrease slowly for distances greater than 1.5 m.

The choice of the location for the reference temperature measurement [sum of $T_0$ and $T_1$ in equation (14)] is particularly important. It should be at a distance sufficient for the influence of the pipe to be negligible—about 15 m. The type of soil and solar history, including shading, at this location should be the same as that over the steam pipe, which implies that this temperature should be measured nearly the same time as those near the pipe.

## 4 An Application

To illustrate the use of this method, near-surface soil temperatures were measured at several locations near an existing 200-mm buried steam line. These data were used to estimate $Q/k$ and $D$ using the method of least squares. The parameter $Q/k$ was chosen for this example because the value of $Q$ is very dependent on the choice of $k$.

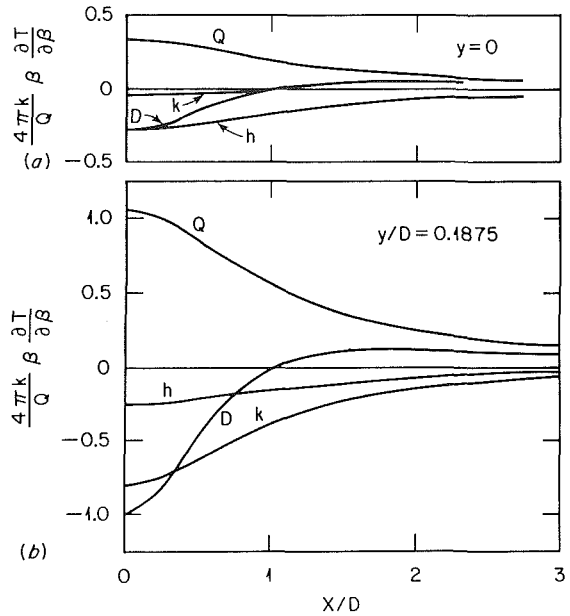


**Fig. 4 Steady-state sensitivity coefficients for Bi = 10**

All the temperature data were measured 0.18 m below the soil surface. At each data collection point, the approximate location of the buried pipe centerline was determined by measuring the ground surface temperatures. At this location, a small diameter (6 mm) hole was drilled. Additional holes were drilled at 0.61 m, 1.22 m, and 1.83 m from this location on each side of the pipe. These distances were selected from the experimental design calculations discussed above. Three additional holes were drilled about 15 m from the pipe to measure the reference temperature. Then, the holes were marked and allowed to dissipate any heat generated in the drilling process. Later, the temperatures at the bottom of the 0.18-m-deep holes were measured, using a thermocouple.

An example of the soil temperatures measured at one of the locations is given in Table 1. The estimated standard error for the measured values is 0.6°C. As for most of the data, the values in Table 1 are skewed, with the measured temperatures on one side of the estimated pipe centerline location being higher than those equidistant on the other side of this location. The sensitivity coefficients, shown in Fig. 4, and the $\Delta_2$ function values, shown in Fig. 5, indicate that the $Q/k$ and $D$ parameters are not very dependent on the precise location of the pipe centerline. A check was made on this, nevertheless, by substituting the value of $x + x_0$ for $x$ in equation (14), where $x_0$ is the difference between the assumed centerline location and the actual centerline location.

The sensitivity coefficients for the parameter $x_0$ were first compared with those for $Q$ and $D$. It was found that the three sensitivity coefficients are linearly independent. Furthermore, the curves for these three coefficients, when plotted as a function of $x$, all have different shapes. This showed that the measured soil temperature data can be used to estimate the parameters $Q/k$, $D$, and $x_0$ simultaneously.

The results of this check showed that the maximum difference between the estimated $Q/k$ values is 2.2 percent, when including the parameter $x_0$ in the estimation procedure as compared to ignoring it in the procedure. Similarly for the estimated $D$ values, the maximum difference was found to be 8.5 percent. The maximum value of $x_0$ was estimated to be about 0.75 m.

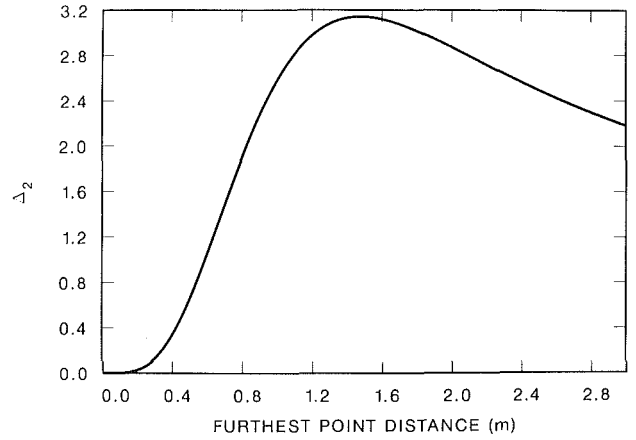


**Fig. 5 Optimal criterion for $n = 7$ and two parameters ($Q$ and $D$)($D = 1.22$ m, $y = 0.23$ m)**

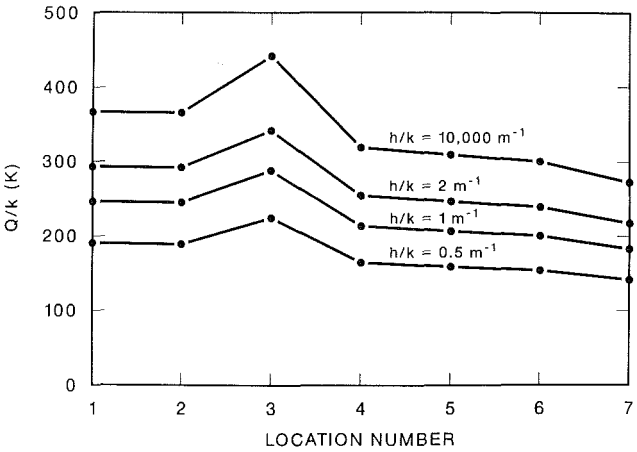


**Fig. 6 $Q/k$ values for soil temperature data; least-squares analysis at each location**

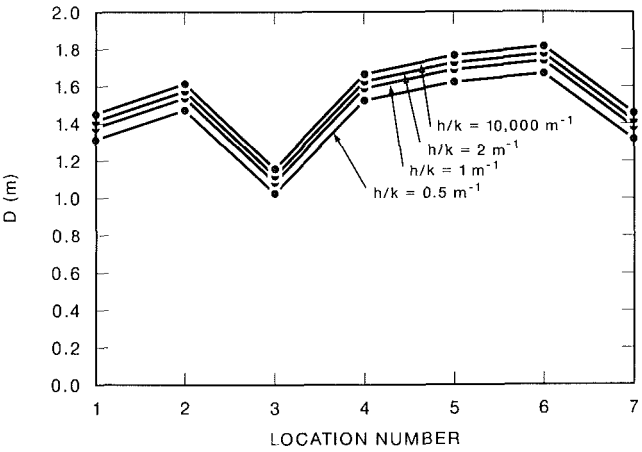


**Fig. 7 $D$ values for soil temperature data; least-squares analysis at each location**

The measured temperature data were used to estimate $Q/k$ and $D$ at each buried pipe location where the data were obtained. The parameter estimation relations, equations (16) and (18), were used together with the soil temperature relation, equation (14), to calculate these values. The reference temperature at each location was assumed to be the average of the three temperatures taken at distances far from the pipe. The value of the parameter $x_0$, in addition to the other two parameters values, was estimated at each location. The impact of ignoring this parameter is small, as shown above.

The estimated values of $Q/k$ and $D$ are displayed in Figs. 6 and 7. These values are shown as a function of the location number and the assumed $h/k$ values. Calculations were made using $h/k$ values of 0.5, 1, 2, and 10,000 m$^{-1}$. The largest value approaches infinity, which corresponds to a constant soil surface temperature. The changes in the value of $Q/k$ are small relative to the changes in the value of $h/k$, particularly at the higher values of this independent variable. When recognizing that $h$ includes radiation from the ground to the sky, the value of $h/k$ generally will be in the range of at least 1 m$^{-1}$ to 2 m$^{-1}$. Except for the extremes, other factors associated with the differences at the different pipe locations result in differences in the same order of magnitude as those associated with the changes in the $h/k$ value.

Results for the estimated values of $D$ show much less sensitivity to the choice of $h/k$. There is greater difference with respect to location than to $h/k$.

The standard errors for the $Q/k$ values were estimated to be $<6$ percent of the calculated values, and those for the $D$ values were estimated to be $<9$ percent of calculated values. These errors were derived by first calculating the variances of these parameters and then finding the positive square roots of these variances. This method is valid for measured soil temperatures that have additive, zero mean, and noncorrelated errors and have constant variances (Beck and Arnold, 1977).

The parameter $k$ was not estimated from the soil temperature data. It is possible to modify the approach described here to estimate simultaneously the values of $Q$ and $k$. However, the values of $D$ and $h$ must be known in this modified approach. Approaches using known heat sources, such as thermal needles, have been used to estimate $k$. In some cases having moist soil conditions, or when the soil temperatures are measured very close to the ground surface, the heat conduction model may not be adequate. In such cases, the parameter estimation method can be used with a more appropriate mathematical heat transfer model.

## 5 Conclusions

A new transient solution describing the heat transfer around a single buried pipe was developed. It is particularly appropriate at distances greater than two or three pipe radii from the pipe. The solution models the pipe as a line heat source and considers a convective boundary condition at the soil surface. It was shown that for large time periods, the solution reduces to a steady-state expression that is believed to describe heat loss rates better than some current, commonly used steady-state relations. Sample calculations indicate that the line heat source (steam pipe) must operate at constant temperatures for several months before the steady-state solution is applicable.

Sensitivity coefficients derived from the solution can be used to design the experiment. They can show which parameters are linearly independent and the optimum locations for the soil temperature measurements.

The methodology was used to estimate linear heat loss rates from an existing 200-mm buried steam line. The method of least squares was used to estimate the $Q/k$ and $D$ values from the measured soil temperatures at each location. The estimated parameters were generally consistent at all locations and only weakly dependent on the $h/k$ values. The effect of miscentering, within 0.75 m, the measurement locations was found to be very small.

The use of near-surface soil temperature measurements shows considerable promise for determining regions having

relatively high heat losses from buried line heat sources. Measuring temperatures and processing the data are relatively simple procedures. The principal uncertainty remaining is the measurement of the soil thermal conductivity. More work needs to be directed in this area to improve the effectiveness of this method.

## 6 Acknowledgments

Research for this work was supported by the U.S. Army Construction Engineering Research Laboratory, Champaign, IL, under U.S. Department of Energy Interagency Agreement No. 40-1716-85, and by the Office of Buildings and Community Systems, U.S. Department of Energy, under Contract No. DE-AC05-84OR21400 with Martin Marietta Energy Systems, Inc.

## References

Abramowitz, M., and Stegun, I. A., eds., 1964, *Handbook of Mathematical Functions*, AMS Series 55, National Bureau of Standards, Gaithersburg, MD.

Bard, Y., 1974, *Nonlinear Parameter Estimation*, Academic Press, New York.

Beck, J. V., 1984, "Green's Function Solution for Transient Heat Conduction Problems," *Int. J. Heat Mass Transfer*, Vol. 27, No. 8, pp. 1235–44.

Beck, J. V., and Arnold, K. J., 1977, *Parameter Estimation in Engineering and Science*, Wiley, New York.

Beck, J. V., and Karnitz, M. A., 1986, *Parameter Estimation Study of Heat Losses From Underground Steam Lines*, ORNL/TM-9928, Oak Ridge National Laboratory, Oak Ridge, TN.

Daniel, C., and Wood, F. S., 1971, *Fitting Equations to Data*, Wiley-Interscience, New York.

Draper, N. R., and Smith, H., 1966, *Applied Regression Analysis*, Wiley, New York.

Eckert, E. R. G., and Drake, R. H., 1957, *Heat and Mass Transfer*, 2nd, ed., McGraw-Hill, New York, pp. 60–64.

Kusuda, T., Aso, S., and Ellis, W., 1983, *A Method for Estimating Heat Loss From Underground Heat Distribution Systems*, National Bureau of Standards, Washington, DC.

Schneider, G. E., 1985, "An Investigation Into the Heat Loss Characteristics of Buried Pipes," ASME JOURNAL OF HEAT TRANSFER, Vol. 107, pp. 696–99.

Schofield, F. H., 1941, "The Steady Flow of Heat From Certain Objects Buried Under Flat-Air-Cooled Surfaces," *Philos. Mag.*, Vol. 31, pp. 471–97.

Sneed, D. M., and King, J. C., 1983, *Energy Conservation: Measuring Heat Loss in Steam Lines*, Tech Data Sheet 83–21, Department of the Navy, Civil Engineering Laboratory.

Thiyagarajan, R., and Yovanovich, M. M., 1974, "Thermal Resistance of a Buried Cylinder With Constant Flux Boundary Condition," ASME JOURNAL OF HEAT TRANSFER, Vol. 96, pp. 249–50.

# ERRATA

Errata for "Non-Darcian Convection in Cylindrical Packed Beds" by M. L. Hunt and C. L. Tien, published in the May 1988 issue of the ASME JOURNAL OF HEAT TRANSFER, Vol. 110, pp. 378-384.

The following correction should be made in equation (2):

Error

$$\frac{\rho}{\epsilon^2}\langle \mathbf{u}\cdot\nabla\mathbf{u}\rangle = -\nabla\langle P\rangle - \frac{\mu}{K}\langle \mathbf{u}\rangle - \mathrm{k}C|\langle \mathbf{u}\rangle|\langle \mathbf{u}\rangle \pm \frac{\mu}{\epsilon}\nabla^2\langle \mathbf{u}\rangle \quad (2)$$

Corrected version

$$\frac{\rho}{\epsilon^2}\langle \mathbf{u}\cdot\nabla\mathbf{u}\rangle = -\nabla\langle P\rangle - \frac{\mu}{K}\langle \mathbf{u}\rangle - \rho C|\langle \mathbf{u}\rangle|\langle \mathbf{u}\rangle + \frac{\mu}{\epsilon}\nabla^2\langle \mathbf{u}\rangle \quad (2)$$

# Inverse Heat Conduction Problem of Periodically Contacting Surfaces

**G. P. Flach**
Assoc. Mem. ASME

**M. N. Özişik**
Fellow ASME

Mechanical and Aerospace Engineering Department,
North Carolina State University,
Raleigh, NC 27695-7910

*An inverse heat conduction method for determining the periodically time-varying contact conductance between two periodically contacting surfaces is presented. The technique is based on solving two single-region inverse problems for the contact surface temperature and heat flux of each solid. The time variation of contact surface temperature is represented with a versatile periodic B-spline basis. The dimension of the B-spline basis is statistically optimized and confidence bounds are derived for the estimated contact conductance. Typical results based on both simulated and actual measurements are given and a parametric study is made to illustrate the general effects of measurement location, number of measurements, etc., on the accuracy of the results.*

## Introduction

Heat transfer between surfaces in imperfect thermal contact occurs in numerous practical situations, and substantial theoretical and experimental effort continues in the measurement and prediction of periodic contact conductance (or contact heat transfer coefficient) (Minges, 1966; Moore, 1967; Moore et al., 1968; Madhusudana and Fletcher, 1981). The special case of heat transfer across periodically contacting surfaces is of interest due to the large number of practical applications. Components in many rotary devices and in automated processes transfer heat periodically across contact surfaces. Examples include heat transfer between a valve and seat in an internal combustion engine, between a soldering iron and work piece on an assembly line, and between a hot workpiece and die under repetitive forming conditions.

Analytical computations of the temperature distribution in periodically contacting regions when the contact conductance is known include the works of Howard and Sutton (1970, 1973) and Vick and Özişik (1981). Howard and Sutton solved finite difference equations using an analogue computer for the situations of perfect (1970) and nonperfect contact (1973). Vick and Özişik (1981) used the integral transform technique to solve a nonperfect contact problem exactly.

Experimental efforts specifically involving periodically contacting surfaces have concentrated on measuring a constant periodic contact conductance during the contact mode of a periodic contact–noncontact operation (McKinzie, 1970; Howard, 1976; Moses, 1985; Moses and Johnson, 1986, 1987). The experimental apparatus typically involved two one-dimensional rods with each of the noncontacting ends held at a closely controlled fixed temperature. The transverse heat transfer was made negligible through insulation around the rods so that the heat transfer was effectively one-dimensional. During the contact mode, the rods were held together under constant pressure. The contact conductance was estimated from surface temperature and heat flux values computed using either the linear (McKinzie, 1970; Howard, 1976) or quadratic (Moses, 1985; Moses and Johnson, 1986, 1987) extrapolation method. The extrapolation method utilizes multiple spatial temperature readings taken physically very close to each contacting surface. A linear or quadratic polynomial is fitted to the spatial data. The value and slope of the extrapolated polynomial at the surface define the estimated surface temperature and heat flux, respectively. Constant values of the contact conductance were determined in each of the experimental investigations. However, Howard (1976) and Moses (1985) both note that the actual contact conductance is not exactly constant during the contact mode even when nominally constant pressure is applied. Howard (1976) cited transients in the contact pressure due to the initial impact and indirectly investigated this point by measuring the instantaneous electrical resistance across the contact surface.

Instantaneous or time-varying values of the periodic contact conductance could not be computed due to inherent deficiencies in the extrapolation method. The extrapolation method can be effective, particularly for determining average or constant values, depending on the particular characteristics of the experiment. Specifically, in order for the extrapolated values to model the true surface temperature and heat flux values accurately, the spatial measurements must be *thermally* extremely close to the contact surface, since the transient effects are not accounted for by the extrapolation method. Otherwise, quite substantial errors occur from the extrapolation process. The extrapolation method is best suited to slow variations in the contact conditions.

However, for many situations, the minimum distance a temperature sensor can be located from the contact surface is limited by practical machining limitations. Also care must be taken not to disturb the surface characteristics under consideration by installing the sensor too close to the surface. For sufficiently fast variations in the contact conditions, the temperature sensor cannot be mounted thermally close to the contact surface. Therefore, an improved method of estimating the instantaneous contact conductance is needed for fast periodic variations in the contact conditions.

Two basic approaches are possible: (1) solve the coupled, two-region inverse heat conduction problem for contact conductance directly, and (2) decouple the regions, solve for the surface temperature and heat flux in each region irrespective of the other, and then construct the contact conductance from its definition. Advantages of the first approach are that continuity of heat flux across the contact interface is required and the functional form of the computed contact conductance can be directly controlled. On the other hand, the second approach promises to be significantly more computationally efficient. The first approach would result in a nonlinear, iterative estimation procedure for contact conductance. In addition, a time-consuming numerical method such as finite differences would be required to solve the direct problem several times at each iteration step. The second approach, when applied to constant thermal property regions, yields two linear estimation problems, which are quickly solved without iteration. Also, a computationally efficient analytical solution is available for evaluating the direct solution. In this work we implement the second approach as follows.

Contributed by the Heat Transfer Division for publication in the JOURNAL OF HEAT TRANSFER. Manuscript received by the Heat Transfer Division November 9, 1987. Keywords: Conduction, Transient and Unsteady Heat Transfer.

A periodic inverse heat conduction method is proposed for processing temperature data taken from one-dimensional experimental thermal contact conductance apparatus. Constant thermal properties are assumed. The method is based on applying a single-region, periodic inverse heat conduction approach proposed recently to each rod separately (Flach and Özişik, 1987). The variation of contact surface temperature with time for each region is represented with periodic *B*-splines. From the surface temperature and heat flux values computed for each region, the periodic contact conductance is determined from its definition. The proposed approach can readily handle thermally fast periodic variations. The method can accommodate an abrupt variation in the contact surface temperature, which might occur due to surfaces that contact and separate periodically, for instance. Continuous variations, due to surfaces that stay in contact but undergo a periodic contact pressure variation, for example, can also be represented by the technique. The method can be classified as "whole-domain" since all the measured temperature data (including "future" data) are used to compute simultaneously the entire periodic contact conductance. The method is statistically optimized and confidence bounds are computed for the estimated contact conductance to ascertain the statistical level of significance that can be assigned to the results. Examples involving both simulated and actual measured temperature data are presented. A parametric error study is also presented.

## Inverse Analysis

The presentation of the inverse analysis is organized in the following order: (1) formulation of the inverse problem, (2) single region analysis for surface temperature and heat flux, (3) determination of periodic contact conductance, and (4) statistical analysis.

**Formulation of the Inverse Problem.** Two periodically contacting, one-dimensional, constant property rods are considered as shown in Fig. 1. The periodic contact conductance

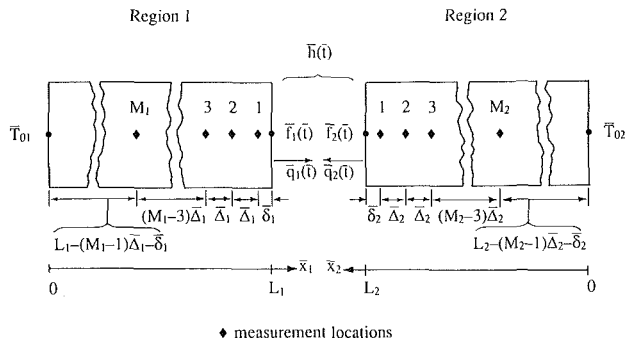


**Fig. 1 Periodic variation of the contact conductance between contacting one-dimensional regions**

$\bar{h}(\bar{t})$ between the two contacting surfaces can vary periodically with time because of contact and noncontact condition at the surfaces or continuous contact but with time variation in contact pressure, for instance. The noncontacting end of each rod is held at a fixed temperature. The inverse problem is concerned with the determination of the unknown periodic contact conductance from temporal interior temperature readings at each of the multiple measurement locations. Here we assume evenly spaced measurement locations as shown in Fig. 1, but arbitrary positions can also be used just as easily.

In each region $k$, $k = 1$ or 2, the governing heat conduction problem in the dimensional form is defined as

$$\frac{\partial^2 \bar{T}_k}{\partial \bar{x}_k^2} = \frac{1}{\alpha_k}\frac{\partial \bar{T}_k}{\partial \bar{t}} \qquad 0<\bar{x}_k<L_k, \quad 0<\bar{t}<\bar{\tau} \tag{1a}$$

$$\bar{T}_k = \bar{T}_{0,k} \qquad \bar{x}_k = 0 \tag{1b}$$

$$\bar{T}_k = \bar{f}_k(\bar{t}) \qquad \bar{x}_k = L_k \tag{1c}$$

$$\bar{T}_k(\bar{x}_k, 0) = \bar{T}_k(\bar{x}_k, \bar{\tau}) \tag{1d}$$

The heat flux at the contacting surface of any region $k$ is given by

## Nomenclature

$B_i(t)$ = *B*-spline function
$c_i$ = *B*-spline coefficient
$d_i(x, t)$ = temperature component defined by equation (10)
$\mathbf{D}$ = matrix of $d_i(x, t)$ functions defined by equation (13)
$\det(\hat{h})$ = deterministic error in $\hat{h}$
$\mathrm{err}(\hat{h})$ = total error in $\hat{h}$
$E(\bullet)$ = statistical expected value operator
$f(t)$ = contact surface temperature
$h(t)$ = periodic contact conductance (or contact heat transfer coefficient)
$k-1$ = *B*-spline order
$l$ = number of *B*-spline intervals
$L$ = region length
$M$ = number of spatial measurement locations
$n$ = number of *B*-spline terms
$N$ = number of measurement times
$P$ = number of points in the time domain
$q(t)$ = contact surface heat flux
SSE = sum of the squared residuals between the measured and estimated data
$\mathrm{sto}(\hat{h})$ = stochastic error in $\hat{h}$
$t$ = time variable
$t^{(q)}$ = measurement times
$T(x, t)$ = interior temperature
$x$ = spatial variable
$x^{(p)}$ = spatial measurement locations
$\alpha$ = thermal diffusivity
$\delta$ = depth below contact surface of first measurement position
$\Delta$ = spacing between measurement positions
$\lambda$ = thermal conductivity
$\nu_i$ = number of *B*-spline continuity requirements at $t=\xi_i$
$\xi_i$ = *B*-spline interval positions in time domain
$\sigma$ = standard deviation
$\tau$ = period

**Subscripts**

0 = condition at noncontacting end
1 = associated with region 1
2 = associated with region 2
$\hat{h}$ = associated with estimated contact conductance
opt = optimal
ref = reference quantity

**Superscripts**

$\bar{}$ = dimensional quantity
$\hat{}$ = estimated quantity
$*$ = associated with periodic *B*-splines as opposed to standard *B*-splines
$\tilde{}$ = measured quantity

$$\bar{q}_k(\bar{t}) = -\lambda_k \frac{\partial \bar{T}_k(L_k, \bar{t})}{\partial \bar{x}_k} \tag{2}$$

The contact conductance between the contacting surfaces is determined from its definition as

$$\bar{h}(t) = \frac{\frac{1}{2}[\bar{q}_1(\bar{t}) - \bar{q}_2(\bar{t})]}{\bar{f}_1(\bar{t}) - \bar{f}_2(\bar{t})} \tag{3}$$

Assuming no losses to the surroundings, the exact heat fluxes, $\bar{q}_1(\bar{t})$ and $\bar{q}_2(\bar{t})$, are equal and $\bar{q}_1(\bar{t}) = -\bar{q}_2(\bar{t}) = \bar{q}_{\text{avg}} = 1/2[\bar{q}_1(\bar{t}) - \bar{q}_2(\bar{t})]$. The average heat flux is preferably used in the numerator of equation (3) since continuity of heat flux is not required in the subsequent decoupled region approach. Computing the average value effectively compensates for any differences (if any) in the individual measured values. In the inverse heat conduction problem (IHCP) defined by equations (1)-(3), the surface temperatures $\bar{f}_k(\bar{t})$, heat fluxes $\bar{q}_k(\bar{t})$, and contact conductance, $\bar{h}(\bar{t})$, are all unknown and to be determined.

The following dimensionless quantities are defined to nondimensionalize the above problem:

$$x_k \equiv \frac{\bar{x}_k}{L_k} = \text{spatial variable} \tag{4a}$$

$$t_k \equiv \frac{\alpha_k \bar{t}}{L_k^2} = \text{time variable} \tag{4b}$$

$$T_k \equiv \frac{\bar{T}_k - \bar{T}_{0,k}}{\bar{T}_{\text{ref},k}} = \text{temperature} \tag{4c}$$

$$f_k \equiv \frac{\bar{f}_k - \bar{T}_{0,k}}{\bar{T}_{\text{ref},k}} = \text{temperature of contacting surface} \tag{4d}$$

$$q_k \equiv \frac{\bar{q}_k}{\lambda_k \bar{T}_{\text{ref},k}/L_k} = \text{heat flux at contacting surface} \tag{4e}$$

$$\tau_k \equiv \frac{\alpha_k \bar{\tau}}{L_k^2} = \text{period} \tag{4f}$$

$$\delta_k \equiv \frac{\bar{\delta}_k}{L_k} = \text{depth below the contacting surface of the first measurement location} \tag{4g}$$

$$\Delta_k \equiv \frac{\bar{\Delta}_k}{L_k} = \text{spacing between measurement points} \tag{4h}$$

$$h \equiv \frac{\bar{h}}{\lambda_1/L_1} = \text{periodic contact conductance} \tag{4i}$$

Then the nondimensional form of the inverse problem becomes

$$\frac{\partial^2 T_k}{\partial x_k^2} = \frac{\partial T_k}{\partial t_k} \qquad 0 < x_k < 1, \quad 0 < t_k < \tau_k \tag{5a}$$

$$T_k = 0 \qquad x_k = 0 \tag{5b}$$

$$T_k = f_k(t_k) \qquad x_k = 1 \tag{5c}$$

$$T_k(x_k, 0) = T_k(x_k, \tau_k) \tag{5d}$$

$$q_k(t_k) = -\frac{\partial T_k(1, t_k)}{\partial x_k} \tag{6}$$

$$h(t) = \frac{\frac{1}{2}\left[q_1 - \frac{\lambda_2}{\lambda_1}\frac{L_1}{L_2}\frac{\bar{T}_{\text{ref},2}}{\bar{T}_{\text{ref},1}} q_2\right]}{f_1 - \frac{\bar{T}_{\text{ref},2}}{\bar{T}_{\text{ref},1}} f_2 + \frac{\bar{T}_{0,1}}{\bar{T}_{\text{ref},1}} - \frac{\bar{T}_{0,2}}{\bar{T}_{\text{ref},1}}} \tag{7}$$

where $f_k(t)$, $q_k(t)$, and $h(t)$ are unknown.

**Single Region Analysis for Surface Temperature and Heat Flux.** To estimate the periodic contact conductance, the surface temperature and heat flux are computed for each region $k$ separately, and then $h(t)$ is estimated from equation (7). That is, two single-region inverse heat conduction problems (IHCP) are solved in order to determine the contact conductance across the regions. Equations (5) define the IHCP for each region $k$, $k = 1$ or 2, where the contact surface temperature, $f_k(t)$, is unknown. The identical IHCP defined by equations (5) has been considered by Flach and Özişik (1987) and their approach utilizing periodic $B$-splines together with the integral transform technique is used in the present analysis. An advantage of the Flach and Özişik (1987) method is that very general functional forms for the surface temperature can be selected, including a discontinuous surface temperature. Since the details of the method have already been documented (Flach and Özişik, 1987), only a brief presentation of the notation is given here in order to provide the starting point for the present extended analysis.

Before summarizing the periodic IHCP method, a brief word concerning the notation used in this paper is in order. First, all quantities considered so far are exact. The corresponding estimated values computed using the inverse analysis are generally inexact due to deterministic and stochastic errors; therefore they will be denoted with a $\hat{}$ over the corresponding symbol used for the exact quantity. In addition, any quantity associated with the estimated result but not having an exact counterpart will also be flagged with a $\hat{}$. Secondly, the notation used by Flach and Özişik (1987) will be preserved in this work for consistency. Finally, the subscript $k$ denoting the region is omitted for brevity unless explicitly needed.

The characteristics of the $B$-spline basis used to represent the contact surface temperature $\hat{f}(t)$ are defined by the following parameter set, where the region $k$ subscript is implicit:

$$\hat{k} - 1 \equiv B\text{-spline order} \tag{8a}$$

$$\hat{I} \equiv \text{number of } B\text{-spline intervals in each period } \tau \tag{8b}$$

$$\hat{\xi}_i \equiv \text{position of the } B\text{-spline interval interfaces in the time domain; } i = 1, \ldots, \hat{I}+1 \tag{8c}$$

$$\hat{\nu}_i \equiv \text{number of continuity conditions required at each interface position, } \hat{\xi}_i;\ i = 1, \ldots, \hat{I}+1 \tag{8d}$$

and the dimension of periodic $B$-spline basis is

$$\hat{n}^* = \sum_{i=1}^{\hat{I}} (\hat{k} - \hat{\nu}_i) \tag{8e}$$

The representation for the surface temperature is written

$$\hat{f}(t) = \sum_{j=1}^{\hat{n}^*} \hat{c}_j^* \hat{B}_j^*(t) = \hat{\mathbf{B}}^{*T} \hat{\mathbf{c}}^* \tag{9}$$

where $\hat{\mathbf{B}}^*$ and $\hat{\mathbf{c}}^*$ are the $B$-spline and coefficient vectors, respectively.

For the surface temperature as defined by this equation, the interior temperature for the medium is readily obtained in terms of the $B$-spline parameters by application of the integral transform technique. The result is expressed in matrix form as

$$\hat{T}(x, t) = \sum_{j=1}^{\hat{n}^*} \hat{c}_j^* \hat{d}_j^*(x, t) = \hat{\mathbf{d}}^{*T} \hat{\mathbf{c}}^* \tag{10}$$

where $\hat{\mathbf{d}}^*(x, t)$ is given by Flach and Özişik (1987). Then, the surface heat flux is computed from

$$\hat{q}(t) = \sum_{j=1}^{\hat{n}^*} \hat{c}_j^* \left(\frac{-\partial \hat{d}_j^*(1, t)}{\partial x}\right) = \frac{-\partial \hat{\mathbf{d}}^{*T}(1, t)}{\partial x} \hat{\mathbf{c}}^* \tag{11}$$

Suppose the measured interior temperature data is available at $M$ spatial locations and $N$ times per period specified as

$$x^{(p)} \equiv \text{measurement locations; } p = 1, \ldots, M \tag{12a}$$

$$t^{(q)} \equiv \text{measurement times; } q = 1, \ldots, N \tag{12b}$$

$\tilde{T}(x^{(p)}, t^{(q)}) \equiv \tilde{T}_i \equiv \tilde{\mathbf{T}} \equiv$ measured temperatures; where for $p = 1, \ldots, M$ and $q = 1, \ldots, N$, $i$ is defined as $i = p + (q-1)M = 1, \ldots, MN$ (12c)

The estimated interior temperatures at these measurement locations and times are computed from equation (10) as

$$\hat{T}_i = \sum_{j=1}^{\hat{n}^*} \hat{c}_j^* \hat{d}_j^*(x^{(p)}, t^{(q)}) = \sum_{j=1}^{\hat{n}^*} \hat{c}_j^* \hat{d}_{ji}^* = \hat{\mathbf{D}}^{*T} \hat{\mathbf{c}}^* \tag{13}$$

The method of least squares is applied to estimate the unknown coefficients $\hat{\mathbf{c}}^*$ from the measured data $\tilde{\mathbf{T}}$ to yield

$$\hat{\mathbf{c}}^* = (\hat{\mathbf{D}}^* \hat{\mathbf{D}}^{*T})^{-1} (\hat{\mathbf{D}}^* \tilde{\mathbf{T}}) \tag{14}$$

All available temperature data are used to estimate simultaneously the coefficients so the approach is "whole domain" in nature. For the standard assumptions of additive, zero mean, constant variance, and uncorrelated errors, an optimal result is obtained if the dimension of the spline representation, i.e., the number of terms, is chosen to be consistent with the error level in the measurements according to

$$\sqrt{\frac{\text{SSE}}{MN}} \cong \sigma \tag{15}$$

where SSE is the sum of the squared errors, $\sigma$ is the standard deviation of the temperature measurements, and $MN$ is the toal number of measurements (Beck et al., 1985).

With the coefficients $\hat{\mathbf{c}}^*$ available from equation (14), the surface temperature and heat flux are computed from equations (9) and (11). The single-region inverse procedure just described is applied to both regions $k$ individually to yield $\hat{f}_1(t), \hat{f}_2(t)$ from equation (9) and $\hat{q}_1(t), \hat{q}_2(t)$ from equation (11).

**Determination of Periodic Contact Conductance.** Now the estimated values of the surface temperature and heat flux being available for each region $k$, $k = 1$ or 2, the estimated periodic contact conductance $\hat{h}(t)$ is readily computed from its definition given previously. We obtain

$$\hat{h}(t) = \frac{\frac{1}{2}\left[\hat{q}_1 - \frac{\lambda_2}{\lambda_1}\frac{L_1}{L_2}\frac{\bar{T}_{\text{ref, 2}}}{\bar{T}_{\text{ref, 1}}}\hat{q}_2\right]}{\hat{f}_1 - \frac{\bar{T}_{\text{ref, 2}}}{\bar{T}_{\text{ref, 1}}}\hat{f}_2 + \frac{\bar{T}_{0,1}}{\bar{T}_{\text{ref, 1}}} - \frac{\bar{T}_{0,2}}{\bar{T}_{\text{ref, 1}}}} \tag{16}$$

The estimated value computed from equation (16) will not be exact, in general. Error is introduced in two distinct ways. First, the true contact conductance cannot generally be resolved exactly if only a discrete number of temperature readings are taken, even when such readings are exact. This is due to incomplete (discrete) input information and the error is deterministic in nature. In this work, the *deterministic error*, denoted $\det(\hat{h})$, is defined to be the total error when exact temperature measurements are used as input to the inverse analysis. A second source of error in $\hat{h}(t)$ is introduced when the input data are inexact due to random measurement errors. Such errors are stochastic in nature and will be denoted by $\text{sto}(\hat{h})$. The *stochastic error* augments the deterministic error to form the *total error*, $\text{err}(\hat{h})$, in $\hat{h}(t)$ when inexact measurements are used as input. A measure of the mean size of the stochastic error is the standard deviation of the estimated contact conductance. Later in the results section, a parametric study will be made to illustrate the effects of measurement location, number of measurements, etc., on the deterministic, stochastic, and total errors. However, before presenting such numerical results, we develop in the next section the standard deviation and statistical confidence bounds of the estimated contact conductance.

**Statistical Analysis.** A statistical analysis of the effects of measurement error on the computed contact conductance is crucial for determining the level of confidence that can be assigned to the results. Since the estimated surface temperature and heat flux are linear functions of the $B$-spline coefficients, the contact conductance is a rational function of the $B$-spline coefficients. Due to this nonlinearity of $\hat{h}(t)$ with respect to the coefficients, an approximate linearized statistical analysis is performed (Gallant, 1987). The variance of $\hat{h}(t)$ is given approximately as

$$\sigma_{\hat{h}}^2 = \left(\frac{\partial \hat{h}}{\partial \hat{\mathbf{c}}^{*T}}\right) E[(\hat{\mathbf{c}}^* - E(\hat{\mathbf{c}}^*))(\hat{\mathbf{c}}^* - E(\hat{\mathbf{c}}^*))^T]\left(\frac{\partial \hat{h}}{\partial \hat{\mathbf{c}}^*}\right) \tag{17}$$

where the coefficient vector $\hat{\mathbf{c}}^*$ is the composite vector of the coefficient vectors from the individual regions, $\hat{\mathbf{c}}_k^*$ with $k = 1$ or 2, given by

$$\hat{\mathbf{c}}^* = \begin{bmatrix} \hat{\mathbf{c}}_1^* \\ \hat{\mathbf{c}}_2^* \end{bmatrix} \tag{18}$$

Differentiation of equation (16) using the quotient rule gives for the derivative vector

$$\begin{aligned}\frac{\partial \hat{h}}{\partial \hat{\mathbf{c}}^*} = \Bigg\{ &\left[\hat{f}_1 - \frac{\bar{T}_{\text{ref, 2}}}{\bar{T}_{\text{ref, 1}}}\hat{f}_2 + \frac{\bar{T}_{0,1}}{\bar{T}_{\text{ref, 1}}} - \frac{\bar{T}_{0,2}}{\bar{T}_{\text{ref, 1}}}\right] \\ &\left[\frac{1}{2}\left(\frac{\partial \hat{q}_1}{\partial \hat{\mathbf{c}}^*} - \frac{\lambda_2}{\lambda_1}\frac{L_1}{L_2}\frac{\bar{T}_{\text{ref, 2}}}{\bar{T}_{\text{ref, 1}}}\frac{\partial \hat{q}_2}{\partial \hat{\mathbf{c}}^*}\right)\right] \\ &- \left[\frac{1}{2}\left(\hat{q}_1 - \frac{\lambda_2}{\lambda_1}\frac{L_1}{L_2}\frac{\bar{T}_{\text{ref, 2}}}{\bar{T}_{\text{ref, 1}}}\hat{q}_2\right)\right] \\ &\left[\frac{\partial \hat{f}_1}{\partial \hat{\mathbf{c}}^*} - \frac{\bar{T}_{\text{ref, 2}}}{\bar{T}_{\text{ref, 1}}}\frac{\partial \hat{f}_2}{\partial \hat{\mathbf{c}}^*}\right]\Bigg\} \\ &\div \left\{\hat{f}_1 - \frac{\bar{T}_{\text{ref, 2}}}{\bar{T}_{\text{ref, 1}}}\hat{f}_2 + \frac{\bar{T}_{0,1}}{\bar{T}_{\text{ref,1}}} - \frac{\bar{T}_{0,2}}{\bar{T}_{\text{ref, 1}}}\right\}^2\end{aligned} \tag{19}$$

where

$$\frac{\partial \hat{f}_1}{\partial \hat{\mathbf{c}}^*} = \begin{bmatrix} \hat{\mathbf{B}}_1^* \\ 0 \end{bmatrix} \tag{20a}$$

$$\frac{\partial \hat{f}_2}{\partial \hat{\mathbf{c}}^*} = \begin{bmatrix} 0 \\ \hat{\mathbf{B}}_2^* \end{bmatrix} \tag{20b}$$

$$\frac{\partial \hat{q}_1}{\partial \hat{\mathbf{c}}^*} = \begin{bmatrix} -\frac{\partial \hat{\mathbf{d}}_1^*}{\partial x} \\ 0 \end{bmatrix} \tag{21a}$$

$$\frac{\partial \hat{q}_2}{\partial \hat{\mathbf{c}}^*} = \begin{bmatrix} 0 \\ -\frac{\partial \hat{\mathbf{d}}_2^*}{\partial x} \end{bmatrix} \tag{21b}$$

from equations (9) and (11). Note that the coefficients $\hat{\mathbf{c}}^*$ associated with the inverse solution appear in the derivative vector. Therefore, the variance cannot be computed until after the inverse solution is computed. The variance-covariance matrix of the composite coefficient vector is determined as

$$E[(\hat{\mathbf{c}}^* - E(\hat{\mathbf{c}}^*))(\hat{\mathbf{c}}^* - E(\hat{\mathbf{c}}^*))^T] = \begin{bmatrix} \sigma_1^2(\hat{\mathbf{D}}_1^{*T}\hat{\mathbf{D}}_1^*)^{-1} & 0 \\ 0 & \sigma_2^2(\hat{\mathbf{D}}_2^{*T}\hat{\mathbf{D}}_2^*)^{-1} \end{bmatrix} \quad (22)$$

Assuming the distribution of $\hat{h}(t)$ is approximately normal and neglecting deterministic error, 99 percent confidence bounds for the estimated contact conductance $\hat{h}(t)$ are

$$\text{Prob}\{\hat{h} - 2.576\sigma_{\hat{h}} < h < \hat{h} + 2.576\sigma_{\hat{h}}\} \cong 99 \text{ percent} \quad (23)$$

Equation (23) provides an approximate measure of the statistical confidence that can be assigned to the estimated result $\hat{h}(t)$.

## Results

Results are given in three phases. For the first two parts, attention is confined to identical regions, with readings taken in one region only, and specifications given in nondimensional terms. The motivation is to reduce the large number of parameters affecting the estimation of contact conductance in the general situation to a manageable level. First, a particular nondimensional reference case, utilizing simulated measured temperature data, is given. Second, a parametric study is made of the overall effects of measurement location, number of measurements, and period on the deterministic, stochastic, and total errors for the case of identical regions in general. In the third portion, dimensional results based on *actual* measured temperature data, taken from both of the contacting regions, are presented to illustrate the practicalness of the present method.

**Reference Case.** Identical regions and temperature readings taken from one region only are chosen for the reference case. The symmetry of the identical regions case allows measurements to be taken in one region only, since the temperature in the other region can be inferred from that of the former. Also the specifications are given in nondimensional terms. With these selections the number of parameters involved is greatly reduced.

Suppose the exact nondimensional contact conductance between two identical regions is chosen as a square wave form of period $\tau = 0.25$ as illustrated in Figs. 2. Such a variation corresponds to the situation in which the rods make contact for $\Delta t = 0.125$ with constant $h$ and then separate for $\Delta t = 0.125$ under insulated conditions. The nondimensional difference in temperature of the noncontacting ends is taken as $(\bar{T}_{0,1} - \bar{T}_{0,2})/\bar{T}_{\text{ref},1} = 2$. The temperature sensor depth parameters shown in Fig. 1 are chosen as $\delta = 0.05$ and $\Delta = 0.10$ for this example. Suppose measurements are taken at four spatial locations (i.e., $M = 4$) and each set of four spatial readings is taken $N = 18$ evenly spaced times per period, that is, nine readings being taken in each subperiod of size $\Delta t = 0.125$. The periods of contact and noncontact are known, but no further information about the functional form of $h(t)$ is considered known. The parameter values selected for this reference case were chosen to be consistent with those reported by Moses and Johnson (1986, 1987).

The $B$-spline representation for the contact surface temperature is chosen with the following characteristics:

$$\hat{k} = 4 \text{ (cubic } B\text{-splines)} \quad (24a)$$

$$\hat{l} = \text{variable} \quad (24b)$$

$$\hat{\xi}_i = \text{evenly spaced } B\text{-spline intervals} \quad (24c)$$

$$\hat{\nu}_i = 3 \text{ (full continuity requirements) except at } t = 0 \text{ and } t = 0.125 \text{ where } \hat{\nu} = 1 \quad (24d)$$

The motivation for selecting these values is as follows. Cubic $B$-splines (i.e., $\hat{k} = 4$) are chosen for their excellent approximating qualities such as smoothness. Evenly spaced splines are chosen since no prior information motivating a clustering of the spline intervals is given. Continuity of contact surface temperature only (i.e., $\hat{\nu} = 1$), and not its time derivatives, at the contact and separation times, $t = 0$ and $t = 0.125$, is chosen since an abrupt change in the surface temperature is expected. Otherwise, the full continuity requirements (i.e., $\hat{\nu} = 3$) are chosen since a smooth variation of contact surface temperature is expected while the surfaces are in contact or separated. In addition we will choose an even integer for $\hat{l}$ so that spline interval breakpoints occur at $t = 0$ and $t = 0.125$ for the evenly spaced intervals.

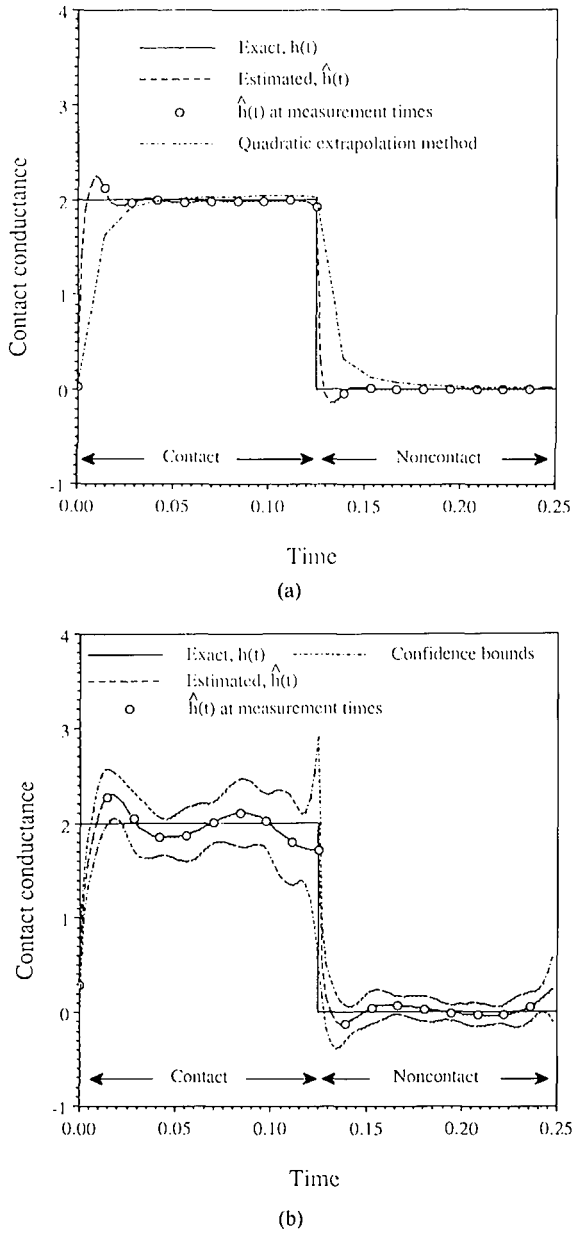


**Fig. 2 Estimated contact conductance using (*a*) exact and (*b*) inexact temperature measurements**

Both exact and inexact measurements are considered. Inexact temperature measurements are simulated by adding normally distributed measurement error with $\sigma = 0.0065$ and zero mean to the exact temperature distribution computed independently using a finite difference approach. These errors are ±5 percent of the largest temperature variation in the identical rods at the 99 percent confidence level. The number of spline intervals $\hat{l}$, or equivalently the number of terms in the $B$-spline representation given by equation (8*e*), is chosen to

**Table 1 Selection of optimal $\hat{n}^*$**

| $\hat{n}^*$ | $\sigma$ | $\sqrt{(\text{SSE}/MN)}$ |
|---|---|---|
| 18 | 0.00650 | 0.00628 |
| 16 | 0.00650 | 0.00635 |
| 14 | 0.00650 | 0.00639 |
| 12 | 0.00650 | 0.00658 |
| 10 | 0.00650 | 0.00675 |
| 8 | 0.00650 | 0.00725 |
| 6 | 0.00650 | 0.01092 |

satisfy best the criterion defined by equation (15). Results based on exact and inexact measurement data are presented in Figs. 2(*a*) and 2(*b*), respectively.

In Fig. 2(*a*), the spline parameter for exact measurements is $\hat{l}=14$. No smoothing is required by criterion (15) when $\sigma=0$, hence we set $\hat{n}^* = N = 18$ for these exact measurement results. The error present in Fig. 2(*a*) for exact input data is purely deterministic. The largest error occurs immediately after the contact and noncontact times since the abrupt change in surface temperature is more difficult to resolve than the slower variation later in the subperiods of size $\Delta t = 0.125$. For comparison, results based on the quadratic extrapolation method are also shown in Fig. 2(*a*). Note the damping and lagging of the estimated contact conductance after the contact and separation times. The faster the period and the greater the distance from the contact surface of the first temperature sensor, the greater the deterministic error becomes for the extrapolation method. Conversely, we show in the next section that the deterministic error for the present inverse analysis is relatively unaffected by $\tau$ and $\delta$.

Figure 2(*b*) shows results based on simulated inexact measurements by taking the optimal spline parameter $\hat{l}_{\text{opt}} = 8$ corresponding to $\hat{n}^*_{\text{opt}} = 12$. Table 1 illustrates the results of the optimization process. Observe that the number of spline terms most closely satisfying equation (15) is $\hat{n}^*_{\text{opt}} = 12$. Smoothing has been added since $\hat{n}^*_{\text{opt}} < N$ for this case. The difference between the results based on inexact measurements (Fig. 2*b*) and exact input data (Fig. 2*a*) is the stochastic error component. The approximate 99 percent confidence bounds, computed from equation (23), largely agree with the exact result $h(t)$, in that the true contact conductance is indeed almost completely within the confidence limits.

**Parametric Study and Error Analysis.** The previous example basically concerns only one selection of the parameters $M$, $N$, $\hat{n}^*$, $\delta$, $\Delta$, and $\tau$, and the functional form of $h(t)$; specifically, $M=4$, $N=18$, $\hat{n}^*=12$ or 18, $\delta=0.05$, $\Delta=0.10$, $\tau=0.25$, and a square wave form were chosen. In order to illustrate the general variation of the deterministic, stochastic, and total errors, a parametric study was prepared. Given the large number of parameter combinations and possible forms for $h(t)$, even for identical, nondimensional regions, only a few of the most important effects can be considered presently. Accordingly, the example shown in Fig. 2 is taken as the basis and the present parametric study is confined to illustrating the overall effect of the number of $B$-spline terms $\hat{n}^*$, depth below the contact surface of the first measurement position $\delta$, and the period $\tau$, on the time-averaged deterministic and stochastic errors. The other parameters and the form of $h(t)$, i.e., square wave form, remain the same as in the initial examples. Exact measurements are used throughout the study so that the deterministic error can be computed by comparison with the exact result. The size of the stochastic error is measured by the normalized standard deviation computed using the exact measurement results to estimate the derivative vector $\partial\hat{h}/\partial\hat{\mathbf{c}}^*$. The deterministic error and stochastic errors are considered first and then the total error.

Recall that the deterministic error is the total error when exact measurements are input to the inverse analysis. The deterministic error is generally not zero, although, if the exactly correct functional form is chosen for representing the surface

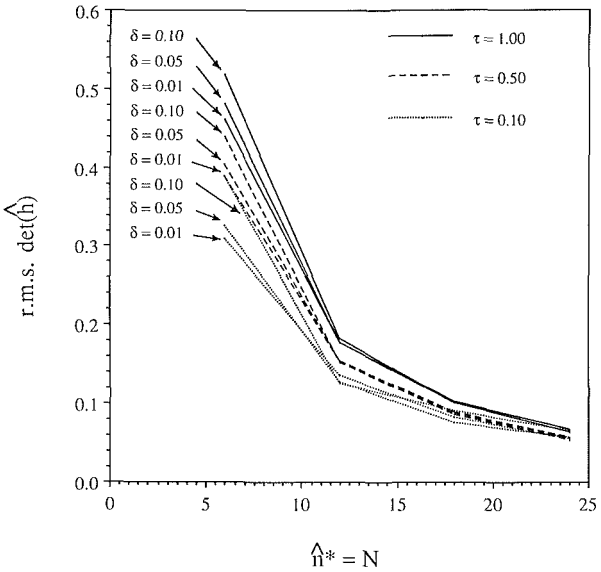


**Fig. 3 Variation in the rms deterministic error with respect to $\hat{n}^*$, $\delta$, and $\tau$**

temperature, the deterministic error is identically zero. Figure 3 shows the rms deterministic error computed according to the discrete formula

$$\text{rms det}(\hat{h}) = \sqrt{\frac{1}{P}\sum_{i=1}^{P}(\hat{h}_i - h_i)^2} \tag{25}$$

where $P$ is the number of points in the time domain. In the present computations 110 points are taken for each case. Note the overall deterministic error is strongly dependent on the number of terms in the representation $\hat{n}^*$, or equivalently the number of measurement times $N$. That is, the more input information provided ($N$) and the more terms used in the model ($\hat{n}^*$), the better the exact variation can be resolved. Clearly, the deterministic error can be made as small as desired through the addition of more data and terms in the $B$-spline series. In contrast, the addition of temperature measurements in the time domain does not improve the accuracy of the extrapolation method since the approach considers only the spatial variation of temperature at a particular time and not the time variation. Also in contrast with the extrapolation method, the depth of the first sensor and period appear weakly to affect the deterministic error for the present inverse method. Note in Fig. 3 that the maximum and minimum rms deterministic errors at a particular value of $\hat{n}^* = N$ deviate small amount with respect to changes in $\delta$ and $\tau$. The reason is that as long as the input temperature data are *exact*, no information about the contact surface is lost through the present inverse analysis by moving away from the surface or decreasing the period. In fact, the deterministic error actually decreased with decreasing period $\tau$ for this particular parametric study.

When inexact measurements due to random errors are used, the total error has a stochastic component too. The standard deviation is a measure of the mean stochastic error. The normalized standard deviation $\sigma_{\hat{h}}(t)/\sigma$ represents the level of magnification of the measurement errors and might be called the sensitivity to measurement error. The time-averaged sensitivity will be taken as the overall measure of the mean normalized stochastic error. That is, overall sensitivity or time-averaged mean normalized error is computed from

$$\frac{\text{avg. sto}_{\text{mean}}(\hat{h})}{\sigma} = \text{avg.}\ \frac{\sigma_{\hat{h}}}{\sigma} = \frac{1}{P}\sum_{i=1}^{P}\left(\frac{\sigma_{\hat{h}}}{\sigma}\right)_i \tag{26}$$

where again $P=110$ points in the time domain are used in each case. All the parameters $\hat{n}^*$, $\delta$, and $\tau$ strongly affect the sen-

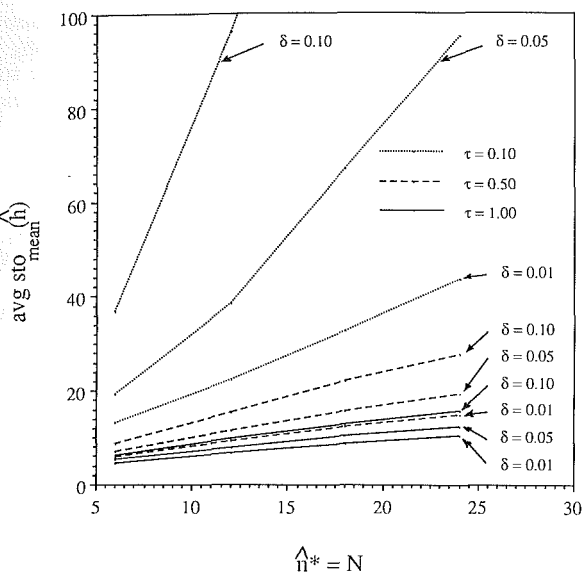


**Fig. 4 Variation in the time-averaged mean normalized stochastic error with respect to $\hat{n}^*$, $\delta$, and $\tau$**

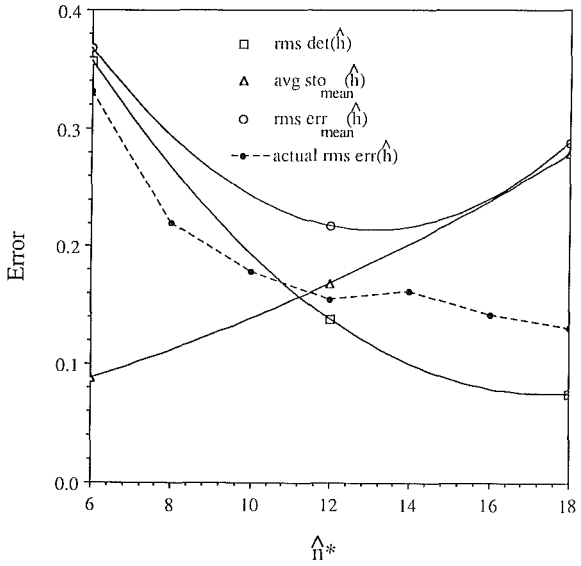


**Fig. 5 Variation in rms mean total error with respect to $\hat{n}^*$**

sitivity to random measurement error. Figure 4 illustrates these effects explicitly for the same region of parameters considered for the deterministic error study above. As one would expect, the sensitivity to measurement error increases with distance of the first sensor from the surface, number of terms in the *B*-spline basis, and decreasing period (i.e., faster transient variations in surface conditions). Increasing the *B*-spline dimension $\hat{n}^*$ allows the *B*-spline representation to vary more readily with changes in the input data including the addition of measurement error. Increasing $\delta$ and decreasing $\tau$ at a fixed absolute level of error $\sigma$ in the temperature measurements increases the *relative* error since the magnitude of the temperature variation away from the contacting surfaces is decreasing.

The previous parametric study involving the deterministic and stochastic components of the total error is quite revealing but of most interest is the total error itself. Recall that the total error, err($t$), is the sum of the deterministic and stochastic errors by the definition of stochastic error

$$\mathrm{err}(\hat{h}(t)) = \mathrm{det}(\hat{h}(t)) + \mathrm{sto}(\hat{h}(t)) \tag{27}$$

Since the stochastic error is a random quantity so is the total error. Let the rms mean total error be given by

$$\mathrm{rms\ err}_{\mathrm{mean}}(\hat{h}) \equiv \sqrt{\frac{1}{P} E\left[\sum_{i=1}^{P} (\mathrm{err}_i)^2\right]}$$

$$= \sqrt{(\mathrm{rms\ det}(\hat{h}))^2 + (\mathrm{rms\ sto}_{\mathrm{mean}}(\hat{h}))^2} \tag{28}$$

Figure 5 illustrates the approximate rms deterministic, time-averaged mean stochastic error, and rms mean total error for the parameters of the reference case illustrated in Fig. 2(*b*), namely, $\tau = 0.25$, $\delta = 0.05$, and $\sigma = 0.00650$. Figure 5 was constructed by quadratically interpolating the data given in Figs. 3 and 4, which are for $\tau = 0.10$, 0.50, and 1.00 and approximating rms mean stochastic error with the time-averaged mean stochastic error in equation (28). The deterministic error decreases and the stochastic error increases with increasing number of spline terms as previously observed. Note that the rms mean total error is a minimum for 12–14 spline terms. That is, Fig. 5 demonstrates the existence of an optimal number of parameters for minimizing the total error and shows the optimal number to be 12 to 14 on average. Recall that criterion (15) picked the optimal number of terms as 12 according to the results given in Table 1 for the reference case discussed previously. Therefore, equation (15) has indeed chosen an optimal number of spline terms. Also shown in Fig. 5 is the actual rms total error for the reference case shown in Fig. 2(*b*). For small $\hat{n}^*$, we expect the actual rms error to follow closely the rms mean error since the stochastic or random component of the total error is small. For large $\hat{n}^*$, the stochastic component of the total error dominates and large deviation between the actual rms total error and the rms mean total error is possible due to the large variance in the total error. In fact, the actual rms error is consistently below the rms mean error for small $\hat{n}^*$ in Fig. 5. The primary reason is that the rms mean total error was computed with $\hat{n}^* = N$ whereas the data were overspecified for the actual case. Overspecified data reduce both the deterministic and stochastic errors at a fixed $\hat{n}^*$. For large $\hat{n}^*$ the actual total error is significantly different from the mean total error, which is not surprising due to the dominant stochastic (random) component. Note that while the optimal number of spline parameters for minimizing the total was chosen as 12 by criterion (15) and 12–14 by observation of the rms mean total error, the total error is actually minimized at $\hat{n}^* = 18$. Certainly neither criterion (15) nor generalized error plots such as Fig. 5 guarantee that the selected optimal number of parameters will necessarily minimize the total error for any particular case. Rather, on average, the optimal estimates are effective.

**Example Utilizing Actual Measured Data.** Finally, we consider an example using actual rather than simulated measured data taken from a contact conductance experiment conducted by Moses (1988). The appendix lists the characteristics of the experiment and specimens and the temperature measurements. The experiment involved identical brass specimens subjected to a moderate temperature difference at the noncontacting ends. The noncontacting-end temperatures are constant. Therefore, the assumptions of the present analysis apply. The regions are in contact for 15 s and separated for 15 s. The nondimensional period in each region is $\tau = 0.10$. The nondimensional distance from the contact surfaces of the first sensor for each region is 0.005, which, compared to the period, is thermally extremely close. Three-dimensional effects at this close distance are possible but will

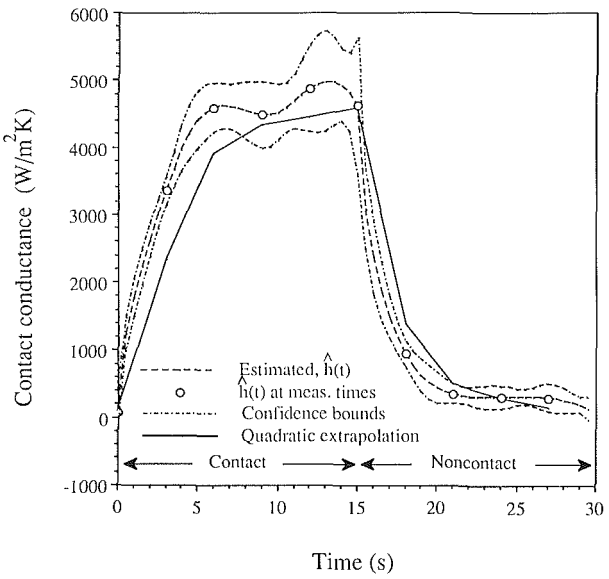


**Fig. 6 Contact conductance example based on actual measured temperature data**

be neglected since we are not in a position to investigate this point further.

We expect the contact conductance to be nominally constant over the first 15 s of a period and nearly zero over the last 15 s. Figure 6 shows the estimated contact conductance determined by using the present inverse method and the quadratic extrapolation method, both based on the experimental data supplied by Moses. Since the first sensors are extremely close to the contact surface in each region, the estimation is comparatively easy. Nevertheless, the extrapolation results still appear to show damping and lagging similar to the results in Fig. 2(*a*). The estimated contact conductance computed using the present inverse analysis is somewhat improved relative to the anticipated true contact conductance. Unfortunately, insufficient temperature data in the time domain (only 10 points) are available to resolve the contact conductance any better using the present method.

## Summary and Conclusions

An inverse heat conduction method for estimating the periodic contact conductance between one-dimensional, constant property contacting regions has been presented. All available temperature data are used to estimate simultaneously the entire contact conductance over a period including "future data." The decoupling approach used promises to be computationally efficient; however, competing inverse approaches have not been published to allow a comparison. The method is statistically optimized and confidence bounds are given for the estimated contact conductance. The method effectively recovers the exact contact conductance when simulated exact measurements are input to the analysis. The present approach is shown to be superior to the extrapolation method. A parametric study of overall deterministic, stochastic, and total error has been presented. The practicalness of the method is shown by an example utilizing data taken from an actual contact conductance experiment.

Extensions of the method would allow the treatment of additional physical problems. For instance, the method can be easily extended to handle variable end temperatures by straightforward addition of an extra term to the analytical solution. Variable thermal property specimens could also be treated using the basic approach given here by replacing the analytical direct solution with, say, a finite difference solution. Then applications involving large temperature variations could be modeled.

## Acknowledgments

The authors wish to express their appreciation to Dr. W. M. Moses for providing experimental data and to the reviewers for suggesting several improvements to the paper. Also, this material is based upon work supported under a National Science Foundation Graduate Fellowship.

## References

Beck, J. V., Blackwell, B., and St. Clair, C. R., Jr., 1985, *Inverse Heat Conduction*, Wiley, New York, pp. 140–141.

Flach, G. P., and Özişik, M. N., 1987, "Periodic *B*-Spline Basis for Quasi-Steady Periodic Inverse Heat Conduction," *Int. J. Heat Mass Transfer*, Vol. 30, pp. 869–880.

Gallant, A. R., 1987, *Nonlinear Statistical Models*, Wiley, New York, p. 47.

Howard, J. R., 1976, "An Experimental Study of Heat Transfer Through Periodically Contacting Surfaces," *Int. J. Heat Mass Transfer*, Vol. 19, pp. 367–372.

Howard, J. R., and Sutton, A. E., 1970, "An Analogue Study of Heat Transfer Through Periodically Contacting Surfaces," *Int. J. Heat Mass Transfer*, Vol. 13, pp. 173–183.

Howard, J. R., and Sutton, A. E., 1973, "The Effect of Thermal Contact Resistance on Heat Transfer Between Periodically Contacting Surfaces," ASME JOURNAL OF HEAT TRANSFER, Vol. 95, pp. 411–412.

Madhusudana, C. V., and Fletcher, L. S., 1981, "Thermal Contact Conductance: A Review of Recent Literature," College of Engineering, Texas A&M University, College Station, TX.

McKinzie, D. J., Jr., 1970, "Experimental Confirmation of Cyclic Thermal Joint Conductance," AIAA Paper No. 70-853.

Minges, M. L., 1966, "Thermal Contact Resistance, Volume 1 – A Review of the Literature," Technical Report AFML-TR-65-375, Wright-Patterson Air Force Base, Dayton, OH.

Moore, C. J., Jr., 1967, "Heat Transfer Across Surfaces in Contact," Ph.D. Dissertation, Southern Methodist University, Dallas, TX.

Moore, C. J., Jr., Atkins, H., and Blum, H. A., 1968, "Subject Classification Bibliography for Thermal Contact Resistance Studies," ASME Paper No. 68-WA/HT-18.

Moses, W. M., 1988, *private communication*.

Moses, W. M., Jr., 1985, "An Experimental Investigation of the Heat Transfer Across Periodically Contacting Surfaces," Ph.D. Dissertation, North Carolina State University, Raleigh, NC.

Moses, W. M., and Johnson, R. R., 1986, "An Experimental Study of the Transient Behavior of the Thermal Contact Conductance and the Temperature Distribution in Periodically Contacting Surfaces," AIAA Paper No. 86-1244.

Moses, W. M., and Johnson, R. R., 1987, "Experimental Results for the Quasi-Steady Heat Transfer Through Periodically Contacting Surfaces," AIAA Paper No. 87-1608.

Vick, B., and Özişik, M. N., 1981, "Quasi-Steady-State Temperature Distribution in Periodically Contacting Finite Regions," ASME JOURNAL OF HEAT TRANSFER, Vol. 103, pp. 739–744.

## APPENDIX

The following experimental data were provided by Dr. W. M. Moses and used to prepare the results given in Fig. 6.

*Contact conductance specimen characteristics:*

| Region 1 | Region 2 |
|---|---|
| Material: brass | Material: brass |
| $\alpha_1 = 3.4 \times 10^{-5} m^2/s$ | $\alpha_2 = 3.4 \times 10^{-5} m^2/s$ |
| $\lambda_1 = 106.1$ W/mK | $\lambda_2 = 106.1$ W/mK |
| $L_1 = 0.10109$ m | $L_2 = 0.10109$ m |
| $\bar{T}_{0,1} = 52.9°C$ | $\bar{T}_{0,2} = 18.7°C$ |
| $\sigma_1 = 0.1°C$ | $\sigma_2 = 0.1°C$ |
| $M = 4$ meas. positions @ | $M = 4$ meas. positions @ |
| $\bar{x}_1^{(1)} = 0.10058$ m | $\bar{x}_2^{(1)} = 0.10058$ m |
| $\bar{x}_1^{(2)} = 0.08839$ m | $\bar{x}_2^{(2)} = 0.08839$ m |
| $\bar{x}_1^{(3)} = 0.07569$ m | $\bar{x}_2^{(3)} = 0.07569$ m |
| $\bar{x}_1^{(4)} = 0.06299$ m | $\bar{x}_2^{(4)} = 0.06299$ m |
| Period, $\bar{\tau} = 30$ s | (15 s contact, 15 s separation) |
| $N = 10$ measurement times | |

*Temperature measurements:*

| | Region 1 temperature @ | | | | Region 2 temperature @ | | | |
|---|---|---|---|---|---|---|---|---|
| $\bar{t}$ (s) | $\bar{x}_1^{(1)}$ (°C) | $\bar{x}_1^{(2)}$ (°C) | $\bar{x}_1^{(3)}$ (°C) | $\bar{x}_1^{(4)}$ (°C) | $\bar{x}_2^{(1)}$ (°C) | $\bar{x}_2^{(2)}$ (°C) | $\bar{x}_2^{(3)}$ (°C) | $\bar{x}_2^{(4)}$ (°C) |
| 0. | 41.2 | 41.6 | 42.6 | 44.1 | 29.5 | 29.1 | 28.2 | 26.9 |
| 3. | 39.8 | 41.8 | 42.8 | 44.2 | 31.6 | 29.0 | 28.0 | 26.7 |
| 6. | 38.7 | 41.1 | 42.8 | 44.3 | 32.5 | 29.7 | 28.1 | 26.6 |
| 9. | 38.3 | 40.7 | 42.6 | 44.3 | 32.8 | 30.2 | 28.3 | 26.7 |
| 12 | 38.1 | 40.4 | 42.4 | 44.2 | 33.0 | 30.5 | 28.5 | 26.7 |
| 15. | 37.9 | 40.2 | 42.2 | 44.1 | 33.1 | 30.6 | 28.7 | 26.8 |
| 18. | 38.9 | 40.1 | 42.1 | 44.0 | 31.7 | 30.6 | 28.8 | 26.9 |
| 21. | 39.8 | 40.5 | 42.1 | 44.0 | 30.9 | 30.2 | 28.8 | 27.0 |
| 24. | 40.4 | 41.0 | 42.3 | 44.0 | 30.3 | 29.8 | 28.6 | 27.0 |
| 27. | 40.9 | 41.3 | 42.4 | 44.0 | 29.9 | 29.4 | 28.4 | 26.9 |

# The Influence of Availability Costs on Optimal Heat Exchanger Design

**L. C. Witte**
Professor of Mechanical Engineering,
University of Houston,
Houston, TX 77004
Fellow ASME

*Optimizing heat exchangers based on second-law rather than first-law considerations ensures that the most efficient use of available energy is being made. In this paper, second-law efficiency is used to develop a new technique for optimizing the design of heat exchangers. The method relates the operating costs of the exchanger to the destruction of availability caused by the exchanger operation. The destruction of availability is directly related to the second-law efficiency of the exchanger. This allows one to find the NTU at which the benefits of reduced availability losses are offset by the costs of added area; this is the optimal point. It can be difficult to determine the proper cost of irreversibility to be used in the optimization process. This issue can be handled by including the irreversibility cost in a dimensionless parameter that represents the ratio of annual ownership costs to annual operating costs that include irreversibility costs. In this way, each heat exchanger designer can estimate the costs of irreversibilities for his particular system, and then use the generalized method that is developed herein for determining the optimal heat exchanger size. The method is applicable to any heat exchanger for which the $\epsilon$-NTU-R relationships are known.*

## Introduction

When designing heat exchangers, it is imperative that due consideration be given to entropy generation because of the irreversibility of the heat transfer process that occurs in the exchanger. This concept, along with the second law of thermodynamics, allows optimal design of exchangers based on the most efficient use of available energy. The impact of entropy generation on optimum design of heat exchangers has been recognized for some time, see e.g., McClintock (1951), Tribus and Evans (1962, 1963), Bejan (1977), and more recently, Witte (1985, 1987).

The most common method of second-law optimization is to perform what has become known as a "thermoeconomic" analysis, a term introduced by Tribus and co-workers that denotes the combined use of second-law efficiency and economics of ownership and operation of an exchanger. Such a process uses the equation for the production of entropy along with the functions that connect various terms in the entropy-production equation to their appropriate costs. This yields an operating cost function. Then the fixed (capital) costs are added to operating costs to form a total annualized cost function for the exchanger. Minimizing the total annualized costs in terms of various parameters yields various points of "optimal" behavior. Fehring and Gaggioli (1977), Tapia and Moran (1986), and Zubair et al. (1987) all give examples of such a process.

Witte and Shamsundar (1983) developed a version of second-law efficiency specifically for heat exchangers that is amenable to a very simple and straightforward method of second-law optimization. Some of the complexities of the method described in the previous paragraph are bypassed by using the second-law efficiency.

## Selecting an Appropriate Second-Law Efficiency

There are several versions of second-law efficiency for heat exchangers that might suffice for use in a thermoeconomic optimization scheme. For example, Moran (1982) has two versions

$$\eta_1 = \frac{\Delta \dot{B}_{\text{cold fluid}}}{\Delta \dot{B}_{\text{hot fluid}}} \tag{1}$$

and

$$\eta_2 = \frac{\dot{B}_{\text{out}}}{\dot{B}_{\text{in}}} \tag{2}$$

while Witte and Shamsundar (1983) introduced the following definition:

$$\eta = 1 - \frac{\dot{I}}{\dot{Q}} \tag{3}$$

where $\dot{Q}$ is the required heat rate for the exchanger, called the "heat duty." Other symbols are defined in the Nomenclature section.

Witte and Shamsundar (1983) pointed out that in many heat exchangers, the coolant is close to ambient temperature, causing $\eta_1$ to be unrealistically close to zero; thus it is rejected for use in an optimization scheme.

Moran's second definition, equation (2), can be written in a manner similar to equation (3) as

$$\eta_2 = 1 - \frac{\dot{I}}{\dot{B}_{\text{in}}} \tag{4}$$

which shows its similarity to equation (3).

It was demonstrated by Witte and Shamsundar (1983) that equation (3) has properties that make it more realistic and more attractive for use in an optimization scheme than equation (4). Primarily this relates to unrealistic behavior of $\eta_2$ in terms of the effectiveness of an exchanger. Figures 1 and 2 demonstrate the inconsistencies between the two definitions. In Fig. 1, equation (3) shows monotonically increasing values of $\eta$ versus $\epsilon$, while Fig. 2 shows that the $\eta_2$ versus $\epsilon$ curves for different capacity ratios exhibit minima. Equation (4) also displays very unrealistic values of unity as $\epsilon$ (or NTU)$\rightarrow 0$ for all values of the capacity ratio. This is caused by the fact that $B_{\text{in}}$ always has a finite value for a heat exchanger while $I$ is reduced toward zero as area is decreased toward zero. It is clear that equation (4) is an inappropriate second-law efficiency for our purposes.

The use of $\eta$, equation (3), has been criticized because its $\eta$-NTU behavior does not correspond to the $\epsilon$-NTU curve, which predicts that $\epsilon = 0$ for NTU $= 0$. Indeed, a proper

Contributed by the Heat Transfer Division for publication in the JOURNAL OF HEAT TRANSFER. Manuscript received by the Heat Transfer Division September 30, 1987. Keywords: Heat Exchangers, Heat Recovery, Thermodynamics and Second Law.

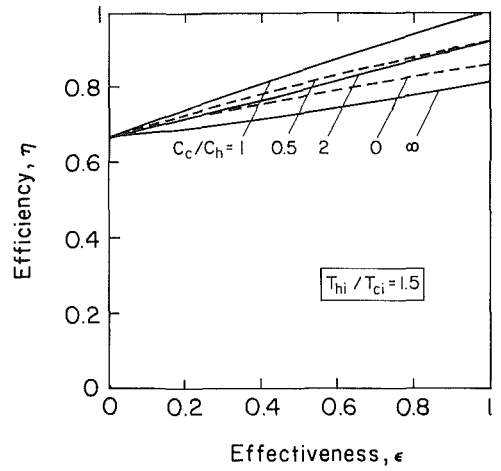


Fig. 1 $\eta$-$\epsilon$ curves for a heat exchanger with an inlet temperature ratio of 1.5

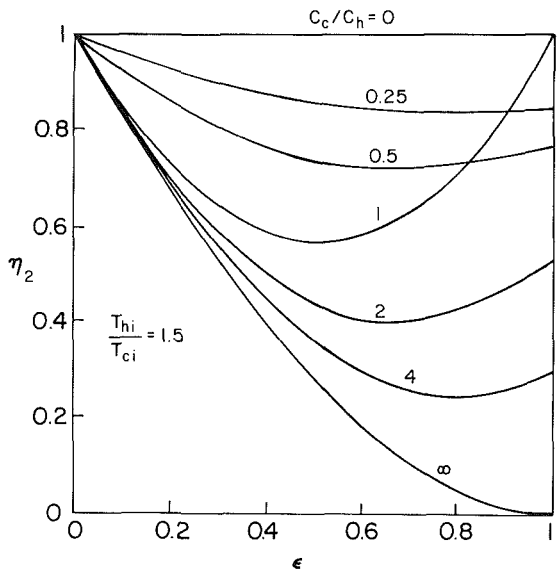


Fig. 2 $\eta_2$-$\epsilon$ curves for a heat exchanger with an inlet temperature ratio of 1.5

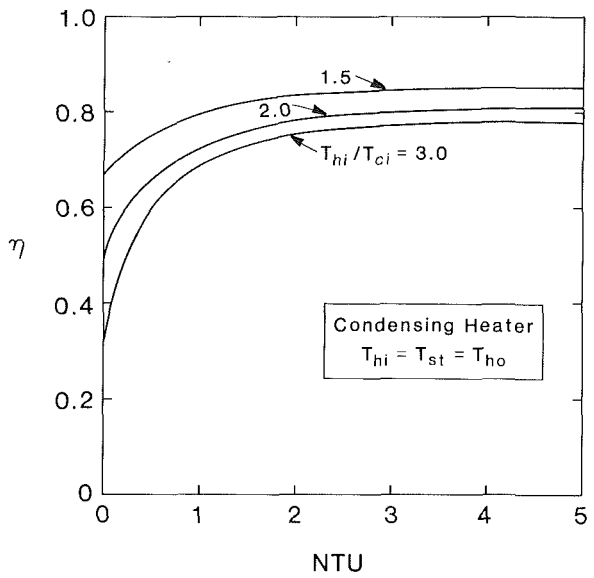


Fig. 3 Second-law efficiency versus NTU for a condensing heater

$\eta$-NTU curve, such as shown in Fig. 3 for a condensing heater, does not behave in this fashion, nor should it. It can be easily shown that as NTU$\rightarrow$0 (or $\epsilon\rightarrow$0), $\eta\rightarrow T_{ci}/T_{hi}$. Thus our theory predicts that as NTU $\rightarrow$0, say by letting $A\rightarrow$0, there is a limiting $\eta$ because for any incremental nonzero area, there will be heat transfer controlled by $T_{ci}$ and $T_{hi}$. Therefore $\eta$ cannot approach zero (or unity for that matter) as NTU$\rightarrow$0.

The total irreversibility rate in an exchanger is made up of two parts, one due to heat transfer and the other due to pressure drop. Thus, equation (3) becomes

$$\eta = 1 - \frac{1}{\dot{Q}} \{\dot{I}_Q + \dot{I}_{\Delta p}\} \tag{5}$$

For many practical cases of interest, the irreversibility rate due to pressure drop is negligible in comparison to that due to heat transfer. Thus for convenience, $\eta$ shall be used to stand for the second-law efficiency neglecting the destruction of availability by pressure drop.

By adopting this simplification $\eta$ can easily be represented in terms of the inlet and outlet temperatures of the exchanger;

## Nomenclature

$A$ = heat exchanger area, m$^2$
$B$ = availability function = $H - T_o\Delta S$, J
$C_{\min}$ = thermal capacitance of heat transfer stream, J/sK
$C_a$ = annual cost of owning heat transfer surface, \$
$c_b$ = heat transfer surface area cost, \$/m$^2$
$C_b$ = annual exchanger operating cost, \$
$c_b$ = unit cost of irreversibility, \$/J
$c_q$ = unit cost of fuel energy, \$/J
$c_p$ = specific heat, J/kg-K
$E_1$ = optimum point, see equation (9)
$E_2$ = optimum point, see equation (10)
$H$ = enthalpy, J
$h$ = enthalpy/unit mass, J/kg
$\dot{I}$ = irreversibility rate, W
$m$ = mass flow rate, kg/s
NTU = number of transfer units = $UA/C_{\min}$
$P$ = perimeter
$p$ = pressure, MPa
$\dot{Q}$ = heat duty, W
$r$ = capital recovery rate, yr$^{-1}$
$t$ = operating time, s/yr
$T$ = temperature, K
$\Delta T_i$ = inlet temperature difference, K
$U$ = overall heat transfer coefficient, W/m$^2$ - K
$T_o$ = ambient temperature, K
$\Gamma$ = pumping power
$\epsilon$ = effectiveness
$\Delta p$ = pressure drop, Pa
$\Delta T$ = temperature difference, K
$\Delta S$ = entropy difference, J/K
$\eta$ = second law efficiency
$\eta_B$ = boiler efficiency

### Subscripts

$c$ = cold
$e$ = exit
$i$, in = inlet
$h$ = hot
opt = optimum
min = minimum
$o$, out = outlet
sat = saturated
1, 2 = various versions of second-law efficiency

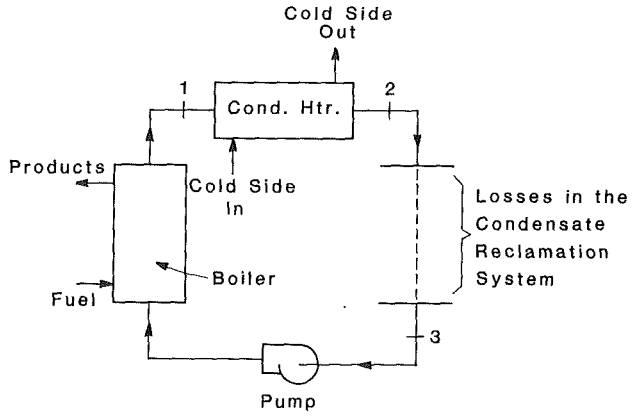


**Fig. 4 Equivalent system for estimating the costs of availability destruction in a condensing heater**

thus it is characteristically "thermodynamic" in that it only reflects the effect of the temperatures in the heat exchanger. Indeed, as shown by Witte and Shamsundar, $\eta$ becomes

$$\eta = 1 + (T_o/\bar{T}_h) - (T_o/\bar{T}_c) \tag{6}$$

where the average stream temperature $\bar{T}$ is defined as

$$\bar{T} = \frac{T_e - T_i}{\ln(T_e/T_i)} \tag{7}$$

However, $\eta$ can be readily related to $\epsilon$, so that the influence of the exchanger operating parameters can be assessed through the dependence of $\epsilon$ on NTU. This is the idea that was followed to produce Fig. 3, which shows the $\eta = \text{NTU}$ curves for a condensing heater in terms of the ratio of inlet temperatures. (We take $T_{ci} = T_o$ for this calculation; this is a matter of convenience only. Allowing these two temperatures to differ adds little complexity to the calculation. It does, of course, add an additional parameter to the problem.)

Equation (3) does not fit the conventional mode of a second-law efficiency because its reference $\dot{Q}$ does not involve the input availabilities of the working fluids. Thus, in the strictest sense it does not tell exactly how much of the input availability was destroyed. However, using the exchanger duty $\dot{Q}$ as a reference makes it a superior tool for optimizing heat exchangers. It has been suggested that $\eta$ be called an "entropy performance factor" rather than a second-law efficiency. It is immaterial what it is called, because it properly reflects the destruction of availability in the exchanger.

## Evaluating the Costs of Irreversibilities

The most difficult aspect of any thermoeconomic analysis is assigning an appropriate cost to the losses due to availability destruction. London and Shah (1983) called this ". . . tying the $-sign to entropy. . .". It is interesting to note that they dealt with this issue by ratioing all the possible irreversibilities in an exchanger to the heat duty of the exchanger. This choice of the rationalizing factor parallels Witte and Shamsundar's choice of $\dot{Q}$ in their definition of $\eta$.

London and Shah pointed out that the assessment of costs due to irreversibilities should be performed taking full account of the complete thermodynamic system in which the exchanger exists. Thus the source of the energy required for the heat duty as well as the sink into which energy must be dissipated from the exhaust streams should be fully accounted for. They classified the possible irreversibilities in an exchanger into the following: heat duty; heat leaks; pressure drops; and mixing of the "purchased" stream with the atmosphere. (The "purchased" stream is the one that must be produced to meet the heat duty of the "required" stream.)

They gave the example of a power plant condenser; in this case, the purchased stream is the cooling water extracted from the surroundings and circulated through the exchanger. The "mixing" irreversibility accounts for the fact that there is a loss of availability between the point where the cooling water is dumped to the atmosphere and where it is extracted from the atmosphere for use in the condenser. Thus even though such mixing availability losses are *external* to the heat exchanger, they should be charged to the exchanger in the same way as $Q$ or $\Delta p$ losses, if appropriate. They found for a 1965 state-of-the-art power plant condenser that the mixing irreversibility accounted for about 35 percent of the losses, the heat duty accounted for about 50 percent, while the remaining losses ($\Delta p$ and heat leaks) accounted for only 15 percent of the losses.

The exact fashion in which costs are assigned is understandably system-dependent. It is not possible to generalize this procedure. For example, Tapia and Moran (1986) recently undertook optimization studies of various types of single-phase exchangers; they evaluated a "unit fuel cost factor" for the energy required to bring the purchased stream to its operating state. Then the actual cost charged to the exchanger is the unit fuel cost multiplied by the irreversibility rate attributed to the exchanger. They pointed out that while this procedure might not be rigorously correct, it allows for the costs of irreversibilities to be accounted for at the design stage without much loss of generality. More appropriate cost functions can be assigned if the exact nature of the thermodynamic system in which the exchanger operates is known, using the ideas proposed by London and Shah.

To illustrate how to evaluate irreversibility costs for a particular system, let us pick a condensing heater system that uses condensing steam as the hot, purchased stream. For different heat duties, or for cases where perhaps fouling has altered the heat transfer characteristics of the system, different steam pressures are required to meet the heat duty. The steam is provided by a boiler that burns fuel priced at $c_q = \$2.84/(10^9\ \text{J})$, and whose efficiency is 80 percent. It is further assumed that the condensate from the heater is fed into a condensate system that eventually feeds a collection main at $p_3 = 0.1014$ MPa (14.7 psia), as shown in Fig. 4.

Even though it might be possible partially to reclaim the energy contained in the heater condensate (from 2 to 3 on Fig. 4), the full amount of energy required to raise the condensate from its condition at the collection main to the boiler outlet, $h_1 - h_3$, will be used to evaluate the factor we shall call $c_b$. This factor is the unit cost of irreversibility (or availability destruction) that is charged to the heat exchanger.

From an energy balance on the system of Fig. 4, $c_b$ is evaluated as

$$c_b = \frac{c_q}{\eta_B} \frac{(h_1 - h_3)}{(h_1 - h_2)} \tag{8}$$

where $c_q$ is the cost of fuel energy and $\eta_B$ is the boiler efficiency. As the required boiler pressure is increased, the latent heat goes down so that the flow rate must increase to meet the heat duty. So even though the cost of energy consumed by the heater remains almost constant, the overall cost increases because of the tariff imposed by the pumping and other losses in the condensate system.

The mixing irreversibility is partially accounted for by the 20 percent inefficiency in the boiler: that is, this recognizes that the available energy in the fuel is not fully released to the steam. Table 1 shows how $c_b$ varies with the steam pressure for this case.

An individual heat exchanger system must be evaluated for its specific irreversibility costs. A single-phase heat exchanger might have a significantly different $c_b$ value than a condensing heater.

Table 1 Unit energy costs for condensing heater supplied by a 80 percent efficient boiler with fuel energy priced at \$2.84/$10^9$ J; see Fig. 4 for Nomenclature

| $p_1$ (MPa) | Tsat (C) | $h_1$ (kJ/kg) | $h_1$-$h_2$ (kJ/kg) | $h_1$-$h_3$ (kJ/kg) | $c_b$ (\$/$10^9$ J) |
|---|---|---|---|---|---|
| 0.1014 | 100 | 2676.1 | 2257.1 | 2257.1 | 3.55 |
| 0.1483 | 110 | 2691.5 | 2230.2 | 2272.5 | 3.62 |
| 0.4154 | 145 | 2740.3 | 2129.6 | 2321.3 | 3.86 |
| 0.7005 | 165 | 2963.5 | 2055.2 | 2344.5 | 4.03 |
| 1.3978 | 195 | 2790.0 | 1960.0 | 2371.0 | 4.29 |
| 2.795 | 230 | 2804.0 | 1813.8 | 2385.0 | 4.67 |
| 5.499 | 270 | 2789.7 | 1505.2 | 2370.7 | 5.24 |

However, in all cases it is advantageous to select one stream as the purchased stream and attach the variable irreversibility costs to it.

## Optimizing an Exchanger

The development that follows takes advantage of equation (3), which is well-suited for an optimization procedure, in a rather simple and straightforward way. Edwards et al. (1979) described a conventional first-law optimization scheme for an exchanger by finding the point on the $\epsilon$-NTU curve where

$$\frac{d\epsilon}{d\text{NTU}} = \frac{r\, c_a}{c_q t U \Delta T_i} = E_1 \tag{9}$$

The slope $E_1$ represents the minimum cost-benefit ratio, and can be used to find the optimal NTU of the exchanger.

By using $\eta$-NTU relationships it can be shown that an exchanger is thermoeconomically optimized at the point on the $\eta$-NTU curve where

$$\frac{d\eta}{d\text{NTU}} = \frac{r\, c_a C_{\min}}{c_b \dot{Q} t U} = E_2 \tag{10}$$

Equations (9) and (10) are similar, but equation (10) involves $c_b$, which reflects the unit cost of energy for the purchased stream related to its availability level. Thus the operational cost of the exchanger is based on the availability destruction of the purchased stream rather than simply on the cost of the fuel required to generate it.

Equation (10) is derived as follows: The benefit of adding area (NTU) is related to $\eta$, and this is compared to the cost of the additional area. Annual operating cost $C_b$ is assumed to be proportional to the availability change in the working fluids: i.e.,

$$C_b \propto \Delta \dot{B} = \Delta \dot{B}_{\text{hot}} + \Delta \dot{B}_{\text{cold}} \tag{11}$$

The irreversibility rate in equation (3) is

$$\dot{I} = \dot{B}_{\text{in}} - \dot{B}_{\text{out}} = \Delta \dot{B} = \Delta(\dot{B}_{\text{cold}} + \dot{B}_{\text{hot}}) \tag{12}$$

Thus, from equation (3), one obtains

$$\dot{Q}\eta = \dot{Q} - (\Delta \dot{B}_{\text{hot}} + \Delta \dot{B}_{\text{cold}}) \tag{13}$$

and, choosing the hot side as the purchased stream

$$d(\dot{Q}\eta) = -d(\Delta \dot{B}_{\text{hot}}) \tag{14}$$

because the heat duty $\dot{Q}$ and the $\Delta \dot{B}_{\text{cold}}$ are fixed quantities according to our definition of $\eta$. Choosing the cold side as the purchased stream does not alter the derivation in any way.

Hence, combining equations (11) and (14) gives

$$-dC_b \propto \dot{Q} d\eta \tag{15}$$

An equation can be written by using the unit cost of available energy $c_b$ along with the annual time of operation of the exchanger as follows:

$$-dC_b = c_b t \dot{Q} d\eta \tag{16}$$

where $-dC_b$ is the incremental reduction in operating costs brought about by a corresponding incremental increase in the efficiency. The unit cost factor $c_b$ must represent all of the cost functions that depend upon operating time, such as heat transfer and pumping power, like

$$c_b = a(\dot{Q}) + b(\Gamma) \tag{17}$$

where $\Gamma$ is the pumping power. Assuming that $\Gamma$ and $\dot{Q}$ are related for a particular heat exchanger configuration, equation (17) can be written as

$$c_b = a(\dot{Q}) + \tilde{b}(\dot{Q}) = \tilde{a}(\dot{Q}) \tag{18}$$

where $\tilde{b}$ is a function that connects pumping power to heat duty. Thus $c_b$ can be written simply in terms of the heat duty of the exchanger.

After Edwards and Matavosian (1982), the added annual cost of increasing the size of an exchanger is taken as

$$dC_a = r c_a P dL \tag{19}$$

where $c_a$ is the unit cost of ownership, including capital and labor costs, taxes, insurance, and other costs that can be attributed to the length $L$, and $r$ is the capital recovery factor. The perimeter length $P$ is usually fixed by selection of tubes so that $PdL$ represents the change in area.

The optimum point on the $\eta$-NTU curve is where the incremental benefit, equation (16), is offset by the cost of adding area, equation (19). By equating the two equations and recognizing that

$$d\eta = \frac{d\eta}{d\text{NTU}} \frac{d\text{NTU}}{dL} dL \tag{20}$$

and that $\text{NTU} = (UPL)/C_{\min}$, one is led to equation (10) as indicated previously.

The slope $E_2$ clearly represents the relative influence of fixed to operating costs. When $E_2$ is low, operating costs dominate fixed costs and a larger exchanger can be justified. If, on the other hand, fixed costs are dominant, the optimal case is a much smaller exchanger.

## The Condensing Heater

For the purposes of illustrating this technique, a condensing heater has been chosen because its $\epsilon$-NTU behavior is unaffected by its capacity ratio $R$, as is the resulting $\eta$-NTU plot (see Fig. 3). Another advantageous factor is that its $\epsilon$-NTU relationship, $\epsilon = 1 - \exp(-\text{NTU})$, is very simple. The discussion that follows applies equally well to other types of exchanger; however, the dependence upon $R$ and geometry must be included.

By differentiating the $\eta$-NTU equation for a given exchanger and setting it equal to $E_2$ as indicated in equation (10), one can find the NTU required for system optimization. Even for a condensing heater, $\eta$ is a fairly complicated function of NTU as shown by equation (21) below

$$\eta = 1 + \frac{T_{ci}}{T_{hi}} - \frac{\ln[(1 - e^{-\text{NTU}})(\{T_{hi}/T_{ci}\} - 1) + 1]}{[(1 - e^{-\text{NTU}})(\{T_{hi}/T_{ci}\} - 1)]} \tag{21}$$

Taking the derivative of equation (21) yields

$$\eta' = \frac{-e^{-\text{NTU}}}{[1 - e^{-\text{NTU}}]^2 [(T_{hi}/T_{ci}) - 1]} \left[ \frac{[1 - e^{-\text{NTU}}][\{T_{hi}/T_{ci}\} - 1]}{[(1 - e^{-\text{NTU}})(\{T_{hi}/T_{ci}\} - 1) + 1]} - \ln[(1 - e^{-\text{NTU}})(\{T_{hi}/T_{ci}\} - 1) + 1] \right] \tag{22}$$

which can be solved implicitly for the appropriate NTU when $\eta'$ is set equal to $E_2$.

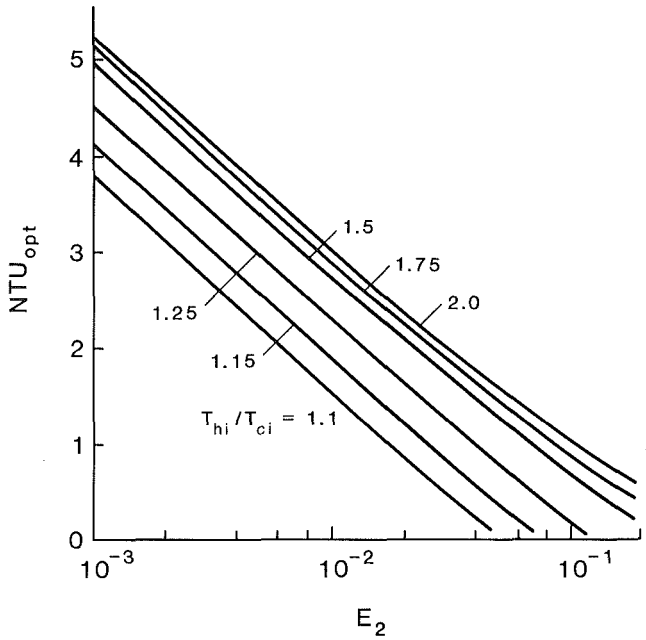


Fig. 5 The $NTU_{opt}$-$E_2$ relationship for a condensing heater for various inlet temperature ratios

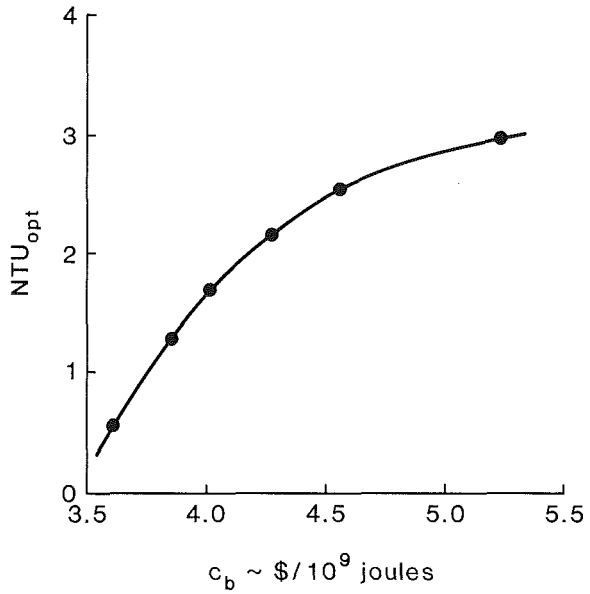


Fig. 6 Optimal NTU as a function of irreversibility cost for the condensing heater of Example 1

Figure 5 contains all the information needed in a general sense to optimize a condensing heat exchanger. Selection of varying $c_b$ values changes the value of $E_2$, which clearly affects the optimal NTU that will result. Thus the effects of the surroundings and the manner of operation of a particular heat exchanger on its irreversibility costs are inherently contained in the curves of Fig. 5. The parameter $T_{hi}/T_{ci}$ ranges from 1.1 to 2.0 in Fig. 5, which covers the operational ranges of most practical heat exchangers.

To illustrate the process of determining the influence of availability costs $c_b$ on the optimal NTU of an exchanger, let us select a simple example case.

**Example 1:** A chemical flowing at 18,182 kg/h with a specific heat of 1.675 kJ/kg-°C is heated by condensing steam. The chemical enters the heater at 21.1°C which is also $T_o$. The heater operates 5000 h/yr with an overall coefficient of 284 W/m²-°C. The $rc_a$ product is taken as \$50/m²-yr. We want to demonstrate the effect of variable irreversibility costs $c_b$ on the optimal NTU. At the same time we will calculate the outlet temperature of the chemical stream to determine the overall heat duty at each optimal point.

Table 2 Optimal values for condensing heater of Example 1

| $p_1$ (MPa) | $c_b$ \$/10⁹J | $NTU_{opt}$ | Q kW | $T_{hi}$ °C | $A_{opt}$ m² |
|---|---|---|---|---|---|
| 0.1014 | 3.55 | -- | -- | -- | -- |
| 0.1433 | 3.62 | 0.47 | 250 | 50.7 | 14.0 |
| 0.4145 | 3.86 | 1.28 | 543 | 85.3 | 38.1 |
| 0.7005 | 4.03 | 1.69 | 855 | 122.1 | 50.3 |
| 1.398 | 4.29 | 2.16 | 1302 | 174.9 | 64.3 |
| 2.795 | 4.67 | 2.53 | 1627 | 214.3 | 75.4 |
| 5.499 | 5.24 | 2.85 | 1995 | 253.0 | 87.9 |

In this case various values of $c_b$ result when the steam pressure is allowed to vary, as demonstrated in the previous section. Table 1 contains all of the pertinent data that we need for this example.

To solve this example, we recognize that for a condensing heater

$$(1-\exp(-\mathrm{NTU}))E_2 = rc_a/c_b t U \Delta T_i \tag{23}$$

The right-hand side of equation (23) is a number fixed by the available data, but the left-hand side is implicit in NTU since $E_2 = \eta'$. $\eta'$ is a function of NTU and the inlet temperature ratio, $T_{hi}/T_{ci}$, so that the $c_b$ value has to be tied to the inlet purchased stream pressure as shown in Table 2, which summarizes the results of Example 1. A trial and error solution using the information contained in Fig. 5 readily yields the $NTU_{opt}$.

Figure 6 shows how optimum NTU behaves in this range of $c_b$. As expected, as $c_b$ increases, the NTU increases, indicating that a larger exchanger is justified. On the other hand, decreasing irreversibility costs in relation to fixed costs justifies a smaller exchanger. It should also be noted that if $c_b$ is too low, a thermoeconomic optimum point might not exist. This is caused by the fact that $\eta'$ approaches a lower limit fixed by the $T_{hi}/T_{ci}$ ratio and if the $E_2$ value is lower than this limit the optimization procedure is not applicable. This generally occurs very near NTU = 0 so it is not of great practical importance. For this example, the initial entry in Table 1, $p_1 = 0.1014$ MPa does not demonstrate an optimal point.

By varying the $rc_a$ product the influence of variable capital costs on the optimal NTU can also be found. In this case, the solution of equation (23) is even simpler because the $T_{hi}/T_{ci}$ ratio is not affected. A simple example demonstrates this effect.

**Example 2.** For the exchanger of Example 1, find the respective sizes of an optimized exchanger for a steam pressure of 0.1440 MPa for two different capital cost factors, $rc_a$ = \$50/m²-yr and \$25/m²-yr.

From our previous calculations, we find that for $rc_a = 50$, $NTU_{opt}$ is 0.47. Then $A_{opt} = NTU_{opt}\, C_{min}/U$, which yields 14.0 m². Using the same procedure as in Example 1, we find that

$$rc_a/c_b t U \Delta T_i = 0.0152$$

For this condition one finds that $NTU_{opt}$ is 1.80, and $A_{opt} = 53.6$ m².

Example 2 shows that halving the capital costs for this exchanger results in the justification of an exchanger almost four times as large. Clearly, decreasing the capital costs has the

same general effect as increasing the operating (irreversibility) costs.

## Optimizing for Different Heat Duties

The method outlined in Examples 1 and 2 is not based on knowing the heat duty a priori. In fact if the heat duty is known for a fixed steam pressure, this fixes all the parameters for a condensing heater. Thus there is no opportunity for optimizing the exchanger.

If a specific heat duty must be matched, then a slightly different procedure is required. Figure 5 can be used directly since it applies to all condensing heaters. The value of $E_2$, see equation (10), is dependent upon pressure because $c_b$ depends upon pressure, as illustrated in Table 1. Thus a pressure that is consistent with the operating parameters of the steam supply system can be picked, the $c_b$ can be calculated using the technique illustrated by Table 1, and the optimal NTU can be determined by the intersection of the temperature ratio curve (determined by the pressure) and the value of $E_2$. Following this, the ability of the exchanger to actually transfer the required heat must be checked using $\epsilon$–NTU relationships. An iteration on pressure until a match on heat duty occurs will complete the optimization procedure. Figure 5 clearly shows that the pressure should be kept as low as feasible so that $NTU_{opt}$ is as low as possible.

## Summary

A method of evaluating the irreversibility costs that occur during heat exchange has been presented in this paper, accompanied by an example of such an evaluation for a system that uses a boiler to provide steam for a condensing heater. The results of this evaluation are then used to demonstrate how the optimization of a heat exchanger is affected by varying values of availability costs and capital costs. The method of optimizing for a required heat duty is also discussed.

Although the techniques demonstrated herein were applied only to a condensing heater, the theory is applicable to any heat exchanger for which the $\epsilon$–NTU–$R$ relationship is known.

## Acknowledgments

The author thanks the University of Houston Energy Laboratory for support of studies of second-law optimization of thermal systems.

## References

Bejan, A., 1977, "The Concept of Irreversibility in Heat Exchanger Design: Counterflow Heat Exchangers for Gas-to-Gas Applications," ASME JOURNAL HEAT TRANSFER, Vol. 99, pp. 374–380.

Edwards, D. K., Denny, V. E., and Mills, A. F., 1979, *Transfer Processes*, 2nd ed., Hemisphere/McGraw-Hill, New York, pp. 292–296.

Edwards, D. K., and Matavosian, R., 1982, "Thermoeconomically Optimum Counterflow Heat Exchanger Effectiveness," ASME JOURNAL HEAT TRANSFER, Vol. 104, pp. 191–193.

Fehring, T., and Gaggioli, R., 1977, "Economics of Feedwater Heater Replacement," ASME *Journal of Engineering for Power*, Vol. 99, p. 482.

London, A. L., and Shah, R. K., 1983, "Costs of Irreversibilities in Heat Exchanger Design," *Heat Transfer Engineering*, Vol. 4, No. 2, pp. 59–73.

Moran, M. J., 1982, *Availability Analysis: A Guide to Efficient Energy Use*, Prentice-Hall, Englewood Cliffs, NJ, p. 100.

McClintock, F. A., 1951, "The Design of Heat Exchangers for Minimum Irreversibility," ASME Paper No. 51-A-108.

Tapia, C. F., and Moran, M. J., 1986, "Computer-Aided Design and Optimization of Heat Exchangers," presented at ASME Winter Annual Meeting, Anaheim, CA, Dec.

Tribus, M., and Evans, R. B., 1962, "A Contribution to the Theory of Thermoeconomics," UCLA Engineering Dept. Report No. 62-36.

Tribus, M., and Evans, R. B., 1963, "The Thermoeconomics of Seawater Conversion," UCLA Engineering Dept. Report No. 62-53.

Witte, L. C., 1985, "Second Law Optimization of Heat Exchangers," *Proc. of Seventh Industrial Energy Technology Conference*, May 12–15, Vol. II, pp. 620–624.

Witte, L. C., 1987, "Second Law Optimization of Heat Exchangers," ASME Paper No. 87-HT-65.

Witte, L. C., and Shamsundar, N., 1983, "A Thermodynamic Efficiency Concept for Heat Exchange Devices," ASME *Journal of Engineering for Power*, Vol. 105, pp. 199–203.

Zubair, S. M., Kadaba, P. V., and Evans, R. B., 1987, "Second-Law-Based Thermoeconomic Optimization of Two-Phase Exchangers," ASME JOURNAL HEAT TRANSFER, Vol. 109, pp. 287–294.

# Transient Response of Rotary Regenerators

**F. E. Romie**
Palos Verdes Estates, CA 90274

*Exit gas temperature responses of the counterflow rotary regenerator are found for a unit step increase of the inlet temperature of either gas. An analytic solution applicable during the first part of the transient shows that the responses cannot be smooth. The overall response is found by dividing the regenerator disk into pie-shaped segments and approximating the area-mean gas temperature leaving a segment as the temperature of the gas leaving a small regenerator located at the center of the segment. The method is shown to give good accuracy and is in agreement with predictions of the analytic solution.*

## Introduction

The counterflow rotary regenerator finds increasingly frequent use in air conditioning systems and as the regenerative heat exchanger for gas turbine engines. It has a long history as the air preheater in steam power plants. Prediction methods for steady-state operation are well established. However the transient response to variation of gas inlet temperature has received relatively little attention. The transient response, particularly for gas turbine applications, is required for control purposes. This paper presents the transient response of the rotary regenerator to a unit step increase of the inlet temperature of either gas. The governing equations are linear and homogeneous with constant coefficients. Thus the response of the regenerator to arbitrary variations of inlet temperatures can be found using standard methods of linear analysis once the responses to unit step excitations are available.

London and co-workers in several papers (summarized in London et al., 1964) give the response of the rotary regenerator to step changes in inlet gas temperatures. In contrast to this paper, their results are restricted to equal capacitance rates for the two gases and to high rotation rates ($C_r^*$ large). The results of this paper are in agreement with their work when these restrictions are observed.

The rotary regenerator analyzed satisfies the following idealizations: (1) The thermal conductances, $(hA)_a$ and $(hA)_b$, for transfer of heat between the gases and the matrix and the gas capacitance rates, $(wc)_a$ and $(wc)_b$, are constant and uniform as is the thermal capacitance $(WC)_t$ of the disk matrix. (2) The rate of rotation is constant. (3) No heat is conducted in the matrix in the direction of fluid flow but the matrix offers no resistance (locally) to heat flow in the direction normal to fluid flow. (4) The ratios of the thermal capacitances of the fluids contained at any instant in the matrix to the thermal capacitance of the containing matrix are negligibly small and are treated as zero. This latter idealization means, in effect, that the fluids must be gases and that transit times for particles of gas to flow through the matrix will be negligibly small compared to the periods $t_a$ and $t_b$.

At the beginning of the transient the disk is considered to be uniformly at temperature zero, which is also the constant inlet temperature of the unstepped gas during the transient. The governing equations are, as noted, linear and homogeneous with constant coefficients. Thus the responses to the unit step excitation are additive to the operating temperatures of the regenerator. The regenerator may be operating at steady state or may be responding to other disturbances of the inlet temperatures or may be in the process of responding to changes in rotation rate or gas capacitance rates and hence thermal conductances. However any changes in rotation rate or gas capacitance rates must occur prior to the unit step excitation because constant coefficients are specified.

Two sets of four parameters are in common use (Shah, 1981) to characterize a regenerator. Either set is sufficient. The first set, $\Lambda_a$, $\Lambda_b$, $\Pi_a$, $\Pi_b$, is most suited to writing the governing equations. The second set, Ntu, $C^*$, $C_r^*$, $(hA)^*$, is commonly used to characterize the rotary regenerator. In this paper the parameter $C_r^*$ will be replaced by its reciprocal $C_{rr}^*$. This replacement is made primarily because of the close relationship between $C_{rr}^*$ and the dimensionless time variable $\theta$. A second reason is that a parameter that falls between 0 and 1 in the range of interest seems aesthetically preferable to one that falls between 1 and infinity. Either set of four parameters can, of course, be translated into the other, as shown in Table 1. For the transient response of the rotary regenerator the angle $\alpha$ formed by the seals (see Fig. 1) is, as will be seen, a fifth parameter that must be specified.

The thermal effectiveness of the rotary regenerator is the same as that of a single stationary regenerator with the same values of the four parameters. A method for rapid calculation of regenerator operation is available (Romie and Baclic, 1988). The referenced paper presents the following equations, which will be used in the analysis of the rotary regenerator.

**Table 1 Parameter equivalents; A = stationary regenerator; B = rotary regenerator**

| | | A | B |
|---|---|---|---|
| Ntu | $\dfrac{\Lambda_a}{1+(hA)^*}$ | same | same |
| $C^*$ | $\dfrac{\Pi_a\Lambda_b}{\Pi_b\Lambda_a}$ | $\dfrac{(wct)_a}{(wct)_b}$ | $\dfrac{(wc)_a}{(wc)_b}$ |
| $C_{rr}^*$ | $\dfrac{\Pi_a}{\Lambda_a}$ | $\dfrac{(wct)_a}{WC}$ | $\dfrac{(wc)_a t_t}{(WC)_t}$ |
| $(hA)^*$ | $\dfrac{\Pi_a}{\Pi_b}$ | $\dfrac{(hAt)_a}{(hAt)_b}$ | $\dfrac{(hA)_a}{(hA)_b}$ |

For stationary regenerators:

$$(WC)_a = (WC)_b = WC$$

For rotary regenerators:

$$\frac{t_a}{(WC)_a} = \frac{t_b}{(WC)_b} = \frac{t_t}{(WC)_t}$$

Contributed by the Heat Transfer Division for publication in the JOURNAL OF HEAT TRANSFER. Manuscript received by the Heat Transfer Division July 8, 1987. Keywords: Heat Exchangers, Transient and Unsteady Heat Transfer.

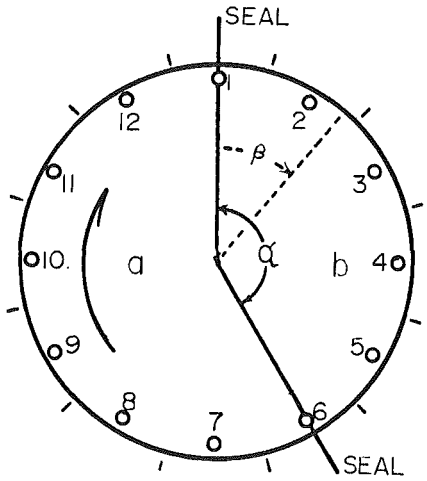


**Fig. 1 Schematic of disk showing small regenerators, stationary seals, and position marks**

The functions $F_n$ and $G_n$ (Romie, 1987) used in the equations are briefly described in the appendix.

In a stationary regenerator let gas $a$ enter ($y=0$) at zero temperature. If at time $t=0$ the temperature distribution of the matrix is expressed as an $N$th degree polynomial of $\Lambda_a y$

$$T_a(0,y)=\sum_{n=0}^{N} A_n \frac{(\Lambda_a y)^n}{n!} \tag{1}$$

then the matrix temperature distribution at later times will be

$$T_a\left(\frac{t}{t_a},y\right)=\sum_{n=0}^{N} A_n F_n\left(\Pi_a \frac{t}{t_a},\Lambda_a y\right) \tag{2}$$

and the exit ($y=1$) temperature of gas $a$ will be

$$\tau_a\left(\frac{t}{t_a},1\right)=\sum_{n=0}^{N} A_n G_n\left(\Pi_a \frac{t}{t_a},\Lambda_a\right) \tag{3}$$

Let the inlet ($y=1$) temperature of gas $b$ be unity and the initial ($t=0$) temperature distribution of the matrix be expressed as an $N$th degree polynomial of $\Lambda_b\,(1-y)$

$$T_b(0,y)=1-\sum_{n=0}^{N} B_n \frac{((1-y)\Lambda_b)^n}{n!} \tag{4}$$

The matrix temperature distribution at later times will be

$$T_b\left(\frac{t}{t_b},y\right)=1-\sum_{n=0}^{N} B_n F_n\left(\Pi_b \frac{t}{t_b},(1-y)\Lambda_b\right) \tag{5}$$

and the exit ($y=0$) temperature of gas $b$ will be

$$\tau_b\left(\frac{t}{t_b},0\right)=1-\sum_{n=0}^{N} B_n G_n\left(\Pi_b \frac{t}{t_b},\Lambda_b\right) \tag{6}$$

## Analytic Solution

During the first part of the rotary regenerator transient, when $t < t_a$, an analytic solution can be derived for the exit temperature response $\tau_b$ of gas $b$ to a unit step change of its inlet temperature. During the time interval $t<t_a$ the temperature of the disk is uniformly zero as it passes the seal and enters region $b$ (see Fig. 1). Thus, from equation (4), $B_0 = 1$ and $B_n = 0$ for $n \neq 0$. At time $t$ the disk will have rotated through an angle $\beta$. The area-mean exit temperature of gas $b$ leaving through the area defined by this angle is

$$\frac{1}{t}\int_0^t \left[1-G_0\left(\Pi_b \frac{t_1}{t_b},\Lambda_b\right)\right]dt_1$$

$$=1-\frac{t_b}{t\Pi_b}\left[\Lambda_b-F_1\left(\Pi_b \frac{t}{t_b},\Lambda_b\right)\right] \tag{7}$$

(See appendix for integral.) In the area defined by the angle $\alpha-\beta$ the exiting gas temperature is uniform, $1-G_0\,(\Pi_b\, t/t_b, \Lambda_b)$. Weighting these two temperatures in accordance with the relative gas capacitance rates ($t/t_b$ and $1-t/t_b$) passing through these two areas and summing the weighted temperatures gives the mixed-mean exit temperature at time $t$

## Nomenclature

$A_n$ = coefficient, equation (1)
$B_n$ = coefficient, equation (4)
$C^*$ = see Table 1
$C_r^*$ = $1/C_{rr}^*$
$C_{rr}^*$ = see Table 1
$F_n(\,)$ = function, see Appendix
$G_n(\,)$ = function, see Appendix
$hA$ = thermal conductance, W/K
$(hA)^*$ = see Table 1
$k$ = index
$N$ = polynomial degree, equations (1) and (4)
$N_a$ = number of disk segments in region $a$
$N_b$ = number of disk segments in region $b$
$N_t$ = total number of disk segments
Ntu = $[(hA)_a/(wc)_a]\,/\,(1+(hA)^*)$
$t$ = time from initiation of unit step, s
$t'$ = time from passing a seal (for SR, $t'$ = t until first seal is passed), s
$t_a$ = time for point on disk to rotate through region $a$, Fig. 1, s
$t_b$ = time for point on disk to rotate through region $b$, Fig. 1, s
$t_t$ = time for one complete revolution, s
$T$ = disk temperature, K
$(wc)$ = capacitance rate of gas, W/K
$(WC)_{a,b}$ = thermal capacitance of disk in regions $a$ and $b$, Fig. 1, J/K
$(WC)_t$ = thermal capacitance of entire disk, J/K
$y$ = fractional distance through disk, measured from gas $a$ entrance plane
$\alpha$ = seal angle subtending area through which gas $b$ flows, deg
$\beta$ = an angle, Fig. 1, deg
$\Delta\theta$ = $C_{rr}^*/N_t$
$\epsilon$ = thermal effectiveness of regenerator
$\theta$ = $(wc)_a t/(WC)_t$, time variable
$\Lambda_{a,b}$ = $(hA)_a/(wc)_a$ and $(hA)_b/(wc)_b$
$\Pi_{a,b}$ = $(hA)_a t_a/(WC)_a$ and $(hA)_b t_b/(WC)_b$
$\tau_{a,b}$ = exit gas temperature response, K

### Subscripts

$a$ = denotes quantities associated with gas having lesser capacitance rate
$b$ = denotes quantities associated with gas having greater capacitance rate

$$\tau_b = 1 - \frac{1}{\Pi_b}\left[\Lambda_b - F_1\left(\Pi_b \frac{t}{t_b}, \Lambda_b\right)\right] - \left(1 - \frac{t}{t_b}\right) G_0\left(\Pi_b \frac{t}{t_b}, \Lambda_b\right) \quad (8)$$

This solution is applicable when $t < t_a$ and $t < t_b$ (i.e., $\beta < \alpha$). During the interval $t_b < t < t_a$, which will occur only if $\alpha <$ 180 deg, the exit temperature is time invariant

$$\tau_b = 1 - \frac{1}{\Pi_b}\left[\Lambda_b - F_1(\Pi_b, \Lambda_b)\right] \quad (9)$$

During this time interval the region $b$ contains only disk that has passed the seal at zero temperature since initiation of the unit step excitation.

Figure 2 shows responses for a specific case. The dimensionless time variable $\theta$ changes by $C^*_{rr}$ for one revolution of the disk. For $\alpha$ = 135 deg the response is constant from $\theta$ = 0.1125 to 0.1875. For $\alpha$ = 180 deg the slope of the response goes to zero at $\theta$ = 0.15.

For the parameters shown in Fig. 2 the final ($\theta \to \infty$) response $\tau_{b\infty}$ is 0.365. Thus the analytic solution covers only a small part of the overall response. Nevertheless the analytic solution is very instructive of some features of the overall response. With $\alpha$ = 135 deg the flat portion of the response, as noted, occurs when region $b$ contains only disk that has passed the seal with the same temperature distribution, which is uniformly zero for the analytic solution. However the following section will make it evident that once each revolution, region $b$ contains only disk that has passed the seal with the same temperature distribution. Thus when gas $b$ is stepped and $\alpha$ is 180 deg or less the slope of the $\tau_b$ response will become zero at times $\theta_m = C^*_{rr}\,\alpha/360 + C^*_{rr}m$ ($m$ = 0, 1, 2, . . . ), and starting at each time $\theta_m$, will remain zero for a duration $\delta\theta = C^*_{rr}\,(1-\alpha/180)$. The analytic solution thus shows that the $\tau_b$ response and, by inference, the $\tau_a$ response will not be smooth.

The same reasoning can be used to find the response of gas $a$ to a unit step change in its inlet temperature during the interval $t < t_b$.

## General Solution

To find the general transient solution the disk is divided into $N_t$ equal pie-shaped segments. The area-mean exiting gas temperature for a segment is approximated as the exit temperature of the gas leaving an elementally small regenerator located on the center radius of the segment. Figure 1 shows the small regenerators (SR) located at the outer ends of the radii but the radial location is arbitrary. Stationary position marks separated by the angle $360/N_t$ are shown outside the disk rim. The dimensionless time required for an SR to rotate from one position mark to the next is $\Delta\theta = C^*_{rr}/N_t$. When the SR are at the position marks region $a$ contains $N_a$ complete segments and region $b$ contains $N_b$ complete segments ($N_a + N_b = N_t$). At these times the exit temperature of gas $b$, $\tau_b$, is calculated as the sum of the gas temperatures leaving the SR in region $b$ divided by $N_b$ and, similarly, the exit temperature $\tau_a$ is the sum of the gas temperatures leaving the SR in region $a$ divided by $N_a$.

The angle $\alpha$ is 360 $N_b/N_t$ so that for $\alpha$ = 150 deg the minimum number for $N_t$ is 12, giving $N_a$ = 7 and $N_b$ = 5; these must, of course, be integers.

Figure 1 shows the SR at their positions at $\theta = 0$ when the inlet temperature of either gas increases by a unit step. Immediately, because particle transit times are zero, the exit temperature of the stepped gas jumps to $\exp(-\Lambda_a)$ if gas $a$ is stepped or $\exp(-\Lambda_b)$ if gas $b$ is stepped (see appendix). Thereafter the exit temperatures are calculated at times ½$\Delta\theta$, 1½$\Delta\theta$, 2½$\Delta\theta$, . . . , these being the times of registry of the SR with the position marks.

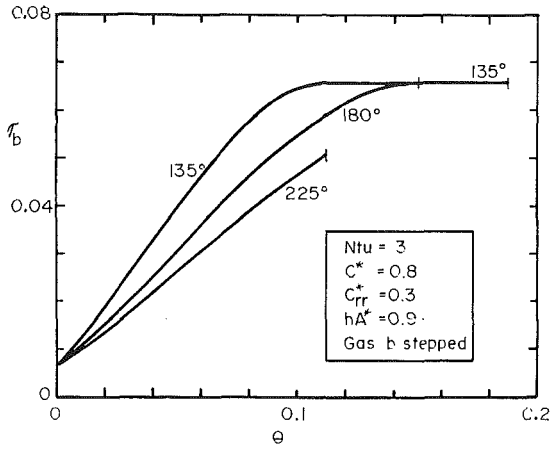


**Fig. 2 Analytic solution for three seal angles**

The details of the analysis will be described for a unit step increase of the inlet temperature of gas $b$ using the regenerator of Fig. 1 for the example. At $\theta = 0$ the entire disk is at zero temperature. Reference to Fig. 1 shows that SR6 through 12 will follow identically the temperature history of SR1, the only difference being that SR12 history will be delayed by 1 $\Delta\theta$, SR11 by 2$\Delta\theta$, and so on to SR6 for which the delay will be 7$\Delta\theta$. Thus only the histories of SR1 through SR5 need be calculated as they rotate about the axis. The procedure will be shown for SR4.

The general form for the exit gas temperature from SR4 during the time it is in region $b$ is

$$\tau_{b4} = 1 - \sum_{n=0}^{N} B_n G_n\left(\Pi_b \frac{t'}{t_b}, \Lambda_b\right) \quad (10)$$

Until SR4 passes the seal for the first time, $t' = t$, $B_0 = 1$, and $B_n = 0$ for $n \neq 0$. At time $\theta$ = ½$\Delta\theta$ ($t'$ = ½$t_b/N_b$), the exit gas temperature is

$$\tau_{b4}(\tfrac{1}{2}\Delta\theta) = 1 - \sum_{n=0}^{N} B_n G_n\left(\frac{1}{2}\frac{\Pi_b}{N_b}, \Lambda_b\right) \quad (11)$$

At time $\theta$ = 1½$\Delta\theta$ ($t'$ = 1½ $t_b/N_b$)

$$\tau_{b4}(1\tfrac{1}{2}\Delta\theta) = 1 - \sum_{n=0}^{N} B_n G_n\left(1\tfrac{1}{2}\frac{\Pi_b}{N_b}, \Lambda_b\right) \quad (12)$$

At time $\theta$ = 2$\Delta\theta$ ($t'$ = 2$t_b/N_b$), SR4 reaches the seal with a matrix temperature distribution

$$T_{b4} = 1 - \sum_{n=0}^{N} B_n F_n\left(2\frac{\Pi_b}{N_b}, (1-y)\Lambda_b\right) \quad (13)$$

On the other side of the seal gas $a$ enters ($y$ = 0) with parameters $\Lambda_a$, $\Pi_a$, and zero temperature. The temperature of the exiting gas in region $a$ is

$$\tau_{a4} = \sum_{n=0}^{N} A_n G_n\left(\Pi_a \frac{t'}{t_b}, \Lambda_a\right) \quad (14)$$

with $t'$ = 0 at the seal. The coefficients $A_n$ are found in terms of the $B_n$ coefficients by noting that the matrix temperature distribution is unchanged on passing the seal

$$\sum_{n=0}^{N} A_n \frac{(y\Lambda_a)^n}{n!} = 1 - \sum_{n=0}^{N} B_n F_n\left(2\frac{\Pi_b}{N_b}, (1-y)\Lambda_b\right) \quad (15)$$

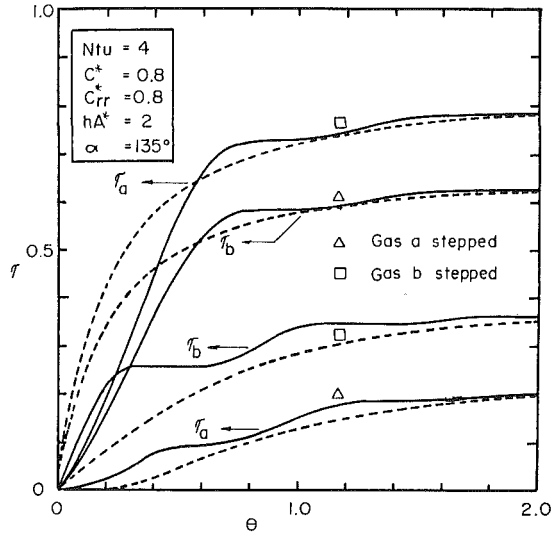


Fig. 3 Exit gas temperature responses for $C^*_{rr} = 0.8$

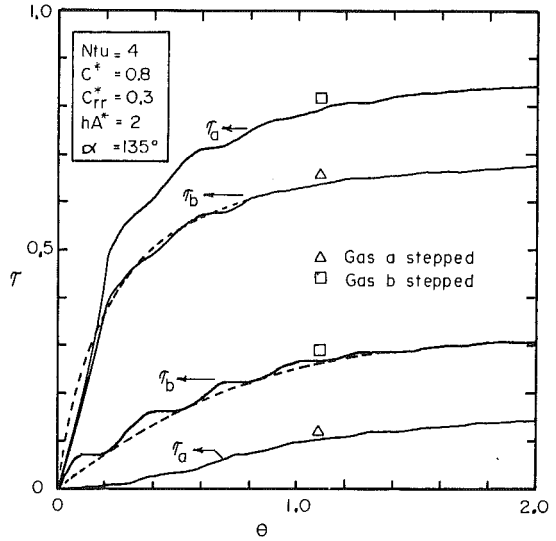


Fig. 4 Exit gas temperature responses for $C^*_{rr} = 0.3$

The successive integral method, SIM (Romie and Baclic, 1988), is used to find the $A_n$ coefficients. SIM gives

$$\sum_{n=0}^{N} A_n \frac{\Lambda_a^n}{n!}\left(\frac{k}{k+n}\right) = 1 - \sum_{n=0}^{N} B_n \frac{k!}{\Lambda_b^k} F_{n+k}\left(2\frac{\Pi_b}{N_b}, \Lambda_b\right) \quad (16)$$

$$k = 1, 2, \ldots, N+1$$

This equation can be represented by an $(N+1) \times (N+1)$ matrix and a column vector. For each value of $k$ the left-hand side gives a row in the matrix and the right-hand side the corresponding entry in the vector. Solution of the system gives the coefficients $A_n$.

At time $\theta = 2\frac{1}{2}\Delta\theta$ $(t' = \frac{1}{2}t_a/N_a)$

$$\tau_{4a}(2\tfrac{1}{2}\Delta\theta) = \sum_{n=0}^{N} A_n G_n\left(\frac{1}{2}\frac{\Pi_a}{N_a}, \Lambda_a\right) \quad (17)$$

and so on until at $\theta = 9\Delta\theta$ $(t' = t_a)$, SR4 rotates past the other seal. The SIM equation to find the new set of $B_n$ coefficients is

$$\sum_{n=0}^{N} B_n \frac{\Lambda_b^n}{n!}\left(\frac{k}{k+n}\right) = 1 - \sum_{n=0}^{N} A_n \frac{k!}{\Lambda_a^k} F_{n+k}(\Pi_a, \Lambda_a) \quad (18)$$

At $\theta = 9\frac{1}{2}\Delta\theta$ $(t' = \frac{1}{2}t_b/N_b)$, the exit gas temperature is

$$\tau_{b4}(9\tfrac{1}{2}\Delta\theta) = 1 - \sum_{n=0}^{N} B_n G_n\left(\frac{1}{2}\frac{\Pi_b}{N_b}, \Lambda_b\right) \quad (19)$$

and so on to the next seal.

The transient response of the rotary regenerator is essentially completed when $\theta = 2$, which means that the five SR are followed for $2/C^*_{rr}$ revolutions of the disk. The time variable $\theta$ can be interpreted as the ratio of the thermal capacitance of the mass of gas that has passed through region $a$ to the thermal capacitance of the entire disk.

If a program is written to compute $\tau_a(\theta)$ and $\tau_b(\theta)$ for a unit step increase in gas $b$ inlet temperature then the same program will compute the responses to a unit step increase in gas $a$ inlet temperature when the numbers of the following pairs are exchanged: $\Lambda_a$ and $\Lambda_b$, $\Pi_a$ and $\Pi_b$, $N_a$ and $N_b$, $\tau_a$ and $\tau_b$.

## Results and Discussion

The solid curves in Figs. 3 and 4 show responses for the same rotary regenerator. Figure 3 shows responses for a rotation period $t_t$ corresponding to $C^*_{rr} = 0.8$. The thermal effectiveness of the regenerator is 0.790. Figure 4 shows responses for a shorter rotation period corresponding to $C^*_{rr} = 0.3$. The thermal effectiveness is 0.849, a value 1.3 percent less than the thermal effectiveness, 0.860, of a counterflow recuperator having the same Ntu and $C^*$. (The thermal effectiveness of the rotary regenerator approaches that of the counterflow recuperator as $C^*_{rr}$ goes to zero.) A value of $C^*_{rr} = 0.8$ is larger than would normally be used with a rotary regenerator, but a large value accentuates some interesting features of the responses.

In Fig. 3 the $\tau_b$ response to a unit step increase of its inlet temperature exhibits flats that, according to the analytical solution, start at times $\theta = 0.3$, 1.1, 1.9, and last for a duration $\delta\theta = 0.2$. The flats last for a longer time indicating a very slow rate of increase of the response following a flat. It can also be observed that the responses of the unstepped gases (the two upper responses) change most rapidly during the times the responses of the stepped gases are responding most slowly.

The two upper responses in Figs. 3 and 4 are, as noted, the responses of the unstepped gases. The top curve is the $\tau_a$ response to a unit step change in gas $b$ inlet temperature. The lower curve is the $\tau_b$ response to a step in gas $a$ inlet temperature and is at all times $C^*$ times the upper response. This characteristic of heat exchangers has been noted for crossflow, counterflow, and parallel-flow recuperators (Romie, 1983, 1984, 1985).

In the range $C^*_{rr} = 0$ to about 0.3 the known (Romie, 1984) response of the counterflow recuperator can be used to approximate closely the responses of the rotary regenerator. For this purpose two functions are used

$$R_1(\theta) = 1 - Ae^{-a\theta} - Be^{-b\theta} \quad (20)$$

$$R_2(\theta) = 1 - Ce^{-c\theta} - De^{-d\theta} \quad (21)$$

For a rotary regenerator with gas $b$ stepped the analogy-predicted exit temperature responses are

$$\tau_b(\theta) = \tau_{b\infty} R_1(\theta) \quad (22)$$

**Table 2 Final gas exit temperature responses to unit step excitation**

| Stepped gas | $\tau_{a\infty}$ | $\tau_{b\infty}$ |
|---|---|---|
| $a$ | $1-\epsilon$ | $\epsilon C^*$ |
| $b$ | $\epsilon$ | $1-\epsilon C^*$ |

**Table 3 Equivalents for gas-to-gas counterflow recuperator**

| This paper | | (Romie, 1984) |
|---|---|---|
| | Always | |
| Ntu | | Ntu |
| $\theta$ | | $\theta$ |
| | Gas $a$ stepped | |
| $C^*$ | | $1/E$ |
| $(hA)^*$ | | $1/R$ |
| | Gas $b$ stepped | |
| $C^*$ | | $E$ |
| $(hA)^*$ | | $R$ |

$$\tau_a(\theta) = \tau_{a\infty} R_2(\theta) \tag{23}$$

If gas $a$ is stepped then

$$\tau_a(\theta) = \tau_{a\infty} R_1(\theta) \tag{24}$$

$$\tau_b(\theta) = \tau_{b\infty} R_2(\theta) \tag{25}$$

The values $\tau_{a\infty}$ and $\tau_{b\infty}$ are the final ($\theta \to \infty$) responses for the rotary regenerator and are expressed in terms of its thermal effectiveness in Table 2. The eight coefficients, $A, a, \ldots, D, d$, are tabulated in the referenced paper for the 24 combinations of Ntu = 1, 2, 4, 8; $C^* = 0.8, 1$; and $(hA)^* = 0.5, 1, 2$. The subscripts and nomenclature used in this paper and the referenced paper are different. Table 3 provides the required translation.

The dashed curves in Figs. 3 and 4 show the responses predicted using the counterflow recuperator analogy. For $C^*_{rr} = 0.8$ (Fig. 3) the agreement is not good but for $C^*_{rr} = 0.3$ (Fig. 4) the agreement is fairly good and is shown only for the two $\tau_b$ responses. The agreement improves as $C^*_{rr}$ becomes smaller.

The very simple form of the functions $R_1$ and $R_2$ means that the response of the rotary regenerator to arbitrary variations of inlet temperatures can be easily computed using Duhamel's integral when $C^*_{rr}$ is less than about 0.3. Rotary regenerators will normally operate in this range of $C^*_{rr}$.

## Concluding Remarks

The four responses given in Figs. 3 and 4 were calculated using $N = 3$, $N_a = 10$, and $N_b = 6$. No change in the computed responses was observed for larger values of these three numbers.

The analogy between the transient responses of the counterflow recuperator and the rotary regenerator can be used in the sense opposite to that used in the preceding section. Specifically, if $C^*_{rr}$ is set equal to a small number, say 0.05, the transient response calculated will be substantially the transient response of the counterflow recuperator having the same Ntu, $C^*$, and $hA^*$. The computation time is less than would be required using a finite difference method. As $C^*_{rr}$ goes to zero the influence of the seal angle on the transient response vanishes insofar as application considerations are concerned. In addition, the number of segments required for a given accuracy decreases. Thus for $C^*_{rr} = 0.05$ the seal angle can be set to 180 deg and $N_t$ set equal to, say, 4 ($N_a = 2$, $N_b = 2$). Using these numbers gives transient responses in excellent agreement with responses for gas-to-gas counterflow recuperators. A program implementing the analysis presented thus serves two purposes.

The analysis given applies equally to disk and drum rotary regenerators.

## References


London, A. L., Sampsell, D. F., and McGowan, J. G., 1964, "The Transient Response of Gas Turbine Plant Heat Exchangers – Additional Solutions for Regenerators of the Periodic-Flow and Direct-Transfer Types," ASME *Journal of Engineering for Power*, Vol. 86, pp. 127–135.

Romie, F. E., 1983, "Transient Response of Gas-to-Gas Crossflow Heat Exchangers With Neither Gas Mixed," ASME JOURNAL OF HEAT TRANSFER, Vol. 105, pp. 563–570.

Romie, F. E., 1984, "Transient Response of the Counterflow Heat Exchangers," ASME JOURNAL OF HEAT TRANSFER, Vol. 106, pp. 620–626.

Romie, F. E., 1985, "Transient Response of the Parallel-Flow Heat Exchanger," ASME JOURNAL OF HEAT TRANSFER, Vol. 107, pp. 727–730.

Romie, F. E., 1987, "Two Functions Used in the Analysis of Crossflow Exchangers, Regenerators and Related Equipment," ASME JOURNAL OF HEAT TRANSFER, Vol. 109, pp. 518–521.

Romie, F. E., and Baclic, B. S., 1988, "Methods for Rapid Calculation of the Operation of Asymmetric Counterflow Regenerators," ASME JOURNAL OF HEAT TRANSFER, Vol. 110, pp. 785–788.

Shah, R. K., 1981, "Thermal Design Theory for Regenerators," *Heat Exchangers, Thermal-Hydraulic Fundamentals and Design*, S. Kakac, A. E. Bergles, and F. Mayinger, eds., Hemisphere, Washington, DC, pp. 721–763.


## APPENDIX

*The functions $F_n$ and $G_n$ satisfy two first-order partial differential equations*

$$-\frac{\partial F_n(u, v)}{\partial u} = F_n - G_n = \frac{\partial G_n(u, v)}{\partial v} \tag{A1}$$

For $n \geq 0$, $F_n(0, v) = v^n/n!$ and $G_n(u, 0) = 0$. Numerical values for $F_n, G_n$, $n = 0, 1, 2, \ldots$ can be found by evaluating just three functions and then using two recurrence equations. The three functions are

$$F_{-1}(u, v) = e^{-(u+v)} \sum_{r=0}^{\infty} \frac{u^{r+1}}{(r+1)!} \frac{v^r}{r!} \tag{A2}$$

$$G_{-1}(u, v) = e^{-(u+v)} \sum_{r=0}^{\infty} \frac{u^r}{r!} \frac{v^r}{r!} \tag{A3}$$

$$G_0(u, v) = e^{-(u+v)} \sum_{r=0}^{\infty} \frac{v^{r+1}}{(r+1)!} \sum_{p=0}^{r} \frac{u^p}{p!} \tag{A4}$$

$F_{-1}$, $G_{-1}$, and $G_0$ can be expressed (Romie, 1987) in terms of modified Bessel functions of the first kind.

The two recurrence equations are

$$F_n(u, v) = G_n(u, v) + G_{n-1}(u, v), \quad \pm \text{integer } n \tag{A5}$$

$$G_{n+1}(u, v) = \frac{1}{n+1}\left[(v-u-1-2n)G_n + (2v-n)G_{n-1} + 2vG_{n-2}\right], \quad n \geq 0 \tag{A6}$$

An integral used in this paper (equation (7)) is

$$\int_0^u G_0(t, v)\,dt = v - F_1(u, v) \tag{A7}$$

The initial ($\theta = 0$) response of the stepped gas can be found by noting that

$$G_0(0, v) = 1 - e^{-v} \tag{A8}$$

**S. H. Chan**
Professor and Chairman.

**H. Rau**
Graduate Student.

**C. DeBellis**
Graduate Student.

**K. F. Neusen**
Associate Professor and
Associate Dean of Graduate School.

Department of Mechanical Engineering,
University of Wisconsin—Milwaukee,
Milwaukee, WI 53201

# Silica Fouling of Heat Transfer Equipment—Experiments and Model[1]

*Silica fouling of heat transfer equipment in geothermal energy systems is studied. The effects of temperature, pH, and salinity on silica solubility and silica polymerization are reviewed. Experimental fouling data are presented for geothermal brines with different pH values, chemical compositions, and thermal-hydraulic conditions. The effects of supersaturation, pH, Reynolds number, and the concentration of ions in the brine solution on the formation of silica scale in the heat exchanger tube are discussed. A silica deposition model is proposed that accounts for supersaturation, pH factor, salinity, and thermal-hydraulic effects. Results based on the analytical model are compared with silica fouling data obtained in the laboratory as well as from two geothermal fields.*

## Introduction

Formation of fouling due to any undesirable deposit on heat transfer surfaces is a subject of considerable economic and technical importance. The economic consequence of fouling, which reduces heat transfer efficiency, is to increase the cost of energy. Pritchard (1981), for example, has estimated that the cost of fouling in British heat exchange equipment equals about 0.5 percent of the British 1976 gross national product. Technically, fouling has been described as "the major unresolved problem in heat transfer" (Taborek et al., 1972a). It is well recognized that the most widely used fouling factor data published by the Tubular Exchange Manufacturers Association provide insufficient information for the design and operation of particular heat exchangers as the data are limited to a small number of fluids and are time independent. Consequently, there are an increasing number of research activities aiming to provide a better understanding of fouling phenomena (Somerscales and Knudsen, 1981; Bryers, 1982).

In geothermal energy utilization, fouling remains one of the key problems to be solved. The major contributors to geothermal fouling are scaling due to silica and calcium carbonate (Wahl, 1977; Ellis and Mahon, 1977). This is a result of the fact that silica is one of the primary components of the earth's crust and so are calcium compounds in some areas.

Calcium scaling in geothermal plants is primarily attributed to pressure reductions, such as scaling found in a wellbore where flashing starts, and in valves, constrictions, or flow measuring instruments. When the pressure of the bulk brine is decreased rapidly, the excess carbon dioxide gas is liberated from the brine due to its decrease in solubility, resulting in a higher pH of the brine. Consequently, the carbonate ion ($CO_3^=$) concentration increases, which causes the deposition and crystal growth of calcium carbonate. The kinetics of this reaction are very fast, causing scale formation immediately downstream of such pressure drops (Wahl, 1977). In some cases this has caused plugging of the pipes, valves, pressure taps, and flow instruments (San Diego Gas and Electric, 1980). Since calcium carbonate solubility decreases with increasing temperature, calcium carbonate scale is also found on heated surfaces.

Silica scaling is quite different. Silica solubility increases with increased brine temperature. Silica, being saturated in geothermal brines in the downhole environment in the monomeric state, can become supersaturated as the brine is cooled through the heat exchanger or when part of the brine is flashed into steam. The supersaturation causes precipitation of silica in an amorphous form on heat exchanger surfaces, separators, well lines, and discharge lines.

Analytical modeling of scale formation in general has been reviewed (Epstein, 1979, 1981; Suitor et al., 1977; Hasson, 1981; Taborek et al., 1972). Due to the complexity of the fouling process, no generalized predictive correlation for the design of heat transfer subject to fouling (*a*) in general and (*b*) when exposed to geothermal brines equipment has yet been established. Some work has been done on the kinetics and crystallization (Loewenthal and Marais, 1976; Reddy and Nancollas, 1971; Nancollas and Reddy, 1971; Roques and Girou, 1974; Wiechers et al., 1975) as well as on modeling and correlation of calcium carbonate deposit formation (Watkinson and Martinez, 1975; Hasson et al., 1962, 1968, 1978, 1981; Gazit and Hasson, 1975; Lee and Knudsen, 1979; Coates and Knudsen, 1980; Knudsen, 1981). Although the majority of these studies are concerned with cooling water fouling or fouling in evaporator and heat exchanger tubes, the fundamentals of calcium carbonate fouling from geothermal brine should be the same. As to silica scale, the deposition mechanism is more complicated than that of the calcium carbonate scale because the dissolved silica can polymerize, forming colloidal particles (Iler, 1955, 1979). Its complex kinetics have recently begun to attract fundamental research (Bohlman et al., 1980; Weres et al., 1979–82; Rothbaum and Rohde, 1979; Barnes, 1979) and some attempts to model and to correlate experimental data have been made (Gudmundsson and Bott, 1979; Lombard, 1978; Fournier, 1970; Felsinger, 1977; The Ben Holt Co., 1978; Bott and Gudmundsson, 1978; Bohlman et al., 1981).

Several previous investigations have reported experimental results for fouling heat transfer with goemetrical brines in tubular heat exchangers. Tests of two 3.05 m horizontal titanium tubes (2.54 cm) were run for 92 h and showed a 60 percent loss in the overall heat transfer coefficient (Felsinger, 1977). Vertical stainless and carbon steel tubes of 1.27 o-d, 45.72 cm long, using natural and synthetic brines were tested (Wahl et al., 1974). Little scaling resulted when the brine was kept in the liquid phase. A test of four 6.1 m long shell-and-tube heat exchangers using 2.54 cm titanium tubes was reported using natural brine (Lombard, 1978). In most instances, linearly increasing fouling resistance was observed due to a silica-based scale. Experiments with 20 ft long horizontal double pipe heat exchangers were made and the

[1]Based mostly on papers presented at the ASME-AIChE National Heat Transfer Conference, 1985 and the ASME-JSME Thermal Engineering Joint Conference, 1983 and 1987.

Contributed by the Heat Transfer Division for publication in the JOURNAL OF HEAT TRANSFER. Manuscript received by the Heat Transfer Division July 28, 1987. Keywords: Fouling, Heat Exchangers.

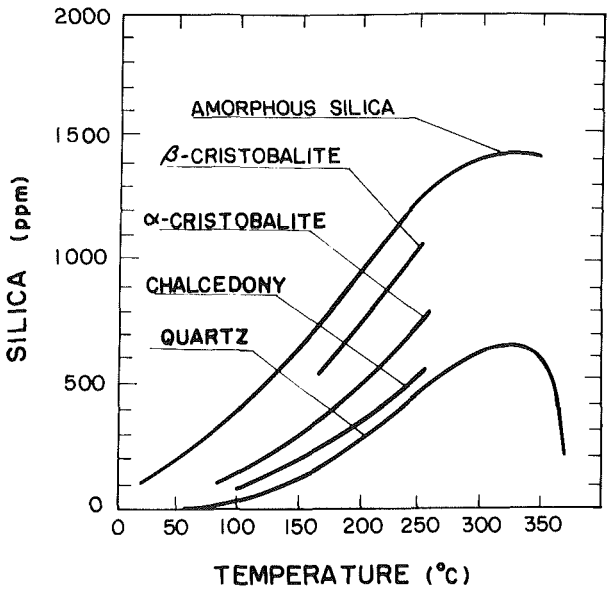


**Fig. 1 Solubilities of various silica phases at various saturation temperatures and pH = 7 (Fournier, 1980)**

observed linear fouling rates were used to design a 5 MW demonstration plant (Mines and Neill, 1978). Studies (Gudmundsson and Bott, 1979) conducted in Iceland were performed at two sites with heat exchangers of the same design but differing flow conditions. At one site, linear fouling was observed but an induction period was indicated at the other site. Geothermal testings in Taiwan (Chou and Lin, 1982; Chou, 1985) indicated that silica concentration in brine seemed to be undersaturated and time dependent, possibly influenced by heavy rainfall, and that little fouling was found in the heat exchanger for most of the time.

An extensive study of fouling with synthetic brines on horizontal 1.83 m long, 0.635 cm titanium pipes was conducted at Oak Ridge National Lab (ORNL) and reported by Bohlman et al. (1981). The heat exchangers were operated in series and overall thermal resistances were reported that varied widely from exchanger to exchanger.

These results are far from conclusive. The complexity of geothermal brine fouling needs a systematic, comprehensive series of experiments to study parameters of importance, the number of which is very large, including various chemical, material, thermal, and hydraulic variables. Therefore an experimental task is undertaken as described later. In the following, the related fundamentals in silica fouling are reviewed first, followed by presentation of an analytical model and experimental data on silica fouling.

## Silica Solubility, Kinetics, and Deposition

**The Solubility of Silica.** Silica exists in both the crystalline and amorphous states (Wahl, 1977; Krauskopf, 1956). Because many possible ordered arrangement of tetrahedra joined by corners are possible, silica forms various crystal structures or polymorphs. The solubilities of the different polymorphs of silica in saturated water at various saturation temperatures are given in Fig. 1. The solubility of the polymorphs increases with increasing temperature up to 300°C; above this temperature the solubility decreases. It can be seen that amorphous silica is more soluble than quartz at all temperatures, but they exhibit similar temperature dependencies. The concentration of silica in underground geothermal brines is usually controlled by the solubility of quartz and downhole temperature so that silica is generally present as quartz (Wahl, 1977; Hoffmann, 1975). However, under most conditions, it appears that silica precipitates out as relatively pure amorphous silica (Wahl, 1977; Weres et al., 1979–1982) whatever the original silica source may be. The reason is that the kinetics of quartz crystallization below 300°C is much slower than that of amorphous silica (Bohlman et al., 1980).

Amorphous silica solubility is a weak function of pressure and therefore the pressure effect can be neglected for most practical applications (Millro, 1982).

In addition to temperature, pH and salinity can also have significant effects on the solubility of silica. Figure 2 shows that at low pH the solubility remains constant, but, beyond a limit, the solubility increases drastically with pH values (Barnes, 1979; Okamota et al., 1957).

## Nomenclature

$A$ = area, $m^2$
$a_j$ = activity of species $j$, molality (m)
$C$ = concentration, molality
$C_e$ = equilibrium concentration, molality
$C_o$ = equilbrium concentration of amorphous silica in pure water, molality
$C_{op}$ = equilibrium concentration of amorphone silica in pure water, ppm
$C_p$ = specific heat at constant pressure
$D$ = diameter, m
$h$ = heat transfer coefficient, $W/m^2°C$
$I$ = ionic strength, molality
$k_f$ = thermal conductivity of fouling film
$K_R$ = rate coefficient for surface crystallization
LMTD = log mean temperature difference
$M_j$ = atomic weight
$m$ = mass of fouling film per unit interface area
$\dot{m}_b$ = brine mass flow rate
NaAc = sodium acetate
$n$ = order of supersaturation
$p$ = correlation constant in equation (1)
$\dot{Q}$ = heat transfer per unit time
$q$ = correlation constant in equation (1)
$R_f$ = thermal fouling resistance, $m^2°C/W$
$R_o$ = thermal resistance in tube between thermocouple location and tube outer surface
$T$ = temperature, K
$T_s$ = temperature at scale-brine interface, K
$t$ = time
$U$ = overall heat transfer coefficient, $W/m^2°C$
$\dot{V}$ = volume flow rate, $m^3/h$
$x$ = axial coordinate, m
$Z_j$ = valence of species $i$
$\gamma_i$ = molal activity coefficient of species $i$
$\epsilon$ = dielectric constant of pure water
$\rho$ = density, $g/cm^3$
$\phi$ = osmotic coefficient

**Subscripts**

$b$ = brine
$c$ = coolant
$cl$ = clean
$f$ = fouling film
$i$ = inside of tube or $i$th location
$o$ = outside of tube
$w$ = wall

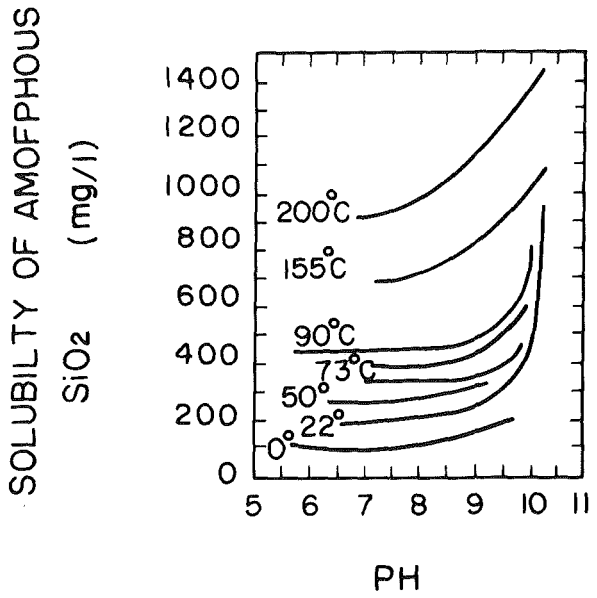


Fig. 2 Solubility of amorphous silica as a function of pH at various temperatures (Goto, 1953)

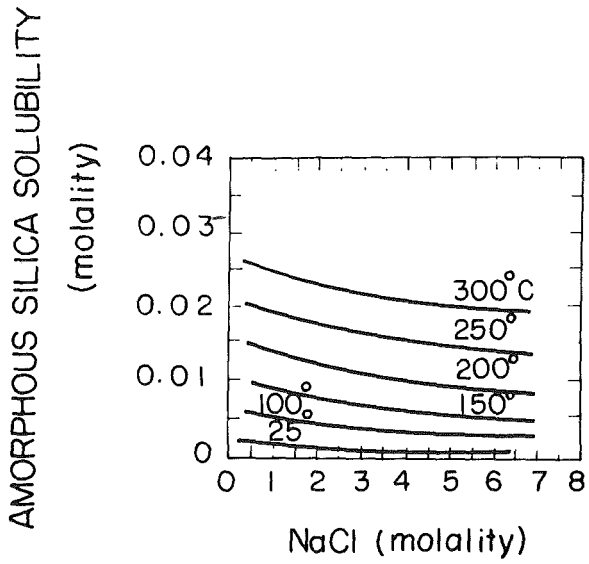


Fig. 3 Molal solubility of amorphous silica in aqueous NaCl solutions, 25-300°C (Chen and Marshall, 1982)

When the salinity of brine is changed due to the addition of salts in the pure water, the magnitude of the activity of water decreases and so does the solubility of silica. Figure 3 shows that the solubility of amorphous silica decreases as the amount of additional NaCl increases at various temperatures.

The solubility of amorphous silica in aqueous sodium nitrate up to 300°C (Marshall, 1980), and in sodium chloride, sodium sulfate, or magnesium sulfate solutions (Chen and Marshall, 1982) up to 350°C has been measured. Other investigators have also studied the solubility in ten (Marshall et al., 1980) and eleven (Chan et al., 1987) different salt solutions (NaCl, NaBr, NaI, LiCl, KCl, $NaNO_3$, NaAc, $Na_2SO_4$, $MgCl_2$, $CaCl_2$, and $SrCl_2$) at 25°C. For a given temperature and salt concentration the effect of different salts on solubility can be correlated by the hydration number of salt cations. The order of decreasing effect of cation on the amorphous silica solubility is found to be (Chan et al., 1987):

$$Mg^{2+} > Ca^{2+} > Sr^{2+} > Li^{+} > Na^{+} > K^{+}$$

Similarly, the effects of the presence of sodium halide salts (NaCl, NaI, and NaBr) in brine solutions were studied. It was found that the gradients of silica concentration with respect to the salt concentration for sodium halide salts can be correlated in terms of the molecular weight of the anionic ions, such that the order of anionic effect can be stated as (Chan et al., 1987):

$$I^{-} > Br^{-} > Cl^{-}$$

and that the solubility of silica $C_{SiO_2}$ (in ppm) in the sodium halide salt solutions can be correlated as a function of salt concentration $C_j$ (in molarity), temperature $T$, and the atomic weight of halide ions $M_j$ as follows:

$$C_{SiO_2} = C_{op} - \frac{11.75[M_j + (378 - T)]}{281 - T} C_j$$

where $C_{op}$ is the silica solubility (in ppm) in pure water; $\log C_{op} = 4.52 - 731/T$.

**Processes of Silica Polymerization and Physical Phenomena of the Deposition of Silica Scale.** The high concentration of silica in most geothermal brines causes the brine solution to become supersaturated when extracted and cooled from the well. This supersaturation is thought to be the main factor in the deposition of silica scale in geothermal energy processes.

Usually, silica precipitates from geothermal brines as amorphous silica or amorphous silicates. The process of amorphous silica precipitation from a supersaturated bulk aqueous phase may consist of the following steps (Weres et al., 1979-1982):

1 Formation of silica polymers of less than critical nucleus size.

2 Nucleation of an amorphous silica phase in the form of colloidal particles that are large enough to grow spontaneously and without interruption, the so-called homogeneous nucleation.

3 Growth of the supercritical amorphous silica particles by further chemical deposition of silicic acid on their surfaces.

4 Coagulation or flocculation of colloidal particles to give a gel.

5 Cementation of the particles in the gel by chemical bonding and further deposition of silica between the particles.

6 Rarely, growth of a secondary phase in the interstices between the amorphous silica particles. Such secondary deposition of FeS and of calcite has been reported, but is not common.

The above homogeneous nucleation processes occur when the concentration of dissolved silica is highly supersaturated. This requires supersaturation by a factor of roughly 2.5 or more. When this condition is met, rapid polymerization occurs, and massive precipitation or scale deposition may follow.

If the concentration of dissolved silica is too low for rapid homogeneous nucleation to occur, relatively slow heterogeneous nucleation and the deposition of dissolved silica directly on solid surfaces become the dominant polymerization processes. The product of the latter process is a dense vitreous silica. At higher temperatures, this process may produce scale at a significant rate.

The polymerization of silica has been studied by some workers (Weres et al., 1979; Rothbaum and Rohde, 1979; Alexander, 1954; Iler, 1953) who employed silica derived from $Na_3SiO_4$, and thus the silica solution contained some significant impurities such as Na. Recently, pure silica from silica gel has been used (Chan et al., 1987). A heated solution with saturated monomeric silica of a high grade of purity was brought to supersaturation by quenching the solution to a lower temperature. The rate of polymerization was determined by measuring the change of the concentration monomeric silica with time. The result showed that the induc-

tion time increases as the pH decreases. The reaction order was found to lie between 1 and 2 and the reaction constant was approximately a linear function of the pH value (Chan et al., 1987).

There are two different types of deposition of silica in the $SiO_2$–$H_2O$ system, namely the depositions from monomeric silicic acid and those from colloidal particles, Monomeric silicic acid forms an impervious glasslike film, whereas colloidal particles form a porous film, often white and opaque when dried (Iler, 1979). The phenomena of both types of deposition are so complicated that, so far, neither has been modeled successfully to yield a general empirical equation for predicting the silica deposition in the geothermal field. In the following, an analytical model is proposed to predict the deposition from monomeric silicic acid brine.

## Silica Deposition Model

The basis of the analytical model is a kinetic study by Bohlman et al. (1980) on simulated geothermal brines in an isothermal system (isothermal in the sense that the supersaturated brine and the deposition surfaces are at the same temperature). They summarized the kinetic reaction rate of silica deposits by a correlation, which shows that the apparent rate constant is independent of system temperature over the rangle of 60 to 100°C and that the apparent kinetic reaction orders for hydroxide ion concentration and the supersaturation of $Si(OH)_4$ are 0.7 and 2, respectively. It is noted that the precise determination of reaction constant and reaction order is difficult, and not unexpectedly somewhat different values are reported by Chan et al. (1987). As pointed out by Fleming (1981), reaction orders in the range of 1 to 4 have been reported.

Assuming that silica scale deposition is surface reaction rate controlled, the kinetic equation for an isothermal system (Bohlman et al., 1980) may be applicable to nonisothermal systems, provided provisions are made for thermal-hydraulic effects. Therefore, it is proposed that the rate of change of fouling resistance (or the mass deposition flux, $dm_f/dt = (dR_f/dt)/\rho_f K_f$) be given as

$$\frac{dR_f}{dt} = K_R \left( \frac{C_b - C_e(T_s)}{C_e(T_s)} \right)^p (C_{OH^-})^q \tag{1}$$

where $C_b$ is the bulk concentration of amorphous silica ($SiO_2$), $C_e$ is the equilibrium solubility of amorphous silica evaluated at the scale-brine interface temperature $T_s$, and $C_{OH^-}$ is the bulk molality concentration of $OH^-$ ions in the brine. The reaction order of silica ($SiO_2$) can be taken as $p=2$, the same as the isothermal system. This is because the fouling rate is expected to be about the same as long as the supersaturation of silica at the interface in the nonisothermal system is the same as that in the isothermal system. The other correlation constants, $K_R$ and $q$, are to be obtained experimentally. As in isothermal systems, the supersaturation and pH effects are explicitly accounted for in equation (1). In addition, salinity effects due to presence of impurities, and thermal-hydraulic effects due to heat transfer and fluid flow, can also be accounted for as described below.

Since the surface kinetic reaction is assumed to be the controlling mechanism for silica deposition, the brine convective diffusion and the heat transfer from the hotter, supersaturated brine to the cooler deposition surface should not affect the deposition mechanism. They can, however, alter the scale-brine interface temperature $T_s$, which in turn has a direct bearing on the deposition rate because the equilibrium solubility $C_e$ in equation (1) is a strong function of temperature. In other words, the model proposed here accounts for thermal-hydraulic effects by evaluating $C_e$ at the interface temperature $T_s$. Normally, overall heat transfer coefficients $U_i$, and the inlet and outlet temperatures of brine and coolant, are measured and reported in the literature (Gudmundsson and Bott, 1979). Then the mean interface temperature can be derived from the simple energy balance

$$\dot{Q} = U_i A_i (\text{LMTD}) = h_i A_i (T_m - T_s) \tag{2}$$

where $h_i$ and $A_i$ are, respectively, the brine side heat transfer coefficient and surface area, LMTD is the log mean temperature difference across a heat exchanger, and $T_m$ is the mean mixed temperature of the brine ($T_m = (T_{i,\text{in}} + T_{i,\text{out}})/2$). For pipe flows with a constant wall temperature, which is equivalent to a mean $T_s$ in the present study, the use of a simple temperature difference as in the thrid term of equation (2) is satisfactory.

The salinity effects due to the presence of impurities other than silica are included in the model by evaluating the equilibrium solubility of water $C_e$ from

$$C_e(T_s)/C_o(T_s) = a^2_{H_2O}/a^2_{H_2O,p} \tag{3}$$

where $C_o$ is the equilibrium solubility of amorphous silica in pure water at the interface temperature (Fournier and Rowe, 1977), i.e.,

$$\log \quad C_o(T_s) = -0.26 - 731/T_s \tag{4}$$

The activity of pure water $a_{H_2O,\,p}$ is one and the activity of water $a_{H_2O}$ in NaCl solution can be evaluated from (Busey and Mesmer, 1976)

$$\log \quad a_{H_2O} = -0.015/\phi I \tag{5}$$

where $I$ is the ionic strength of all ion components in the brine

$$I = \frac{1}{2}\sum_i C_i Z_i^2 \tag{6}$$

with $C_i$ and $Z_i$ standing for, respectively, molality and ionic strength of ion $i$. The osmotic coefficient ($\phi$) for water solutions of NaCl can be found in Lin and Lindsay (1972), which provides a table of the coefficient as a function of temperature and salt (NaCl) concentration. The salt concentration can be replaced by the ionic strength of the brine if all the ions in the brine are assumed to have the same effect on the osmotic coefficient as NaCl salt.

To include the effect of salinity on the concentration of hydroxide ions, $C_{OH^-}$ in equation (1) is calculated from

$$\log \quad C_{OH^-} = \log Q_w + \text{pH} + \log \quad \gamma_{H^+} \tag{7}$$

$Q_w$ is the dissociation quotient of water, which is a function of temperature and ionic strength (Busey and Mesmer, 1976). The molal activity coefficient of $H^+$ ions is calculated from (Truesdell and Jones, 1974)

$$\log \quad \gamma_{H^+} = -C_1 Z^2_{H^+} \sqrt{I}/(1 + b_{H^+} C_2 \sqrt{I}) \tag{8}$$

where

$$\begin{aligned} b_{H^+} &= 9 \text{ Å} \\ C_1 &= 1.82483 \times 10^{-6} \times \rho_b^{1/2}/(\epsilon T)^{3/2} \quad (\text{molality})^{1/2} \\ C_2 &= 50.2916 \times \rho_b^{1/2}/(\epsilon T)^{1/2}, \quad (\text{Å})^{-1}(\text{molality})^{-1/2} \\ Z_{H^+} &= 1 \end{aligned}$$

and $\epsilon$ is the dielectric constant of pure water (Malmberg and Maryott, 1956; Akerlof and Ashry, 1950).

The density of the brine solution is evaluated from

$$\rho_b = \rho_w + 0.0073 wt(1 + 1.6 \times 10^{-6}(T - 273)^2)$$

where $\rho_w$ is the water density at $T$ and $wt$ is the concentration of salts in terms of the weight percentage of the total dissolved solids (TDS) in brine. Finally, it is noted that $T$ in the above equations is evaluated at the interface temperature. The accuracy of the model will be assessed later when a comparison is made with experimental data.

## Experimental Setup, Procedures, and Results of Geothermal Brine Fouling

**Experimental Setup and Procedure.** Recently, a high-

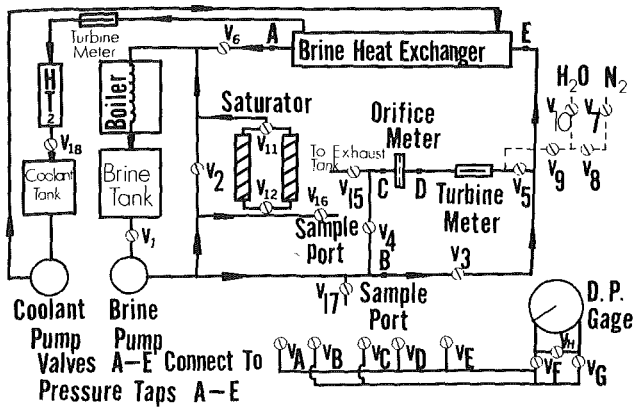


Fig. 4 Schematic of geothermal fouling loop

pressure (1.58 MPa), high-temperature (190°C), and corrosion resistant brine loop has been built in the Geothermal Fouling Test Laboratory at the University of Wisconsin—Milwaukee to investigate the effects of silica supersaturation, brine pH, Reynolds number, and contents of sodium, chloride, and other ions on formation of silica scale. The major components of the loop are shown in Fig. 4. The details of the design were given in Chan et al. (1982) and will not be reiterated here. All experiments were performed on the same cocurrent, double-tube heat exchanger with brine on the tube side and distilled deonized water on the shell side. The inner tube was a 2.82 m long, 2.54 cm diameter titanium tube with a 0.165 cm wall thickness. Thermocouples were also imbedded in 0.0635 cm holes drilled through the titanium tube, using an E.D.M. machine, at 30.48 cm intervals along the tube length.

A calibration was performed on the brine tube prior to scaling runs with distilled water in the brine loop and a special bulk fluid temperature probe inserted in the center of the titanium tube. Its purpose was to obtain the thermal resistance $R_{oi}$ between each of the eight thermocouples in the tube wall and the outer tube surface on the coolant side. From the results for a clean tube, it is possible to calculate the local overall heat transfer coefficients for a fouled heat exchanger. The method is that of Wilson as modified by Fisher et al. (1975).

The loop is instrumented to yield both overall and local transient fouling resistances for all experiments. The overall fouling resistance (over the entire length of a heat exchange) is reduced from

$$R_f = 1/U_{of} - 1/U_{ocl}$$

where

$$U_o = \dot{Q}/A_o \mathrm{LMTD}$$

The log mean temperature difference and $\dot{Q}(=\dot{m}_b C_{pb} \Delta T_b)$ are calculated from the experimental brine mass flow rate, and the mixed mean inlet and outlet temperatures of brine and coolant. $C_{pb}$ and $\rho_b$ of the brine are calculated from Wahl (1977). The $U_{ocl}$ values are listed in Table 2.

With thermocouple readings in the wall and coolant $(T_w, T_c)_i$, and the modified Wilson plot results, $(R_o + 1/h_o)_i$, the local thermal fouling resistance at station $i$ is calculated from

$$R_{fi}(t) = 1/U_{of}(t)_{i-1,i+1} - 1/U_{ocl}(t=0)_{i-1,i+1} \tag{9}$$

$U_{of}$ is evaluated from the energy balance

$$\Delta Q_{i-1,i+1} = (T_w - T_c)_i \pi D_o \Delta x_i / (R_o + 1/h_o)_i \tag{10}$$

$$= U_{ofi-1,i+1} \mathrm{LMTD}_{i-1,i+1} \pi D_o \Delta x_{i-1,i+1}$$

with

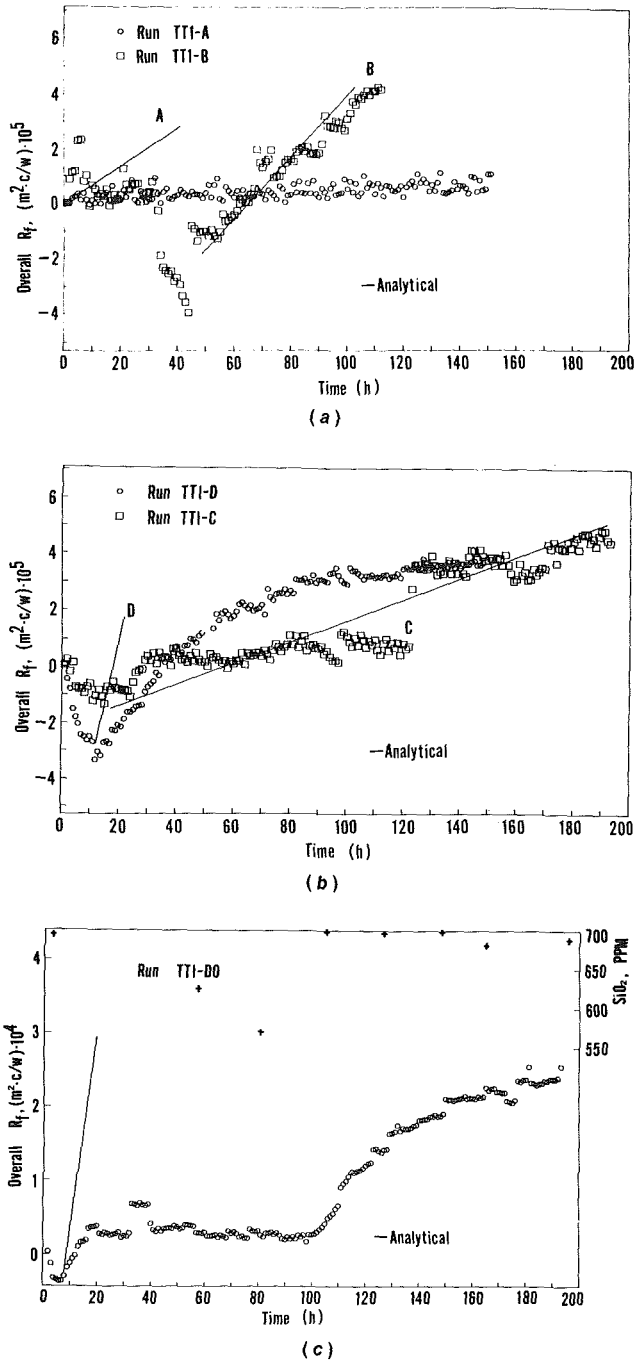


Fig. 5 Overall thermal fouling resistance curves

$$\mathrm{LMTD}_{i-1,i+1} = \frac{(T_{bi+1} - T_{ci+1}) - (T_{bi-1} - T_{ci-1})}{\ln[(T_{bi+1} - T_{ci+1})/(T_{bi-1} - T_{ci-1})]} \tag{11}$$

The necessary $T_b$ at thermocouple locations are evaluated as follows. The first $T_{b1}$ is calculated by a linear interpolation using the measured inlet and outlet brine temperatures, because a linear brine temperature profile is expected due to a high brine mass flow rate in the tube and the small $\Delta T$ drop in the coolant side. For other points, a combination of equation (10) and $d\dot{Q} = \dot{m}_b C_{pb} dT_b$ yields

$$T_{bi} - T_{bj} = \frac{D_o \pi}{\dot{m}_b C_{pb}} \int_{x_i}^{x_j} \frac{T_w - T_c}{R_o + 1/h_o} dx \tag{12}$$

from which $T_{b2}$ is calculated using a two-point numerical in-

tegration. For the third points ($j=i+2$) and beyond, Simpson's integration rule was used.

**Experimental Results and Discussion.** The solubility of amorphous silica in the brine of the Geothermal Testing Loop also has been measured to ensure that the brine supplied to the test section is maintained at the same saturated silica concentration level during the course of the experiment. Table 1 shows the average values of the monomeric and total silica concentrations in brines taken from the brine reservoir tank during the course of all experiments. The monomeric silica concentration was measured by an Auto-analyzer from Technicon Instruments Corp. (automated method for molybdate-reactive silica) and the total silica concentration was determined by an Atomic Absorption Spectrophotometer. Since their values are almost identical and are in agreement with the equilibrium solubility curve reported by previous workers, it can be concluded that the silica in the brine is indeed maintained all the time in the form of the monomeric acid without polymerization all the time. Thus the loop has correctly simulated natural brines containing monomeric acid.

**Table 1 Monomeric silica and total silica in brine drawn from brine tank**

| Run No. | TT1-A | TT1-B | TT1-C | TT1-D | TT1-DO |
|---|---|---|---|---|---|
| Monomeric acid, ppm $SiO_2$ | 670 | 590 | 570 | 660 | 680 |
| Total silica, ppm $SiO_2$ | 587 | ---- | 560 | 662 | 668 |

The results of five typical experiments using synthetic brine are presented in Figs. 5 and 6. The thermal hydraulic conditions and chemistry for each run are given in Tables 2 and 3, respectively. Runs A to C used distilled deionized water at nominal pH of 6 and a variation in NaCl concentration. Runs D and DO used sodium acetate as a buffer to change the pH of the brine to above 7.

Run A contains pure silica solution only without any impurity. Very little scale was found in this run. This indicates that although silica is the major constituent of the scale, other chemical species must be present to ensure the formation of a significant deposit.

In comparing the results of these five runs, the effect of sodium chloride concentration will be examined first. In runs A, B, and C, the NaCl concentration varied from 0.0, 0.1, to 1.0 molar, respectively. The linear fouling rates (Table 4) indicate a nonlinear relationship between the NaCl concentration and fouling rate. This is unexpected. One would expect the fouling rate to increase with concentration. One explanation for the higher fouling rate in run B could be the higher pH of 6.8. Since pH is a major variable affecting fouling, it may overshadow the NaCl concentration. Another explanation might be that the tube was not chemically cleaned prior to running in run B. Therefore, silica nucleation sites could have

**Table 2 Thermal hydraulic conditions in fouling experiments**

| Run No. | $Re_b$ | $T_{b\,in}$ | $T_{b\,out}$ | $T_{c\,in}$ | $T_{c\,out}$ | $\dot{V}_b$ | $\dot{V}_c$ | $U_{ocl}$ | $t_{tp}$ |
|---|---|---|---|---|---|---|---|---|---|
| TT1-A | 73,130 | 438.6 | 396.6 | 344.5 | 345.6 | 0.94 | 169.5 | 2715.3 | 150 |
| TT1-B | 77,500 | 436.9 | 396.4 | 343.9 | 345.0 | 0.98 | 168.5 | 2709.1 | 133 |
| TT1-C | 75,790 | 438.2 | 397.4 | 344.3 | 345.4 | 0.95 | 167.8 | 2614.8 | 193 |
| TT1-D | 76,150 | 437.8 | 397.8 | 344.9 | 345.9 | 0.96 | 168.9 | 2608.0 | 148 |
| TT1-DO | 51,920 | 439.0 | 389.4 | 343.7 | 344.9 | 0.68 | 110.0 | 2257.1 | 193 |

$T_{h\,out}$ and $T_{c\,out}$ are based on beginning value of run: $Re_b$ based on $D_i$, $T_b$, and water properties; $U_o$ in units of W/m$^2$°C; $t_{tp}$ = test period in *h*.

**Table 3 Chemical composition in fouling experiments**

| Run No. | $SiO_2$[1] | NaCl[2] | NaAc | pH | TDS[3] |
|---|---|---|---|---|---|
| TT1-A | 0.0111 (670) | 0 | 0 | 5.9 | 670 |
| TT1-B | 0.0098 (590) | 0.1 (58500) | 0 | 6.8 | 6440 |
| TT1-C | 0.0095 (570) | 1.0 (58500) | 0 | 5.8 | 59070 |
| TT1-D | 0.0109 (660) | 0 | 0.1 (13610) | 7.3 | 14250 |
| TT1-DO | 0.0113 (680) | 0 | 0.1 (13610) | 7.4 | 14290 |

[1] Saturation concentration.
[2] Units of $SiO_2$, NaCl, and NaAC concentrations in molarity and (ppm).
[3] Total dissolved solids in ppm.

**Table 4 Comparison of fouling behavior**

| Run No. | Characteristic fouling behavior and value | Percent increase in $\Delta p$ across heat exchanger | $\rho f k_f$, kgW/m$^3$°C |
|---|---|---|---|
| TT1-A | Linear 0.399[1] | 0 | |
| TT1-B | Linear 6.144[1] | 200 | 541 |
| TT1-C | Linear 2.314[1] | 64 | 355 |
| TT1-D | Asymptotic 4.4[2] | 193 | 1504 |
| TT1-DO | Asymptotic 24.9[2] | 317 | 687 |

[1] Linear fouling rate (m$^2$°C/W/h) × $10^5$
[2] Fouling resistance at end of run (m$^2$°C/W) × $10^5$.

**Table 5 Scale deposition and composition**

| Run No. | TT1-A | TT1-B | TT1-C | TT1-D | TT1-DO |
|---|---|---|---|---|---|
| $m \times 10^3$ | Neg. | 23.2 | 18.2 | 66.2 | 171.2 |
| $\dot{m} \times 10^5$ | ___ | 20.6 | 9.4 | 44.7 | 139.[2] |
| $SiO_2$[1] | ___ | 87.6 | 82.3 | 84.9 | 97.1 |
| $Na_2O$[1] | ___ | ___ | ___ | 2.3 | 1.3 |
| $Cl$[1] | ___ | ___ | <1 | ___ | ___ |
| $CaO$[1] | ___ | <1 | ___ | 1.7 | ___ |
| $FeO$[1] | ___ | 4.7 | 9.3 | 5.6 | 1.6 |
| $ZNO$[1] | ___ | 6.2 | 6.3 | 5.6 | ___ |

[1] Composition in weight percent of total sample.
[2] Time = (193 h) − (70 h of zero fouling) = 123h; $m$ and $\dot{m}$ in kg/m$^2$ and kg/m$^2$h, respectively.

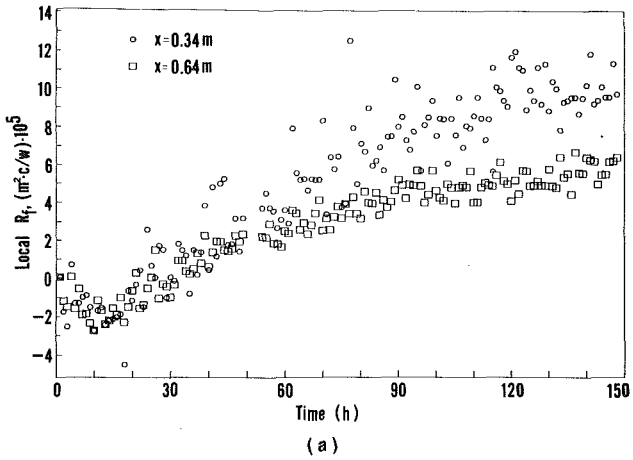


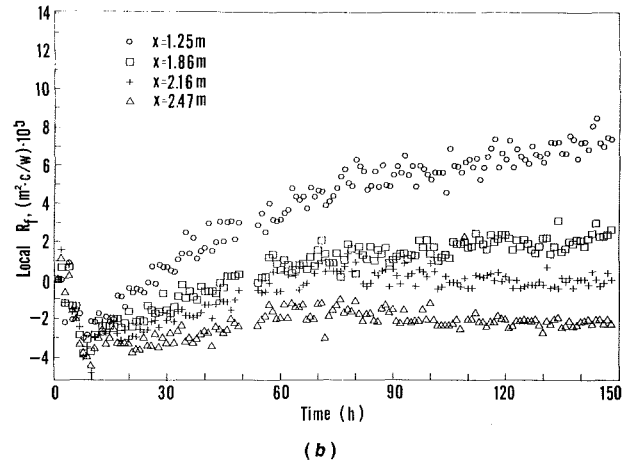


**Fig. 6 Local thermal fouling resistance curves**

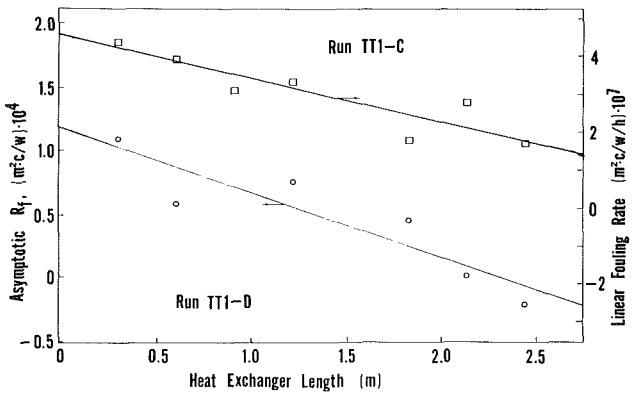


**Fig. 7 Variation of local fouling**

been present prior to the experiment, which would accelerate the fouling process. Run B might have to be repeated because of these factors.

The effect of pH is not completely clear at this time since runs D and DO (pH above 7) had asymptotic fouling rates while those with a pH below 7 had linear fouling rates. However, a comparison of run B with runs A and C would indicate that a higher pH increases the fouling rate as described earlier.

To demonstrate the effect of Reynolds number, runs D and DO can be compared. Before comparison is made, it is noted that the flat curve between 20 and 100 h of run DO was accidently caused by an insufficient amount of silica placed in saturators of the loop as indicated by the drop in the silica concentration level in the brine (see crosses in Fig. 5, run DO). If that flat portion of data is ignored, run DO has the same shape as run D. However, the asymptotic fouling resistance in run DO is 466 percent higher than that of run D (see Table 4). This corresponds to a 32 percent lower Reynolds number in run DO. Therefore the lower Reynolds number increased the fouling rate in this brine chemistry. This would confirm Wahl's (Wahl et al., 1974) conclusion and refute others (Gudmundsson and Bott, 1979; Felsinger, 1977).

The characteristic shapes of the fouling curves show an "induction period" and an initial drop in resistance for the runs with NaCl and sodium acetate (NaAc). With the exception of TT1B (the induction period of which is not as clearly defined as others, which exhibit a spoon shape), experiments C, D, and DO show that the "induction period" is reduced as pH increases, in agreement with the batch type of experiments (Weres et al., 1979; Rothbaum and Rohde, 1979). The initial drop in resistance was reported in Gudmundsson and Bott (1979) and Bohlman et al. (1981). It is explained as an initial enhancement in heat transfer caused by scale-induced turbulence, which is eventually overcome by the increasing thermal resistance of the deposit. Since the fouling resistance $R_f$ is defined as the difference between the later and the initial total resistances, $R_f = 0$ initially. However, with heat transfer enhancement, the later total resistance is reduced afterward, resulting in negative $R_f$ values as shown in Figs. 5 and 6. All curves then proceed with increasing fouling functions, i.e., linear or asymptotic.

Figure 6 shows the transient local thermal fouling resistance at different locations in the heat exchanger for run TT1-D. This has the same shape as the TT1-D overall curve in Fig. 5. In comparing the curves, there is a drop in the rate of change and in the asymptotically achieved value of resistance at 148 h, as the heat exchanger length (this refers to distance from the inlet of the heat exchanger) increases. Figure 7 is a graph of the asymptotic fouling resistance versus heat exchanger length. The asymptotic value of resistance is reached faster at

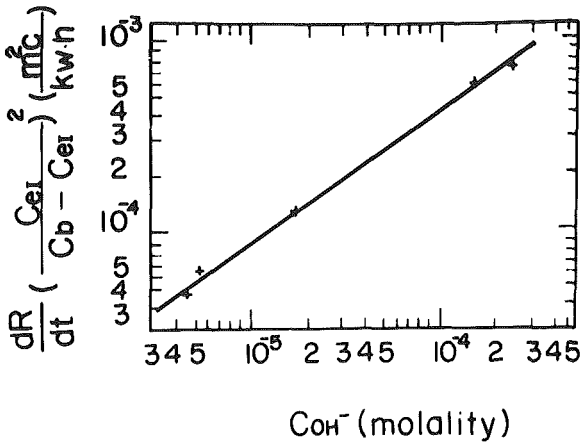


**Fig. 8 Correlation of silica deposition data from two geothermal fields**

the exit than at the inlet locations. For other runs, the local curves have the same shape as the overall curves. For example, for the runs without NaAc (TT1A to TT1C), both local curves and overall curves appear to be linear. From a linear regression analysis (least-square method) undertaken to obtain the local fouling rate ($dR_{fi}/dt$), it is found that the fouling rate decreases with heat exchanger length. Figure 7 also shows the variation in fouling rate versus heat exchanger length for run TT1-C. This contradicts the findings that fouling was heavier at the exit (Gudmundsson and Bott, 1979). The disagreement may be explainable because the latter was based on visual observation of scale thickness while the current study is based on the actual measurement of thermal resistance itself. Examination of fouling surface in our experiments by a boroscope revealed that the scale near the exit had a rough and rippled appearance transverse to the flow direction with high pointed ridges and valleys that left the tube surface exposed. The scale near the inlet had a smoother layer that covered the entire surface, resulting in a higher thermal fouling resistance.

A quantitative chemical analysis of the scale was carried out following the removal of the deposit from the heat transfer surface with a high-pressure water jet. The method of analysis was x-ray spectrometry using a scanning electron microscope. The major component of the scale in all runs as shown in Table 5 is silica, in agreement with the chemicals added in the experimental loop as well as with a survey of natural brine scales made by Wahl (1977).

Even with the high sodium and chlorine content of runs B and C, little of these constituents was found in the scale. However, their presence in the brine makes a great difference in the fouling rate, as seen in Table 4.

## Comparison Between Analytical Predictions and Experimental Results

The analytical model given by equation (1) is used to correlate or to predict silica fouling from natural and synthetic brines. The data and experimental conditions of silica deposition rate on heat transfer surfaces at two geothermal fields in Iceland as reported in Gudmundsson and Bott (1979) appear to be of sufficient detail that meaningful calculations can be made to incorporate supersaturation, pH factor, salinity, and thermal-hydraulic effects in the model.

Figure 8 shows that the experimental deposition rates of silica from both fields can be correlated surprisingly well by equation (1) with $K_R = 0.9954$ and $q = 0.862$. As discussed before, a second order of reaction for dissolved silica (i.e., $p = 2$) has been assumed. However, the comparison of the analytical calculations with the synthetic brine data is not totally satisfactory (see Fig. 5). In Fig. 5, the analytical lines are placed through the lowest values of the resistance curves. The fouling model is not expected to predict run A data since no scale was found in this case. The comparison of run DO is not as poor as it appears since, as discussed above, the flat portion of data was caused by an experimental error and could be ignored. Better agreements are indicated for other runs. But in any case, a further refinement of the analytical model is desirable.

## Conclusions

A review has been made of the fundamental information relevant to silica deposition in aqueous solution. An analytical model and expermental measurements of silica scale deposit have also been presented and discussed. Comparisons between analytical predictions with experimental data are encouraging but are not yet all satisfactory. Due to the complex nature of geothermal fouling and because relatively few quantitative measurements are available, continuation of systematic measurements is needed before a general fouling model can be developed.

## Acknowledgments

This research was sponsored by the National Science Foundation (NSF Grant No. CBT-8311788). The authors also wish to express their gratitude for the assistance of D. Alberts, D. Doers, D. Z. Zhou, and L. S. Lee in the Geothermal Fouling Test Laboratory.

## References

Akerlof, G. C., and Ashry, H. I., 1950, "The Dielectric Constant of Water at High Temperatures and in Equilibrium With Its Vapor," *Am. Chem. Soc. J.*, Vol. 72, pp. 2044–2847.

Alexander, G. B., 1954, "The Polymerization of Monosilicic Acid," *J. Phys. Chem.*, Vol. 76, pp. 2094–2096.

Barnes, H. L., 1979, *Geochemistry of Hydrothermal Ore Deposits*, 2nd ed., Wiley, New York.

Ben Holt Co., 1978, "Geothermal Heat Exchanger Test at Heber, California," RP-846-1, EPRI ER-572, Aug.

Bohlman, E. G., Mesmer, R. E., and Berlinski. P., 1980, "Kinetics of Silica Deposition From Simulated Geothermal Brine," *Society of Petroleum Engineers Journal*, pp. 239–248.

Bohlman, R. G., Shor, A. J., Berlinski, P., and Mesmer, R. R., 1981, "Silica Scaling in Simulated Geothermal Brines," Oak Ridge National Laboratory Report No. ORNL/TM-7681.

Bott, T. R., and Gudmundsson, J. S., 1978, "Rippled Silica Depositions in Heat Exchanger Tubes," *Proceedings of 6th International Heat Transfer Conference*, Toronto, Canada, Aug. 7–11.

Bryers, R. W., 1982, *Fouling of Heat Exchanger Surface*, Proceedings of the Engineering Foundation Conference, White Haven, PA, Oct. 31–Nov. 5.

Busey, R. H., and Mesmer, R. E., 1976, "The Ionization of Water in NaCl Media to 300°C," *J. of Solution Chemistry*, Vol. 5, No. 2, pp. 147–152.

Chan, S. H., Neusen, K. F., Shadid, J., Chou, S. F., and Lin, C. C., 1982, "Geothermal Transient Fouling Heat Transfer Measurements," *Fouling of Heat Exchanger Surfaces*, R. W. Byers, ed., Engineering Foundation, NY.

Chan, S. H., Neusen, K. F., and Chang, C. T., 1987, "The Solubility and Polymerization of Amorphous Silica in Geothermal Energy Applications," *Proceedings of 1987 ASME-JSME Thermal Engineering Joint Conference*, Vol. 3, pp. 103–108.

Chen, C. T. A., and Marshall, W., 1982, "Amorphous Silica Solubilities. IV. Behavior in Pure Water and Aqueous Sodium Chloride, Sodium Sulfate, Magnesium Chloride, and Magnesium Sulfate Solutions up to 350°C," *Geochemica et Cosmochimica Acta*, Vol. 46, pp. 279–287.

Chou, S. F., and Lin, C. C., 1982, "Transient Fouling Heat Transfer in Geothermal Energy," *Proceedings of 1982 Symposium on Transport Phenomena and Application*, Taipei, Taiwan, pp. 14–27.

Chou, S. F., 1985, "An Experimental Study on the Geothermal Fouling in Heat Exchanger," *Proceedings of 1985 Symposium on Transport Phenomena and Applications*, Taipei, Taiwan, pp. 184–189.

Coates, K. E., and Knudsen, J. G., 1980, "Calcium Carbonate Scaling Characteristics of Cooling Tower Water," *ASHRAE Transactions*, Vol. 86, Part 2.

Ellis, A. J., and Mahon, W. A. J., 1977, *Chemistry and Geothermal Systems*, Academic Press, NY.

Epstein, N., 1979, "Fouling in Heat Exchangers," *Heat Transfer 1978—Proceedings of the Sixth International Heat Transfer Conference*, Hemisphere, NY, Vol. 6, pp. 235–253.

Epstein, N., 1981, "Fouling: Technical Aspects (Afterword to Fouling in

Heat Exchangers)," in: *Fouling of Heat Transfer Equipment*, E.F.C. Somerscales and J. G. Knudsen, eds., Hemisphere, Washington, DC, pp. 31–53.

Eusey, R. H., and Mesmer, R. E., 1976, "The Ionization of Water in NaCl Media to 300°C," *J. Solution Chemistry*, Vol. 5, No. 2, pp. 147–152.

Felsinger, D. E., Mulliner, D. K., and Bishop, H. K., 1973, "Geothermal Field Tests Heat Exchanger Evaluation," San Diego Gas & Electric Co. report.

Fischer, P., Suitor, J. W., and Ritter, R. B., 1975, "Fouling Measurement Techniques," *Chem. Eng. Prog. Symp. Ser.*, Vol. 17, No. 7, pp. 66–72.

Fleming, B. A., 1981, *Polymerization Kinetics and Ionization Equilibria in Aqueous Silica Solutions*, Ph.D. Dissertation, Dept. Chem. Eng., Princeton University, Princeton, NJ.

Fournier, R. O., 1970, "Silica in Thermal Waters: Laboratory and Field Investigations," in: *Proc. Int. Symp. on Hydrogeochemistry and Biogeochemistry*, Tokyo, Sept. 7–9, pp. 122–139.

Fournier, R. P., and Rowe, J. J., 1977, "The Solubility of Amorphous Silica in Water at High Temperatures and Pressure," *American Mineralogist*, Vol. 52, pp. 1052–1056.

Gazit, E., and Hasson, D., 1975, "Scale Deposition From an Evaporating Falling Film," *Desalination*, Vol. 17, pp. 339–351.

Gudmundsson, J. S., and Bott, T. R., 1979, "Deposition of Silica From Geothermal Waters on Heat Transfer Surfaces," *Desalination*, Vol. 28, pp. 125–145.

Hasson, D., 1962, "Rate of Decrease of Heat Transfer Due to Scale Deposition," *Deutsche Gesellschaft fur Chemisches Apparatewesen*, Vol. 47, pp. 233–252.

Hasson, D., Avriel, M., Resnick, W., Rozenman, T., and Windreich, S., 1968, "Mechanism of Calcium Carbonate Scale Deposition on Heat-Transfer Surfaces," *I&EC Fundamentals*, Vol. 7, No. 1, pp. 59–65.

Hasson, D., Sherman, H., and Biton, M., 1978, "Prediction of $CaCO_3$ Scaling Rates," *Proceedings 6th International Symposium Fresh Water From the Sea*, Vol. 2, 1978, pp. 193–199.

Hasson, D., and Pearl, I., 1981a, "Scale Deposition in a Laminar Falling-Film System," *Desalination*, Vol. 37, pp. 279–292.

Hasson, D. 1981b, "Precipitation Fouling," in: *Fouling of Heat Transfer Equipment*, E.F.C. Somerscales and J. G. Knudsen, eds., Hemisphere, Washington, DC, pp. 527–268.

Hoffmann, M. R., 1975, "Brine Chemistry—Scaling and Corrosion—Geothermal Research Study in the Salton Sea Region of California," Environmental Quality Laboratory, California Institute of Technology, EQL Memorandum No. 14.

Iler, R. K., 1953, "Polymerization of Polysilicia Acid Derived from 3.3 Ratio Sodium Silicate," *J. Phys. Chem.*, Vol. 56, pp. 604–607.

Iler, R. K., 1955, *The Colloid Chemistry of Silica and Silicates*, Cornell University Press, Ithaca, NY.

Iler, R. K., 1979, *The Chemistry of Silica—Solubility, Polymerization, Colloid and Surface Properties, and Biochemistry*, Wiley, NY.

Kern, D. Q., and Seaton, R. E., 1959, "A Theoretical Analysis of Thermal Surface Fouling," *British Chemical Engineering*, Vol. 4, pp. 258–262.

Knudsen, J. G., 1981, "Cooling Water Fouling—A Brief Review," *Fouling in Heat Exchange Equipment*, HTD-Vol. 17, 20th ASME/AIChE Heat Transfer Conference, Milwaukee, WI, Aug. 2–5.

Krauskopf, K. B., 1956, "Dissolution and Precipitation of Silica at Low Temperature," *Geochimica et Cosmochimica Acta*, Vol. 10, pp. 1–26.

Lee, S. H., and Knudsen, J. G., 1979, "Scaling Characteristics of Cooling Tower Water," *ASHRAE Transactions*, Vol. 85, Part I.

Lin, C., and Lindsay, W. T., 1972, "Thermodynamics of Sodium Chloride Solutions at High Temperature," *J. of Solution Chemistry*, Vol. 1, No. 1, pp. 45–69.

Lowenthal, R. E., and Marais, G. V. R., 1976, *Carbonate Chemistry of Aquatic Systems: Theory and Application*, Ann Arbor Science, Ann Arbor, MI.

Lombard, G. L., 1978, "Heat Exchanger Tests With Moderately Scaling Geothermal Brine," *AIChE Symp. Series No. 174*, Vol. 74, pp. 281–287.

Malmberg, C. G., and Maryott, A. A., 1956, "Dielectric Constant of Water From 0° to 100°C," *J. of Research of the National Bureau of Standards*, Vol. 56, No. 1, pp. 1–8.

Marshall, W. L., 1980a, "Amorphous Silica Solubilities—I. Behavior in Aqueous Sodium Nitrate Solutions; 20–300°C, 0-6 Molal," *Geochimica et Cosmochimica Acta*, Vol. 44, pp. 907–913.

Marshall, W. L., and Warakomski, J. M., 1980b, "Amorphous Silica Solubilities—II, Effect of Aqueous Salt Solutions at 25°C," *Geochimica et Cosmochmica Acta*, Vol. 44, pp. 915–924.

Millro, F. J., 1982, "The Effect of Pressure on the Solubility of Minerals in Water and Seawater," *Geochimica et Cosmochimica Acta*, Vol. 46, pp. 11–22.

Mines, G. L., and Neill, D. I., 1978, "Analysis of Raft River Heat Exchanger Fouling Data Using a Multivariate Regression Technique," EG&G Inc., Idaho Falls, ID.

Nancollas, G. H., and Reddy, M. M., 1971, "The Crystallization of Calcium Carbonate. II. Calcite Growth Mechanism," *J. of Colloid and Interface Science*, Vol. 37, No. 4, pp. 824–830.

Okamota, G., Okura, T., and Goto, K., 1957, "Properties of Silica in Water," *Geochimica et Cosmochimica Acta*, Vol. 12, pp. 123–132.

Pritchard, A. M., 1981, "Fouling—Science or Art? An Investigation of Fouling and Anti-fouling Measures in the British Isles," in: *Fouling of Heat Transfer Equipment*, E.F.C. Somerscales and J. G. Knudsen, eds., Hemisphere, Washington, DC, pp. 513–523.

Reddy, M. M., and Nancollas, G. H., 1971, "The Crystallization of Calcium Carbonate, I. Isotopic Exchange and Kinetics," *J. of Colloid and Interface Science*, Vol. 36, p. 166.

Roques, H., and Girou, A., 1974, "Kinetics of the Formation Conditions of Carbonate Tartars," *Water Research*, Vol. 8, pp. 907–920.

Rothbaum, H. P., and Rohde, A. G., 1979, "Kinetics of Silica Polymerization and Deposition From Dilute Solutions Between 5 and 180°C," *J. of Colloid and Interface Science*, Vol. 71, No. 3, pp. 533–559.

San Diego Gas and Electric, 1980, "Geothermal Loop Experimental Facility," DOE Contract #DE-AC03-76ETZ8443, Final Report.

Somerscales, E. F. C., and Knudsen, J. G., ed., 1981, *Fouling of Heat Transfer Equipment*, Hemisphere, Washington, DC.

Suitor, J. W., Marner, W. J., and Ritter, R. B., 1977, "The History and Status of Research in Fouling of Heat Exchangers in Cooling Water Service," *The Canadian Journal of Chemical Engineering*, Vol. 55, pp. 374–380.

Taborek, J., Aoki, T., Ritter, R. B., Palen, J. W., and Knudsen, J. G., 1972, 1972a, "Fouling: The Major Unresolved Problem in Heat Transfer (Parts I and II)," *Chemical Engineering Program*, Vol. 68, No. 2, pp. 59–67; Vol. 68, No. 7, pp. 69–78.

Taborek, J., Aoki, T., Ritter, R. B., Palen, J. W., and Knudsen, J. G., 1972b, "Predictive Methods for Fouling Behavior," *Chemical Engineering Progress*, Vol. 68, No. 7, pp. 69–78.

Truesdell, A. H., and Jones, B. F., 1974, "Water, a Computer Program for Calculating Chemical Equilibrium of Natural Waters," *J. Research U. S. Geol. Survey*, Vol. 2, No. 2, pp. 233–248.

Wahl, E. F., Yen, I. K., and Bartel, W. J., 1974, "Silica Scale Control in Geothermal Brines," Office of Saline Water, U.S. Department of Int., Washington, DC, Report #14-30-3-41.

Wahl, E. F., 1977, *Geothermal Energy Utilization*, Wiley, NY.

Watkinson, A. P., and Martinez, O., 1975, "Scaling of Heat Exchanger Tubes by Calcium Carbonate," ASME JOURNAL OF HEAT TRANSFER, Vol. 97, pp. 504–508.

Weres, O., Yee, A. W., and Tsao, L., 1979, "Kinetic Equations and Type Curves for Predicting the Precipitation of Amorphous Silica From Geothermal Brines," SPE of AIME International Symposium on Oilfield and Geothermal Chemistry, Houston, TX, Jan. 22–24, paper SPE 7888.

Weres, O., Yee, A., and Tsao, L., 1980, "Kinetics of Silica Polymerization," Lawrence Berkeley Laboratory, Report LBL-7033.

Weres, O., Yee, A., and Tsao, L., 1981, "Kinetics of Silica Polymerization," *J. of Colloid and Interface Science*, Vol. 84, No. 2, pp. 379–402.

Weres, O., Yee, A., and Tsao, L., 1982, "Equations and Type Curves for Predicting the Polymerization of Amorphous Silica in Geothermal Brines," *Society of Petroleum Engineers J.*, Feb., pp. 9–16.

Wiechers, H. N. S., Sturrock, P., and Marais, G. V. R., 1975, "Calcium Carbonate Crystallization Kinetics," *Water Research*, Vol. 9, pp. 835–845.

# Analytical Solution for Unsteady Heat Transfer in a Pipe

**J. Sucec**
Professor of Mechanical Engineering,
University of Maine,
Orono, ME 04469
Mem. ASME

*Under consideration is transient, convective heat transfer to a fluid flow within a pipe due to a sudden change in the temperature of the ambient medium outside the pipe. A solution is developed by the Laplace transformation, for the fastest portion of the transient, which gives the pipe wall temperature, surface heat flux, and fluid bulk mean temperature. These analytical results are compared with available finite difference results and with quasi-steady solutions. A criterion is developed that indicates when the zero thermal capacity wall solution can be used with adequate accuracy.*

## Introduction

In the design and analysis of coolant passages in gas turbine power plants, nuclear reactors, and heat exchangers, knowledge of transient forced convection heat transfer to a fluid in a pipe is required as a function of time.

Normally, the fastest portion of the transient occurs in time domain I where downstream locations in the pipe have not yet been reached by any of the fluid that was at the pipe inlet at the start of the transient.

The simplest approach to unsteady-state convective heat transfer analysis is the quasi-steady approach, which usually uses a constant surface coefficient of heat transfer $h$. Tan and Spinner (1978) and Li (1986) give solutions by this quasi-steady approach. One of the factors controlling the rapidity of the transient convection process is the ratio of the thermal energy storage capacity of the fluid to that of the wall; for large values of this ratio, the quasi-steady results may be suspect.

Krishnan (1982) analyzes the case of a pipe undergoing a transient due to a step change in either surface temperature or heat flux at its outside surface. An analytical solution is found by Laplace transforms for the inside pipe wall temperature in time domain I for times short enough to allow a thermal boundary layer. Chen et al. (1983) employ finite differences on a problem similar to that of Krishnan.

Lin et al. (1983) consider the unsteady-state situation in which an outside, ambient fluid has its temperature suddenly changed and through a constant heat transmission coefficient between it and the inside pipe wall, communicates this change to the fluid inside the pipe.

## Analysis

In the physical situation, a fluid, initially at temperature $T_i$ throughout, is moving within a circular pipe of radius $R$ in a constant property, laminar, fully developed hydrodynamically fashion without appreciable viscous dissipation. A sudden change in the outside ambient medium temperature to $T_L$ initiates the unsteadiness. Axial conduction is neglected, as is the temperature drop across the pipe wall of thickness $b$.

For the conditions stated, an energy balance on the fluid and then on the wall of thickness $b$ and use of the conjugation conditions of flux and temperature continuity at $y=0$ give the partial differential equations along with their side conditions.

In time domain I, $t<x/u_{\max}$, so that for the boundary condition being considered, $\partial T/\partial x=0$, and the nondimensional problem statement becomes as follows in terms of a dimensionless radial coordinate $z=r/R$. In time domain I, $F\leq X/2$,

$$\frac{\partial^2\phi}{\partial z^2}+\frac{1}{z}\frac{\partial\phi}{\partial z}=\frac{\partial\phi}{\partial F} \tag{1}$$

$$\phi(0,z)=0,\quad z=0,\quad F>0,\quad \partial\phi/\partial z=0 \tag{2}$$

$$z=1,\ F>0,\quad \frac{\partial\phi}{\partial z}=S(1-\phi)-\frac{(1+b/2R)}{\hat{a}}\frac{\partial\phi}{\partial F} \tag{3}$$

The velocity profile, which is needed even in time domain I so that the bulk mean temperature can be calculated, is given by

$$u(z)=2u_m[1-z^2] \tag{4}$$

## Solution of Equations

Applying the Laplace transform with respect to $F$ to equations (1)-(3) gives

$$\frac{d^2\bar{\phi}}{dz^2}+\frac{1}{z}\frac{d\bar{\phi}}{dz}=p\bar{\phi} \tag{5}$$

At $z=0$, $d\bar{\phi}/dz=0$

$$z=1,\quad \frac{d\bar{\phi}}{dz}=S\left(\frac{1}{p}-\bar{\phi}\right)-\frac{p}{\hat{a}}(1+b/2R)\bar{\phi} \tag{6}$$

Solving equation (5) and applying the conditions of equation (6) gives the solution in the transform plane as

$$\bar{\phi}(z,p)=\frac{I_o(\sqrt{p}z)}{p\left\{\left[1+\dfrac{p(1+b/2R)}{\hat{a}S}\right]I_o(\sqrt{p})+\dfrac{\sqrt{p}}{S}I_1(\sqrt{p})\right\}} \tag{7}$$

The wall temperature in the transform plane is found by setting $z=1$ in equation (7).

Next, for the limiting condition, $\hat{a}\to\infty$, considered by Lin et al. (1983), where the storage capacity of the wall material is small compared to that of the fluid, the term containing $\hat{a}$ in the denominator of equation (7) vanishes. This condition may occur if a liquid is the flowing fluid in the pipe. A criterion that establishes the conditions under which an actual, finite value of $\hat{a}$ can be adequately represented by the solution for $\hat{a}\to\infty$ will be developed later.

Since the analysis is already restricted to time domain I, which, relatively speaking, occurs at the shorter times $F$, corresponding to large $p$ in the transform plane, a short-time solution is sought by using the large-argument expansions of the Bessel functions of equation (7) as available in Abramowitz and Stegun (1965). This type of solution is more appropriate than is the direct eigenfunction solution of equation (1) because of the number of terms that would be required for adequate convergence at small values of time $F$. In addition, the type of solution being developed here can, without too much more additional effort, be applied to cases of finite

Contributed by the Heat Transfer Division and presented at the ASME Winter Annual Meeting, Anaheim, California, December 7-12, 1986. Manuscript received by the Heat Transfer Division July 27, 1987. Keywords: Forced Convection, Heat Exchangers, Transient and Unsteady Heat Transfer.

$\hat{a}$ by retention of the term containing $\hat{a}$ in equation (7). This extension is not possible for the eigenfunction solution procedure since the problem is no longer of the Sturm Liouville type. After introducing these expansions into equation (7), setting $z=1$, performing the division, and inverting the result term by term, one gets the analytical solution for the wall temperature as given next:

$$\phi_w(F) = S\left\{\frac{2\sqrt{F}}{\sqrt{\pi}} + (b_1 - C_{01})F + \frac{4e_1F^{3/2}}{3\sqrt{\pi}} + \frac{(e_2 - C_{01}e_1)F^2}{2} + \frac{8f_1F^{5/2}}{15\sqrt{\pi}} + (f_2 - C_{01}f_1)\frac{F^3}{6} + \frac{16g_1F^{7/2}}{105\sqrt{\pi}} + (g_2 - C_{01}g_1)\frac{F^4}{24} + \frac{32h_1F^{9/2}}{945\sqrt{\pi}} + (h_2 - C_{01}h_1)\frac{F^5}{120} + \frac{64i_1F^{11/2}}{10{,}395\sqrt{\pi}} + \frac{(i_2 - C_{01}i_1)F^6}{720} + \ldots\right\} \quad (8)$$

$$r_n = \frac{(4k^2-1^2)(4k^2-3^2)\ldots(4k^2-[2n-1]^2)}{n!8^n} \quad (9)$$

$$a_n = |r_n|_{k=1}, \quad b_n = |r_n|_{k=0}, \quad C_{n,n+1} = Sb_n - a_{n+1} \quad (10)$$

$$e_n = b_{n+1} - C_{n,n+1} - C_{n-1,n}(b_1 - C_{01}) \quad (11)$$

$$f_n = e_{n+2} - C_{n,n+1}e_1 - C_{n-1,n}(e_2 - C_{01}e_1) \quad (12)$$

$g_n$ is given by equation (12) with the $e$ values replaced by $f$ on the right side, $h_n$ is given by equation (12) with the $e$'s replaced by corresponding $g$'s, and $i_n$ is found by replacing the $e$'s on the right side of equation (12) by $h$ values.

In order to get an expression for the bulk mean temperature, its definition, equation (13), is put into nondimensional form, then the velocity profile, equation (4), is inserted and the Laplace transform is taken. This gives

$$T_B = \frac{2}{R^2}\int_0^R \frac{u}{u_m} Tr dr \quad (13)$$

$$\bar{\phi}_B(p) = 4\int_0^1 (z - z^3)\bar{\phi} dz \quad (14)$$

After inserting $\bar{\phi}(z, p)$ from equation (7), integration by parts and using an integral given in Luke (1962) yields,

$$\bar{\phi}_B(p) = \frac{8SI_2(\sqrt{p})}{p^2[\sqrt{p}I_1(\sqrt{p}) + SI_o(\sqrt{p})]} \quad (15)$$

(In the event that time $F$ is large enough so that the eigenfunction solution would be used instead, a referee has kindly pointed out that the bulk mean temperature can be found by means of the same integration that gave equation (15) if one replaces the modified Bessel function $I$ by the ordinary Bessel function $J$.)

After employing the large-argument expansions in equation (15), dividing and inverting term by term results in

$$\phi_B(F) = 8S\left\{\frac{4F^{3/2}}{3\sqrt{\pi}} - (w_1 + C_{01})\frac{F^2}{2} + \frac{8l_1}{15\sqrt{\pi}}F^{5/2} + (l_2 - C_{01}l_1)\frac{F^3}{6} + \frac{16m_1}{105\sqrt{\pi}}F^{7/2} + (m_2 - C_{01}m_1)\frac{F^4}{24} + \frac{32n_1F^{9/2}}{945\sqrt{\pi}} + \frac{(n_2 - C_{01}n_1)F^5}{120} + \frac{64q_1F^{11/2}}{10{,}395\sqrt{\pi}} + \ldots\right\} \quad (16)$$

$$w_n = |r_n|_{k=2}, \quad l_n = w_{n+1} - C_{n,n+1} + C_{n-1,n}(w_1 + C_{01}) \quad (17)$$

$$m_n = l_{n+2} - C_{n,n+1}l_1 - C_{n-1,n}(l_2 - C_{01}l_1) \quad (18)$$

$n_n$ is given by the right side of equation (18) with $l$ replaced by $m$ and $q_n$ is given by equation (18) when $l$ is replaced by $n$.

The nondimensional flux $Q_w$ can be obtained, for $\hat{a} \to \infty$, by the following simple expression:

$$Q_w = 2S[1 - \phi_w] \quad (19)$$

For very large values of $S$, it is found that the series solutions, equations (8) and (16), are convergent only for very small values of time $F$. This is remedied by a rearrangement of the expansions used in the divisions required by equations (7) and (15) so that, in effect, the quotient is given in terms of powers of $S^{-1}$ instead of $S$.

Defining

$$a'_n = a_n/S, \quad C'_{n,n+1} = b_n - a'_{n+1}, \quad d_{n,n+1} = C'_{n,n+1}/C'_{01} \quad (20)$$

## Nomenclature

$\hat{a}$ = $\rho c_p R/\rho_w c_{pw} b$ = ratio of thermal energy storage capacity of fluid to wall material

$b$ = pipe wall thickness

$B_0, B_1, B_2$ = series defined by equations (21), (22), and (23)

$c_p, c_{pw}$ = specific heat capacity of fluid and pipe wall, respectively

$F$ = $\alpha t/R^2$ = Fourier number

$h$ = local surface coefficient of heat transfer between inside of pipe wall and inside flowing fluid

$I_0, I_1, I_2$ = modified Bessel functions of the first kind

$k$ = thermal conductivity of the inside fluid; also, an index used in equations (9), (10), and (17)

Nu = $h(2R)/k$ = Nusselt number

$n$ = index

$p$ = Laplace transform parameter

$q_w$ = local, instantaneous surface heat flux at inside of pipe

$Q_w$ = $2Rq_w/k(T_L - T_i)$ = nondimensional surface heat flux

$r$ = radial coordinate from pipe center line

$R$ = pipe inside radius

$S$ = $UR/k$

$t$ = time

$T$ = local instantaneous fluid temperature

$T_B, T_L, T_i$ = bulk mean, ambient, and initial, as well as inlet, temperature, respectively

$U$ = overall heat transmission coefficient between ambient fluid outside of pipe and inside pipe wall, based on inside surface area

$u, u_m, u_{\max}$ = local, mass average and maximum, fluid velocity

$x$ = space coordinate along pipe

$X$ = $\alpha x/R^2 u_m$

$y$ = space coordinate perpendicular to pipe wall

$z$ = $r/R$

$\alpha$ = $k/\rho c_p$ = thermal diffusivity of inside fluid

$\theta$ = $(T(x, y, t) - T_L)/(T_i - T_L) = 1 - \phi$

$\theta_w, \theta_B$ = $1 - \phi_w, 1 - \phi_B$, respectively

$\rho, \rho_w$ = mass density of inside fluid and wall, respectively

$\phi$ = $(T(x, y, t) - T_i)/(T_L - T_i)$

$\phi_w, \phi_B$ = wall and bulk mean values of $\phi$, respectively

$|\ |$ = absolute value of

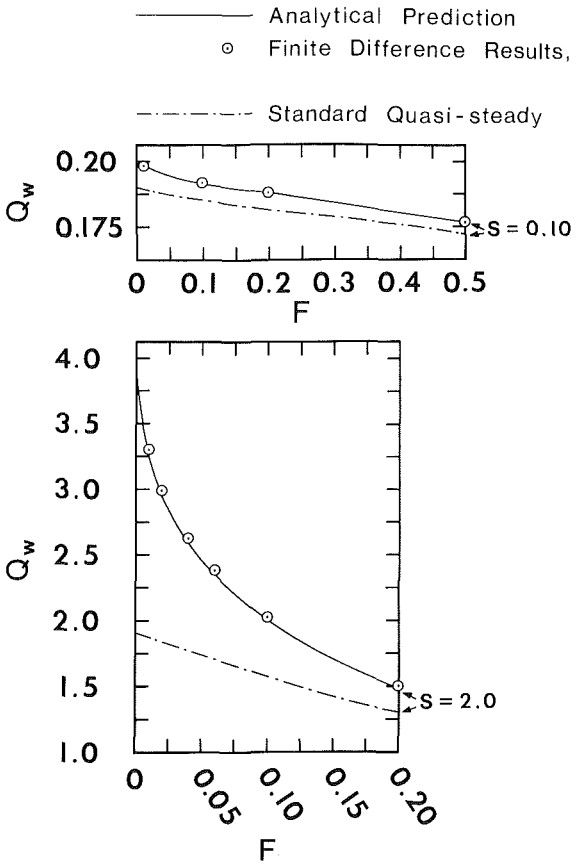


Fig. 1 Comparison of analytical, finite difference (Lin et al., 1983) and quasi-steady solutions for surface heat flux

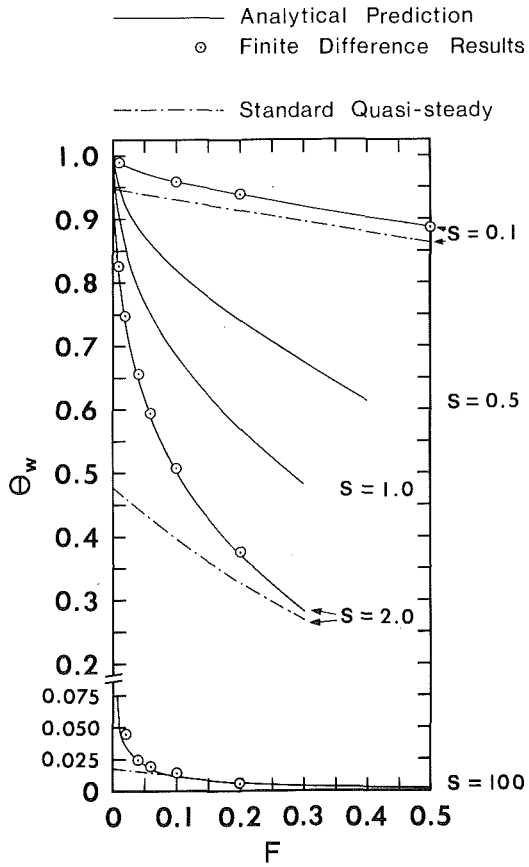


Fig. 2 Wall temperature, $\theta_w = 1 - \phi_w$, versus time and comparison with finite difference (Lin et al., 1983) and quasi-steady solutions

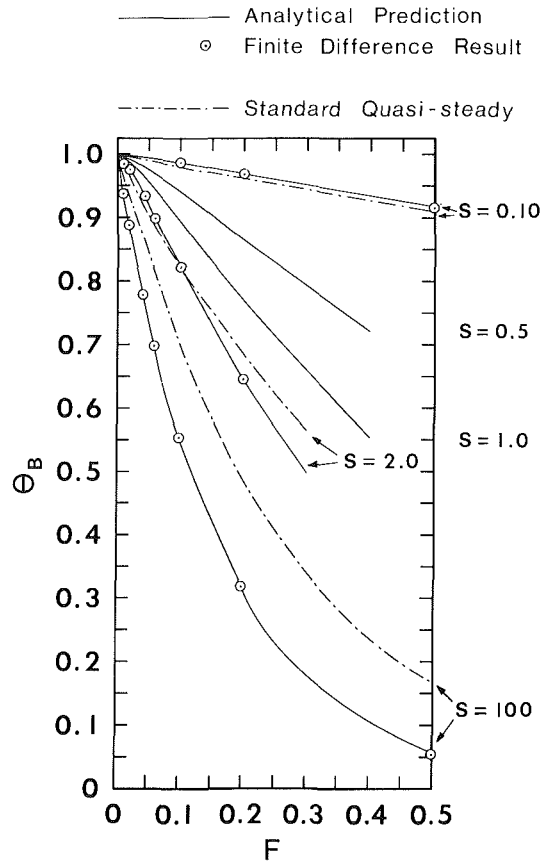


Fig. 3 Bulk mean temperature, $\theta_B = 1 - \phi_B$, versus time and comparison with finite difference (Lin et al., 1983) and quasi-steady solution

$$B_o = \frac{1}{p^{1/2}} + \frac{d_{12}}{p} + \ldots + \frac{d_{n,n+1}}{p^{(n+1)/2}} + \ldots + \frac{1}{SC'_{01}} \tag{21}$$

$$B_1 = \frac{8}{C'_{01}p^{5/2}}\left[1 - \frac{w_1}{p^{1/2}} + \frac{w_2}{p} + \ldots + \frac{w_n}{p^{n/2}} + \ldots\right] \tag{22}$$

$$B_2 = \frac{1}{C'_{01}p^{3/2}}\left[1 + \frac{b_1}{p^{1/2}} + \frac{b_2}{p} + \ldots + \frac{b_n}{p^{n/2}} + \ldots\right] \tag{23}$$

Then, for large values of $S$

$$\theta_w(F) = B_2/B_o, \quad \theta_B(F) = B_1/B_o \tag{24}$$

The divisions in equation (24) lead to recursive-type relations of a form similar to those previously given as equations (17), (18), etc. If desired, the transient Nusselt number can now be found as $\mathrm{Nu} = Q_w/(\phi_w - \phi_B)$.

## Quasi-Steady Approach

Energy balances on the moving fluid and solid wall, respectively, in time domain I, give

$$\frac{\partial \phi_{BqS}}{\partial F} = \mathrm{Nu}(\phi_{wqS} - \phi_{BqS}) \tag{25}$$

$$\frac{2}{\hat{a}}\frac{\partial \phi_{wqs}}{\partial F} + \mathrm{Nu}[\phi_{wqs} - \phi_{Bqs}] = 2S[1 - \phi_{wqS}] \tag{26}$$

Solving equations (25) and (26) simultaneously leads to the following quasi-steady response functions for $\hat{a} \to \infty$:

$$\phi_{wqS} = 1 - \left(\frac{\mathrm{Nu}}{\mathrm{Nu} + 2S}\right)e^{-2S\mathrm{Nu}F/(\mathrm{Nu}+2S)} \tag{27}$$

$$\phi_{BqS} = 1 - e^{-2S\mathrm{Nu}F/(\mathrm{Nu}+2S)} \tag{28}$$

## Criterion for Validity of $\hat{a} \to \infty$ Solution

To develop an analytic criterion to determine the range of

finite $\hat{a}$ values for which the limiting "no wall" solution, $\hat{a}\to\infty$, is an acceptable approximation, equations (25) and (26) will be considered further. A simple and easy-to-study solution can be effected by successive approximations as follows. As a first approximation for $\phi_{BqS}$, take $\phi_{BqS}\approx 0$, which is essentially correct at very low $F$. This is then used in equation (26) to solve for $\phi_{wqs}$, which is then used in equation (25) to get an improved approximation to $\phi_{Bqs}$. Using this, the ratio of $\phi_{Bqs}$ for finite $\hat{a}$ to that for $\hat{a}\to\infty$ is formed to yield the following, after definition of $V$ as $V=\hat{a}(\mathrm{Nu}+2S)/2\mathrm{Nu}$:

$$\frac{(\phi_{Bqs})_{\hat{a}}}{(\phi_{Bqs})_{\hat{a}\to\infty}}=1-\frac{[e^{-V\mathrm{Nu}F}-e^{-\mathrm{Nu}F}]}{(1-V)[1-e^{-\mathrm{Nu}F}]} \tag{29}$$

Requiring that the bulk mean temperature excess for finite $\hat{a}$ be within 5 percent of the value for $\hat{a}\to\infty$ for all $F>0.02$ yields the criterion $\hat{a}\geq 520/(1+2S/\mathrm{Nu})$. Next, equations (25) and (26) were solved without any approximations and the comparison of the solutions for finite $\hat{a}$ to those for $\hat{a}\to\infty$ leads to a criterion virtually the same as the one arrived at with the approximate solution of equation (29). The 520 becomes 540 and this number exhibits a separate dependence upon $\mathrm{Nu}/2S$, so slight as to be negligible. Thus, we take the criterion to be as follows:

$$\hat{a}\geq\frac{540}{1+2S/\mathrm{Nu}} \tag{30}$$

## Results and Discussion

The main analytical results of the present work are given by equations (8) and (24) for the wall temperature, equations (16) and (24) for the bulk mean temperature of the fluid, and equation (19) for the surface heat flux, all as functions of nondimensional time $F$, and the parameter $S$. Values of $S$ included those of Lin et al. (1983), namely, 0.10, 2.0, and 100, as well as 0.5 and 1.0 as typical of this parameter's size over a wide range of $S$. Plots of the results are given in Figs. 1–3.

The analytical solution of the present work and the finite difference solution of Lin et al. (1983) were both compared, for $S=100$, to the limiting, $S\to\infty$, exact solution given in Siegel (1960). It was found that the numerical results of Lin et al. (1983) for the surface heat flux were 70 percent too high at $F=0.01$ and about 5 percent high at $F=0.10$ because the lattice was not sufficiently refined during the most rapid part of the transient, a lack of agreement also noted by the authors in Lin et al. (1983). On the other hand, the present analytical results are virtually coincident with those of Siegel (1960).

Comparison between the present analytical predictions and the finite difference predictions of Lin et al. (1983) are shown in Figs. 1, 2, and 3 for the heat flux, wall temperature, and fluid bulk mean temperature respectively. Agreement is seen to be excellent for $S=0.10$ up to $F=0.5$, which is also the point at which the series in equations (8) and (16) begins to exhibit tendencies that, at larger $F$, will lead to nonconvergence. For the more rapid transient, $S=2.0$, agreement between the present analytical series solutions and the finite difference results of Lin et al. (1983) is very good up to $F=0.20$ with the above-noted tendency toward divergence being first evident at $F=0.30$. At the largest value of $S$, $S=100.0$, the series in equations (8) and (16) diverges at very small values of $F$, necessitating the rearrangement of the expansions as shown in equations (20)–(23), giving equation (24), which is used for the $S=100$ case. Once again it is seen that the agreement between the analytical predictions and the finite difference results of Lin is very good.

With the dimensionless time, $F$, region of validity established for the analytical solution, in the first time domain, the analytical solution complements the numerical solution of Lin et al. (1983) at the low times and the high values of $S$, which would require extremely small time steps to achieve convergence. Extension of the results takes place when the analytical solution is used to generate the response functions at values of $S$ other than the three given in Lin et al. (1983), such as was done at $S=0.5$ and 1.0 in Figs. 2 and 3. This can be done quickly and economically since only elementary functions are required.

The quasi-steady predictions given by equations (27) and (28) are plotted as dashed dot curves in Figs. 1, 2, and 3, and it is evident that its performance is acceptable only for $S\leq 0.10$, which corresponds to the slowest of the transients.

Finally, the question of assuming negligible thermal energy storage capacity of the pipe wall relative to that of the inside fluid, letting $\hat{a}\to\infty$ as was done in Lin et al. (1983) and in equation (7) of the present work, is dealt with. In particular, the practically important question is for what conditions, such as values of $\hat{a}$, will the solutions for $\hat{a}\to\infty$ adequately predict the results for finite $\hat{a}$ ? Tan and Spinner (1978) give some very rough, incomplete criteria in their work. Thus, it was decided to derive an appropriate criterion by making the analytical study which culminated in equation (30).

The criterion, equation (30), was based on fluid bulk mean temperature, because the wall temperature requires a much less severe criterion and hence is even more closely approximated by the $\hat{a}\to\infty$ solutions when equation (30) is satisfied. For example, at $F=0.02$, when the equal sign in equation (30) leads to 5 percent agreement in $\phi_B$, the agreement for $\phi_w$ is within 0.7 percent. Additional support for the criterion, equation (30), was generated by comparison of the finite $\hat{a}$ and infinite $\hat{a}$ fluid temperature solutions given in Clark et al. (1958), for a different type of transient, namely a step change in generation within the pipe wall and no convection to the ambient. If $S$ is set equal to zero in equation (30), the criterion $\hat{a}\geq 540$ serves very well in this case also. Unpublished finite difference results by the author for a different geometry, the parallel plate duct, also show acceptable agreement with equation (30) for the case of $S=2.0$. Since the solutions given in Tan and Spinner (1978), Clark et al. (1958), and as equation (29) of this work are quasi-steady solutions, the value of Nu used in equation (30) for the various comparisons was $\mathrm{Nu}=3.66$. Of course, since the criterion was based on quasi-steady solutions, it must be treated as a guide for an actual transient as to when the limiting solution of $\hat{a}\to\infty$ will acceptably represent the case of finite $\hat{a}$.

It is interesting to see the wide range of minimum values of $\hat{a}$ required, in order that the $\hat{a}\to\infty$ solution be adequate, depending upon the value of $S$. From equation (30), it is found that for $S=0.1$, $\hat{a}\geq 512$, for $S=2.0$, $\hat{a}\geq 258$, and for $S=100$, $\hat{a}\geq 10$.

It is felt that the criterion, equation (30), is an important result because it allows effective, practical use and application of the limiting solution presented in this work, as well as that of Lin et al. (1983), Li (1986), and numerous other transient convection solutions in the literature that utilize the limit of $\hat{a}\to\infty$.

## Conclusion

The analytical solution developed for the unsteady pipe wall temperature, surface heat flux, and fluid bulk mean temperature represents an easier, faster to use, more economical alternative to finite difference solutions in the most rapid part of the transient in the first time domain. Furthermore, the basic procedure can be easily extended to handle the more general case of finite $\hat{a}$.

By working in the Laplace transform plane, the bulk mean temperature can be predicted without knowledge of the moving fluid's temperature profile in the physical plane.

The criterion developed in the present work allows one to apply the various available solutions for the limiting situation of $\hat{a}\to\infty$ to practical cases of finite values of $\hat{a}$ for both the

type of transient convection problem considered here and for other types as well.

For the transients considered herein, the quasi-steady approach can be badly in error and should not be employed unless $S \leq 0.10$.

## References


Abramowitz, M., and Stegun, I., eds., 1965, *Handbook of Mathematical Functions*, Dover, New York.

Chen, S. C., Anand, N. K., and Tree, D. R., 1983, "Analysis of Transient Laminar Convective Heat Transfer Inside a Circular Duct," ASME JOURNAL OF HEAT TRANSFER, Vol. 105, pp. 922–924.

Clark, J. A., Arpaci, V. S., and Treadwell, K. M., 1958, "Dynamic Response of Heat Exchangers Having Internal Heat Sources – Part I," *Trans. ASME*, Vol. 80, pp. 612–624.

Krishnan, B., 1982, "On Conjugated Heat Transfer in Fully Developed Flow," *Int. J. Heat Mass Transfer*, Vol. 25, pp. 288–291.

Li, Chung-Hsiung, 1986, "Exact Transient Solutions of Parallel-Current Transfer Processes," ASME JOURNAL OF HEAT TRANSFER, Vol. 108, pp. 365–369.

Lin, T. F., Hawks, K. H., and Leidenfrost, W., 1983, "Unsteady Thermal Entrance Heat Transfer in Laminar Pipe Flows With Step Change in Ambient Temperature," *Warme- und Stoffubertragung*, Vol. 17, pp. 125–132.

Luke, Y. H., 1962, *Integrals of Bessel Functions*, McGraw-Hill, New York.

Siegel, R., 1960, "Heat Transfer for Laminar Flow in Ducts With Arbitrary Time Variations in Wall Temperature," ASME *Journal of Applied Mechanics*, Vol. 27, pp. 241–249.

Tan, K. S., and Spinner, I. H., 1978, "Dynamics of a Shell and Tube Heat Exchanger With Finite Tube Wall Capacity and Finite Shell Side Resistance," *Ind. Eng. Chem. Fundam.*, Vol. 17, pp. 353–358.

# Three-Dimensional Laminar Heat Transfer and Fluid Flow Characteristics in the Entrance Region of a Rhombic Duct

**Y. Asako**
Associate Professor,
Department of Mechanical Engineering,
Tokyo Metropolitan University,
Tokyo, 158, Japan

**M. Faghri**
Associate Professor,
Department of Mechanical Engineering,
University of Rhode Island,
Kingston, RI 02881
Mem. ASME

*A solution methodology is developed to obtain three-dimensional fluid flow and heat transfer characteristics in the entrance region of a rhombic duct. Owing to the complexity of the geometry, the literature results are limited to the fully developed values. The numerical methodology is based on an algebraic coordinate transformation technique, which maps the complex cross section onto a rectangle, coupled with a calculation procedure for three-dimensional parabolic flows, which reduces the problem to a series of two-dimensional problems. The Nusselt number and friction factor results are obtained for boundary conditions of uniform wall heat flux and uniform wall temperature. The asymptotic values of the Nusselt numbers and friction factors approach the available fully developed results. The entry length results for the limiting case of $\phi = 90$ deg are in perfect agreement with the available experimental and numerical results for a rectangular duct.*

## Introduction

A summary of the literature on heat transfer in laminar duct flows has been brought together in a book by Shah and London (1978). From a study of this information, it is apparent that only limited consideration has been given to three-dimensional duct problems. The pioneering work is by Patankar and Spalding (1972) who developed a calculation procedure for three-dimensional parabolic flows. This procedure was adopted by Prakash and Liu (1985) to study forced convection flow and heat transfer in the entrance region of an internally finned circular duct. Recently, Karki and Patankar (1985) applied this method to determine augmentation due to buoyancy effects in the entrance region of a shrouded fin array. The aforementioned duct problems are such that the cross-sectional boundaries lie along the coordinate axes and are classified as regular domain problems. A careful search of the literature failed to disclose any prior work on the hydrodynamic and thermal entrance region characteristics of a rhombic duct and many other ducts with irregular cross section. This has motivated the present study to obtain solutions for the entrance region of a rhombic duct. However, the methodology can be applied to other ducts with irregular cross sections.

The numerical methodology that was used in this paper utilizes an algebraic coordinate transformation developed in previous papers by Faghri et al. (1984) and Asako and Faghri (1987) to map the irregular cross section onto a rectangle. This method was coupled with the calculation procedure for three-dimensional parabolic problems developed by Patankar and Spalding (1972) to obtain solutions in the downstream region from the upstream information. The numerical solutions were carried out for both uniform wall temperature and uniform wall heat flux and for four values of the duct angle ($\phi = 30$, 45, 60, and 90 deg) and for four values of the Prandtl number (Pr = 0, 0.7, 8, and $\infty$). The Nusselt number and pressure drop results were compared with the available fully developed values and also with the entrance region results for the limiting case where $\phi = 90$ deg. In this case, the rhombic duct reduces to a rectangular duct.

Contributed by the Heat Transfer Division and presented at the AIAA/ASME Thermophysics and Heat Transfer Conference, Boston, Massachusetts, June 2–4, 1986. Manuscript received by the Heat Transfer Division July 30, 1986. Keywords: Forced Convection, Heat Exchangers, Numerical Methods.

## Formulation

**Description of the Problem.** The problem to be considered in this study is schematically depicted in Fig. 1(*a*). It involves the determination of heat transfer and fluid flow characteristics for laminar, incompressible, forced convection in the entrance region of a rhombic duct. As seen in this figure, the fluid enters the duct with a uniform velocity $\bar{w}$ and a uniform temperature $T_i$. Two types of thermal boundary condition are considered: a uniform heat input per unit axial length with a uniform temperature at any cross section, and a uniform temperature both axially and peripherally. These are the *H*1 and *T* boundary conditions, respectively, of Shah and London (1978). Figure 1(*b*) pictures the cross section of the duct. As seen in this figure, two walls of the duct lie along the $x$ axis, while the other walls do not lie along the $y$ axis, but they make an angle $\phi$ with the $x$ axis. The deviation from the $y$ axis is denoted by $\epsilon(y)$. Then, the methodology set forth in

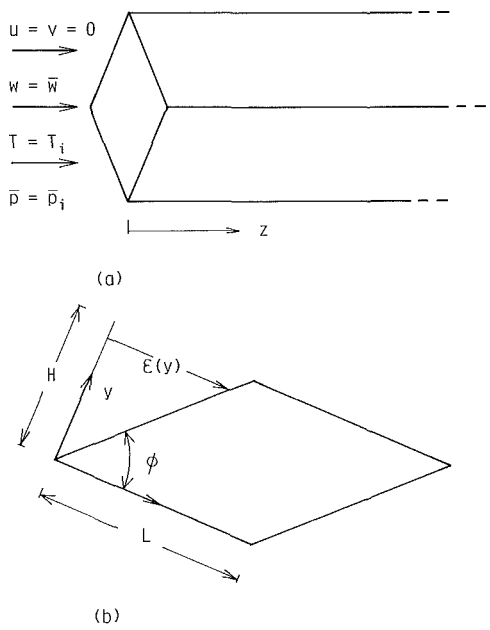


**Fig. 1** (*a*) An axial coordinate of the rhombic duct; (*b*) a cross section of the rhombic duct

papers by Faghri et al. (1984) and Asako and Faghri (1987) can be used to map the cross section onto a rectangle. The geometry of the duct is specified by length $L$, height $H$, and the angle $\phi$. If $H$ is chosen as a reference length, then $L/H$ and $\phi$ are the geometric parameters. However, $L/H$ can be expressed in terms of $\phi$. Therefore, the only geometric parameter of the problem is the duct angle $\phi$.

The duct problem under consideration is a three-dimensional problem. However, because of the predominant flow in the $z$ direction, the problem is assumed to be parabolic in this direction and the calculation procedure developed by Patankar and Spalding (1972) is adopted. In this method, like other boundary layer problems, the diffusion is neglected along the predominant flow direction. Also, along this direction, the pressure is assumed to be "one way." With this assumption, the longitudinal and lateral pressure gradients are uncoupled (i.e., $p = p' + \bar{p}$ where $p'$ is pressure variation in the cross-stream direction and $\bar{p}$ is the cross-sectional averaged pressure). Therefore, like other parabolic problems, the marching procedure is employed in the $z$ direction, and the problem numerically reduces to a two dimensional problem.

**Conservation Equation.** The governing equations to be considered are the continuity, momentum, and energy equations. Constant thermophysical properties are assumed and natural convection is excluded. The following dimensionless variables are used:

$$X = x/D_h, \quad Y = y/D_h, \quad Z = z/(D_h \mathrm{Re}),$$

$$U = uD_h/\nu, \quad V = vD_h/\nu, \quad W = w/\bar{w},$$

$$P = p/(\rho \bar{w}^2), \quad P' = p' D_h^2/(\rho \nu^2),$$

$$\theta = (T - T_i)/(T_w - T_i) \text{ for the } T \text{ boundary},$$

$$\theta = (T - T_i)/(Q'/K) \text{ for the } H1 \text{ boundary} \tag{1}$$

where $D_h$ is the hydraulic diameter, $D_h = 4(\text{area})/(\text{perimeter}) = 4HL/(4L) = H$; Re is the Reynolds number, $\mathrm{Re} = \bar{w} D_h/\nu$; and $Q'$ is the heat input per unit axial length. Then, upon the introduction of the dimensionless variables, the parabolized governing equations take the following forms:

$$\partial U/\partial X + \partial V/\partial Y + \partial W/\partial Z = 0 \tag{2}$$

$$\partial(UU)/\partial X + \partial(VU)/\partial Y + \partial(WU)/\partial Z = \nabla^2 U - \partial P'/\partial X \tag{3}$$

$$\partial(UV)/\partial X + \partial(VV)/\partial Y + \partial(WV)/\partial Z = \nabla^2 V - \partial P'/\partial Y \tag{4}$$

$$\partial(UW)/\partial X + \partial(VW)/\partial Y + \partial(WW)/\partial Z = \nabla^2 W - \partial \bar{P}/\partial Z \tag{5}$$

$$\partial(U\theta)/\partial X + \partial(V\theta)/\partial Y + \partial(W\theta)/\partial Z = (1/\mathrm{Pr})\nabla^2 \theta \tag{6}$$

where

$$\nabla^2 = \partial^2/\partial X^2 + \partial^2/\partial Y^2 \tag{7}$$

The streamwise second derivatives are neglected on the right hand side of equations (3)–(6) because of the predominant flow direction. To complete the formulation of the problem, it remains to discuss the boundary conditions. These are:

*at duct inlet*

$$u = v = 0$$

$$w = \bar{w}\text{: uniform}$$

$$T = T_i\text{: uniform}$$

$$\bar{p} = p_i\text{: uniform} \tag{8}$$

*at wall*

$$u = v = w = 0$$

$$T = T_w \tag{9}$$

## Nomenclature

$C_p$ = specific heat of the fluid
$D_h$ = equivalent hydraulic diameter = $H$
$f$ = friction factor, equation (25)
$H$ = height of a rhombic duct
$K$ = incremental pressure drop, equations (26)
$k$ = thermal conductivity
$L$ = length of a side of a rhombic duct
$\dot{m}$ = total mass flow rate
Nu = Nusselt number
Pr = Prandtl number
$p$ = pressure
$p'$ = pressure driving the cross-stream flow
$\bar{p}$ = cross-sectional average pressure
$p_i$ = pressure at the inlet plane
$Q$ = total heat transfer up to $z$
$Q'$ = heat input per unit axial length for the $H1$ boundary condition
Re = Reynolds number = $\bar{w} D_h/\nu$
$T$ = temperature
$T_b$ = bulk temperature, equation (27)
$T_i$ = uniform temperature of the fluid at the inlet plane
$T_w$ = wall temperature
$U, V$ = dimensionless velocity components, equation (1)
$u, v$ = velocity components
$W$ = dimensionless axial velocity component, equation (1)
$w$ = axial velocity component
$\bar{w}$ = uniform axial velocity at the inlet plane
$X, Y$ = dimensionless coordinates: $X = x/D_h$, $Y = y/D_h$
$x, y$ = coordinates
$Z$ = dimensionless axial coordinate = $(z/D_h)/\mathrm{Re}$
$z$ = axial coordinate
$\alpha$ = geometric function, equation (19)
$\beta$ = geometric function, equation (15)
$\delta(Y)$ = dimensionless deviation from $y$ axis = $\epsilon(y)/D_h$
$\epsilon(y)$ = deviation from $y$ axis
$\eta$ = transformed coordinate = $(x - \epsilon)/D_h$
$\Theta$ = diffusion term = $-\partial\Phi/\partial\xi$
$\theta$ = dimensionless temperature, equation (1)
$\Lambda$ = pseudodiffusion term = $\beta(\partial\Phi/\partial\xi)$
$\mu$ = viscosity
$\nu$ = kinematic viscosity
$\xi$ = transformed coordinate = $Y$
$\rho$ = density of the fluid
$\phi$ = angle of rhombic duct
$\Phi$ = general dependent variable
$\Psi$ = pseudodiffusion term = $\beta(\partial\Phi/\partial\eta)$
$\Omega$ = diffusion term = $-\alpha(\partial\Phi/\partial\eta)$

**Subscripts**

$fd$ = refers to the fully developed conditions
$H1$ = refers to the case of uniform heat input per unit axial length with a peripherally uniform temperature at any cross section—the H1 boundary condition
$T$ = refers to the case of a uniform temperature both axially and peripherally—the $T$ boundary condition

**Numerical Solutions.** The solution methodology consists of two steps. The first step is to introduce a transformation of coordinates, which maps the duct cross-section onto a rectangle. The second step is to reduce the three-dimensional problem computationally into a series of two-dimensional problems. The methodology to accomplish the first step is documented in earlier papers by Faghri et al. (1984) and Asako and Faghri (1987). Therefore, only a brief description will be given here. In this methodology, the $X$, $Y$ coordinates are first transformed into $\eta$, $\xi$ coordinates by the relation

$$\eta = X - \delta(Y),\ \xi = Y \text{ where } \delta(Y) = \epsilon(y)/D_h \tag{10}$$

In terms of the new coordinates, the solution domain is defined by $0 < \eta < L/H$, $0 < \xi < 1$. The exact values of $\delta(Y)$ and its derivatives are as follows:

$$\delta = Y \tan(90 - \phi) \tag{11}$$

$$d\delta/dY = \tan(90 - \phi) \tag{12}$$

$$d^2\delta/dY^2 = d^3\delta/dY^3 = 0 \tag{13}$$

Then, a new velocity component $U_\eta$ is introduced as

$$U_\eta = U - \beta V \tag{14}$$

where $\beta$ is a function of $Y$ and is expressed as

$$\beta = \partial\delta/\partial Y \tag{15}$$

Combining equaitons (3), (4), and (14), the $U_\eta$ momentum equation can be obtained as follows:

$$U(\partial U_\eta/\partial X) + V(\partial U_\eta/\partial Y) + W(\partial U_\eta/\partial Z) - (\partial^2 U_\eta/\partial X^2)$$

$$-(\partial^2 U_\eta/\partial Y^2) = -\partial P'/\partial X + \beta\partial P'/\partial Y - V(\partial\beta/\partial Y)$$

$$+ V(\partial^2\beta/\partial Y^2) + 2(\partial V/\partial Y)(\partial\beta/\partial Y) \tag{16}$$

This equation will be solved instead of the $U$ momentum equation. Interested readers may refer to the paper by Faghri et al. (1984) for its derivation.

Attention will now be focused on the solution methodology. The governing equations (2), (4), (5), (6), and (16) are first integrated over a control volume in physical space bounded by lines of constant $\eta$ and constant $\xi$ using the divergence theorem. Then, a formal coordinate transformation is performed from $X$, $Y$ to $\eta$, $\xi$ by using the following transformations:

$$(\partial/\partial X)_Y = (\partial/\partial\eta)_\xi$$

$$(\partial/\partial Y)_X = -\beta(\partial/\partial\eta)_\xi + (\partial/\partial\xi)_\eta \tag{17}$$

Finally, the integrated transformed governing equations are written in the following common form:

$$\int_1 [V\Phi + \Gamma(\Theta + \Psi)]d\eta - \int_3 [V\Phi + \Gamma(\Theta + \Psi)]d\eta$$

$$+ \int_2 [U_\eta\Phi + \Gamma(\Omega + \Lambda)]d\xi - \int_4 [U_\eta\Phi + \Gamma(\Omega + \Lambda)]d\xi$$

$$= -\int_\forall W(\partial\Phi/\partial Z)d\eta d\xi + b \tag{18}$$

where $\Phi$ stands for $U_\eta$, $V$, $W$, or $\theta$, and $\Gamma$ is the diffusion coefficient, which is equal to 1 for the momentum equations and 1/Pr for the energy equation. The variables $\Omega$, $\Theta$, $\Lambda$, and $\Psi$ are abbreviations, which are defined as follows:

$$\Omega = -\alpha(\partial\Phi/\partial\eta),\quad \Theta = -(\partial\Phi/\partial\xi),$$

$$\Lambda = \beta(\partial\Phi/\partial\xi),\quad \Psi = \beta(\partial\Phi/\partial\eta)\quad \text{where } \alpha = 1 + \beta^2 \tag{19}$$

The $b$ term in the $U_\eta$ momentum equation is obtained from the right-hand side of equation (16), which simplifies to

$$b = -\int_\forall [\alpha(\partial P'/\partial\eta) - \beta(\partial P'/\partial\xi)]d\eta d\xi$$

$$-\int_\forall [V^2(\partial^2\delta/\partial\xi^2) - V(\partial^3\delta/\partial\xi^3)$$

$$+ 2\beta(\partial V/\partial\eta)(\partial^2\delta/\partial\xi^2) - 2(\partial V/\partial\xi)(\partial^2\delta/\partial\xi^2)]d\eta d\xi \tag{20}$$

and for the $V$ momentum equation reduces to

$$b = -\int_\forall [(\partial P'/\partial\xi) - \beta(\partial P'/\partial\eta)]d\eta d\xi \tag{21}$$

and for the $W$ momentum equation is given by

$$b = -\int_\forall (\partial\bar{P}/\partial Z)d\eta d\xi \tag{22}$$

Finally, the $b$ term is zero for the energy equation.

The methodology to accomplish the second step is fully described by Patankar and Spalding (1972). The discretized procedure of the transformed equation is based on the power-law scheme of Patankar (1981), and the discretized equations are solved by using a line-by-line method. The lateral pressure and velocity are linked by the SIMPLE algorithm of Patankar (1980) while the longitudinal pressure is corrected by the pressure correction methodology based on the total mass flow rate suggested by Patankar and Spalding (1972).

From an examination of the governing equations (2) to (6) and also the geometry of the problem, there are two parameters whose values have to be specified prior to the initiation of the computation. These are the Prandtl number, Pr, and the duct angle $\phi$. In this paper, values of 0, 0.7, 8, and $\infty$ are selected for Pr and the selected values of $\phi$ are 30, 45, 60, and 90 deg. When $\phi = 90$ deg, the rhombic duct reduces to a rectangular duct.

The computation are performed with $(22 \times 22)$ grid points. These grid points are distributed in a nonuniform manner with higher concentration of grids close to the walls in both directions. Each interior control volume contains one grid point while the boundary adjacent control volume contains two grid points. Supplementary runs are performed with $(8 \times 8)$, $(12 \times 12)$, $(18 \times 18)$, and $(26 \times 26)$ grid points to investigate grid size effect.

**Solution Procedure for H1 Boundary Condition.** For the case of isothermal walls, the $T$ boundary condition, the temperature $T_w$ is known and there is no difficulty. However, for the second type of thermal boundary condition, the $H1$ boundary condition, there is some difficulty. A solution procedure for this condition was described by Prakash et al. (1985). The temperature $T_w$ is unknown and is a function of $z$. Instead, the bulk temperature is known, and can be obtained by a heat balance as

$$T_b = T_i + Q'z/(\dot{m}c_p) \tag{23}$$

In the procedure suggested by Prakash et al. (1985), the wall temperature is adjusted iteratively until the computed bulk temperature is in agreement with the exact bulk temperature given by equation (23). In other words, if $T_w^k$ is the wall temperature at the location $z$ at the $k$th iteration, leading to a computed bulk temperature $T_b^k$, then in the next iteration, $T_w$ is adjusted by the equation

$$T_w^{k+1} = (T_w^k)(T_b/T_b^k) \tag{24}$$

where $T_b$ is the desired bulk temperature given by equation (23). When the problem converges, $T_b = T_b^k$, and $T_w^{k+1} = T_w^k$. About 40 to 50 iterations are required to get the convergence of the wall temperature to five significant digits.

Table 1 Fully developed values of ($f$Re) and incremental pressure drop $K$

| $\phi$ | $(f\,Re)_{f.d.}$ | | $K(\infty)$ | |
|---|---|---|---|---|
| | Present work | Shah (1975) | Present work | Shah (1975) |
| 90 | 14.108 | 14.227 | 1.445 | 1.551 |
| 60 | 13.729 | 13.830 | 1.538 | 1.673 |
| 45 | 13.302 | 13.381 | 1.673 | 1.850 |
| 30 | 12.800 | 12.803 | 1.883 | 2.120 |

Table 2 Grid size effect on ($f$Re)

| Grid Points | $(f\,Re)_{f.d.}$ | error |
|---|---|---|
| ( 8 X 8) | 12.590 | 5.9 % |
| (12 X 12) | 13.118 | 2.0 % |
| (18 X 18) | 13.253 | 0.96% |
| (22 X 22) | 13.302 | 0.59% |
| (26 X 26) | 13.325 | 0.42% |
| Shah (1975) | 13.381 | |

**Fully Developed Region.** Sufficiently far downstream from the inlet plane, the flow becomes fully developed. The equations governing the flow in this region are obtained from equations (2) to (6) by setting $u=0$, $v=0$, and assuming $w$ to be independent of $z$. The fully developed results are obtained by solving these equations separately.

**Computational Procedure.** The fully developed results are obtained first. Then the results in the developing region are computed. The computation is continued far downstream so that the Nusselt numbers agree with their fully developed values to within 1 percent. At each marching step, sufficient number of iterations are performed. About 40 to 50 iterations are required to get the convergence of $W$ and $\theta$ to five significant digits. About 100 iterations (maximum) are required for the convergence of the $U$, $V$, and $\bar{P}$ equations. This is because of the presence of the extra terms (e.g., $\Lambda$, $\psi$, and $b$ in equation (18)), which arose from the coordinate transformation methodology. These extra terms were incorporated in the source term. Therefore, a large number of iterations is required. The first dimensionless step size is taken as $2\times10^{-5}$. Starting with this value, subsequent step sizes are gradually increased using the relation $\Delta Z=(1.1)$(previous $\Delta Z$) until $\Delta Z<(\Delta\eta)^2_{\min}/5$ where $(\Delta\eta)_{\min}$ is the minimum value of the control volume size in the $\eta$ direction. The maximum step size $\Delta Z$ is $8.3\times10^{-5}$, $1.1\times10^{-4}$, $1.6\times10^{-4}$ and $3.1\times10^{-4}$ for $\phi=90$, 60, 45, and 30 deg, respectively. This criterion was determined empirically to obtain a stable solution. Thus, marching to $Z=0.1$ requires in excess of 1000 longitudinal steps.

**Hydrodynamic Results.** The local friction factor $f$ is defined as

$$f=\frac{(-d\bar{p}/dz)D_h/4}{(\rho\bar{w}^2)/2} \tag{25}$$

In the fully developed region, the friction factor becomes inversely proportional to the Reynolds number, and ($f$Re) becomes independent of $z$. The pressure drop from the inlet up to $z$ is defined as $\Delta p=p_i-\bar{p}(z)$ where $p_i$ is the pressure at the inlet plane. This pressure drop can be expressed as

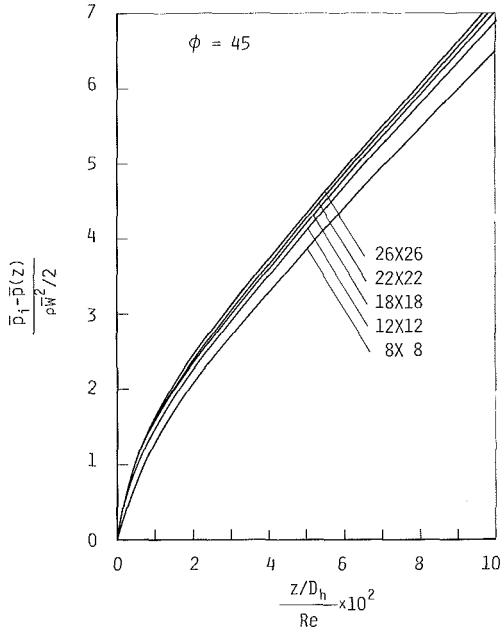


Fig. 2 Effect of mesh size on the pressure drop

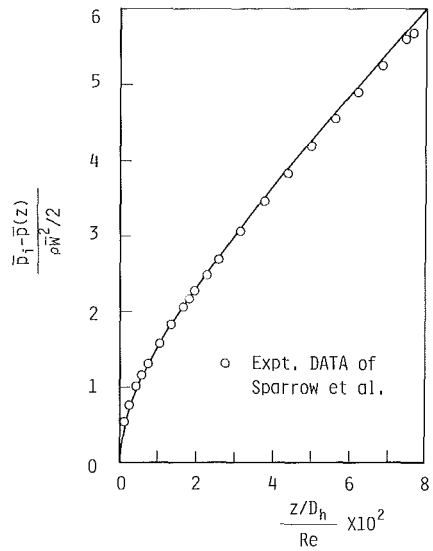


Fig. 3 Comparison of the pressure drop for computational and experimental results ($\phi=90$ deg)

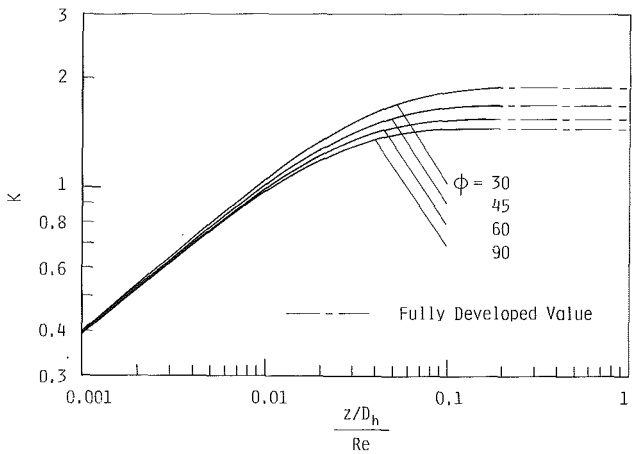


Fig. 4 Incremental pressure drop $K$ as a function of dimensionless axial length

$$\frac{p_i - \bar{p}(z)}{(\rho \bar{w}^2)/2} = (f\mathrm{Re})_{fd}\left(\frac{4z}{D_h \mathrm{Re}}\right) + K(z) \tag{26}$$

where $(f\mathrm{Re})_{fd}$ refers to the fully developed values. $(f\mathrm{Re})_{fd}(4z/D_h\mathrm{Re})$ represents the pressure drop if the flow were fully developed all the way from the inlet. $K(z)$ is the incremented pressure drop due to the entrance effect.

## Results and Discussion

**Friction Factor for Fully Developed Flow.** The computed fully developed friction factors are given in Table 1. Shah (1975) analyzed the fully developed flow in a rhombic duct and obtained the values of $(f\mathrm{Re})_{fd}$. His results are also listed in Table 1. As seen from this Table, the $(f\mathrm{Re})_{fd}$ values of the present computation are slightly lower than the values of Shah.

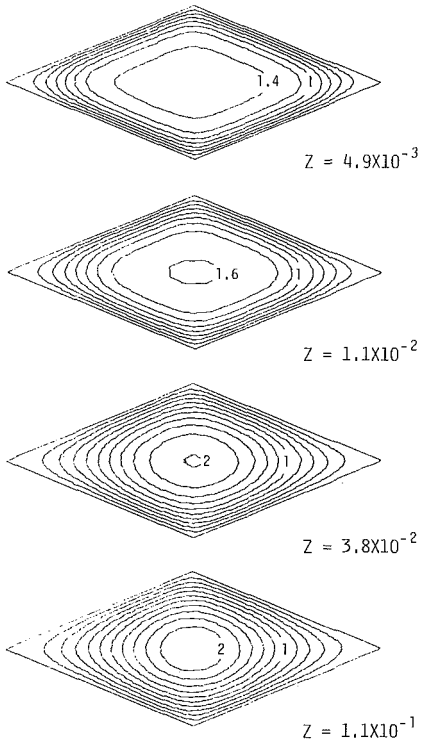


Fig. 5(a) Axial velocity $W$ contours ($\phi = 45$ deg)

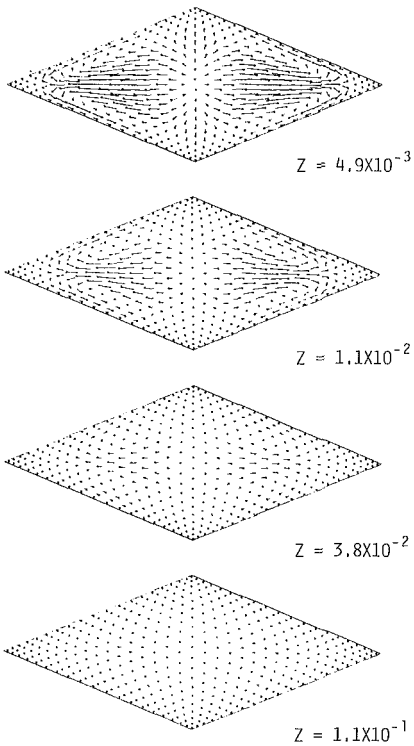


Fig. 5(c) Velocity vectors ($\phi = 45$ deg)

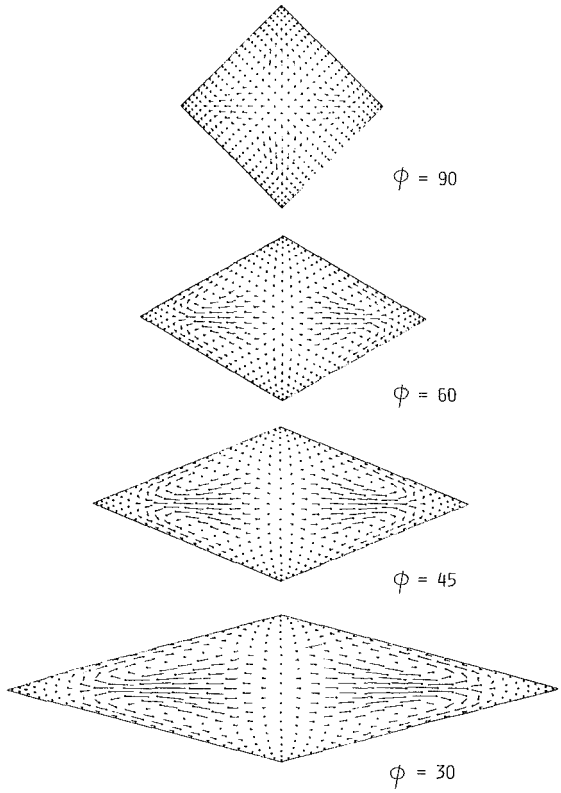


Fig. 5(b) Velocity vectors $[(z/D_h)/\mathrm{Re} = 1.1 \times 10^{-2}]$

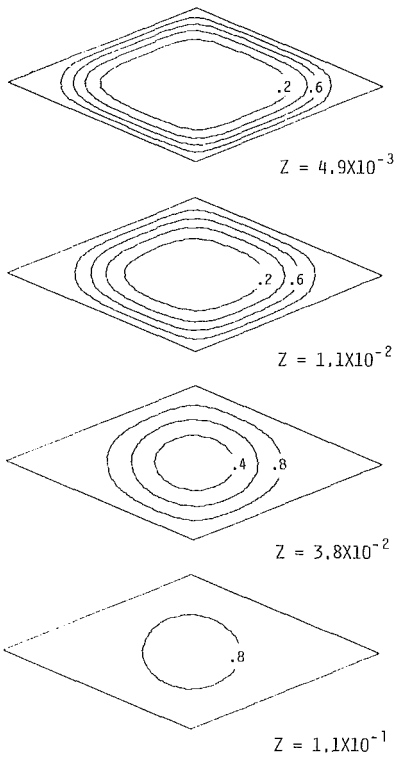


Fig. 5(d) Contours of $(T - T_i)/(T_w - T_i)$ for $T$ boundary condition ($\mathrm{Pr} = 0.7$, $\phi = 45$ deg)

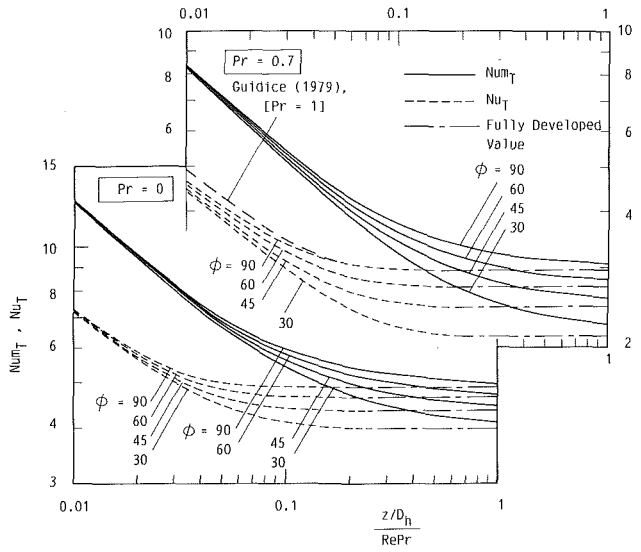


Fig. 6 Nusselt number with $T$ boundary as a function of dimensionless axial length (Pr = 0 and 0.7)

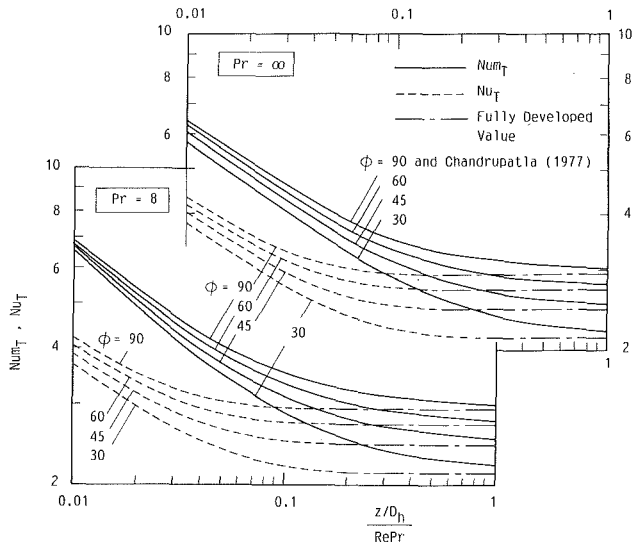


Fig. 7 Nusselt number with $T$ boundary condition as a function of dimensionless axial length (Pr = 8 and ∞)

**Mesh Size Effect.** Axial pressure distributions for $\phi = 45$ deg under different mesh sizes are given in Fig. 2. Inspection of this figure indicates that the normalized pressure defect depends strongly on the mesh size when the mesh size is coarse.

Comparisons of the $(f\mathrm{Re})_{fd}$ for $\phi = 45$ deg under various mesh sizes with the values of Shah (1975) are made in Table 2. Thus a $(22 \times 22)$ mesh is chosen to maintain relatively moderate computing costs.

**Comparisons With Previous Results.** The comparison of the axial pressure distribution for $\phi = 90$ deg is given in Fig. 3 with the experimental data of Beavers et al. (1970). As seen from this figure, the result of the present computation agrees well with the experimental data. Patankar and Spalding (1972) have numerically obtained an axial pressure distribution for $\phi = 90$ deg, which is also in perfect agreement with the presently computed results.

**Incremental Pressure Drop in the Entrance Region.** Results for the incremental pressure drop $K$ are plotted in Fig. 4 with the angle $\phi$ as a curve parameter. As expected, $K$ increases with $z$ and approaches asymptotically a constant value at a large axial distance. It is noteworthy that the value of $K$ is independent of the angle $\phi$ near the inlet.

The asymptotic value of $K$ for large $z$ is called $K(\infty)$, and it represents the total incremental pressure drop due to the entrance effect. This value is obtained graphically by extrapolating the results of Fig. 4, as is summarized in Table 1, and is compared with the values by Shah (1975). The results indicate that the total incremental pressure drop $K(\infty)$ increases with the angle $\phi$. The dashed lines in Fig. 4 indicate the total incremental pressure drop $K(\infty)$.

**Axial Velocity Contours, Velocity Vectors, and Contours of Isotherms.** Representative contours of the axial velocity $W$ are presented in Fig. 5(*a*). This figure is for $\phi = 45$ deg, and for the dimensional axial distance $Z\ [= (z/D_h)/\mathrm{Re}]$ ranging from $4.9 \times 10^{-3}$ to $1.1 \times 10^{-1}$. As seen from this figure, the axial velocity at the central point of the cross plane increases with the distance $z$ from the inlet plane, and it approaches the fully developed value ($W = 2.23$) far from the inlet plane.

Representative velocity vectors of the cross-stream flow are presented in Fig. 5(*b*) at $Z\ [= (z/D_h)/\mathrm{Re}] = 1.1 \times 10^{-2}$. As seen from this figure, the cross-stream velocity vectors of the rhombic duct are stronger than that of the rectangular duct at the same location from the inlet plane.

Representative velocity vectors of the cross-stream flow are also presented in Fig. 5(*c*). This figure is for $\phi = 45$ deg and for the dimensionless axial distance $Z$ ranging from $4.9 \times 10^{-3}$ to $1.1 \times 10^{-1}$. As seen from this figure, the cross-stream flow is diminished far from the inlet plane.

Representative contours of $(T - T_i)/(T_w - T_i)$ for the $T$ boundary are presented in Fig. 5(*d*). This figure is for $\phi = 45$ deg and Pr = 0.7, and the dimensionless axial distance $Z$ ranging from $4.9 \times 10^{-3}$ to $1.1 \times 10^{-1}$. As seen from this figure, the temperature at the central point of the cross plane increases with the distance $z$ from the inlet plane, and approaches the wall temperature far from the inlet plane.

**Thermal Results: Isothermal Duct—The T Boundary Condition.** The $T$ boundary condition corresponds to a uniform temperature $T_w$ both axially and peripherally. The bulk temperature $T_b(z)$ at an axial location $z$ is given by

$$T_b(z) = \frac{1}{\dot{m} C_p} \int_A C_p \rho w T \, dA \tag{27}$$

and the heat transfer $Q(z)$ up to a distance $z$ is equal to

$$Q(z) = \dot{m} C_p (T_b - T_i) \tag{28}$$

The averaged Nusselt number up to the axial location $z$ and the local peripheral average Nusselt number at an axial location are defined as

$$\mathrm{Num}_T = \frac{Q/(4L)z}{(T_w - T_b)} \frac{D_h}{k}$$

$$\mathrm{Nu}_T = \frac{dQ/dZ}{(T_w - T_b)} \frac{D_h}{k} \tag{29}$$

where $(\overline{T_w - T_b})$ is the log-mean temperature difference given by

$$\overline{T_w - T_b} = \frac{(T_w - T_i) - (T_w - T_b)}{\ln[(T_w - T_i)/(T_w - T_b)]} \tag{30}$$

The fully developed Nusselt number values for the developed flow (Pr = ∞) are listed in Table 3. Shah (1975) did not present these values for the $T$ boundary condition. The fully developed Nusselt number values for the slug flow (Pr = 0) are also listed in Table 3. They differ from those obtained for the developed flow.

Results for the $\mathrm{Num}_T$ and $\mathrm{Nu}_T$ are plotted in Figs. 6 and 7

**Table 3 Fully developed Nusselt number values**

| $\phi$ | $Num_T$ | | | $Nu_{H1}$ | | |
|---|---|---|---|---|---|---|
| | Developed Flow | | Slug Flow | Developed Flow | | Slug Flow |
| | Present work | Shah (1975) | Present work | Present work | Shah (1975) | Present work |
| 90 | 2.974 | 2.976 | 4.912 | 3.610 | 3.608 | 7.054 |
| 60 | 2.743 | - | 4.657 | 3.378 | 3.367 | 6.865 |
| 45 | 2.471 | - | 4.353 | 3.107 | 3.080 | 6.651 |
| 30 | 2.136 | - | 3.966 | 2.777 | 2.722 | 6.400 |

with the angle $\phi$ as the curve parameter. The dashed lines in these figures indicate the local peripheral average Nusselt number $Nu_T$. The fully developed Nusselt number values are also plotted in these figures by chain lines. As expected, $Num_T$ and $Nu_T$ decrease with $z$ and approach the fully developed values. It is noteworthy that the thermal entrance length depends slightly on the angle $\phi$, tending to decrease with $\phi$. Comparisons of the Nusselt number with the literature for $\phi = 90$ deg are given in Figs. 6 and 7. An extremely good agreement is obtained for $Pr = \infty$. Note that the Nusselt number values by Guidice et al. (1979) is for $Pr = 1$.

**Thermal Results: Uniform Heat Input per Unit Axial Length—H1 Boundary.** The local Nusselt number is defined as

$$Nu_{H1} = \frac{Q'/(4L)}{(T_w - T_b)} \frac{D_h}{K} \tag{31}$$

where $T_w$ is the wall temperature, which is uniform peripherally, and $T_b$ is the local bulk temperature given by equation (23).

The fully developed Nusselt number values for the fully developed flow ($Pr = \infty$) are listed in Table 3 as well as the values by Shah (1975). The present computed results are in perfect agreement with the values obtained by Shah. The fully developed Nusselt number values for the slug flow ($Pr = 0$) are also listed in Table 3. They differ from those for the fully developed flow.

Results for the $Nu_{H1}$ are plotted in Figs. 8 and 9 with the angle $\phi$ as the curve parameter. The fully developed Nusselt number values are also plotted in these figures by chain lines. As expected, $Nu_{H1}$ decreases with $z$ and approaches the fully developed values. It is noteworthy that the thermal entrance length depends slightly on the angle $\phi$. The comparisons of the Nusselt number for $\phi = 90$ deg are given in Figs. 8 and 9. Small deviations can be seen in these figures. The Nusselt number value by Chandrupatla et al. (1978) is for $Pr = 1$.

## Concluding Remarks

Three-dimensional heat transfer and fluid flow characteristics in the entrance region of a rhombic duct are obtained numerically by a coordinate transformation technique coupled with a calculation procedure for three-dimensional parabolic flows. The fully developed values of the Nusselt numbers and friction factors approach the available asymptotic results. The entry length results for the limiting case of rectangular duct are in perfect agreement with the experimental and numerical results.

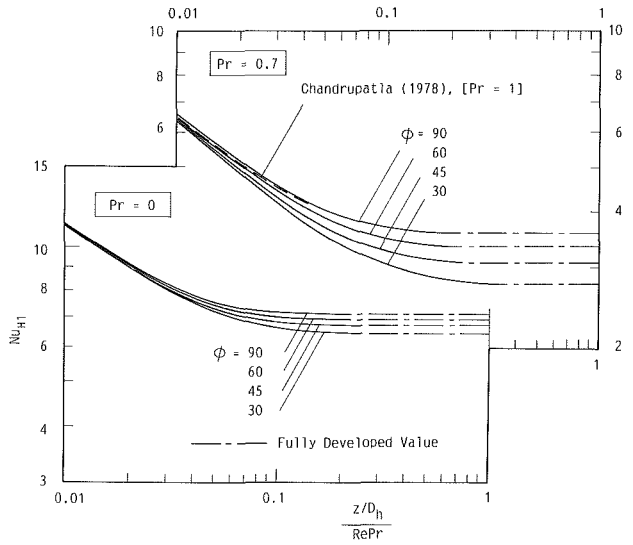


**Fig. 8 Nusselt number with *H*1 boundary condition as a function of dimensionless axial length (Pr = 0 and 0.7)**

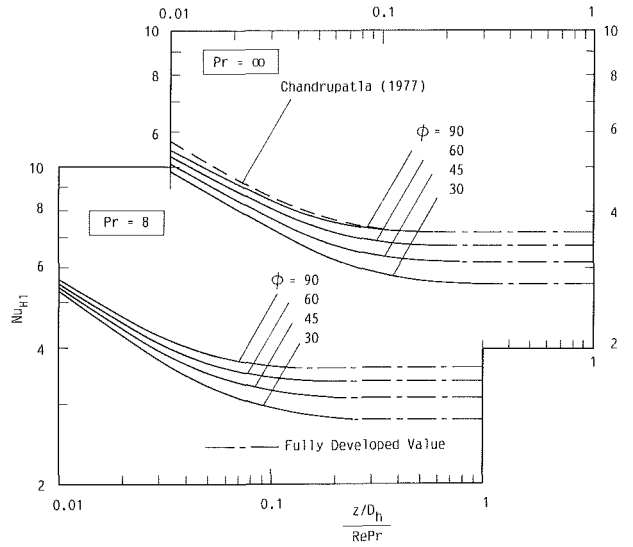


**Fig. 9 Nusselt number with *H*1 boundary condition as a function of dimensionless axial length (Pr = 8 and ∞)**

## References


Asako, Y., and Faghri, M., 1987, "Finite-Volume Solutions for Laminar Flow and Heat Transfer in a Corrugated Duct," ASME JOURNAL OF HEAT TRANSFER, Vol. 109, pp. 627–634.

Beavers, G. S., Sparrow, E. M., and Magnuson, R. A., 1970, "Experiments on Hydrodynamically Developing Flow in Rectangular Ducts of Arbitrary Aspect Ratio," *Int. J. Heat Mass Transfer*, Vol. 13, pp. 689–702.

Chandrupatla, A. R., and Sastri, V. M. K., 1977, "Laminar Forced Convection Heat Transfer of a Non-Newtonian Fluid in a Square Duct," *Int. J. Heat Mass Transfer*, Vol. 20, pp. 1315–1324.

Chandrupatla, A. R., and Sastri, V. M. K., 1978, "Laminar Flow and Heat Transfer to a Non-Newtonian Fluid in an Entrance Region of a Square Duct With Prescribed Constant Axial Wall Heat Flux," *Numerical Heat Transfer*, Vol. 1, pp. 243–254.

Faghri, M., Sparrow, E. M., and Prata, A. T., 1984, "Finite Difference Solutions of Convection-Diffusion Problems in Irregular Domains Using a Non-orthogonal Coordinate Transformation," *Numerical Heat Transfer*, Vol. 7, pp. 183–209.

Guidice, S. D., Strada, M., and Gomini, G., 1979, "Laminar Heat Transfer in the Entrance Regions of Ducts," *Numerical Heat Transfer*, Vol. 2, pp. 487–496.

Karki, K. C., and Patankar, S. V., 1985, "Heat Transfer Augmentation Due to Buoyancy Effects in the Entrance Region of a Shrouded Fin Array," 23rd National Heat Transfer Conference, Denver, CO (ASME HTD-Vol. 43).

Patankar, S. V., and Spalding, D. B., 1972, "A Calculation Procedure for Heat, Mass and Momentum Transfer in Three-Dimensional Parabolic Flows," *Int. J. Heat Mass Transfer*, Vol. 15, pp. 1787–1805.

Patankar, S. V., 1980, *Numerical Heat Transfer and Fluid Flow*, McGraw-Hill, New York.

Patankar, S. V., 1981, "A Calculation Procedure for Two-Dimensional Elliptic Situations," *Numerical Heat Transfer*, Vol. 4, pp. 409–425.

Prakash, C., and Ye-Di Liu, 1985, "Analysis of Laminar Flow and Heat Transfer in the Entrance Region of an Internally Finned Circular Duct," ASME JOURNAL OF HEAT TRANSFER, Vol. 107, pp. 84–91.

Shah, R. K., 1975, "Laminar Flow Friction and Forced Convection Heat Transfer in Ducts of Arbitrary Geometry," *Int. J. Heat Mass Transfer*, Vol. 18, pp. 849–862.

Shah, R. K., and London, A. L., 1978, *Laminar Flow Forced Convection in Ducts*, Academic Press, New York.

# Turbulent Transport on the Endwall in the Region Between Adjacent Turbine Blades

**R. J. Goldstein**

**R. A. Spores**

University of Minnesota,
Department of Mechanical Engineering,
Minneapolis, MN 55455

*The complex three-dimensional flow in the endwall region near the base of a turbine blade has an important impact on the local heat transfer. The initial horseshoe vortex, the passage vortex, and resulting corner vortices cause large variations in heat transfer over the entire endwall region. Due to these large surface gradients in heat transfer, conventional measurement techniques generally do not provide an accurate determination of the local heat transfer coefficients. In the present study, the heat/mass transfer analogy is used to examine the local transport coefficients for two different endwall boundary layer thicknesses and two free-stream Reynolds numbers. A linear turbine blade cascade is used in conjunction with a removable endwall plate. Naphthalene ($C_{10}H_8$) is cast into a mold on the plate and the rate of naphthalene sublimation is determined at 6000+ locations on the simulated endwall by employing a computer-aided data acquisition system. This technique allows one to obtain detailed contour plots of the local convection coefficient over the entire endwall. By examining the mass transfer contours, it is possible to infer information on the three-dimensional flow in the passage between the blades. Extremely high transport coefficients on the endwall indicate locations of potential overheating and failure in an actual turbine.*

## Introduction

To increase the efficiency and power of modern aircraft gas turbine engines, designers are continually trying to raise the maximum turbine inlet temperature. Over the last decade the temperature has risen from 1500 K to 1750 K in some high-performance engines. Of this 250 K increase, only about 25 percent can be attributed to improved alloys (Hennecke, 1982). New materials, such as ceramics, could help increase this maximum temperature even more in the future. However, most of the recent improvements in inlet temperature come from better cooling of the blades and a greater understanding of the heat transfer and three-dimensional temperature distribution in the turbine passage. Higher gas temperature generally causes increased blade temperatures and greater temperature gradients, both of which can have a detrimental effect on service life. In some situations, an increase in metal temperature of 15°C can reduce a component's life by half (Metzger and Mayle, 1983).

The goal of gas turbine heat transfer analysis is to obtain a detailed cooling scheme, for the turbines, blades, and endwall structures between the blades, that allows for maximum inlet temperature. Most studies on heat transfer to gas turbine components deal with the two-dimensional flow region far from the blade endwall. Even here, the flow and transport mechanisms are complex. The present study considers the even more complex endwall region and how the endwall secondary flows influence the heat transfer. Analysis of the flow and heat transfer in this region is extremely difficult. Although impressive strides have been made recently in predicting the major secondary flow phenomena (saddle point on endwall, leading edge horseshoe vortex, Hah, 1984), modern computational schemes still do not have the needed accuracy to calculate heat transfer in the endwall region. This implies that at present industry must resort to experimentation for heat transfer design improvements and the data base needed for future numerical work.

The flow field near the endwall generates a complex pattern in the convective heat transfer distribution on both the passage endwall and the blades. Knowledge of the local heat transfer distribution throughout the passage is essential in understanding the flow field's effect on heat transfer. This study provides detailed results for the endwall region of a particular blade configuration by employing the heat/mass transfer analogy.

Several investigators have already looked at endwall heat transfer in a cascade. Blair (1974) investigated the film cooling effectiveness and convection heat transfer coefficient distributions on the endwall of a large-scale turbine vane passage. Graziani et al. (1980) looked at heat transfer to both the airfoil and the passage endwall in a blade cascade using a series of strip heaters in combination with an array of thermocouples. Georgiou et al. (1979) studied iso-heat-transfer-rate lines on the endwall by using an isentropic compression tube facility along with thin film heat transfer gages. York et al. (1984) obtained endwall heat transfer results using measurements from a double layer grid of thermocouples as input to a finite element solution. A comparison was made by Gaugler and Russell (1984) between heat transfer distributions and visualized secondary flows on a turbine endwall.

The present study uses a mass transfer system to study the transport coefficient on the endwall. Related mass transfer results include: Goldstein and Karni (1984) and Sparrow et al. (1984) who both investigated the effects of an endwall boundary layer on a cylinder in crossflow using mass transfer; Goldstein and Taylor (1982) looked at mass transfer in the neighborhood of film cooling holes. In addition, Kan et al. (1971) conducted a local mass transfer experiment on a two-dimensional blade in a cascade.

One important advantage of the mass transfer technique is that much greater detail of the local transfer coefficient can be obtained. In the present study, measurements were taken at

Contributed by the Heat Transfer Division and presented at the ASME Winter Annual Meeting, Boston, Massachusetts, December 13-18, 1987. Manuscript received by the Heat Transfer Division August 6, 1987. Keywords: Mass Transfer, Measurement Techniques, Turbines.

6387 locations over the test area, in comparison to fewer than 200 points for any of the previous endwall studies. Another advantage of mass transfer is that regions of high gradients are more easily determined; conduction in the test plate that smooths out local extremes in heat flux is not a problem.

## Experimental Apparatus and Procedure

This study has been carried out at the University of Minnesota Heat Transfer Laboratory using an open circuit wind tunnel with a test section 46.9 cm wide by 60 cm high. The test section has a steel floor, plexiglass sides and top, and contains a rectilinear turbine blade cascade consisting of six scaled-up high-performance (G.E. CF6-50 Stage One High Pressure) turbine blades running the height of the test section. The blades have a chord length and aspect ratio of 16.91 and 3.55, respectively. The turbine blade coordinates can be found in Ito (1976). The top of the test section has a hole cut out for the insertion of a test plate, which contains a flat molded-naphthalene surface positioned on top of the third, fourth, and fifth blades of the cascade.

A drawing of the test plate used to contain the naphthalene is shown in Fig. 1. The leading edge of the plate is at the same angle to the oncoming flow as the cascade to provide similar upstream boundary conditions for equivalent locations in both of the active mass transfer endwall passages. Three thermocouples are embedded just under the naphthalene surface at different positions on the plate. These thermocouples measure the temperature near the naphthalene-air interface to determine the surface vapor pressure. All thermocouple readings are within 1 mV (~ 0.02°C) of each other, indicating that the temperature variation along the plate is insignificant.

A brief outline of the data acquisition system follows; a more complete discussion of the system is given by Goldstein et al. (1985). Two stepper-motor-driven positioning tables provide controlled measurement over the entire naphthalene surface. The test plate is mounted on the lower positioning table while the upper table moves a depth gage over the naphthalene surface. This depth gage is a Linear Variable Differential Transformer (LVDT) with a linear operating range of 0.020 in. (0.51 mm) and resolution of about 2.0 $\mu$in. (50 $\mu$m). The LVDT is connected to a signal conditioner, which supplies excitation and converts the a-c signal output of the gage to a calibrated d-c voltage. A voltmeter reads the voltage output and sends the signal to a minicomputer for data reduction. To control the stepper-motors, a HP-85 microcomputer is used. Between this computer and the motors is a hardware interfacing component, which converts the HP-85 commands from digital signals into a number of properly sequenced phase control signals, which instruct the stepper-motors physically to move.

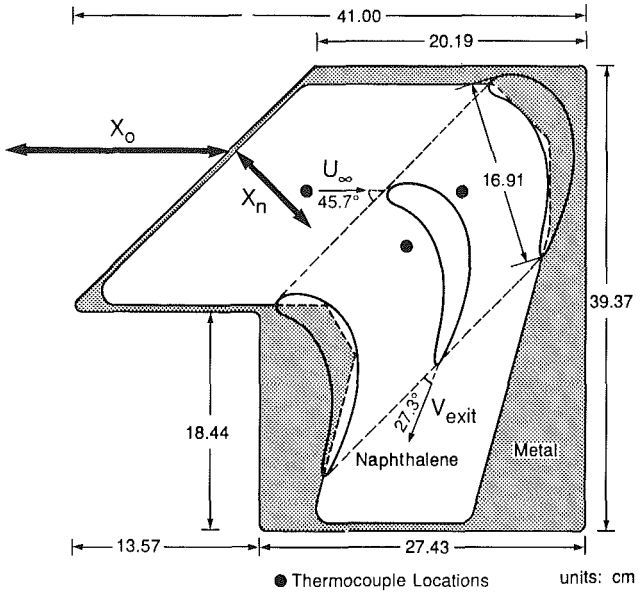


**Fig. 1 Test plate showing naphthalene surface**

Prior to a wind tunnel test, the test plate, which has been cast with naphthalene, is mounted on the lower positioning table of the data acquisition system. The initial naphthalene surface profile is measured over a specified nonuniform rectangular grid of points on the test plate. In regions where steep gradients are known to exist (from preliminary tests), more points are taken. After these initial measurements, the plate is removed from the positioning tables, enclosed in a special carrying case (to eliminate sublimation during transport), and moved to the wind tunnel room. The test plate is placed in the test section on top of the turbine blades and exposed to the air stream for a period of 90–120 min, depending on run conditions. A second set of naphthalene surface measurements is taken next at the same specified locations on the test plate as the preliminary measurements. Reference points on the metal surface are also taken during the initial and final runs. These reference points are used to calculate reference planes from which the local naphthalene surface profiles are measured. The actual amount sublimed at each location is determined by subtracting the final local measurement from the initial one, where both measurements are taken with respect to their reference planes. Based on test conditions and the amount of

## Nomenclature

$C$ = axial chord length = 16.91 cm
$D$ = diffusion coefficient
$h_m$ = local mass transfer coefficient
$h_{mo}$ = local mass transfer coefficient for flat plate case
Pr = Prandtl number = $\nu/\alpha$
$\mathrm{Re}_c$ = free-stream Reynolds number based on axial chord length and $U_\infty$
$\mathrm{Re}_x$ = Reynolds number based on distance from virtual origin to location of interest and $U_\infty$
Sc = Schmidt number = $\nu/D$
$\mathrm{St}_h$ = local heat transfer Stanton number
$\mathrm{St}_{ho}$ = local heat transfer Stanton number for flat plate case
$\mathrm{St}_m$ = local mass transfer Stanton number = $h_m/U_\infty$
$\mathrm{St}_{mo}$ = local mass transfer Stanton number for flat plate case = $h_{mo}/U_\infty$
$T$ = local temperature
$U$ = local flow velocity
$U_\infty$ = mean velocity of approaching main stream flow, measured 22.9 cm upstream of blade leading edge
$U_{exit}$ = mean velocity of flow leaving turbine passage
$w$ = mass concentration
$X$ = effective distance from the virtual origin of the turbulent boundary layer to location of interest in a turbine passage = $X_n + X_o$
$X_n$ = the portion of length $X$ actually on the naphthalene surface
$X_o$ = distance from virtual origin of boundary layer to the start of the naphthalene surface
$y$ = distance from endwall
$\alpha$ = thermal diffusivity
$\delta$ = boundary layer thickness
$\nu$ = kinematic viscosity

naphthalene sublimed, the local mass transfer Stanton number is calculated. Note that sublimation occurs continuously throughout the measurement process, but even at the locations of least mass transfer this is only about 7 percent of the total local sublimation. A correction is applied in the data reduction for the amount sublimed during handling and the measurement process. For all data runs, the maximum sublimation never exceeded 0.254 mm (0.01 in.) or 0.15 percent of the blade's chord length; thus change in geometry of the passage is not a problem.

An uncertainty analysis using the method outlined in Moffat (1982) reveals that the technique used has an overall error margin of 4.7 percent. The largest sources of uncertainty are in the test plate alignment process and in the naphthalene vapor pressure, which is used to calculate the mass transfer Stanton numbers. Deviations between the individual runs are usually less than 3 percent in the passage, while slightly greater discrepancies were found in the region upstream of the blades. Preliminary tests that included several passages showed that the periodicity of the measurements from blade passage to passage are likewise typically within 3 percent.

## Heat-Mass Transfer Analogy

The analogy is based on the fact that the governing differential equations for mass and energy transport are essentially the same. One merely has to replace the nondimensional parameters in the energy equation by the corresponding parameters (e.g., $T$ and Pr, by $w$ and Sc) to obtain the mass transfer equation. This analogy is valid only for a constant property fluid, which can be assumed as long as the transported quantities (heat or mass) are not creating large gradients in the flow (Eckert, 1972, 1976). In using mass transfer results for heat transfer predictions, care must be taken when the value of the Schmidt number in the mass transfer study differs from the Prandtl number in the heat transfer application. Basically this is equivalent to doing a parallel heat transfer study with a fluid of different Prandtl number from the one of interest in an application. In either event, one needs to be aware that there is a variation in convective transport with Prandtl (Schmidt) number and that this variation is generally a function of both geometry and Reynolds number. Many analogies and anslyses have been used to predict this Prandtl number variation in pure heat transfer cases, but even today this is not completely established, especially with intense vortices such as those encountered in the present work. Although the Schmidt number for naphthalene diffusion in air is approximately 2.0,[1] the primary application for turbine heat transfer would be in air, which has a Prandtl number of approximately 0.7. This difference (2.0 versus 0.7) is relatively small compared to variations that occur in a number of other mass/heat transfer analogies. Even so, it is desirable to reduce the problem of comparing heat (or mass) transfer results using several fluids, each with a different Prandtl (or Schmidt) number, by using relative measurements. In the present study this means dividing the local mass transfer results in a turbine passage ($St_m$) by the local mass transfer measurements taken on the flat surface in the absence of turbine blades ($St_{mo}$) to give a ratio, $St_m/St_{mo}$. There still could be a Prandtl (Schmidt) number influence when translating this to a different Prandtl (Schmidt) number since the Stanton number variation with Prandtl (Schmidt) number could be different for the cases with and without blades present. However, it appears to be a reasonable approach because the difference in Prandtl (Schmidt) number dependence for the two cases is probably not very large.

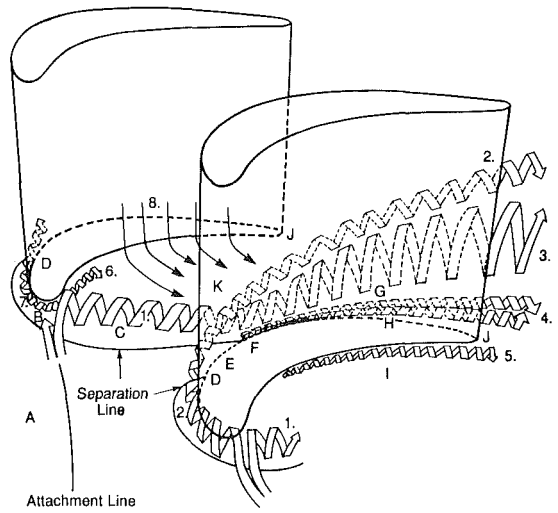


1. Leading edge pressure side vortex
2. Leading edge suction side vortex
3. Passage vortex
4. Suction side corner vortices
5. Pressure side corner vortex
6. Pressure side leading edge corner vortex
7. Suction side leading edge corner vortex
8. Downward velocity component on pressure side

**Fig. 2 The three-dimensional flow field in the endwall region**

The values of $St_{mo}$, actually used, are determined experimentally in the same test section and under the same conditions as $St_m$ with the exception that the blades are absent. For verification, the values of $St_{mo}$ are also compared with a standard correlation and found to be in good agreement. Flat plate mass transfer Stanton numbers can be calculated using a relation by von Karman between the coefficients of heat transfer and skin friction along with an equation for local skin friction along a flat plate (Schlichting, 1979). An expression for the unheated starting length is added and then the heat-mass transfer analogy is employed. The final equation used is

$$St_{mo} = \frac{1.60\ (\ln Re_X)^{-2.584}}{1 + 14.62\ (\ln Re_X)^{-1.292}} \left[1 - \left(\frac{X_0}{X}\right)^{.9}\right]^{-1/9}$$

A 3 percent difference between experiment and calculations is observed for the main test case. When calculating $St_{mo}$ for each particular point in a run, a length $X$ is used from the effective origin of the turbulent boundary layer. The question then arises as to how this length should be taken on the naphthalene surface between the blades. It was decided to take that portion of length $X$ that lies on the plate surface, $X_n$, as the perpendicular distance from the leading edge of the naphthalene to the particular point of interest, instead of a curved streamline through the passage (see Fig. 1).

## Flow Field

The heat (mass) transfer variation in the endwall region is closely related to the fluid flow in the turbine passage. For this reason, a discussion of the fluid mechanics inside a turbine passage is a prerequisite to discussing the results. Figure 2 shows our present concept of the fluid mechanics in the passage. Much of this is derived from flow visualization and direct measurements by a number of investigators including: Marchal and Sieverding (1977), Langston (1980), Sieverding (1985), and Sonoda (1985). Figure 2 shows the major vortices, labeled 1 through 7, and the primary regions of interest, labeled A through K, in the passage. The secondary flows of the endwall region are primarily the result of two main pressure gradients in the passage. The pressure variation at the leading edge-endwall intersection (due to both the boundary

[1] The value of Sc chosen does not significantly affect $St_m/St_{mo}$ in the present study because of the small range of test conditions. This value is somewhat different from that usually used in the past, which comes from a re-analysis of data for the diffusion coefficient. A review of the mass transfer physical properties is being prepared for publication.

layer velocity distribution and the stagnation of flow on the blade) forces the flow down toward the endwall, where it rolls up into the leading edge (horseshoe) vortex. The two legs of the leading edge vortex can be seen in Fig. 2 as Vortices 1 and 2. The turning of the mainstream flow between the turbine blades results in the second pressure variation – a strong gradient across the passage. This gradient affects the paths of both legs of the leading edge vortex and the low-momentum flow adjacent to the endwall. It also generates a downflow on the pressure surface and upflow on the convex surface. The concave (pressure) side leg of the leading edge vortex (Vortex 1) combines with the low-momentum flow near the endwall to form what is known collectively as the passage vortex (Vortex 3). Upon reaching the suction side, the passage vortex lifts off the endwall and continues downstream along the suction side of the passage. In contrast, the suction side leg of the leading edge vortex (Vortex 2) continues from its inception, along the blade-endwall junction until it reaches the separation line of the endwall boundary layer at region D. At the separation line the suction side leg of the leading edge vortex lifts off the endwall and continues downstream along the suction surface adjacent to the passage vortex. Sieverding (1985) indicates that Vortex 2 wraps itself around the passage vortex and the actual position of Vortex 2 depends on cascade geometry and overall flow conditions. Both Vortices 1 and 2 are believed to lift off the endwall surface due to the higher average velocities, and lower pressures, found away from the endwall along the suction surface.

Two reference lines are shown in the endwall flow visualization photograph, Fig. 3 (Goldstein and Chen, 1985). $S_1$-$S_2$ delineates the separation line of the endwall boundary layer as it approaches the turbine blades. $A_1$-$A_2$, often called the attachment line, extends from the incoming flow to the stagnation point on the front of the turbine blade. This attachment line divides the incoming boundary layer flow entering a blade passage from the flow entering the adjacent passage. The intersection of these two lines is a saddle point.

The transverse pressure gradient affects the mainflow as much as a chord length away from the endwall. For example, the downwash (toward the endwall) on the pressure surface is so strong that flow visualization by Marchal and Sieverding (1977) reveals a small corner separation line in the endwall region of the pressure side. They likewise observed a suction side-endwall corner separation similar to the one on the pressure side and believe that both separation lines are accompanied by small vortices (Vortices 4 and 5); further justification of Vortices 4 and 5 will be shown in the present study. Note that near the suction side corner, both the mass transfer results of the present study and the work of Sonoda (1985) imply the existence of two suction side corner vortices. These suction side corner vortices originate just downstream of where the passage vortices lift off from the endwall (region F) and appear to be driven by an interaction of the passage vortex with the suction surface. The pressure side corner vortex first becomes apparent on the endwall approximately 1/3 of the way back from the blade's leading to its trailing edge.

Sonoda (1985) discusses in more detail the development of the suction side corner vortex pair. He found these vortices originate just downstream of the $S_1$-$S_2$ separation line near the suction surface and are slightly away from the endwall, whereas this study observes the effects of this pair directly on the endwall. Sonoda suggests that these vortices form due to an interaction of the leading edge suction side vortex (instead of passage vortex as suggested above) with the suction surface.

The formation of the leading edge (horseshoe) vortex acts as the driving force for another corner vortex. The leading edge corner vortices (referring to Vortices 6 and 7), which are the most intense vortices in a turbine blade passage, originate in the same region as the horseshoe vortex but have a rotation in the opposite direction. This observation of an intense corner vortex underneath the horseshoe vortex is also found at the front base of a circular cylinder in crossflow (Goldstein and Karni, 1984).

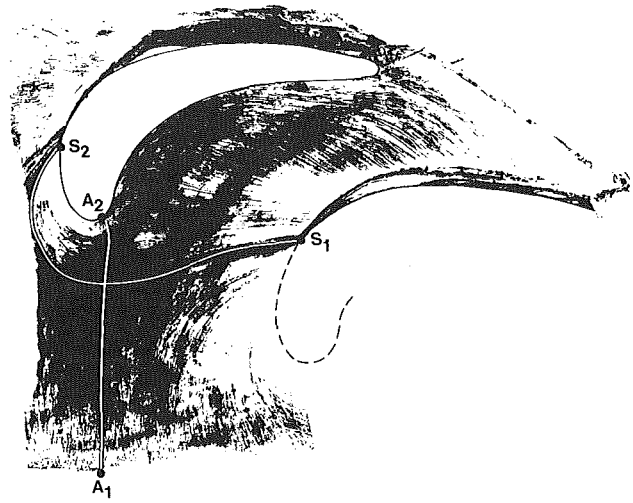


Fig. 3 Flow visualization of endwall (Goldstein and Chen, 1985)

**Table 1 Test conditions**

| | Case 1 | Case 2 | Case 3 |
|---|---|---|---|
| Free-stream velocity | 13.19 m/s | 13.23 m/s | 8.23 |
| Reynolds number $Re_c$ | $1.42\times10^5$ | $1.42\times10^5$ | $8.86\times10^4$ |
| Boundary layer thickness 0.99U | 1.504 cm | 2.913 cm | 1.171 cm |
| Displacement thickness | 0.213 cm | 0.378 cm | 0.170 cm |
| Momentum thickness | 0.151 cm | 0.284 cm | 0.116 cm |
| $U/U_\infty=(y/\delta)^{1/n}$ | $n=5.90$ | $n=6.90$ | $n=5.43$ |
| Turbulence intensity | 1.20% | 1.20% | 1.22% |
| $St_{mq}$ (at leading edge of blades) | $1.472\times10^5$ | $1.376\times10^{-3}$ | $1.563\times10^{-3}$ |

The final region to be discussed is the wake region just downstream of the turbine blade trailing edge (region J). As the high-pressure fluid from one side of the blade meets the low-pressure fluid from the other side, a highly mixed and large eddy flow region results. Gaugler and Russell (1984) observed a diverging flow pattern on the endwall in this region by using ink dot flow visualization. This seems to indicate an impingement of flow onto the endwall, which as seen later results in high local heat transfer coefficients.

## Operating Conditions

Three test conditions were studied, encompassing two Reynolds numbers and two separate boundary layer thicknesses. The mainstream velocities used are 8.2 m/s and 13.2 m/s. In the mainstream flow, the turbulence intensity is measured via hot-wire anemometry as 1.22 percent for the low-speed case and 1.20 percent for the higher speed. The turbulence measurements were taken in the free stream 21 cm in front of the cascade and in the middle of the test section. Test conditions for the three cases studied are summarized in Table 1.

The free-stream velocity is measured at a point 22.9 cm in front of the cascade, while all boundary layer measurements are taken 15.2 cm in front of the cascade.

Temperature variation throughout the run is kept to within 0.20°C, which corresponds to a 2.0 percent variation in

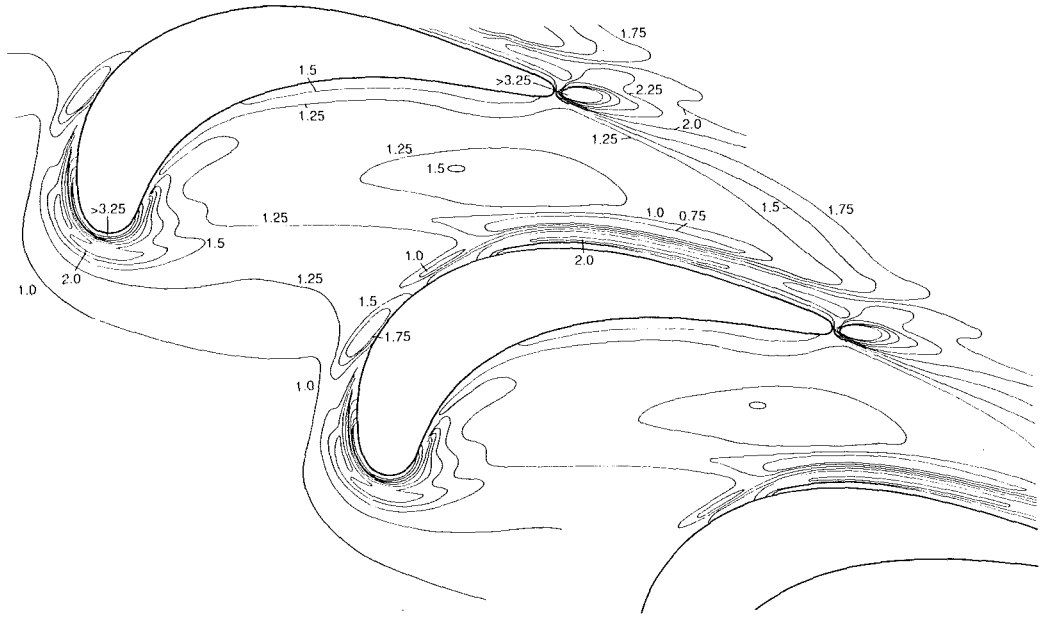


Fig. 4(*a*) Case 1, main test case; contours of $St_m/St_{mo}$ = 0.75, 1.0, 1.25, 1.5, 1.75, 2.0, 2.25, 2.5, 2.75, 3.0, 3.25

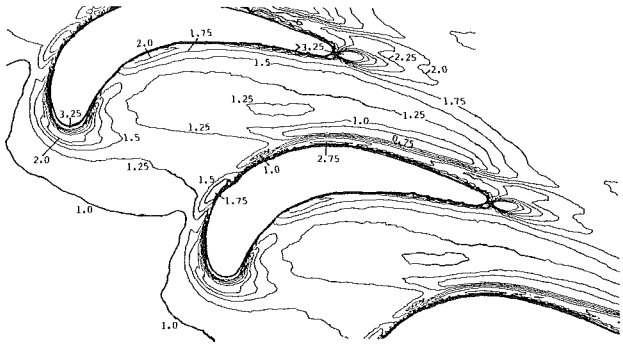

Fig. 4(*b*) Case 2, thick boundary layer case; contours of $St_m/St_{mo}$ = 0.75, 1.0, 1.25, 1.5, 1.75, 2.0, 2.25, 2.5, 2.75, 3.0, 3.25

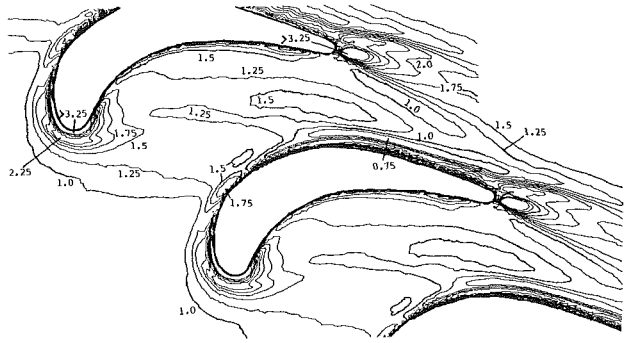

Fig. 4(*c*) Case 3, low Reynolds number case; contours of $St_m/St_{mo}$ = 0.75, 1.0, 1.25, 1.5, 1.75, 2.0, 2.25, 2.5, 2.75, 3.0, 3.25

naphthalene vapor pressure. The vapor pressure of naphthalene, and consequently the sublimation rate, are highly dependent on surface temperature. Accurately monitoring and stabilizing the temperature is critical in naphthalene mass transfer experiments.

The constant vapor pressure condition that exists over the naphthalene endwall corresponds to an isothermal boundary condition for the heat transfer case, while the non-naphthalene turbine blades correspond to adiabatic walls in heat transfer. These boundary conditions differ from those in an actual turbine passage where the blades and endwall are all active. This is not considered a significant problem. Other mass transfer studies with simpler geometries have shown only minor differences between having active or inactive boundaries adjacent to the surface of interest.

## Results – Mass Transfer on the Endwall

Nondimensionalized mass transfer contours of constant $St_m/St_{mo}$ for Case 1 (the main test case) are shown in Fig. 4(*a*). Figures 4(*b*) and 4(*c*) represent runs with a thickened boundary layer (Case 2) and a lower $Re_c$ (Case 3), respectively. These figures are generated using a computer plotting program that interpolates between the data points to draw line segments. Note that smoothing out of the contour lines is involved and that these figures, which show mass transfer for two adjacent passages, are actually the data from just one rectangular region, printed twice. The steep reduction in mass transfer near the turbine blades results in many contour lines around the blade surfaces; note that the mass transfer actually goes to zero right at the turbine surfaces. These lines adjacent to the blades have been eliminated for clarity. Figure 4(*a*) is a completely smoothed-out version while Figs. 4(*b*) and 4(*c*) show the original computer-generated contours. Case 1 will be discussed in detail with follow-up comments on how the other cases deviate from Case 1. The regions referred to in the discussion are shown on Fig. 2.

Mass transfer for the endwall region upstream of the turbine cascade (region A) is essentially that for an isothermal flat plate and the ratio equals just under 1.00. As the flow approaches the leading edge of a turbine blade (region B), a sharp increase in mass transfer is noticed as a result of the rollup of the oncoming boundary layer into the horseshoe vortex, which scrubs this area of the endwall very effectively. The Stanton number ratio increases up to its highest value on the endwall, $St_m/St_{mo}$ = 5.28, very close to the leading-edge-endwall junction as a result of the intense leading edge corner vortices, which wrap tightly around the front of the blade. Figure 5 is a one-dimensional plot showing the variation in $St_m/St_{mo}$ straight out (into the direction of $U_\infty$) from the leading edge of a blade. Note the double maximum in the profile; the dominant peak is a result of the leading edge corner vortex while the lesser peak is a result of the horseshoe vortex.

The contour plots show a rapid decrease in mass transfer as both sets of leading edge vortices travel around the blade. The

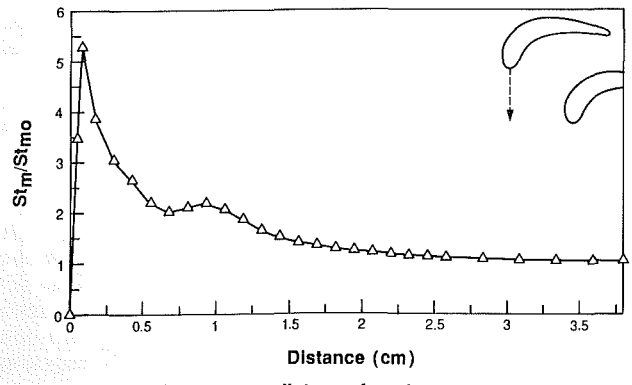


Fig. 5 $St_m/St_{mo}$ versus distance from leading edge (Case 1)

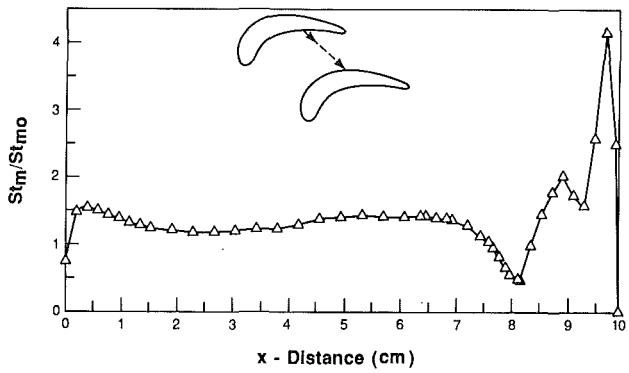


Fig. 6 $St_m/St_{mo}$ versus distance across passage (Case 1)

leading edge suction side vortex quickly lifts off the endwall as it traverses around the nose and the suction leg of the leading edge corner vortex does likewise. As these suction side vortices separate they create a small region of relatively low mass transfer on the endwall where $St_m/St_{mo} \sim 1.0$ (region D). The leading edge region of high mass transfer continues around the concave side as a result of the pressure side leg of the leading edge corner vortex (Vortex 6). As on the suction side, the Stanton number ratio quickly drops off close to the wall as Vortex 6 appears to diminish or lift off the endwall. In contrast, Vortex 1 affects a much larger area, region C.

The passage vortex increases the ratio of $St_m/St_{mo}$ up to 1.36 in a band (region C) extending from the leading edge of one blade to the suction surface of the adjacent blade. Note that in the separation region just upstream of the passage vortex, near where the fluid lifts off the endwall or changes direction by approximately 90 deg in order to flow with the vortex, there is no noticeable reduction in mass transfer. However, near where the passage vortex encounters the suction surface there is a relatively large increase in mass transfer on the upstream side of the location (region E) and low mass transfer on the downstream side (region F).

The high mass transfer zone, region E, is the result of a localized region of highly turbulent flow caused by the transverse pressure gradient turning the upstream boundary layer flow and forcing it to flow toward the suction surface. Note that this local peak (region E) occurs in front of the separation line and is consequently not believed to be the result of a stagnation point due to the passage vortex. The low mass transfer area, region F, on the other hand is due to a "dead zone" on the surface, created underneath the lift off of the passage vortex as it climbs up the suction surface.

The midpassage of the endwall, region K, is an area of approximately uniform mass transfer, which contrasts to large variations near the suction surface and the increase near the pressure side. Figure 6 is a one-dimensional plot of $St_m/St_{mo}$ through region K from pressure side to suction side taken 70 percent of the chord length back from the leading edge. This figure reveals a slight peak in mass transfer near the concave side, due to the weak pressure side corner vortex (region I, Vortex 5) generated under the downwash from the pressure surface. This pressure side corner vortex increases the convection ratio, $St_m/St_{mo}$, to 1.56. Near the suction side, Fig. 6 shows a dramatic decrease in mass transfer where the boundary layer separates off the endwall (region G), followed by a strong increase as a result of the suction side corner vortices (region H).

The narrow strip of reduced mass transfer, region G, is due to separation of the new passage boundary layer (which forms behind Vortex 1) as it feeds the passage vortex, which at this point is well off the endwall and traveling along the suction surface. This strip is the largest region on the endwall where the flow pattern reduces the mass transfer below the flat plate case. In region G, $St_m/St_{mo}$ decreases to as low as 0.44 (cf. Fig. 6). Note in Fig. 4(*a*) that the lowest contour shown in this region is 0.75 as the 0.5 contour would be an extremely narrow strip.

Closer to the suction surface (region H), the mass transfer steeply increases again as a result of the two suction side corner vortices (Vortices 4 in Fig. 2). Although only affecting a thin region in the corner, the vortex closest to the suction surface on the endwall attains a peak mass transfer ratio, $St_m/St_{mo} = 4.2$, while the outer vortex of the pair attains a maximum of approximately half this value. Both strips of increased convection start at region F on the endwall but are indistinguishable from one another at the trailing edge where both have a Stanton number ratio of about 2.0. The increased transport caused by the inner (more intense) suction side corner vortex has reduced to $St_m/St_{mo} \sim 3.0$ by the 80 percent axial chord point through the passage.

In addition to the extensive increase in mass transfer at the leading edge and along the suction surface of the blade, another significant increase can be found at the blade trailing edge (region J). A double peak in mass transfer is found in this region with the more significant peak a result of the strong recirculating wake behind the blade. The lesser peak, always located on the suction side of the main peak, is believed to be caused by the suction side corner vortices continuing past the blade trailing edge to interact with the recirculating fluid and form another region of large eddies. The primary peak reaches a $St_m/St_{mo}$ ratio of 4.6 while the lesser peak is 2.25. Figure 7 is a graph of $St_m/St_{mo}$ from the trailing edge of a blade through the primary peak in mass transfer induced by the recirculation fluid. The peak coincides with the direction of the exit velocity in the passage. Note that the Stanton number ratio remains about 2.0 well downstream of the trailing edge.

**Effect of Thicker Boundary Layer.** The differences between test Cases 1 and 2 (Figs. 4*a* and 4*b*) are rather minor. The displacement thickness has been increased by 77 percent for Case 2 by placing a trip wire on the test section floor 50 cm upstream of the cascade. Note that the $St_m/St_{mo}$ contours are very similar for both cases. Both figures show the 0.75 contour just off the suction surface and peaks in excess of 3.25 over similar-sized areas at both the leading and trailing edges of the blades. Further, it appears that the thicker boundary layer has little effect on the mass transfer in region C; the horseshoe vortex causes essentially the same increase in mass transfer for both test cases.

There are, however, some small differences in the mass transfer between Case 1 and Case 2. The contour plots indicate that for Case 1 the mass transfer near the pressure side is larger; it is over 2.0 for the thick boundary layer case while it only reached a maximum of 1.56 for Case 1. Also note how the mass transfer ratio is greater than 1.25 near the pressure surface over a much greater area for Case 2. This increased mass transfer indicates that the downwash off the pressure surface and/or the pressure side corner vortex are stronger for

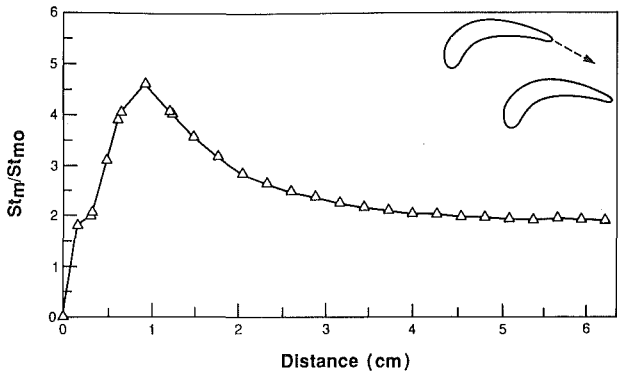


Fig. 7 $St_m/St_{mo}$ versus distance from trailing edge

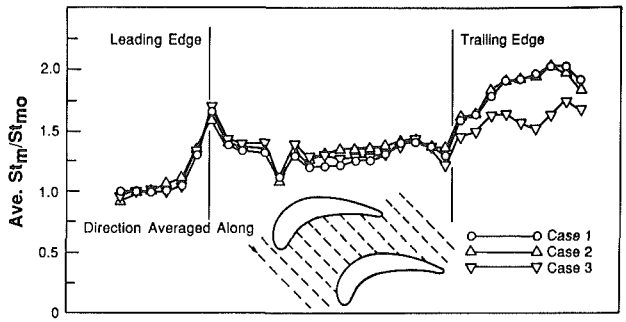


Fig. 8 Average $St_m/St_{mo}$ along turbine passage

the thick boundary layer case. In contrast, mass transfer in the midpassage and near the suction side is smaller for the thicker boundary layer case. The reduction at midpassage is best seen by comparing the closed contour of $St_m/St_{mo} = 1.25$ at midpassage for both cases. From the $St_m/St_{mo}$ contours of 1.0 and 0.75 in region G it is apparent that the reduction in mass transfer for Case 2 continues all the way to the suction surface. Interestingly, the reduced mass transfer from midpassage to the suction surface nearly compensates for the increase near the pressure surface to yield average values across the passage that are nearly equal for the two flow conditions.

**Effect of Changing Reynolds Numbers.** Between Cases 1 and 3 there is a decrease in Reynolds number of 38 percent and a decrease in displacement thickness of 20 percent. Even though the differences in mass transfer ratio are again not large, they are more pronounced than between Cases 1 and 2. First, Case 3 indicates an increase in mass transfer over Case 1 in the center of the passage where a larger portion of area is enclosed by both the 1.25 and 1.5 contours. However, the contour plots are somewhat misleading and this increase is not really significant. Although a larger area at midpassage is enclosed by the 1.5 contours for the lower Reynolds number (Case 3), the same area has a $St_m/St_{mo}$ ratio just below 1.5 (at about 1.45) for Case 1. Another difference can be seen at the exit plane of the cascade. Notice the closed contour of $St_m/St_{mo} = 1.0$ just upstream of the gradual rise in mass transfer from the wake behind each turbine blade; this contour is absent in the other test cases. The drop in mass transfer appears to be the result of a stagnant zone that occurs as the endwall boundary layer encounters the wake from the pressure side blade of the passage. It also should be pointed out that Case 3 has a significantly lower average value of $St_m/St_{mo}$ downstream of the blades, which can be attributed to the area of reduced mass transfer (region G) extending well past the trailing edge.

**Average Mass Transfer in the Passage.** Figure 8 is another approach to presenting the mass transfer data. The Stanton number ratio for a strip of endwall across the passage is averaged and plotted as a function of the distance transversed through the passage. This graph of average $St_m/St_{mo}$ is slightly biased upstream and downstream of the cascade since only the rectangular regions shown in the contour plots are included in the averaging. The ratio is 1.0 upstream of the blades (as expected), but quickly rises near the line connecting the leading edges of the blades. This steep increase is a result of the two leading edge vortices (horseshoe and leading edge corner), which greatly increase the mass transfer. Downstream of this peak there is a sharp minimum in the average mass transfer. This region of reduced mass transfer corresponds to the area just downstream of the passage vortex sweeping across the endwall; in this region the boundary layer is starting over and the momentum of the flow is weak. Another significant finding observed on this graph is that the turbulent wake behind the blades results in an average convection coefficient double that for the flat plate case.

Note how the profiles follow one another for all three test cases. As mentioned earlier, the averages for Cases 1 and 2 are nearly the same even though the mass transfer is greater near the pressure surface and less near the suction surface for the thicker boundary layer flow. The only significant deviation among the three cases is in the wake region where the flow in Case 3 (lower Reynolds number) results in a much lower average value as the strip of reduced mass transfer (region G) extends past the trailing edge to cover a much greater area.

The differences among the contour maps themselves are minor. The fact that the results are quite similar despite significant variation in the parameters is not unusual. Georgiou et al. (1979) and Graziani et al. (1980) likewise found little disparity in the contours as the major parameters were changed. Differences between runs are even less for this study because variations in the boundary layer thickness and Reynolds number are taken into account in the divisor $St_{mo}$. For example, $St_{mo}$ is about 6.5 percent lower over the endwall for the thicker boundary layer case and about 6.2 percent higher for the low $Re_c$ case, both compared to Case 1. However, $St_m$ with the blades present also varies by similar amounts yielding ratios that are approximately equivalent to the main test case.

When the ratio $St_m/St_{mo}$ is averaged over the entire endwall region between adjacent turbine blades, from the leading edges of two blades to the trailing edges (i.e., in the region between the two vertical lines shown in Fig. 8), the overall average Stanton number ratio is found to be 1.31 for Case 1. The secondary flows increase the convection mass transfer on the endwall by 31 percent over the flat plate case.

**Comparison With Heat Transfer Results.** Comparisons were made of the transport coefficients measured in this study with the results of Blair (1974), Georgiou et al. (1979), Graziani et al. (1980), Gaugler and Russell (1984), and York et al. (1984). It should be pointed out that all these studies, except Graziani et al. (1980), are for inlet guide vanes, unlike the present study, which takes measurements around a rotor blade. Blair (1974) and Georgiou et al. (1979) present results similar to each other with the minor difference that Georgiou et al. (1979) reports two regions of low heat transfer, one near the inlet at midpassage and the other a strip just off the suction surface, farther upstream than Blair does. The data of Gaugler and Russell (1984) and York et al. (1984) show the same trends of reduced heat transfer plus quite distinctly revealing regions of increased heat transfer at both the leading edges of the blades (due to the horseshoe vortices) and in the blade wake region (due to the mixing of pressure and suction side flows). All these major trends are also found in the data presented here; however, the region of reduced (mass) transfer near the inlet of the passage is only subtly shown while the other features are obvious from the contour maps. The region of reduced transfer can best be seen in Fig. 8, which shows a

large decrease in average mass transfer downstream of the leading edge.

The data of Graziani et al. (1980) agree the best with the present study, particularly their thick boundary layer case and the thick boundary layer case of this report. Although the free-stream Reynolds number is four times greater for Graziani, both cases have virtually identical displacement thicknesses. In addition to agreeing with the major trends already pointed out, the two studies also agree in magnitude and area on the effect from the leading edge vortex traversing the endwall between blades. Their thick boundary layer case even shows hints of two vortices at the blade leading edge. A one-dimensional comparison was made between strip-averaged values across the passage for $St_m/S_{mo}$ from this study and strip-averaged values for $St_h/St_{ho}$ from their thick boundary layer case. Except for the region close to the trailing edge, the agreement is within 10 percent throughout the passage.

Contributions to the current understanding of heat transfer on the endwall not found in previous studies include: observing an increase in the convection on both the pressure side–endwall junction and the suction side–endwall junction from corner vortices; although the study of Graziani et al. (1980) shows some signs of the leading edge corner vortex, the present study is the first to reveal the effects of this vortex in detail. The other studies, which used heat transfer, do not show as great extremes in convective coefficient values or as much detail in their contour maps.

## Summary and Conclusions

1. Much greater detail of the convection process can be obtained using a local mass transfer technique as compared with conventional heat transfer instrumentation. Regions of high turbulent transport are more easily determined using mass transfer since conduction in a test plate tends to smooth out regions of high heat transfer gradient. Due to the potentially greater density of measurement locations, it is much easier to correlate the convection patterns with the secondary flows than in heat transfer studies. The mass transfer results can be used to predict the heat transfer for an equivalent flow.

2. Presenting the data in the form of $St_m/St_{mo}$ appears to be a convenient way of expressing the results. As shown in Fig. 8 and by an examination of the contour plots, data from all three test cases are very similar when standardized in this manner.

3. This study helps to confirm the existence of several flow features in a turbine cascade that have only recently been observed. These features include the corner vortices at the pressure side–endwall junction, the pair of vortices at the suction side–endwall junction, and the leading edge corner vortices.

4. The secondary flows in a turbine passage result in a complex distribution of convection coefficients that vary by more than an order of magnitude over the endwall. Two-dimensional boundary layer analysis would not accurately describe the variations in convection throughout the passage.

5. The secondary flow between turbine blades has an overall effect of increasing convection on the passage endwall by a factor of 1.31 over the flat plate case. However, localized increases up to 5.28 are present, which, with the large gradients in transport coefficient, could lead to significant thermal stresses.

## References


Blair, M. F., 1974, "An Experimental Study of Heat Transfer and Film Cooling on Large-Scale Turbine Endwalls," ASME JOURNAL OF HEAT TRANSFER, Vol. 96, p. 524.

Eckert, E. R. G., and Drake, R. M., 1972, *Analysis of Heat and Mass Transfer*, McGraw-Hill, New York, p. 728.

Eckert, E. R. G., 1976, "Analogies to Heat Transfer Processes," *Measurements in Heat Transfer*, Hemisphere Publishing, New York, pp. 399–403.

Gaugler, R. E., and Russell, L. M., 1984, "Comparison of Visualized Turbine Endwall Secondary Flows and Measured Heat Transfer Patterns," ASME *Journal of Engineering for Gas Turbines and Power*, Vol. 104, p. 715.

Georgiou, D. P., Godard, M., and Richards, B. E., 1979, "Experimental Study of the Iso-Heat-Transfer-Rate Lines on the End-wall of a Turbine Cascade," ASME Paper No. 79-GT-20.

Goldstein, R. J., and Chen, H. P., 1985, "Film Cooling on a Gas Turbine Blade Near the End Wall," ASME *Journal of Engineering for Gas Turbines and Power*, Vol. 107, p. 117.

Goldstein, R. J., Chyu, M. K., and Hain, R. C., 1985, "Measurement of Local Mass Transfer on a Surface in the Region of the Base of a Protruding Cylinder With a Computer-Controlled Data Acquisition System," *International Journal of Heat and Mass Transfer*, Vol. 28, p. 977.

Goldstein, R. J., and Karni, J., 1984, "The Effect of a Wall Boundary Layer on Local Mass Transfer From a Cylinder in Crossflow," ASME JOURNAL OF HEAT TRANSFER, Vol. 106, p. 260.

Goldstein, R. J., and Taylor, J. R., 1982, "Mass Transfer in the Neighborhood of Jets Entering a Crossflow," ASME JOURNAL OF HEAT TRANSFER, Vol. 104, p. 715.

Graziani, R. A., Blair, M. F., Taylor, J. R., and Mayle, R. E., 1980, "An Experimental Study of Endwall and Airfoil Surface Heat Transfer in a Large Scale Turbine Blade Cascade," ASME *Journal of Engineering for Power*, Vol. 102, p. 257.

Hah, C. A., 1984, "A Navier-Stokes Analysis of Three-Dimensional Turbulent Flows Inside Turbine Blade Rows at Design and Off-Design Conditions," ASME *Journal of Engineering for Gas Turbines and Power*, Vol. 106, No. 2, p. 421.

Hennecke, D. K., 1982, "Turbine Blade Cooling in Aeroengines," von Karman Institute for Fluid Dynamics, Lecture Series 1982–02, and personal communication.

Ito, S., 1976, "Film Cooling and Aerodynamic Loss in a Gas Turbine Cascade," Ph.D. Thesis, University of Minnesota, Minneapolis, MN, p. 127.

Kan, S., Miwa, K., Morishita, T., Munakata, Y., and Normura, M., 1971, "Heat Transfer of a Turbine Blade," *Tokyo Joint Int. Gas Turbine Conf.*, Paper No. JSME-30.

Langston, L. S., 1980, "Crossflows in a Turbine Cascade Passage," ASME *Journal of Engineering for Power*, Vol. 102, p. 866.

Marchal, Ph., and Sieverding, C. H., 1977, "Secondary Flows Within Turbomachinery Bladings," AGARD Conf. Proc., No. 214.

Metzger, D. E., and Mayle, R. E., 1983, "Gas Turbine Engines," *Mechanical Engineering*, p. 44.

Moffat, R. J., 1982, "Contribution to the Theory of Single Sample Uncertainty Analysis," ASME *Journal of Fluids Engineering*, Vol. 104, pp. 250.

Schlichting, H., 1979, *Boundary Layer Theory*, 7th ed., McGraw-Hill, New York, pp. 641, 710.

Sieverding, C. H., 1985, "Recent Progress in the Understanding of Basic Aspects of Secondary Flows in Turbine Blade Passages," ASME *Journal of Engineering for Gas Turbines and Power*, Vol. 107, pp. 248–257.

Sonoda, T., 1985, "Experimental Investigation on Spatial Development of Streamwise Vortices in a Turbine Inlet Guide Vane Cascade," ASME Paper No. 85-GT-20.

Sparrow, E. M., Stahl, T. J., and Traub, P., 1984, "Heat Transfer Adjacent to the Attached End of a Cylinder in Crossflow," *Int. Journal Heat Mass Transfer*, Vol. 27, No. 2, pp. 273–242.

York, R.E., Hylton, L. D., and Mihelc, M. S., 1984, "An Experimental Investigation of Endwall Heat Transfer and Aerodynamics in a Linear Vane Cascade," ASME *Journal of Engineering for Gas Turbines and Power*, Vol. 106, p. 159.

# A Numerical Study of Turbulent Heat Transfer in a Spherical Annulus

**W. Stein**
Engineer,
Lawrence Livermore National Laboratory,
Livermore, CA 94550
Assoc. Mem. ASME

**H. Brandt**
Professor,
Mechanical Engineering Dept.,
University of California, Davis,
Davis, CA 95616
Mem. ASME

*A numerical study of steady, buoyant, incompressible water flow and heat transfer through a spherical annulus has been made. A two-dimensional computer code based on the TEACH code was rewritten in spherical coordinates to model the Navier-Stokes equation and to model fluid turbulence with a k–ϵ turbulence model. Results are given for the total system Nusselt number, local heat transfer rate, and fluid flow characteristics for both buoyant and nonbuoyant laminar and turbulence modeled flow. Incorporating both the turbulence model and buoyancy into the calculations improves the results.*

## Introduction

The objective of this study is to predict the heat and momentum transfer of fluid flow through a spherical annulus. This problem is of interest in the temperature control of gyroscope gimbals, the cooling of spherical fuel elements in homogeneous nuclear reactors, and the guard cooling of the spherical containers.

The problem analyzed involves the upward flow of water vertically into the annulus space between two concentric spheres as shown in Fig. 1. As the fluid enters the annulus and begins flowing around the spherical shape, its cross-sectional area increases considerably, which in turn decreases its fluid velocity. The fluid decreases in velocity until it reaches the equator. After the equator, the fluid velocity increases as the flow cross-sectional area decreases. The fluid flow pattern exhibits a recirculation zone along the outer sphere in the entry region due to the sharp corner where the entrance pipe joins the annulus. The flow also exhibits changing patterns as it moves along the annulus. The flow exhibits aspects of a stagnation flow on the inner sphere upon entering, a boundary layer jet flow along the inner sphere as the fluid flows toward the equator, and then separation of the boundary layer along the inner sphere with a resultant recirculation region downstream of the separation point. In the region downstream of the equator, the flow assumes a velocity profile similar to that in the space between flat plates.

In this study the inner sphere is maintained at a temperature near 0°C, and the outer sphere is insulated. The fluid entering is water at a temperature of 50°C. The water cools as is flows around the annulus and exits at the top. The water temperature is coolest near the inner sphere with the majority of heat transfer occurring in the entrance region along the inner sphere. The cooled fluid along the inner sphere generates buoyancy forces that retard the flow and may cause boundary layer separation.

Theoretical studies of flow through a spherical annulus have been reported by several investigators. Cobble (1963) assumed a simplified tangential velocity distribution and then calculated heat transfer based on the energy equation. Bird et al. (1964) presented the solution to isothermal creeping flow in a spherical annulus. Astill (1976) analyzed laminar forced convection flow with simplified boundary layer assumptions for air flowing between isothermal spheres. Ramadyani et al. (1983) and Tuft and Brandt (1982) analyzed laminar forced convection in a spherical annulus without considering buoyancy-driven natural convection. Brown (1967) analyzed natural convection flow in a closed spherical annulus, and Ramadhyani et al. (1984) analyzed combined natural and forced convection laminar flow at low gap Reynolds numbers.

Experimental studies have been reported by many investigators for various combinations of sphere and annulus size. Ward (1966) and Bozeman and Dalton (1970) provided a flow visualization study of isothermal flow in a spherical annulus. Rundell et al. (1968) observed a flow rate independent separation point located approximately 45 deg downstream from the inlet along the inner sphere. Upstream of the separation point, the flow is characterized by a high-velocity jet of fluid along the inner sphere with a relatively low-velocity return flow along the outer sphere. The region of high velocity jetting fluid upstream of the separation point is a region of high heat transfer. Beyond the separation point, a return flow eddy is followed by a relatively tranquil flow. This region exhibits a relatively low heat transfer rate. Rundell measured temperature profiles and total heat transfer for steady flow for

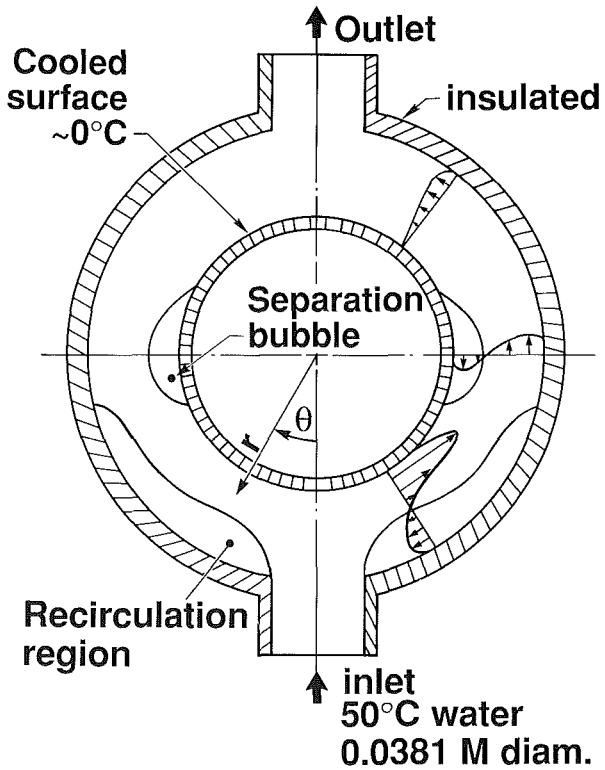


**Fig. 1 Geometry of the spherical annulus heat exchanger analyzed and typical flow phenomena computed**

Contributed by the Heat Transfer Division for publication in the JOURNAL OF HEAT TRANSFER. Manuscript received by the Heat Transfer Division June 12, 1987. Keywords: Enclosure Flows, Forced Convection, Heat Exchangers.

two sets of sphere sizes. Astill et al. (1978) and Newton (1977) investigated spherical annulus flow and heat transfer experimentally. They presented a correlation based on total heat transfer measurements. Tuft and Brandt (1982) investigated spherical annulus flow for the case of a constant temperature inner sphere and an adiabatic outer sphere. They measured local and total heat transfer as well as temperature profiles and separation point location. They also analyzed laminar nonbuoyant flow through the annulus configuration shown in Fig. 1.

In this paper an extensive numerical study of spherical annulus fluid flow is presented with detailed comparisons with the experimental data of Tuft and Brandt (1982). The laminar analysis is extended by incorporating the effects of buoyancy. The analyses were further extended by modeling the fluid turbulence with a two-equation ($k$–$\epsilon$) turbulence model. This work is believed to be the first two-dimensional analysis of the full Navier–Stokes equations with a $k$–$\epsilon$ turbulence model for steady, incompressible, spherical coordinate fluid flow and convective heat transfer. This work evaluates the $k$–$\epsilon$ turbulence model by comparing it with experimentally determined total Nusselt numbers, with local heat transfer rates, with temperature profiles, and with inner sphere boundary layer separation point locations. Ranges of fluid flow for gap Reynolds numbers Re of 110 to 1086 were investigated with water entering the annulus at 50°C and with convective cooling caused by a nominally 0°C inner sphere. The Richardson number $R_i$ for this flow varied from 0.001 to 0.4.

## Mathematical and Physical Model

**Governing Equations.** The numerical model is based on the solution of the steady two-dimensional incompressible form of the time-averaged Navier–Stokes equation, incorporating the Boussinesq turbulent-viscosity concept. The turbulent viscosity is calculated from the two-equation high Reynolds number form of the $k$–$\epsilon$ turbulence model developed by Launder and Spalding (1974) and Chieng and Launder (1980). The governing equations in spherical coordinates may be written in the following general form:

$$\frac{1}{r^2}\frac{\partial}{\partial r}(r^2\rho V\phi)+\frac{1}{r\sin\theta}\frac{\partial}{\partial\theta}(\rho U\sin\theta\phi)$$

$$=\frac{1}{r^2}\left[\frac{\partial}{\partial r}\left(r^2\Gamma\frac{\partial\phi}{\partial r}\right)+\frac{1}{\sin\theta}\frac{\partial}{\partial\theta}\left(\sin\phi\Gamma\frac{\partial\phi}{\partial\theta}\right)\right]+S_\phi \qquad (1)$$

where $\phi$ represents the dependent variables of longitudinal velocity $U$, radial velocity $V$, fluid temperature $T$, turbulent kinetic energy per unit mass $k$, and dissipation rate of turbulent kinetic energy per unit mass $\epsilon$. A summary of these equations is given in Table 1. The constants applicable to the $k$ and $\epsilon$ transport equations are given in Table 2.

**Near-Wall Model.** Viscous effects, due to the no-slip condition on the smooth spherical walls, are very influential on the flow. Within the near-wall boundary layer, the velocity typically follows a logarithmic law behavior. Two versions of the high Reynolds number form of the $k$–$\epsilon$ turbulence model were evaluated.

The version of Launder and Spalding (1974) gives the relationship between the velocity at the node adjacent to the wall and shear stress, $\tau_w$, as

$$\frac{U_p}{\tau_{w/\rho}}C_\mu^{1/4}k_p^{1/2}=\frac{1}{\kappa}\ln\left[Ey_p\frac{(C_\mu^{1/2}k_p)^{1/2}}{\nu}\right] \qquad (2)$$

This relationship should be applied at a dimensionless wall distance $y^+$, whose values are in the range $20<y^+<200$. At values of $y^+\leq 20$, the flow is assumed laminar. The dissipation $\epsilon$ at the first node adjacent to the wall is evaluated by

$$\epsilon_p=\frac{C_\mu^{3/4}k_p^{3/2}}{y_p} \qquad (3)$$

## Nomenclature

$A$ = surface area of inner sphere
$C_\mu$, $C_1$, $C_2$ = coefficients in turbulence model
$C_p$ = specific heat at constant pressure
$E$ = von Karman constant
$g$ = acceleration of gravity
$g_r$ = acceleration of gravity in radial direction
$g_\theta$ = acceleration of gravity in longitudinal direction
$h$ = heat transfer coefficient
$k$ = turbulent kinetic energy per unit mass
$K$ = thermal conductivity of fluid
$m$ = fluid mass flow rate
$Nu_g$ = total system Nusselt number
$P$ = mean generation rate of turbulent kinetic energy per unit mass
$P*$ = heat transfer $P$-function
$p$ = pressure
$q_w$ = wall heat flux
$r$ = radial coordinate
$r_i$ = outside radius of inner sphere (=0.1397 m)
$r_o$ = inside radius of outer sphere = 0.1683 m
$R_i$ = Richardson number $=\beta g(r_o-r_i)\cdot(T_{in}-T_{out})/V_{in}^2$
Re = gap Reynolds number $=\rho U_A(r_o-r_i)/\nu$
$T$ = temperature
$T_A$ = average radial temperature
$T_i$ = average temperature of inner sphere surface
$T_B$ = bulk fluid temperature $=(T_{in}+T_{out})/2$
$T_W$ = wall temperature
$U$ = mean longitudinal velocity
$U_A$ = average velocity at equator
$U*$ = friction velocity $=(\tau_w/\rho)^{1/2}$
$V$ = mean radial velocity
$y$ = distance from wall
$y^+$ = dimensionless wall distance $=y_pk_p^{1/2}/\nu$
$\beta$ = water volume coefficient of expansion
$\Gamma$ = effective diffusivity
$\epsilon$ = dissipation rate of turbulent kinetic energy per unit mass
$\theta$ = longitudinal coordinate
$\kappa$ = von Karman constant
$\mu$ = dynamic viscosity
$\mu_T$ = turbulent viscosity
$\nu$ = kinematic viscosity
$\rho$ = density
$\sigma$ = Prandtl number
$\sigma_k$, $\sigma_\epsilon$, $\sigma_T$ = turbulent Prandtl numbers for diffusion of $k$, $\epsilon$, and $T$
$\tau_w$ = wall shear force
$\phi$ = variable

**Subscripts**

in = values in inlet region
$e$ = values at the edge of cell adjacent to the wall
out = values at exit region
$p$ = values at node point adjacent to wall
$v$ = values at the edge of the viscous sublayer

**Table 1 Summary of equations solved**

| | | | |
|---|---|---|---|
| Continuity | $\phi = 1$ | $\Gamma = 0$ | $S\phi = 0$ |
| Energy | $\phi = T$ | $\Gamma = \frac{\mu}{\sigma} + \frac{\mu_T}{\sigma_T}$ | $S\phi = 0$ |
| Turbulence energy | $\phi = k$ | $\Gamma = \frac{\mu_T}{\sigma_K}$ | $S\phi = \rho P - \rho\epsilon$ |
| Energy dissipation | $\phi = \epsilon$ | $\Gamma = \frac{\mu_T}{\sigma_\epsilon}$ | $S\phi = C_1 \frac{\epsilon}{k} P - C_2 \frac{\epsilon^2}{k}$ |

$U$-momentum $\phi = U \quad \Gamma = \mu + \mu_T \quad S_\phi = -\frac{1}{r}\frac{\partial}{\partial\theta}p - \frac{\rho UV}{r}$

$$+\Gamma\frac{\partial}{dr}\left(\frac{U}{r}\right)+\frac{1}{r^2}\frac{\partial}{\partial r}\left(r\Gamma\left(U+\frac{\partial V}{\partial\theta}\right)\right)+\frac{\Gamma}{r^2}\frac{\partial V}{\partial\theta}$$

$$+\frac{1}{r^2\sin\theta}\frac{\partial}{\partial\theta}\left(\frac{\Gamma}{r}\sin\theta\left(\frac{\partial U}{\partial\theta}+2V\right)\right)+\rho g_\theta\beta(T-T_{\text{in}})$$

$V$-momentum $\phi = V \quad \Gamma = \mu + \mu_T \quad S\phi = -\frac{\partial p}{\partial r} + \frac{\rho U^2}{r}$

$$-\frac{2\Gamma}{r^2}\left(\frac{\partial U}{\partial\theta}+V\right)+\frac{1}{r\sin\theta}\frac{\partial}{\partial\theta}\left(r\Gamma\sin\theta\frac{\partial}{\partial r}\left(\frac{U}{r}\right)\right.$$

$$\left.+\frac{1}{r^2}\frac{\partial}{\partial r}\left(r^2\Gamma\frac{\partial V}{\partial r}\right)+\rho g_r\beta(T-T_{\text{in}})\right.$$

where: $\mu_T = \rho c_\mu k^2/\epsilon$

$$P=\mu_T\left[2\left[\left(\frac{\partial V}{\partial r}\right)^2+\left(\frac{\partial U}{r\partial\theta}+\frac{V}{r}\right)^2\right.\right.$$

$$\left.\left.+\left(\frac{V}{r}+\frac{U}{r}\cot\theta\right)^2\right]+\left(r\frac{\partial}{\partial r}\left(\frac{U}{r}\right)+\frac{\partial V}{r\partial\theta}\right)^2\right]$$

**Table 2 Turbulence model constants**

| $C_\mu$ | $C_1$ | $C_2$ | $\sigma_k$ | $\sigma_\epsilon$ | $\sigma_T$ |
|---|---|---|---|---|---|
| 0.09 | 1.44 | 1.92 | 1.0 | 1.3 | 0.9 |

and the average value of $\epsilon$ over the control volume at the wall is evaluated by

$$\int_0^{y_p}\epsilon dy = C_\mu^{3/4}\frac{k_p^{3/2}}{\kappa}\ln\left[Ey_p\frac{(C_\mu^{1/2}k_p)^{1/2}}{\nu}\right] \tag{4}$$

The second version of the $k$-$\epsilon$ model evaluated is that of Chieng and Launder (1980). Figure 2 shows the assumed approach where the control volume around the wall adjacent node $p$ contains a viscous sublayer out to a distance $y_v$ from the wall, and the turbulent kinetic energy varies linearly from the node adjacent to the wall to $y_v$. The connection between the velocity at the node adjacent to the wall and the wall shear stress $\tau_w$ is given by

$$\frac{U_p C_\mu^{1/4}k_v^{1/2}}{\tau_{w/\rho}} = \frac{1}{\kappa}\ln\left[Ey_p\frac{(C_\mu^{1/2}k_v)^{1/2}}{\nu}\right] \tag{5}$$

with the kinetic energy of the turbulence $k$ evaluated at the edge of the viscous sublayer.

The dissipation $\epsilon$ is again evaluated at the first nodal point adjacent to the wall by

$$\epsilon_p = \frac{C_\mu^{3/4}k_p^{3/2}}{y_p} \tag{6}$$

Other models in the near wall region for $\epsilon$, in the $\epsilon$ equation,

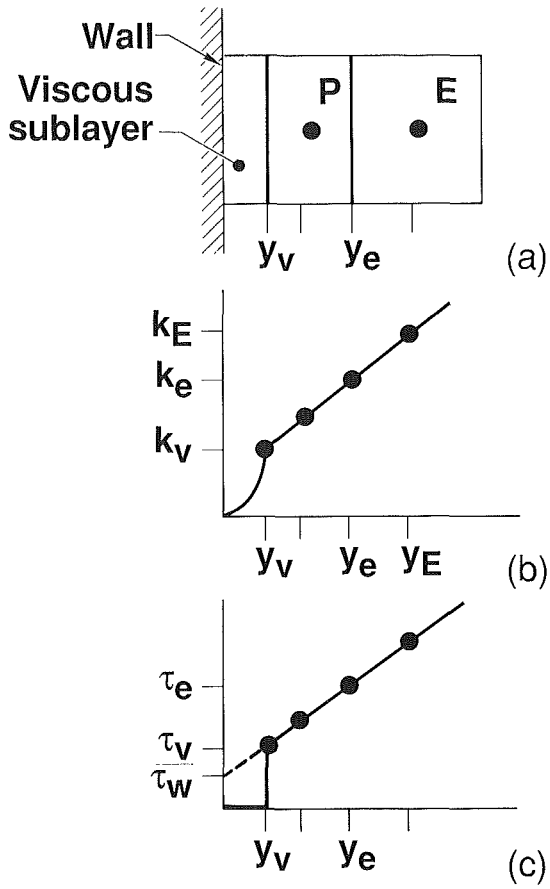


**Fig. 2 The model for (a) the near wall adjacent cell, (b) the assumed variation of turbulence kinetic energy, and (c) the assumed distribution of turbulent shear stress**

were considered. The Amano and Jensen (1982) two-layer model, as applied to impinging jet flow, showed little improvement in heat transfer over the Chieng and Luander (1980) model. The Amano (1984) two and three-layer models, as applied to an abrupt pipe expansion case, did show a significant improvement. Heat transfer in our spherical annulus occurs only on the inner sphere and represents a case similar to impinging jet flow, and thus the Amano and Jensen (1982) model is expected to give similar results compared to the model by Chieng and Launder (1980).

The mean generation rate $P$ of the turbulent kinetic energy at the first node adjacent to the wall is given by

$$P = \frac{\tau_w(U_e - U_v)}{y_e} + \frac{\tau_w(\tau_e - \tau_w)}{\rho\kappa C_\mu^{1/4}k_v^{1/2}y_e}\left(1-\frac{y_v}{y_e}\right) \tag{7}$$

and the mean dissipation rate $\epsilon_m$ is given by

$$\epsilon_m = \frac{2k_v^{3/2}}{y_e R_v} + \frac{1}{2.55y_e}\left[\frac{2}{3}(k_e^{3/2}-k_v^{3/2})\right.$$

$$\left.+2a(k_e^{1/2}-k_v^{1/2})+\lambda\right] \tag{8}$$

where

$$\lambda = a^{3/2}\ln\left[\frac{(k_e^{1/2}-a^{1/2})(k_v^{1/2}+a^{1/2})}{(k_v^{1/2}-a^{1/2})(k_e^{1/2}+a^{1/2})}\right] \text{ if } a>0 \tag{9}$$

$$= 2(-a)^{3/2}\left[\tan^{-1}\frac{k_e^{1/2}}{(-a)^{1/2}}-\tan^{-1}\frac{k_v^{1/2}}{(-a)^{1/2}}\right] \text{ if } a<0 \tag{10}$$

and where

$$a = k_p - \frac{(k_p - k_E)}{(y_p - y_E)} y_p \tag{11}$$

and

$$R_v = \frac{y_v k_v^{1/2}}{\nu} = 20 \tag{12}$$

The local wall heat flux and near wall temperature profile are given as

$$\frac{\rho C_p C_\mu^{1/4} k_p^{1/2} (T_w - T_p)}{q_w} = \sigma_T \left[ \frac{1}{\kappa} \ln \left( E y_p \frac{(C_\mu^{1/2} k_p)^{1/2}}{\nu} \right) + P* \right] \tag{13}$$

where $P*$ is the $P$ function given by Jayatilleke (1969)

$$P* = 9.24((\sigma/\sigma_T)^{3/4} - 1)(1 + 0.28\exp(-0.007\,\sigma/\sigma_T)) \tag{14}$$

**Numerical Solution Procedure.** The method used for solving equation (1) is the solution procedure of the TEACH code (Patankar, 1980). This program takes a control volume approach with scalar variables evaluated at the center of a control volume and the velocity vector quantities evaluated at the control volume boundaries. The TEACH code version used in this study uses a hybrid differencing scheme in which central differencing is used when the control volume Peclet number is less than 2 and upwind differencing is used for Peclet numbers greater than 2. The problem of determining the pressure distribution and satisfying mass conservation is overcome by adjusting the pressure field so as to satisfy mass conservation. This method is the so-called semi-implicit method for pressure-linked equations (SIMPLE) algorithm.

For this study the TEACH code was rewritten from cylindrical coordinates into spherical coordinates. The energy equation to model the heat transfer was added as well as the near-wall models for the $k$–$\epsilon$ equations.

At the inflow boundary region, a uniform temperature and velocity profile is given. The turbulence intensity ($k/V_{\text{in}}^2$) is assumed to be in the range of 0.005, and the turbulent length scale ($k^{3/2}/\epsilon$) is given by 0.03 $r_o$. At the outflow boundary region, the flow is assumed to be of the parabolic type. The inner sphere temperature is specified and the outer sphere is assumed to be adiabatic. A no-slip velocity boundary condition is applied at the sphere walls, and symmetry is assumed about the vertical centerline.

Computations for laminar flow were made primarily with a uniform mesh of 36 node points in the radial direction and 60 node points in the longitudinal direction. Under relaxation of the conservation equations was required for convergence. Typically the momentum equations required a relaxation parameter of 0.5, and the pressure correction equation required relaxation parameters from 0.8 for nonbuoyant flow to 0.2 for buoyant flows. Convergence occurred usually in fewer than 600 iterations, with one iteration representing a solution of each conservation equation. The convergency criteria were based on a normalized mass error balance, with convergence assumed for values below $1 \times 10^{-5}$. The balance was calculated by summing the absolute values of the mass flow errors at each node point divided by the total mass flow rate. The computations were run on a CRAY-1 computer and, for a $60 \times 36$ mesh, required approximately 2 min of computer time.

Mesh independence studies for laminar flow were made at $R_e = 110$. Increasing the mesh longitudinally by 52 percent resulted in 1 percent increase in total system Nusselt number $\text{Nu}_g$, and the flow separation point shifted upstream by 3 percent. The mean longitudinal velocity $U$ varied by 5 percent in the inlet region to less than 1 percent in the downstream regions. Increasing the mesh radially by 55 percent resulted in a 5 percent decrease in total system Nusselt number $\text{Nu}_g$, and the flow separation point shifted downstream by 4 percent. The mean longitudinal velocity $U$ varied by 4 percent in the inlet region to less than 1 percent in the downstream regions.

Computations for turbulent flow were made primarily using a mesh with 12 radial nodes and 60 longitudinal nodes. Underrelaxation of the conservation equations for turbulent calculations was also required. Typically the momentum equations required a relaxation parameter of 0.5, the pressure correction equation required relaxation parameters down to 0.2, and the $k$ and $\epsilon$ equations required relaxation parameters of 0.3. Applying a convergence criterion similar to that for laminar flow resulted in convergence after approximately 1500 iterations. Increasing the mesh longitudinally by 52 percent at $\text{Re} = 1086$ resulted in a 2 percent decrease in total system Nusselt number $\text{Nu}_g$. The mean longitudinal velocity $U$, and turbulent kinetic energy $k$, varied by 2 percent and 3 percent, respectively, in the inlet region. In the relatively quiescent downstream regions, the mean longitudinal velocity $U$ varied by 3 percent and the turbulent kinetic energy $k$ decreased as much as 14 percent. Increasing the mesh radially by 40 percent resulted in a 3 percent increase in total system Nusselt number $\text{Nu}_g$. The longitudinal velocity $U$ varied by less than 2 percent throughout the flow. The turbulent kinetic energy $k$ varied by 2 percent in the inlet regions to values decreased by as much as 14 percent in the downstream regions. The computations were run on a CRAY-1 computer and, for a $60 \times 12$ mesh, required approximately 2-1/2 min of computer time.

## Results and Discussion

**Laminar Flow.** Analysis of laminar flow through a heated spherical annulus, without buoyancy effects considered, was performed by Ramadyani et al. (1983). Ramadhyani's analyses were duplicated in this study using the spherical coordinate version of the TEACH code in an effort to verify proper operation of the code. The results gave identical flow patterns with a recirculation zone along the wall of the outer sphere and separation of the flow along the wall of the inner sphere occurring approximately 3/4 around the sphere. Further work by Ramadhyani et al. (1984) in which the buoyancy effects were modeled showed a strong effect on the laminar flow patterns caused by buoyancy. Duplication of these calculations again produced identical flow patterns and showed that buoyancy effects may have a strong impact on heated flow in a spherical annulus.

Computational results were obtained for the total Nusselt number as a function of the gap Reynolds number for hot water flow through the spherical annulus configuration shown in Fig. 1. The total Nusselt number $\text{Nu}_g$ is calculated from average inner sphere temperature, average inlet and exit temperatures, and the fluid mass flow rate by:

$$\text{Nu}_g = \frac{mC_p (T_{\text{out}} - T_{\text{in}})(r_o - r_i)}{A(T_i - T_B)K} \tag{15}$$

Results were obtained for laminar flow with and without buoyancy effects incorporated into the momentum equations. Figure 3 shows results for total system Nusselt number for laminar buoyant flow. The results show that the laminar buoyant model underpredicts the total Nusselt number by 16 percent at a gap Reynolds number of 110. At a gap Reynolds number of 1086 the total Nusselt number is overpredicted by 12 percent. For the nonbuoyant laminar case, the total system Nusselt number is lower initially at a gap Reynolds number of 110, but soon increases and equals the values for the laminar buoyant case for gap Reynolds numbers of 180 and above. The results for both the laminar buoyant and nonbuoyant cases show an improvement over results calculated by Tuft and Brandt (1982) as shown in Fig. 3. The calculations in this study for laminar flow were performed with a mesh that had

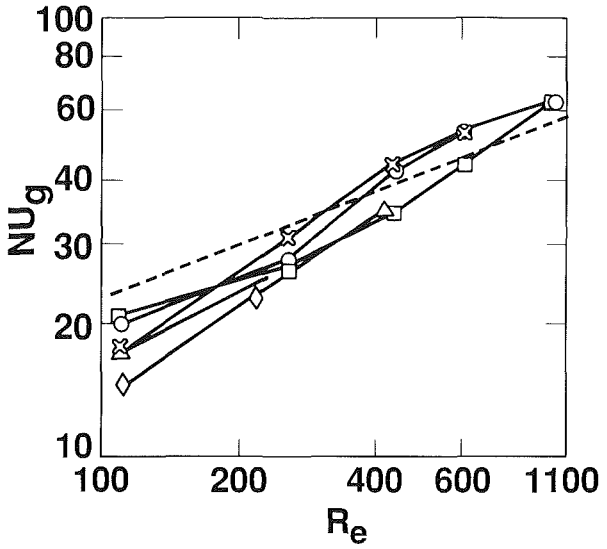


Fig. 3 Measured and calculated total-system Nusselt number: _ _ _ _ experiment (Tuft and Brandt, 1982); calculated: ◇ laminar (Tuft and Brandt, 1982); ⋈ laminar, nonbuoyant; ○ laminar, buoyant; □ $k$-$\epsilon$ model, buoyant; △ $k$-$\epsilon$ model, nonbuoyant

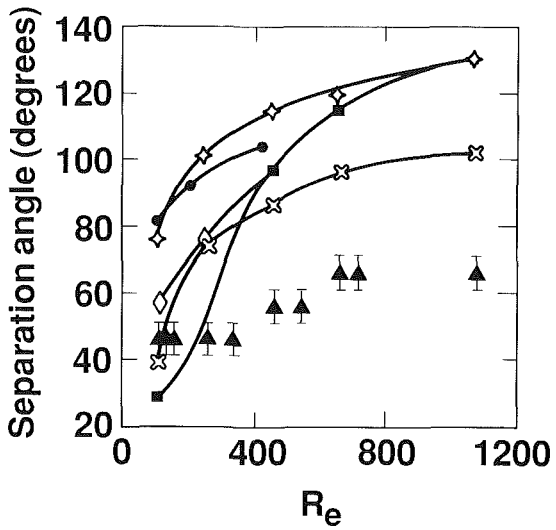


Fig. 4 Measured and calculated separation angles: ▲ experiment (Tuft and Brandt, 1982); calculated: ■ laminar, buoyant; ✧ laminar, nonbuoyant; ● laminar, (Tuft and Brandt, 1982); ◇ $k$-$\epsilon$ model; ⋈ mixing length model

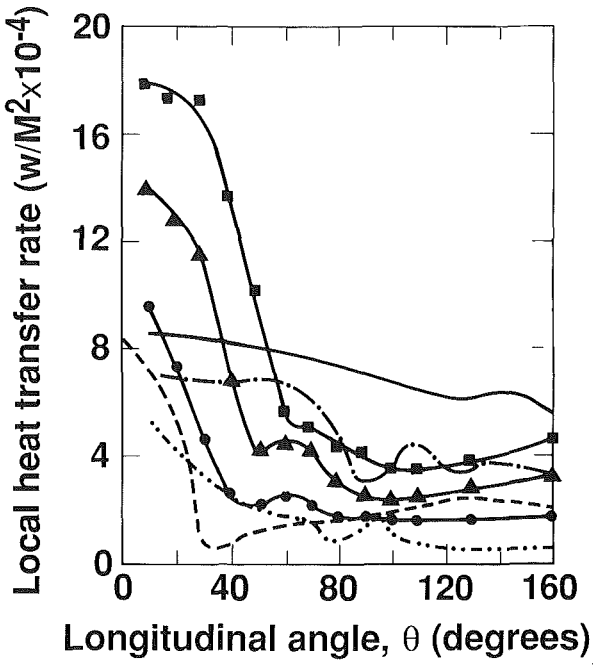


Fig. 5 Local heat transfer rate based on a laminar flow calculation: experiment (Tuft and Brandt, 1982): ■ Re = 1086; ▲ Re = 465; ● Re = 110; calculated: ___ Re = 1086; _ . _ Re = 465; _ _ _ Re = 110; _ . . . _ Re = 110, nonbuoyant

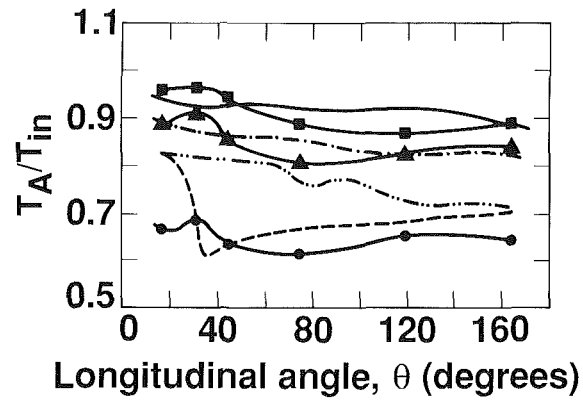


Fig. 6 Normalized radial average annulus water temperature distribution based on a laminar flow calculation: experiment (Tuft and Brandt, 1982): ■ Re = 1086; ▲ Re = 465; ● Re = 110; calculated: ___ Re = 1086; _ . _ Re = 465; _ _ _ Re = 110; _ . . . _ Re = 110, nonbuoyant

60 longitudinal nodes and 36 radial nodes, which is finer than the 16 radial nodes used by Tuft and Brandt (1982).

The calculational results for the location of the separation point of the boundary layer along the inner sphere are given in Fig. 4. The results for laminar nonbuoyant flow, as well as the results of Tuft and Brandt (1982) for laminar nonbuoyant flow, show a separation point near 80 deg at a gap Reynolds number of 110. The separation point is located in a region of adverse pressure gradient with the experimental wall jet separating sooner than predicted due to observed vortex motion and flow instabilities. Incorporating the effects of buoyancy into the laminar calculations, however, shows in Fig. 4 that buoyancy has a marked effect on the location of the separation point. The cooling of the fluid on the inner sphere wall gives rise to negative buoyancy forces that act against the flow direction and thus aid in causing separation. Incorporating buoyancy improves the calculation of the location of the separation point at lower gap Reynolds numbers but does not affect the results at higher gap Reynolds numbers. The calculational results do show the trend of the separation point moving downstream with increases in gap Reynolds number.

Figure 5 shows calculated and experimental local heat transfer rate for gap Reynolds numbers of 110, 465, and 1086 for laminar buoyant flow. The maximum heat transfer rate occurs in the inlet region where maximum wall jet velocities occur on the inner sphere. The heat transfer rate decreases with increasing angle due to the deceleration of the wall jet. A local minimum heat transfer rate occurs at the location of the separation point where the velocity gradient is zero and the fluid is stagnant. Downstream of the separation point, a region of reverse flow exists and the heat transfer rate increases. The flow reattaches downstream of the separation point, and the heat transfer rate assumes a relatively flat profile in the downstream low-velocity region. Also shown is the calculated local heat transfer rate for laminar nonbuoyant flow at a gap Reynolds number of 110. At higher gap Reynolds numbers, the difference between buoyant and nonbuoyant cases become small. The computed heat transfer rate in the inlet region is considerably underpredicted. Experimen-

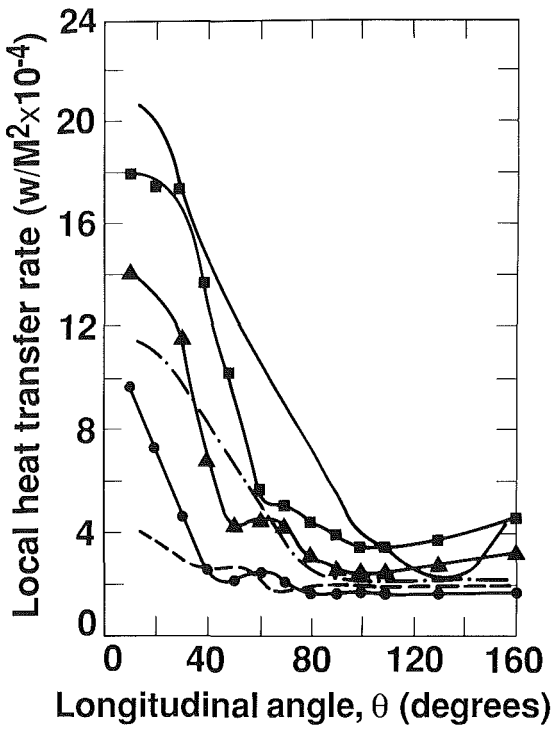


**Fig. 7 Local heat transfer rate based on a $k$–$\epsilon$ turbulence model calculation: experiment (Tuft and Brandt, 1982): ■ Re = 1086; ▲ Re = 465; ● Re = 110; calculated: ___ Re = 1086; _ . _ Re = 465; _ _ _ Re = 110**

tal observations show vortex motion, large temperature fluctuations, and unstable flow geometry in this region, which suggest that the flow is turbulent with an associated increased heat transfer rate.

Calculated profiles of normalized average radial temperature are shown in Fig. 6. For laminar buoyant flow the profile at a gap Reynolds number of 110 shows a profile that is much improved over the nonbuoyant case. At higher gap Reynolds numbers of 465 and 1086, the profiles that are shown in Fig. 6 for laminar buoyant flow are also found to be very similar to the nonbuoyant case. The temperature profiles are very much dependent on the location of the separation point. Since the local minimum in heat transfer rate, velocity gradient, and temperature is associated with the separation point, the accuracy of these profiles improve as separation is more accurately predicted.

## Turbulent Flow

The buoyant laminar flow analysis was extended by incorporating a $k$–$\epsilon$ turbulence model (Launder and Spalding, 1974) to calculate a turbulent viscosity.

Calculational results for local heat transfer rate at gap Reynolds numbers of 110, 465, and 1086 are shown in Fig. 7. The results show a high local heat transfer rate in the entrance region, which falls rather sharply until it levels off to a fairly constant value in the quiescent regions of the flow. Comparing the turbulent calculations to the buoyant laminar flow results of Fig. 6 shows that the $k$–$\epsilon$ model results are improved in the entrance region and follow more closely the experimentally determined slope of the local heat transfer curve at gap Reynolds numbers of 465 and 1086. The higher heat transfer rates in the inlet region along the inner sphere are due to large velocity gradients in the wall jets. These large velocity gradients produce high turbulent kinetic energies and associated high turbulent viscosities and heat transfer coefficients. The wall jet velocity drops off rapidly as the equator is approached

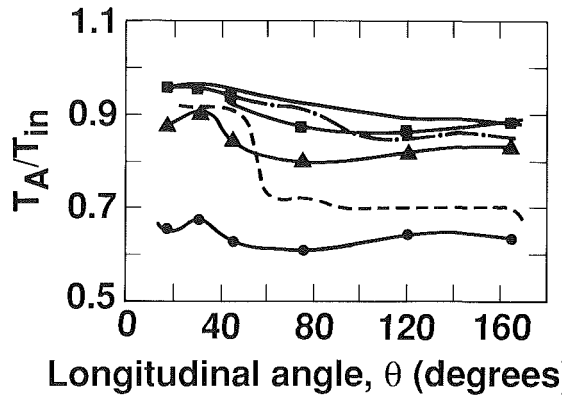


**Fig. 8 Normalized radial average annulus water temperature distribution based on a $k$–$\epsilon$ turbulence model calculation: experiment (Tuft and Brandt, 1982): ■ Re = 1086; ▲ Re = 465; ● Re = 110; calculated: ___ Re = 1086; _ . _ Re = 465; _ _ _ Re = 110**

and results in an associated drop in turbulent heat transfer coefficient. The values of dimensional wall distance $y^+$ vary considerably along the inner sphere wall. In the entrance region where a wall jet along the inner sphere exists, the values of $y^+$ are initially very high and remain relatively high until either the flow approaches the equator or boundary layer separation occurs. Farther downstream, the flow is relatively quiescent and $y+$ becomes smaller. At a higher gap Reynolds of Re = 1086, the values of $y^+$ vary from 233 to 43 in the first half of the annulus. In the annulus downstream of the equator, the values of $y^+$ vary from 34 to 19. For a gap Reynolds number of 465, the values of $y^+$ from the entrance to the separation point vary from 92 to 20, but downstream of separation the values of $y^+$ are below 20, and the flow is assumed to be in the laminar sublayer.

Results for total Nusselt number based on a $k$–$\epsilon$ turbulent flow analysis are also given in Fig. 3. For buoyant calculations the $k$–$\epsilon$ model gives similar results when compared to the laminar buoyant analyses, especially at high and low Reynolds numbers. The results for nonbuoyant turbulent flow shown in Fig. 3 are not as accurate as those for buoyant flow at a Reynolds number of 110 but soon equal the buoyant turbulent case results at higher Reynolds numbers. The buoyant turbulent analysis, at Re = 110, predicts more accurately than the nonbuoyant case the boundary layer separation on the inner sphere and thus results in a more accurate caculation of heat transfer. Applying the boundary conditions from the $k$–$\epsilon$ model of Chieng and Launder (1980) gave total Nusselt number results that changed little from those of the Launder and Spalding (1974) model.

Normalized average radial temperature profiles based on turbulent flow are given in Fig. 8. The calculated profile at a gap Reynolds number of 1086 is more accurate than that at a low gap Reynolds number of 110. Comparing the turbulent calculation to the laminar buoyant flow calculation shows better agreement at a gap Reynolds number of 110 for laminar flow and better agreement for the $k$–$\epsilon$ turbulence model at a gap Reynolds number of 1086. Figures 9 and 10 show typical calculated horizontal velocity and temperature profiles across the annulus at several locations for a gap Reynolds number of 260.

Results for the location of the separation point using the buoyant $k$–$\epsilon$ model are shown in Fig. 4. The results fall between the data of the nonbuoyant and the buoyant laminar cases. At high gap Reynolds numbers, the buoyant $k$–$\epsilon$ model did not give any separation. Flow in the annulus up to the annulus equator experiences a positive gradient along the boundary layer due to increasing cross-sectional area and decelerating fluid. Boundary layer separation occurs if the momentum of the boundary layer cannot overcome the

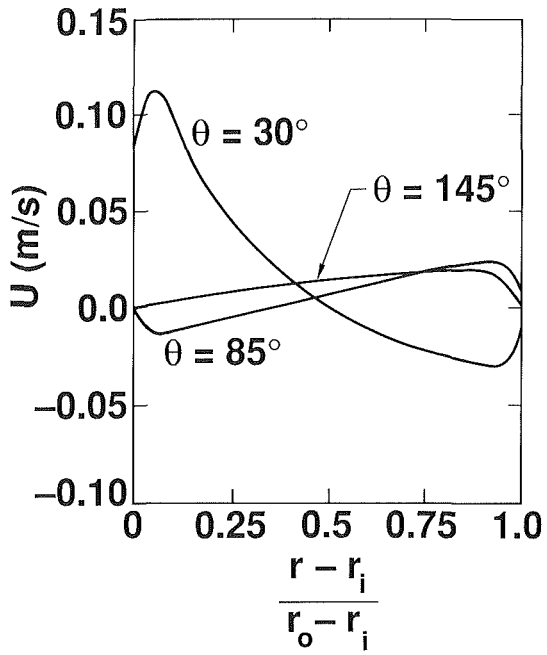


**Fig. 9 Horizontal velocity profiles for flow at a gap Reynolds number of 260 at longitudinal coordinates $\theta$ of 30, 85, and 145 deg**

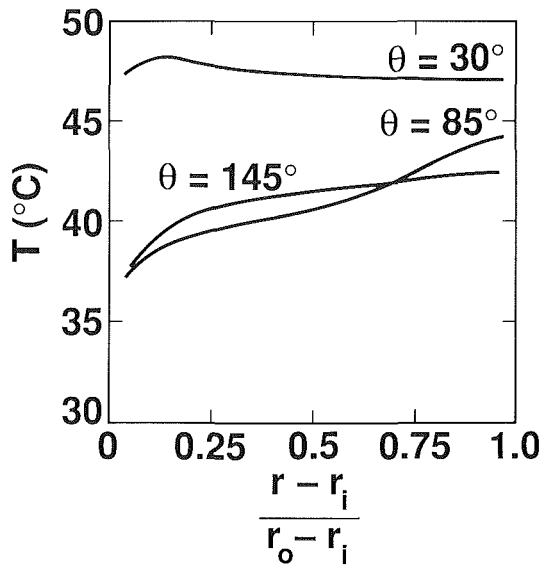


**Fig. 10 Temperature profiles for flow at a gap Reynolds number of 260 at longitudinal coordinates $\theta$ of 30, 85, and 145 deg**

pressure gradient. Downstream of the equator, a negative pressure gradient exists, and flows that have not yet separated will tend not to separate. The nonbuoyant $k$–$\epsilon$ model calculation did not predict any separation occurring over the range of gap Reynolds number from 110 to 1086. In an attempt to obtain a better calculation of separation point location, a simple mixing length model ($l_m = \kappa y_p$) was incorporated into the laminar analysis at the wall adjacent node. The results show in Fig. 4 that this mixing length model gives the best results over the range of gap Reynolds numbers considered.

## Conclusions

It is believed that this study is the first analysis in which the two equation $k$–$\epsilon$ turbulence model and the full axisymmetric Navier–Stokes equations have been applied to steady spherical annulus turbulent forced convection flow.

There are four main conclusions from this study of fluid flow and heat transfer in a spherical annulus:

1 Incorporating a two-equation $k$–$\epsilon$ turbulence model improves the computation of local heat transfer over a laminar model calculation, especially in the entrance region where a high-velocity stream of fluid flows along the inner sphere wall.

2 Incorporating buoyancy into the computations shows that buoyancy forces are significant at lower gap Reynolds numbers and strongly affect both the fluid flow pattern and the location of the boundary layer separation point on the inner sphere.

3 The location of the separation point of the boundary layer along the inner sphere moves downstream with increases in the gap Reynolds number.

4 Prediction of the location of the boundary layer separation point along the inner sphere wall was more accurate at lower gap Reynolds numbers than at higher gap Reynolds numbers.

## Acknowledgments

This work was performed under the auspices of the U.S. Department of Energy by Lawrence Livermore National Laboratory under Contract No. W-7405-Eng.-48.

## References

Amano, R. S., and Jensen, M. K., 1982, "A Numerical and Experimental Investigation of Turbulent Heat Transport of an Axisymmetric Jet Impinging on a Flat Plate," ASME Paper No. 82-WA/HT-55.

Amano, R. S., 1984, "Development of a Turbulence Near-Wall Model and Its Application to Separated and Reattached Flows," *Numerical Heat Transfer*, Vol. 7, pp. 59–75.

Astill, K. N., 1976, "An Analysis of Laminar Forced Convection Between Concentric Spheres," ASME JOURNAL OF HEAT TRANSFER, Vol. 98, pp. 601–608.

Astill, K. N., Kerney, P. J., and Newton, R. L., 1978, "An Experimental Investigation of Forced Convection Between Concentric Spheres at Low Reynolds Number," *Proceedings of the Sixth International Heat Transfer Conference*, Vol. 5, pp. 179–184.

Bird, R. B., Stewart, W. E., and Lightfoot, E. N., 1964, *Transport Phenomena*, Wiley, New York, pp. 117–118.

Bozman, J. D., and Dalton, C., 1970, "Flow in the Entrance Region of a Concentric Sphere Heat Exchanger," ASME JOURNAL OF HEAT TRANSER, Vol. 92, pp. 184–185.

Brown, J. R., 1967, "Natural Convection Heat Transfer Between Concentric Spheres," Ph.D. Dissertation, University of Texas, Austin, TX.

Cobble, M. H., 1963, "Spherical Shell Heat Exchanger—Dirichlet Problem," *Journal of the Franklin Institute*, pp. 197–198.

Chieng, C. C., and Launder, B. E., 1980, "On the Calculation of Turbulent Heat Transfer Downstream From an Abrupt Pipe Expansion," *Numerical Heat Transfer*, Vol. 3, pp. 189–207.

Jayatilleke, C. L., 1969, "The Influence of Prandtl Number and Surface Roughness on the Resistance of the Laminar Sub-Layer to Momentum and Heat Transfer," *Progress in Heat and Mass Transfer*, Vol. 1, pp. 193–329.

Launder, B. E., and Spalding, D. B., 1974, "The Numerical Computation of Turbulent Flows," *Computer Methods in Applied Mechanics and Engineering*, Vol. 3, pp. 269–289.

Newton, R. L., 1977, "An Experimental Investigation of Forced Convection Between Concentric Spheres," Master's Thesis, Tufts University, Medford, MA.

Patankar, S. V., 1980, *Numerical Heat Transfer and Fluid Flow*, Hemisphere Publishing Corp.

Ramadhyani, S., Torbaty, M., and Astill, K. N., 1983, "Laminar Forced Convection Heat Transfer in Spherical Annuli," ASME JOURNAL OF HEAT TRANSFER, Vol. 105, pp. 341–349.

Ramadhyani, S., Zenouzi, M., and Astill, K. N., 1984, "Combined Natural and Forced Convective Heat Transfer in Spherical Annuli," ASME JOURNAL OF HEAT TRANSFER, Vol. 106, pp. 811–816.

Rundell, H. A., Ward, E. G., and Cox, J. E., 1968, "Forced Convection in Concentric-Sphere Heat Exchangers," ASME JOURNAL OF HEAT TRANSFER, Vol. 90, pp. 125–129.

Tuft, D. B., and Brandt, H., 1982, "Forced Convection Heat Transfer in a Spherical Annulus Heat Exchanger," ASME JOURNAL OF HEAT TRANSFER, Vol. 104, pp. 670–677.

Ward, E. G., 1966, "Flow Through the Annulus Formed Between Concentric Spheres," Master's Thesis, University of Houston, Houston, TX.

**C. H. Stern**
Department of Mechanical Engineering,
Virginia Polytechnic Institute
and State University,
Blacksburg, VA 24061

**R. Greif**

**J. A. C. Humphrey**

Department of Mechanical Engineering,
University of California, Berkeley,
Berkeley, CA 94720

# An Experimental Study of Natural Convection in a Toroidal Loop

*Velocity and temperature profiles were measured at the entrance and exit to the heating section of a toroidal thermosyphon loop operating under steady flow conditions for a range of heat inputs. Velocity measurements were made with a laser-Doppler velocimeter and temperature measurements with a small thermocouple probe. Detailed results are presented for the longitudinal and circumferential components of the velocity for four heat inputs. The data for cross-stream secondary flows and streamwise flow reversals emphasize the importance of including three-dimensional effects in analyses of these systems.*

## 1 Introduction

A thermosyphon loop is a natural circulation loop in which the flow is driven by thermally generated density gradients. Applications for natural convection loops include solar heating and cooling, geothermal power production, permafrost protection, engine cooling, and cooling of nuclear reactors. In a thermosyphon important design considerations are the magnitude and the stability of the resulting flow rate of the working fluid. In order to facilitate the design of effective and reliable thermosyphons, the basic characteristics of these flows must be understood. This requires a knowledge of the physics of the flow and how the flow affects the heat transfer, as well as an experimental data base for appraising numerical models.

In order to obtain a better understanding of the flow and heat transfer mechanism in thermosyphons, measurements of the velocity and temperature profiles were carried out in a toroidal thermosyphon loop (Fig. 1). The lower half of the water-filled thermosyphon is heated with a constant heat flux, while the upper half is cooled at a constant wall temperature. The toroidal loop is mounted vertically and can be rotated in the vertical plane about its center to any angle $\theta_0$ (see Fig. 1) in the longitudinal ($\theta$) direction. The value of $\theta_0$ directly affects the stability of the flow in the thermosyphon.

Nondimensionalization of the governing equations shows that the Prandtl number, the Grashof number, and the Froude number are important parameters in the thermosyphon flow (see Nomenclature). The Prandtl number varies from 4 to 7, corresponding to the variation of the properties of water with respect to temperature. The Grashof number and the Froude number vary with changing heat input. Choosing the tube diameter as the characteristic length $L$, and using the characteristic velocity $V$ (see Nomenclature) from Creveling et al. (1975), the Grashof number is defined as $\mathrm{Gr} = g\beta\Delta TL^3/\nu^2$, with $\Delta T = Q/(\dot{m}c)$.

Increasing the heat input corresponds to an increase in the buoyant driving force and heat inputs varying from 145 W to 875 W result in Grashof numbers ranging from $1.4 \times 10^5$ to $8.9 \times 10^5$. The Froude number, a measure of inertia relative to gravity, increases from 0.002 to 0.042 with the increase in heat input. The ratio of the toroid radius to the tube radius is $R/a = 24.6$, which results in significant curvature effects on the flow field.

Several reviews of thermosyphon flows and their applications are available. Japikse (1973) lists many practical applications for buoyancy-driven heat transfer. Zvirin (1981) provides both a review of natural circulation loops for nuclear reactor cooling and a listing of important parameters for characterizing these flows. He also recommends that measurements be made of the temperature and the velocity profiles within these loops. Mertol and Greif (1985) provide a comprehensive review of natural circulation loops, including a summary of the analyses done on the toroidal thermosyphon.

In pioneering experiments on the toroidal loop, Creveling et al. (1975) and Damerell and Schoenhals (1979) measured the temperature at the entrance to and the exit from the heating section. These measurements were made at a fixed radial location in the tube where the temperature was considered to be approximately equal to the bulk temperatures of the flow, assuming steady, forced, laminar flow. The mass flow rate was estimated using an energy balance based on the heat input and the measured temperature difference of the fluid from the inlet to the outlet of the heating section.

The measurements of Stern and Greif (1987) showed that the temperature profiles in the toroidal loop vary significantly in three dimensions and differ from the profiles assumed in previous studies. In the present work, measurements of the velocity and temperature profiles have been obtained for several heat inputs. The flow is examined both quantitatively, based on the recorded temperature and velocity data, and qualitatively, utilizing flow visualization. The results obtained are believed to represent the first laser-Doppler measurements of the velocity profile in a toroidal thermosyphon loop.

The results show that very complex secondary and longitudinal recirculating flow patterns are present. Previous flow visualization tests have reported the presence of secondary and reversed flows, but no quantitative data have been presented. While the one-dimensional analyses of Creveling et

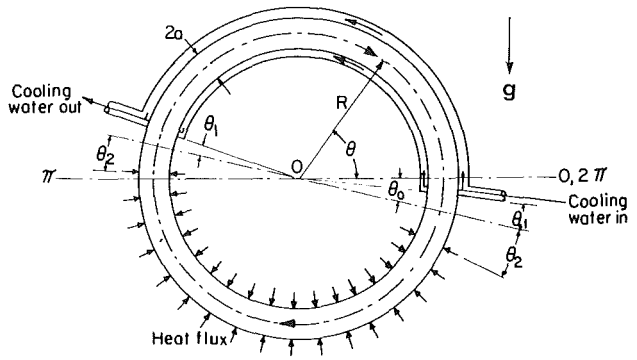


Fig. 1 Toroidal thermosyphon

Contributed by the Heat Transfer Division for publication in the JOURNAL OF HEAT TRANSFER. Manuscript received by the Heat Transfer Division September 17, 1987. Keywords: Heat Pipes and Thermosyphons, Natural Convection.

al. (1975), Damerell and Schoenhals (1979), and Greif et al. (1979), as well as the two-dimensional analysis of Mertol et al. (1982), neglect these flow characteristics, the three-dimensional numerical analysis of Lavine (1984) clearly predicts them. The analyses of Lavine (1984) and Lavine et al. (1986, 1987) predict regions of longitudinal (streamwise) flow reversal, as well as secondary, circumferential (cross-stream) flow patterns resulting from the curvature of the thermosyphon tube. However, numerical limitations restricted these three-dimensional analyses to low Grashof numbers. If water is the working fluid, the temperature differences at these Grashof numbers are too small to measure accurately. It is important to have velocity data for the development and testing of improved numerical models as well as for advancing fundamental understanding of these flows.

## 2 Experimental Apparatus and Procedure

**Description of the Thermosyphon.** The torus of the thermosyphon (see Fig. 1) was fabricated from 1.22 in. (31 mm) i.d. Pyrex glass tubing with a major diameter of 30 in. (76.2 cm). The tube wall thickness is 0.079 in. (2 mm). The torus has three ball joints in the bottom half to permit thermal expansion. The working fluid in the thermosyphon tube is distilled water.

The thermosyphon is cooled by means of a water jacket, which surrounds the upper portion of the torus. The jacket is made from clear Plexiglas and is a square cross section, 2 in. $\times$ 2 in. (5.08 cm $\times$ 5.08 cm). The Plexiglas allows visual observation of the flow over the entire cooled section of the thermosyphon. A high coolant flow rate for all the experimental runs resulted in a nearly constant wall temperature over the cooling section. The temperature difference of the coolant fluid, between the inlet and the outlet of the cooling jacket, was always less than 0.5°C.

The thermosyphon is heated with 1/2 in. (1.27 cm) wide nichrome heater tapes that are wound evenly around the lower half of the torus. Power is supplied to the heater tapes with a 0-115 VAC Powerstat variable transformer. The experimental runs have been conducted at power levels ranging from 145 to 875 W corresponding to wall heat fluxes ranging from 1400 to 8410 W/m$^2$. The area of the heated section is 0.104 m$^2$. The heated section of the torus is covered with multiple layers of fiberglass blanket approximately 3 in. (7.6 cm) thick.

Construction considerations required that the exterior heating and cooling sections of the thermosyphon each cover slightly less than one half of the entire surface of the torus. As shown in Fig. 1, a sector of 14 deg ($\theta_1$ = 4 deg and $\theta_2$ = 10 deg) was left exposed on either side of the torus to permit optical access. Comparison of fluid temperature measurements for insulated and uninsulated conditions at these locations confirmed that this wall condition has no discernible effect on the measured temperature profiles.

The torus is made with glass nipples at the inlet and outlet to the heated section. These serve as access ports to permit measurement of the fluid temperature profiles at these locations. The nipples accommodate rubber stoppers, which are flush with the inner wall and are located at an angle of 9 deg below the major diameter of the torus; i.e., at $\theta = -(\theta_0 + 9$ deg) and $\theta = 180$ deg $+ 9$ deg $- \theta_0)$ on the right-hand and left-hand sides, respectively, in Fig. 1. Further details on the temperature measurements are presented in Stern and Greif (1987).

**Laser-Doppler Anemometry System and Measurement Procedure.** The laser-Doppler anemometer (LDA) system that is used to make velocity measurements in the thermosyphon is a DISA (Dantec) two-component system, operated in the backscatter made with frequency shifting. The optimum frequency shift for the measured velocities and the signal processing equipment used in this study was determined experimentally to be between 60 and 80 kHz. Details on the LDA system and measurement procedure are given in Stern (1986).

Only one component of velocity was measured at any one time in the loop because of the curvature of the glass tube wall. All of the LDA measurements require passing the two incident laser beams through curved Pyrex glass walls. Since the glass walls and the water in the loop have indices of refraction that differ from air (1.474 and 1.333, respectively), these refracting interfaces are accounted for in both the positioning of the measuring volume and the calibration of the frequency signal collected. The index of refraction corrections needed for both velocity components measured in this study (longitudinal and circumferential) have been derived by Azzola and Humphrey (1984).

With the LDA technique, the velocity that is measured is that of the particles seeded in the flow and not that of the fluid. Polystyrene latex microspheres were chosen as seed particles because of their uniformly spherical shape and selected size. With a density of 1.05 g/ml, these particles are almost neutrally buoyant in water at room temperature. A particle diameter of 2.9 $\mu$m was chosen to maximize the SNR for an interference fringe spacing of 2.2 $\mu$m in the probe volume. These seeding particles follow all oscillation frequencies believed to be present in the flow. The optimum particle concentration was determined to be about 1 drop of aqueous solution (10 percent solids by weight) per 2000 ml distilled water.

Data collection and reduction are performed by the PDP 11/34 minicomputer. The number of data points collected at

## Nomenclature

$a$ = radius of thermosyphon tube
$c$ = specific heat of fluid
Fr = Froude number = $V^2/gL$
$g$ = gravitational constant
Gr = Grashof number = $g\beta\Delta TL^3/\nu^2$
$L$ = characteristic length scale
$\dot{m}$ = mass flow rate
Pr = Prandtl number
$Q$ = heat input (into heating section)
$r$ = radial coordinate in thermosyphon tube
$R$ = large radius of toroid (radius of curvature)
SNR = signal-to-noise ratio
$T$ = fluid temperature
$T_c$ = cooling water temperature
$U_\phi$ = circumferential (cross-stream) fluid velocity
$U_\theta$ = longitudinal (streamwise) fluid velocity
$V$ = characteristic velocity = $(g\beta Q/4\pi^3\mu c)^{1/2}$
$\beta$ = thermal expansion coefficient of fluid
$\Delta T$ = characteristic bulk fluid temperature difference = $Q/\pi a^2\rho cV$
$\theta$ = longitudinal coordinate around toroid
$\theta_0$ = rotational tilt angle imposed on toroid
$\theta_1$ = exposed sector of tube between center and cooling section
$\theta_2$ = exposed sector of tube between center and heating section
$\mu$ = fluid viscosity
$\nu$ = fluid kinematic viscosity
$\rho$ = fluid density
$\phi$ = circumferential coordinate in thermosyphon tube

*Table 1 Summary of measurement uncertainties*

| Variable | Type of Uncertainty | | | |
|---|---|---|---|---|
| | Systematic | | Random | |
| | Typical | Maximum [1] | Typical | Maximum [1] |
| $T - T_c$ (°C) | 1 | 1 | ±0.3 | ±0.3 |
| $U_\theta$ (%) [2] | 7.7 | 14 | ±5.0 | ±15.3 |
| $U_\phi$ (%) [3] | 33 | 70 | ±20 | ±20 |
| r (mm) | 1.6 | | ±0.5 | |
| θ (deg) | 0.1 | | ±0.5 | |
| φ (mm) | 1.0 | | ±0.1 | |

1. Restricted to small region of flow
2. As percentage of $U_\theta$ at centerline
3. As percentage of $U_\phi$ = 0.010 m/s

each position was determined to give an average that was independent of the sample size. A sample size of 1000 points at an average rate of 20 Hz with 30 percent validation results in a collection period of several minutes ensuring that the measurement period is substantially longer than any periods of oscillation in the flow. Sample sizes of 100, 200, 500, 1000, and 2000 were taken to compare the mean velocity profiles. A sample size of 1000 points was found to be sufficient, except for the low heat input case in the inner wall region where the flow enters the heating section.

## 3 Experimental Uncertainty

The experimental uncertainties for all of the measured variables are listed in Table 1. Systematic sources of uncertainty were summed to calculate the tabulated upper bound. Random sources of uncertainty were combined by taking the square root of the sum of the squares to give the listed values. The typical uncertainties that are listed in Table 1 represent the largest uncertainties expected in the data over most of the region that was measured. However, for some regions more extreme uncertainties can occur. These uncertainties are designated as maximum uncertainties and are restricted to specific locations in the flow. A detailed evaluation of the uncertainties in the measurements of both the temperatures and the velocities is given in Stern (1986). A description of the more significant uncertainties in the velocity measurement is presented here.

The uncertainties in the longitudinal velocity measurement are given as a percentage of the values at the center of the tube. Values at the tube center could not be used to normalize the circumferential velocity uncertainties because it was not possible to obtain circumferential velocities at this location. Therefore, these uncertainties are shown as a percentage of a characteristic value of 0.010 m/s.

Several of the error sources (e.g., nonuniform tube cross section, tube wall surface irregularities, probe reference location uncertainty, index of refraction gradients, etc.) contributed to both the uncertainty in the probe location coordinate and the uncertainty in the velocity measurements since the velocity that is measured may not be at the specified location. Uncertainties in the velocity resulting from errors in the location of the probe volume are dependent on the local gradient of the velocity. In most of the flow these errors would be small since the gradients are not large. However, these errors can be significant near the wall where the velocity gradient is large. The uncertainties in the probe location are evaluated solely as uncertainties in the location; i.e., their direct effect on the velocity is not included in the calculated uncertainties. However, it is noted that the errors in the probe location are primarily systematic so that the shape of the velocity profile will be much less affected by these uncertainties than will the absolute magnitude of the velocities.

Velocity bias occurs when the photodetector output in a fluctuating flow records a larger number of faster moving particles than slower moving particles in a given interval of time. The fluctuations in the thermosyphon flow are sufficiently large that velocity biasing should be considered. The velocity data from the thermosyphon show that the root-mean-square (rms) value of the longitudinal velocity increases with heat input. The exception to this trend is for the lowest heating case (145 W) when the recirculating region at the entrance to the heating section induces additional fluctuations at this location. For all the heat inputs the rms value of the longitudinal velocity is fairly uniform over the central portion of the cross section but decreases near the wall. The velocity bias error can be expected to increase with increasing rms values.

Mean velocities in the flow were calculated using equal weighting (unweighted or arithmetic mean) and with the inverse velocity weighting of McLaughlin and Tiederman (1973) (weighted mean approximating a time-weighted averaged). While the latter weighting should provide a more accurate value for the mean longitudinal velocity in this flow, problems occur when the velocity is small because the inverse velocity weighting becomes large. Therefore, the mean becomes biased toward the lower values of the velocities. For the 145 W heating case, the longitudinal velocities frequently fluctuated so as to yield negative velocities causing the weighted mean to deviate from the actual mean much further than does the unweighted mean. The mean velocity should be bounded by the weighted mean (biased toward low velocities) and the unweighted mean (biased toward high velocities). Thus, these extreme values provide a convenient estimate of the maximum error resulting from the velocity bias. An uncertainty of 5 percent in $U_\theta$ was estimated for the longitudinal velocity measurements. The maximum error in $U_\theta$ of 10 percent occurs for the 145 W heating case at the entrance to the heating section because of the presence of the reverse flow in this region. Both weighted and unweighted mean velocities are presented in the tabulated data of Stern (1986), but only unweighted velocity data are presented here because this is a better overall choice in view of the difficulties with the weighting method. Velocity bias probably does not affect the circumferential velocity measurements because the number of particles in the probe volume is not strongly correlated to the magnitude of this velocity component.

The velocity spectrum measured by the LDA technique is "broadened" by the velocity gradient because the probe records data from a finite control volume and the particles traversing the probe volume have a range of velocities. This contribution to uncertainty in the mean velocity is greatest where the velocity gradient changes most drastically (at a "corner" of the flow profile). Therefore, the maximum uncertainties listed in Table 1 correspond to corner regions of the flow profile for the mean velocities.

The uncertainties caused by a deviation in the orientation angle of the laser beams from the direction of the velocity component being measured were calculated for the condition of a (maximum) deviation of ±4 deg in the orientation angle. It is unlikely that the error in the circumferential mean velocity would be as large as the calculated value of 65 percent because the angular deviation is anticipated to be less than 4 deg. This effect leads to a significant uncertainty, but it is systematic so that the general shape of the measured velocity profile is valid despite the uncertainty in the magnitude. To reduce this uncertainty would require extremely precise dimensional tolerances in the tube to permit accurate alignment of the laser beams along the desired coordinate directions.

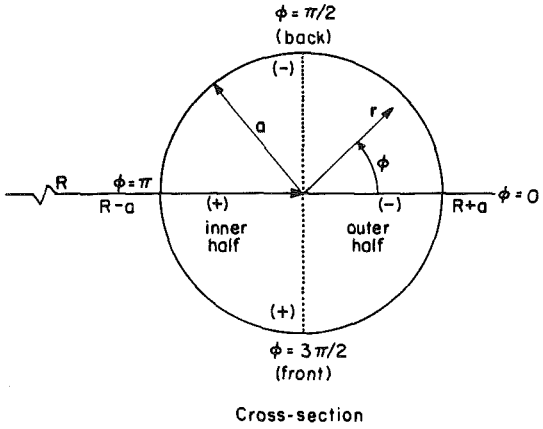


Cross-section

**Fig. 2 Thermosyphon tube cross section**

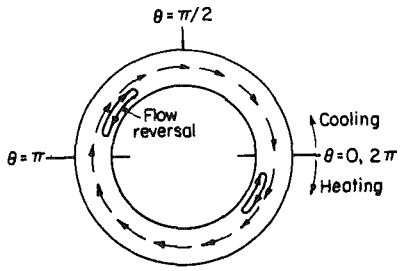


a. Recirculating Flow

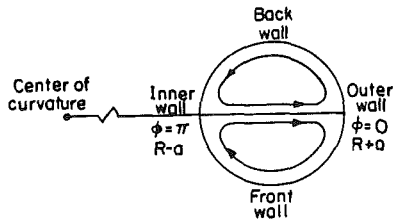


b. Secondary Flow

**Fig. 3 *Features of the thermosyphon flow***

## 4 Results and Discussion

**Flow Visualization.** Flow visualization techniques were used to observe the complex flow field in the thermosyphon. Pearl essence particles suspended in the working fluid reflected light, which permitted the fluid motion to be observed. In addition, density gradients in the thermosyphon permitted flow observation when light from a point source passed through the fluid and projected shadows on a surface behind the flow.

Several important characteristics of the fluid motion have been observed including flow recirculation in the longitudinal coordinate direction and circumferential secondary flows, as shown in Fig. 3. (The flow visualization was conducted at a tilt angle $\theta_0$ of 10 deg. To simplify the figure this tilt angle is not shown and is not used in identifying angles in this discussion, consistent with the qualitative nature of this section.) The former pattern was reported by Creveling et al. (1975). The regions of recirculation were detected by noting that the fluid motion in the region near the inner wall was opposite to the direction of the bulk flow. The inner wall refers to the portion of the thermosyphon tube cross section closest to the center of the torus. This is the region near $\phi = \pi$ (radial location $R-a$) in Fig. 2. The outer wall refers to the portion farthest from the center of the torus, i.e., near $\phi = 0$ $(R+a)$. The front wall region, that region through which most optical observations are made, is defined to be at $\phi = 3\pi/2$ and the back wall refers to the portion of $\phi = \pi/2$.

Longitudinal (or streamwise) flow recirculation was observed in the region entering the cooling section (between $\theta = \pi$ and $\theta = \pi/2$ in Fig. 3*a*) for clockwise flow at all heating levels. A similar recirculating flow region is also expected in the region where the flow enters the heating section, i.e., between $\theta = 0$ (or $2\pi$) and $\theta = 3\pi/2$. The extremity of the latter recirculation region was confirmed from the velocity measurements. Both of these recirculating flow regions were predicted in the three-dimensional numerical analysis of Lavine (1984) at Grashof numbers one order of magnitude lower.

The streamwise recirculating flow regions at the entrances to both the heating and cooling sections are caused by density changes in the fluid near the inner wall and are aided by the secondary motion. As the fluid travels upward into the cooling section (at $\theta = \pi$), it is rapidly cooled along the wall, which is maintained at $T_c$. This denser fluid is carried by the secondary motion to the inner wall where it falls under the force of gravity. The portion of the fluid that falls along the inner wall is moving opposite to the hot fluid rising upward from the heating section, thereby creating the recirculation region. A similar effect occurs in the entrance region to the heating section where hotter (less dense) fluid rises upward, along the inner wall, against the main flow.

The flow reversal works to reduce the friction on the fluid in the vicinity of these recirculation regions (cf. Lavine et al., 1984, 1986, 1987). However, the total buoyancy force is reduced by the recirculation regions. This is because the average temperature of the fluid decreases more rapidly near the cooling section entrance and increases more rapidly at the heating section entrance. The three-dimensional computations of Lavine et al. (1984, 1986, 1987) predict the flow reversal in the heating section to be stronger than the reversal in the cooling section. As the Grashof number increases the recirculation region in the heating section is expected to penetrate back into the cooling section. This is verified by the velocity measurements of this study.

Several types of cross-stream secondary flow pattern are evident in the thermosyphon. A secondary motion in the thermosyphon refers to fluid motion in the $r$, $\phi$ plane, i.e., perpendicular to the longitudinal or $\theta$ direction. Although the longitudinal velocity is at least an order of magnitude greater than the components of velocity in the $r$ or $\phi$ directions, the secondary motions are very important to both the fluid flow and heat transfer since they can strongly influence the velocity and temperature gradients near the wall.

The secondary flow shown in Fig. 3(*b*) is an expected pattern in a curved pipe flow. Berger et al. (1983) describe the origin and manner of the flow field in a curved pipe in forced convection. As the fluid flows around the center of curvature of the torus, centrifugal acceleration results in a cross-stream flow from the inner wall toward the outer wall along the symmetry plane of the tube extending from $R-a$ to $R+a$. The pressure gradient from the stagnation region near $\phi = 0$ $(R+a)$ then drives the fluid back toward the inner wall (along the curved front and back walls) resulting in the two-cell pattern shown in Fig. 3(*b*). This secondary circumferential flow has been predicted and described in the steady-state analysis of Lavine (1984) and measured in this study.

A transient secondary motion was observed in the second half of the cooling section (i.e., between $\theta = \pi/2$ and $\theta = 0$) for a clockwise flow. This motion appeared as a serpentine waviness of the observable density gradients across the vertical "symmetry" plane containing the circle of radius $R$ formed by the tube centerline. This motion may be a result of instabilities as the secondary flow (described in the previous paragraph) approaches the wall and divides at $\phi = 0$.

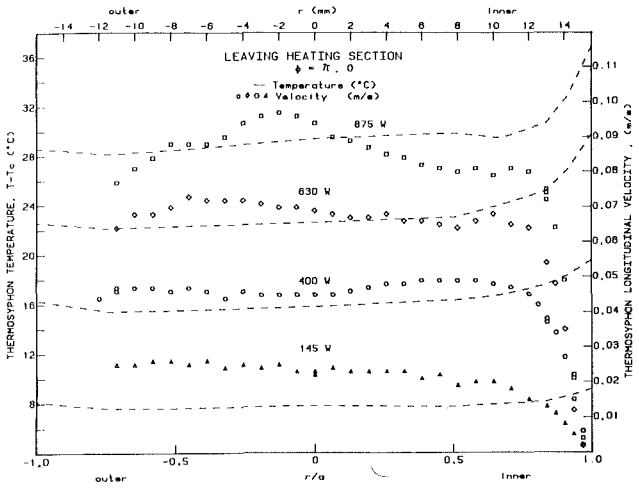


Fig. 4 Temperature and velocity profiles leaving heating section: $\phi = \pi$, 0

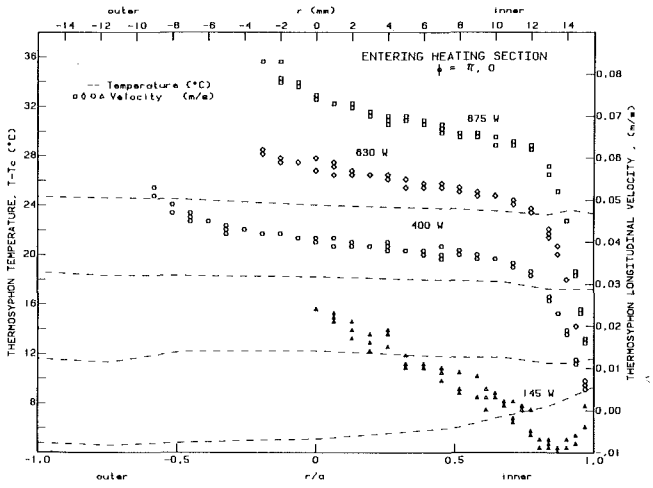


Fig. 6 Temperature and velocity profiles entering heating section: $\phi = \pi$, 0

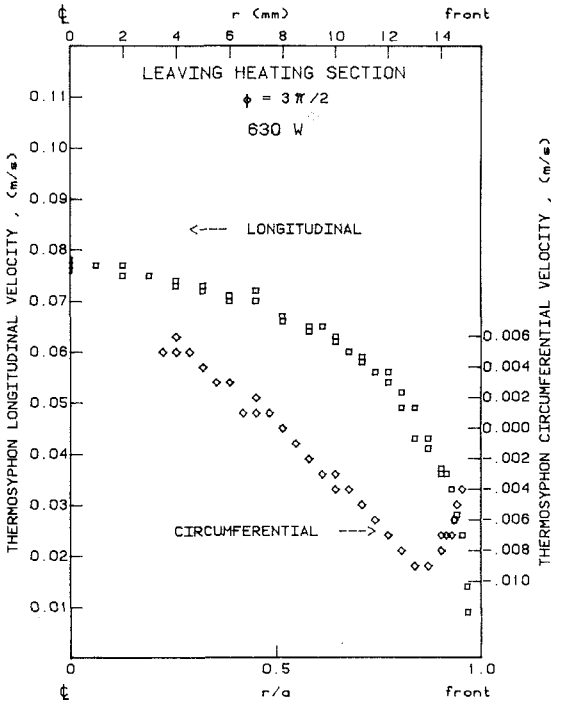


Fig. 5 Velocity leaving heating section: $\phi = 3\pi/2$, 630 W

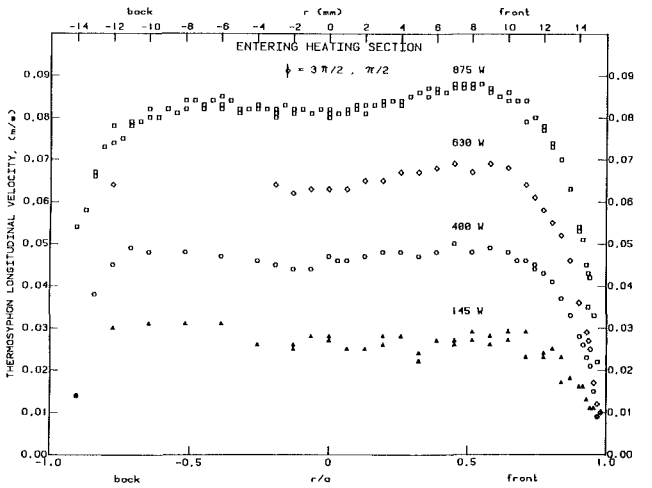


Fig. 7 Longitudinal velocity entering heating section: $\phi = 3\pi/2$, $\pi/2$

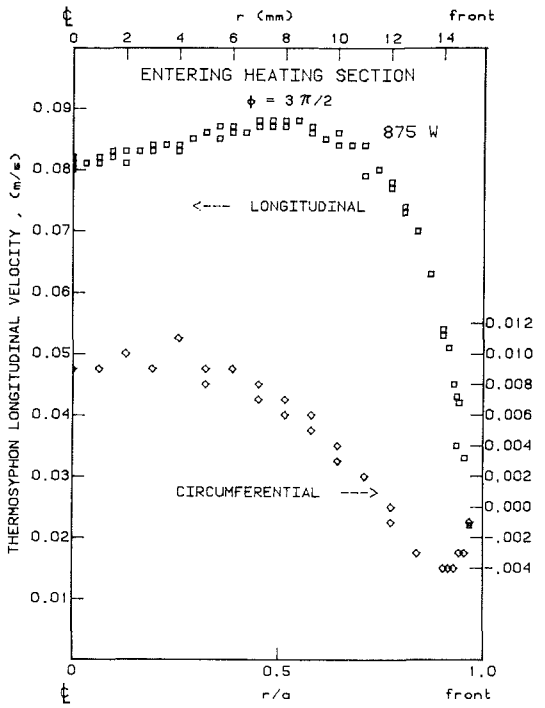


Fig. 8 Velocity entering heating section: $\phi = 3\pi/2$, 875 W

**Velocity Measurements.** LDA measurements were made in the thermosyphon, tilted at an angle $\theta_0 = 10$ deg, at locations leaving and entering the heating section; $\theta = 176.8 \pm 0.5$ deg and $\theta = 341.7 \pm 0.5$ deg, respectively, in Fig. 1. Mean velocity profiles along cross-sectional diameters from the inner wall toward the outer wall (from $R - a$ along $\phi = \pi$ toward $R + a$ along $\phi = 0$ in Fig. 2) and from the front wall toward the back wall ($\phi = 3\pi/2$ to $\phi = \pi/2$ in Fig. 2) are given in Figs. 4 through 8. These data are representative of the more extensive data in Stern (1986). The thermosyphon heating was set at four different levels; 145 W, 400 W, 630 W, and 875 W. These heat inputs correspond to a Grashof number range of $1 \times 10^5$ to $9 \times 10^5$.

Utilizing a mirror mounted at 45 deg to the central axis of the toroid, the incident laser beams were reflected along the major radius of the thermosyphon and the flow velocity was measured near the inner wall region ($\phi = \pi$, $R - a$) of the cross section. This mirror was mounted on the left-hand side of the thermosyphon as viewed in Fig. 1. To obtain measurements

near the inner wall in regions both leaving and entering the heating section, the thermosyphon was tilted clockwise and counterclockwise, respectively. This was possible because of the symmetry in the boundary conditions about the diameter from $\theta = \pi/2 - \theta_0$ to $\theta = 3\pi/2 - \theta_0$ in Fig. 1. A clockwise (downward) tilt is defined to be a positive value of $\theta_0$ in Fig. 1 and results in a steady-state bulk clockwise flow. A counterclockwise (upward) tilt is a negative value of $\theta_0$ and results in a counterclockwise flow.

The velocity data are plotted with either the inner or the front wall (depending on $\phi$) on the right side of the graph and the outer or the back wall on the left side (see Fig. 2). This eliminates confusion about whether the data were collected on the right- or left-hand side of the thermosyphon. The coordinate is given as both a dimensionless radial location, $r/a$, and a dimensional radial location, $r$, in mm with positive and negative values consistent with the sign convention of Fig. 2. Each longitudinal velocity data point (see Figs. 4–8) represents the mean of 1000 velocity measurements at the specified location in the cross section. Each circumferential velocity data point (see Figs. 5 and 8) represents the mean of at least 500 measurements. The velocity measurements were collected over a period of several minutes (up to a maximum of 15 min) at a data rate of 1–50 Hz.

Mean velocity data in the circumferential direction are shown in Figs. 5 and 8. Along the radius $\phi = 3\pi/2$ in Fig. 2, a positive velocity is defined to be flow from the inner wall toward the outer wall. This corresponds to the secondary motion along the central diameter of Fig. 3($b$). The velocities along the front and back walls in the cross-section in Fig. 3($b$) are toward the inner wall and have negative velocities. Thus, the circumferential velocity is considered to be positive when the flow is from the inner wall toward the outer wall (i.e., from $R - a$ toward $R + a$ in Fig. 2) and negative when the flow is toward the inner wall.

**Velocity Profiles Leaving Heating Section.** The data for the mean longitudinal velocity of the flow leaving the heating section are given in Figs. 4 and 5. The reduced intensity and increased noise of the optical signal prevented measurement of the velocity beyond $r = -12$ mm. (Note that the tube centerline is not expected to be a point of symmetry on the diameter $\phi = \pi$ to 0 in Fig. 4). The shape of the velocity profile changes as the heating level is varied. In particular, the velocity gradient near the inner wall becomes much larger as the heating rate is increased. Thus, as the fluid leaves the heating section, the velocity is larger near the inner wall for the higher heating rates. The steep gradients at the wall indicate an increasing frictional force with increased heating.

The velocity profiles are relatively flat in the core region of the flow. The flow leaving the heating section is measured at $\theta = 176.8$ deg in Fig. 1 ($\theta_0 = 10$ deg) so that gravity is almost aligned with the tube centerline. The buoyancy force on the heated fluid acts upward and apparently overcomes the inertial force on the flow which would tend to move the fluid toward the outer wall. Secondary motion, evident in the circumferential velocity profiles of Fig. 5, may act to flatten the velocity profiles at this location. In Fig. 4 the velocity data at 875 W exhibit a slight peak near the inner wall, which may be caused by the greater effect of buoyancy at this higher heat input.

Data for the longitudinal velocity of the flow leaving the heating section along the diameter extending from $\phi = 3\pi/2$ to $\pi/2$ (from the front wall toward the back wall) were obtained. Figure 5 shows data for the 630 W heat input from the front wall to the tube centerline. The signal intensity and data rate from the back half of the flow (tube radial locations beyond $-10$ mm) decreased and it was not possible to obtain an accurate velocity measurement in this region. Thus a definitive check could not be made of the anticipated symmetry of the flow about $r = 0$ on this diameter. However, a comparison was possible between 0 and 10 mm radial locations over both the front half and back half sections. Although the uncertainty of the measured velocity increased as the probe was traversed into the back half of the flow, the flow did exhibit symmetry about $r = 0$.

For all heat inputs the circumferential velocities in the region leaving the heating section exhibit the secondary flow pattern of Fig. 3($b$) (cf. Fig. 5). Note that the ratio of $U_\phi$ to the longitudinal velocity $U_\theta$ remains roughly the same for all heat inputs. The secondary motion in the cross stream alters the longitudinal velocity and convects thermal energy in the circumferential direction and results in the flattening of both the temperature and velocity profiles in the longitudinal ($\theta$) direction. The distribution of $U_\phi$ over the cross section as illustrated in Fig. 3($b$) will cause the heat transfer coefficient to be a strong function of $\phi$. Clearly, a complete understanding of this flow requires three-dimensional measurements and calculations.

**Velocity Profiles Entering Heating Section.** The data for the mean longitudinal velocity of the flow entering the heating section at $\theta = 341.7$ deg (cf. Fig. 1, $\theta_0 = 10$ deg) are given in Figs. 6–8. Along $\phi = \pi$ toward $\phi = 0$ it was possible to measure the velocity slightly beyond the center as shown in Fig. 6. Data could not be obtained beyond approximately $r = 0$ (except for the 400 W case) because of the reduced signal quality. For the 145 W heat input the recirculating flow region is evident from the negative velocities near the inner wall ($r = 12$ to $r = 15$ mm). This result is not present in any of the other velocity profiles (which are at the higher heating levels) and may indicate that the recirculating region at the higher heating rates is located farther downstream (into the heating section). A further indication of the flow disturbance caused by the prominent recirculating region is the larger scatter of the data at this low heat input. The recirculating flow region may also be responsible for the dip in the velocity profiles of Fig. 7; that is, the reversed flow near the inner wall may affect the velocity upstream to the extent that it reduces the velocity in the central portion (along the diameter extending from $\phi = 3\pi/2$ to $\phi = \pi/2$ in Fig. 2). From Fig. 6, the maximum value in the velocity profiles appears to be in the outer portion of the flow. This could be due to the diversion of the flow around the recirculation region and (or) the buoyancy force causing the cooled fluid to move toward the outer wall (note that at $\theta = 341.7$ deg the gravity force is directed toward the outer wall, cf. Fig. 1).

At the thermosyphon cross section where the flow is entering the heating section it was possible to measure the velocity from the front wall almost to the back wall (i.e., from $\phi = 3\pi/2$ toward $\phi = \pi/2$). These velocity profiles are shown in Fig. 7 and display good symmetry about the center, as expected. It is noted that the uncertainty in the data in the back half of the diameter is greater than that in the data in the front half.

In Fig. 7 the velocity gradients near the walls again become steeper with increased heating levels. Now, however, the maximum velocity does not occur at the center but at a location between the radial locations of 6 and 12 mm. There is a small dip in the velocity profile in the central region of the cross section at all of the heating levels. The increased scatter of the multiple data points at the low-heat condition, 145 W, suggests that the flow is less stable.

The circumferential velocity data for the flow entering the heating section (Fig. 8) show the same trend as the data for the flow leaving the heating section (Fig. 5). The magnitude of the circumferential velocity is slightly less entering the heating section than leaving the heating section. This may indicate that there is less secondary motion entering the heating section and may be a consequence of the recirculation region being in closer proximity to this location.

**Discussion of Temperature and Velocity Measurements.** The temperature and the velocity measurements shown in Figs. 4 and 6 were made along the diameter from $\phi = \pi$ to $\phi = 0$ for the flow leaving and entering the heating section. The temperature and velocity values were not measured at exactly the same $\theta$ location. Leaving the heating section the temperatures were measured 0.7 deg closer to the heating section than were the velocities. Entering the heating section the temperatures were measured 2.2 deg closer to the heating section than were the velocities. Although the temperature at the wall and the velocity profiles were recorded simultaneously, the temperature profiles were not recorded at the same time. The specific temperature data that were used in Figs. 4 and 6 gave the best agreement with the wall temperature value that had been recorded with the velocity measurement.

From Fig. 4 it is evident that for the flow leaving the heating section the thermal and momentum boundary layers have about the same thickness at the inner wall. At the outer wall the temperature profile is flat; the velocity data did not extend to this region, but would presumably be small near the wall. In the core of the flow, thermal and momentum transfer are apparently enhanced by the secondary motions resulting in the relatively flat profiles that were measured.

For the flow entering the heating section, the temperature peak at the inner wall for the low heat input (cf. Fig. 6 for the 145 W case) corresponds to the prominent recirculation region (negative values of $U_\theta$ at 145 W). At the higher heat inputs, the temperature profiles are much flatter. The recirculation region results in the upward transport of the hotter fluid from the heating section (opposite to the main flow) resulting in the temperature peak at 145 W at the inner wall. For the other heating cases, the recirculation region does not influence the velocity as strongly and the temperature is primarily influenced by the upstream conditions in the cooling section. The relatively flat temperature profile, even with the nonsymmetric velocity profile, indicates rapid cross-stream transfer of the thermal energy.

The circumferential velocity was also measured along the diameter $\phi = \pi$, 0 (Fig. 2) for flow leaving and entering the heating section. Within the uncertainty of the LDA measurements in the circumferential direction this velocity was negligible in the mean and confirms that the plane along $\phi = \pi$ and $\phi = 0$ is a flow symmetry plane in the time-averaged sense.

From the velocity data it is clear that the motion in the thermosyphon is three-dimensional. Therefore, a two-dimensional model of the flow, allowing $U_\theta$ to vary only with $r$ and assuming $U_\phi = 0$, is inadequate. Furthermore, the bulk velocity cannot be found by simply integrating the velocity profiles along the diameters from $\phi = \pi$ to 0 and from $\phi = 3\pi/2$ to $\pi/2$ alone. For the flow entering the heating section it appears (cf. Fig. 6) that the mass flow does not vary linearly with $U_\theta$ at the centerline.

## 5 Conclusions

Temperature and velocity were measured on the fluid in the regions leaving and entering the heating section of a toroidal thermosyphon. The temperature data were obtained with miniature thermocouple probes and the velocity data with an LDA system. The measurements were made with the thermosyphon tilted at an angle $\theta_0 = 10$ deg. Tests were carried out at four heat inputs: 145, 400, 630, and 875 W.

A detailed analysis indicates that the largest uncertainties in the velocity measurements are related to the nonuniform cross section of the thermosyphon tube; uncertainty in the initial location of the probe volume; tube wall surface irregularities; and uncertainty in the orientation angle of the laser beams. Most of these uncertainties were systematic so that the shape of the profile was very accurate, although the absolute value may be in error.

The velocity in the thermosyphon was measured along two diameters in the cross section, along $\phi = \pi$, 0 and $\phi = 3\pi/2$, $\pi/2$ in Fig. 2. Mean velocities in both the longitudinal and the circumferential directions were obtained. The magnitudes of both the velocities and the velocity gradients near the wall increased as the heat input was increased for the flow leaving and entering the heating section. The velocity profiles along $\phi = \pi$, 0 for the flow leaving the heating section were relatively flat in the core region indicating that the buoyancy force (upward) counteracted the inertia of the fluid (toward the outer wall). Along the $\phi = 3\pi/2$, $\pi/2$ diameter the time-averaged flow appeared to be symmetric. The maximum velocity was located at the centerline, but the profile was relatively flat.

For the flow entering the heating section the velocity profiles along the radius at $\phi = \pi$ showed evidence of a prominent recirculation region for a heat input of 145 W. For this heat input, negative velocities, i.e., velocities opposite to the bulk flow direction, and larger velocity fluctuations occurred at the inner wall region. The recirculation region apparently resulted in a reduction of the momentum in the core region of the profiles along the diameter extending from $\phi = 3\pi/2$ to $\pi/2$. The velocity profiles were symmetric along this diameter.

The circumferential component of the velocity in the regions leaving and entering the heating section exhibited the secondary, cross-stream motion characteristic of curved-pipe flow. The magnitude of this component of velocity increased with increasing heat input and was roughly proportional to the longitudinal velocity. The secondary velocity affected the longitudinal velocity and convected thermal energy in the circumferential direction. This contributed to the flattening of both the velocity and temperature profiles in the longitudinal direction. The presence of this significant circumferential motion indicated that the accurate determination of the heat transfer requires three-dimensional modeling and measurement.

The velocity and temperature profiles along the $\phi = \pi$, 0 diameter for the flow leaving and entering the heating section show the effect of the recirculation region and secondary flow on the temperature profiles. The recirculating region near the entrance to the heating section results in upstream (upward) transport of hotter fluid from the heating section. Secondary (cross-stream) flows flatten both the velocity and temperature profiles by increasing the cross-sectional redistribution of momentum and thermal energy.

The following is a summary of the main findings of this study:

1 The three-dimensional nature of the flow field, previously reported in flow visualization studies and calculated numerically, has been confirmed quantitatively from LDA velocity measurements. However, the numerical results of Lavine et al. (1984, 1986, 1987) cannot be directly compared with these measurements since the Grashof number range is several orders of magnitude greater in this study.

2 For the lowest heat input the presence of the prominent recirculating flow region at the entrance to the heating section strongly affected both the temperature and the velocity data.

3 A circumferential flow pattern similar to that found in forced-convection curved-pipe flows was measured in this buoyancy-driven flow.

4 An extensive evaluation of the uncertainties involved in toroidal thermosyphon measurements provides a firm foundation for the utilization of the data presented.

5 The measured temperature and velocity profiles contribute to the fundamental understanding of buoyancy-driven flows and provide an important data base for the validation of numerical calculations of the flow in a toroidal thermosyphon.

## Acknowledgments

The authors are grateful to the National Science Foundation and the University of California, Berkeley for their support of this research.

## References

Azzola, J., and Humphrey, J. A. C., 1984, "Developing Turbulent Flow in a 180° Curved Pipe and Its Downstream Tangent," presented at the Second International Symposium on Applications of Laser Anemometry to Fluid Mechanics, Lisbon, Portugal, July 2–4; also available as LBL Report No. 17681, University of California, Berkeley.

Berger, S. A., Talbot, L., and Yao, L.-S., 1983, "Flow in Curved Pipes," *Annual Review of Fluid Mechanics*, Vol. 15, pp. 461–512.

Creveling, H. F., DePaz, J. F., Baladi, J. Y., and Schoenhals, R. J., 1975, "Stability Characteristics of a Single-Phase Free Convection Loop," *Journal of Fluid Mechanics*, Vol. 67, pp. 65–84.

Damerell, P. S., and Schoenhals, R. J. 1979, "Flow in a Toroidal Thermosyphon With Angular Displacement of Heated and Cooled Sections," ASME JOURNAL OF HEAT TRANSFER, Vol. 101, pp. 672–676.

Greif, R., Zvirin, Y., and Mertol, A., 1979, "The Transient and Stability Behavior of a Natural Convection Loop," ASME JOURNAL OF HEAT TRANSFER, Vol. 101, pp. 684–688.

Japikse, D., 1973, "Advances in Thermosyphon Technology," in: *Advances in Heat Transfer*, T. F. Irvine, Jr., and J. P. Harnett, eds., Vol. 9, Academic Press, New York, pp. 1–111.

Lavine, A. G., 1984, "A Three-Dimensional Analysis of Natural Convection in a Toroidal Loop," Ph.D. Dissertation, University of California, Berkeley, CA.

Lavine, A. S., Greif, R., and Humphrey, J. A. C., 1986, "A Three-Dimensional Analysis of Natural Convection in a Toroidal Loop: Effect of Tilt Angle," ASME JOURNAL OF HEAT TRANSFER, Vol. 108, pp. 796–805.

Lavine, A. S., Greif, R., and Humphrey, J. A. C., 1987, "A Three-Dimensional Analysis of Natural Convection in a Toroidal Loop—The Effect of Grashof Number," *International Journal of Heat and Mass Transfer*, Vol. 30, pp. 251–262.

McLaughlin, D. K., and Tiederman, W. G., 1973, "Biasing Correction for Individual Realization of Laser Anemometer Measurements in Turbulent Flows," *Physics of Fluids*, Vol. 16, pp. 2082–2088.

Mertol, A., and Greif, R., 1985, "A Review of Natural Circulation Loops," in: *Natural Convection: Fundamentals and Applications*, W. Aung, S. Kakac, and R. Viskanta, eds., Hemisphere Publishing Corp., New York, pp. 1033–1071.

Mertol, A., Greif, R., and Zvirin, Y., 1982, "Two Dimensional Study of Heat Transfer and Fluid Flow in a Natural Convection Loop," ASME JOURNAL OF HEAT TRANSFER, Vol. 104, pp. 508–514.

Stern, C. H., 1986, "An Experimental Study of the Flow and Heat Transfer in a Toroidal Thermosyphon," Ph.D. Dissertation, University of California, Berkeley, CA.

Stern, C., and Greif, R., 1987, "Measurements in a Natural Convection Loop," *Warme- und Stoffubertragung*, Vol. 21, No. 5, pp. 277–282.

Zvirin, Y., 1981, "A Review of Natural Circulation Loops in Pressurized Water Reactors and Other Systems," *Nuclear Engineering and Design*, Vol. 67, pp. 203–225.

# Buoyancy-Driven Exchange Flow Through Small Openings in Horizontal Partitions

**M. Epstein**
Fauske & Associates, Inc.,
Burr Ridge, IL 60521

*This paper describes an experimental study of the phenomenon of buoyancy-driven exchange (countercurrent) flow through openings in a horizontal partition. A density-driven exchange flow was obtained by using brine above the partition and fresh water below the partition. In the first part of the study, flow measurements were made with a single opening, for opening ratios* L/D *in the range 0.01 to 10.0, where* L *and* D *are the length of the opening (in the direction normal to the partition) and the diameter of the opening, respectively. Four different flow regimes are identified as* L/D *is increased through this range. As a result of the competition between two of these regimes, the exchange flow rate versus* L/D *relation exhibits a peak. The exchange flow rate was found, for all practical purposes, to be independent of viscosity, enabling a universal correlation between Froude number (dimensionless exchange flow rate) and* L/D. *The second part of the study was an experimental investigation of the same phenomenon, but with two openings in the horizontal partition. Two openings were observed to give rise to three different flow configurations involving both one-way and countercurrent flows within the openings.*

## Introduction

The consideration of air flow indoors requires an understanding of buoyancy-driven fluid motion through apertures connecting rooms in buildings. Despite the outpouring of research on natural convection, relatively few papers have dealt with this type of natural convection problem. In this paper fundamental experiments are described on buoyancy-driven exchange flow through a single opening in a horizontal partition that separates two rectangular compartments. The area of the opening is small compared with the horizontal extent of the partition so that the major resistance to flow is posed by the opening. This paper also presents a limited amount of data on exchange flow when two openings penetrate the horizontal partition. The density of the atmosphere (gas) that fills the upper compartment exceeds that of the lower compartment. Under conditions of practical interest, such as during building fires, the density difference between the two compartments arises partly from the difference in composition and partly from the difference in temperature. The density difference makes for a buoyancy-driven downflow of the heavier fluid from the upper compartment to the lower compartment. Since the compartments are sealed, mass conservation dictates an upflow of the lighter gas. In the case of a single opening, this situation gives rise to an interesting countercurrent exchange flow across the opening. As will be seen, countercurrent exchange flow is also possible in the case of multiple openings.

The experimental technique described below makes use of the fact that salty water is denser than fresh water. This attractively simple choice of materials to represent buoyancy-driven gas movement between rooms is valid so long as molecular viscosity and thermal diffusivity are not important parameters, that is in the limit of purely density-driven flow. The effect of viscosity on the fluid exchange rate will be discussed and will be seen to be small. The brine-water technique has some advantages over performing a heat transfer experiment with gas as the working fluid. There is no need to cover the test section with insulation as the density-driven flow is isothermal, and there is no waiting time requirement for steady state to be reached. The maximum compartment-to-compartment density difference ratio $\Delta\rho/\bar{\rho}$ that can be achieved with the brine–water system is approximately 0.2, where $\bar{\rho}$ is the average density. This corresponds to a gas exchange rate driven by a temperature difference of 100 K between two rooms when the average temperature is 500 K.

From a survey of the literature, it appears that the only prior papers dealing with *vertical* buoyancy-driven exchange flow between two compartments connected by a single opening are those of Brown (1962) and Mercer and Thompson (1975). In Brown's experiments air was used as the fluid medium and the countercurrent flow through square apertures was investigated by imposing a temperature difference between the two compartments. His tests covered ratios of opening length (or partition thickness) to the side of the square opening, $L/S$, in the range 0.0825 to 0.66. Brown interpreted the countercurrent flow as a heat transfer phenomenon and expressed his results in terms of a Nusselt number Nu, versus Grashof number Gr, correlation. However, by introducing the definitions for Nu and Gr, and canceling viscosity and thermal conductivity, his correlation can be re-expressed, for all practical purposes, in the form of a single functional relationship between the exchange flow rate and $\Delta\rho/\bar{\rho}$, $L/S$, and $S$, as would be suggested by a balance between the inertia and buoyancy terms of Bernoulli's equation. A major result of Brown's investigation is that the exhcange flow rates increase with increasing $L/S$.

Experiments on buoyancy-driven flow through inclined, short tubes were reported by Mercer and Thompson (1975). The density difference between the two compartments was accomplished by using brine and water as the working fluids. Their experimens with vertical tubes, which are of interest here, covered a tube length-to-diameter ratio ($L/D$) range of 3.5 to 18. Interestingly enough, the exchange flow rates were observed to decrease with increasing $L/D$. This behavior is opposite to that observed by Brown and suggests that, for a single opening, a maximum exchange flow rate exists at an $L/D$ or $L/S$ between 0.66 and 3.5.

It is also relevant to take note of prior work on exchange flow through openings in vertical partitions. Experiments on

Contributed by the Heat Transfer Division for publication in the JOURNAL OF HEAT TRANSFER. Manuscript received by the Heat Transfer Division May 5, 1987. Keywords: Building Heat Transfer, Enclosure Flows, Natural Convection.

exchange flow through openings of small $L/S$ (windows or doors) were reported by Brown and Solvason (1962) and Shaw (1971). Shaw also studied combined buoyancy-driven and forced air flow across a door in a vertical partition. Buoyancy-driven flow through a horizontal duct or tube connecting two compartments was studied experimentally by Leach and Thompson (1975) and by Bejan and Rossie (1981). In the latter study the countercurrent flow through the duct was controlled by the boundary layers that covered the walls of the compartments. Therefore, this study is not directly relevant here. Experimental and theoretical studies of steady-state fire-induced flow through a window or door were conducted by Prahl and Emmons (1975), Steckler et al. (1982), and Stecker et al. (1984). In a later paper by Steckler et al. (1985) the brine-water technique was used to model the buoyantly driven flow of fire gases within a multicompartment structure. Comparison of the small-scale experimental results with previously conducted fire tests in a full-scale facility demonstrated the utility of the brine-water technique in predicting full-scale results with hot gases.

## Experimental Apparatus and Procedures

Most of the experiments were carried out with a single opening. The essential features of the experimental apparatus for the case of a single opening will be described with the aid of Fig. 1. The test unit consists of a large rectangular tank fabricated from plexiglass; it is 0.55 m square and 0.762 m deep. A horizontal plexiglass partition located 0.33 m above the bottom of the tank divides the tank into an upper compartment and a lower compartment. At the center of the partition there is an aperture whose cross-sectional area is large compared with the openings used in the experiments.

Two types of opening were employed in the experiments. In one, the countercurrent brine-water flow was directed through a simple orifice, which was constructed by cutting a circular hole in a thin metal plate. In the other, the brine-water flow passed through a plexiglass tube that was bounded by a plexiglass support plate.[1] The thin metal orifice plate or the plexiglass support plate was mounted on the partition. Figure 1 illustrates the tube arrangement. As shown there, the centerline of the tube is in alignment with the centerline of the aperture cut in the partition. The support plate and the partition were pressed together by bolts to prevent leaks between compartments. Five round openings of different diameters and lengths were fabricated from tubes or holes cut in the partition plate. A square orifice also served as an opening. The diameters of the round openings were 0.0254, 0.0339, 0.0437, 0.0445, and 0.0525 m. The length of a side of the square opening was 0.0292 m. This combination of orifices and tubes resulted in an exchange-flow-path length $L$ that varied from 0.015 to 10 opening diameters. Openings with $L/D < 0.3$ were orifices and $L$ for this configuration actually corresponds to the thickness of the orifice plate. The $L/D > 0.3$ were achieved with tubes or ducts, and $L$ for this geometry is simply the tube or duct length. Tests were carried out with average brine densities over the duration of a run in the range of 1028–1188 kg m$^{-3}$ The corresponding average density dif-

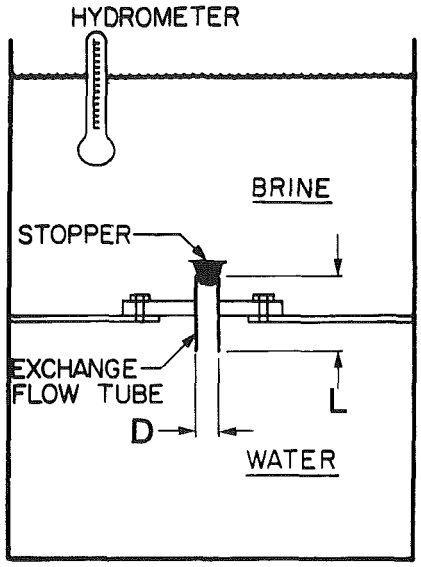


**Fig. 1 Schematic diagram of the apparatus**

[1] The tubes are meant to simulate exchange flow between rooms connected by stairwells or equipment transfer shafts.

## Nomenclature

$A$ = flow area of opening
$D$ = diameter of circular opening (aperture or tube)
$D_t$ = eddy diffusivity
$g$ = acceleration due to gravity
Gr = Grashof number based on partition thickness = $g\Delta\rho L^3/(\bar{\rho}\nu)$
$J_{0,1}$ = Bessel's functions of zero and order one
$H$ = level of opening 1 above partition in two-opening system
$k$ = wave number
$K$ = opening entrance and exit pressure losses or dimensionless constant in eddy diffusivity relation (12)
$L$ = axial length of opening (partition thickness or tube length)
$n$ = wave growth parameter at the brine-water interface
Nu = Nusselt number based on partition thickness
$P_L$ = pressure in light fluid
$P_H$ = pressure in heavy fluid
Pr = Prandtl number = $\nu/\alpha$
$q$ = flooding or purging flow rate
$Q$ = buoyancy-driven exchange flow rate
$r$ = radial coordinate measured from the center of an aperturelike opening
$R$ = radius of circular opening
$S$ = length of a side for a square opening
$t$ = time
$t_b$ = departure time of brine-water interface
$u$ = velocity of fluid within opening
$V_H$ = volume of upper compartment
$V_L$ = volume of lower compartment
$x$ = vertical location within tube
$Y$ = mass fraction of less dense liquid
$\alpha$ = thermal diffusivity
$\delta$ = thickness of partition in two-opening system
$\Delta\rho$ = density difference = $\rho_H - \rho_L$
$\eta$ = location of brine-water interface at given time and position $r$ within aperture
$\eta_b$ = value of $\eta$ breakoff condition
$\eta_0$ = amplitude of initial brine-water interface disturbance
$\nu$ = kinematic viscosity
$\rho_L$ = density of light fluid
$\rho_H$ = density of heavy fluid
$\bar{\rho}$ = mean density = $(\rho_H + \rho_L)/2$

### Subscripts

0 = pertains to initial conditions
1 = refers to diffusion zone in flow regime III or opening 1 in two-opening configuration
2 = refers to Bernoulli flow zone in flow regime III or opening 2 in two-opening configuration

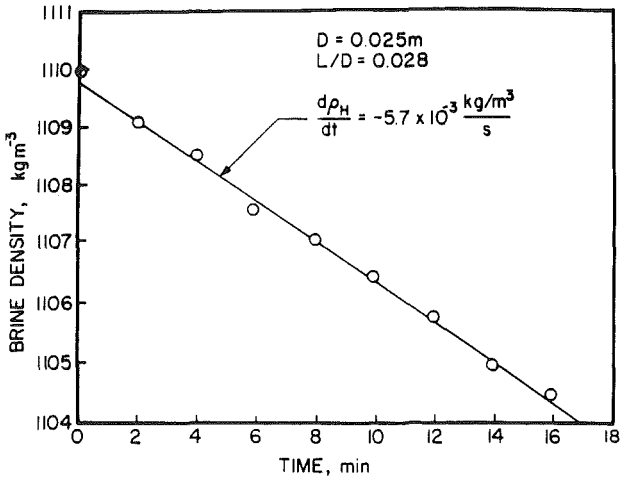


Fig. 2 Typical density versus time plot for the heavier upper fluid (brine)

ference ratio range was $\Delta\rho/\bar{\rho} = 0.024$–$0.17$.

To carry out an experiment, the lower compartment was filled with water. The opening (orifice or tube) that penetrated the partition was then sealed with a rubber stopper and brine was introduced into the upper compartment. The density of the brine-filled upper compartment was determined by means of a hydrometer. The 0.1 kg m$^{-3}$ resolution of the hydrometer readily accommodated the ~10 kg m$^{-3}$ change of density during a run. A run was initiated by removing the rubber stopper. A countercurrent flow of water and brine was observed within the opening. The density of the brine in the upper compartment was measured at regular intervals. This was accomplished by resealing the hole and carefully measuring the submergence of the hydrometer. A subsequent hydrometer reading was taken after mechanically stirring the brine solution, and this information was used to correct for any stratification in the upper compartment.

The volume rate of flow $Q$ (the exchange rate in m$^3$ s$^{-1}$) from the upper compartment to the lower compartment or vice versa in terms of rate of dilution of the brine can be shown to be given by (see appendix)

$$Q = \frac{-V_H(d\rho_H/dt)}{(\rho_H - \rho_{L,0}) - \frac{V_H}{V_L}(\rho_{H,0} - \rho_H)} \quad (1)$$

where $V_H$ and $V_L$ are the volume of the heavy liquid (brine) in the upper compartment and the volume of the less dense liquid (water) in the lower compartment, respectively, $\rho_H$ is the density of the brine solution at time $t$, and $\rho_{L,0}$ and $\rho_{H,0}$ are the densities of the contents of the water- and brine-filled compartments at zero time. Thus, to obtain $Q$, $\rho_H$ was plotted against time $t$ and differentiated graphically.

A typical plot of the brine density versus time, as determined from the hydrometer readings, is shown in Fig. 2. The duration of the run (or the total number of hydrometer readings) was selected to limit the brine density reduction to a linear function of time. A best-fit slope was superimposed upon this linear segment of the density–time plot, and the volume rate of exchange flow was thus calculated from equation (1). The uncertainty associated with both reading the hydrometer and graphically determining $d\rho_H/dt$ was arrived at through repeated experiments at fixed initial density conditions. The uncertainty in the exchange flow rate measurements, as determined in this manner, are about ±10 percent.

As was already mentioned, experiments were also carried out with two openings in the horizontal partition. The two-opening configuration studied is presented in Fig. 4. The

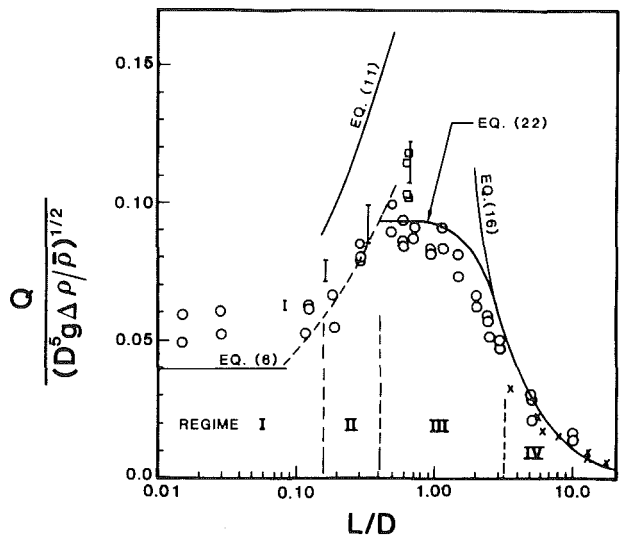


Fig. 3 Experimental results for countercurrent exchange flow through a single opening; see Table 1 for explanation of symbols

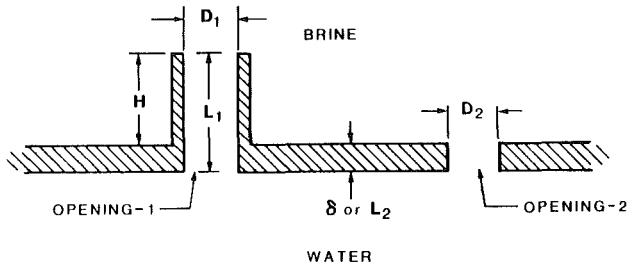


Fig. 4 Schematic of two-opening configuration

discussion of this figure is postponed until the presentation of the data for the case of two openings. The experimental procedure was essentially the same as that described in the foregoing for the single opening, except that each data run began with the placement of two rubber stoppers, one in each opening. The flow was initiated by removing each stopper simultaneously. The flow directions within each opening, cocurrent or countercurrent, were readily visible owing to refraction effects. A clear turbulent plume is formed by the fluid, water into brine or brine into water, just beyond the exit planes of the opening.

## Single Opening: Results and Discussion

Figure 3 has been prepared to illustrate the results obtained in the present study of natural convection flow through a single opening. Also plotted in Fig. 3 are the heat transfer data obtained by Brown (1962) with air as the fluid medium, and the brine-water data of Mercer and Thompson (1975). The various experimental conditions are tabulated in Table 1. In Fig. 3, the volume exchange rate is plotted in the form of a dimensionless Froude number, $Q/(D^5 g\,\Delta\rho/\bar{\rho})^{1/2}$, as a function of the length-to-diameter ratio of the opening, $L/D$. For the case of square openings the symbol $S$ should replace $D$ in the coordinates of Fig. 3. The measured exchange flow rates are given in Table 2.

For a given opening geometry characterized by $L/D$, a set of experiments was performed. Most of the sets involved only two experiments, one with $\Delta\rho/\bar{\rho} = 0.04$ while in the other $\Delta\rho/\bar{\rho} = 0.09$. The results of these experiments suggested that there exists an influence of the density ratio on the Froude number $Q/(D^5 g\Delta\rho/\bar{\rho})^{1/2}$, especially at low $L/D$ where an increase from $\Delta\rho/\bar{\rho} = 0.04$ to 0.09 was observed to give rise to modest reductions in the Froude number (~20 percent). Ac-

cordingly, a few experimental sets were carried out for three or four density ratios to quantify better the separate effect of $\Delta\rho/\bar{\rho}$ on the Froude number. Further increases in $\Delta\rho/\bar{\rho}$ above 0.09 or, for that matter, decreases below 0.04, were found not to lead to significant additional changes in the Froude number. Thus it was concluded that no additional density parameter is needed to characterize the results.

As expected from the discussion in the introduction, the flow rate attains a maximum at an $L/D$ of about 0.6. At lower $L/D$ the flow rate decreases and appears to be tending toward a constant value as $L/D \to 0$. At the higher $L/D$ the opposite behavior is noted, with the flow rate decreasing with increasing $L/D$.

We will now attempt to explain the flow behavior that leads to the data trends conveyed in Fig. 3. Also, we will provide some justification for the dimensionless coordinates used in the construction of Fig. 3. It is speculated here that the maximum in the countercurrent, exchange flow curve reflects a competition between an orifice flow regime (or Bernoulli-type flow) at low $L/D$ and a process of turbulent binary diffusion in the "tube flow regime" at high $L/D$. One might argue that the tube flow regime should be modeled as a viscous phenomenon and that the inverse relationship between $Q$ and $L/D$ in this regime indicates the importance of wall boundary layers. The fact that a maximum is attained at an $L/D$ as small as 0.6, however, suggests that a boundary layer model would not properly describe the measurements. We will return to this issue later on.

For convenience, the experimental curve shown in Fig. 3 has been divided into the following exchange flow regimes: (I) an oscillatory exchange flow regime, (II) a countercurrent Bernoulli flow regime, (III) a regime of combined turbulent binary diffusion and Bernoulli flow, and (IV) a region of pure turbulent binary diffusion.

**Oscillatory Exchange Flow (Regime I).** At very small $L/D$ the thickness of the partition is reduced enough so that the pressure at the level of the opening is essentially the same in both bodies of water. One would suppose, therefore, that in this limit there would be no exchange flow through the opening. However, in spite of the equalization of pressures at the opening in the limit $L \to 0$, a layer of denser fluid overlying a layer of lighter fluid is unstable and subject to any small, random disturbances in the system. As a result of this so-called "Taylor instability" (1950) some of the lighter water protrudes upward through the orifice and some of the denser brine protrudes downward. This intrusion of each liquid on each other's domain is responsible for the nonzero flow rate in the limit $L \to 0$. Visual observations revealed upward and downward plumes or fingers of fresh and salt water, respectively, periodically breaking through the opening. Presumably the fresh and salt water plumes appear in the opening simultaneously in order to conserve volume in the lower compartment, although the cycle of the oscillation was too short to tell if this was the case with any certainty. Unfortunately, there was no support for flow visualization by photographic reproduction to be included as part of this study.

**Table 1 Symbol key for data plotted in Fig. 3**

| Reference | Opening | D or S,m | Fluid(s) | $\Delta\rho/\bar{\rho}$ | Symbol Used in Figure |
|---|---|---|---|---|---|
| Present Data | Round | 0.025-0.053 | Brine/Water | 0.03-0.17 | ○ |
| Present Data | Square | 0.029 | Brine/Water | 0.024-0.15 | □ |
| Mercer & Thompson | Round | 0.05-0.2 | Brine/Water | ~ 0.1 | X |
| Brown | Square | 0.15-0.3 | Air | ~ 0.02-0.09 | I |

An approximate expression for the motion of the interface that separates the brine and water is, as suggested from the linearized Taylor-wave theory for a standing-wave perturbation in cylindrical geometry,

$$\eta = \eta_0 e^{nt}[J_0(kr) - J_0(kR)] \tag{2}$$

where $\eta$ is the interface displacement relative to the level of the opening, $r$ is the radial distance measured from the center of the opening, $\eta_0$ is the initial disturbance at time $t=0$, $k$ is the wave number, and $n$ is the growth parameter given by

$$n = \left(\frac{kg\ \Delta\rho}{2\bar{\rho}}\right)^{1/2} \tag{3}$$

This analysis thus presumes a central finger of outer radius in the plane of the opening at $kr_1 = 2.678$ and an oppositely directed annular ring wave of fluid in the interval $r_1 < r < R$, where $kR = 5.135$, as dictated by the condition that the volume of the finger equals that of the annular wave. Actually, equation (2) does not satisfy some of the potential flow conditions on each side of the interface. We have contented ourselves with this form because it has approximately the correct shape and it allows fluid volume to be conserved in the lower compartment.

Based on visual observations, it is assumed that the water finger "separates" from the opening when its length (amplitude) is of the order of the diameter of the opening. Therefore, from equation (2), the volume of the finger at breakoff is

$$\int_0^D \pi r^2 d\eta = \pi D k \int_0^{r_1} r^2 J_1(kr)\, dr = 0.088 D^3 \tag{4}$$

Also, the time necessary for the interface to grow to a height equal to the amplitude at breakoff, $\eta = D$, is from equation (2)

**Table 2 Measured buoyancy-driven exchange flows through single openings**

| Opening | D(m) or S(m) | L(m) | $\rho_H$(kg m$^{-3}$) | $\rho_L$(kg m$^{-3}$) | Q(m$^3$s$^{-1}$) x $10^6$ |
|---|---|---|---|---|---|
| Square | 0.0292 | 0.0191 | 1169.6 | 1007.2 | 17.61 |
| Square | 0.0292 | 0.0191 | 1110.2 | 1003.7 | 17.09 |
| Square | 0.0292 | 0.0191 | 1066.2 | 1003.9 | 12.82 |
| Square | 0.0292 | 0.0191 | 1028.1 | 1003.5 | 7.27 |
| Round | 0.0437 | $6.55 \times 10^{-4}$ | 1100.4 | 1004.6 | 18.78 |
| Round | 0.0437 | $6.55 \times 10^{-4}$ | 1043.3 | 1003.9 | 14.47 |
| Round | 0.0254 | $7.11 \times 10^{-4}$ | 1107.3 | 1002.8 | 5.36 |
| Round | 0.0254 | $7.11 \times 10^{-3}$ | 1039.8 | 1005.1 | 3.62 |
| Round | 0.0525 | $6.35 \times 10^{-3}$ | 1088.7 | 1006.0 | 29.75 |
| Round | 0.0525 | $6.35 \times 10^{-3}$ | 1044.3 | 1003.3 | 25.15 |
| Round | 0.0525 | $6.35 \times 10^{-3}$ | 1039.0 | 1008.5 | 20.55 |
| Round | 0.0339 | $6.35 \times 10^{-3}$ | 1098.7 | 1005.3 | 10.73 |
| Round | 0.0339 | $6.35 \times 10^{-3}$ | 1044.8 | 1004.8 | 8.75 |
| Tube | 0.0254 | $7.62 \times 10^{-3}$ | 1044.0 | 1003.1 | 5.46 |
| Tube | 0.0254 | $7.62 \times 10^{-3}$ | 1091.5 | 1003.5 | 7.33 |
| Tube | 0.0254 | $7.62 \times 10^{-3}$ | 1187.9 | 1004.4 | 10.55 |
| Tube | 0.0445 | 0.0222 | 1043.6 | 1003.5 | 25.56 |
| Tube | 0.0445 | 0.0222 | 1098.4 | 1008.1 | 33.99 |
| Tube | 0.0254 | 0.0152 | 1105.4 | 1004.4 | 8.39 |
| Tube | 0.0254 | 0.0152 | 1052.3 | 1004.2 | 6.55 |
| Tube | 0.0254 | 0.0152 | 1049.7 | 1006.9 | 5.57 |
| Tube | 0.0445 | 0.0334 | 1040.6 | 1005.0 | 21.48 |
| Tube | 0.0445 | 0.0334 | 1089.5 | 1007.1 | 33.27 |
| Tube | 0.0254 | 0.0229 | 1048.3 | 1003.7 | 5.63 |
| Tube | 0.0254 | 0.0229 | 1105.5 | 1004.5 | 8.12 |
| Tube | 0.0445 | 0.0507 | 1048.5 | 1004.4 | 24.31 |
| Tube | 0.0445 | 0.0507 | 1089.6 | 1004.7 | 31.42 |
| Tube | 0.0445 | 0.0668 | 1052.0 | 1005.0 | 22.72 |
| Tube | 0.0445 | 0.0668 | 1101.9 | 1006.7 | 29.21 |
| Tube | 0.0445 | 0.0890 | 1101.0 | 1006.1 | 24.61 |
| Tube | 0.0445 | 0.0890 | 1051.5 | 1004.5 | 18.61 |
| Tube | 0.0254 | 0.0635 | 1044.6 | 1006.9 | 3.60 |
| Tube | 0.0254 | 0.0635 | 1093.6 | 1001.5 | 5.27 |
| Tube | 0.0254 | 0.0635 | 1087.8 | 1007.3 | 4.50 |
| Tube | 0.0445 | 0.1335 | 1047.3 | 1002.8 | 13.82 |
| Tube | 0.0445 | 0.1335 | 1100.4 | 1003.8 | 18.81 |
| Tube | 0.0445 | 0.2225 | 1083.3 | 1012.3 | 10.40 |
| Tube | 0.0445 | 0.2225 | 1093.0 | 1002.5 | 11.30 |
| Tube | 0.0445 | 0.2225 | 1045.3 | 1006.3 | 5.40 |
| Tube | 0.0254 | 0.254 | 1098.0 | 1004.0 | 1.40 |
| Tube | 0.0254 | 0.254 | 1044.4 | 1001.8 | 1.11 |

$$t_b = \frac{1}{n} \ln \frac{D}{\eta_0} \tag{5}$$

The ratio of the finger departure amplitude to the initial disturbance $\eta_0$ is assumed to be a constant and the term $\ln(D/\eta_0)$ is taken to be a constant of proportionality between the growth parameter $n$ and the interface breakoff time $t_b$. Lewis' (1950) classical experimental results on Taylor instability show that when the interface attains an amplitude of the order of $\ln(\eta/\eta_0) \sim 5$ it rapidly changes from a wave form into fingers of one of the fluids penetrating into the other. Since the brine-water interface takes on the appearance of a finger just before it pinches off the fluid protruding through the opening, it seems reasonable to conclude that $\ln(D/\eta_0) \sim 5$. The volume exchange rate is the product of $1/t_b$ and the volume of the finger at $t_b$, or from equations (3) and (5) and the fact that $k = 5.135/R$

$$Q = \frac{0.1\ D^3}{t_b} = 0.04(D^5 g \Delta\rho/\bar{\rho})^{1/2} \tag{6}$$

This prediction is only slightly below the data in the oscillatory exchange flow regime (see Fig. 3). Of course, this agreement between theory and experiment is not conclusive because of the more or less arbitrarily selected values of the size of the departing fluid finger and $\eta/\eta_0$ at departure. Nevertheless, the constant Froude number result tends to support the validity of the Taylor-wave mechanism of fluid exchange at very low opening $L/D$.

**Bernoulli Flow (Regime II).** An examination of Fig. 3 and Table 1 reveals that the exchange flow data with air reported by Brown (1962) lie within or just outside flow regime II. The vertical bars shown in Fig. 3 represent the range of measured volumes for each opening $L/S$. Brown correlated his net heat flow data through square openings in the form of a Nusselt number correlation. By simply introducing the definitions for Nu, Gr, and Pr (see nomenclature), the flow Froude number can be expressed in terms of these quantities as

$$\frac{Q}{(S^5 g \Delta\rho/\bar{\rho})^{1/2}} = \frac{\mathrm{Nu}}{\mathrm{PrGr}^{1/2}} \cdot \left(\frac{L}{S}\right)^{1/2} \tag{7}$$

Brown reported Nu/Pr and Gr numbers for each $L/S$ investigated in his experiments. This information, together with equation (7), was used to plot the results of his heat transfer tests in Fig. 3.

From Fig. 3 it will be noted that agreement of the heat transfer data with the brine-water data is fairly good, but that the brine-water results are somewhat lower than the air data. The reason for the discrepancy is simply due to the difference in opening geometry—square openings in Brown's work versus mostly round openings in the present study. A few experiments were made to measure the brine/water exchange flow through a square opening of $L/S = 0.65$. The results, shown as square data points in Fig. 3, are very similar to the air data of Brown when plotted as Froude number against $L/S$. Thus, whether dealing with liquid or gas, the experiments give rise to exchange flow rates that lie within the scatter of the experimental data. It would appear from Fig. 3 that the range of $L/D$ covered in Brown's experiments is just short of what is required to observe the peak in the $Q$ versus $L$ relation.

If the opening is square, having a side of length $S$, then $D$ in Fig. 3 should be viewed as the diameter that a round opening would attain if it had the same area as the square opening, namely

$$D = \sqrt{\frac{4}{\pi}}\, S = 1.128\ S \tag{8}$$

The actual value of the effective diameter that best brings the round and square opening data together in Fig. 3 is found to be

$$D = 1.1\ S \tag{9}$$

Brown developed an expression for inviscid exchange flow by applying Bernoulli's equation and assuming that the pressure losses are due entirely to entrance and exit losses. His analysis shows that the speed of either fluid at the opening is

$$u = \left(\frac{1}{3} \frac{\Delta\rho g L}{\bar{\rho}}\right)^{1/2} \tag{10}$$

based on a pressure loss of $1/4\ \rho u^2$ at the entrance and $1/2\ \rho u^2$ at the exit of the opening. Brown converted equation (10) into a heat transfer correlation by introducing the Nusselt, Prandtl, and Grashof number definitions. Here we simply convert equation (10) into an expression for the exchange flow

$$Q = \frac{1}{2} \frac{\pi D^2}{4} u = 0.23\ (D^5 g \Delta\rho/\bar{\rho})^{1/2} (L/D)^{1/2} \tag{11}$$

Figure 3 compares the data with the theoretical prediction and with a line (dashed) with the Froude number equal to 0.64 times its theoretical value. Since the condition of the liquid flow at the opening is observed to be unstable and since some interchange of brine and water must take place at the opening, both of which the theory does not account for, the absence of a perfect match between equation (11) and experiment is understandable. The $Q \sim (L/D)^{1/2}$ behavior appears to represent the data in regime II reasonably well, although the experimental accuracy of the data is not sufficient to determine the effect of the term $L/D$ with great accuracy.

**Turbulent Diffusion (Regime IV).** The progress of each liquid into the other was observed to be much slower in vertical tubes with large $L/D$ (regime IV) than in the other three regimes investigated. The countercurrent flow within the tube appeared to comprise packets of water and packets of brine and the motion of the packets was chaotic and random in appearance. This violent motion was observed for some time after the tube was sealed with a rubber stopper. Kubie studied the rate of advance of two initially separated liquids in a tube closed at each end and observed similar fluid motions. This unpublished work was referenced by Gardner (1977) who viewed the process as one of turbulent diffusion. He postulated that the turbulent liquid-liquid diffusivity $D_t$ must be the same as that proposed by Baird and Rice (1975) for correlating axial dispersion data in bubble and liquid-liquid spray columns; namely,

$$D_t = K(uD^4 g \Delta\rho/\bar{\rho})^{1/3} \tag{12}$$

where $K$ is a constant to be determined from experiment.

If $u$ designates the average flow (superficial velocitiy) of, say, the lighter liquid of mass fraction $Y$ at vertical location $x$ within the tube, then

$$u = -D_t \frac{\partial Y}{\partial x} \tag{13}$$

Since

$$\frac{\partial Y}{\partial x} = -\frac{1}{L} \tag{14}$$

and the volume flux of water is

$$Q = \frac{\pi D^2}{4} u \tag{15}$$

we therefore find that by eliminating $D_t$ between equations (12) and (13) the flux of water through the tube is

$$Q = \frac{\pi}{4} K^{3/2} (D^5 g \Delta\rho/\bar{\rho})^{1/2} (L/D)^{-3/2} \tag{16}$$

This result, first obtained by Gardner (1977), is plotted in Fig. 3 with $K=0.55$. (Baird and Rice (1975) recommended $K=0.35$ for correlation of bubble column data.) The measured rates are in approximate agreement with the function $Q \sim (L/D)^{-3/2}$ for large $L/D$ but do not follow this form as $L/D$ is decreased. It would appear that a useful next step in the theory is to link the Bernoulli and turbulent diffusion approaches, and this is the subject of the next section.

Before leaving this section on regime IV, it is worth noting that Mercer and Thompson's (1975) results fall within this regime and pertain to the exchange flow of brine and water in rather large diameter tubes (see Fig. 3 and Table 1). The fact that their data and the present data are very well correlated by the Froude number shows that there is negligible Grashof number dependence, and that the countercurrent flow through tubes or ducts with $L/D$ at least as large as 10 can, indeed, be treated as inviscid.

**Combined Turbulent Diffusion and Bernoulli Flow (Regime III).** To explain the trend of the data in regime III, the countercurrent exchange flow domain of length $L$ is divided into two subdomains by a mixing front of nominal thickness small compared to $L$. The lighter and heavier fluids within zone 1 are assumed to be unmixed and the exchange flow within this zone is well represented by the corrected form of Bernoulli's equation, equation (11). In zone 2 the two liquids are well mixed and the exchange flow takes place by turbulent binary diffusion, as represented by equation (16). It is recognized that the division of the flow into unmixed and mixed zones is, to say the least, an oversimplification. The complete conditions within the exchange flow opening (tube), especially with respect to the inflows and outflows of the heavier and lighter fluids, are complex, and the exact nature of the flow must remain a matter for speculation. The chief test of the appropriateness of the theoretical approach will be the correct trend of the Froude number with respect to $L/D$. A three-zone model with two Bernoulli flow zones, one at each end of the tube, and one central diffusion zone may appear to be more valid than the two-zone model proposed here. However, since two identical Bernoulli-flow zones must be assumed in order to reduce the number of unknown quantities and close the problem, the two-zone model can be shown to be equivalent to the three-zone model.

As discussed above, the exchange flow in zone 1 is given by

$$Q=0.147(D^5 g\Delta\rho_1/\bar{\rho})^{1/2}(L_1/D)^{1/2} \tag{17}$$

where $\Delta\rho_1$ is the density "jump" across $L_1$, the length of zone 1. The numerical coefficient 0.147 is required to bring experiment and theory together in region II. Recall that equation (17) is the corrected version of equation (11) and is represented by the dashed curve in Fig. 3.

The exchange flow rate within the diffusion zone (2) must also equal $Q$, and equation (16) with $K=0.55$ provides the relation between $Q$ and $L_2$ and $\Delta\rho_2$

$$Q=0.32(D^5 g\Delta\rho_2/\bar{\rho})^{1/2}(L_2/D)^{-3/2} \tag{18}$$

The total length of the exchange flow path and the total density change are given by summing $L_1$ and $L_2$, and $\Delta\rho_1$ and $\Delta\rho_2$, respectively

$$L=L_1+L_2 \tag{19}$$

$$\Delta\rho=\Delta\rho_1+\Delta\rho_2 \tag{20}$$

Eliminating $\Delta\rho_1$ and $\Delta\rho_2$ between equations (17), (18), and (20) yields

$$\frac{Q}{(D^5 g\Delta\rho/\bar{\rho})^{1/2}}=\frac{0.147(L_1/D)^{1/2}}{\left[1+0.21\left(\frac{L_1}{D}\right)\left(\frac{L_2}{D}\right)^3\right]^{1/2}} \tag{21}$$

On the assumptions that $L_1/D$ is constant and is the length-to-diameter ratio corresponding to the intersection of flow regimes II and III in Fig. 3 and above which mixing of the two opposing "Bernoulli streams" becomes pronounced, the magnitude of $L_1/D$ can be estimated. In other words, $L_1$ is regarded as an entrance length for the diffusion zone 2. Based on Fig. 3 we estimate that $L_1/D \simeq 0.4$. Introducing this value and equation (19) into equation (21) gives the sought result for the exchange flow rate in regime III; that is

$$\frac{Q}{(D^5 g\Delta\rho/\bar{\rho})^{1/2}}=\frac{0.093}{[1+0.084(L/D-0.4)^3]^{1/2}} \tag{22}$$

The comparison of equation (22) with the measured exchange flow rates in regime III shows rough agreement as to trend, with the data being somewhat lower than the predictions. A more detailed treatment, including the effects of finite mixing rates, may be required to rationalize the observed reduction in Froude number with $L/D$ ratio.

**Empirical Correlation of Data.** The theory together with the experimental results presented in the foregoing suggest that viscous effects are small and, therefore, the volume exchange rate $Q$ is appropriately expressed in terms of the Froude number $Q/(D^5 g\Delta\rho/\bar{\rho})^{1/2}$, and that the Froude number is only a function of the length-to-diameter ratio of the opening. An additional, purely empirical correlation for the exchange flow rate was computed over the entire range of $L/D$ investigated. The result is

$$\frac{Q}{(D^5 g\Delta\rho/\bar{\rho})^{1/2}}=\frac{0.055[1+400(L/D)^3]^{1/6}}{[1+0.00527(1+400(L/D)^3)^{1/2}((L/D)^6+117(L/D)^2)^{3/4}]^{1/3}} \tag{23}$$

It can be shown by reference to a plot that the data presented in Fig. 3 are equally distributed on either side of the curve corresponding to equation (23).

The parameter ranges covered in the experiments are

$$0.01<L/D<20 \text{ and } 0.025<\Delta\rho/\bar{\rho}<0.17$$

but the equation should be correct for higher values of $\Delta\rho/\bar{\rho}$. Equation (23) should prove useful in computer-coded analyses of the natural convection flow in actual buildings. Again, while the above correlation is based mainly on data with round openings, the evidence suggests that equation (23) can be applied with reasonable accuracy to square openings of characteristic dimension $S$ (length of a side) by making the identification $D=1.1\ S$.

## Multiple Openings: Results and Discussion

The buoyancy-driven exchange flow pattern between two compartments separated by a horizontal partition with multiple openings is, under certain conditions, complex. In this section we discuss the exchange rates observed with a partition penetrated by two openings.

**Flow Configuration.** Experiments for two openings in a common partition were conducted in the rectangular tank described previously. The geometric configuration of the openings is shown in Fig. 4. One of the flow paths connecting the two compartments, labeled opening 1 in the figure, was a tube of diameter $D_1$ and length $L_1$, whose lower end was flush with the lower surface of the partition. The upper end of opening 1 extended a distance $H$ into the heavier liquid in the upper compartment. An opening of circular cross section served as the other flow path and is denoted by opening 2. Opening 2 was fabricated by simply drilling a hole through the partition, so that $L_2$ is equal to the thickness of the partition $\delta$. The

openings were separated by a distance of approximately 0.15 m. The effect, if any, of the spacing between openings was not explored in the present study.

Unlike the case of a single opening, the flow through each opening in a multiple opening system may be unidirectional and form the convective loop illustrated in Fig. 5(*a*). On the other hand, simultaneous unidirectional flow and countercurrent (bidirectional) flow may occur, as illustrated in Fig. 5(*b*). These two flow configurations were observed during the experimental investigation. It is relevant to note that the bidirectional flow shown in Fig. 5(*b*) is different from that encountered in a system with only one opening in that in the former case the upward flow rate is not equal to the downward flow rate. With downward unidirectional flow occurring in opening 2, continuity demands that the upward flow exceed the downward flow within opening 1. It is apparent from this study and from closely related work reported in the literature (see below) that the flow within any opening of a multiple opening system may be bidirectional if the unidirectional flow established throughout the system is not high enough to arrest the opposing flow in the opening. In other words some minimum unidirectional, "purging" or "flooding" velocity is required to prevent countercurrent flow within the opening. In the flow configuration shown in Fig. 5(*a*) the strength of the unidirectional convective loop is sufficient to prevent the downward flow of heavier liquid into opening 1 and the upward flow of lighter liquid into opening 2. In the situation depicted in Fig. 5(*b*), however, the loop flow is not strong enough to oppose the downward movement of heavier fluid at opening 1. In some cases the unidirectional convective loop may be too weak to prevent bidirectional flow at both openings. This situation was observed with two orifices (i.e., $H=0$ in Fig. 4) and is illustrated in Fig. 5(*c*).

**Unidirectional Flow and the Flooding Velocity.** The forced flow of brine in horizontal and vertical ducts in opposition to the buoyancy-driven flow of fresh water was investigated experimentally by Leach and Thompson (1975) and by Mercer and Thompson (1975), respectively. They demonstrated that it is possible to form a wedge of water, with zero net flow rate, on the inside surface of the duct by flowing brine through the duct. Indeed, at high brine velocities the water was entirely prevented from entering the duct. In a system with more than one opening the countercurrent flow in one or more of the openings may be suppressed without fluid being supplied from an external source. The natural one-way flow pattern established in such a system by the gravitational head may, in magnitude, be more than what is required to prevent countercurrent exchange at an opening. The gravitational head for the system shown in Fig. 4 is $\Delta\rho g L_1$. An expression for the exchange flow rate for the one-way flow configuration illustrated in Fig. 5(*a*) can be obtained by application of the Bernoulli equation.

For the upward flow through opening 1, we have

$$P_L - P_{H,1} = \frac{1}{2}\rho_L u_1^2 + \frac{K_1}{2}\rho_L u_1^2 + \rho_L g(H+\delta) \qquad (24)$$

where $P_L$ is the pressure beneath the openings, $P_{H,1}$ is the pressure above opening 1, $u_1$ is the fluid velocity within opening 1, and $K_1$ is the loss coefficient for the entrance flow into opening 1. The first term on the right-hand side of the above equation is the loss due to the re-entrant flow from opening 1. The Bernoulli equation applied to opening 2 gives

$$P_{H,2} - P_L = \frac{1}{2}\rho_H u_2^2 + \frac{K_2}{2}\rho_H u_2^2 - \rho_H g\delta \qquad (25)$$

where $P_{H,2}$ is the pressure above opening 2, $u_2$ is the downward directed velocity within opening 2, and $K_2$ is the loss coefficient for the entrance flow into opening 2. The vertical pressure difference in the upper fluid is

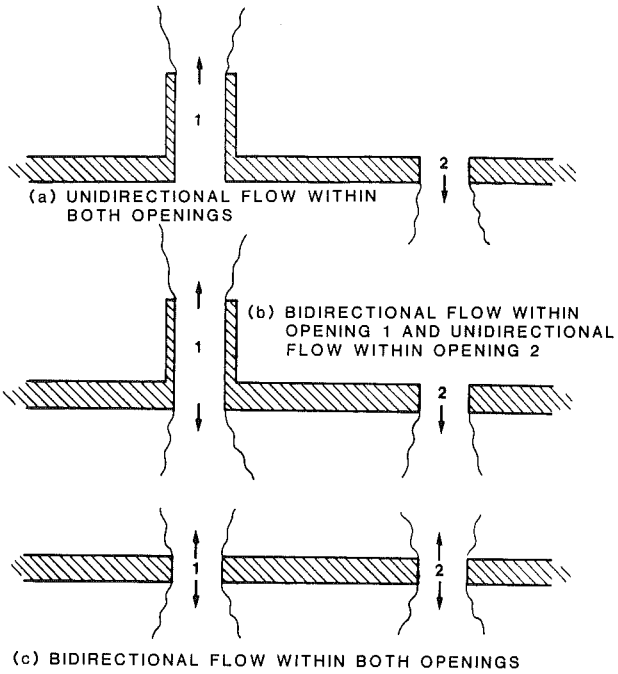


**Fig. 5 Illustration of observed flow configurations with the two-opening system**

$$P_{H,2} - P_{H,1} = \rho_H g H \qquad (26)$$

Substitution of equations (24) and (25) into (26) results in

$$\frac{1}{2}\rho_L(1+K_1)u_1^2 + \frac{1}{2}\rho_H(1+K_2)u_2^2 = (\rho_H - \rho_L)gL_1 \qquad (27)$$

Denoting the unidirectional flow rate by the symbol $Q_u$ and assuming no net volumetric flow to each compartment, we have

$$Q_u = A_1 u_1 = A_2 u_2 \qquad (28)$$

Assuming that the entrance flow loss coefficients for openings 1 and 2 are the same and are equal to 1/2, equation (27) becomes

$$Q_u = 1.15\left[\frac{A_1^2 g \Delta\rho L_1}{\rho_L + \rho_H\left(\frac{A_1}{A_2}\right)^2}\right]^{1/2} \qquad (29)$$

It is important to note that equation (29) cannot be used when the exchange flow through one or both of the openings is strongly bidirectional (see below). The experimental results presented below show that the functional form of equation (29) is probably correct but that the coefficient is too great. Apparently additional contractions and losses reduce the exchange flow to about 70 percent of the theoretical. Thus the final corrected form of equation (29) is obtained by replacing the coefficient 1.15 with 0.805. Recall that a similar correction factor was required to bring the Bernoulli equation (11) into line with the data for countercurrent exchange flow through a single opening.

A total of nine experiments were performed with two openings. In Experiments 1-8, $L_1$ and $D_1$ were fixed and the ratio $A_1/A_2$ was varied systematically by making use of different opening 2 diameters. These experiments were designed to observe the flow transition from bidirectional to unidirectional flow within opening 1 as $D_2$ was increased and, therefore, as the unidirectional flow was increased. A final experiment (9) was conducted in which the lengths of the two openings were identical and equal to the thickness of the parti-

Table 3 Measured buoyancy-driven exchange flows through two openings

| Expt. No. | $D_1$ (m) | $D_2$ (m) | $L_1$ [1] (m) | $\rho_H$ (kg m$^{-3}$) | $\rho_L$ (kg m$^{-3}$) | Flow Regime (see Fig. 5) | $Q \times 10^6$ ($m^3 s^{-1}$) Expt'l | $Q \times 10^6$ ($m^3 s^{-1}$) Eq. 23 [3] | $Q_u \times 10^6$ ($m^3 s^{-1}$) Eq. 29 |
|---|---|---|---|---|---|---|---|---|---|
| 1 | 0.0445 | 0.0127 | 0.0231 | 1114 | 1011 | (b) | 43.8 | 37.8 | 14.7 |
| 2 | 0.0445 | 0.0191 | 0.0231 | 1110 | 1011 | (b) | 48.0 | 37.2 | 32.1 |
| 3 | 0.0445 | 0.0294 | 0.0231 | 1117 | 1012 | (b) | 76.9 | 38.1 | 73.5 |
| 4 | 0.0445 | 0.0353 | 0.0231 | 1115 | 1012 | (b) | 96.7 | 38.5 | 97.3 |
| 5 | 0.0445 | 0.0385 | 0.0231 | 1117 | 1008 | (a) [2] | 101.2 | 38.9 | 113.2 |
| 6 | 0.0445 | 0.0445 | 0.0231 | 1110 | 1013 | (a) [2] | 127.5 | 36.7 | 127.0 |
| 7 | 0.0445 | 0.0516 | 0.0231 | 1112 | 1009 | (a) | 148.5 | - | 149.3 |
| 8 | 0.0445 | 0.0643 | 0.0231 | 1115 | 1012 | (a) | 184.0 | - | 169.6 |
| 9 | 0.0525 | 0.0127 | 0.00635 | 1136 | 1010 | (c) | 36.3 | 39.1 [4] | 8.5 |

[1] $L_2 = \delta = 0.0063$ m.

[2] Unstable flow.

[3] Based on isolated bidirectional flow within opening 1.

[4] Based on isolated bidirectional flow within each opening.

tion (i.e., $H=0$). If a unidirectional flow existed in this experiment it was too weak to be detected visually. The flow through each opening was bidirectional and appeared to act independently as if the other opening was not present (see Fig. 5*c*).

Table 3 has been prepared to convey the results obtained from the experiments with two openings and to compare these results with the exchange flow rates predicted with equations (23) and (29). The table should be used along with Fig. 5 to aid in visualizing the flow configuration observed in each experiment. In Experiments 1–4 the flow within opening 1 was definitely countercurrent although increases in the diameter of opening 2 led to progressively increasing unidirectional flow strengths. An examination of the last three columns of Table 3 shows that equation (23) applied to opening 1 is in closer agreement with the exchange rates recorded in Experiments 1 and 2 than the predictions obtained with equation (29) for one-way flow through each of the openings. This indicates that countercurrent flow through opening 1 was the major contributor to the exchange flow in these experiments for which $A_2/A_1 \ll 1$. The measured volumetric exchange rates in Experiments 3–8 are in good agreement with equation (29) for one-way flow. It should be noted that countercurrent flow within opening 1 was observed in Experiments 3 and 4. Apparently the countercurrent exchange rates were not high enough to be significant and were nearly completely purged by the one-way flow superimposed on the system. This suggests that the $A_2/A_1$ parameter regime in which both one-way and countercurrent flow contribute significantly to the overall exchange rate is rather narrow.

The flow observed within opening 1 in Experiments 6 and 7 can best be described as unstable unidirectional flow. The flow was generally upward with periodic pulses of downward heavier fluid. This condition represented a boundary between the cocurrent flow observed in Experiments 1–4 and the pure unidirectional flow observed in Experiments 7 and 8. Based on the measured flow rate in Experiment 6, we conclude that the critical flow rate $q$ above which the heavier fluid is prevented from entering opening 1 is, in dimensionless form

$$\frac{q}{(D^5 g \Delta\rho/\bar{\rho})^{1/2}} = 0.32 \tag{30}$$

Interestingly enough, by invoking the approximation $\bar{\rho} \simeq \rho_L$ in equation (30) we recover the flooding correlation of Wallis (1969) for the critical gas velocity required to force liquid up and out of a vertical tube. If, indeed, the transition from bidirectional to unidirectional flow is a flooding phenomenon, that is a wedge of stationary fluid held in place by lighter or heavier fluid flowing over it, the substitution $\bar{\rho} = \rho_L$ should be made so that equation (30) truly expresses a balance between inertial forces in the lighter fluid and buoyancy. However, the difference between $\bar{\rho}$ and $\rho_L$ for the brine–water system is too small to warrant an examination of the influence of the density ratio on the critical water velocity.

While equation (30) is probably a valid criterion for flooding in buoyancy-driven exchange flow, it would seem reasonable to perform additional experiments to see what happens when $L/D$ is varied over a wide range, especially at very small $L/D$. Equation (30) predicts bidirectional flow in opening 2 of Experiments 7 and 8. This contrasts with the unidirectional flow that was observed within this opening of $L/D = 0.1$.

## Conclusions

An experimental program of buoyancy-driven exchange flow through small openings in horizontal partitions has been carried out in order to deepen our understanding of the character of air flow within buildings. Attention has been focused mainly on the bidirectional exchange flow between compartments connected by a single opening. These results are of immediate utility. The limited set of experiments with two openings showed that both unidirectional and bidirectional flow patterns are possible. Initial indications are that a flooding mechanism accounts for the transition between one-way and countercurrent flow in an opening, much as has been observed in vertical two-phase flows. Further measurements will be required to determine the rules that govern the flow

patterns and exchange rates between compartments separated by a horizontal partition with more than one opening.

## Acknowledgments

The author is grateful for Electric Power Research Institute (EPRI) funding and the support provided by Dr. Edward L. Fuller, EPRI Project Manager. The assistance of Mr. Alan S. La Croix and Mr. Verden R. Fletcher in conducting the experiments is also gratefully acknowledged.

## References

Baird, M. H. I., and Rice, R. G., 1975, "Axial Dispersion in Large Unbaffled Columns," *Chem. Engng. J.*, Vol. 9, pp. 171–174.

Bejan, A., and Rossie, A. N., 1981, "Natural Convection in Horizontal Duct Connecting Two Fluid Reservoirs," ASME JOURNAL OF HEAT TRANSFER, Vol. 103, pp. 108–113.

Brown, W. G., 1962, "Natural Convection Through Rectangular Openings in Partitions—2. Horizontal Partitions," *Int. J. Heat Mass Transfer*, Vol. 5, pp. 869–878.

Brown, W. G., and Solvason, K. R., 1962, "Natural Convection Through Rectangular Openings in Partitions—Vertical Partitions," *Int. J. Heat Mass Transfer*, Vol. 5, pp. 859–867.

Gardner, G. C., 1977, "Motion of Miscible and Immiscible Fluids in Closed Horizontal and Vertical Ducts," *Int. J. Multiphase Flow*, Vol. 3, pp. 305–318.

Leach, S. J., and Thompson, H., 1975, "An Investigation of Some Aspects of Flow Into Gas Cooled Nuclear Reactors Following an Accidental Depressurization," *J. Br. Nucl. Energy Soc.*, Vol. 14, pp. 243–250.

Lewis, D. J., 1950, "The Instability of Liquid Surfaces When Accelerated in a Direction Perpendicular to Their Planes II," *Proc. Roy. Soc.*, Vol. A202, pp. 81–96.

Mercer, A., and Thompson, H., 1975, "An Experimental Investigation of Some Further Aspects of the Buoyancy-Driven Exchange Flow Between Carbon Dioxide and Air Following a Depressurization Accident in a Magnox Reactor, Part I: The Exchange Flow in Inclined Ducts," *J. Br. Nucl. Energy Soc.*, Vol. 14, pp. 327–334.

Mercer, A., and Thompson, H., 1975, "An Experimental Investigation of Some Further Aspects of the Buoyancy-Driven Exchange Flow Between Carbon Dioxide and Air Following a Depressurization Accident in a Magnox Reactor, Part II: The Purging Flow Requirements in Inclined Ducts," *J. Br. Nucl. Soc.*, Vol. 14, pp. 335–340.

Prahl, J., and Emmons, H. W., 1975, "Fire Induced Flow Through an Opening," *Combustion and Flame*, Vol. 25, pp. 369–385.

Shaw, B. H., 1971, "Heat and Mass Transfer by Natural Convection and Combined Natural Convection and Forced Air Flow Through Large Rectangular Openings in a Vertical Partition," *Symposium on Heat and Mass Transfer by Combined Forced and Natural Convection*, IMechE, Sept. 15, Paper No. C117/71.

Steckler, K. D., Quintiere, J. G., and Rinkinen, W. J., 1982, "Flow Induced by Fire in a Compartment," *19th Symposium (Int.) on Combustion*, The Combustion Institute, pp. 913–920.

Steckler, K. D., Baum, H. R., and Quintiere, J. G., 1984, "Fire Induced Flows Through Room Openings—Flow Coefficients," *20th Symposium (Int.) on Combustion*, The Combustion Institute, pp. 1591–1600.

Steckler, K. D., Baum, H. R., and Quintiere, J. G., 1985, "Salt Water Modeling of Fire Induced Flows in a Multiroom Enclosure," in: *Chemical and Physical Processes of Combustion*, Fall Technical Meeting, Philadelphia, PA, pp. 58/1-58/4.

Taylor, G. I., 1950, "The Instability of Liquid Surfaces When Accelerated in a Direction Perpendicular to Their Planes," *Proc. Roy. Soc.*, A, Vol. 201, pp. 192–196.

Wallis, G. B., 1969, *One-Dimensional Two-Phase Flow*, McGraw-Hill, New York, p. 339.

## APPENDIX

Equation (1) was obtained as follows: Mass balances on the brine and water compartments give

$$V_H \frac{d\rho_H}{dt} = -Q\rho_H + Q\rho_L \tag{A1}$$

$$V_L \frac{d\rho_L}{dt} = -Q\rho_L + Q\rho_H \tag{A2}$$

Solving equation (A1) for $Q$ yields

$$Q = \frac{-V_H d\rho_H/dt}{\rho_H - \rho_L} \tag{A3}$$

Adding equations (A1) and (A2) and integrating the result from the initial densities $\rho_{H,0}$ and $\rho_{L,0}$, we obtain

$$V_H(\rho_H - \rho_{H,0}) + V_L(\rho_L - \rho_{L,0}) = 0 \tag{A4}$$

Equation (1) is then derived by solving the above expression for $\rho_L$ and substituting the result into equation (A3).

# Natural Convection Heat Transfer of Cold Water Within an Eccentric Horizontal Cylindrical Annulus

**C. J. Ho**
Professor.
Assoc. Mem. ASME

**Y. H. Lin**
Graduate Student.

Department of Mechanical Engineering,
National Cheng Kung University,
Tainan, Taiwan 70101

*Natural convection heat transfer of cold water, encompassing a density inversion, within an eccentric horizontal annulus made of two isothermal cylinders, is numerically studied via a finite difference method. Numerical results have been obtained for an annular radius ratio 2.6 with Rayleigh number ranging from $10^3$ to $10^6$, the inversion parameter being 0.0 to 1.0, the eccentricity varying from 0 to 0.8, and the orientation angle of the inner cylinder between 0 and $\pi$. Results indicate that the flow patterns and heat transfer characteristics are strongly influenced by the combined effect induced by the density inversion of water and the position of the inner cylinder of the annulus. For the cases considered in the present study, a minimum in heat transfer arises with the inversion parameter between 0.4 and 0.5 depending primarily on the position of the inner cylinder.*

## Introduction

The problem of natural convection heat transfer in the annulus between two horizontal cylinders is of fundamental importance due to its association with numerous practical applications of current engineering interest. Common examples of applications are found in energy conversion systems, thermal energy storage systems, cooling of electronic systems, underground electric transmission lines, and many others. As a result, a considerable number of theoretical and experimental studies have been conducted to investigate the effect of the various parameters on the heat transfer process. A comprehensive literature review on the subject was given by Kuehn and Goldstein (1976); a more up-to-date extensive bibliography can be found in the paper of Rao et al. (1985). Previous studies were concerned with natural convection in annuli filled with a Boussinesq fluid (which has a linear relation between fluid density and temperature), which is valid for most fluids. However, for cold water at temperature near the freezing point, a well-known nonlinear density inversion phenomenon exists such that the maximum density occurs at about 4°C. Due to the effect of density inversion, the natural convective motion in cold water is developed in a considerably complicated manner. Moreover, in view of the fact that natural convection of cold water plays an important role over a wide range of occurrences in nature and technology, many studies on natural convection heat transfer of cold water with density inversion have been performed.

Seki et al. (1975) investigated experimentally the natural convection of water with density inversion in a horizontal concentric cylindrical annulus. The inner cylinder was maintained at 0°C while the temperature of the outer cylinder was kept at various temperatures above 0°C. They reported the appearance of bicellular flow patterns in the annulus, and that the average heat transfer coefficient exhibited a minimum value when the two counterrotating eddies were of approximately the same size. Recently, theoretical studies on the similar problem of Seki et al. (1975) have been carried out by Nguyen et al. (1982) and Vasseur et al. (1983) by means of perturbation and finite difference methods, respectively.

The present study originated primarily while investigating the natural convection of molten water during melting of ice around a heated cylinder. Specifically, natural convection of cold water, encompassing a density inversion, within an eccentric horizontal cylindrical annulus, is studied numerically via a finite difference method. The eccentric annulus is transformed in the radial coordinate direction such that a regular computational domain can be obtained. The primary objective of the present numerical study is to analyze the effects of eccentricity and orientation of the inner cylinder on natural convection heat transfer of cold water in a cylindrical annulus.

## Problem Formulation

Figure 1 illustrates schematically the physical problem of steady natural convection of cold water within an eccentric horizontal annulus made of two isothermal cylinders of radius $r_o$ and $r_i$, respectively. The outer and inner cylinders are kept at different temperatures $T_o$ and $T_i$ ($T_i > T_o$), respectively. A mathematical formulation of the problem is made in cylindrical coordinates with the origin at the center of the inner cylinder. The following assumptions are made:

1 The water is a Newtonian fluid.
2 The fluid motion is two-dimensional and laminar.
3 The physical properties of water, except density, are temperature-independent and evaluated at the mean temperature $T_f = (T_o + T_i)/2$.
4 The Boussinesq approximation is employed such that the variation of density with temperature can be neglected except for the buoyancy force terms.
5 The viscous dissipation is negligible.

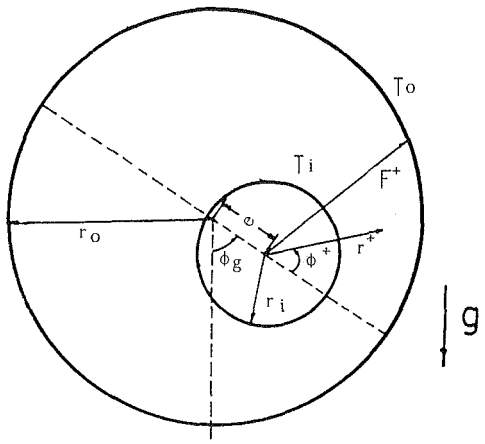


Fig. 1 Schematic representation of the physical problem

Contributed by the Heat Transfer Division and presented at the AIAA/ASME Thermophysics and Heat Transfer Conference, Boston, Massachusetts, June 2-4, 1986. Manuscript received by the Heat Transfer Division March 18, 1986. Keywords: Enclosure Flows, Natural Convection.

To account for the density inversion effect of cold water, the following density relation of water, proposed by Gebhart and Mollendorf (1977), is employed:

$$\rho(T) = \rho_m[1 - \text{rsp}\,|T - T_m|^q] \tag{1}$$

where $\rho_m = 999.9720\ \text{kg/m}^3$, $\text{rsp} = 9.297173 \times 10^{-6}(°\text{C})^{-q}$, $T_m = 4.029325°\text{C}$, and $q = 1.894816$.

In dealing with the irregular solution domain of the eccentric annulus, applicable mathematical techniques include the bipolar coordinate transformation (Wood, 1957; Pepper and Cooper, 1983) and the radial coordinate transformation (Yao, 1980; Ho and Viskanta, 1984). In view of the inherent restriction that a perfectly concentric annulus is not possible using bipolar coordinates, the radial coordinate transformation is adopted in the present paper and a new radial coordinate is defined as

$$\eta = (r - R_i)/(F(\phi) - R_i) \tag{2}$$

where $F(\phi)$ denotes the radial profile of the outer cylinder measured from center of the inner cylinder and is given as

$$F(\phi) = [R_o^2 - \epsilon^2 \sin^2(\phi_o\phi)]^{1/2} - \epsilon\cos(\phi_o\phi) \tag{3}$$

Consequently, the eccentric annulus is mapped into a unit circle. The normalized governing equations and boundary conditions in the transformed plane can be written in terms of the stream-function vorticity formulation as follows:

$$\hat{\nabla}^2\psi = -\omega \tag{4}$$

$$\frac{1}{\phi_o r}\frac{\partial\eta}{\partial r}\left(\frac{\partial\psi}{\partial\phi}\frac{\partial\omega}{\partial\eta} - \frac{\partial\psi}{\partial\eta}\frac{\partial\omega}{\partial\phi}\right) = \text{Pr}\,\hat{\nabla}^2\omega + \text{PrRa}\left\{[\cos\phi_g \sin(\phi_o\phi) + \sin\phi_g\cos(\phi_o\phi)]\frac{\partial\eta}{\partial r}\frac{\partial}{\partial\eta}|\theta - \theta_m|^q + [\cos\phi_g\cos(\phi_o\phi) - \sin\phi_g\sin(\phi_o\phi)]\frac{1}{\phi_o r}\left[\frac{\partial}{\partial\phi}|\theta-\theta_m|^q + \frac{\partial\eta}{\partial\phi}\frac{\partial}{\partial\eta}|\theta-\theta_m|^q\right]\right\} \tag{5}$$

$$\frac{1}{\phi_o r}\frac{\partial\eta}{\partial r}\left(\frac{\partial\psi}{\partial\phi}\frac{\partial\theta}{\partial\eta} - \frac{\partial\psi}{\partial\eta}\frac{\partial\theta}{\partial\phi}\right) = \hat{\nabla}^2\theta \tag{6}$$

where

$$\frac{\partial\eta}{\partial r} = \frac{1}{F - R_i} \tag{7a}$$

$$\frac{\partial\eta}{\partial\phi} = \frac{-\eta}{F - R_i}\frac{\partial F}{\partial\phi} \tag{7b}$$

$$\frac{\partial^2\eta}{\partial\phi^2} = \frac{-1}{F - R_i}\left(\eta\frac{\partial^2 F}{\partial\phi^2} + 2\frac{\partial\eta}{\partial\phi}\frac{\partial F}{\partial\phi}\right) \tag{7c}$$

$$\hat{\nabla}^2 \equiv \left[\left(\frac{\partial\eta}{\partial r}\right)^2 + \left(\frac{1}{\phi_o r}\frac{\partial\eta}{\partial\phi}\right)^2\right]\frac{\partial^2}{\partial\eta^2} + \frac{2}{(\phi_o r)^2}\frac{\partial\eta}{\partial\phi}\frac{\partial^2}{\partial\eta\partial\phi} + \frac{1}{(\phi_o r)^2}\frac{\partial^2}{\partial\phi^2} + \left[\frac{1}{r}\frac{\partial\eta}{\partial r} + \frac{1}{(\phi_o r)^2}\frac{\partial^2\eta}{\partial\phi^2}\right]\frac{\partial}{\partial\eta} \tag{7d}$$

subject to

(*i*) *For* $\phi_g = 0$ *or* $\pi$,

$$\phi = 0 \text{ or } 1; \quad \frac{\partial\theta}{\partial\phi} = \psi = \omega = 0 \tag{8a}$$

$$\eta = 0; \quad \theta = 1, \quad \psi = \frac{\partial\psi}{\partial\eta} = 0 \tag{8b}$$

$$\eta = 1; \quad \theta = 0, \quad \psi = \frac{\partial\psi}{\partial\eta} = 0 \tag{8c}$$

(*ii*) *For* $0 < \phi_g < \pi$,

$$\theta(\eta, \phi = 0) = \theta(\eta, \phi = 1) \tag{9a}$$

$$\psi(\eta, \phi = 0) = \psi(\eta, \phi = 1) \tag{9b}$$

$$\omega(\eta, \phi = 0) = \omega(\eta, \phi = 1) \tag{9c}$$

$$\eta = 0; \quad \theta = 1, \quad \psi = \frac{\partial\psi}{\partial\eta} = 0 \tag{9d}$$

$$\eta = 1; \quad \theta = 0, \quad \psi = \frac{\partial\psi}{\partial\eta} = 0 \tag{9e}$$

It should be noted that the adoption of the boundary conditions of $\psi(\eta = 0) = \psi(\eta = 1) = 0$ in equations (9*d*) and (9*e*), which preclude the occurrence of a net circulating flow around the inner cylinder, is based on experiments done with eccentric annuli (Kuehn and Goldstein, 1978).

An inspection of the foregoing governing equations and boundary conditions, equations (4)–(9), reveals that the governing parameters for the present problem include the Rayleigh number Ra, the radius ratio $r_o/r_i$, eccentricity $\epsilon$, the orientation angle of the inner cylinder $\phi_g$, formed by the line joining the centers of the inner and outer cylinders and the gravitational direction, and the inversion parameter $\theta_m$.

In addition to the flow field and temperature distributions,

## Nomenclature

$C_p$ = specific heat
$e$ = eccentricity
$F^+$ = radial profile of outer cylinder
$F$ = dimensionless radial profile of outer cylinder = $F^+/Lr$
$g$ = gravitational acceleration
$Lr$ = radius gap = $(r_o - r_i)$
Nu = overall Nusselt number
Pr = Prandtl number = $\nu/\alpha$
$q$ = coefficient of density relation
$r^+$ = radial coordinate
$r$ = dimensionless radial coordinate = $r^+/Lr$
Ra = Rayleigh number = $\text{rsp}\,gLr^3(T_i - T_o)^q/\{\alpha\nu(1 - \text{rsp}\,|T_f - T_m|^q)\}$
$r_i$ = radius of inner cylinder
$R_i$ = dimensionless radius of inner cylinder = $r_i/Lr$
$r_o$ = radius of outer cylinder
$R_o$ = dimensionless radius of outer cylinder = $r_o/Lr$
rsp = coefficient of density relation
$T$ = temperature
$\alpha$ = thermal diffusivity
$\epsilon$ = dimensionless eccentricity = $e/Lr$
$\eta$ = radial coordinate
$\theta$ = dimensionless temperature = $(T - T_o)/(T_i - T_o)$
$\theta_m$ = inversion parameter = $(T_m - T_o)/(T_i - T_o)$
$\nu$ = kinematic viscosity
$\rho$ = density
$\phi^+$ = angular coordinate
$\phi$ = dimensionless angular coordinate = $\phi^+/\phi_o$
$\phi_g$ = orientation angle of inner cylinder
$\phi_o$ = angular range of solution domain = $\pi$ or $2\pi$
$\psi^+$ = stream function
$\psi$ = dimensionless stream function = $\psi^+/\alpha$
$\omega^+$ = vorticity
$\omega$ = dimensionless vorticity = $L_r^2\omega^+/\alpha$
$\hat{\nabla}^2$ = Laplace operator in transformed plane

**Subscripts**

$i$ = inner cylinder surface
$m$ = physical properties of water at 4.029325°C
$f$ = physical properties of water at film temperature
$o$ = outer cylinder surface

the physical quantities of primary interest are the overall Nusselt numbers at the inner and outer cylinder, which are defined as follows:

$$\overline{\mathrm{Nu}_i} = \log(r_o/r_i)\int_0^1 \frac{\partial\eta}{\partial r}\frac{\partial\theta}{\partial\eta}\bigg|_{\eta=0} R_i d\phi \qquad (10a)$$

$$\overline{\mathrm{Nu}_o} = \log(r_o/r_i)\int_0^1 - \left[1+\left(\frac{1}{\phi_o F}\frac{\partial F}{\partial\phi}\right)^2\right]^{1/2}\frac{\partial\eta}{\partial r}\frac{\partial\theta}{\partial\eta}\bigg|_{\eta=1} F d\phi \qquad (10b)$$

## Numerical Method

The system of equations (4)–(7) together with the boundary conditions, equations (8) and (9), was solved numerically via a finite difference method. The solution of the system of steady equations was obtained by using a pseudotransient formulation approach in which a fictitious transient term was introduced to each equation (Peyret and Taylor, 1983). The governing equations were then discretized by employing central difference approximations for the spatial derivatives and forward difference approximations for the time derivatives, except for the convective terms, for which the second upwind difference scheme was used (Roache, 1976). Furthermore, a two-dimensional alternating directional implicit (ADI) splitting scheme was adopted to arrange the resulting set of algebraic finite difference equations in the convenient tridiagonal form; and Thomas algorithm was used to solve the system of algebraic equations. The cross-differential terms were always evaluated from the values of variables at the previous time step.

The solution procedure was initiated by advancing the temperature distribution one time step through solution of the energy equation. The vorticity equation was then solved for all the interior grid points. Next, the stream function equation was solved. From the solution of the stream function equation the wall vorticities were updated. The procedure was then repeated for a new time step until a pre-established convergence criterion was satisfied for all field variables ($\xi = \psi, \omega, \theta$):

$$\frac{|\xi_{i,j}^{n+1} - \xi_{i,j}^{n}|_{\max}}{|\xi_{i,j}^{n+1}|_{\max}} \le 5\times 10^{-5} \qquad (11)$$

where the superscripts $n$ and $(n+1)$ indicate the $n$th and $(n+1)$th time step, respectively. A further check on the convergence of the steady-state solution was made by comparing the overall Nusselt number for the inner and outer cylinder.

Two grid systems were utilized for the computation depending on the flow domain. For the cases of symmetric flow, a grid system of 45 nodes in the $\eta$-direction by 31 nodes in the $\phi$-direction was used, while a $45\times 61$ mesh was employed for the asymmetric annular flows. The selection of the foregoing grid systems was considered to represent a reasonable compromise between accuracy and computing cost on a basis of a series of grid size studies, in which various grids of $23\times 21$, $45\times 31$, $45\times 41$, and $61\times 51$ were considered. For instance, for $\phi_g = 0$, $\theta_m = 0$, $\epsilon = -0.8$, and $\mathrm{Ra} = 10^6$, the values of the overall Nusselt number and the maximum stream function

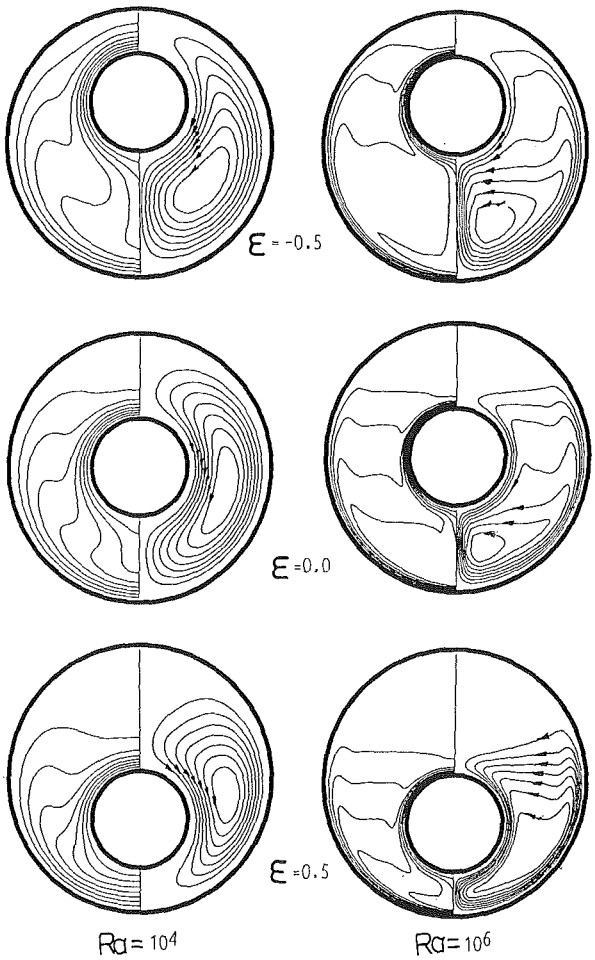


Fig. 2 Streamline and isotherm patterns for $\theta_m = 1.0$

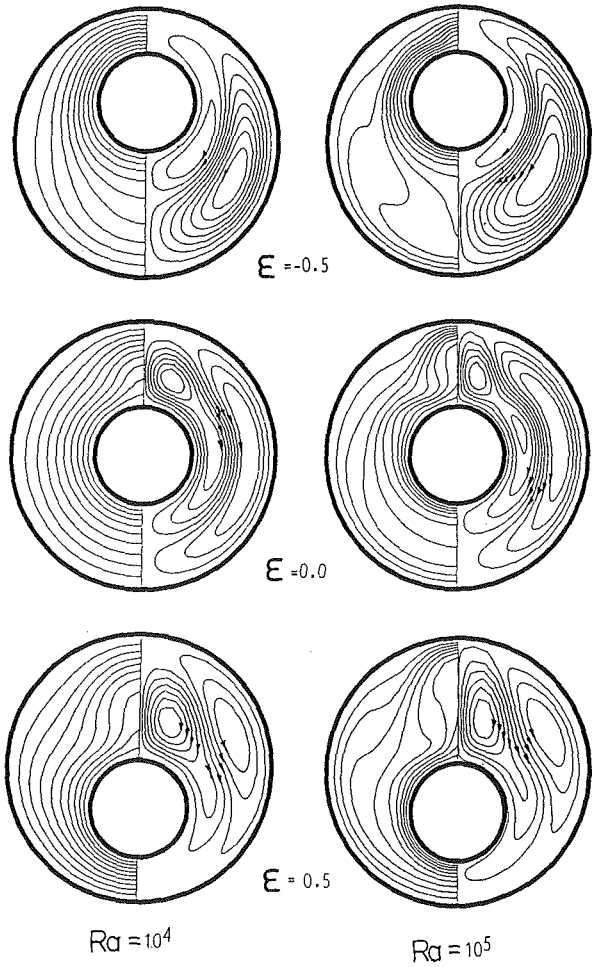


Fig. 3 Streamline and isotherm patterns for $\theta_m = 0.4$

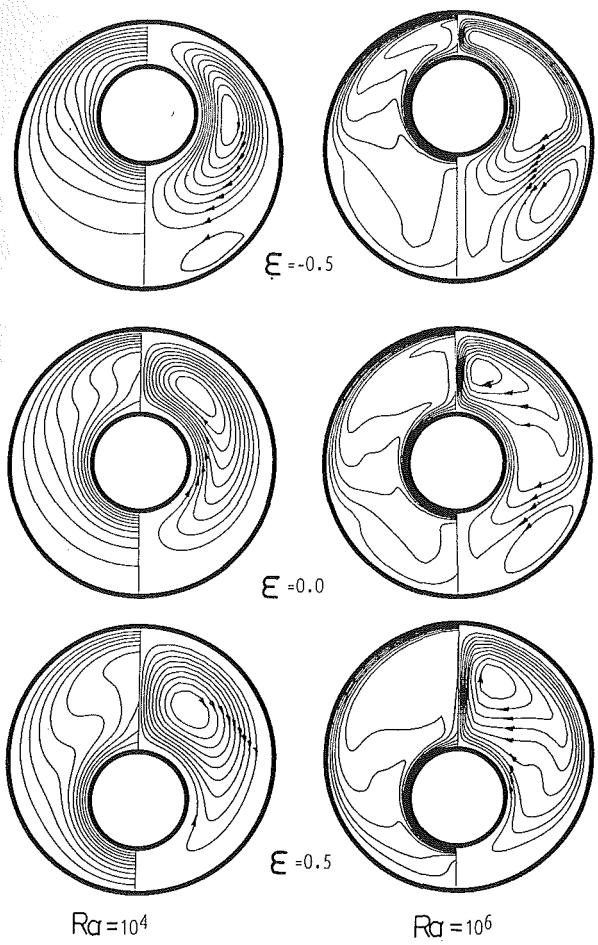


**Fig. 4 Streamline and isotherm patterns for $\theta_m = 0.2$**

changed by less than 2 and 3 percent, respectively, between the $45 \times 31$ and $61 \times 51$ grids.

## Results and Discussion

In order to assess the validity of the numerical results, test calculations were conducted for air within a horizontal eccentric cylindrical annulus, which could be directly compared with experimental results reported by Kuehn and Goldstein (1978). Additionally, preliminary computations were performed for the case of cold water with density inversion within a horizontal concentric cylindrical annulus; a comparison with the published results of Vasseur et al. (1983) was made to check the accuracy of the density relation of water adopted in this study. These test computations for the flow patterns as well as the temperature distributions were in excellent agreement with the published results.

Based on the numerical results in the preliminary calculations, numerical results were obtained for an annulus of radius ratio 2.6, with the Rayleigh number ranging from $10^3$ to $10^6$, the inversion parameter being 0.0 to 1.0, the eccentricity varying from 0 to 0.8, and the orientation angle of the inner cylinder between 0 and $\pi$. Emphases on the effects of the density inversion of cold water and eccentricity as well as the orientation angle of the inner cylinder are stressed.

**Flow Patterns and Isotherm Distributions.** Representative predicted flow patterns and temperature distributions are presented in the form of streamline and isotherm contour plots. Figures 2 to 4 show the results for annuli with vertical eccentricity of $-0.5$ and 0.5 at two values of Ra for $\theta_m = 1.0$, 0.4, and 0.2, respectively. For the situation of $\theta_m = 1.0$ (e.g., $T_i = 4°C$ and $T_o = 0°C$) the water in the vicinity of the inner cylinder is at a higher density than that near the outer cylinder. Thus water near the surface of the inner cylinder moves downward while the relatively lighter water near the outer cylinder moves upward and a single-circulation pattern results, as seen in Fig. 2. Moreover, a thermal plume originates at the bottom of the inner cylinder, impinging on the outer cylinder. As the inner cylinder is shifted downward along the vertical axis, defined as a positive eccentricity, the vortex center moves upward while the convective circulation as well as the thermal plume activity appear to be markedly impeded. Conduction is the dominant heat transport mechanism in the bottom region of the annulus. Furthermore, the top of the inner cylinder exhibits an enlarged, stagnant, isothermal region of water. When the inner cylinder moves toward the top, the circulation and thermal plume are greatly intensified in both size and strength, thus increasing the heat transfer rate. As expected, the convective flow in the annulus is enhanced with increasing Rayleigh number. Except for the reverse flow motion in the water due to its density anomaly, the characteristics of the flow and isotherm patterns for $\theta_m = 1.0$ are quite similar to those for ordinary fluids such as air (Kuehn and Goldstein, 1978).

Figure 3 presents the flow patterns and isotherm distributions for $\theta_m = 0.4$ (e.g., $T_i = 10°C$, $T_o = 0°C$). The flow field is characterized by the presence of two counterrotating circulations in the half-annulus. This is apparently a direct effect of the density inversion of the water enclosed in the annulus. With increasing positive eccentricity, the vortex center of the outer circulation near the outer cylinder shifts to the top; increasing thermal plume activity is detected. When the inner cylinder is moved upward, the vortex centers of both inner and outer circulation move downward. Meanwhile the inner circulation in the bottom region of the annulus is further subdued by the expanding outer circulation. Accordingly, a significant temperature inversion occurs in the region. Moreover, there is no thermal plume activity above the inner cylinder in the negatively eccentric annulus; conduction-controlling heat transport in the region can be readily recognized. Further decreasing the inversion parameter results in an opposite trend in the combined effect of eccentricity and density inversion on the flow and isotherm pattern. For $\theta_m = 0.2$ (Fig. 4) both the inner circulation and thermal plume arising above the inner cylinder appear to intensify with increasing positive eccentricity; for negative eccentricity the effect is reversed. The flow field becomes dominated by the inner circulation while the outer circulation is severely subdued, and even disappears completely. This clearly represents the decay of the density-inversion effect; the maximum density of the water for these cases occurs essentially along the outer cylinder, as evidenced from the isotherm plots. The flow and isotherm patterns appear similar to those of ordinary fluids.

Further examination of the isotherm plots in Figs. 2 to 4 reveals that for the cases considered, a thermal boundary layer always exists around the inner cylinder while the presence of a boundary layer along the outer cylinder depends on the position of the inner cylinder and the inversion parameter. For $\theta_m = 1.0$ and 0.4, a thermal boundary layer develops everywhere along the outer cylinder as the inner cylinder moves toward the top of the annulus. Conversely, when the inner cylinder shifts downward, there is no boundary layer along the top region of the outer cylinder. Boundary layer development in the opposite direction observed for $\theta_m = 0.2$ is similar to that reported by Kuehn and Goldstein (1978) for an eccentric annulus filled with ordinary fluids.

Next, the influence of orientation angle of the inner cylinder is examined by varying $\phi_g$ from 0 to $\pi$ with the fixed eccentricity. With the nonvertical eccentricity, the flow patterns and temperature distributions, as expected, are no longer symmetric with respect to the vertical axis of the inner cylinder.

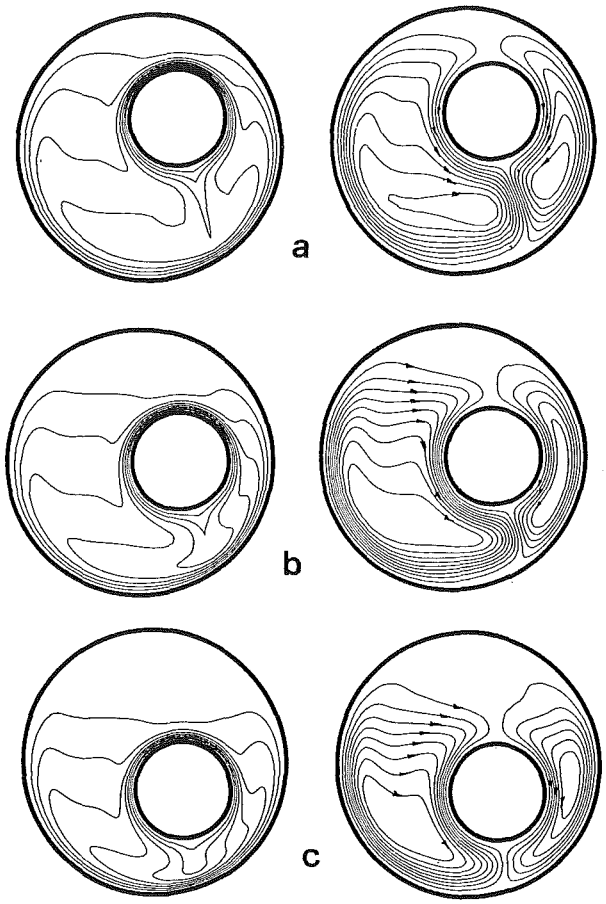


Fig. 5 Flow structures and temperature distributions for $\theta_m = 1.0$, $Ra = 10^5$, $\epsilon = 0.5$, $\phi_g =$ (*a*) 45 deg, (*b*) 90 deg, (*c*) 135 deg

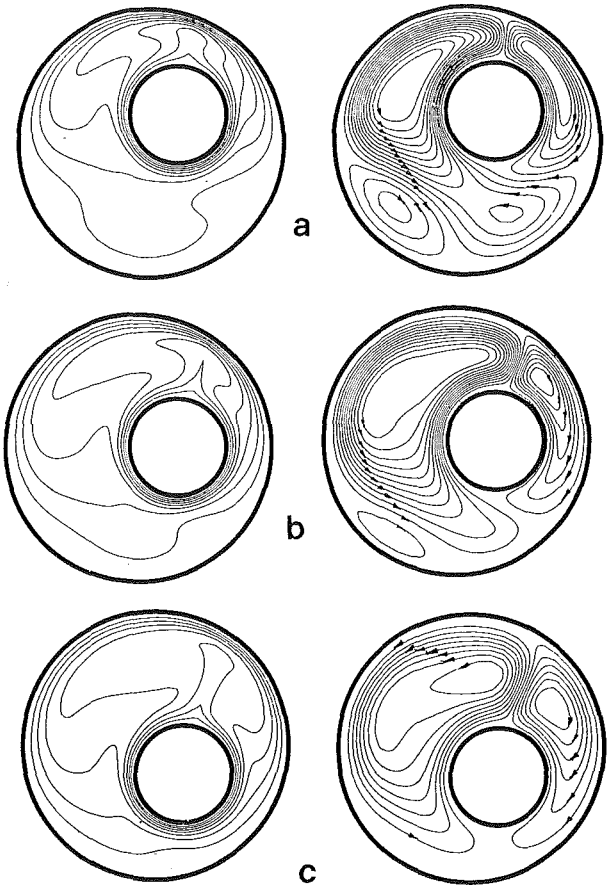


Fig. 6 Flow structures and temperature distributions for $\theta_m = 0.2$, $Ra = 10^5$, $\epsilon = 0.5$, $\phi_g =$ (*a*) 45 deg, (*b*) 90 deg, (*c*) 135 deg

Furthermore, the thermal plume activity does not rise vertically above or below the inner cylinder. Representative flow and isotherm patterns are shown in Figs. 5 and 6 for $\theta_m = 1.0$ and 0.2, respectively. In general, the flow patterns are complicated by the relative diminishing and/or intensifying of the counter-rotating convective circulations to both sides of the inner cylinder with increasing $\phi_g$.

**Overall Heat Transfer Results.** Attention will now be focused on the overall heat transfer results for all cases under consideration. First of all, the effect of the eccentricity of the inner cylinder $\epsilon$ on the rate of heat transfer is considered by plotting the overall Nusselt number versus the eccentricity, while keeping the orientation angle and Rayleigh number unchanged; the representative result is shown in Fig. 7. As seen from the figure, there exists a value of eccentricity that yields minimum heat transfer for most cases considered. The occurrence of minimum heat transfer signifies the onset of a regime where the increase in conduction in the eccentric annulus is enough to offset the decrease in convection. The specific value of such eccentricity appears to depend on the Rayleigh number, the orientation angle, and the inversion parameter. Qualitatively it appears that the minimum heat transfer rate always occurs at some positive and negative eccentricity for $\theta_m = 0.5$–$1.0$ and $\theta_m = 0.4$–$0.0$, respectively. For ordinary fluids, the variation of the overall heat transfer coefficient with eccentricity has been investigated numerically by Cho et al. (1982) and Projahn et al. (1981); results appear to be very similar to those predicted for the cases of $\theta_m = 0.0$–$0.4$ in the present study. Moreover, results tend to demonstrate that with an increase of Rayleigh number, the effect of eccentricity on the overall Nusselt number is more pronounced.

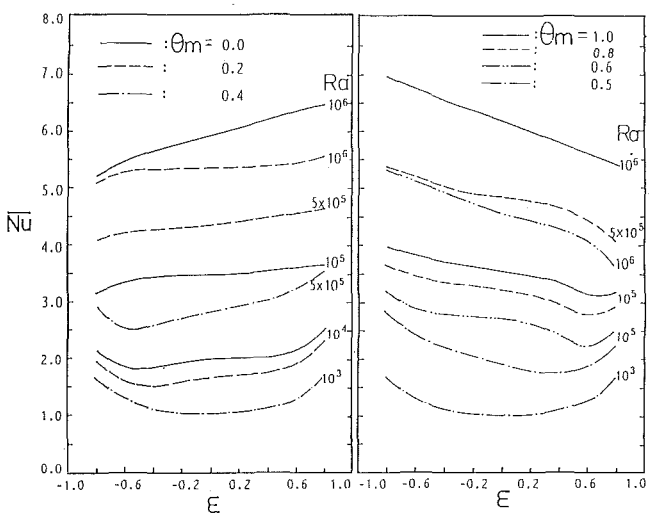


Fig. 7 Effect of eccentricity on overall Nusselt number

Next, in Figs. 8(*a*) and 8(*b*) are shown the representative influence of the inversion parameter on the overall Nusselt number for various eccentricity, orientation angle, and Rayleigh number. It can be observed from the figures that a minimum in heat transfer arises within the range $0.4 \leq \theta_m \leq 0.5$ depending primarily on the position of the inner cylinder. This is due to the presence of bicellular flow structure of approximately equal strength in the annulus within this range of $\theta_m$, yielding more mixing of the water and hence increasing the

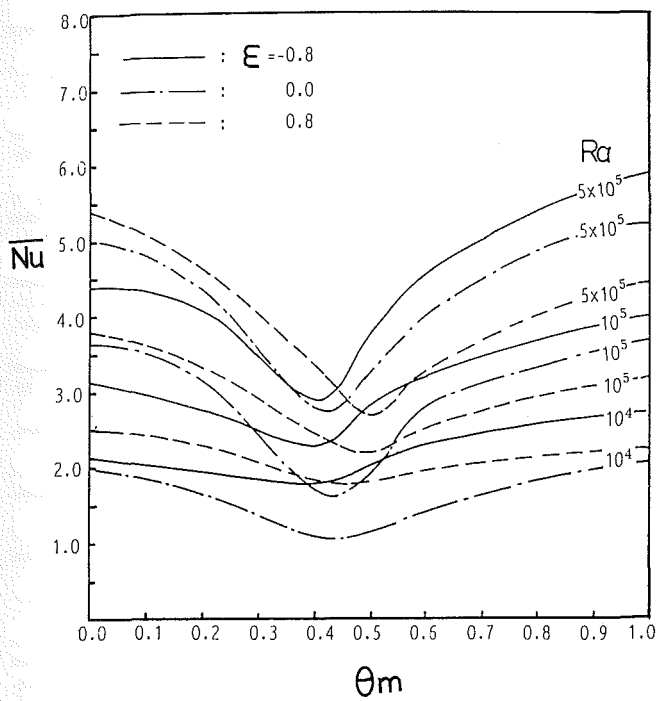


Fig. 8(*a*) Dependence of the overall heat transfer on the inversion parameter for vertically eccentric annulus

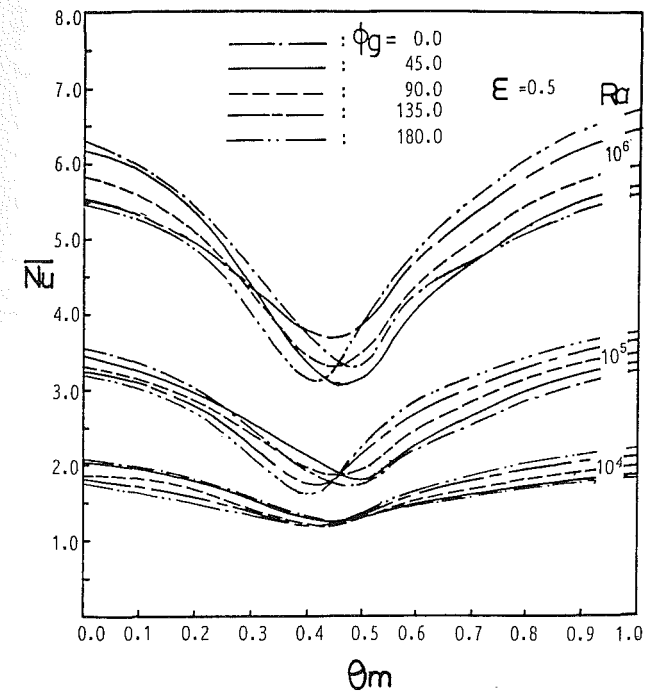


Fig. 8(*b*) Dependence of the overall heat transfer on the inversion parameter for various orientation angles

thermal resistance for heat transport across the annulus. An inspection of Fig. 8(*a*) reveals that for a concentric annulus, $\epsilon = 0$, the minimum heat transfer occurs at about $\theta_m \simeq 0.44$ (e.g., $T_i = 9°C$, $T_o = 0°C$). This value of critical $\theta_m$ is different from that predicted by Vasseur et al. (1983), $\theta_m \simeq 0.375$, for similar geometric configuration. This can be attributed to the difference in the physical configuration considered by Vasseur and his co-workers, in which the inner cylinder is cooled while the outer cylinder is heated. As for the vertically eccentric annulus, the occurrence of the minimum

**Table 1 Constants of equation (12) for various inversion parameters and vertical eccentricities**

| $\theta_m$ | ε | C | n | Ra | ε | C | n | Ra |
|---|---|---|---|---|---|---|---|---|
| 0.0 | -0.8 | 0.3560 | 0.1920 | $10^4$-$10^6$ | 0.8 | 0.7087 | 0.1411 | $10^3$-$10^5$ |
| | -0.6 | 0.2058 | 0.2385 | $10^4$-$10^6$ | 0.6 | 0.2377 | 0.2373 | $10^4$-$10^6$ |
| | -0.4 | 0.1966 | 0.2440 | $10^4$-$10^6$ | 0.4 | 0.2508 | 0.2311 | $10^3$-$10^6$ |
| | -0.2 | 0.2068 | 0.2419 | $10^3$-$10^6$ | 0.2 | 0.2165 | 0.2413 | $10^3$-$10^6$ |
| | 0.0 | 0.2014 | 0.2457 | $10^3$-$10^6$ | | | | |
| 0.2 | -0.8 | 0.1358 | 0.2607 | $10^5$-$10^6$ | 0.8 | 0.3916 | 0.1894 | $10^4$-$10^6$ |
| | -0.6 | 0.1449 | 0.2586 | $10^4$-$10^6$ | 0.6 | 0.2309 | 0.2272 | $10^4$-$10^6$ |
| | -0.4 | 0.1243 | 0.2715 | $10^4$-$10^6$ | 0.4 | 0.1907 | 0.2414 | $10^4$-$10^6$ |
| | -0.2 | 0.1444 | 0.2607 | $10^4$-$10^6$ | 0.2 | 0.2032 | 0.2354 | $10^4$-$10^6$ |
| | 0.0 | 0.1910 | 0.2396 | $10^3$-$10^6$ | | | | |
| 0.5 | -0.8 | 0.4319 | 0.1650 | $10^4$-$10^6$ | 0.8 | 1.0735 | 0.0602 | $10^3$-$10^5$ |
| | -0.6 | 0.1853 | 0.2243 | $10^4$-$10^6$ | 0.6 | 0.6849 | 0.0836 | $10^3$-$10^5$ |
| | -0.4 | 0.1207 | 0.2534 | $10^4$-$10^6$ | 0.4 | 0.0614 | 0.2921 | $10^5$-$10^6$ |
| | -0.2 | 0.1003 | 0.2643 | $10^4$-$10^6$ | | | | |
| | 0.0 | 0.0677 | 0.2910 | $10^5$-$10^6$ | | | | |
| 0.6 | -0.8 | 0.6669 | 0.1351 | $10^3$-$10^5$ | 0.8 | 0.5057 | 0.1422 | $10^4$-$10^6$ |
| | -0.6 | 0.2195 | 0.2264 | $10^4$-$10^6$ | 0.6 | 0.5313 | 0.1226 | $10^3$-$10^5$ |
| | -0.4 | 0.1498 | 0.2536 | $10^4$-$10^6$ | 0.4 | 0.1520 | 0.2430 | $10^4$-$10^6$ |
| | -0.2 | 0.1818 | 0.2610 | $10^4$-$10^6$ | 0.2 | 0.1327 | 0.2561 | $10^4$-$10^6$ |
| | 0.0 | 0.1331 | 0.2580 | $10^4$-$10^6$ | | | | |
| 0.8 | -0.8 | 0.6264 | 0.1531 | $10^3$-$10^5$ | 0.8 | 0.7613 | 0.1151 | $10^3$-$10^5$ |
| | -0.6 | 0.3555 | 0.1966 | $10^3$-$10^5$ | 0.6 | 0.4128 | 0.1638 | $10^3$-$10^5$ |
| | -0.4 | 0.2453 | 0.2287 | $10^3$-$10^5$ | 0.4 | 0.1369 | 0.2575 | $10^4$-$10^6$ |
| | -0.2 | 0.2067 | 0.2412 | $10^3$-$10^6$ | 0.2 | 0.1595 | 0.2587 | $10^4$-$10^6$ |
| | 0.0 | 0.1918 | 0.2454 | $10^3$-$10^6$ | | | | |
| 1.0 | -0.8 | 0.6162 | 0.1617 | $10^3$-$10^5$ | 0.8 | 0.7053 | 0.1291 | $10^3$-$10^5$ |
| | -0.6 | 0.3116 | 0.2208 | $10^3$-$10^6$ | 0.6 | 0.2192 | 0.2341 | $10^4$-$10^6$ |
| | -0.4 | 0.2522 | 0.2351 | $10^3$-$10^6$ | 0.4 | 0.2315 | 0.2327 | $10^3$-$10^6$ |
| | -0.2 | 0.2208 | 0.2435 | $10^3$-$10^6$ | 0.2 | 0.2103 | 0.2429 | $10^3$-$10^6$ |
| | 0.0 | 0.2063 | 0.2467 | $10^3$-$10^6$ | | | | |

overall Nusselt number is shifted toward lower and higher value of $\theta_m$ for negative and positive eccentricity, respectively, as the Rayleigh number increases. Furthermore, the effect of eccentricity on heat transfer rate elucidated in Fig. 7 can be further inferred from Fig. 8(*a*). Moreover, as depicted in Fig. 8(*b*), the minimum in heat transfer arises at a lower value of $\theta_m$ with increasing orientation angle as the Rayleigh number increases with fixed eccentricity. Another important fact that can be seen in Fig. 8(*b*) is that the overall Nusselt number can be significantly affected by the change of the orientation of the inner cylinder. Depending on the Rayleigh number, a monotonic decreasing trend of the overall Nusselt number with the increasing orientation angle such as that found for the ordinary fluid (Cho et al., 1983) is predicted for $\theta_m$ below a lower bound. On the other end, an opposite trend is detected for $\theta_m$ beyond an upper bound. For instance, for $Ra = 10^5$ with $\theta_m \leq 0.25$, the overall Nusselt number decreases as the orientation angle increases, such that the maximum heat transfer occurs at the positive vertical eccentricity; for $\theta_m \geq 0.46$ a reversed trend results. As for the intermediate values of $\theta_m$, a somewhat complex trend appears in that the extreme in heat transfer rate does not always arise at the vertical orientations. The effect of the orientation angle tends to be enhanced with increasing Rayleigh number.

Finally, using a least-squares regression analysis, the overall heat transfer results for most cases of vertical eccentricity can be well correlated in the form

$$\overline{\mathrm{Nu}} = C\mathrm{Ra}^n \tag{12}$$

where values of $C$ and $n$ are presented in Table 1 for various eccentricity and inversion parameter. The maximum deviations of these correlations from the numerical data are within 5 percent. Little success was obtained in an attempt to attain a global correlation of the heat transfer results for all the cases investigated in the present study.

## Conclusion

The steady laminar natural convection of cold water within an eccentric horizontal cylindrical annulus has been studied numerically via a finite-difference method. A radial coordinate transformation technique was employed to solve for the flow and temperature within the eccentric annulus. Results indicate that the density anomaly of water exhibited in the inversion parameter range considered causes the convective flow developed in the annulus to be more complex than for ordinary fluids. Accordingly, the heat transfer characteristics are strongly influenced by the combined effects of the density inversion of water and the position of the inner cylinder. Specifically, there exists a value of eccentricity that yields minimum heat transfer for most cases under consideration. The specific value of such eccentricity appears to depend on the Rayleigh number, the orientation angle, and the inversion parameter. As the Rayleigh number increases, the effect of eccentricity on the overall Nusselt number increases. For the cases considered in the present study, a minimum in heat transfer arises within the range $0.4 \leq \theta_m \leq 0.5$, depending primarily on the position of the inner cylinder of the annulus.

## Acknowledgments

The authors wish to acknowledge National Cheng Kung University for providing the necessary computer time. The constructive comments made by the reviewers are also highly appreciated.

## References

Cho, C. H., Chang, K. S., and Park, K. H., 1982, "Numerical Simulation of Natural Convection in Concentric and Eccentric Horizontal Cylindrical Annulus," ASME JOURNAL OF HEAT TRANSFER, Vol. 104, pp. 624–630.

Gebhart, B., and Mollendorf, J., 1977, "A New Density Relation for Pure and Saline Water," *Deep-Sea Research*, Vol. 124, pp. 831–848.

Ho, C. J., and Viskanta, R., 1984, "Heat Transfer During Melting in a Horizontal Tube," *International Journal of Heat and Mass Transfer*, Vol. 27, No. 5, pp. 705–716.

Kuehn, T. H., and Goldstein, R. J., 1976, "Correlating Equations for Natural Convection Heat Transfer Between Horizontal Circular Cylinders," *International Journal of Heat and Mass Transfer*, Vol. 10, pp. 1127–1134.

Kuehn, T. H., and Goldstein, R. J., 1978, "An Experimental Study of Natural Convection Heat Transfer in Concentric and Eccentric Horizontal Cylindrical Annuli," ASME JOURNAL OF HEAT TRANSFER, Vol. 100, pp. 635–640.

Nguyen, T. H., Vasseur, P., and Robillard, L., 1982, "Natural Convection Between Horizontal Concentric Cylinders With Density Inversion of Water for Low Rayleigh Numbers," *International Journal of Heat and Mass Transfer*, Vol. 25, No. 10, pp. 1559–1568.

Pepper, D. W., and Cooper, R. E., 1983, "Numerical Solution of Natural Convection in Eccentric Annuli," *AIAA Journal*, Vol. 21, No. 19, pp. 1331–1337.

Peyret, R., and Taylor, T. D., 1983, *Computational Methods for Fluid Flow*, Springer-Verlag, New York.

Projahn, U., Rieger, H., and Beer, H., 1981, "Numerical Analysis of Laminar Convection Between Concentric and Eccentric Cylinders," *Numerical Heat Transfer*, Vol. 4, pp. 131–146.

Rao, Y.-F., Miki, Y., Fukuda, K., and Takata, Y., 1985, "Flow Patterns of Natural Convection in Horizontal Cylindrical Annuli," *International Journal of Heat and Mass Transfer*, Vol. 28, No. 3, pp. 705–714.

Roache, P. J., 1976, *Computational Fluid Dynamics*, Hermosa, Albuquerque, NM.

Seki, N., Fukusako, S., and Nakaoka, M., 1975, "Experimental Study on Natural Convection Heat Transfer With Density Inversion of Water Between Two Horizontal Concentric Cylinders," ASME JOURNAL OF HEAT TRANSFER, Vol. 97, pp. 556–561.

Vasseur, P., Robillard, L., and Chandra Shekar, B., 1983, "Natural Convection Heat Transfer of Water Within a Horizontal Cylindrical Annulus With Density Inversion Effects," ASME JOURNAL OF HEAT TRANSFER, Vol. 105, pp. 117–123.

Wood, W. W., 1957, "The Asymptotic Expansion at Large Reynolds Numbers for Steady Motion Between Non-coaxial Rotating Cylinders," *Journal of Fluid Mechanics*, Vol. 3, pp. 159–175.

Yao, L. S., 1980, "Analysis of Heat Transfer in Slightly Eccentric Annuli," ASME JOURNAL OF HEAT TRANSFER, Vol. 102, pp. 270–284.

# Combined Forced and Free Laminar Convection in the Entrance Region of an Inclined Isothermal Tube

**D. Choudhury**

**S. V. Patankar**

Department of Mechanical Engineering,
University of Minnesota,
Minneapolis, MN 55455

*An analysis is made of the combined forced and free convection for laminar flow in the entrance region of isothermal, inclined tubes. This involves the numerical calculation of the developing flow with significant buoyancy effects. Three independent parameters are introduced: the Prandtl number Pr, a modified Rayleigh number Ra*, and Ω, a parameter that measures the relative importance of free and forced convection. The inclination angle does not appear explicitly in the formulation. Numerical results are obtained for Pr = 0.7, 5, and 10, and representative values of Ra* and Ω. The axial development of the velocity profiles, temperature field, local pressure gradient, and the Nusselt number are presented. These results reveal that the buoyancy effects have a considerable influence on the fluid flow and heat transfer characteristics of the development flow. A comparison of the numerical results with the available experimental data is also presented.*

## Introduction

The convection heat transfer coefficient and fluid flow characteristics of duct flows are often affected by the presence of gravity forces, particularly at low or moderate flow rates. The orientation of the duct can have a considerable influence on the velocity and temperature profiles and the associated heat transfer and friction coefficients in the duct. For horizontal tubes, the buoyancy forces are perpendicular to the main flow direction and they give rise to secondary currents in the cross section. For vertical tubes, the gravity forces are in the main flow direction, and axial symmetry is preserved since there is no secondary flow in the cross section. In inclined tubes, however, buoyancy forces act in both the main flow and the cross-stream directions. In practice, this situation is commonly encountered in heat exchanger equipment and in solar collectors.

Laminar combined free and forced convection in horizontal and vertical pipes has been studied theoretically and experimentally by many investigators in recent years. Yousef and Tarasuk (1982) have reviewed much of the published work for horizontal, isothermal tubes, and Collins (1980) has reviewed analytical and experimental studies of flow and heat transfer in vertical, isothermal tubes. The literature on buoyancy-affected flow and heat transfer in inclined ducts is sparse, and, to the authors' knowledge, no theoretical work has been published for developing laminar mixed convection in inclined, isothermal tubes. Iqbal and Stachiewicz (1966), Cheng and Hong (1972a), Cheng and Hong (1972b), Ou et al. (1976), and Sabbagh et al. (1976) have studied fully developed flow and heat transfer in inclinded tubes with the constant heating rate thermal boundary condition. Abdelmeguid and Spalding (1979) have presented numerical predictions of fully developed turbulent flow and heat transfer in uniformly heated, inclined tubes.

In many practical situations, the length of the channel is not long enough for the flow to become fully developed and the problem of mixed convection in the entrance region becomes important. Recently, Abou-Ellail and Morcos (1980) have presented entrance region calculations for uniformly heated inclined rectangular channels. In a later publication Morcos and Abou-Ellail (1983) have studied a similar problem as applied to solar collector channels. In the case of the isothermal boundary condition, the only publication has been a flow visualization study by Cheng and Yuen (1985) in which photographs of secondary flow patterns in the entrance region of inclined isothermal tubes are presented.

The purpose of this paper is to present a numerical study of the developing laminar flow and heat transfer in an inclined isothermal tube in which the heating from the tube wall leads to significant buoyancy effects in the upward flow. In the formulation presented here, only three independent parameters (the Prandtl number Pr, a modified Rayleigh number Ra*, and Ω, a parameter related to the relative magnitude of buoyancy and inertial forces) appear explicitly in the governing equations. With suitable choices of these parameters, the vertical and horizontal orientations of the heated tube can be recovered as limiting cases. The Prandtl number is assigned values of 0.7, 5, and 10 so that the range of air and water fluids is covered. Solutions are obtained over a range of Ra* and Ω such that a wide variation of buoyancy and inclination effects is encountered. The present investigation is restricted to only heated upflow (or cooled downflow). For this situation, the effect of buoyancy is to accelerate the flow near the tube wall while retarding the flow in the core. At certain combinations of Ra* and Ω, the acceleration of the flow near the wall tends to cause reverse flow. Since the numerical method employed in this study is limited to boundary layer type flows, the computations are not carried out beyond these critical values of Ra* and Ω. The results obtained from the computations include Nusselt numbers, friction factors, velocity profile, isotherm maps, and secondary flow patterns in the entrance region of the tube. Comparisons with experimental and numerical data for horizontal and vertical pipes are also presented.

## Analysis

**Problem Statement.** The inclined tube under consideration is shown schematically in Fig. 1 together with a typical cross section of the tube perpendicular to the main flow direction. The fluid enters the tube with a uniform velocity $w_{in}$ and at a uniform temperature $T_{in}$. The tube wall temperature is held constant at $T_w$. The problem to be analyzed in this work

Contributed by the Heat Transfer Division and presented at the ASME Winter Annual Meeting, Anaheim, California, December 7-12, 1986. Manuscript received by the Heat Transfer Division April 20, 1987. Keywords: Mixed Convection, Numerical Methods.

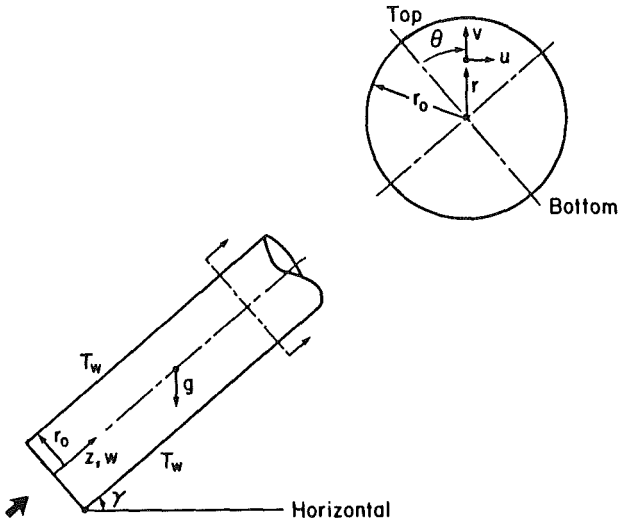


Fig. 1 The geometry considered

is that of simultaneously developing laminar flow and heat transfer with appreciable buoyancy effects in an isothermally heated tube inclined at an angle $\gamma$ to the horizontal. Because of the symmetry inherent in the problem, the calculations can be restricted to a solution domain that comprises one-half of the circular region as shown in Fig. 1.

**Governing Equations.** The equations governing the present problem are those of conservation of mass, momentum, and energy expressed in cylindrical coordinates. The pressure gradient and body force terms in the radial momentum equation are

$$-\partial p/\partial r - \rho g \cos\theta \cos\gamma \tag{1}$$

where $r$, $\theta$, and $\gamma$ are measured as shown in Fig. 1. The density $\rho$ appearing in equation (1) can be related to the temperature via the Boussinesq approximation in which the variation of density $\rho$ is included only in the calculation of the buoyancy terms. The density $\rho$ is given by

$$\rho = \rho_w[1 - \beta(T - T_w)] \tag{2}$$

where $\rho_w$ is the density evaluated at the reference temperature $T_w$. With a modified pressure $p^*$ defined as

$$p^* = p + \rho_w g r \cos\theta \cos\gamma \tag{3}$$

equation (1) may be rewritten as

$$-\partial p^*/\partial r + \rho_w g\beta(T - T_w)\cos\theta\cos\gamma \tag{4}$$

A similar manipulation of the pressure and body forces in the tangential ($\theta$-direction) momentum equation yields

$$-(\partial p^*/\partial\theta)/r - \rho_w g\beta(T - T_w)\sin\theta\cos\gamma \tag{5}$$

Invoking the Boussinesq approximation, the pressure gradient and body force terms in the axial momentum equation are

$$-\partial p/\partial z - \rho_w g\sin\gamma + \rho_w\beta(T - T_w)\sin\gamma \tag{6}$$

The flow is assumed to be parabolic and in the axial momentum equation a space-averaged pressure $\bar{p}$ is supposed to prevail at each cross section, thus permitting a decoupling from the pressure $p^*$ in the cross-sectional momentum equation. This "pressure uncoupling" follows the parabolic-flow practice and, together with the assumption that neither momentum nor heat is diffused in the axial direction, permits a marching-integration calculation procedure. Using this practice and absorbing the term $\rho_w g \sin\gamma$ in the definition of $\bar{p}$, equation (6) becomes

$$-d\bar{p}/dz + \rho_w g\beta(T - T_w)\sin\gamma \tag{7}$$

## Nomenclature

$c_p$ = constant pressure specific heat
$D$ = tube diameter
$f$ = friction factor, equation (27)
Gr = Grashof number, equation (26)
$g$ = acceleration due to gravity
$h$ = circumferential average heat transfer coefficient, equation (30)
$h_m$ = mean heat transfer coefficient, equation (33)
$k$ = thermal conductivity
$m$ = mass flow rate
Nu = circumferential average Nusselt number, equation (30)
$\mathrm{Nu_m}$ = mean Nusselt number, equation (33)
$P$ = dimensionless mean pressure, equation (8)
$P^*$ = dimensionless cross-sectional pressure, equation (8)
Pr = Prandtl number $= c_p\mu/k$
$p$ = pressure
$\bar{p}$ = modified mean pressure
$p^*$ = modified cross-sectional pressure, equation (3)
$q$ = average heat flux at a cross section
Ra = Rayleigh number, equation (8)
Ra* = modified Rayleigh number, equation (12)
Re = Reynolds number, equation (8)
$r$ = radial coordinate
$T$ = temperature
$T_b$ = bulk temperature at a cross section, equation (31)
$T_{in}$ = uniform entrance temperature
$T_m$ = mean temperature at a cross section, equation (29)
$\Delta T_m$ = average mean temperature difference, equation (34)
$U, V, W$ = dimensionless velocities, equation (8)
$u, v, w$ = velocity components in $\theta$, $r$, $z$ directions
$w_{in}$ = uniform entrance velocity
$Z$ = dimensionless axial coordinate, equation (8)
$Z^+$ = dimensionless axial coordinate, equation (32)
$z$ = axial coordinate
$\alpha$ = thermal diffusivity
$\beta$ = thermal expansion coefficient
$\gamma$ = tube inclination angle
$\eta$ = dimensionless radial coordinate $= r/D$
$\theta$ = angular coordinate
$\mu$ = molecular viscosity
$\nu$ = dynamic viscosity
$\rho$ = density
$\rho_w$ = density at the reference wall temperature $T_w$
$\phi$ = dimensionless temperature, equation (8)
$\phi_b$ = dimensionless bulk temperature, equation (31)
$\phi_m$ = dimensionless mean temperature, equation (28)
$\Omega$ = mixed convection parameter, equation (13)

As a final step, dimensionless variables are introduced as follows:

$$\eta = r/D, \quad Z = z/(D\mathrm{RePr}), \quad \mathrm{Re} = w_{in}D/\nu, \quad \mathrm{Pr} = \nu/\alpha$$

$$U = uD/\alpha, \quad V = vD/\alpha, \quad W = w/w_{in}$$

$$P = \bar{p}/(\rho w_{in}^2 \mathrm{Pr}), \quad P^* = p^* D^2 \mathrm{Pr}/(\rho\nu^2) \tag{8}$$

$$\phi = (T - T_w)/(T_{in} - T_w), \quad \mathrm{Ra} = g\beta(T_w - T_{in})D^3/(\nu\alpha)$$

The nondimensionalized body force terms in the radial, tangential, and axial momentum equations then become

$$\mathrm{Ra}\phi \sin\theta \cos\gamma \tag{9}$$

$$-\mathrm{Ra}\phi \cos\theta \cos\gamma \tag{10}$$

and

$$\mathrm{Ra}\phi \sin\gamma/(\mathrm{RePr}) \tag{11}$$

respectively. Expressions (9), (10), and (11) can be presented in a compact fashion by introducing two new parameters

$$\mathrm{Ra}^* = \mathrm{Ra} \cos\gamma \tag{12}$$

and

$$\Omega = (\mathrm{Ra}/\mathrm{Re}) \sin\gamma \tag{13}$$

With these definitions, and the assumptions made earlier, the equations expressing the conservation of mass and of $r$, $\theta$, and $z$ momentum are

$$[\partial(\eta V)/\partial\eta + \partial U/\partial\theta]/\eta + \partial W/\partial Z = 0 \tag{14}$$

$$[(U/\eta)\partial U/\partial\theta + V\partial U/\partial\eta + UV/\eta + W\partial U/\partial Z]\mathrm{Pr} =$$

$$-(\partial P^*/\partial\theta)/\eta + \nabla^2 U + 2(\partial V\partial/\partial\theta)/\eta - U/\eta^2 + \mathrm{Ra}^*\phi \sin\theta \tag{15}$$

$$[(U/\eta)\partial V/\partial\theta + V\partial V/\partial\eta - U^2/\eta + W\partial V/\partial Z]/\mathrm{Pr} =$$

$$-\partial P^*/\partial\eta + \nabla^2 V - 2(\partial U/\partial\theta)/\eta^2 - V/\eta^2 \mathrm{Ra}^*\phi \cos\theta \tag{16}$$

and

$$[(U/\eta)\partial W/\partial\theta + V\partial W/\partial\eta + \partial W/\partial Z]/\mathrm{Pr} = -dP/dZ$$

$$+ \nabla^2 W - \Omega\phi/\mathrm{Pr} \tag{17}$$

Neglecting viscous dissipation and compression work, as is appropriate for incompressible laminar flows, the energy equation is written as

$$(U/\eta)\partial\phi/\partial\theta + V\partial\phi/\partial\eta + W\partial\phi/\partial Z = \nabla^2\phi \tag{18}$$

In equations (14)–(18), $\nabla^2$ is the Laplace operator in cylindrical coordinates

$$\nabla^2 = (1/\eta^2)\partial^2/\partial\theta^2 + (1/\eta)\partial(\eta\partial/\partial\eta)/\partial\eta \tag{19}$$

**Boundary Conditions.** As mentioned earlier, because of the symmetry about the vertical center line shown in Fig. 1, it is sufficient to solve the equations over only the right half of the circular cross section. The boundary conditions for this domain are given by

$$\eta = 0.5: \qquad U = V = W = \phi = 0 \tag{20}$$

$$\theta = 0 \text{ and } \theta = \pi: \quad U = 0, \ \partial V/\partial\theta = \partial W/\partial\theta = \partial\phi/\partial\theta = 0 \tag{21}$$

Further, at the inlet of the tube

$$Z = 0: \qquad U = V = 0, \quad W = 1, \quad \phi = 1 \tag{22}$$

**Governing Parameters.** The governing equations (14)–(18) contain three independent parameters: Ra*, Ω, and Pr. Ra* is a modified Rayleigh number given by equation (12) and Ω is a parameter defined by equation (13) that contains the ratio of the Rayleigh number, Ra, to the Reynolds number Re, modified by an inclination angle factor sin γ. An examination of the dimensionless equations (14)–(18) shows that the inclination angle γ does not explicitly appear in the formulation; hence, the introduction of the dimensionless parameters Ra* and Ω has reduced the number of independent parameters from four to three. Moreover, from equations (12) and (13), it is obvious that as

$$\gamma \to 0, \quad \sin\gamma \to 0, \quad \mathrm{Ra}^* \to \mathrm{Ra}, \quad \Omega \to 0 \tag{23}$$

and equations (14)–(18) become the governing equations for a horizontal isothermal tube. Also, as

$$\gamma \to \pi/2, \quad \sin\gamma \to 1, \quad \mathrm{Ra}^* \to 0, \quad \Omega \to \mathrm{Ra}/\mathrm{Re} \tag{24}$$

and the buoyancy term in the axial momentum equation (17) becomes

$$\gamma \to \pi/2, \quad \Omega\phi/\mathrm{Pr} \to \mathrm{Ra}\phi(\mathrm{RePr}) = (\mathrm{Gr}/\mathrm{Re})\phi \tag{25}$$

which is the correct buoyancy parameter for the axial momentum equation in a vertical tube. Here Gr is the Grashof number defined as

$$\mathrm{Gr} = \mathrm{Ra}/\mathrm{Pr} \tag{26}$$

Thus, it is noted that when $\gamma = \pi/2$, equations (14)–(18) become the conservation equations for buoyancy-affected flow in a vertical isothermal tube. It is clear, then, that the introduction of Ra* and Ω as independent parameters has not only reduced the number of governing parameters of the problem but has permitted a compact formulation in which all inclination angles, including the limiting cases of vertical and horizontal tubes, can be recovered.

The computations were carried out for the Prandtl numbers of 0.7, 5, and 10. Ra* was varied between 0 and $10^6$ and Ω was taken between 0 and 500. This choice of parameters covers a wide range of possible combinations of fluid properties, flow rate, temperature differences, and inclination angles.

**Solution Procedure.** The governing equations were solved numerically by a modified version of the finite-difference method for three-dimensional parabolic flows described by Patankar and Spalding (1972). The modifications included the use of the SIMPLER procedure of Patankar (1980) for handling the pressure–velocity coupling in the cross section of the tube and the incorporation of the method described by Raithby and Schneider (1979) to calculate the streamwise pressure gradient.

**Computational Details.** The computations were performed on a $22 \times 32$ grid in $\theta$–$r$ coordinates. In the $\theta$ direction, a uniform grid spacing was chosen, while the $r$ direction grid spacing was nonuniform, with grid lines being more closely packed near the tube wall. The axial step size $\Delta Z$ was varied from $10^{-6}$ near the tube entrance to about $10^{-2}$ near the fully developed flow region. The value of $\Delta Z$ was adjusted so that at each station the selected step size would cause the bulk temperature of the flow to rise by approximately 1 percent of the maximum possible change $(T_w - T_{in})$. With this continuously varying step size, about 120 forward steps were needed to reach the fully developed region. At each marching step, a sufficient number of iterations (about 6 to 8) were performed to ensure that the velocity and temperature fields converged to four significant digits. Exploratory runs on finer grids ($38 \times 50$) and double the number of forward steps at high Ra* values changed the predicted heat transfer and friction coefficients by less than 1.5 percent for $Z$ values less than $5 \times 10^{-4}$ and by lesser amounts for larger values of $Z$. Typical computation times encountered on a CRAY-1A computer were of the order of 120 cpu seconds.

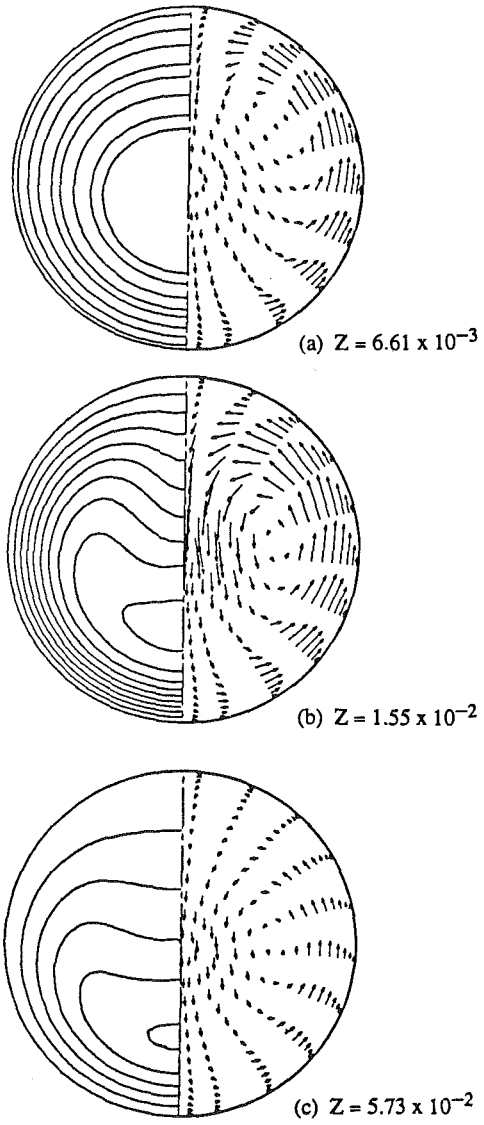


**Fig. 2 Cross-stream flow and isotherm maps for Pr = 0.7, Ra* = $10^5$, Ω = 500**

As a partial verification of the computational procedure, results were initially obtained for simultaneously developing fluid flow and heat transfer in an isothermal tube for pure forced convection (Ra* = 0, Ω = 0) with Pr = 0.7 and Pr = 5. The results for fluid flow and heat transfer were compared with those of Liu (1974) and Hwang and Sheu (1974) as tabulated by Shah and London (1978). The friction factors and Nusselt numbers were found to agree within 1 and 1.5 percent, respectively, for axial stations downstream of $Z = 3 \times 10^{-4}$.

## Results and Discussion

In the presentation that follows, detailed results for a few of the cases studied are given consideration. Most of the results are shown for the Prandtl number of 0.7; the results for Pr = 5 and Pr = 10 are qualitatively similar. Information about the flow and temperature field development is provided via vector plots, velocity profiles, and isotherm maps. Overall quantities that are of most direct relevance to applications, like the Nusselt number and the friction factor, are presented in more detail. Finally, a comparison of the present results with some experimental and numerical results for vertical and horizontal tubes is presented.

**Development of Secondary Flow and Temperature Field.** Figure 2 displays the buoyancy-induced secondary flow pattern and the temperature distribution in the cross section of the tube for the case Pr = 0.7, Ra* = $10^5$, and Ω = 500 at three axial locations. This choice of parameters represents a case in which buoyancy and inclination effects are insignificant. Because of the symmetry about the vertical diameter, the isotherms are plotted in the left half and the velocity vectors in the right half of the circular region. In the absence of buoyancy forces, only the radial component of velocity would be present and the secondary flow associated with the growth of the boundary layer would be directed away from the tube wall. In the presence of free convection, this flow pattern changes. At the first axial station, $Z = 6.61 \times 10^{-3}$ in Fig. 2(*a*), it is seen that the flow pattern is already affected by the buoyancy forces. The fluid rises along the heated wall with a relatively high velocity and falls slowly toward the center where it is carried away by the main flow. Since most of the fluid is still at a temperature close to $T_{in}$, the relative magnitudes of the velocities, except very near the tube wall, are rather small. The center of circulation appears to be in the upper half of the tube. The isotherm contours at the same axial locations are presented with increments of 0.1 in the nondimensional temperature $\phi$. Since the axial location is very near the entrance of the tube, the isotherms are nearly circular and are virtually unaffected by the secondary flow pattern.

As the fluid moves downstream, the buoyancy forces are in effect for a longer distance and the strength of the secondary flow increases. This can be seen in Fig. 2(*b*) at $Z = 1.55 \times 10^{-2}$ where the secondary flow is most intense. The center of circulation moves downward to a location close to the horizontal diameter of the tube. The magnitudes of the velocity vectors are appreciably larger compared to those in Fig. 2(*a*) ($Z = 6.61 \times 10^{-3}$). At the bottom of the domain, the secondary flow is rather sluggish. The isotherms in the lower part of the cross section are nearly circular, just as in Fig. 2(*a*), due to this weak secondary flow. The stronger secondary flow elsewhere, however, causes a very noticeable distortion in the temperature field with the isotherms being sparsely spaced in the upper region of the cross section. Consequently, in the upper section, pronounced peripheral variations are expected in the local wall shear stress and heat transfer coefficients. The fact that the secondary flow is most intense at this axial location causes the friction factor and Nusselt number to have their maximum values at this station.

Farther downstream, at $Z = 5.73 \times 10^{-2}$, the secondary flow becomes weaker due to the disappearance of free convection effects (Fig. 2*c*). At sufficiently far downstream locations, the secondary flow disappears altogether as the fluid reaches the wall temperature and the flow becomes fully developed.

**Development of Axial Velocity Profiles.** The developing profiles of the axial velocity $W$ along the vertical symmetry line are illustrated in Fig. 3. The axial velocity profiles for pure forced convection are symmetric about the central axis of the tube. With the influence of buoyancy effects, the symmetric velocity profile is still preserved along the horizontal center line ($\theta = \pi/2$). However, except for the case of a vertical tube, this symmetry is lost along the vertical center line ($\theta = 0$ and $\theta = \pi$). The profiles in Figs. 3(*a, b, c, d*) have been presented for Pr = 0.7 and for various combinations of Ra* and Ω that introduce an inclination angle effect. In each subplot, the $W$ profiles have been plotted at five axial locations starting from near the entrance of the tube (curve A) to location in the fully developed region (curve E). Near the entrance, the velocity profile is nearly uniform over the cross section as shown by curve A in all the subplots. At the farthest downstream locations, corresponding to curve E, the effect of free convection vanishes and a fully developed parabolic profile for Poiseuille flow is attained in all cases. At intermediate axial locations,

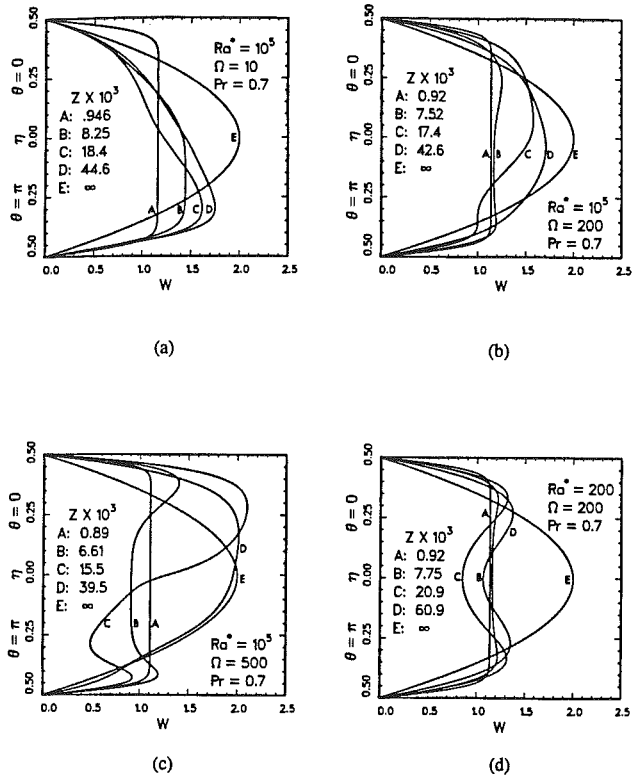


**Fig. 3 Development of axial velocity profiles for Pr = 0.7**

the curves are distorted due to buoyancy effects, and the nature of the distortion depends on the magnitude of Ra* and Ω. The development of $W$ profiles for Pr = 5 and Pr = 10 is qualitatively the same although the distortion due to buoyancy effects is less pronounced.

Figure 3($a$) shows the $W$ profiles for $Ra^* = 10^5$ and $\Omega = 10$. Returning to the definitions of Ra* and Ω (equations (12) and (13) and the arguments presented earlier for recovering the limiting case of a horizontal tube (expression (23)), it is seen that this combination of a large Ra* and a small value of Ω yields the case of a horizontal tube. Alternatively, if the momentum equations (15)–(17) are examined, it is observed that the buoyancy term in the axial momentum equation (equation (17)) becomes small. However, because Ra* is larger, the cross-stream buoyancy terms are important and the resulting equations are for a horizontal tube orientation. As depicted by the developing velocity profiles B, C, and D in Fig. 3($a$), the maximum velocity is displaced toward the bottom wall. This is typical of horizontal, heated tubes and the profiles in this figure show good qualitative agreement with those presented by Hishida et al. (1982) in their study of mixed convection in the entrance region of an isothermally heated horizontal tube.

Increasing the value of Ω while keeping Ra* fixed introduces an interesting buoyancy effect on the developing velocity profiles, as seen in Figs. 3($b$) and 3($c$). With finite values of Ω, the buoyancy term in the axial momentum equation (equation (17)) becomes significant and the $W$ profiles are affected by the cross-stream buoyancy as well as by the aiding buoyancy force in the main flow direction. The combination of Ra* and Ω values chosen in Figs. 3($b$) and 3($c$) is reasonable for a heated tube inclined at an angle $\gamma$ between 0 and $\pi/2$ radians. In contrast to Fig. 3($a$), the maximum velocity is now displaced toward the top tube wall; in the heated upflow the aiding buoyancy force pulls the hot fluid toward the top of the tube. The distortion of the $W$ profiles is very evident in Fig. 3($c$) for $Ra^* = 10^5$ and $\Omega = 500$. The flow accelerates near the heated tube wall, which results in profiles with maxima and minima behavior. The tendency toward flow reversal is in evidence, especially in curve C, which is at $Z = 1.55 \times 10^{-3}$, a location where the buoyancy effect and the secondary flow are most intense. Higher parameter values would lead to backflow in the axial direction.

The last subplot (Fig. 3$d$) presents developing $W$ profiles for a case in which $Ra^* = 200$ and $\Omega = 200$. Following the argument presented earlier in expression (24), this situation is that of a heated tube that is almost vertical. The only significant buoyancy term in the momentum equations (15)–(17) is the one in the axial direction momentum equation (17). Thus, the developing velocity profiles in Fig. 3($d$) show no influence of cross-stream buoyancy forces and the curves are symmetric about the central axis of the tube ($\eta = 0$). The curves show good qualitative agreement with the developing velocity profiles for a vertical isothermal tube as presented by Zeldin and Schmidt (1971). The curves have maxima near the tube wall and a minimum at the center of the tube, indicating that at sufficiently high heating rates, flow reversal may take place.

**Axial Variation of the Friction Factor and the Nusselt Number.** The results of the local pressure gradient in the entrance region of the inclined tube may be presented through the value of $f$ Re, where $f$ is a dimensionless friction factor given by

$$f = (-d\bar{p}/dz - \rho g \sin\gamma)/(1/2\rho_w w_{in}^2) \tag{27}$$

and Re is the tube Reynolds number given by equation (8). A direct effect of the buoyancy forces can be obtained from the values of $f\,\mathrm{Re}/(f\,\mathrm{Re})_0$ in which $(f\,\mathrm{Re})_0$ is the forced convection value of 64. Figures 4, 6, 8, and 10 illustrate the effect of Ra*, Ω, and Pr on the values of $f\,\mathrm{Re}/(f\,\mathrm{Re})_0$ at different axial locations. A quantity related to the dimensionless mean temperature, given by

$$1 - \phi_m = (T_m - T_{in})/(T_w - T_{in}) \tag{28}$$

is also plotted in each figure so that, if needed, $d\bar{p}/dz$ can be extracted from the values of $f$ at each axial location $Z$ by using equation (27). The mean temperature is evaluated as

$$T_m = \int\int Tr dr d\theta / (\int\int r dr d\theta) \tag{29}$$

The Nusselt number behavior is of importance because it is directly related to the heat transfer coefficient. The circumferentially averaged heat transfer coefficient and the corresponding Nusselt number are defined as

$$h = q/(T_w - T_b), \quad \mathrm{Nu} = hD/k \tag{30}$$

where $q$ is the circumferential average heat flux at the tube wall at an axial location $Z$ and $T_b$ is the bulk temperature at the cross section. It may be noted that the heat transfer coefficient $h$, and the Nusselt number Nu, in equation (30) are local quantities that are computed at each axial location. $T_b$ and its nondimensional equivalent $\phi_b$ are calculated from

$$T_b = \int\int wTr dr d\theta / (\int\int w r dr d\theta)$$

$$\phi_b = (T_b - T_w)/(T_{in} - T_w) \tag{31}$$

where the integrations are performed over a cross section of the tube at an axial location $Z$. The bulk temperature is a good indication of the thermal development because it represents the heat absorbed by the fluid until the axial location $Z$ where the bulk temperature is calculated. Figures 5, 7, 9, and 11 pre-

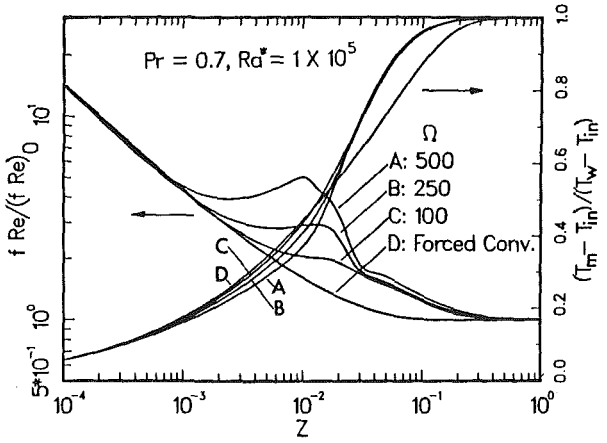


Fig. 4 Effect of Ω on $f$ Re and $(1-\phi_m)$ for Pr = 0.7, Ra* = $10^5$

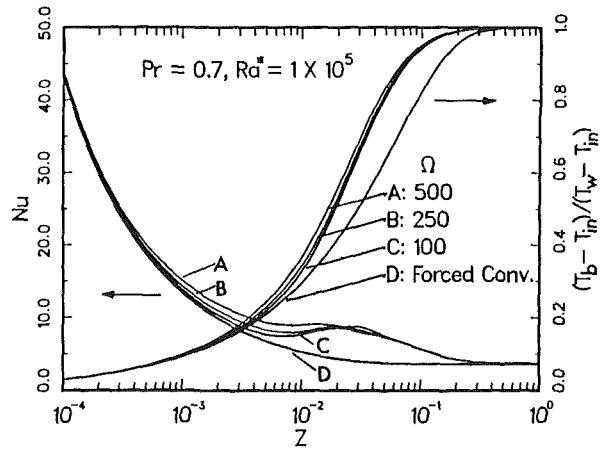


Fig. 5 Effect of Ω on Nu and $(1-\phi_b)$ for Pr = 0.7, Ra* = $10^5$

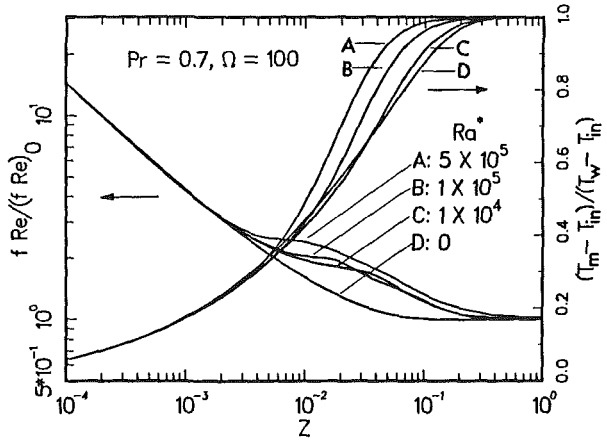


Fig. 6 Effect of Ra* on $f$ Re and $(1-\phi_m)$ for Pr = 0.7, Ω = 100

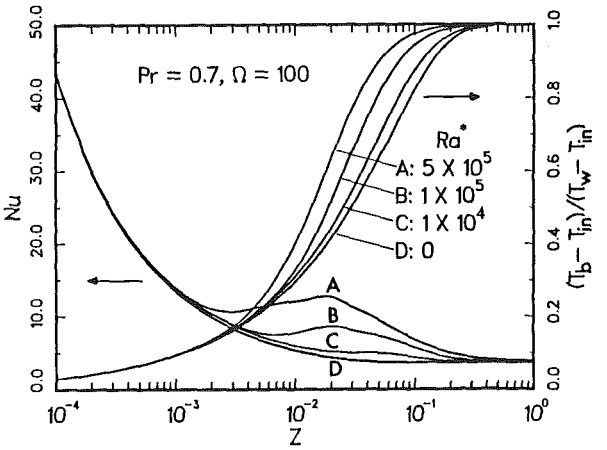


Fig. 7 Effect of Ra* on Nu and $(1-\phi_b)$ for Pr = 0.7, Ω = 100

sent the axial variation of Nu and the dimensionless quantity $(1-\phi_b) = (T_b - T_{in})/(T_w - T_{in})$ for different Ra*, Ω, and Pr parameter values.

The effect of increasing Ω on the $f$ Re and Nu at a fixed value of Ra* = $10^5$ and Pr = 0.7 is shown in Figs. 4 and 5, respectively. The pure forced convection curve, denoted by curve D in all the plots, has been obtained by setting Ra* and Ω to be equal to zero. Near the inlet, the free convection effects are insignificant and all the curves follow the forced convection curve. As the buoyancy effects become important (at about $Z = 10^{-3}$), the Nu and $f$ Re curves for mixed convection rise above the forced convection curve. The buoyancy effects are the most pronounced at the highest value of Ω since this parameter represents a ratio of free convection to forced convection effects. At Ω = 500, the maximum values of $f$ Re and Nu occur at approximately $Z = 10^{-2}$ and $Z = 1.5 \times 10^{-2}$, respectively, near the location where the secondary flow and the buoyancy effects are the strongest. The vigorous secondary flow results in an increase in the flow resistance and heat transfer. After attaining a maximum, the Nu and $f$ Re curves decrease asymptotically to the fully developed forced convection values of 3.658 and 64, respectively. It may be noted that for Ω = 500, the enhancement in heat transfer and flow resistance can be as much as 100 percent (heat transfer) and 225 percent (flow resistance). In Figs. 4 and 5, a comparison of the behavior of the mean bulk temperature curves leads to an interesting observation. With increasing values of Ω, the $T_b$ curves rise more rapidly with $Z$ as compared with the forced convection curve. The bulk temperature $T_b$ is a measure of the heat added to the fluid and since heat transfer coefficients are consistently higher for mixed convection, larger $T_b$ values are expected. In contrast, the mean temperature ($T_m$) curves for mixed convection are below the forced convection curve until about $Z = 2 \times 10^{-2}$, where they cross over. This tendency is more pronounced with increasing values of Ω and can be explained by the following argument. Near the entrance, the buoyancy forces tend to make the secondary flow rise along the heated wall and fall along the vertical center line. However, in pure forced convection, the secondary flow near the entrance is directed radially inward away from the tube wall. Consequently, at the same axial location close to the entrance of the duct, the fluid at the center is warmer for the forced convection case because of the thicker thermal boundary layer. Since the mean temperature $T_m$ is space averaged over the cross section, it is higher for forced convection compared to mixed convection. Farther downstream, however, the buoyancy effects lead to greater heat transfer and better mixing compared to forced convection and the $T_m$ for the mixed convection cases becomes greater.

Figures 6 and 7 represent the axial variation of $f$ Re and Nu for different modified Rayleigh numbers at Ω = 100 and Pr = 0.7. From the defining equations of Ra* and Ω (equations (12) and (13)) it is seen that holding Ω fixed while increasing Ra* is like decreasing the inclination angle $\gamma$ and simultaneously increasing the Rayleigh number Ra, at a fixed value of the Reynolds number Re. Alternatively, the same effect can be obtained at a fixed inclination angle $\gamma$ by increasing Ra and Re simultaneously such that the value of Ω remains the same. In any case, the effect of increasing Ra* at a fixed Ω is to

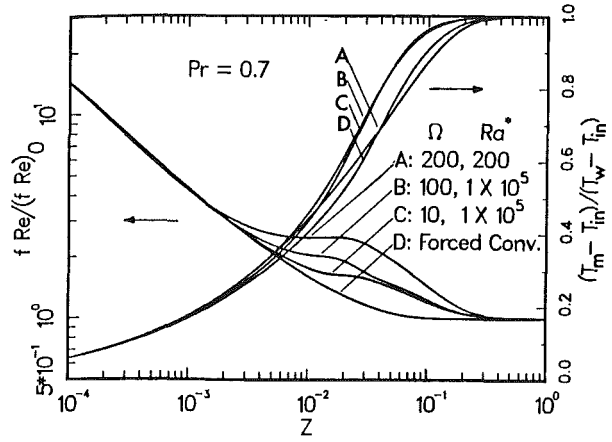


Fig. 8 Axial variation of $f$ Re and $(1-\phi_m)$ with Ra* and Ω for Pr = 0.7

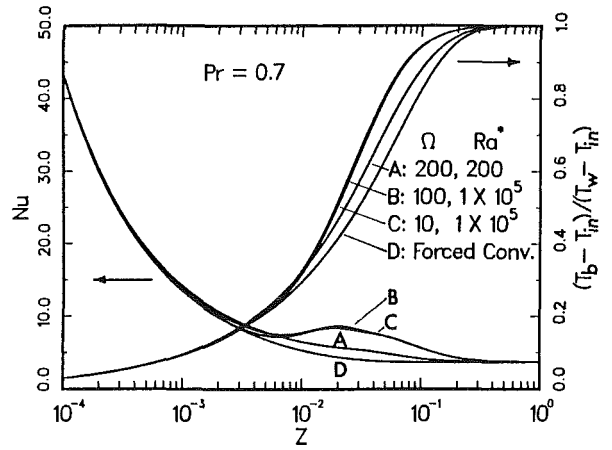


Fig. 9 Axial variation of Nu and $(1-\phi_b)$ with Ra* and Ω for Pr = 0.7

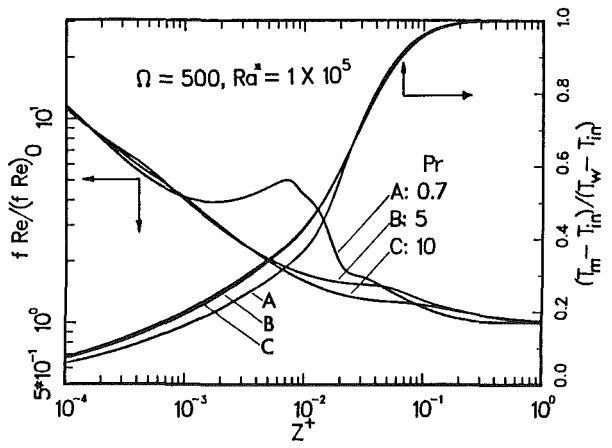


Fig. 10 Effect on Pr on $f$ Re and $(1-\phi_b)$ for Ra*$10^5$, Ω = 500

increase the buoyancy effect as seen in Figs. 6 and 7. At $Ra^* = 5\times10^5$, $Z = 2\times10^{-2}$ the enhancement in the Nusselt number is about 200 percent compared to the corresponding forced convection value. The increase in the $f$ Re value over the forced convection $f$ Re is only 55 percent at $Z = 10^{-2}$. The bulk temperature $T_b$ rises at a faster rate along the length of the tube as the value of Ra* is increased, indicating that the heat transfer performance improves. A similar behavior is observed for the $f$ Re curves.

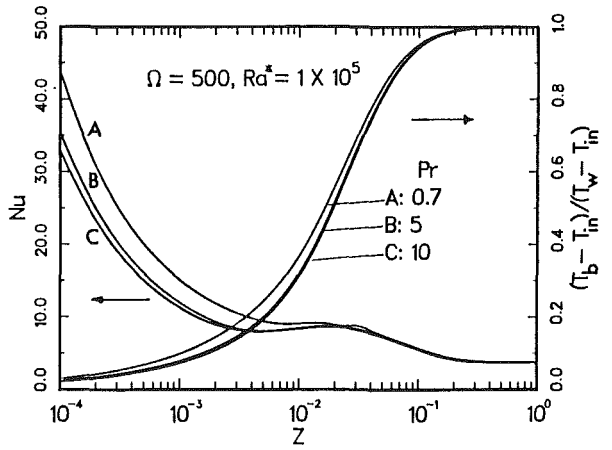


Fig. 11 Effect on Pr on Nu and $(1-\phi_b)$ for Ra*$10^5$, Ω = 500

In Figs. 8 and 9 the axial variation of $f$ Re and the Nusselt number is presented for three combinations of Ra* and Ω for Pr = 0.7. Curve A represents a choice of parameter values that yields a nearly vertical tube (Ra* = 200, Ω = 200). Curve C (Ra* = $10^5$, Ω = 10) is for a nearly horizontal tube. Curve B represents an intermediate case of a heated, inclined tube (Ra* = $10^5$, Ω = 100). The axial momentum equation buoyancy term is relatively large for the nearly vertical tube and this leads to higher friction factors compared to the other cases. The Nusselt number curves B and C are nearly coincident and in both cases the values of Nusselt number are significantly higher than those of the vertical tube (curve A). Evidently, the buoyancy-induced secondary flow in the horizontal and the inclined tube leads to a better enhancement in heat transfer when compared to the nearly vertical tube in which the secondary flow is insignificant. This observation is reinforced by the behavior of the bulk temperature curves in Fig. 9.

The Prandtl number effect is shown in Figs. 10 and 11 for Ra* = $10^5$ and Ω = 500. In Fig. 10, the $f$ Re/($f$ Re)$_0$ has been plotted against a dimensionless axial distance $Z^+$ defined as

$$Z^+ = z/(D\mathrm{Re}) \tag{32}$$

The quantity $(1-\phi_m) = (T_m - T_{in})/(T_w - T_{in})$, however, has been plotted against the usual dimensionless distance $Z$. The Prandtl number effect is nonexistent very near the entrance (where there are no buoyancy effects) and in the fully developed region where the buoyancy-induced secondary flow disappears. However, in the region where buoyancy is significant, the Pr = 0.7 curve is markedly different compared to the Pr = 5 and Pr = 10 curves. The diminished influence of buoyancy on $f$ Re for fluids of higher Prandtl number may be attributed to the dampening of the secondary flow velocities due to the higher viscosities of such fluids. When the Prandtl number is increased from 5 to 10, the behavior of the $f$ Re/($f$ Re)$_0$ curves is not altered drastically. In fact, for larger values of the Prandtl number, the friction factor variation would become identical with the force convection curve. Figure 11 depicts the influence of the Prandtl number on the Nusselt number and the bulk temperature variation in the entrance region. Near the entrance, the Nusselt number and the bulk temperature at a given $Z$ location is lower for the higher Prandtl number fluids. The effect of the Prandtl number is significant only for $Z$ values less than about 0.04. The curves for all Prandtl numbers attain the same fully developed forced convection value of the Nusselt number (3.658). The Nusselt number results show a diminishing influence of increasing the Prandtl number from 5 to 10. This indicates that an infinite Prandtl number assumption (an assumption that greatly simplifies the computational task) should be good for fluids

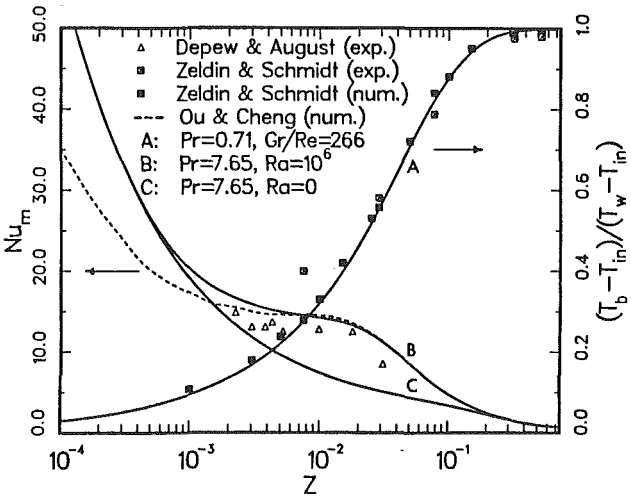


**Fig. 12 Comparison of $Nu_m$ and $T_b$ with experimental and numerical data**

with Prandtl numbers greater than 10. The bulk temperature curves exhibit the same trend as the Nusselt number curves.

**Comparison With Experimental and Numerical Results.** Since no experimental or numerical data for developing mixed convection in inclined circular tubes are available in the literature, comparisons have been made for the limiting cases of a vertical and a horizontal tube. Figure 12 presents a comparison of the calculated bulk temperature $(T_b - T_{in})/(T_w - T_{in})$ in a vertical tube with the experimental and numerical results of Zeldin and Schmidt (1971). For this case, the relevant parameter values are $Ra^* = 0$, $\Omega/Pr = Gr/Re = 266$, and $Pr = 0.71$. The agreement with the numerical results is excellent. The experimental data compare well except at $Z = 7.5 \times 10^{-3}$, where the discrepancy may be attributed to the fact that Zeldin and Schmidt (1971) noted problems with the preheating of the fluid. Also presented in Fig. 12 is the mean Nusselt number variation for a horizontal tube ($\Omega = 0$) with $Ra^* = Ra = 10^6$ and $Pr = 7.65$. The mean Nusselt number $Nu_m$ has been computed to permit easy comparison with the available data. $Nu_m$ is defined as

$$Nu_m = h_m D/k = mc_p \Delta T_m/(\pi kz) \tag{33}$$

where $\Delta T_m$ is the average temperature difference calculated as

$$\Delta T_m = [(T_{in} - T_w) + (T_b - T_w)]/2 \tag{34}$$

The calculated mean Nusselt numbers are compared to the numerical solution of Ou and Cheng (1977) and the experimental data of Depew and August (1971). It is noted that the numerical results of Ou and Cheng (1977) are for the Graetz problem with a large Prandtl number assumption for $Ra = 8 \times 10^5$. In their work, the velocity profile is assumed to be fully developed at the entrance. Consequently, a comparison with the present results shows that the $Nu_m$ values of Ou and Cheng (1977) for $Z$ less than $5 \times 10^{-3}$ are underpredicted. For larger values of $Z$, the agreement is very good. The experimental data of Depew and August (1971) are for a range of Rayleigh numbers ($Ra = 0.84 \sim 1.2 \times 10^6$) and for a fully developed velocity profile at the inlet of the tube. The calculated mean Nusselt numbers are somewhat higher than the experimental values but are within the range of experimental uncertainty. Although not presented here, the range of the data of Oliver (1962) ($Ra = 1.46 \sim 1.84 \times 10^6$, $Pr = 16.85$) and of Depew and Zenter (1969) ($Ra = 3.64 \times 10^5$, $Pr = 13.4$) brackets the values of $Nu_m$ predicted in the present work. A detailed comparison of the data for horizontal isothermal pipes has been made by Ou and Cheng (1977).

## Concluding Remarks

The equations governing the developing laminar mixed convection in the entrance region of an isothermal, inclined circular tube have been solved using a three-dimensional parabolic computational technique. The formulation presented in this work permits a study of the buoyancy and inclination angle effects without the need for a numerical solution for each inclination angle. The solutions have mainly been presented for an air flow of Prandtl number 0.7; however, the Prandtl number effect has been demonstrated.

The effect of the secondary flow and the aiding main flow direction buoyancy force has been found to be significant. The buoyancy effects increase with the axial direction until they reach a maximum and then decay as the fully developed situation is attained. The secondary flow distorts the axial velocity and temperature distributions and the nature of the distortion depends on the relative magnitudes of $Ra^*$ and $\Omega$. The circumferential average Nusselt number and the friction factor reach a local maximum at an axial location where the buoyancy effects are the most intense. Increases in the Nusselt number and the friction factor over the forced convection values may be as much as 200 and 225 percent, respectively.

The effect of the Prandtl number is diminished for Prandtl numbers greater than 10. Comparisons with numerical and experimental results for the vertical and horizontal tube orientations show reasonably good agreement for the mean Nusselt number and bulk temperature variations in the entrance region of the tube. The solutions presented here serve as useful data and provide insight into the complex interaction of fluid flow and heat transfer in the entrance region of inclined tubes.

## Acknowledgments

This research was partially supported by a grant from the Minnesota Supercomputer Institute.

## References

Abou-Ellail, M. M. M., and Morcos, S. M., 1980, "Combined Forced and Free Laminar Convection in the Entrance Region of Inclined Rectangular Channels," *Proceedings of the International Conference on Numerical Methods for Non-Linear Problems*, C. Taylor et al., eds., Pineridge Press, Swansea, United Kingdom, pp. 807–821.

Abdelmeguid, A. M., and Spalding, D. B., 1979, "Turbulent Flow and Heat Transfer in Pipes With Buoyancy Effects," *Journal of Fluid Mechanics*, Vol. 94, Part 2, pp. 383–400.

Cheng, K. C., and Hong, S. W., 1972a, "Effect of Tube Inclination on Laminar Convection in Uniformly Heated Tubes for Flat-Plate Solar Collectors," *Solar Energy*, Vol. 13, pp. 363–371.

Cheng, K. C., and Hong, S. W., 1972b, "Combined Free and Forced Laminar Convection in Inclined Tubes," *Applied Scientific Research*, Vol. 27, pp. 19–38.

Cheng, K. C., and Yuen, F. P., 1985, "Flow Visualization Studied on Secondary Flow Pattern for Mixed Convection in the Entrance Region of Isothermally Heated Inclined Pipes," *Fundamentals of Forced and Mixed Convection*, ASME HTD-Vol. 42, pp. 121–130.

Collins, M. W., 1980, "Finite Difference Analysis for Developing Laminar Flow in Circular Tubes Applied to Forced and Combined Convection," *International Journal of Numerical Methods in Engineering*, Vol. 15, pp. 381–404.

Depew, C. A., and August, S. E., 1971, "Heat Transfer Due to Combined Free and Forced Convection in a Horizontal and Isothermal Tube," ASME JOURNAL OF HEAT TRANSFER, Vol. 93, pp. 380–384.

Depew, C. A., and Zenter, R. C., 1969, "Laminar Flow Heat Transfer and Pressure Drop With Freezing at the Wall," *International Journal of Heat and Mass Transfer*, Vol. 12, pp. 1710–1714.

Hishida, M., Nagano, Y., and Montesclaros, M. S., 1982, "Combined Forced and Free Convection in the Entrance Region of an Isothermally Heated Horizontal Pipe," ASME JOURNAL OF HEAT TRANSFER, Vol. 104, pp. 153–159.

Hwang, G. J., and Sheu, J. P., 1974, "Effect of Radial Velocity Component on Laminar Forced Convection in Entrance Region of a Circular Tube," *International Journal of Heat and Mass Transfer*, Vol. 17, pp. 372–375.

Iqbal, M., and Stachiewicz, J. W., 1962, "Influence of Tube Orientation on Combined Free and Forced Laminar Convection Heat Transfer," ASME JOURNAL OF HEAT TRANSFER, Vol. 88, pp. 109–116.

Liu, J., 1974, "Flow of a Bingham Fluid in the Entrance Region of an Annular Tube," M.S. Thesis, University of Wisconsin—Milwaukee.

Morcos, S. M., and Abou-Ellail, M. M. M., 1983, "Buoyancy Effects in the Entrance Region of an Inclined Multirectangular-Channel Solar Collector," ASME *Journal of Solar Energy Engineering*, Vol. 105, pp. 157–162.

Oliver, D.R., 1962, "The Effect of Natural Convection on Viscous-Flow Heat Transfer in Horizontal Tubes," *Chemical Engineering Science*, Vol. 17, pp. 335–350.

Ou, J. W., Cheng, K. C., and Lin, R. C., 1976, "Combined Free and Forced Laminar Convection in Inclined Rectangular Channels," *International Journal of Heat and Mass Transfer*, Vol. 19, pp. 277–283.

Ou, J. W., and Cheng, K. C., 1977, "Natural Convection Effects on Graetz Problem in Horizontal Isothermal Tubes," *International Journal of Heat and Mass Transfer*, Vol. 20, pp. 953–960.

Patankar, S. V., 1980, *Numerical Heat Transfer and Fluid Flow*," McGraw-Hill, New York.

Patankar, S. V., and Spalding, D. B., 1972, "A Calculation Procedure for Heat, Mass and Momentum Transfer in Three-Dimensional Parabolic Flows," *International Journal of Heat and Mass Transfer*, Vol. 15, pp. 1784–1806.

Raithby, G. D., and Schneider, G. E., 1979, "Numerical Solution of Problems in Incompressible Fluid Flow: Treatment of the Velocity–Pressure Coupling," *Numerical Heat Transfer*, Vol. 2, pp. 417–440.

Sabbagh, J. A., Aziz, A., El-Ariny, A. S., and Hamad, G., 1976, "Combined Free and Forced Convection in Inclined Circular Tubes," ASME JOURNAL OF HEAT TRANSFER, Vol. 98, pp. 322–324.

Shah, R. K., and London, A. L., 1978, *Laminar Forced Convection in Ducts*," Academic Press, New York.

Yousef, W. W., and Tarasuk, J. D., 1982, "Free Convection Effects on Laminar Forced Convective Heat Transfer in a Horizontal Isothermal Tube," ASME JOURNAL OF HEAT TRANSFER, Vol. 104, pp. 145–152.

Zeldin, B., and Schmidt, F. W., 1971, "Developing Flow With Combined, Forced-Free Convection in an Isothermal Vertical Tube," *ASME–AIChE Heat Transfer Conference*, Paper No. 71-HT-6.

# Flows in Vertical Channels With Asymmetric Wall Temperatures and Including Situations Where Reverse Flows Occur

**D. B. Ingham**

**D. J. Keen**

Department of Applied Mathematical Studies,
University of Leeds,
Leeds, United Kingdom

**P. J. Heggs**

Schools of Chemical Engineering,
Unviersity of Bradford,
Bradford, United Kingdom

*Numerical investigations are conducted into steady laminar combined convection flows in vertical parallel plate ducts with asymmetric constant wall temperature boundary conditions. The streamwise diffusion terms in the governing equations are neglected and the resulting parabolic equations are expressed in an implicit finite difference scheme and solved using a marching technique. In certain situations the combination of the size of the ratio |Gr/Re| and the difference in temperature between the walls of the duct is such that the fully developed flow profile, as the streamwise coordinate tends toward infinity, includes reverse flow in the vicinity of the cold wall. Techniques first used in a previous study are employed in finding a solution through the whole domain of the fluid for those situations involving reverse flow in the fully developed region. Comparisons with existing data near the duct entrance and far along the duct show very good agreement.*

## 1 Introduction

The problem of obtaining numerical solutions for combined convection flows in vertical parallel plate ducts with asymmetric wall temperature boundary conditions has received increasing attention recently because of its relevance to, for example, the modeling of the cooling processes in modern electronic devices in which vertically mounted circuit cards are positioned in such a way as to form vertical channels (Aung et al., 1973; Aung, 1973; Aung and Worku, 1986a). During their operation the temperature of these electronic devices must be carefully controlled in order to maintain good performance and reliability. In many situations cooling is carried out using only natural convection (Aung et al., 1973; Aung, 1973), however more recently higher density packaging has meant that in some devices it is necessary to cool using forced flow, but even in these situations natural convection can still be very significant (Aung and Worku, 1986a, 1986b).

Combined convection flows are often modeled by neglecting the streamwise diffusion terms in the momentum and energy equations. The relevance of the streamwise diffusion terms is, in general, dependent upon the magnitude of the Reynolds and Peclet numbers. In situations where the Reynolds and Peclet numbers are relatively large, Re, $\mathrm{Pe} \gg 1$, it can be seen using a suitable nondimensionalization that the transverse diffusion terms in the governing momentum and energy equations, respectively, are far more important than the streamwise diffusion terms. In this study the streamwise diffusion terms are assumed to be negligible and the problem reduces to solving the boundary layer equations. These equations are parabolic in nature and are solved using finite difference methods and a marching technique. This method requires the specification of boundary conditions at the entrance of the channel and then the solution can be calculated up to a point where either the flow becomes fully developed or reverse flow is first detected. The governing equations of these types of flow can be nondimensionalized in such a way that the solution is only dependent upon three nondimensional quantities, namely the Prandtl number Pr, the ratio of the Grashof number to the Reynolds number Gr/Re, and $\theta_R = (T_{WL} - T_{WR})/(T_e - T_{WR})$, where $T_e$ is the entry temperature of the fluid, $T_{WR}$, and $T_{WL}$ are the temperatures of the walls, and $T_{WR} \geq T_{WL} \geq T_e$ or $T_{WR} \leq T_{WL} \geq T_e$ depending upon whether Gr/Re is less than or greater than zero, respectively. In certain circumstances the ratio |Gr/Re| can become sufficiently large to produce a flow reversal at some point in the flow. In these situations a marching solution procedure may diverge because the flow in the reverse flow region is in the opposite direction to the direction of the marching, and hence information vital to the upstream solution is ignored. The flow reversals occur either near the center of the duct or adjacent to the cold wall or in both positions. In this paper emphasis is placed on situations where the flow reversals are adjacent to the cold wall. Flow reversals near the center of the duct were dealt with by Ingham et al. (1987) for the case of symmetrically heated ducts and they may be treated in a similar manner for the asymmetric heating situation. This is however beyond the scope of the present investigation. Aung and Worku (1986a, 1986b) in their recent papers discuss the problems encountered with flow reversal and they indicate the need for more work to be performed in this area. In particular they consider situations where flow reversal is present in the fully developed flow region and they predict asymptotic solutions in the fully developed region by assuming parallel flow and a constant pressure gradient along the duct. Although they were able to compute solutions up to the first point of reverse flow, they were not able in general to march from this point through to the fully developed flow region.

In this paper the problem, as considered by Aung and Worku (1986a), is formulated in terms of a nondimensional stream function, vorticity, and temperature. The solution procedure used is of a marching type, although the direction of the marching may be varied, and the governing nondimensional parameters are Pr, Gr/Re, and $\theta_R$ as above. In situations where no flow reversal is present the governing implicit finite difference equations are solved by marching from the entry of the duct into the region of fully developed flow. In situations where |Gr/Re| is sufficiently large to cause flow separation at the cold wall an approximation similar to the FLARE approximation, used by Reyner and Flügge-Lotz (1968) and Cebeci et al. (1982), is introduced in order to allow the marching to be continued into the fully developed flow

Contributed by the Heat Transfer Division for publication in the JOURNAL OF HEAT TRANSFER. Manuscript received by the Heat Transfer Division June 30, 1987. Keywords: Flow Separation, Mixed Convection, Numerical Methods.

region. The solution thus obtained can be iterated upon using a method similar to that employed by Williams (1975). The techniques used in this paper are the same as those used by Ingham et al. (1987) for the solution of the boundary layer equations in a parallel plate duct with symmetric wall temperature boundary conditions.

Complete solutions have been obtained for developing flows in which flow separation is present. The results achieved using this new numerical technique are in full agreement with those obtained by Aung and Worku (1986a, 1986b) both near the entry of the duct and in the fully developed region.

There is in the types of flow considered in this paper the possibility of instabilities occurring in both the developing and fully developed regions of the flow. A stability analysis of a related problem is considered by Yao (1987) and regions of both stable and unstable flow are identified. An experimental investigation is carried out by Morton et al. (1987) into another related problem and photographs of stable configurations are displayed for developing recirculating flows. A stability analysis is however beyond the scope of the present paper.

## 2 Model and Governing Equations

Steady laminar combined convection of a fluid with velocity $(u, v)$ between two vertical parallel plates in the semi-infinite domain $-a \le x \le a$, $0 \le y < \infty$ as illustrated in Fig. 1 is the situation under consideration. In the model, fluid at constant temperature $T = T_e$ is assumed to flow from the semi-infinite domain $-\infty < x < \infty$, $-\infty < y < 0$ into a parallel plate duct in such a way that the velocity at $y = 0$, $-a \le x \le a$, $(0, v_e)$, is constant and upward in the $y$ direction. The walls of the duct are at constant temperatures, $T_{WR}$ and $T_{WL}$, where $T_{WR} \ge T_{WL} \ge T_e$ or $T_e \ge T_{WL} \ge T_{WR}$ but in general $T_{WR}$ is not equal to $T_e$ so that the effects of natural convection on the system are significant. The acceleration due to gravity, $g$, acts vertically downward in the opposite direction to the forced convection. The fluid is considered to be Newtonian with constant dynamic viscosity, thermal conductivity, specific heat capacity, and coefficient of expansion. Density variations are assumed to be negligible except in the buoyancy term of the vertical momentum equation (Boussinesq approximation). The above assumptions are made in order to keep the model as simple as possible, although inclusion of variations in some of the physical properties should not in theory be difficult to introduce into the numerical analysis. Viscous dissipation is ignored in the energy equation as it was shown to have only a small effect (Collins, 1975).

The governing equations are the continuity, transverse momentum, streamwise momentum, and energy equations and these can be reduced using the same theory and notation as used by Ingham et al. (1987) to the following nondimensional form:

$$\Omega = \frac{\partial^2 \psi}{\partial X^2} \tag{1}$$

$$\frac{\partial \psi}{\partial X}\frac{\partial \Omega}{\partial Y} - \frac{\partial \psi}{\partial Y}\frac{\partial \Omega}{\partial X} = \frac{\partial^2 \Omega}{\partial X^2} + \frac{\mathrm{Gr}}{\mathrm{Re}}\frac{\partial \theta}{\partial X} \tag{2}$$

$$\frac{\partial \psi}{\partial X}\frac{\partial \theta}{\partial Y} - \frac{\partial \psi}{\partial Y}\frac{\partial \theta}{\partial X} = \frac{1}{\mathrm{Pr}}\frac{\partial^2 \theta}{\partial X^2} \tag{3}$$

where $\mathrm{Re} = a u_m / \nu$ is the Reynolds number, $a$ the half-width of the duct, $u_m$ a characteristic velocity taken in this study to be the mean velocity, $\nu$ the kinematic viscosity, $\mathrm{Pr} = \nu/\alpha$ the Prandtl number, $\alpha$ the molecular thermal diffusivity of the fluid, $\mathrm{Gr} = g\beta(T_e - T_{WR})a^3/\nu^2$ the Grashof number, $\beta = (-1/\rho)/(\partial\rho/\partial T)$ the coefficient of expansion with respect to $T$, and $\rho$ the density of the fluid. The coordinates $(X, Y)$ are nondimensional and are defined by $a(X, \mathrm{Re}\,Y) = (x, y)$ and $\psi$, $\Omega$, and $\theta$ are the nondimensional stream function, vorticity, and temperature, respectively; these are defined as follows:

$$U = -\frac{1}{\mathrm{Re}}\frac{\partial \psi}{\partial Y}, \quad V = \frac{\partial \psi}{\partial X} \tag{4}$$

$$\Omega = \frac{\partial V}{\partial X} - \frac{1}{\mathrm{Re}}\frac{\partial U}{\partial Y} \tag{5}$$

$$\theta = (T - T_{WR})/(T_e - T_{WR}) \tag{6}$$

where $(U, V)$ are the nondimensional velocities defined by $u_m(U, V) = (u, v)$. The streamwise diffusion terms, which are

## Nomenclature

$a$ = half-width of the duct
$A_c$ = flow cross-sectional area
$f$ = friction factor
$g$ = acceleration due to gravity
Gr = Grashof number $= g\beta(T_e - T_{WR})a^3/\nu^2$
$h$ = local heat transfer coefficient
$H$ = finite difference step size across the duct
$k$ = thermal conductivity of the fluid
$K$ = finite difference step size along the duct
$N$ = number of finite difference steps across the duct
$NN$ = number of finite difference steps along the duct
Nu = Nusselt number $= ha/k$
Pe = Peclet number = RePr
Pr = Prandtl number $= \nu/\alpha$
Re = Reynolds number $= au_m/\nu$
$T$ = temperature
$u$ = transverse velocity
$U$ = dimensionless transverse velocity $= u/u_m$
$u_m$ = mean velocity
$v$ = streamwise velocity
$V$ = dimensionless streamwise velocity $= v/u_m$
$x$ = transverse coordinate
$X$ = dimensionless transverse coordinate $= x/a$
$y$ = streamwise coordinate
$Y$ = dimensionless streamwise coordinate $= y/a\mathrm{Re}$
$\alpha$ = molecular thermal diffusivity
$\beta$ = coefficient of thermal expansion $= (-1/\rho)(\partial\rho/\partial T)$
$\delta$ = average change for the step doubling test
$\epsilon$ = small parameter
$\theta$ = dimensionless temperature $= (T - T_{WR})/(T_e - T_{WR})$
$\theta_R$ = value of $\theta$ on wall at $X = -1 = (T_{WL} - T_{WR})/(T_e - T_{WR})$
$\nu$ = kinematic viscosity
$\rho$ = density
$\psi$ = dimensionless stream function
$\Omega$ = dimensionless vorticity

**Subscripts**

$e$ = entry value
$i$ = transverse finite difference suffix
$j$ = streamwise finite difference suffix
$m$ = flow average value
$WL$ = value at the inside of the wall at $X = -1$
$WR$ = value at the inside of the wall at $X = 1$
$\infty$ = value in the fully developed region of the duct

**Superscripts**

$*$ = value calculated at $X = -1$

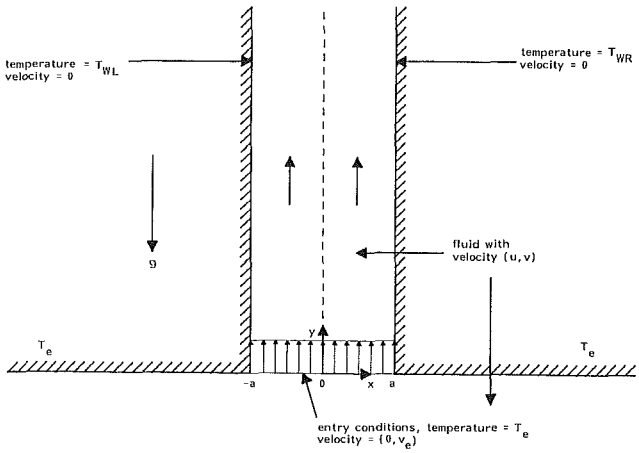


**Fig. 1 Schematic view of the mathematical model and the solution domain**

of order $1/\mathrm{Re}^2$, have been neglected in the above reduction.

The nondimensional boundary conditions for this problem are as follows:

$$\text{At } X=-1, \quad 0\le Y<\infty: \quad \psi=-1, \quad \frac{\partial\psi}{\partial X}=0, \quad \theta=\theta_R \tag{7}$$

$$\text{At } X=1, \quad 0\le Y<\infty: \quad \psi=1, \quad \frac{\partial\psi}{\partial X}=0, \quad \theta=0 \tag{8}$$

$$\text{At } Y=0, \quad -1\le X\le 1: \quad \psi=X, \quad \Omega=0, \quad \theta=1 \tag{9}$$

where $\theta_R$ is equal to $(T_{WL}-T_{WR})/(T_e-T_{WR})$. Equations (1)–(3) are parabolic in nature and hence no boundary condition as $Y\to\infty$ is needed in order to solve them. Equations (1)–(3) give the desired description of the flow under consideration and they are solved subject to the boundary conditions given by equations (7)–(9).

## 3 Solution Technique

The solution to the problem is obtained by expressing the governing equations (1)–(3) in finite difference form and solving them using a marching procedure subject to the boundary conditions (7)–(9). The finite difference scheme used is as used by Ingham et al. (1987), a fully implicit scheme with backward differences being used in the streamwise direction and central differences in the transverse direction. The compatible finite difference forms of equations (1)–(3) are (Ingham et al., 1987)

$$\Omega_{i,j+1}=\frac{1}{H^2}(\psi_{i+1,j+1}-2\psi_{i,j+1}+\psi_{i-1,j+1}) \tag{10}$$

$$\frac{1}{2HK}\{(\psi_{i+1,j+1}-\psi_{i-1,j+1})(\Omega_{i,j+1}-\Omega_{i,j}) - (\psi_{i,j+1}-\psi_{i,j})(\Omega_{i+1,j+1}-\Omega_{i-1,j+1})\} = \frac{1}{H^2}(\Omega_{i+1,j+1}-2\Omega_{i,j+1}+\Omega_{i-1,j+1}) + \frac{\mathrm{Gr}}{2\mathrm{Re}H}(\theta_{i+1,j+1}-\theta_{i-1,j+1}) \tag{11}$$

$$\frac{1}{2HK}\{(\psi_{i+1,j+1}-\psi_{i-1,j+1})(\theta_{i,j+1}-\theta_{i,j}) - (\psi_{i,j+1}-\psi_{i,j})(\theta_{i+1,j+1}-\theta_{i-1,j+1})\} = \frac{1}{\mathrm{Pr}H^2}(\theta_{i+1,j+1}-2\theta_{i,j+1}+\theta_{i-1,j+1}) \tag{12}$$

The suffices $(i, j)$ refer to the point at $X=(i-1)H$ on the $j$th streamwise location, $H$ and $K$ are the step sizes in the $X$ and $Y$ directions, respectively, and $H=1/N$, where $N$ is the number of steps used across the duct. The solution technique is such that the step size in the streamwise direction can be doubled at selected axial locations if loss of accuracy in doing so is seen to be negligible. The number of steps taken in the axial direction $NN$ is chosen in such a way as to allow the marching to proceed right through to the region of fully developed flow. The above scheme allows information to be calculated at consecutive streamwise locations by starting at the duct entrance and marching in the same direction as the flow. The boundary conditions, equations (7)–(9), are treated in a similar way to the paper by Ingham et al. (1987), the vorticity on the boundaries being determined to second-order accuracy using Taylor series expansions of $\Omega$ and $\psi$ on $X=1$ and $X=-1$, using the fact that $\partial\psi/\partial X=0$ at $X=\pm 1$ and equation (1) evaluated at $X=\pm 1$. This leads to

$$\Omega_{1,j+1}=\frac{3}{H^2}(1+\psi_{2,j+1})-\frac{1}{2}\Omega_{2,j+1} \tag{13}$$

$$\Omega_{N+1,j+1}=-\frac{3}{H^2}(1-\psi_{N,j+1})-\frac{1}{2}\Omega_{N,j+1} \tag{14}$$

Equations (10)–(14) represent $3N-1$ equations in $3N-1$ unknowns and hence provide sufficient information to solve the problem at streamwise step $j+1$ given the solution at step $j$.

As they stand, equations (11) and (12) include nonlinear terms, so in order to be able to apply Gaussian elimination to the whole system it is necessary to replace terms such as $(\psi_{i+1,j+1}-\psi_{i-1,j+1})$ by $(\psi_{i+1,j}-\psi_{i-1,j})$ in order to linearize the system. This does not affect the compatibility of any of the equations, although the accuracy of the solution may suffer slightly. It is thus possible using Gaussian elimination to solve the problem at streamwise location $j+1$ using information from streamwise location $j$ and hence to march along the duct computing solutions until the fully developed region is reached.

In flows where hydrodynamic and thermal development are relatively slow, many streamwise steps may have to be taken to march through to the fully developed region. Due to limitations in both computing time and storage space there is therefore a need occasionally to double the streamwise step size; this is carried out in the following way. Consider the marching procedure to be at the stage where the solution has just been computed at streamwise locations $j+1$ and $j$ using a step size $K$ and information from locations $j$ and $j-1$, respectively. The streamwise step size is now doubled if doing so does not greatly affect the accuracy of the solution. The loss of accuracy is determined by calculating the solution at streamwise location $j+1$ using the solution from location $j-1$ and a step size of $2K$ and then calculating the quantity $\delta$ given by

$$\delta=\frac{1}{3N-1}\sum_i\{\,|\psi^K_{i,j+1}-\psi^{2K}_{i,j+1}|+|\Omega^K_{i,j+1}-\Omega^{2K}_{i,j+1}| + |\theta^K_{i,j+1}-\theta^{2K}_{i,j+1}|\,\} \tag{15}$$

where the superscripts refer to the step size used in the calculation of the finite difference variables. If $\delta<\epsilon$, where $\epsilon$ is usually taken to be about $10^{-3}$, the streamwise step size is increased to $2K$ and the calculation at $j+2$ started. For convenience in programming this test is only carried out at most at every second step, although in practice it is only carried out every four or five steps.

In situations where $\theta_R$ is relatively close to 1 or $|\mathrm{Gr}/\mathrm{Re}|$ is large or for certain other combinations of $\theta_R$ and $|\mathrm{Gr}/\mathrm{Re}|$ flow separation from the colder wall may take place. In many situations the flow never rejoins the cold wall and reverse flow

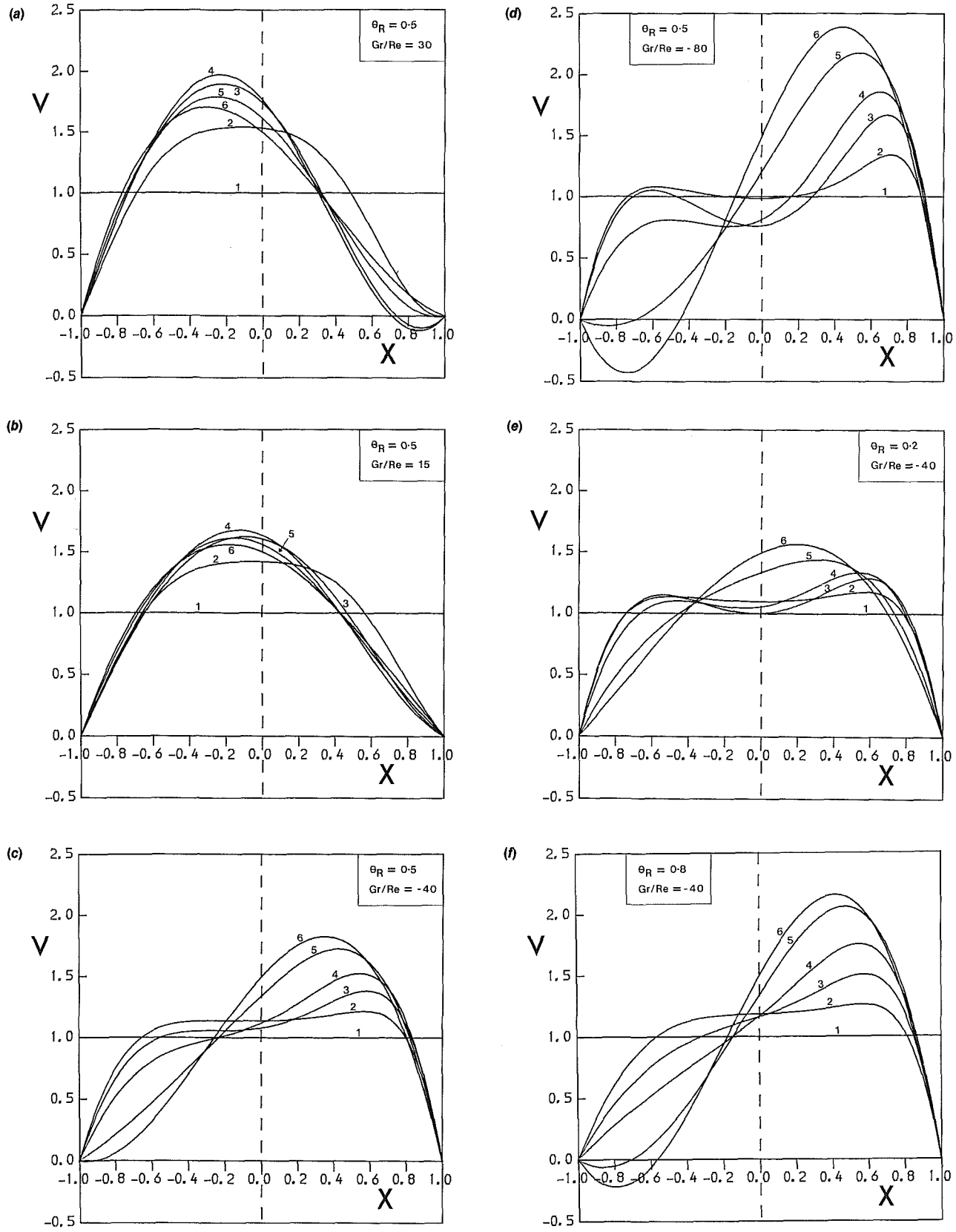


Fig. 2

is present in the fully developed flow profile. In general when reverse flow occurs the numerical solution procedure becomes unstable because information is traveling in the direction opposite to the direction of the marching. When the reverse flow is very weak it is often possible to march through to the fully developed flow region without the solution procedure becoming unstable; however this is the exception rather than the rule and when the reverse flow is reasonably strong problems are encountered with the solution technique. These problems are overcome by first constructing an approximate solution throughout the region of reverse flow and then iterating upon this approximation using techniques very similar to those

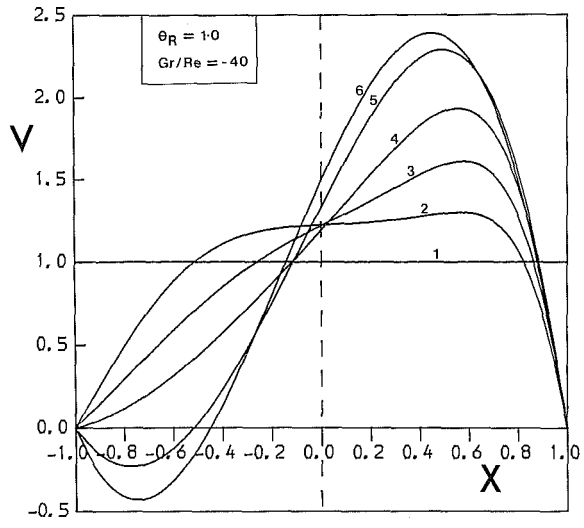


**Fig. 2 Streamwise velocity profiles for the indicated values of Gr/Re and $\theta_R$ at $Y=0$ (1), 0.048 (2), 0.12 (3), 0.232 (4), 0.648 (5), and $\infty$ (6)**

employed by Ingham et al. (1987). In the paper of Ingham et al. (1987) an approximation is calculated in the reverse flow region by modifying the $\psi$ profile at a particular streamwise location $j$, in such a way as to make it monotonic increasing, $\psi_{i+1,j} \geq \psi_{i,j}$, $i=1, N$, so that no negative streamwise velocities can be present for the calculation at streamwise step $j+1$. After the calculation at streamwise step $j+1$ the old $\psi$ profile is replaced at step $j$. Using the above technique an approximate solution to the finite difference equations can generally be obtained in situations where reverse flow is present. An iteration is then carried out by marching backwards and calculating a new approximation in the reverse flow region only, where forward differences must be used in the streamwise direction in order to maintain stability, and then marching forward and calculating a new approximation in the forward flow region only. Boundary condition points are taken to be the first point in the forward flow region for the backward sweep and the first point in the reverse flow region for the forward sweep. At the boundary condition points $\psi$, $\Omega$, and $\theta$ are assumed to be constant and are put equal to their values calculated during the previous forward or backward sweep, respectively. After each iteration a test for convergence is carried out; when the convergence criterion is satisfied the iteration procedure is terminated and marching is continued beyond the region of the duct containing the region of reverse flow until a point is reached where the flow profile is fully developed. The only difference in this paper is the fact that in many of the situations considered reverse flow is present in the fully developed flow profile so whereas in the paper by Ingham et al. (1987) the approximation marching sweep is stopped a few steps beyond the last point at which reverse flow is detected, here the marching must be continued well into the fully developed flow region. The iteration procedure is then carried out in the same manner as before, but when convergence is achieved the solution is complete and no further marching is necessary. This iterative scheme allows the reverse flow region to change its shape gradually because the upstream sweep modifies the boundary condition for the downstream sweep and the downstream sweep modifies the boundary condition for the upstream sweep. This technique clearly only allows a very slow change in the position of the dividing streamline but this is exactly what is required in order to maintain stability.

## 4 Results

The results presented in this paper are calculated on a finite difference grid consisting of 40 uniform steps across the width of the duct and up to 160 steps of nonuniform length along the duct. A comparison between a particular set of these results and the corresponding results computed on a grid involving 80 transverse steps would suggest that the results obtained for the stream function when 40 transverse steps are used are correct to within $2\times10^{-2}$ near the leading edges of the duct and to within $2\times10^{-3}$ elsewhere. The initial streamwise step length used in the calculations is $10^{-3}$. Problems are encountered in reducing this step size below $5\times10^{-4}$ and these problems can only be overcome by increasing the number of finite difference steps across the width of the duct.

The situations investigated in this paper involve cases where the free convection aids the forced convection, for example heating of the fluid in upflow, and where the free convection opposes the forced convection, for example cooling of the fluid in upflow. The Prandtl number Pr is chosen to be 0.72 as this value is characteristic of many common gases, in particular, air. In general the value of $\theta_R$ is chosen to be nonzero although a few calculations carried out with $\theta_R=0$, including one in the forced convection limit, were found to agree with the results for the stream function of Ingham et al. (1987) to within $2\times10^{-5}$ at every point on the finite difference grid. Further comparisons were made in the forced convection limit, Gr/Re = 0, with the results of Aung and Worku (1986a) and the two sets of solutions were found to be graphically indistinguishable.

The results obtained in situations where reverse flow is present in the fully developed flow region can be compared with the exact solution in the fully developed flow region, as determined by Aung and Worku (1986b). This exact solution can be expressed, in the slightly different notation used in this paper, as follows:

$$\theta=\frac{\theta_R}{2}(1-X) \tag{16}$$

$$V=\theta_R\frac{\mathrm{Gr}}{\mathrm{Re}}\frac{X}{12}(X^2-1)+\frac{3}{2}(1-X^2) \tag{17}$$

It can be deduced from equation (17) that for a given value of $\theta_R$ reverse flow is present in the fully developed flow profile if

$$\left|\frac{\mathrm{Gr}}{\mathrm{Re}}\right|>\frac{18}{\theta_R} \tag{18}$$

so the sign of Gr/Re is not important when determining whether or not a flow reversal is present.

The results are presented in such a way as to allow the behavior of the solution to be studied as one of the governing parameters, $\theta_R$ or Gr/Re, is varied while the other is held constant. Firstly consider $\theta_R$ to be fixed at 0.5 so that the wall at $X=-1$ is at a temperature exactly halfway between the temperature of the wall at $X=1$ and the entry temperature of the fluid. Figures 2(*a-d*) illustrate velocity profiles for the situations where Gr/Re = 30, 15, −40, and −80, respectively, where the first two values correspond to cases where the free convection opposes the forced convection and the last two values correspond to cases where the free convection aids the forced convection. In each diagram the streamwise velocity distributions corresponding to the streamwise distances $Y=0$, 0.048, 0.12, 0.232, 0.648, and $\infty$ are displayed and they are numbered in such a way that 1 corresponds to $Y=0$, 2 to $Y=0.048$, etc. The general characteristics of these types of flow are a reduction in the streamwise velocity of the fluid, with respect to the entry velocity, near the colder of the two walls and a peak in the velocity profile in the half of the duct adjacent to the hotter wall at any particular streamwise location. It is found from the numerical results that an increasing positive value of Gr/Re leads to separated flow from the cold

wall, which, because these situations correspond to cooling in upflow, is the wall at $X=1$. This trend is illustrated in Figs. 2($a$) and 2($b$). When Gr/Re = 30 the flow rejoins the wall at around $Y=0.88$; however this is not always the case and for larger values of Gr/Re there may be reverse flow present in the fully developed flow profile. Figures 2($c$) and 2($d$) give an illustration of the fact that for decreasing negative Gr/Re reverse flow again appears at the cold wall, which in these situations corresponding to heating in upflow is at $X=-1$. In both of these cases reverse flow is present in the fully developed velocity profile, as would be expected from equation (18), although it is quite clearly very much more significant for Gr/Re = −80 than for Gr/Re = −40.

Now consider the value of Gr/Re to be fixed at −40 in order to investigate the effects of varying $\theta_R$ on the mathematical model. Streamwise velocity distributions corresponding to values of $\theta_R$ of 0.2, 0.5, 0.8, and 1.0 are displayed in Figs. 2($e$), 2($c$), 2($f$), and 2($g$), respectively. The numbers on the plots correspond to the same values of $Y$ as before. In all four situations the colder wall is at $X=-1$ and hence the peak in streamwise velocity is between $X=0$ and $X=1$. It is interesting to notice that for $Y<0.048$ the differences in the velocity profiles in Figs. 2($a$) to 2($g$) are relatively small in comparison with the differences further along the duct. Figures 2($c$), 2($f$), and 2($g$) all show reverse flow in the fully developed flow profile as would be expected from equation (18) and a second-order extrapolation between solutions calculated for $\theta_R=0.5$ with 20 and 40 finite difference steps across the width of the duct shows an agreement with the exact solution in the fully developed flow region, as given by equation (17), to within $10^{-3}$ at every transverse location.

In order to examine the effects of the above flows on the temperature distributions, contour plots of temperature and flow average temperature distributions were considered. It was found that the presence of reverse flow does not produce any significant change in the temperature contours. For this reason and for ease of comparison between different situations only the flow average temperature distributions are presented in this paper. The flow average or mixing cup temperature at any particular streamwise location can be expressed as follows (Shah and London, 1978):

$$T_m=\frac{1}{A_c u_m}\int_{A_c} vTdA_c \tag{19}$$

where $A_c$ is the flow cross-sectional area. For the situation under consideration equation (19) can be reduced to

$$\theta_m=\frac{1}{2}\int_{-1}^{1}\frac{\partial\psi}{\partial X}\,\theta dX \tag{20}$$

$\theta_m$ is evaluated using Simpson's rule and its value is plotted against $Y$ in Figs. 3($a$) and 3($b$) for all the situations considered previously. $\theta_R$ is fixed at 0.5 in Fig. 3($a$) where $\theta_m$ is also plotted for the case of pure forced convection, Gr/Re = 0, and Gr/Re is fixed at −40 in Fig. 3($b$) where $\theta_m$ is also plotted for the symmetric case, $\theta_R=0$. From Fig. 3($a$) it can be seen that $\theta_m$ decreases more rapidly when Gr/Re is large and negative and this implies that heat transfer takes place more efficiently when the free convection aids the forced convection. It can also be seen from Fig. 3($a$) that when the free convection opposes the forced convection the heat transfer is inhibited when compared to pure forced convection, as would be expected. The fully developed values of $\theta_m$ are different for each of the situations illustrated in Fig. 3($a$) because they are dependent upon the fully developed velocity profiles, which were seen to be considerably different earlier. In Fig. 3($b$) $\theta_m$ is seen to decrease with $\theta_R$ at every streamwise location, as would be expected. The temperature in the fully developed

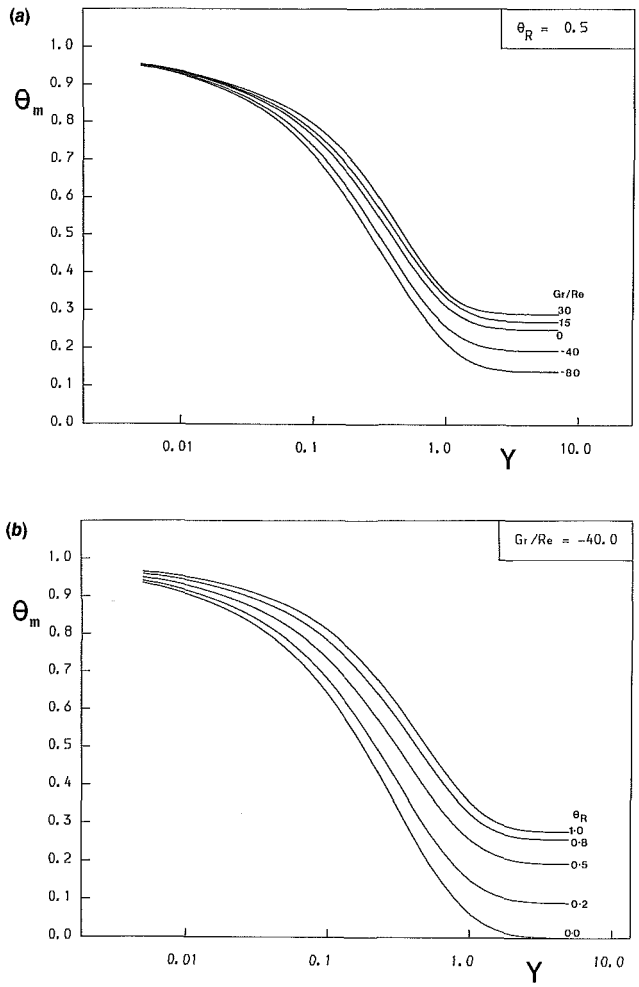


**Fig. 3 Dimensionless mean temperature distributions for (*a*) $\theta_R=0.5$, (*b*) Gr/Re = −40**

region of the duct can be deduced exactly from equations (16) and (17) to be the following:

$$\theta_{m,\infty}=\frac{\theta_R}{2}+\frac{\theta_R^2}{180}\,\frac{\mathrm{Gr}}{\mathrm{Re}} \tag{21}$$

Each of the plots in Figs. 3($a$) and 3($b$) was found to be in agreement with equation (21) to within $5\times10^{-3}$ for large $Y$.

A simple heat balance at the wall of the duct at $X=1$ leads to the following expression:

$$h(T_m-T|_{X=1})=-\frac{k}{a}\,\frac{\partial T}{\partial X}\bigg|_{X=1} \tag{22}$$

where $h$ is the local heat transfer coefficient between the fluid and the wall and $k$ is the thermal conductivity of the fluid. Defining the Nusselt number Nu to be equal to $ha/k$, and expressing $T$ in terms of $\theta$, leads to

$$\mathrm{Nu}=-\frac{\partial\theta}{\partial X}\bigg|_{X=1}\Big/(\theta_m-\theta|_{X=1}) \tag{23}$$

As a comparison now define the local Nusselt number at $X=-1$, Nu*, to be the temperature gradient at $X=-1$ divided by the same reference temperature gradient as used in equation (23)

$$\mathrm{Nu}^*=\frac{\partial\theta}{\partial X}\bigg|_{X=-1}\Big/(\theta_m-\theta|_{X=1}) \tag{24}$$

Nu and Nu* are plotted against $Y$ in Figs. 4($a$) and 4($b$) for the same parameter values as were used in Figs. 3($a$) and

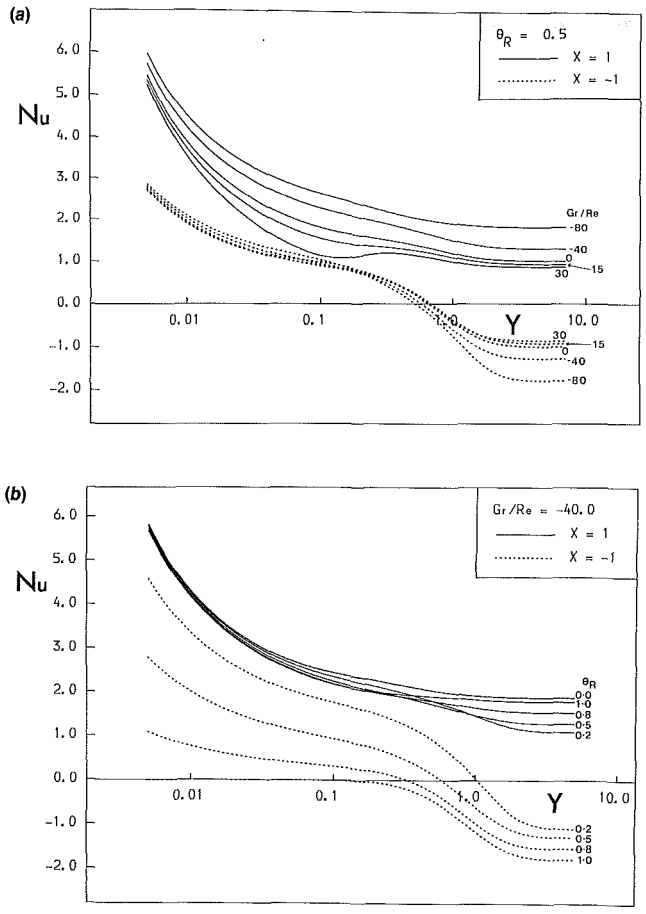


Fig. 4 Local Nusselt number distributions for (*a*) $\theta_R = 0.5$, (*b*) Gr/Re = −40

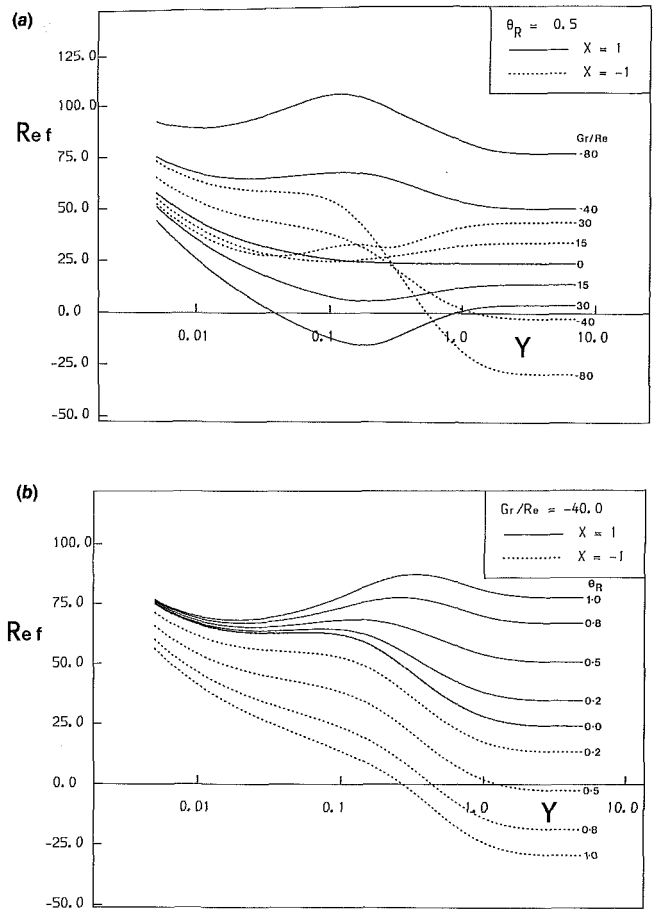


Fig. 5 Friction factor times Reynolds number plotted against streamwise distance for (*a*) $\theta_R = 0.5$, (*b*) Gr/Re = −40

3(*b*), respectively, with Nu being represented by solid lines and Nu* by broken lines. From Fig. 4(*a*) it can be seen that Nu is large for large negative Gr/Re again implying that heat transfer is more efficient in flows where the free convection aids the forced convection. The Nu* profiles also imply more efficient heat transfer at $X = -1$ for Gr/Re large and negative because over most of the length of the duct the magnitude of |Nu*| is greatest when Gr/Re is large and negative. Of particular interest in Fig. 4(*a*) is the behavior of Nu when Gr/Re = 30. For $Y < 0.1$ the curve for Gr/Re = 30 follows the pattern exhibited by the other four curves; however for $0.1 < Y < 1.0$ the effects of the flow separation on the Nusselt number become very apparent. Heat transfer is clearly enhanced by the recirculation region and it is only when $\theta_m$ falls below the value of $\theta_R$ that the Nusselt number begins to fall again toward its fully developed value. In Fig. 4(*b*) it can be seen that heat transfer seems to take place most efficiently for $\theta_R$ close to 1. The plot for $\theta_R = 0$, that is the symmetric case, does not however seem to fit in with the trends of the other curves. This is due to the fact that when $\theta_m$ falls below the value of $\theta_R$ there is a relatively rapid fall in the values of both Nu and Nu*. Since for $\theta_R = 0$ it must always hold that $\theta_m > \theta_R$ this rapid fall never occurs in the symmetric case. This can be verified by performing a calculation with $\theta_R = 10^{-5}$; in this situation Nu and Nu* are found to follow the curves for $\theta_R = 0$ until $\theta_m$ falls below $\theta_R$, when they fall very quickly to fully developed vaues, which agree with the trends in Fig. 4(*b*). It is also apparent from Fig. 4(*b*) that the presence of reverse flow adjacent to the wall at $X = -1$ produces an enhancement of the heat transfer at the wall at $X = 1$ and this has the effect of partially cancelling out the fall in Nu as described above. This means that any two independent curves with $\theta_R \neq 0$ cross over at some point on the graph. The exact fully developed values of equations (23) and (24) are given respectively as follows:

$$\mathrm{Nu}_\infty = \left\{1 + \frac{\theta_R}{90}\,\frac{\mathrm{Gr}}{\mathrm{Re}}\right\}^{-1} \tag{25}$$

$$\mathrm{Nu}^*_\infty = -\left\{1 + \frac{\theta_R}{90}\,\frac{\mathrm{Gr}}{\mathrm{Re}}\right\}^{-1} \tag{26}$$

Equations (25) and (26) agree to within $5 \times 10^{-3}$ with the values plotted in Figs. 4(*a*) and 4(*b*) for large $Y$.

The friction factor at the wall $x = a$ at any particular streamwise location can be expressed as follows (Özişik, 1985):

$$f = -\frac{8a}{\mathrm{Re}u_m}\,\frac{\partial v}{\partial x}\bigg|_{x=a} \tag{27}$$

Putting $v = u_m V$ and $x = aX$ and using $V = \partial\psi/\partial X$ and equation (1), equation (27) reduces to

$$f = -\frac{8}{\mathrm{Re}}\,\Omega\,|_{X=1} \tag{28}$$

Similarly the friction factor at the wall $X = -1$, $f^*$, can be expressed in the form

$$f^* = \frac{8}{\mathrm{Re}}\,\Omega\,|_{X=-1} \tag{29}$$

Re$f$ and Re$f^*$ are plotted against $Y$ in Figs. 5(*a*) and 5(*b*) for the same parameter values as were used in Figs. 3(*a*) and 3(*b*), respectively, with Re$f$ being represented by solid lines and Re$f^*$ by broken lines. In Figs. 5(*a*) and 5(*b*) negative values for Re$f$ and Re$f^*$ imply flow separation from either

$X=1$ or $X=-1$, respectively, and large positive values of Re$f$ and Re$f^*$ imply streamwise velocity peaks in the half of the duct adjacent to $X=1$ or $X=-1$, respectively. In Fig. 5($a$) it can be seen that large negative values of Gr/Re produce flow separation from the wall at $X=-1$ and that large positive values of Gr/Re produce flow separation from the wall at $X=1$, which is in agreement with earlier results. Figure 5($b$) shows that as $\theta_R$ is increased the velocity profile begins to peak near the wall at $X=1$ and flow separation occurs from the wall at $X=-1$. The exact fully developed values of equations (28) and (29) are given, respectively, as follows:

$$f_\infty = \frac{8}{\mathrm{Re}}\left\{3 - \frac{\theta_R}{6}\frac{\mathrm{Gr}}{\mathrm{Re}}\right\} \tag{30}$$

$$f^*_\infty = \frac{8}{\mathrm{Re}}\left\{3 + \frac{\theta_R}{6}\frac{\mathrm{Gr}}{\mathrm{Re}}\right\} \tag{31}$$

Equations (30) and (31) agree with the values displayed in Figs. 5($a$) and 5($b$) to within $5\times10^{-2}$.

Where comparisons were possible the results obtained in this investigation, near the entrance of the duct, were found to be graphically indistinguishable from those of Aung and Worku (1986a).

## 5 Conclusions

Solutions to combined convection flows in vertical parallel plate ducts with asymmetric wall temperature boundary conditions are presented. The solution technique is of a marching nature and when regions of reverse flow are encountered the solution is formed by using an iteration technique based on marching only in regions where the flow is in the same direction as the direction of the marching. When reverse flow is present, either over a finite length of the duct or in the fully developed flow profile, the whole development of the flow is presented, from entry through to the fully developed region, for all the situations considered. Comparisons with existing literature, where possible, show very good agreement.

Results presented for heat transfer data imply that for a fixed value of $\theta_R$ heat transfer is most efficient for Gr/Re large and negative and that for a fixed value of Gr/Re heat transfer is most efficient when the entry temperature of the fluid is equal to the temperature of the cold wall. The results confirm the expected conclusion that compared to the pure convection case, aiding free convection enhances the heat transfer, whereas opposing free convection inhibits the heat transfer. It is also found that over sections of the duct containing reverse flow there is a significant improvement in the heat transfer.

The techniques presented in this paper open the way for many more new investigations into problems involving asymmetric wall boundary conditions where the effects of natural convection are very significant.

## Acknowledgments

D. J. Keen would like to thank the SERC for providing a research studentship for the duration of his studies.

## References

Aung, W., Kessler, T. J., and Beitin, K. I., 1973, "Free Convection Cooling of Electronic Systems," *IEEE Transactions on Parts Hybrids and Packaging*, Vol. 9, No. 2, pp. 75–86.

Aung, W., 1973, "Heat Transfer in Electronic Systems With Emphasis on Asymmetric Heating," *Bell Systems Technical Journal*, Vol. 52, pp. 907–925.

Aung, W. and Worku, G., 1986a, "Developing Flow and Flow Reversal in a Vertical Channel With Asymmetric Wall Temperatures," ASME JOURNAL OF HEAT TRANSFER, Vol. 108, pp. 229–304.

Aung, W., and Worku, G., 1986b, "Theory of Fully Developed Mixed Convection Between Parallel Vertical Plates," ASME JOURNAL OF HEAT TRANSFER, Vol. 108, pp. 485–488.

Cebeci, T., Khattab, A. A., and Lamont, R., 1982, "Combined Natural and Forced Convection in Vertical Ducts," *Heat Transfer 1982, Proceedings of the 7th International Heat Transfer Conference*, Munich, West Germany, Vol. 3, pp. 419–424.

Collins, M. W., 1975, "Viscous Dissipation Effects on Developing Laminar Flow in Adiabatic and Heated Tubes," *Proceedings of the Institution of Mechanical Engineers*, Vol. 189, pp. 129–137.

Ingham, D. B., Keen, D. J., and Heggs, P. J., 1987, "Two Dimensional Combined Convection in Vertical Parallel Plate Ducts, Including Situations of Flow Reversal," submitted for publication to the *International Journal for Numerical Methods in Engineering*.

Morton, B., Ingham, D. B., Keen, D. J., and Heggs, P. J., 1987, "Experimental and Numerical Investigations Into Recirculating Combined Convection in Laminar Pipe Flow," *Proceedings of The International Symposium on Natural Circulation*, ASME Winter Annual Meeting, Boston, MA, Dec.

Özişik, M. N., 1985, *Heat Transfer, A Basic Approach*, McGraw-Hill, New York.

Reyhner, T. A., and Flügge-Lotz, I., 1968, "The Interaction of a Shock Wave With a Laminar Boundary Layer," *International Journal of Non-Linear Mechanics*, Vol. 3, pp. 173–199.

Shah, R. K., and London, A. L., 1978, *Advances in Heat Transfer, Supplement 1, Laminar Flow Forced Convection in Ducts*, Academic Press, London.

Williams, P. G., 1975, "A Reverse Flow Computation in the Theory of Self Induced Separation," *Lecture Notes in Physics*, Vol. 35, pp. 445–451.

Yao, L. S., 1987, "Is a Fully-Developed and Non-isothermal Flow Possible in a Vertical Pipe?" *International Journal of Heat and Mass Transfer*, Vol. 30, pp. 707–716.

# Molten Metal Flow Around the Base of a Cavity During a High-Energy Beam Penetrating Process

**Peng Sheng Wei**
Associate Professor.

**Lih Ren Chiou**
Graduate Student.

Department of Mechanical Engineering,
National Sun Yat-Sen University,
Kaohsiung, Taiwan

*An axisymmetric, quasi-steady-state model for the flow of molten metal in a thin layer surrounding the lower region of a vapor-filled cavity formed during a high-energy beam penetrating process is investigated for the first time. The shape of the vapor–liquid interface is determined by solving the momentum and energy equations and satisfying global mass conservation. Results show that the effective surface pressure and the force caused by the surface tension induce the upward flow of the liquid layer, which is responsible for the formation of the cavity. Distributions of the cavity temperatures, the liquid layer thickness, and the tangential velocity are also presented in this initial study.*

## Introduction

High-energy beam welding or drilling is characterized by a narrow and deep vapor-filled cavity. The current hypothesis given, for example, by Schiller et al. (1982) and Connor et al. (1987) for the formation of the cavity is that, at a high power density, and for a temperature rise at the surface on which the beam impinges, the vapor pressure increases and results in the formation of a needlelike vapor-filled cavity, which is surrounded by molten material. As a result of this cavity the beam can penetrate deep into the workpiece. When the power density rises to extreme values, both the vapor pressure and the evaporation rate become so high that the whole melt is ultimately ejected by the vapor stream and a deep and narrow cavity is finally formed. Due to the complexity of the process, understanding of the formation of the cavity and its penetrating phenomena are still lacking at the present time.

A systematic study of the high-energy beam penetrating process is of practical importance. Leskov et al. (1975) used a piezoelectric sensing element to record the reaction forces on the lower surface of a welding cavity. Intensive vaporization was found to take place at the base of the cavity only. As a jet of vapor moves upward, a projection occurs on the surface of the liquid layer due to an interfacial pressure. If the projection is in the path of the high-energy beam, the upper liquid surface will be heated to a very high temperature and the pressure induced from the vapor generated (the recoil pressure) associated with this high temperature will drive the projecting liquid toward the bottom of the cavity. Possible instability of penetration is associated with the formation and movement of projections toward the cavity base. Arata et al. (1976) observed the molten metal flow by utilizing a fluoroscopic technique and proposed that the formation of the weld defect known as spiking is a result of the breakdown of the balance between the vapor pressure and the hydrostatic head of the melt. Schauer and Giedt (1978) found that the imbalance of the vapor pressure and the surface tension force has a close relationship with the spiking tendency.

Hashimoto and Matsuda (1965) studied the forces acting on the cavity during the electron beam welding process. The forces due to the beam impulse of the electrons on the material surface, and the electromagnetic effect of the beam current, are small. Only the repulsive force due to evaporation of metal was significant. The repulsive force in the cavity could be modeled by the saturation pressure acting on a small area related to the cavity diameter and the results showed general agreement with experimental data for both steel and aluminum. The evaporation rate was also evaluated by substituting the temperature measured by a thermocouple and the corresponding saturation pressure into the equilibrium equation developed by Langmuir (1913). Good agreement was achieved by comparing with the weight difference before and after welding.

The variation of the surface tension due to nonuniform surface temperatures (the thermocapillary force) was found by Ol'Shanskii et al. (1974) to be the driving force causing the liquid layer to flow from the front of the cavity to the rear. His assessment was later confirmed by Giedt and Wei (1982), and Wei and Giedt (1985) by calculating the fluid flow in the liquid layer around an electron beam welding cavity. Due to the small radius of curvature of the free surface and the large vertical temperature gradient measured by Schauer et al. (1978) and calculated by Wei and Wu (1987), the force induced by the surface tension should be responsible for the fluid flow in the liquid layer during the penetrating process.

In this study, to provide an exploratory understanding of the complicated high-energy beam penetrating process, an axisymmetric, quasi-steady state model for the flow of molten metal in a thin layer surrounding the lower region of a vapor-filled cavity, formed during high-energy beam penetrating process, is investigated. Both the effective surface pressure, which is the sum of the gas pressure near the surface of the liquid layer and the pressure due to evaporation, and the force induced by the surface tension are taken into account. Results obtained for free surface temperature distributions, velocity profiles, and liquid layer thickness distributions are presented.

## Analysis

During a high-energy beam welding or drilling process, a narrow and deep vapor-filled cavity is formed as shown in Fig. 1. In this study, an $rz$ coordinate system is assumed to move into the solid at a steady penetrating velocity. The shape of the liquid–solid interface is fixed in this coordinate system. The penetrating process is thus simplified to an axisymmetric, quasi-steady flow in this moving coordinate system. The beam energy density is assumed to be a Gaussian distribution. Consequently, the melting rate has a maximum value at the cavity

Contributed by the Heat Transfer Division for publication in the JOURNAL OF HEAT TRANSFER. Manuscript received by the Heat Transfer Division August 10, 1987. Keywords: Laser Processing, Materials Processing and Manufacturing Processes, Thermocapillary Flows.

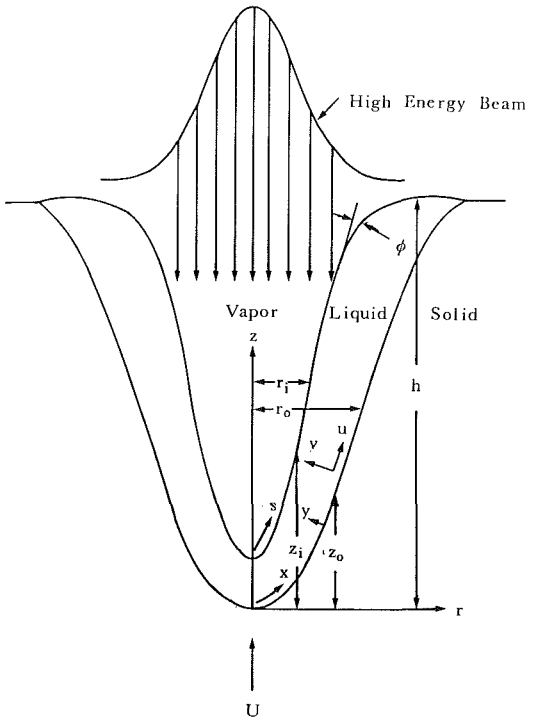


**Fig. 1 Flow model and coordinate system for a high-energy beam welding or drilling cavity liquid layer**

base and decreases to zero at the edge of the cavity. The melting rate of the incoming solid material across the liquid-solid interface is thus assumed to have a Gaussian distribution in the $r$ coordinate direction. The temperature profile across the liquid layer is assumed to be linear since the ratio of the liquid layer thickness to the cavity minor radius has been found to be less than 7 percent (see Giedt and Wei, 1982, and Wei and Giedt, 1985). Radiative heat transfer was estimated to be only 0.2 percent of the beam power of 3 kW at a typical cavity radius 1 mm and a cavity temperature 2350 K, and was assumed to be negligible.

**Governing Equations and Boundary Conditions.** With the above assumptions and estimated Reynolds and Peclet numbers on the order of 2400 and 60, respectively, the continuity, momentum, and energy equations of an axisymmetric flow can be described by planar flow equations for a curvilinear coordinate system

$$\frac{\partial r_o u}{\partial x}+\frac{\partial r_o v}{\partial y}=0 \tag{1}$$

$$u\frac{\partial u}{\partial x}+v\frac{\partial u}{\partial y}=-\frac{1}{\rho_l}\frac{dp_l}{dx}+\nu\frac{\partial^2 u}{\partial y^2}-g\frac{\partial z}{\partial x} \tag{2}$$

$$\frac{\partial^2 T_l}{\partial y^2}=0 \tag{3}$$

The shape of the liquid-solid interface is defined by a Gaussian distribution

$$z_o=h(t)[1-\exp(-r_o^2/2\sigma^2)] \tag{4}$$

Relative velocity components of the solid with respect to the moving coordinate system at the liquid-solid interface $y=0$ are

$$u=\frac{U\beta\exp(-r_o^2/2\sigma^2)}{\sqrt{1+\beta^2}} \tag{5}$$

$$v=\frac{U\exp(-r_o^2/2\sigma^2)}{\sqrt{1+\beta^2}} \tag{6}$$

where the penetrating velocity $U = dh/dt$ is assumed to be constant as found by the experimental measurements conducted by Arata and Miyamoto (1973). The energy balance equation and the temperature of the liquid at the liquid-solid interface are

$$k_l\frac{\partial T_l}{\partial y}\bigg|_{y=0^+}=k_s\frac{\partial T_s}{\partial y}\bigg|_{y=0^-}+\rho_l v L_{sl} \tag{7}$$

$$T_l=T_m \tag{8}$$

At the vapor-liquid interface $y = \delta(x)$, the force balance equations in the tangential and normal directions are, respectively,

$$\sigma_T\frac{\partial r_i}{\partial s}+r_i\frac{\partial \sigma_T}{\partial s}=\mu r_i\frac{\partial u}{\partial y} \tag{9}$$

$$p_v+j^2\left(\frac{1}{\rho_v}-\frac{1}{\rho_l}\right)=p_l+\sigma_T\left(\frac{1}{R_1}+\frac{1}{R_2}\right) \tag{10}$$

where the first term on the left of equation (9) represents the force induced by the surface tension due to the change in the radius of the cavity, and the second term denotes the force

## Nomenclature

$A$ = empirical constant
$c$ = specific heat
$F$ = objective function
Fr = Froude number = $U/(gh)^{0.5}$
$g$ = gravitational acceleration
$G$ = $\sigma_m/\rho_l U^2 h$
$h$ = penetration depth
$j$ = evaporation rate
$K$ = $k_s/k_l$
$k_l$, $k_s$ = liquid and solid thermal conductivity
$L_{lv}$, $L_{sl}$ = latent heat of evaporation and melting
Pe = Peclet number = $Uh/\alpha_l$
$p_l$, $p_v$ = liquid and vapor pressure
$p_l^*$ = $p_l/\rho_l U^2$
$r$, $r^*$ = dimensional and dimensionless radial coordinate; $r^* = r/h$
$R$ = specific gas constant
Re = Reynolds number = $Uh/\nu$
$R_1$, $R_1^*$; $R_2$, $R_2^*$ = dimensional and dimensionless radii of principal curvature; $R_1^* = R_1/h$, $R_2^* = R_2/h$
$s$ = distance measured along free surface from cavity base
$S$ = $\mu U/\sigma_m$
Ste = Stefan number = $cT_m/L_{sl}$
$t$ = time
$T_l$, $T_m$, $T_s$ = liquid, melting, and solid temperature
$T_\infty$ = ambient temperature
$u$ = dimensional longitudinal velocity component
$U$ = penetration velocity
$\bar{u}$, $\tilde{u}$ = longitudinal velocity components; $\bar{u}$, defined in equation (15), $= -\partial\bar{\Psi}/\partial\bar{y}$, $\tilde{u} = -\partial\Psi^*/\partial\eta$
$v$ = dimensional transverse velocity component
$V$ = $U/(2\pi RT_m)^{0.5}$
$\bar{v}$ = velocity, defined in equation (15), $= \partial\bar{\Psi}/\partial\bar{x}$
$x$, $x^*$ = dimensional and dimensionless longitudinal coordinate; $x^* = \bar{x}/h$

caused by the surface tension due to the temperature variation, namely, the thermocapillary force. In equation (10) $p_v$ is the gas pressure near the liquid surface, and the second term on the left expresses the pressure due to evaporation, which can be determined from the equilibrium equation developed by Langmuir (1913). If equilibrium conditions are not satisfied, the gas pressure near the surface is less than the saturation pressure corresponding to the local surface temperature. Knight (1982) investigated transient evaporation from a flat surface into vacuum and found that the gas pressure near the evaporating surface is 20.6 percent of the saturation pressure when the Mach number of the evaporating molecules is equal to 1. This would be expected to occur at the cavity base due to the strong evaporation into a vacuum. As the average evaporating velocity decreases to zero, the vapor pressure approaches the saturation value. The recoil pressure has a minimum value around a half of the saturation pressure when the evaporating molecules have a Mach number M = 1. However, this would occur only when the cavity is initially formed. After it has penetrated even a short distance the vapor in the cavity will retard the outflow. Force balances made by Schauer et al. (1978) showed that vapor pressure must be very close to saturation values at the cavity base. For this reason, in this study the gas pressure near the liquid surface is assumed to be the saturation vapor pressure, which can be simply determined from the Clausius-Clapeyron equation (Giedt, 1971). To be conservative the total or effective gas pressure was then taken to be the total of $p_v$ plus the recoil pressure determined from the Langmuir equation.

The radii of the principal curvatures $R_1$ and $R_2$ are determined from the equation of the liquid–vapor interface

$$\frac{1}{R_1}=\frac{\partial^2 z_i}{\partial r_i^2}\Big/\left[1+\left(\frac{\partial z_i}{\partial r_i}\right)^2\right]^{3/2} \tag{11}$$

$$\frac{1}{R_2}=\frac{1}{r_i}\frac{\partial z_i}{\partial r_i}\Big/\sqrt{1+\left(\frac{\partial z_i}{\partial r_i}\right)^2} \tag{12}$$

The evaporation rate $j$, which can be calculated by the Langmuir equation, yields

$$j=\rho_l v \tag{13}$$

At $x=0$, $u=0$ to satisfy the axisymmetric boundary condition.

**Mangler Transformation.** Mangler (1948) discovered a transformation that reduced equations (1) and (2) to an orthogonal coordinate system by assuming the liquid layer thickness to be much smaller than the radius of the cavity. The Mangler transformation is

$$\bar{x}=\int_0^x\left(\frac{r_o}{h}\right)^2 dx \qquad \bar{y}=\frac{r_o}{h}\,y \tag{14}$$

$$\bar{u}=u \qquad \bar{v}=\frac{h}{r_o}\left(v+\frac{h}{r_o}\frac{\partial \bar{y}}{\partial x}\,\bar{u}\right) \tag{15}$$

where $h$ is assumed to be a constant in this initial study. The transformed equations (1) and (2) become

$$\frac{\partial \bar{u}}{\partial \bar{x}}+\frac{\partial \bar{v}}{\partial \bar{y}}=0 \tag{16}$$

$$\bar{u}\frac{\partial \bar{u}}{\partial \bar{x}}+\bar{v}\frac{\partial \bar{u}}{\partial \bar{y}}=-\frac{1}{\rho_l}\frac{dp_l}{d\bar{x}}+\nu\frac{\partial^2 \bar{u}}{\partial \bar{y}^2}-g\frac{\partial z}{\partial \bar{x}} \tag{17}$$

Introducing the stream function $\bar{\Psi}$ to eliminate the continuity equation (16), the momentum equation (17) in the dimensionless form becomes

$$\frac{\partial \Psi^*}{\partial y^*}\frac{\partial^2 \Psi^*}{\partial x^* \partial y^*}-\frac{\partial \Psi^*}{\partial x^*}\frac{\partial^2 \Psi^*}{\partial y^{*2}}=-\frac{dp_l^*}{dx^*}-\frac{1}{\mathrm{Re}}\frac{\partial^3 \Psi^*}{\partial y^{*3}}-\frac{1}{\mathrm{Fr}^2}\frac{\partial z^*}{\partial x^*} \tag{18}$$

**Immobilization Transformation.** Since this is a free surface problem, the domain of the flow field is unknown. A simple way to provide a rectangular mesh convenient for finite difference computations in this case is to introduce new independent variables defined by

$$\xi=x^* \qquad 0\le\xi\le 1$$

$$\eta=y^*/\delta^* \qquad 0\le\eta\le 1$$

Equation (18) becomes

$$\frac{\partial \Psi^*}{\partial \eta}\frac{\partial^2 \Psi^*}{\partial \xi \partial \eta}-\frac{1}{\delta^*}\frac{\partial \delta^*}{\partial \xi}\left(\frac{\partial \Psi^*}{\partial \eta}\right)^2-\frac{\partial \Psi^*}{\partial \xi}\frac{\partial^2 \Psi^*}{\partial \eta^2}=-\delta^{*2}\frac{dp_l^*}{d\xi}-\frac{1}{\delta^*\mathrm{Re}}\frac{\partial^3 \Psi^*}{\partial \eta^3}-\frac{\delta^{*2}}{\mathrm{Fr}^2}\frac{\partial z^*}{\partial \xi} \tag{19}$$

Equation (19) is reduced to two equations for numerical computation

## Nomenclature (cont.)

$\bar{x}$ = longitudinal coordinate, defined in equation (14)
$y, y^*$ = dimensional and dimensionless transverse coordinate; $y^* = \bar{y}/h$
$\bar{y}$ = transverse coordinate, defined in equation (14)
$z, z^*$ = dimensional and dimensionless vertical coordinate; $z^* = z/h$
$\alpha$ = effective surface pressure correction factor
$\alpha_l$ = liquid thermal diffusivity
$\beta$ = $dz_0/dr_0$
$\Gamma$ = $(d\sigma_T/dT)T_m/\sigma_m$
$\delta, \delta^*$ = dimensional and dimensionless liquid layer thickness; $\delta^* = \delta/h$
$\eta$ = immobilization coordinate = $y^*/\delta^*$
$\theta_l, \theta_s$ = dimensionless liquid and solid temperature; $\theta_l = T_l/T_m$, $\theta_s = (T_s-T_\infty)/(T_m-T_\infty)$
$\theta_\infty$ = $T_\infty/T_m$
$\mu$ = dynamic viscosity
$\nu$ = kinematic viscosity
$\xi$ = immobilization coordinate, = $x^*$
$\Pi$ = $L_{lv}/RT_m$
$\rho_l, \rho_v$ = liquid and vapor density
$\sigma, \sigma^*$ = dimensional and dimensionless shape parameter of liquid-solid interface; $\sigma^* = \sigma/h$
$\sigma_m, \sigma_T$ = surface tension at $T_m$ and $T_l$, respectively; $\sigma_T = \sigma_m + (d\sigma_T/dT)(T_l-T_m)$
$\phi$ = angle between energy beam and free surface
$\bar{\Psi}, \Psi^*$ = dimensional and dimensionless stream function; $\Psi^* = \bar{\Psi}/Uh$
$\tilde{\Psi}_j$ = stream function determined from equation (26)

**Subscripts**

$i$ = vapor–liquid interface
$o$ = liquid–solid interface

$$\tilde{u}\frac{\partial \tilde{u}}{\partial \xi}-\frac{1}{\delta^*}\frac{\partial \delta^*}{\partial \xi}\tilde{u}^2+\frac{\partial \Psi^*}{\partial \xi}\frac{\partial \tilde{u}}{\partial \eta}$$

$$=-\delta^{*2}\frac{dp_l^*}{d\xi}+\frac{1}{\delta^*\mathrm{Re}}\frac{\partial^2\tilde{u}}{\partial\eta^2}-\frac{\delta^{*2}}{\mathrm{Fr}^2}\frac{\partial z^*}{\partial\xi} \tag{20}$$

$$\tilde{u}=-\frac{\partial\Psi^*}{\partial\eta} \tag{21}$$

Boundary conditions (5) and (6) at $\eta=0$ become

$$\tilde{u}=\frac{\delta^*\beta\exp(-r_o^{*2}/2\sigma^{*2})}{\sqrt{1+\beta^2}} \tag{22}$$

$$\Psi^*=\sigma^{*2}z_o^* \tag{23}$$

Boundary conditions (9), (10), and (13) at $\eta=1$ become

$$[1+\Gamma(\theta_l-1)]\frac{\partial r_l^*}{\partial\xi}+\Gamma r_l^*\frac{\partial\theta_l}{\partial\xi}=\frac{S}{\delta^{*2}}\frac{\partial\tilde{u}}{\partial\eta} \tag{24}$$

$$\alpha A\exp(-\Pi/\theta_l)=p_l^*+G[1+\Gamma(\theta_l-1)]\left(\frac{1}{R_1^*}+\frac{1}{R_2^*}\right) \tag{25}$$

$$\Psi^*=VA\int_o^\xi \exp(-\Pi/\theta_l)/\sqrt{\theta_l}r_l^*ds^* \tag{26}$$

$\alpha = 1.16$ by assuming that the gas pressure near the liquid layer surface equals the saturation vapor pressure and a strong evaporation occurs. The axisymmetric boundary conditions are

$$\tilde{u}=0,\quad \Psi^*=0 \qquad \text{at } \xi=0 \tag{27}$$

The liquid temperature $\theta_l$, which is found by integrating equation (3) subject to boundary conditions (7) and (8), yields

$$\theta_l=1+\left[K(1-\theta_\infty)\left.\frac{\partial\theta_s}{\partial\eta}\right|_{\eta=0^-}+\mathrm{Pe}\delta^*\exp(-r_o^{*2}/2\sigma^{*2})/\mathrm{Ste}r_o^*\sqrt{1+\beta^2}\right]\eta \tag{28}$$

where the heat conduction to the solid $K\,\partial\theta_s/\partial\eta$ at $\eta=0^-$ is calculated by solving the energy equation of solid.

Solutions are then obtained by substituting equations (11), (12), and (28) into equations (20)–(27).

**Solution Procedure.** The key steps for solving this problem are the following:

1 $\delta_j^*$, $j = 1, 2, 3$ at the first three grid locations are guessed.

2 The stream function $\Psi_j^*$ at the vapor–liquid interface is calculated by substituting $\delta_j^*$ into the momentum equations (20) and (21).

3 The stream function at the vapor–liquid interface $\tilde{\Psi}_j$ is also determined from the evaporation rate equation (26).

4 An objective function $F=\sum_{j=1}^{3}|\Psi_j^*-\tilde{\Psi}_j|$ is defined; this is minimized by using the Box optimization technique, which is described in detail by Wei and Giedt (1985). The desired distribution of $\delta_j^*$ ($j = 1, 2$, and 3) is determined when $F$ becomes less than a specified minimum value ($1\times10^{-2}$ in the present study).

5 With the first three values of $\delta_j^*$ known, computation can proceed in the longitudinal $x$ direction. The difference in $\Psi_j^*$ and $\tilde{\Psi}_j$ for $j \geq 4$ is minimized by iterations at each longitudinal location.

## Results and Discussion

The governing equations and their associated boundary conditions involve the thermal and fluid properties of the solid and liquid phases of the material being drilled. In view of the limited data available at the temperatures involved, it was decided to make initial calculations with values appropriate for aluminum. Values used in the final calculations, based on Brandes (1983), are listed in Table 1.

**Table 1 Properties of aluminum**

| | |
|---|---|
| Dynamic viscosity $\mu$, kg/m-s | $2.0\times10^{-3}$ |
| Solid conductivity $k_s$, W/m-K | 220 |
| Liquid conductivity $k_l$, W/m-K | 106 |
| Melting temperature $T_m$, K | 933 |
| Liquid thermal diffusivity $\alpha_l$, $m^2/s$ | $3.8\times10^{-5}$ |
| Latent heat of evaporation $L_{lv}$, J/kg | $1\times10^{7}$ |
| Latent heat of melting $L_{sl}$, J/kg | $3.7\times10^{5}$ |
| Thermocapillary force constant $d\sigma_T/dT$, N/K-m | $-3.5\times10^{-4}$ |
| Surface tension at melting temperature $\sigma_m$, N/m | 0.914 |
| Density $\rho_l$, $kg/m^3$ | 2124 |

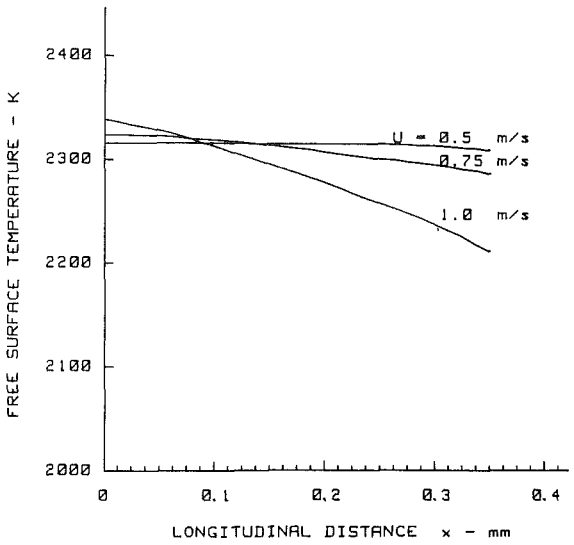


**Fig. 2 Variation of free surface temperature distribution with penetrating velocity for drilling aluminum ($h$ = 2 mm, $\sigma$ = 1 mm)**

Quantitative understanding of a high-energy beam penetrating process is still lacking at the present time. For clarity, dimensional figures are provided to quantify physical phenomena occurring during a high-energy beam penetrating process in this initial study. Temperature distributions near the bottom of the cavity for different penetrating velocities are shown in Fig. 2. The cavity base temperature is found to be 2340 K for the penetrating velocity $U = 1.0$ m/s and decreases to 2315 K for $U = 0.5$ m/s. It is obvious that the penetrating velocity, which is proportional to the intensity of the energy beam, has little effect on the cavity base surface temperature. Since the variation of the cavity base temperature with the beam power and the welding speed is less than 1 percent as shown by Wei and Wu (1987), the measurement of an electron beam welding cavity temperature distribution at a beam power 1.96 kW and speed of 4.4 mm/s conducted by Schauer et al. (1978) is a relevant comparison. According to their results, the cavity base temperature was found to be 2170 K. Hence the difference between the measured and the calculated cavity base temperatures is less than 10 percent. The temperature gradient along the liquid surface calculated near the cavity base is around 370 K/mm for a penetrating velocity $U = 1.0$ m/s, which is in accord with 350 K/mm for the experimental results. Figure 2 also reveals that the temperature gradient increases with increasing penetration velocity. Consequently, an intense energy beam can readily produce a deep and narrow cavity since the effect of a temperature gradient increase is to increase the force induced by the surface tension and the effective surface pressure, which cause upward flow of the liquid layer.

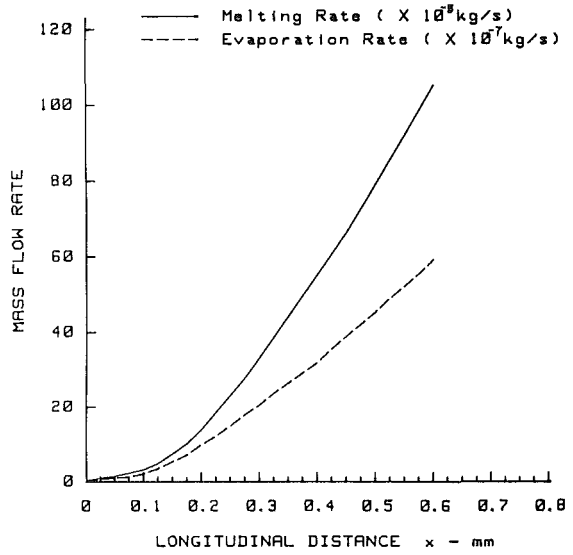


Fig. 3 Comparison between rates of melting and evaporation for drilling aluminum ($h$ = 3 mm, $\sigma$ = 1 mm, $U$ = 0.75 m/s)

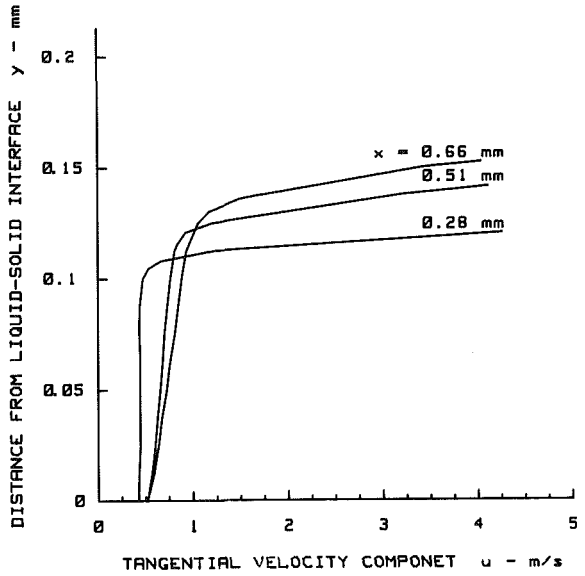


Fig. 5 Tangential velocity distributions in liquid layer for drilling aluminum ($h$ = 3 mm, $\sigma$ = 1 mm, $U$ = 0.75 m/s)

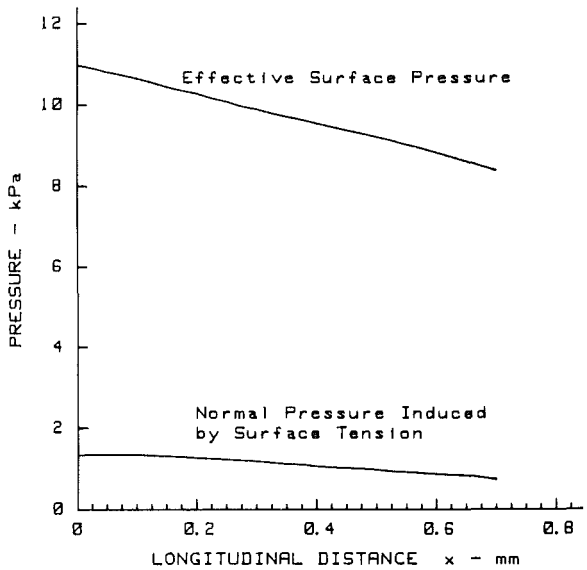


Fig. 4 Distributions of effective surface pressure and normal pressure induced by surface tension for drilling aluminum ($h$ = 3 mm, $\sigma$ = 1 mm, $U$ = 0.75 m/s)

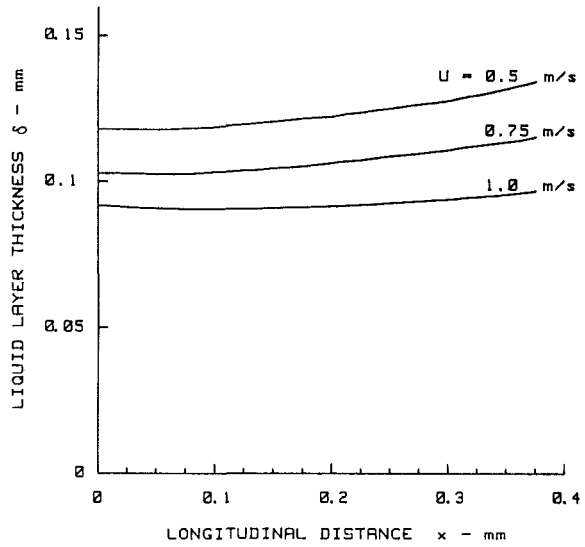


Fig. 6 Variation of liquid layer thickness distribution with penetrating velocity ($h$ = 2 mm, $\sigma$ = 1 mm)

Both the variation of the evaporation rate and the melting rate with distance from the base are shown in Fig. 3. It is interesting to find that the mass melted at the distance 0.6 mm from the bottom of the cavity is $1.1 \times 10^{-3}$ kg/s, which is around 200 times larger than the $6 \times 10^{-6}$ kg/s of mass evaporated. Hence most of the solid material melted is convected upward. The formation of the cavity is primarily due to the melting rate and the upward motion of the liquid layer rather than due to evaporation as suggested by Schiller et al. (1982) and Connor et al. (1987).

The effective surface pressure and the normal pressure induced by the surface tension acting along the vapor–liquid interface are shown in Fig. 4. The effective surface pressure is found to be around $1.1 \times 10^4$ Pa and the normal pressure induced by the surface tension is $1.3 \times 10^3$ Pa at the cavity base. The effective surface pressure is dominant in the lower region of the cavity and decrease more rapidly than the normal pressure caused by the surface tension. It is possible that the latter is greater than the former in the upper region of the cavity and results in spiking, which is suggested by Schauer and Giedt (1978). Evaluation of the effective surface pressure is still not definitive since it involves the interaction with the vapor flow and the nonequilibrium phenomena near the cavity surface as mentioned previously. In this study, the vapor pressure is assumed to be the saturation pressure, as suggested by Hashimoto and Matsuda (1965). The pressure due to evaporation is found from the Langmuir equation by assuming ideal evaporation. Based on the measurements conducted by Hashimoto and Matsuda (1965), the effective surface pressure predicted will be of the right order of magnitude.

Figure 5 shows velocity profiles across the liquid layer at a depth of penetration $h$ = 3 mm, a penetrating velocity $U$ = 0.75 m/s, and cavity shape parameter $\sigma$ = 1 mm. Velocities increase very rapidly near the vapor–liquid interface due to a strong force induced by the surface tension. Free surface velocities are found to be around 4 m/s and decrease in the longitudinal direction.

The liquid layer thickness distributions for various penetrating velocities are shown in Fig. 6. The liquid layer

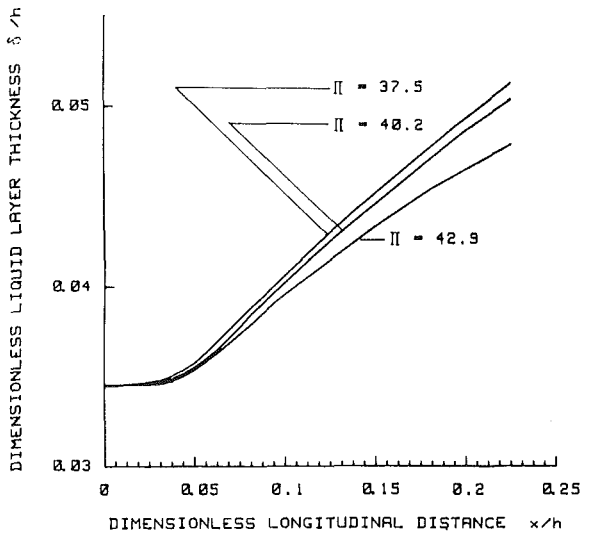


**Fig. 7 Variation of liquid layer thickness distribution with effective surface pressure distribution parameter ($G = 0.26$, $K = 2.08$, Re = 2390, $S = 1.6 \times 10^{-3}$, $V = 5.6 \times 10^{-4}$, and $\Gamma = -0.36$)**

thickness increases from the bottom of the cavity to the upper region. The thickness at the bottom of the cavity is found to be 0.09 mm for $U = 1$ m/s and increases to 0.12 mm at $U = 0.5$ m/s. It is obvious that increasing the penetrating velocity decreases the liquid layer thickness. This is indicative of the strong influence that the force induced by the surface tension can have on fluid flow, since increasing the penetrating velocity results in an increase in the temperature gradient. Ratios of the liquid layer thickness to the local cavity radius are found to be less than 10 percent, which satisfies the assumption for thin liquid layer flow in this study. The effect of the effective surface pressure distribution parameter on the liquid layer thickness for $G = 0.26$, $K = 2.08$, Re = 2390, $S = 1.6 \times 10^{-3}$, $V = 5.6 \times 10^{-4}$, and $\Gamma = -0.36$ is shown in Fig. 7. Increasing $\Pi$ indicates a greater pressure drop as can be seen in equation (25). Hence the increase of the liquid layer thickness with distance $x$ is lowered.

From this study, the description of the mechanism of the high-energy density beam penetrating process is that, when a high-energy beam hits the surface of a workpiece, it produces a small molten pool. Increasing the power density causes surface temperatures and temperature gradients of the molten pool to increase. Significant effective surface pressure and the force caused by the surface tension then push the melt flow outward and upward and a shallow cavity with the metal liquid in a thin layer flowing along the wall is formed. Energy from the beam can readily melt the solid through this molten metal layer and induce high surface temperature gradients, which result in further increases in the effective surface pressure and the force induced by the surface tension and an upward motion of the liquid layer. This process is continued and a deep and narrow cavity is finally formed.

## Conclusions

Conclusions drawn are as follows:

1 A detailed mechanism of the high-energy beam penetrating process is provided in this study. Due to high surface temperatures and temperature gradients of the molten metal layer, the effective surface pressure and the force induced by the surface tension cause the liquid layer to flow upward and result in a deep and narrow cavity. Since the liquid metal evaporation rate is only 1/200 of the melting rate, it is believed that factors affecting the formation of a cavity are primarily the melting rate and the upward motion of the liquid layer rather than evaporation.

2 The penetrating velocity, which is proportional to the intensity of the energy beam, has little effect on the cavity base surface temperature. The liquid surface temperature gradient increases with increasing penetration velocity. Hence an intense energy beam can readily produce a deep and narrow cavity due to the increase of the force induced by the surface tension and the effective surface pressure drop.

3 Velocity profiles at different longitudinal locations are presented. The velocity increases very rapidly, for example, from 0.5 m/s at the liquid–solid interface to 4 m/s near the vapor–liquid interface due to the strong action of the force induced by the surface tension.

4 The liquid layer thickness increases from the bottom of the cavity to the upper region. The liquid layer thickness decreases with increasing penetration velocity of the cavity. Increasing the effective surface pressure has the effect of reducing the increase of the liquid layer thickness.

5 For a given cavity, the effective surface pressure is dominant in the lower region of the cavity and drops more rapidly than the normal pressure induced by the surface tension. It is possible that the latter becomes larger than the former in the upper region of the cavity and gives rise to instability.

## References


Arata, Y., Abe, E., and Fujisawa, M., 1976, "A Study on Dynamic Behaviors of Electron Beam Welding (Report I)–The Observation by a Fluoroscopic Method," *Transactions of JWRI*, Vol. 5, pp. 1–9.

Arata, Y., and Miyamoto, I., 1973, "Processing Mechanism of High Energy Density Beam (Report I)–Mechanism of Drilling," *Transactions of JWRI*, Vol. 2, pp. 19–22.

Brandes, E. A., 1983, *Smithells Metals Reference Book*, Butterworth & Co., Boston.

Conner, L. P., ed., 1987, *Welding Handbook*, 8th ed., American Welding Society, Miami, Vol. 1, p. 40.

Giedt, W. H., 1971, *Thermophysics*, Van Nostrand Reinhold Co., New York, pp. 387–388.

Giedt, W. H., and Wei, P. S., 1982, "Temperature and Velocity Distributions in the Liquid Flowing Around the Front of an Electron Beam Welding Cavity," *Proceedings, 7th International Heat Transfer Conference*, Hemisphere, Washington, DC, Vol. 6, pp. 403–408.

Hashimoto, T., and Matsuda, F., 1965, "Penetration Mechanism of Weld Beads in Electron-Beam Welding–Studies on EB Weldings No. 6," *Transactions of National Research Institute for Metals*, Vol. 7, pp. 12–20.

Knight, C. J., 1982, "Transient Vaporization From a Surface Into Vacuum," *AIAA Journal*, Vol. 20, pp. 950–954.

Langmuir, I., 1913, "The Vapor Pressure of Metallic Tungsten," *The Physical Review*, Vol. 2, pp. 329–342.

Leskov, V. I., Trunov, E. N., and Zhivada, L. I., 1975, "Mechanism in Deep Weld Pools During Electron-Beam Welding," *Avt. Svarka*, No. 1, pp. 12–15.

Mangler, W., 1948, "Zusammenhang zwischen ebenen und rotationssymmetrischen Grenzschichten in kompressiblen Flüssigkeiten," *Z. Angew. Math. Mech.*, Vol. 28, pp. 97–103.

Ol'Shanskii, N. A., et al., 1974, "Movement of Molten Metal During Electron-Beam Welding," *Svar. Proiz.*, No. 9, pp. 12–14.

Schauer, D. A., and Giedt, W. H., 1978, "Prediction of Electron Beam Welding Spiking Tendency," *Welding Journal*, Vol. 57, pp. 189-s to 195-s.

Schauer, D. A., Giedt, W. H., and Shintaku, S. M., 1978, "Electron Beam Welding Cavity Temperature Distributions in Pure Metals and Alloys," *Welding Journal*, Vol. 57, pp. 127-s to 133-s.

Schiller, S., Heisig, U., and Panzer, S., 1982, *Electron Beam Technology*, Wiley, New York, pp. 289–290.

Wei, P. S., and Giedt, W. H., 1985, "Surface Tension Gradient-Driven Flow Around an Electron Beam Welding Cavity," *Welding Journal*, Vol. 64, pp. 251-s to 259-s.

Wei, P. S., and Wu, T. H., 1987, "Effects of Welding Parameters on Three-Dimensional Geometry and Temperatures of a High Energy Beam Welding Cavity," to appear in ASME JOURNAL OF HEAT TRANSFER.

# Evaporative Cutting of a Semitransparent Body With a Moving CW Laser

**H. Abakians**
University of Southern California,
Department of Mechanical Engineering,
Los Angeles, CA 90089-1453

**M. F. Modest**
The Pennsylvania State University,
Department of Mechanical Engineering,
University Park, PA 16802

*The formation of a groove by partial evaporation of a moving semi-infinite and semitransparent solid is considered. Evaporative removal of material is achieved by focusing a high-power, highly concentrated Gaussian laser beam of continuous wave (CW) onto the surface of the solid. Surface heat losses due to radiation and convection are assumed to be negligible, and conductive losses are treated in an approximate fashion using a simple integral method. The relevant nonlinear partial differential equations are solved numerically, and results for groove depth and shape are presented for a variety of laser and solid parameters.*

## Introduction

Shortly after the invention of the laser in 1960, researchers found that the beam from a ruby laser could melt and vaporize small amounts of material. From 1960 until the early 1970s, lasers were primarily laboratory equipment that required a lot of maintenance and had a very high operating cost. All of them operated in the pulsed mode, and had a low pulsing frequency. In the early 1970s, laser processing advanced further with the development of the $CO_2$ laser. Prior to the advent of the $CO_2$ laser, laser melting or vaporization of materials was confined to thin metal sheets ($\simeq 2$ mm) and small samples; however, with the new $CO_2$ laser, much thicker metal sheets and larger samples could be processed. From the early 1970s on, the application of lasers in industry increased tremendously. Presently laser applications include welding, drilling, cutting, machining and heat treatment of materials, fabrication of electronic components, medical surgery, and production of charged particles to name a few.

Most of the theoretical work on laser-treatment heat transfer to date has centered on the solution of the classical heat conduction equation for a stationary or moving solid. In these attempts, cases with and without phase change, and a variety of irradiation or source conditions have been studied. The simplest case without phase change arises when a semi-infinite half-space is heated uniformly over its entire boundary surface. This type of problem was first addressed by Podolsky (1951), Carslaw and Jaeger (1959), White (1963a, 1963b) and Rykalin et al. (1967). The more realistic case of a disk-shaped source (pulsed or constant in time) was addressed by Paek and Gagliano (1972) and Bunting and Cornfield (1975). Further refinement of the theory was achieved by assuming the laser beam intensity to have a Gaussian distribution, i.e., the intensity decreases exponentially from the center of the beam with the square of radial distance; this type of problem has been addressed by Ready (1971), Cline and Anthony (1977), and Nissim et al. (1980).

A number of authors have considered laser heating of metals with temperature-dependent material properties (absorptivity, thermal conductivity, and specific heat). Dobrovol'skii and Uglov (1974) analyzed the effect of heating a semi-infinite slab with a Gaussian laser, where the surface absorptivity varied linearly with temperature. They solved for the two-dimensional temperature distribution and compared the result of their theory to a one-dimensional model neglecting radial effects (solved exactly by Laplace transform of the conduction equation). Warren and Sparks (1979) presented the solution for the same one-dimensional problem (Dobrovol'skii et al.) and gave asymptotic approximations for the temperature distribution of an insulated slab with variable absorptivity. Rykalin et al. (1977) considered laser heating of a slab with absorptivity and specific heat as linear functions of temperature. Recently Rykalin et al. (1982) solved the temperature distribution in a laser-heated slab numerically, with absorptivity, thermal conductivity, and specific heat varying with temperature; they showed that the combined effect of nonlinearities gives substantially new results in a number of cases. Some researchers, in particular Brugger (1972) and Maydan (1970, 1971), have solved the stationary semi-infinite slab problem assuming that the intensity of the incident beam decays exponentially with distance into the material (internal absorption). In a recent paper, Modest and Abakians (1986a) considered a penetrating laser (CW and pulsed) irradiating a moving slab, and obtained exact solutions to the temperature distribution.

The problem is considerably more complicated when phase transition takes place. Cases studied include stationary or moving sources with a variety of source conditions. Soodak (1943) was the first to address the problem of melting with complete removal of melt. He considered constant heating of the surface, and numerically evaluated the steady-state melting rate. Landau (1950) considered melting of a one-dimensional slab with complete removal of melt (subjected to time-varying heating on one end, and insulated conditions on the other). He obtained the time-varying temperature distribution in the solid, and the unsteady position of the moving surface; he also evaluated the limiting speed of the melting front. Masters (1956) considered the time-varying case of a one-dimensional slab irradiated by a uniform heat source, and analyzed the effect of melt on the temperature distribution of the slab during the heat pulse. Rogerson and Chayt (1971) calculated the total melting time of a one-dimensional ablating slab subjected to constant heating (time and space) with complete removal of melt. They showed that the resultant time is independent of the transport properties of the material.

The theory of laser processing is further refined by allowing laser penetration into the material. Dabby and Paek (1972) considered such problems assuming that the material vaporizes at the surface; however, below the surface, the material is heated by absorption of laser energy and is allowed

Contributed by the Heat Transfer Division and presented at the ASME-JSME Thermal Engineering Joint Conference, Honolulu, Hawaii, March 22-27, 1987. Manuscript received by the Heat Transfer Division November 21, 1986. Keywords: Evaporation, Laser Processing, Materials Processing and Manufacturing Processes.

to attain temperatures higher than the vaporization temperature. These supercritical temperatures give rise to high pressures, and consequently material is expelled violently during the heating process. They used this model to explain the drilling process qualitatively. Wagner (1974) also considered drilling processes; however, unlike Paek and Gagliano, the absorption of heat was assumed to take place at the constant vaporization temperature. In a recent paper, Boersch-Supan et al. (1984) solved the steady conduction equation for a stationary semi-infinite medium under constant, but penetrating, irradiation. They overcome the difficulty of the moving boundary by allowing the solid to absorb radiation in-depth, which induces an in-depth solid-to-gas reaction. The newly formed gas escapes as rapidly as it is formed carrying sensible heat with it. The position of the moving boundary will now depend on the value of the local material density, since no distinct boundary exists, i.e., large values of density will denote the solid (unvaporized) region, and small values of it will correspond to the vaporized parts of the medium.

A further complication of the problem arises if the irradiation source is moved across the surface (cutting rather than drilling). Gonsalves and Duley (1972), by considering a uniform disk source, found the melting isotherm for a given fraction of absorbed laser energy. Modest and Abakians (1986b), by considering a CW Gaussian laser irradiating a moving semi-infinite slab, solved the steady conduction problem, and obtained the shape of the groove formed by this vaporization process.

In the present paper, the problem of partially vaporizing the surface of a moving semi-infinite body by irradiation from a penetrating CW laser with Gaussian intensity distribution is considered. We adopt the formalism introduced by Boersch-Supan et al. (1984), i.e., by assuming that the material removal is a volume rather than a surface phenomenon, which causes a change in the local density distribution. Assuming heat losses to be small, these losses are treated in an approximate fashion by a novel integral method using cubic splines for a profile. The resultant nonlinear equations are then solved numerically, and the result for the groove shape is presented for a variety of laser and solid parameters.

## Analysis

In order to obtain a realistic yet feasible description of the evaporation front on a solid irradiated by a moving Gaussian laser beam, the following simplifying assumptions will be made:

1 The solid moves at a constant velocity $u$;

2 All material properties such as thermal conductivity $k$, specific heat $c$, density $\rho$, and extinction coefficient $\beta$ are taken to be independent of temperature. Since in cutting applications conduction losses should be relatively small, temperature dependence of these properties is expected to have only a minor effect on the results.

3 Change of phase of the medium from solid to vapor occurs in one step at a single evaporation temperature $T_{ev}$; therefore, material is evaporating within a certain volume where the temperature is constant at $T_{ev}$. Since the medium is semitransparent, evaporation is expected to occur in-depth rather than only on the surface. Thus the energy lost to material removal will be accounted for by a change in the density. Material removal may be by complete evaporation (sublimation), or may be accompanied by the expulsion of liquid droplets and/or solid particles (micro-explosive removal). While the theoretical model based on this assumption will not predict a zero density groove anywhere, the groove is formed by blowing away those parts of the evaporating region with density below a certain (small) threshold. It is then possible to think of the evaporating region as a porous plug where the density varies between a minimum at the top flat surface of the body and $\rho_s$ at the solid surface. Thus, the extinction coefficient is assumed to be proportional to density $\rho$, or

$$\beta = \left(\frac{\beta_s}{\rho_s}\right)\rho \tag{1}$$

since $\beta$ should be zero where the density is zero, and should increase with density to a maximum value inside the solid; similarly, the thermal conductivity in the evaporating region is assumed to be proportional to density; however, since material removal takes place at a single temperature, the porous plug is isothermal without any conductive losses (regardless of the value of thermal conductivity in this region).

4 The evaporated material does not interfere with the laser beam reaching the surface. This will be a good assumption if the material is evaporated completely (and the vapor has no absorption band at the laser wavelength), or if a strong jet assist is employed to blow particles out of the laser irradiation path.

5 Multiple reflections and beam guiding (important for metals) of laser radiation within the groove are neglected. This is a severe limitation that restricts the present model to materials with high absorptivities (even at grazing angles), e.g., if the evaporation surface is rough. This would most likely occur in nonhomogeneous materials with stepwise evaporation; the present model is not suitable for materials with strong beam guiding, such as metals.

6 Surface heat losses due to convection and radiation are neglected since in a previous paper Modest and Abakians (1986b) showed that the effect of these surface losses on the final groove shape is indeed negligible, even in the presence of strong gas jets.

## Nomenclature

$c$ = specific heat
$F_o$ = laser flux at center of beam
$h_r$ = heat of material removal
$\hat{\mathbf{i}}, \hat{\mathbf{j}}, \hat{\mathbf{k}}$ = unit vectors in $x, y, z$ directions
$k$ = thermal conductivity
$\hat{\mathbf{n}}$ = unit vector normal to groove surface
$N_e$ = evaporation-to-laser power parameter
$N_k$ = conduction-to-laser power parameter
$R$ = effective laser beam radius
$s, S$ = groove depth
$S_{\max}$ = maximum groove depth
$S_\infty(\eta)$ = established groove cross section
$T$ = temperature
$T_{ev}$ = evaporation temperature
$T_\infty$ = ambient temperature
$u$ = laser scanning speed
$U$ = laser-to-diffusion speed parameter $= uR/\alpha$
$x, y, z$ = Cartesian coordinates
$\beta$ = material extinction coefficient
$\beta_s$ = extinction coefficient in the solid region
$\delta$ = thermal penetration depth
$\eta_{\max}(\xi)$ = local half-width of the groove
$\theta$ = nondimensional temperature
$\theta_o$ = nondimensional surface temperature
$\tau$ = nondimensional extinction coefficient $= \beta_s R$
$\rho$ = density
$\rho^*$ = nondimensional density
$\rho_s$ = density in the solid region
$\xi, \eta, \zeta$ = nondimensional $x, y, z$ coordinates

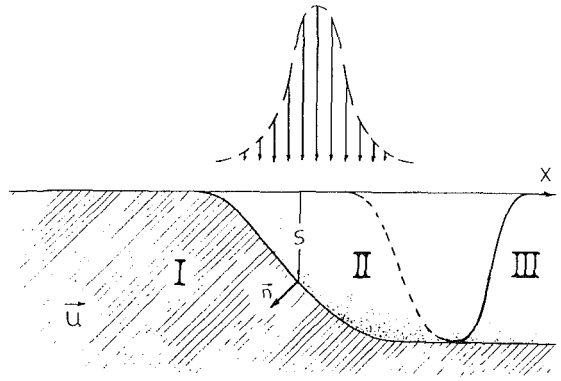


**Fig. 1 Identification of different regimes**

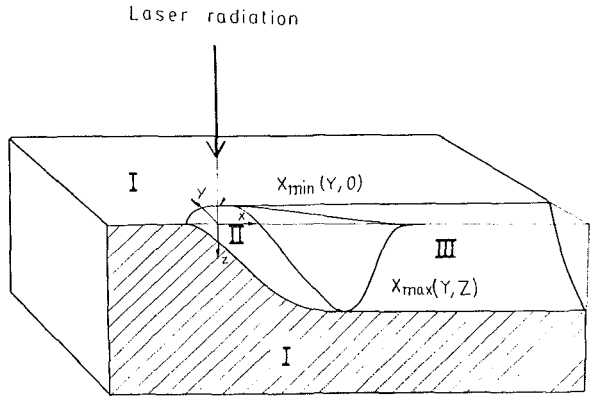


**Fig. 2 Coordinate system for groove formation**

We distinguish between three different regions (cf. Figs. 1 and 2). Region I is the entire semi-infinite body except for the evaporated region. It extends from $-\infty$ to $\infty$ in the $x$ and $y$ directions, and $S$ to $\infty$ in the $z$ direction ($S$ is the groove depth). This region is too far away laterally from the center of the beam (on the surface of the semi-infinite body, $x<x_{\min}(y, 0)$, or $|y|>y_{\max}$, where $y_{\max}$ is the half-width of the established groove), or too deep in the $z$ direction to ever undergo evaporation. Region II, or the porous plug, is the region closest to the center of the laser beam where evaporation is taking place. In this region the medium is at constant temperature $T_{ev}$ (assumption 3), while $\rho$ and $\beta$ are spatially varying, i.e., $\rho$ is minimum on the surface $z=0$, and increases sharply to $\rho=\rho_s$ within a thin layer near the solid body (region I). Finally, region III is the established tail of region II. Since the laser beam has moved too far away from this region, evaporation has ceased and the temperature has dropped below the evaporation temperature $T_{ev}$.

Under the above assumptions the steady-state heat transfer in region I for a moving body and stationary laser, with the coordinate system fixed at the center of the laser beam, is governed by

$$\rho_s c u\frac{\partial T}{\partial x}=k\nabla^2 T$$

$$+\beta_s F_o\exp\left\{-\frac{x^2+y^2}{R^2}-\beta_s(z-S)-\frac{\beta_s}{\rho_s}\int_0^S\rho dz\right\} \tag{2}$$

subject to the boundary conditions

$$x\to\pm\infty,\quad y\to\pm\infty,\quad z\to\infty:\quad T\to T_\infty \tag{3}$$

The necessary boundary condition at the surface $z=S$ is obtained from an energy balance on the surface adjoining regions I and II, resulting in $\hat{\mathbf{n}}\cdot(k\nabla T)|_{\text{regionII}}=\hat{\mathbf{n}}\cdot(k\nabla T)|_{\text{regionI}}=0$, since region II is isothermal and laser energy is delivered as a volume source, or

$$z=S,\quad x<x_{\max}(y, z),\quad |y|<\infty:\quad \hat{\mathbf{n}}\cdot\nabla T=0 \tag{4}$$

(This boundary condition is also valid in the warmup region, $x<x_{\min}(y, 0)$, since surface losses by convection and radiation are neglected.) Since evaporation takes place at a constant evaporation temperature $T_{ev}$, continuity of temperature between regions I and II additionally demands that

$$z=S,\quad x_{\max}(y, z)<x<x_{\min}(y, z),\quad |y|<y_{\max}(x):\quad T=T_{ev} \tag{5}$$

Here $T$ is the temperature of the medium, $u$ is the speed of the solid (in the positive $x$-direction) with respect to the stationary laser, and $\hat{\mathbf{n}}$ is the inward surface normal to region I (cf. Fig. 2). $F_o$ is the absorbed laser flux at the center of the beam, $R$ is the effective beam radius, and $S$ is the depth of the groove. For $x<x_{\min}(y, 0)$, $S$ is zero, and the source decay in the $z$ direction will be simply proportional to $\exp(-\beta_s z)$. The surface $x_{\max}(y, z)$ denotes the beginning of region III, i.e., the region where the temperature within the porous layer falls below the evaporation temperature $T_{ev}$.

To complete the system of equations, it is necessary to obtain a condition describing the variation of $\rho$ in the porous region. This is obtained by a volume energy balance in region II, resulting in

$$\frac{\beta_s}{\rho_s}\rho F_o\exp\left\{-\frac{x^2+y^2}{R^2}-\frac{\beta_s}{\rho_s}\int_0^z\rho dz\right\}+h_r u\frac{\partial\rho}{\partial x}=0 \tag{6}$$

subject to

$$x=x_{\min}(y, z):\quad \rho(x, y, z)=\rho_s \tag{7}$$

where $h_r$ is the heat of material removal (energy required to remove material per unit mass), be it by complete evaporation, or micro-explosive material removal.

Before attempting to solve the above set of equations, it is advantageous to introduce a number of nondimensional variables and parameters, viz.:

$$\xi=x/R,\quad \eta=y/R,\quad \zeta=z/R,\quad r^2=\xi^2+\eta^2; \tag{8}$$

$$s=S(x, y)/R,\quad \theta=(T-T_\infty)/(T_{ev}-T_\infty); \tag{9}$$

$$N_e=\rho_s h_r u/F_o,\quad N_k=k(T_{ev}-T_\infty)/RF_o,\quad U=\rho_s cuR/k; \tag{10}$$

$$\tau=\beta_s R,\quad \rho^*=\rho/\rho_s \tag{11}$$

Employing the definitions of equations (8) through (11), equations (2) to (7) may be rewritten as

$$U\frac{\partial\theta}{\partial\xi}=\nabla^2\theta+\frac{\tau}{N_k}\exp\left\{-r^2-\tau(\zeta-s)-\tau\int_0^\zeta\rho^*d\zeta\right\} \tag{12}$$

$$\xi\to\pm\infty,\quad \eta\to\pm\infty,\quad \zeta\to\infty:\quad \theta\to 0 \tag{13}$$

$$\zeta=s,\quad \xi<\xi_{\max}(\eta, \zeta),\quad |\eta|<\infty:\quad \mathbf{n}\cdot\nabla\theta=0 \tag{14}$$

$$\zeta=s,\quad \xi_{\min}(\eta, \zeta)<\xi<\xi_{\max}(\eta, \zeta),\quad |\eta|<\eta_{\max}(\xi, \zeta):\quad \theta=1 \tag{15}$$

$$\tau\rho^*\exp\left\{-r^2-\tau\int_0^\zeta\rho^*d\zeta\right\}+N_e\frac{\partial\rho^*}{\partial\xi}=0 \tag{16}$$

$$\xi=\xi_{\min}(\eta, \zeta):\quad \rho^*(\xi, \eta, \zeta)=1 \tag{17}$$

Equation (16) may be integrated exactly by first letting

$$\phi=\tau\int_0^\zeta\rho^*d\zeta \tag{18}$$

leading to

$$\ln\left(\frac{e^{\phi}-1}{e^{\phi_o}-1}\right)=-\frac{\tau\sqrt{\pi}}{2N_e}e^{-\eta^2}[\mathrm{erf}(\xi)-\mathrm{erf}\{\xi_{\min}(\eta,\ \zeta)\}] \tag{19}$$

where $\xi_{\min}(\eta,\ \zeta)$ is the $\xi$ location of the surface $s=s(\xi,\ \eta)$ for given $\eta$ and $s=\zeta$, and $\phi_o=\phi(\zeta=s)$. Employing equation (18) one may obtain the equation describing the variation of $\rho^*$ in region II as a function of $\xi$, $\eta$, and $\zeta$ as

$$\rho^*(\xi,\ \eta,\ \zeta)=\frac{1-e^{-\phi}}{1-e^{-\phi_o}}\left\{1+e^{-r2}\{e^{-\phi o}-1\}\{1-e^{-\xi 2-\xi^2_{\min}}\}\Big/\left(N_e\frac{\partial s}{\partial\xi}\right)\right\} \tag{20}$$

To complete the solution, $\phi_o$ must be determined. This is done by integrating equation (16) over $\zeta$ from 0 to $s$, and manipulating it somewhat to get

$$-e^{-r2}\{1-e^{-\phi_o}\}=\frac{N_e}{\tau}\frac{\partial\phi_o}{\partial\xi}-N_e\frac{\partial s}{\partial\xi} \tag{21}$$

with the boundary condition

$$\xi=\xi_{\min}(\eta,\ 0):\quad \phi_o=0 \tag{22}$$

Equation (12) with its boundary conditions (13), (14) describes the temperature field within the solid region, and equation (16) along with its boundary condition (17), or its solution equations (19) to (21), describes the density within the evaporating porous plug. The additional condition, equation (15), is required to determine the interface $s(\xi,\ \eta)$ between the two regions.

Since for a vast majority of applications depth, width, and general shape of the groove are desired (rather than accurate knowledge of the temperature field), and since the overall conduction losses are expected to be small, emphasis will be given to the groove geometry, and the heat losses will be handled only approximately. The condition loss (equation (12)) is modeled by making two additional assumptions:

7 Since the temperature drop inside the medium is strongest normal to the surface, the three-dimensional diffusion term may be replaced by a one-dimensional term in the direction normal to the surface, i.e., $\nabla^2\theta\simeq\partial^2\theta/\partial n^2$, where $n$ is distance along the surface normal $\hat{\mathbf{n}}$.

8 The conduction equation may be solved by the integral method, for which the temperature profile in the direction normal to the surface will be approximated by cubic splines.

In order to invoke assumption (7), one may introduce a coordinate transformation as: $\xi=\xi$, $\eta=\eta$, $n=n(\xi,\ \eta,\ \zeta)$; then equation (12) becomes

$$U\left\{\frac{\partial\theta}{\partial\xi}-\frac{\partial s}{\partial\xi}\frac{\partial\theta}{\partial n}\Big/\sqrt{1+\left(\frac{\partial s}{\partial\xi}\right)^2+\left(\frac{\partial s}{\partial\eta}\right)^2}\right\}=\frac{\partial^2\theta}{\partial n^2}+\frac{\tau}{N_k}e^{-r2}G(\xi,\ \eta,\ n) \tag{23}$$

$$\xi\to\pm\infty,\quad \eta\to\pm\infty,\quad n\to\infty:\quad \theta\to 0 \tag{24}$$

$$n=0:\quad \frac{\partial\theta}{\partial n}=0 \tag{25}$$

$$n=0,\quad \xi_{\min}(\eta,\ 0)<\xi<\xi_{\max}(\eta,\ 0),\quad |\eta|<\eta_{\max}(\xi):\quad \theta=1 \tag{26}$$

and

$$G(\xi,\ \eta,\ n)=\exp[-n^2\{(\hat{\mathbf{n}}\cdot\hat{\mathbf{i}})^2+(\hat{\mathbf{n}}\cdot\hat{\mathbf{j}})^2\}-n\{2\xi(\hat{\mathbf{n}}\cdot\hat{\mathbf{i}})+2\eta(\hat{\mathbf{n}}\cdot\hat{\mathbf{j}})\}-\phi_o(\xi+n\hat{\mathbf{n}}\cdot\hat{\mathbf{i}},\ \eta+n\hat{\mathbf{n}}\cdot\hat{\mathbf{j}})-\tau\{s(\xi,\ \eta)+n\ \hat{\mathbf{n}}\cdot\hat{\mathbf{k}}-s(\xi+n\ \hat{\mathbf{n}}\cdot\hat{\mathbf{i}},\ \eta+n\ \hat{\mathbf{n}}\cdot\hat{\mathbf{j}})\}] \tag{27}$$

is the source term in the new coordinate system.

To apply the integral method, the cubic splines must be determined first. It is expected that the temperature profile in the normal direction $\hat{\mathbf{n}}$ experiences an inflection point at some point, say $n=\delta_s$. This partial penetration depth $\delta_s$ is approximately the location where the effect of the heat source has become negligible, and beyond which (for $n>\delta_s$) the temperature profile in the medium is entirely due to heat diffusion. Thus, the temperature profile in the $n$ direction is described by two cubic splines, i.e., one for $0<n<\delta_s$, and one for $\delta_s<n<\delta$. To obtain the location of the inflection point approximately, we assume the heat source $G(\xi,\ \eta,\ n)$ in equation (23) to have a simple quadratic form, i.e., $G\simeq G_{os}(1-n/\delta_s)^2$, where $G_{os}$ is the source at $n=0$. Requiring this expression to have the same slope at $n=0$, and the same amount of total energy release in the $n$ direction as the source term $G(\xi,\ \eta,\ n)$, gives $\delta_s$ as

$$\delta_s^2=\frac{6H(\xi,\ \eta)}{\tau\sqrt{1+\left(\frac{\partial s}{\partial\xi}\right)^2+\left(\frac{\partial s}{\partial\eta}\right)^2}+(\hat{\mathbf{n}}\cdot\hat{\mathbf{i}})\left(\frac{\partial\phi_o}{\partial\xi}+2\xi\right)+(\hat{\mathbf{n}}\cdot\hat{\mathbf{j}})\left(\frac{\partial\phi_o}{\partial\eta}+2\eta\right)} \tag{28}$$

where

$$H(\xi,\ \eta)=\int_0^{\infty}G(\xi,\ \eta,\ n)dn \tag{29}$$

Eight conditions are required for the complete description of the two cubic splines; they are selected as:

(*a*) continuity of functional value at $\delta_s$,
(*b*) continuity of slope at $\delta_s$,
(*c*) continuity of curvature at $\delta_s$,
(*d*) zero curvature at $\delta_s$,
(*e*) satisfying equation (23) at $n=0$,
(*f*) surface temperature to be $\theta_o$ at $n=0$,
(*g*) zero temperature at $n=\delta$ ($\delta$ is the total penetration depth), and
(*h*) zero slope at $n=\delta$.

Satisfying the conduction equation at $n=0$ gives

$$\frac{\partial\theta_o}{\partial\xi}=-\frac{3\theta_o}{U\delta\delta_s}+\frac{\tau}{UN_k}e^{-r2-\phi o} \tag{30}$$

Invoking the other spline assumptions along with the boundary condition (26), equation (23) yields, after integrating over $n$,

$$\frac{\partial}{\partial\xi}\{\theta_o(3\delta+2\delta_s)\}+8\theta_o\frac{\partial s}{\partial\xi}\Big/\sqrt{1+\left(\frac{\partial s}{\partial\xi}\right)^2+\left(\frac{\partial s}{\partial\eta}\right)^2}=\frac{8\tau}{UN_k}e^{-r2}H(\xi,\ \eta) \tag{31}$$

with boundary conditions

$$\xi\to-\infty:\quad \theta\to 0,\quad \delta=\text{finite} \tag{32}$$

and the additional condition for determining $s(\xi,\ \eta)$

$$\xi_{\min}(\eta,\ 0) < \xi < \xi_{\max}(\eta,\ 0): \quad \theta = 1 \tag{33}$$

Despite the great simplifications introduced here, the problem requires the solution of four coupled equations (21), (28), (30), (31); three of these are first-order nonlinear partial differential equations in the region $-\infty < \xi < \xi_{\max}$, and $0 < \eta < \eta_{\max}(\xi)$ (the groove is symmetric about $\eta = 0$, although there may be a sharp apex at that location). However, the approach is simple and straightforward. Since for $\xi < \xi_{\min}(\eta,\ 0)$, $s = \phi_o = 0$, equation (28) simply reduces to $\delta_s = \sqrt{6}/\tau$; therefore, equations (30) and (31) are integrated in the $\xi$ direction from $-\infty$ to $\xi = \xi_{\min}(\eta,\ 0)$ at which point $\theta_o = 1$. We now have the equation for the boundary $\xi = \xi_{\min}(\eta,\ 0)$, along with initial values for $\delta$ and $\delta_s$. For $\xi_{\min}(\eta,\ 0) < \xi < \xi_{\max}(\eta,\ 0)$, equation (31) is discretized by a simple explicit-implicit scheme, which is unconditionally stable, and since $\theta_o = 1$, equation (30) takes the simple form of $\delta = 3N_k \exp(r^2 + \phi_o)/\tau\delta_s$. Thus, in order to predict $s$ at node $(\xi_i,\ \eta_j)$, it is assumed that all variables ($s$, $\delta$, $\delta_s$, $\phi_o$, and $\theta_o$) are known for every $\xi < \xi_i$, and $\eta > \eta_j$, and the iteration scheme proceeds by first assuming an $s$ for node $(i,\ j)$, then obtaining $\phi_o$ from equation (21), calculating $\delta_s$ from equation (28) and $\delta$ from equation (30); substituting $s$, $\phi_o$, $\delta$, $\delta_s$ into equation (31) gives the surface temperature $\theta_o$; the iteration on $s$ stops when $\theta_o$ is equal to 1. The solution for a given $\xi_i$ is started at $\eta = \eta_{\max}(\xi_i)$ (where $s = 0$), and marched inward in the $\eta$ direction toward $\eta = 0$.

## Discussion of Results

Figure 3 depicts the effect of variation of the nondimensional extinction coefficient $\tau$ on the evaporation zone. Here $U = 10$, $N_e = 0.1$, and $N_k = 0.1$. Due to diminishing conductive losses (increasing $\delta$, $\delta_s$) along the periphery of the groove, the maximum width is attained at a $\xi$ larger than zero. Beyond the maximum width (larger values of $\xi$), $\eta_{\max}$ decreases sharply back to zero because the slope of the groove becomes so large that the conductive heat losses use up most of the laser energy.

The influence of the latent heat-to-laser power parameter $N_e$ on the groove shape and depth is shown in Fig. 4. Here $U = 10$, $N_k = 0.1$ have been selected as representative, and the medium is taken to be moderately transparent at $\tau = 25$. Large values of $N_e$ ($N_e \simeq 1.0$) generally mean shallow grooves, and therefore relatively small heat losses (the ratio of groove surface to that normal to the laser beam is relatively small due to shallowness of the groove). A small $N_e$ implies large laser power $F_o$, or a small heat of removal $h_r$. Decreasing $N_e$ will increase the groove depth, but because of simultaneous increase of groove surface area, conductive losses will increase even though $N_k$ will remain unchanged. The broken line represents the depth at which the density attains 1 percent of its maximum value, $\rho_s$. As it is seen, the change in the density along the $z$ direction (near the surface $z = S$) is extremely sharp even for relatively large $N_e$ (for $N_e \leq 0.1$, the 1 percent density level nearly coincides with the solid lines where $\rho = \rho_s$), and only at a distance very near the solid surface does $\rho$ increase appreciably.

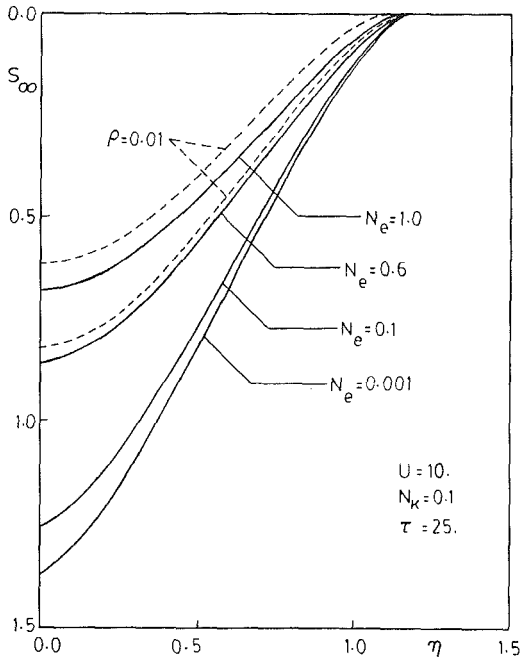


**Fig. 4 Influence of latent heat-to-laser power $N_e$ on groove depth and shape**

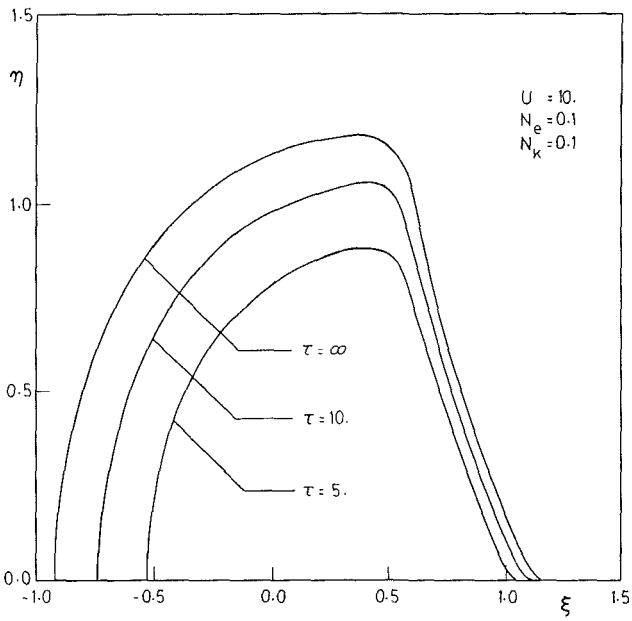


**Fig. 3 Top view of evaporation region for different extinction coefficient levels**

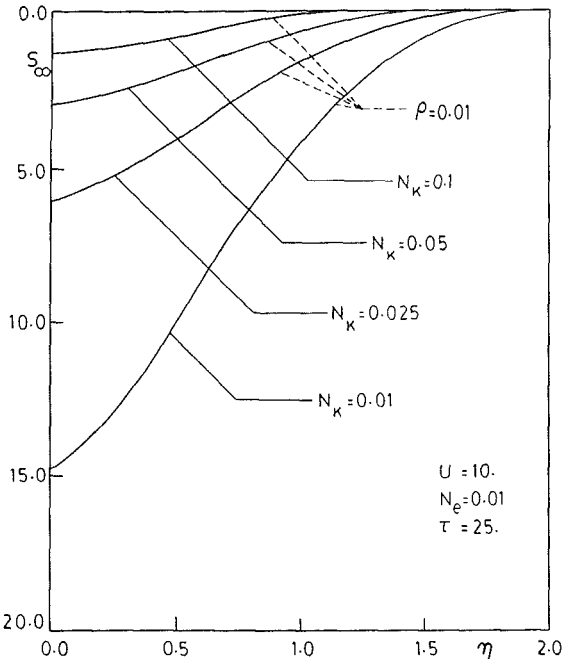


**Fig. 5 Influence of conduction losses on groove and shape**

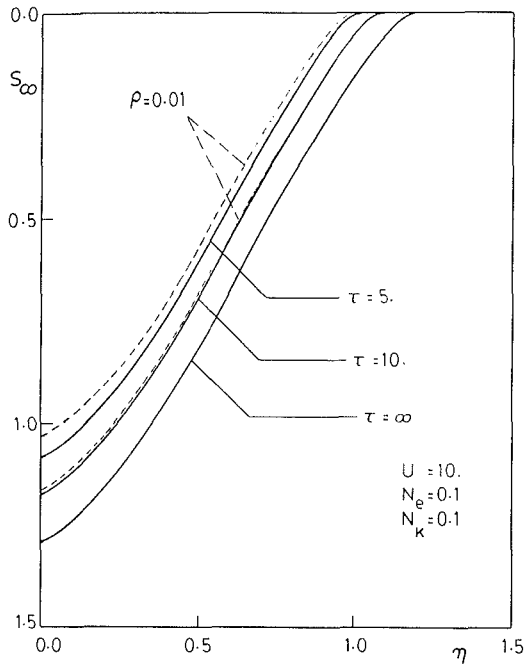


**Fig. 6 Influence of the extinction coefficient on groove depth and shape**

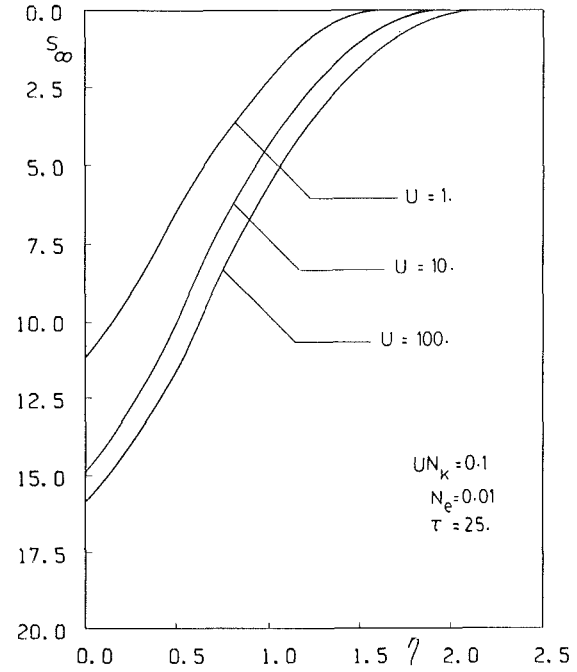


**Fig. 7 Influence of laser scanning speed $U$ on groove depth and shape**

Changes in the groove shape and depth for different values of the conduction loss parameter $N_k$ are shown in Fig. 5. In this plot $U=10$, $N_e=0.01$, and $\tau$ is taken to be 25. For large values of $N_k$, the laser energy is mostly taken away by conductive losses, explaining the shallow groove. Decreasing $N_k$ will reduce conductive losses, but this decrease will not be as rapid as the decrease in $N_k$, since for a deep groove (small $N_e$), the ratio of the groove area to area normal to the laser beam becomes very large. For moderate $N_e$ ($N_e \simeq 0.01$) the 1 percent density line nearly coincides with the solid surface even for relatively large values of $N_k$, as indicated in the figure.

The effect of the nondimensional extinction coefficient $\tau$ on the final groove shape and depth is depicted in Fig. 6. $U=10$, and $N_k$, $N_e$, are both taken relatively large as 0.1. For $\tau=\infty$ the entire laser energy is deposited on the surface; thus as $\tau$ is decreased, the surface temperature is lowered and, consequently, the evaporation zone and the maximum groove depth are reduced. The broken lines again represent the depth at which density attains 1 percent of its maximum value. As $\tau$ is decreased, the 1 percent density line drifts away from the solid surface, and the porous region begins to fill up (ideally, for $\tau=0$, the porous region will be totally filled, and no evaporation will take place). Despite a different approach in this paper (including a somewhat different conduction model), the solution for $\tau=\infty$ coincides exactly with previous results (cf. Modest and Abakians, 1986b).

Figure 7 shows the effect of $U$, the ratio of laser scanning speed to that of heat diffusion into the medium, on the final groove depth $s_\infty$. In this case the medium is taken to be fairly opaque at $\tau=25$, $N_e$ is at a relatively small value of 0.01, and $U\times N_k$ is kept constant at 0.01. Keeping $U\times N_k$ constant ensures that the irradiated energy/unit area will remain constant. Thus increasing $U$ will decrease conduction losses, and the maximum groove depth will increase.

Finally, Fig. 8 depicts the variation of total material removal (per unit time) as a function of the extinction coefficient $\tau$. Here $U=10$, $N_k$ is taken as 0.1. For small $\tau$, the source penetrates a large distance into the medium making the penetration depth ($\delta_s$, $\delta$) very large. This in turn reduces the evaporation zone, and very little material is removed;

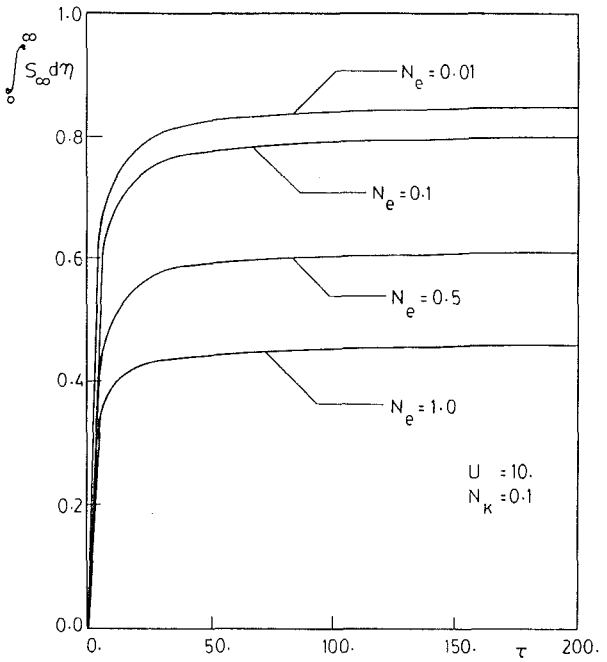


**Fig. 8 Total material removal as a function of extinction coefficient for different $N_e$ levels**

however, for large $\tau$ the source is concentrated close to the surface, and material removal attains its maximum value.

## Summary

A fairly simple model has been developed to predict the shape of a groove formed by partially evaporating the surface of a semi-infinite, semitransparent body using a moving, Gaussian laser beam. It is observed that already for moderately small extinction coefficients ($\tau \simeq 10$), the maximum groove depth and shape is not very different from the surface deposition case ($\tau \to \infty$). Therefore, one of the major conclusions of

the present work is that, unless the medium is very transparent, laser deposition of energy may usually be treated as a surface phenomenon.

At this point the model is still fairly primitive, but it will be useful for predicting the ranges of values for which the nondimensional parameters $N_e$, $N_k$, $U$, and $\tau$ will produce an efficient laser cut. The model will also be able to predict groove depths quantitatively for a few idealized situations. For accurate quantitative results, a number of the simplifying assumptions need to be relaxed in future development; in particular assumptions (3) (evaporation mechanism), and (5) (beam guiding, to include more realistic materials with moderate absorptivities).

## Acknowledgments

Support of this work by the National Institute of Arthritis, Diabetes, Digestive, and Kidney Diseases under Grant No. AM30240 is gratefully acknowledged.

## References

Boersch-Supan, W., Hunter, L. W., and Kuttler, J. R., 1984, "Endothermic Gasification of a Solid by Thermal Radiation Absorbed in Depth," *Int. J. Heat Mass. Trans.*, Vol. 27, pp. 1171–1182.

Brugger, K., 1972, "Exact Solutions for the Temperature Rise in a Laser Heated Slab," *J. Appl. Phys.*, Vol. 43, pp. 577–583.

Bunting, K. A., and Cornfield, G., 1975, "Toward a General Theory of Cutting: a Relationship Between the Incident Power Density and the Cut Speed," ASME JOURNAL OF HEAT TRANSFER, Vol. 97, pp. 116–121.

Carslaw, H. S., and Jaeger, J. C., 1959, *Conduction of Heat in Solids*, 2nd ed., Oxford University Press, United Kingdom.

Cline, H. E., and Anthony, T. R., 1977, "Heat Treating and Melting Material With a Scanning Laser or Electron Beam," *J. Appl. Phys.*, Vol. 48, pp. 3895–3900.

Dabby, F. W., and Paek, U.-C., 1972, "High-Intensity Laser-Induced Vaporization and Explosion of Solid Material," *IEEE J. Quant. Elect.*, Vol. QE-8, pp. 106–111.

Dobrovol'skii, I. P., and Uglov, A. A., 1974, "Analysis of the Heating of Solids by Laser Radiation Allowing for the Temperature Dependence of the Absorptivity," *Soviet Physics—Doklady*, Vol. 4, pp. 788–790.

Gonsalves, J. N., and Duley, W. W., 1972, "Cutting Thin Metal Sheets With the CW $CO_2$ Laser," *J. Appl. Phys.*, Vol. 43, pp. 4684–4687.

Landau, H. G., 1950, "Heat Conduction in a Melting Solid," *Quart. Appl. Math.*, Vol. 8, pp. 81–94.

Masters, J. I., 1956, "Problem of Intense Surface Heating of a Slab Accompanied by Change of Phase," *J. Appl. Phys.*, Vol. 27, pp. 477–484.

Maydan, D., 1970, "Fast Modulator for Extraction of Internal Laser Power," *J. Appl. Phys.*, Vol. 41, pp. 1552–1559.

Maydan D., 1971, "Micromachining and Image Recording on Thin Films by Laser Beams," *Bell System Technical Journal*, Vol. 50, pp. 1761–1789.

Modest, M. F., and Abakians, H., 1986a, "Heat Conduction in a Moving Semi-infinite Solid Subjected to Pulsed Laser Irradiation," ASME JOURNAL OF HEAT TRANSFER, Vol. 108, pp. 597–601.

Modest, M. F., and Abakians, H., 1986b, "Evaporative Cutting of a Semi-infinite Body With a Moving CW Laser,"ASME JOURNAL OF HEAT TRANSFER, Vol. 108, pp. 602–607.

Nissim, Y. I., Lietoila, A., Gold, R. B, and Gibbons, J. F., 1980, "Temperature Distributions Produced in Semiconductors by a Scanning Elliptical or Circular CW Laser Beam," *J. Appl. Phys.*, Vol. 51, pp. 274–279.

Paek, U.-C., and Gagliano, F. P., 1972, "Thermal Analysis of Laser Drilling Processes," *IEEE J. Quant. Electronics*, Vol. QE-8, pp. 112–119.

Podolsky, B., 1951, "A Problem in Heat Conduction," *J. Appl. Phys.*, Vol. 22, pp. 581–585.

Ready, J. F., 1971, *Effects of High Power Laser Radiation*, Academic Press, New York.

Rogerson, J. E., and Chayt, G. A., 1971, "Total Melting Time in the Ablating Slab Problem," *J. Appl. Phys.*, Vol. 42, pp. 2711–2713.

Rykalin, N. N., Uglov, A. A., and Makarov, N. I., 1967, "Effects of Peak Frequency in a Laser Pulse on the Heating of Metal Sheets," *Soviet Physics—Doklady*, Vol. 12, pp. 644–646.

Rykalin, N. N., Uglov, A. A., and Nizametdinov, M. M., 1977, "Calculation of the Heating of Materials by Laser Radiation Allowing for the Temperature Dependences of Thermal Properties," *Soviet Physics—Doklady*, Vol. 17, pp. 853–856.

Rykalin, N. N., Uglov, A. A., and Smurov, I. Yu., 1982, "Nonlinearities of Laser Heating of Metals," *Soviet Physics—Doklady*, Vol. 27, pp. 970–972.

Soodak, H., 1943, *Effects of Heat Transfer Between Gases and Solids*, Ph.D. Thesis, Duke University, Durham, NC.

Wagner, R. E., 1974, "Laser Drilling Mechanics," *J. Appl. Phys.*, Vol. 45, pp. 4631–4637.

Warren, R. E., and Sparks, M., 1979, "Laser Heating of a Slab Having Temperature Dependences of Thermal Properties," *J. Appl. Phys.*, Vol. 50, pp. 7952–7957.

White, R. M., 1963a, "Elastic Wave Generation by Electron Bombardment or Electromagnetic Wave Absorption," *J. Appl. Phys.*, Vol. 34, pp. 2123–2124.

White, R. M., 1963b, "Generation of Elastic Waves by Transient Surface Heating," *J. Appl. Phys.*, Vol. 34, pp. 3559–3567.

# Effects of Natural Convection on Ice Formation Around an Isothermally Cooled Horizontal Cylinder

K. C. Cheng

H. Inaba[1]

R. R. Gilpin[2]

Department of Mechanical Engineering,
University of Alberta,
Edmonton, Alberta, Canada T6G 2G8

*The effects of maximum density near 4°C on steady-state, two-dimensional ice formation around an isothermally cooled horizontal cylinder in a quiescent water bath are studied experimentally for ambient water temperature $T_\infty = 1.9$ to 18.0 °C and cylinder surface temperature $T_w = -20.0$ to $-16.2$°C. The stagnation point Nusselt number, local heat transfer coefficient, and average Nusselt number behavior at the ice-water interface are studied using such parameters as ambient temperature, Rayleigh number, and a modified Grashof number $Gr_d^*$. The temperature field in the ice layer is determined from the measured ice profiles by a point-matching method using a series solution of the Laplace equation in the ice. The average ice layer thickness and total low-temperature heat stored in the ice layer can be correlated using the parameter $Gr_d^{*0.5}/\theta_c^2$. A flow direction inversion region exists in the range $T_\infty = 5.2$ to 8.1°C, $Gr_d^* = 3.8 \times 10^4$ to $1.3 \times 10^5$, and a minimum Nusselt number behavior occurs at $T_\infty = 5.2$°C. Flow visualization photographs of the flow patterns near the ice surface are presented for $T_\infty = 3.8$, 5.2, 8.1, and 12.1°C.*

## 1 Introduction

Freezing and melting heat transfer problems involving ice-water systems occur in various industrial processes and natural phenomena, and have been studied by many investigators in recent years. The classical Stefan problem is a limiting case considering only the conduction process. For practical problems, one must consider natural, forced, or mixed convection effects. Consideration is given here to the natural convection effects only. Water exhibits maximum density at 3.98°C, and the conventional Boussinesq approximation for a monotonic density-temperature relationship is not applicable. Thus, the theoretical analysis for the freezing or melting heat transfer problem in ice-water systems at 4°C becomes rather difficult and is limited to such geometric shapes as vertical plates, vertical or horizontal cylinders, and spheres for the case of external flow.

Phase-change (solidification and melting) heat transfer problems have been well reviewed by Viskanta (1983) and Epstein and Cheung (1983, 1984) recently. The effects of maximum density on natural convection around melting ice spheres were studied by Dumore et al. (1953), Merk (1954), Schenk and Schenkels (1968), Vanier and Tien (1969), and others. Similar work on a vertical ice slab immersed in cold water was reported by Bendell and Gebhart (1976), where further references can be found. Saitoh (1976) reported theoretical (numerical) and experimental studies on natural convection heat transfer from a melting horizontal ice cylinder and observed three-dimensional instability phenomena for a bulk temperature of 6.0°C. It is of interest to note that these studies reveal minimum stagnation point Nusselt number behavior in a flow reversal region due to the maximum density effect. In Saitoh's experiments, the measurement of the stagnation point heat transfer coefficient for a melting horizontal ice cylinder and the understanding of heat transfer mechanism in flow inversion region were the primary goals. The peculiar minimum heat transfer behavior for melting ice spheres observed first by Dumore et al. (1953) and Merk (1954) in the flow inversion region was confirmed by Saitoh (1976) for the case of a melting horizontal ice cylinder.

The effect of natural convection on ice formation around an isothermally cooled horizontal cylinder in water was studied numerically by Saitoh and Hirose (1981). They clarified the steady freezing front contour, the temperature distribution in the solid phase, isotherm, streamlines, and the variations of the average and forward stagnation Nusselt numbers with water temperature, cooled cylinder surface temperature, and cylinder diameter. The effect of natural convection on transient freezing of superheated water around an isothermal, horizontal cylinder was studied experimentally by Herrmann et al. (1984). Flow visualization by shadowgraph technique for flow around test cylinder (dia = 25 mm) in a cylindrical test cell of 100 mm diameter and 76 mm length revealed dendritic ice formation and convective instability causing waviness of the ice-water interface. Ice contours during freezing of water and variation of frozen volume as a function of dimensionless time are presented. Heat transfer during the unsteady outward solidification of paraffin around a cooled horizontal cylinder was studied experimentally and analytically by Bathelt et al. (1979) and the results show significant natural convection effects. Similar ice formation problems involving vertical cylinders were studied by Chao and Schoenhals (1981) and Cheng and Sabhapathy (1985) recently.

The purpose of this paper is to report experimental results on steady-state ice formation around an isothermally cooled cylinder in a body of quiescent water in the temperature range $T_\infty = 1.9$ to 18.0°C. The local and average heat transfer coefficients at the ice-water interface were determined from measured ice profiles from photographs of an ice layer by a collocation method using an exact series solution of the Laplace equation in the ice layer. Flow visualization photographs for natural convection flow near the ice surface obtained by dye injection method are also presented. The present results and the earlier results from experimental investigation of ice formation around isothermally cooled

[1] Present address: Department of Mechanical Engineering, Kitami Institute of Technology, Hokkaido, Japan.

[2] Deceased in 1982.

Contributed by the Heat Transfer Division for publication in the JOURNAL OF HEAT TRANSFER. Manuscript received by the Heat Transfer Division December 18, 1986. Keywords: Flow Visualization, Natural Convection, Phase-Change Phenomena.

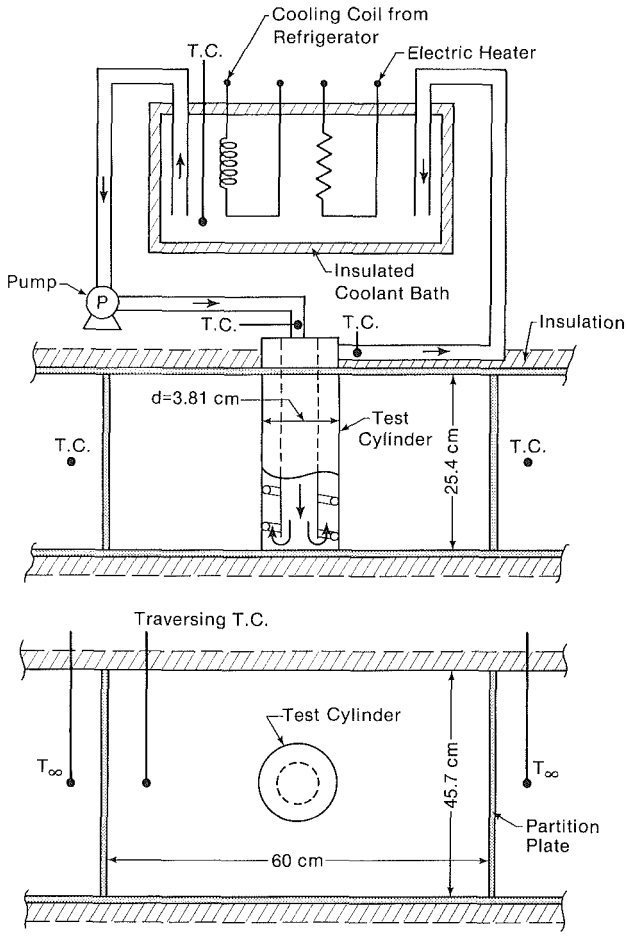


**Fig. 1 Schematic diagram of experimental apparatus**

cylinder in crossflow (Cheng et al., 1981) have application in cold storage systems for cooling applications. The correlation equations obtained using the characteristic ice formation parameter $Gr_d^{*0.5}/\theta_c^2$ enable one to estimate the amount of ice formation and low-temperature heat storage in an ice layer around a cylinder. The experimental results for stagnation point Nusselt number are compared with the experimental results from a melting horizontal ice cylinder by Saitoh (1976).

## 2 Experimental Apparatus and Procedure

A schematic of the experimental apparatus is shown in Fig. 1. The present experimental apparatus is modified from that used by Cheng et al. (1981) by introducing two vertical partition plates. The rectangular test vessel measures 25.4 cm wide, 45.7 cm high, and 60 cm long. The copper test cylinder (38.1 mm o.d., wall thickness 1.5 mm, and length 254 mm) was placed horizontally at the center of the test section. A coiled spring was inserted in the annular space (see Fig. 1) in order to promote turbulence of the coolant (a mixture of glycol, alcohol, and water) circulating in the test cylinder for high heat transfer rates. The coolant was circulated at a high velocity between the test cylinder and a temperature-controlled bath with a temperature range of 0 to $-25°C$. The nearly constant surface temperature of the test cylinder was confirmed since the inlet and outlet temperatures of the coolant at the test cylinder were within 0.1°C of each other. The ambient water temperatures on both sides of each partition plate were controlled at a given temperature between 1.9 and 18°C. Other side walls of the test section were covered with insulation materials. The two dimensionality of the flow and temperature fields around the horizontal cylinder were confirmed by the observation that the ice layer around the cylinder was axially uniform except for a small region near the transparent wall of the rectangular test section.

After reaching a steady state by checking the given experimental conditions and the termination of ice growth with time as shown by a constant ice layer thickness, the ice contour was recorded photographically. Steady state was reached in 20 to 50 h depending on experimental conditions. The flow pattern for natural convection flow around the cylinder was visualized by injecting black drawing ink through a small stainless steel tube (0.8 mm dia) near the ice surface. A 76-$\mu$m-dia copper-constantan thermocouple formed in the shape of a

## Nomenclature

$A$ = temperature difference ratio $=(T_m-T_\infty)/(T_f-T_m)$
$A_0, B_0, A_n, B_n$ = coefficients defined in equation (3)
$C_{pi}$ = specific heat of ice
$Ds$ = effective diameter of ice near forward stagnation point
$D_m$ = mean diameter of ice layer
$d$ = cylinder diameter
$Gr_d^*$ = modified Grashof number
$g$ = gravitational acceleration
$h$ = heat transfer coefficient
$h_m, h_{n,\phi}$ = average and local heat transfer coefficients
$k_i, k_w$ = thermal conductivities for ice and water
$L_i$ = latent heat of fusion per unit volume
$Nu_d, Nu_{Ds}$ = Nusselt numbers $=h_m d/k_w$ (average) and $hDs/k_w$ (stagnation point)
$Q_t$ = total heat stored in ice layer per unit axial length, m
$R, R_1, R_2$ = radial coordinate, outside radius of cylinder, and radial coordinate of ice-water interface
$Ra_{Ds}$ = Rayleigh number $=g\beta\Delta TDs^3/\nu\alpha$
$r$ = dimensionaless radial coordinate $=R/R_1$
$T$ = temperature
$T_f, T_m, T_w, T_\infty$ = freezing temperature of water, temperature at maximum density, surface temperature of cylinder, and ambient temperature
$\Delta T$ = temperature difference $=(T_\infty-T_f)$
$V_i$ = ice volume per unit length of cylinder, m
$\alpha$ = thermal diffusivity
$\beta$ = coefficient of thermal expansion
$\gamma_i$ = specific weight of ice
$\gamma_1, \gamma_2$ = temperature coefficients of density-temperature relationship (Sun et al., 1969), $\gamma_1=0.793953\times10^{-5}$ °C$^{-2}$, $\gamma_2=-0.655908\times10^{-7}$ °C$^{-3}$
$\delta_{im}$ = mean ice layer thickness
$\theta$ = dimensionless temperature $=(T-T_w)/(T_f-T_w)$
$\theta_c$ = cooling temperature ratio $=(T_f-T_w)/(T_\infty-T_f)$
$\nu$ = kinematic viscosity
$\phi$ = angular position measured from the top of cylinder
$\Psi$ = angle defined in Fig. 2

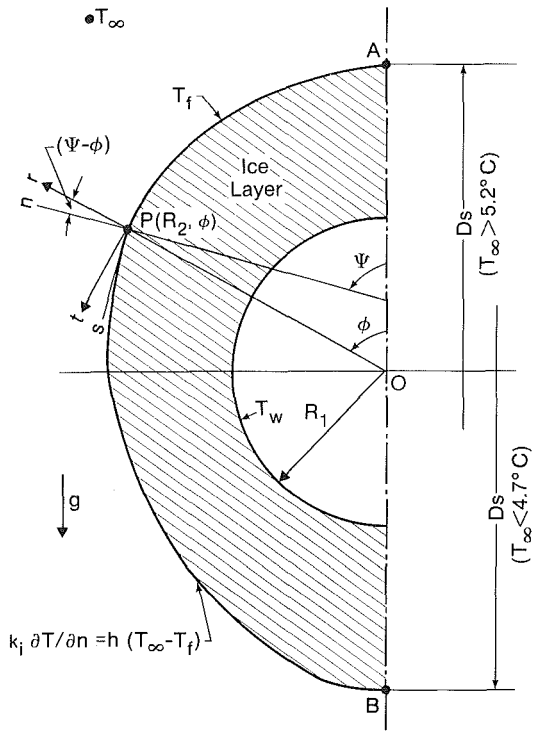


**Fig. 2 Coordinate system and ice layer around cylinder**

loop was mounted on a traversing system. A standard thermometer was used to measure the ambient water temperature.

## 3 Data Reduction

**3.1 Temperature Field in Ice Layer.** At steady state the temperature field must satisfy the Laplace equation and the boundary conditions (see Fig. 2)

$$\frac{\partial^2\theta}{\partial r^2}+\frac{1}{r}\frac{\partial\theta}{\partial r}+\frac{1}{r^2}\frac{\partial^2\theta}{\partial\phi^2}=0 \tag{1}$$

$$\theta=0(T=T_w) \text{ at } r=1 \quad \text{(cylinder surface)}$$

$$\theta=1(T=T_f) \text{ at } r=R_2/R_1 \quad \text{(interface)} \tag{2}$$

Considering symmetry of the ice layer profile with respect to the vertical axis, the exact series solution (Hildebrand, 1962) becomes

$$\theta=A_0+B_0\ln r+\sum_{n=1,2,3,\ldots}^{\infty}(A_n r^n+B_n r^{-n})\cos n\phi \tag{3}$$

The boundary condition at cylinder surface ($r=1$) $\theta=0$ can be satisfied exactly and the unknown coefficients can be determined by a point-matching method satisfying the boundary condition $\theta=1$ at 20 equi-angular spaced points ($n=20$) along the ice profile AB (see Fig. 2) It is noted that supercooling will occur before the nucleation of ice on cylinder surface. After the ice formation, supercooling will not occur at the ice-water interface. Thus, the interface temperature is 0°C. The maximum error for $\theta$ occurs at the interface boundary. Maximum boundary errors were found to be less than $\pm 10^{-8}$ in comparison with the exact value $\theta=1$. This observation confirms the convergence of the solution and the accuracy of the numerical method used is similar to that described in Cheng et al. (1981). The point-matching method is known to provide accurate numerical solution when the deviation of the boundary shape from circular is not appreciable.

**Table 1 Ranges of experimental parameter values**

| Symbols | $T_w$, °C | $T_\infty$, °C | $\theta_c$ | $Gr^*_d$ |
|---|---|---|---|---|
| ○ | -19.0 | 1.9 | 10.0 | $2.29 \times 10^4$ |
| ● | -19.6 | 2.7 | 7.28 | $3.28 \times 10^4$ |
| ◑ | -19.7 | 3.4 | 5.79 | $4.17 \times 10^4$ |
| ◐ | -19.1 | 3.8 | 5.03 | $4.85 \times 10^4$ |
| ◓ | -17.5 | 4.7 | 3.72 | $6.18 \times 10^4$ |
| ◒ | -19.9 | 5.2 | 3.83 | $6.97 \times 10^4$ |
| ⊕ | -16.3 | 6.0 | 2.72 | $8.24 \times 10^4$ |
| □ | -19.9 | 6.3 | 3.16 | $8.76 \times 10^4$ |
| ■ | -19.0 | 6.8 | 2.79 | $9.60 \times 10^4$ |
| ⊖ | -16.5 | 7.0 | 2.36 | $9.95 \times 10^4$ |
| ◨ | - 19.9 | 7.4 | 2.69 | $1.07 \times 10^5$ |
| ◧ | -16.2 | 8.0 | 2.03 | $1.17 \times 10^5$ |
| ◑ | -16.7 | 8.1 | 2.06 | $1.19 \times 10^5$ |
| △ | -20.0 | 8.1 | 2.47 | $1.19 \times 10^5$ |
| ◐ | -19.8 | 8.6 | 2.30 | $1.28 \times 10^5$ |
| ◔ | -18.5 | 9.8 | 1.89 | $1.52 \times 10^5$ |
| ▽ | -19.7 | 11.4 | 1.73 | $1.84 \times 10^5$ |
| ▲ | -16.5 | 11.7 | 1.41 | $1.91 \times 10^5$ |
| ⊕ | -16.2 | 12.1 | 1.34 | $2.00 \times 10^5$ |
| ▼ | -19.0 | 14.1 | 1.35 | $2.80 \times 10^5$ |
| ◔ | -19.8 | 18.0 | 1.10 | $3.35 \times 10^5$ |

**3.2 Determination of Local Heat Transfer Coefficient.** At steady state, the local heat transfer coefficient $h$ at the ice-water interface can be determined from

$$h(T_\infty-T_f)-k_i\frac{\partial T}{\partial n}\bigg|_{R=R_2}=0 \tag{4}$$

At any angular position $\phi$, the local heat transfer coefficient $h_n,\phi$ can be written as

$$h_{n,\phi}=k_i\frac{(T_f-T_w)}{(T_\infty-T_f)}\frac{1}{R_1}\left[\frac{(\sin\bar{\Psi}-\phi)}{r_2}\frac{\partial\theta}{\partial\phi}\bigg|_{r=r_2}+\cos(\bar{\Psi}-\phi)\frac{\partial\theta}{\partial r}\bigg|_{r=r_2}\right] \tag{5}$$

The direction of the external normal $n$ at any point on the ice-water interface was determined by considering the chord subtended by the two neighboring points located at $\pm 2.5$ deg from an angle $\phi$. The accuracy of the calculation was also confirmed from the agreement of the total heat transfer rates through the cooling cylinder surface and the ice-water interface within 1 percent. In order to minimize the measuring errors of the ice profiles, the photographs of the ice layer were enlarged two to three times.

## 4 Results and Discussion

The ranges of experimental conditions in this study are shown in Table 1. The ranges of the dimensionless parameters, modified Grashof number $Gr^*_d$ (Sun et al., 1969) and cooling temperature ratio $\theta_c$, defined below, are

$$Gr^*_d = (gd^3/\nu^2)[2\gamma_1 A(\Delta T)^2](1+(3\gamma_2/2\gamma_1)A\Delta T)$$

$$= 2.3\times 10^4 \sim 3.4\times 10^5$$

$$\theta_c = (T_f-T_w)/(T_\infty-T_f)=1.10\sim 10.0$$

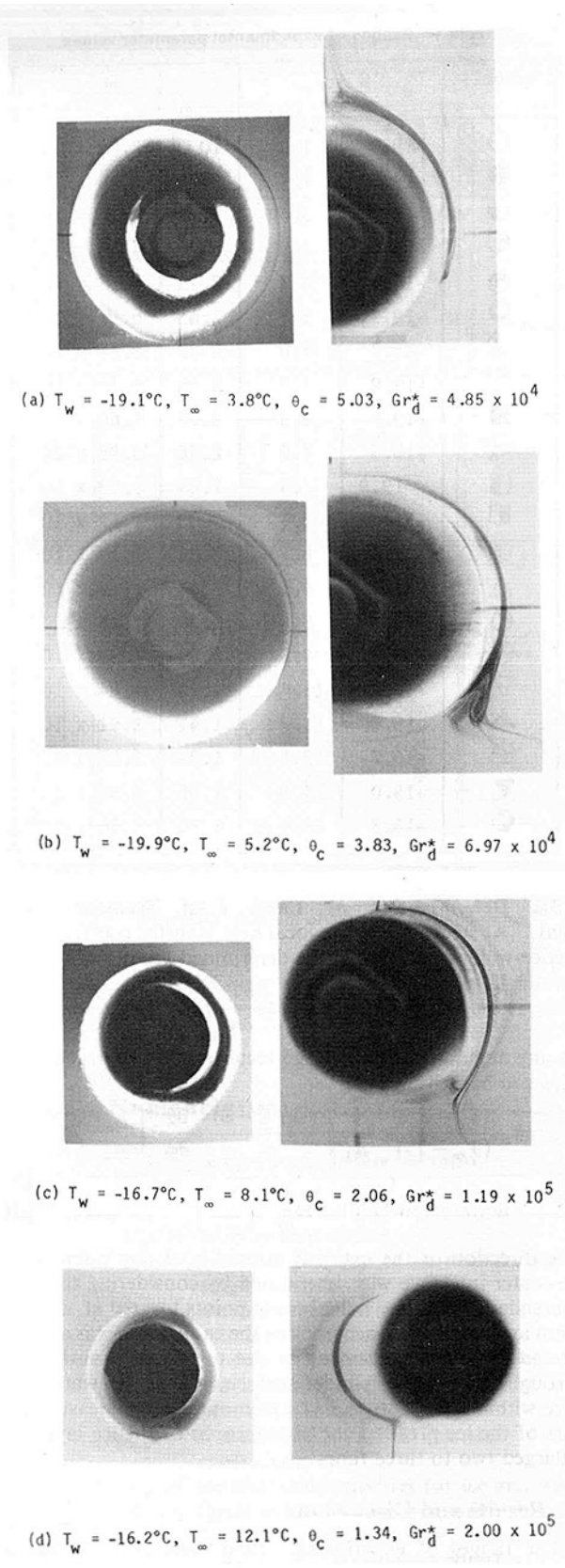


**Fig. 3 Photographs of ice profile and flow pattern**

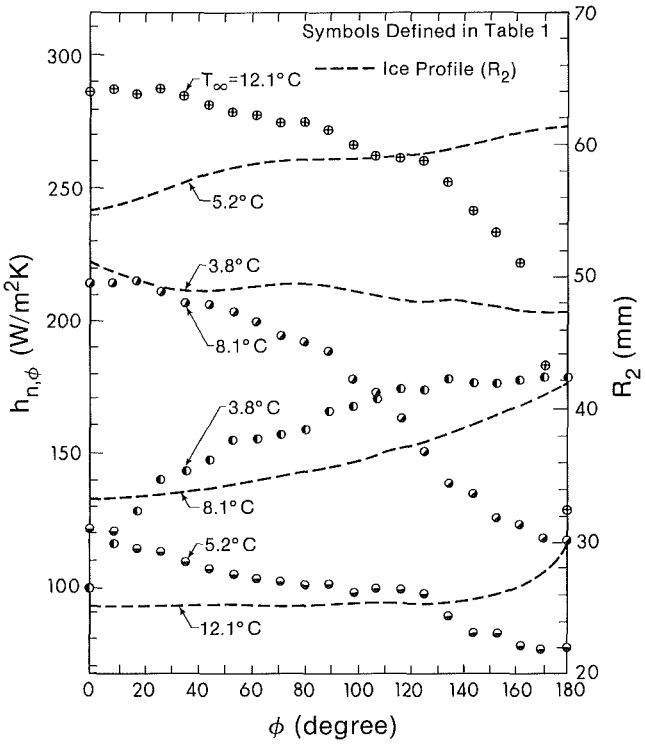


**Fig. 4 Local heat transfer coefficient distributions and ice profiles for $T_\infty = 3.8$, 5.2, 8.1, and 12.1°C**

**4.1 Ice Layer Profile and Flow Visualization.** Photographs in Fig. 3 show the shape of the steady-state ice layer and the flow pattern of natural convection flow around the cylinder for four different conditions. The deviation of the ice-water interface from the circular represents the natural convection effect. The ice thickness as shown in Fig. 3(*a*) for $T_w = -19.1$°C and $T_\infty = 3.8$°C increases gradually from the bottom of the cylinder ($\phi = 180$ deg) toward the top of the cylinder ($\phi = 0$ deg). The water flow near the ice-water interface is from bottom to top, and the boundary layer thickness increases gradually toward the top. The stagnation point is located at the bottom. It is noted that a negative thermal expansion coefficient exists for this case.

For the case with $T_w = -19.9$°C and $T_\infty = 5.2$°C as shown in Fig. 3(*b*), the near flow is from top to bottom and the ice layer thickness increases gradually from top to bottom. A vortex flow can be seen near the bottom; the complex flow pattern with upward flow near the ice surface and downward flow away from the ice surface is due to the density inversion near 4°C. Apparently, boundary layer theory is not applicable in this region.

For the case in which $T_w = -16.7$°C and $T_\infty = 8.1$°C as shown in Fig. 3(*c*), the flow is basically downward and the ice layer thickness is seen to be smaller than that of Figs. 3(*a*) and 3(*b*). The natural convection effect is seen to be large. The ice thickness at the top is considerably smaller than that at the bottom. The convective inversion effect is smaller for this case.

For the case in which $T_w = -16.2$°C and $T_\infty = 12.1$°C as shown in Fig. 3(*d*), the boundary layer for downward flow is seen to be relatively small and the upward flow near the bottom observed in Figs. 3(*b*) and 3(*c*) disappears. Thus, it appears that the density inversion may be neglected when $T_\infty \gtrsim 10$°C. The ice thickness at the bottom is seen to be quite large due to the merging of the two boundary layers there. Thus, a sharp tail may appear under certain conditions. With water near 4°C, the flow visualization using dye injection becomes difficult because of weak natural convection flow. The intention here is to show the shape of the ice profile and the general idea of flow pattern.

**4.2 Local Heat Transfer Coefficient.** The ice profile and the variation of local heat transfer coefficient with angle $\phi$ for

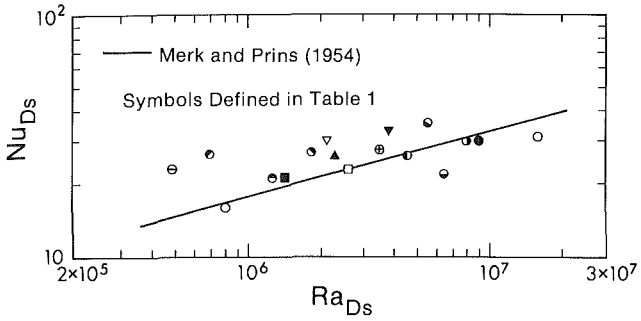


**Fig. 5 $Nu_{Ds}$ versus $Ra_{Ds}$ relationship for cases with and without maximum density effect**

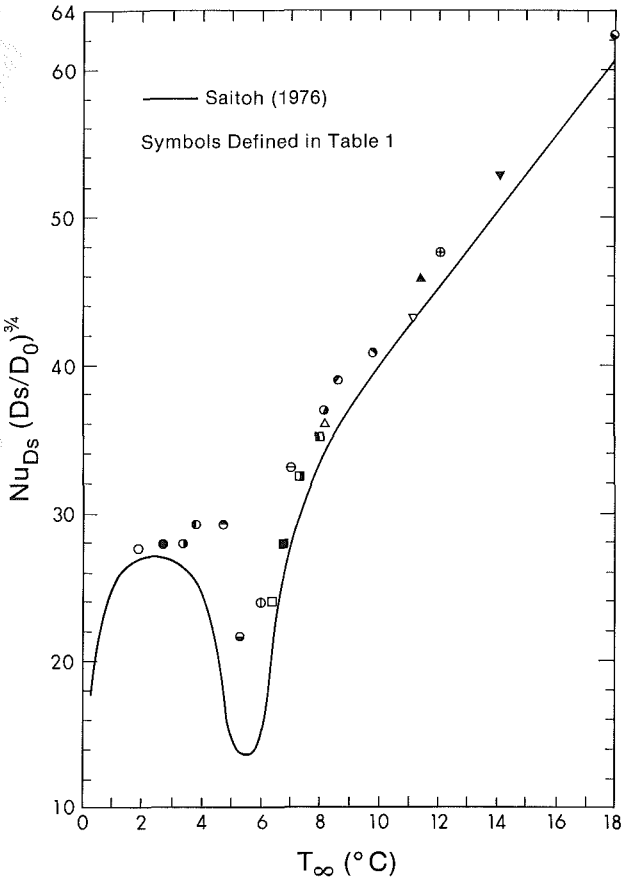


**Fig. 6 Comparison between present results for stagnation point Nusselt number for the freezing problem and previous results (Saitoh, 1976) from a melting experiment**

the four cases shown in Fig. 3 are presented in Fig. 4. For $T_\infty = 3.8°C$, the maximum heat transfer coefficient exists near the bottom of the cylinder. The local heat transfer variation is similar to that of a heated horizontal cylinder in a fluid without the maximum density effect. For $T_\infty = 5.2°C$, the convective inversion occurs and the trend of the distribution of $h_{n,\phi}$ is seen to be opposite to that of $T_\infty = 3.8°C$. The variation is seen to be small. For $T_\infty = 8.1°C$, the value of $h_{n,\phi}$ decreases rapidly with $\phi$ except in the range $\phi > 150$ deg due to predominantly downward flow. The variation becomes small in the range $\phi > 150$ deg due to the weak upward flow. For $T_\infty = 12.1°C$, the flow is downward and the density inversion effect is negligible. The rapid decrease of $h_{n,\phi}$ in the range $\phi > 170$ deg corresponds to the rapid increase of ice thickness near $\phi = 180$ deg. It is expected that a sharp tail may appear

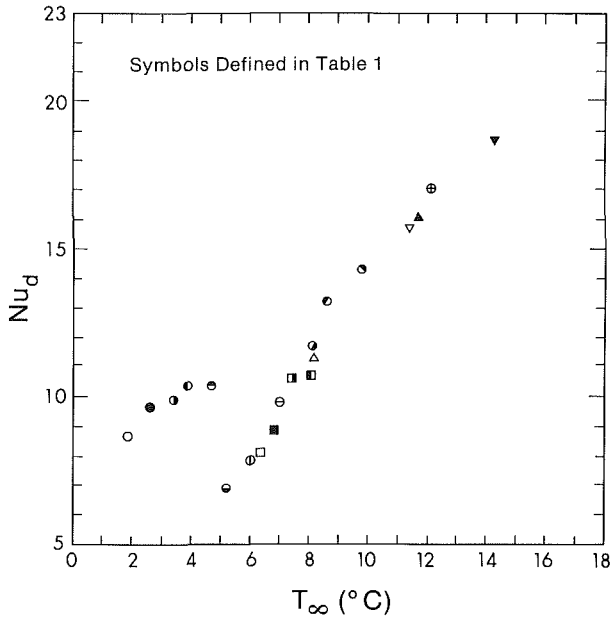


**Fig. 7 Relationship between average Nusselt number $Nu_d$ and ambient temperature $T_\infty$**

for the ice profile near $\phi = 180$ deg. It is seen that the value of $h_{n,\phi}$ increases with $T_\infty$ for $T_\infty > 5.2°C$, thus indicating the increasing natural convection effect. One also notes that the variation of $h_{n,\phi}$ with $\phi$ near the forward stagnation point is rather small.

**4.3 Heat Transfer Coefficient at Forward Stagnation Point.** Near the forward stagnation point, the ice profile can be approximated by a circle. In this region the heat transfer rates may be compared to those for a horizontal circular cylinder without the maximum density effect. The experimental data for Nusselt number at stagnation point $Nu_{Ds}$ are compared with the prediction of Merk and Prins (1954) in Fig. 5. The physical properties for $Nu_{Ds}$ and $Ra_{Ds}$ are evaluated at $(T_f + T_\infty)/2$. The experimental data near $T_\infty = 8°C$ were deleted in Fig. 5 since the thermal expansion coefficient of water becomes zero near 4°C. The difference between experimental data and the prediction may be attributed to evaluation of the thermal expansion coefficient $\beta$ and the density inversion effect.

It is of interest to compare the stagnation point Nusselt numbers from this study with the theoretical results of Saitoh (1976) for the case of melting of a horizontal ice cylinder at constant temperature in water. The results are shown in Fig. 6. It is noted that theoretical results for ice formation are not available for direct comparison. The Nusselt number was divided by $(Ds/D_0)^{3/4}$ since $Nu_{Ds}$ is proportional to the reference length to the 3/4 power in the range where the laminar boundary layer approximation is valid. The reference diameter was taken as $D_0 = 0.1$ m. It is seen that the trend of the present results roughly agrees with those of the melting problem, although the values from this study are somewhat higher. The difference is apparently due to the different heat transfer mechanism (melting and subcooling) and the different temperature field in ice. The existence of minimum Nusselt number between $T_\infty = 5$ and 6°C for both freezing and melting problems is noteworthy. The Nusselt number increases rapidly with $T_\infty$ in the range $T_\infty > 6°C$. The boundary layer approximation appears to be valid in the range $T_\infty > 8°C$ (Saitoh, 1976).

**4.4 Average Nusselt Number at the Ice-Water Interface.** The relationship between Nusselt number $Nu_d$ and am-

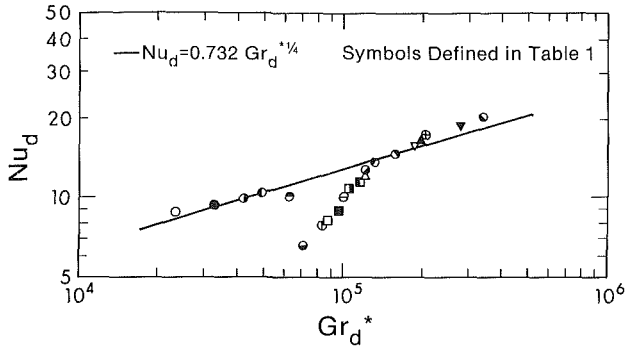


Fig. 8 Relationship between average Nusselt number $Nu_d$ and modified Grashof number $Gr_d^*$

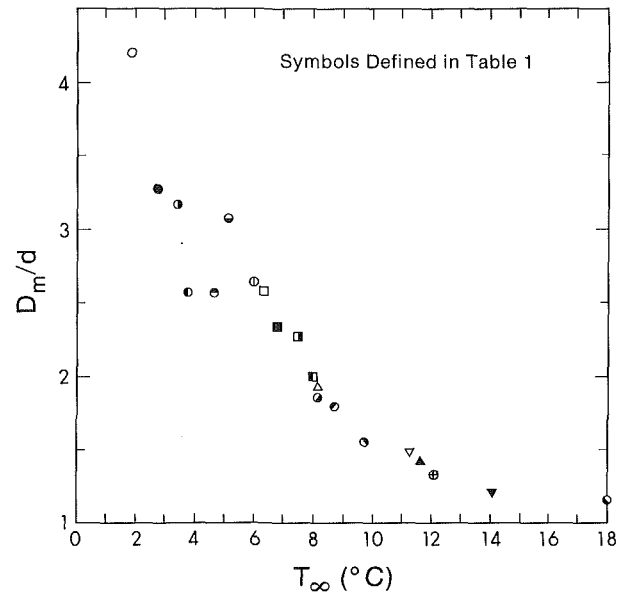


Fig. 9 Relationship between $D_m/d$ and $T_\infty$

bient temperature $T_\infty$ is shown in Fig. 7. The diameter of the cooling cylinder $d$ was used as a characteristic length since the ice shape on the cylinder becomes complicated depending on experimental conditions. The experimental data are also plotted in the form of $Nu_d$ as a function of modified Grashof number $Gr_d^*$ in Fig. 8. It is clearly seen that the density inversion effect exists in the range $T_\infty = 4$ to 8°C. In this flow reversal region, the boundary layer approximation may not be applicable. The existence of a minimum average Nusselt number is clearly seen.

Saitoh (1976) observed the existence of a flow instability phenomenon in the form of an irregular melting front contour at $T_\infty = 6.0$°C. The instability phenomenon was not observed in the present freezing experiments. The heat conduction in the ice layer may have a stabilizing effect.

In Fig. 8, the density inversion effect appears in the range $Gr_d^* = 5\times10^4$ to $1.6\times10^5$. The following correlation equation is applicable (±5 percent scatter) excluding the flow reversal region:

$$Nu_d = 0.732 Gr^{*1/4}_d \tag{6}$$

A minimum value of $Nu_d$ appears at around $Gr_d^* = 7.0\times10^4$. It appears that $Gr_d^*$ is a reasonable parameter for the present freezing problem with maximum density effect.

**4.5 Amount of Ice Growth Around the Cylinder.** For low-temperature heat storage in ice and other applications, the amount of ice growth around the cylinder is of particular interest. The relationship between dimensionless mean ice diameter $D_m/d$ and ambient water temperature $T_\infty$ is shown in Fig. 9. The decrease of $D_m/d$ in the range $T_\infty = 3.8$ to 4.7°C is of interest. The increase of mean ice thickness in the range $T_\infty = 4.7$ to 5.2°C is due to the decrease of natural convection caused by the density inversion of water, as can be seen in Fig. 7.

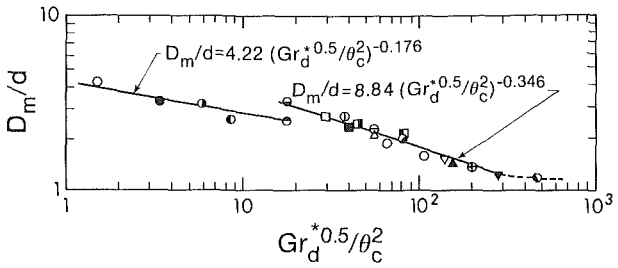


Fig. 10 Relationship between $D_m/d$ and $Gr^{*0.5}_d/\theta_c^2$

It is desirable to correlate the amount of ice growth by a simple one-dimensional analysis. By assuming a linear temperature profile through the ice layer, one obtains the following expression from the energy balance at the ice-water interface:

$$h_m(T_\infty - T_f) = k_i(T_f - T_w)/\delta_{im} \tag{7}$$

The mean Nusselt number $Nu_d$ can now be written as

$$Nu_d = \frac{h_m d}{k_w} = \frac{k_i}{k_w}\frac{(T_f - T_w)}{(T_\infty - T_f)}\frac{d}{\delta_{im}} = \frac{k_i}{k_w}\theta_c\frac{d}{\delta_{im}} \tag{8}$$

As shown in Fig. 8, $Nu_d$ is the proportional to $Gr^{*1/4}_d$. Thus, one obtains

$$\frac{\delta_{im}}{d} \sim \frac{D_m}{d} \sim \frac{k_i}{k_w}\theta_c/Gr^{*1/4}_d \tag{9}$$

Figure 10 shows the relationship between $D_m/d$ and $Gr^{*0.5}_d/\theta_c^2$. Excluding the region with $Gr^{*0.5}_d/\theta_c^2 = 18\sim19$ where the change of flow pattern due to density inversion is appreciable, the experimental data can be correlated within the relative error of ±10 percent by the following expressions:

$$D_m/d = 4.22(Gr^{*0.5}_d/\theta_c^2)^{-0.176} \tag{10}$$

for $1.5 < Gr^{*0.5}_d/\theta_c^2 < 18$, $1.9°C < T_\infty < 4.7°C$;

$$D_m/d = 8.84(Gr^{*0.5}_d/\theta_c^2)^{-0.346} \tag{11}$$

for $19 < Gr^{*0.5}_d/\theta_c^2 < 300$, $5.2°C < T_\infty < 14°C$.

Two limiting cases are of special interest. As $Gr^{*0.5}_d/\theta_c^2 \to 0$ ($Gr^{*0.5}_d \to 0$ or $\theta_c^2 \to \infty$), the effect of natural convection on overall heat transfer disappears and conduction heat transfer in the ice layer increases due to $Gr_d^* \to 0$ or $\theta_c \to \infty$. The heat transfer mechanism is then dominated by transient heat conduction in the ice layer and the growth of the ice layer continues indefinitely. On the other hand, as $Gr^{*0.5}_d/\theta_c^2 \to \infty$ ($Gr^{*0.5}_d \to \infty$ or $\theta_c^2 \to 0$), the influence of conduction heat transfer in the ice layer vanishes and the convective heat transfer at the ice-water interface dominates. As a result, the ice layer around the cylinder disappears and $D_m/d = 1$ is approached. It is to be expected that, with $Gr^{*0.5}_d/\theta_c^2 \geq 4.8\times10^2$ ($T_\infty = 18$°C), the value of $D_m/d$ becomes quite small and eventually the ice layer vanishes.

**4.6 Amount of Low-Temperature Heat Storage in Ice Layer for Cooling.** It is of practical interest to estimate the heat storage in the ice layer around a horizontal cylinder in natural convection. The amount of heat stored in the ice layer $Q_t$ represents the sum of latent and sensible heat as

$$Q_t = \gamma_i V_i[L_i + C_{pi}(T_f - T_w)] \quad [W/m] \tag{12}$$

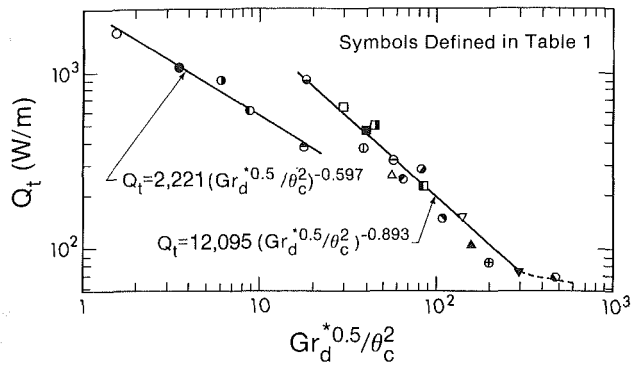


**Fig. 11 Relationship between low-temperature heat stored $Q_t$ and $Gr^{*0.5}_d/\theta^2_c$**

where $V_i$ is the volume of ice layer per unit length (m). Figure 11 shows the relationship between the stored heat $Q_t$ and the parameter $Gr^{*0.5}_d/\theta^2_c$. Excluding the region $Gr^{*0.5}_d/\theta^2_c = 17$ to 18, the experimental data can be correlated by the following two expressions within a relative error of $\pm 10$ percent:

$$Q_t = 2221(Gr^{*0.5}_d/\theta^2_c)^{-0.597} \quad [W/m] \tag{13}$$

for $1.5 < Gr^{*0.5}_d/\theta^2_c < 18$, $1.9°C < T_\infty < 4.7°C$;

$$Q_t = 12{,}095(Gr^{*0.5}_d/\theta^2_c)^{-0.893} \quad [W/m] \tag{14}$$

for $18 < Gr^{*0.5}_d/\theta^2_c < 300$, $5.2°C < T_\infty < 14°C$. Thus, one may estimate the low-temperature heat storage in ice layer after evaluating the parameter $Gr^{*0.5}_d/\theta^2_c$. The parameter is derived in equation (9) and is seen to be very useful for the present freezing problem with maximum density effect. In this connection it should be pointed out that the dimensionless mean ice layer thickness ($\delta_{im}/d$) in equation (9) is somewhat analogous to the well-known dimensionless laminar boundary layer thickness, $\delta/x = 4.64/Re^{1/2}$, or the thermal boundary layer thickness on a constant temperature flat plate by noting the correspondence between Reynolds number in laminar forced convection and Grashof number in natural convection. The parameter $Gr^{*1/2}_d/\theta^2_c$ represents the balance between natural convection and heat conduction through the ice layer. This parameter determines the ice layer thickness depending on the given thermal and hydrodynamic conditions for cooling. The parameter is important for ice formation problems and the observation is also confirmed in an earlier work (Cheng et al., 1981).

## 5 Concluding Remarks

The effects of maximum density on steady-state ice formation around an isothermally cooled horizontal cylinder in quiescent water have been studied experimentally for ambient water temperature $T_\infty = 1.9$ to 18.0°C and cylinder surface temperature $T_w = -20.0$ to $-16.2$°C. Particular emphasis is placed on the effect of the density inversion for the liquid water surrounding the ice layer, and its effect on the natural convection process and, in turn, on the shape of the ice-water interface profile.

It has been found that for $T_\infty < 4.7°C$, upflow occurs and the stagnation point with maximum heat transfer rate is located at the bottom of the cylinder. For $T_\infty > 5.2°C$, downflow is observed and the stagnation point is at the top of the cylinder. In the range $T_\infty = 5$ to 8°C, flow direction inversion due to maximum density occurs, and a minimum Nusselt number phenomenon similar to that noted in the melting problem is observed at $T_\infty = 5.2°C$. For $T_\infty > 8°C$, a boundary layer approximation may be applicable. The stagnation point Nusselt number, local heat transfer coefficient, and average Nusselt number behavior were studied using such parameters as ambient temperature, Rayleigh number, and modified Grashof number considering maximum density. It is found that the average ice layer thickness and heat stored in the ice layer can be correlated using the parameter $Gr^{*0.5}_d/\theta^2_c$ with reasonable accuracy. The derived characteristic parameter $Gr^{*0.5}_d/\theta^2_c$ (see equation (9)) is useful in correlating average ice layer thickness and is not unlike the parameter in the expression for velocity boundary layer thickness in Blasius flow on a flat plate or thermal boundary layer thickness in laminar forced convection on a flat plate. The analogy is of particular interest for ice formation problem.

The heat transfer mechanism for the freezing problem is different from that of the melting problem. The stagnation point Nusselt number for the freezing problem is found to be higher than that of the melting problem. In the flow reversal region ($Gr^*_d = 3.8\times10^4$ to $1.3\times10^5$, $T_\infty = 5.2$ to 8.1°C) the heat transfer rate decreases and then increases due to the existence of very slow flows. It is noted that theoretical results for the present freezing problem are not available in the literature.

## Acknowledgments

This work was supported by a grant from the Natural Sciences and Engineering Research Council of Canada. The experiments were performed in 1980. This paper is dedicated to the memory of the late Professor R. R. Gilpin (1942–1982).

## References

Bathelt, A. G., Van Buren, P. O., and Viskanta, R., 1979, "Heat Transfer During Solidification Around a Cooled Horizontal Cylinder," *AIChE Symposium Series*, Vol. 75, No. 189, pp. 103–111.

Bendell, M., and Gebhart, B., 1976, "Heat Transfer and Ice-Melting in Ambient Water Near Its Density Extremum," *Int. J. Heat Mass Transfer*, Vol. 19, pp. 1081–1087.

Chao, S. L., and Schoenhals, R. J., 1981, "An Experimental Study of a Closed Two-Phase Thermosyphon for Ice Production," ASME Paper No. 81-HT-16.

Cheng, K. C., Inaba, H., and Gilpin, R. R., 1981, "An Experimental Investigation of Ice Formation Around an Isothermally Cooled Cylinder in Crossflow," ASME JOURNAL OF HEAT TRANSFER, Vol. 103, pp. 733–738.

Cheng, K. C., and Sabhapathy, P., 1985, "An Experimental Investigation of Ice Formation Over an Isothermally Cooled Vertical Circular Cylinder in Natural Convection," ASME Paper No. 85-HT-1.

Cheung, F. B., and Epstein, M., 1984, "Solidification and Melting in Fluid Flow," *Advances in Transport Processes*, Vol. 3, pp. 35–117.

Dumore, J. M., Merk, H. J., and Prins, J. A., 1953, "Heat Transfer From Water to Ice by Thermal Convection," *Nature*, Vol. 172, pp. 460–461.

Epstein, M., and Cheung, F. B., 1983, "Complex Freezing–Melting Interfaces in Fluid Flow," *Ann. Rev. Fluid Mech.*, Vol. 15, pp. 293–319.

Herrmann, J., Leindenfrost, W., and Viskanta, R., 1984, "Effect of Natural Convection on Freezing of Water Around an Isothermal, Horizontal Cylinder," *Int. Comm. Heat Mass Transfer*, Vol. 11, pp. 391–310.

Hildebrand, F. B., 1962, *Advanced Calculus for Applications*, Prentice-Hall, New York, pp. 434–435.

Merk, H. J., 1954, "The Influence of Melting and Anomalous Expansion on the Thermal Convection in Laminar Boundary Layers," *Appl. Sci. Res.*, Vol. 4A, pp. 435–452.

Merk, H. J., and Prins, J. A., 1954, "Thermal Convection in Laminar Boundary Layers III," *Appl. Sci. Res.*, Vol. 4A, pp. 207–221.

Saitoh, T., 1976, "Natural Convection Heat Transfer From a Horizontal Ice Cylinder," *Appl. Sci. Res.*, Vol. 32, pp. 429–451.

Saitoh, T., and Hirose, K., 1981, "Numerical Method for the Two-Dimensional Freezing Problem Around a Horizontal Cylinder Encompassing a Density Inversion Point," *Bulletin of the JSME*, Vol. 24, pp. 147–152.

Schenk, J., and Schenkels, F. A. M., 1968, "Thermal Free Convection From an Ice Sphere in Water," *Appl. Sci. Res.*, Vol. 19, pp. 465–476.

Sun, Z. S., Tien, C., and Yen, Y. C., 1969, "Thermal Instability of a Horizontal Layer of Liquid With Maximum Density," *AIChE Journal*, Vol. 15, pp. 910–915.

Vanier, C. R., and Tien, C., 1970, "Free Convection Melting of Ice Spheres," *AIChE Journal*, Vol. 16, pp. 76–82.

Viskanta, R., 1983, "Phase-Change Heat Transfer," *Solar Heat Storage: Latent Heat Materials*, G. A. Lane, ed., CRC Press, Boca Raton, FL, pp. 153–222.

# Network Thermodynamic Modeling With Bond Graphs for Membrane Transport During Cell Freezing Procedures

K. R. Diller

J. J. Beaman

J. P. Montoya[1]

Department of Mechanical Engineering,
Bio-Heat Transfer Laboratory,
The University of Texas,
Austin, TX 78712

P. C. Breedfeld

Department of Electrical Engineering,
Twente University of Technology,
Enschede, The Netherlands

*Freezing procedures for preservation of living cells create osmotic stresses associated with the addition and removal of cryoprotective agents and with ice formation in the extracellular solution, causing a concomitant segregation of electrolytes into the remaining liquid phase. When these osmotic stresses are introduced, coupled flows of water and permeable solute are induced across the plasma membrane. A network thermodynamic model of this process is presented, based on development according to the principles of bond graphs. The model is a complete representation of the equations that describe the process, and the bond graph can be interpreted directly in terms of the relevant energy flows during membrane transport and the topology of the system. Determination of the transient cell volume during addition of glycerol to an erythrocyte suspension is used to demonstrate the model.*

## Introduction

The freezing of living cells is governed by the coupled membrane transport of water and cryoprotective additives (CPA), which results from the concentration of extracellular solutes during solidificaton. The optimal design of cryopreservation protocols is dependent on a rational basis for controlling the governing transport processes. Therefore, membrane transport models are useful for process design and analysis and are requisite to obtaining values of the relevant permeability parameters from experimental data.

Traditionally, the osmotic process experienced by a cell suspended in anisotonic solutions with CPAs has been modeled with the Kedem-Katchalsky (K-K) coupled flow equations, which are derived from irreversible thermodynamics assuming dilute intracellular and extracellular solutions (Kedem and Katchalsky, 1958). An alternative way of describing the system behavior is to apply the methods of network thermodynamics to model the coupled transport across a membrane; the advantages of this technique are that it provides additional insight into the system topology and permits a systematic and organized perspective for analysis and solution similar to that used in network and control theory of dynamic systems (Oster et al., 1973). Implementation with bond graph methodology (Paynter, 1961) results in a graphic representation that depicts the physical processes that drive the system behavior in a manner that can be directly interpreted visually. The technique lends itself well to hierarchical model building by organizing fundamental physical building units into meaningful arrangements that represent complex behavior patterns. Furthermore, the governing equations can be generated automatically from a properly executed graphic description of the system, providing a convenient means of evaluating perturbations in system configuration and composition.

In this paper a network thermodynamic model for cell membrane coupled flow of water and a permeable CPA during freezing is introduced in the form of a bond graph. The basis of the network thermodynamics approach will be discussed briefly, followed by application to the coupled process of water and CPA membrane transport during CPA addition and removal and cell freezing. Equivalence of the network thermodynamic method with the irreversible thermodynamic method will be demonstrated for the case in which the necessary simplifying assumptions are invoked.

## Network Thermodynamic Analysis

The initial publication describing the network thermodynamic method presented a number of application examples dealing with membrane fluxes under various conditions (Oster et al., 1973). These authors used the bond graph method (Paynter, 1961) to apply the theory, although electrical circuit simulation methods have also been used successfully (Mikulecky, 1983). Although bond graphs make use of a somewhat abstract graphic language that is not immediately decipherable to the uninitiated, they may be understood with a relatively short learning period, and they offer advantages in the rigor and degree of generality in presentation. Our model is based on the bond graph presentation method.

The bond graph method incorporates a top-down approach to system simulation. The implementation consists of starting with an overall description of a system of interest and proceeds to a state in which focus is directed to the specific details of the constitutive components. In developing the bond graph of a system, the immediate goal may not be the generation of a set of governing equations. Rather, the bond graph affords a way to define the structure and constitutive equations of the system prior to having to deal with appropriate mathematical representations. Standard bond graph elements are used to build a model of the structure of the system; inherent to this model is the complete set of equations describing the system behavior. Automated computer techniques have been developed to generate these equations, and alternative methods for deriving equivalent block diagrams are also available. Current automated equation generation routines are generally limited to linear systems, whereas block diagrams can handle nonlinear systems. We are presently working on an algorithm that will deal effectively with nonlinear system equations, but in this paper we have implemented the bond graph by a block diagram technique.

An elementary method of implementing a bond graph is to illustrate the system components and their interconnections with words and arrows, i.e., by building a word bond graph.

[1]Present address: Department of Mechanical Engineering, The University of Michigan, Ann Arbor, MI 48104.

Contributed by the Heat Transfer Division and presented in preliminary form at the ASME-JSME Thermal Engineering Joint Conference, Honolulu, Hawaii, March 22-27, 1986. Manuscript received by the Heat Transfer Division November 17, 1986. Keywords: Biotechnology, Nonequilibrium Flows, Thermophysical Properties.

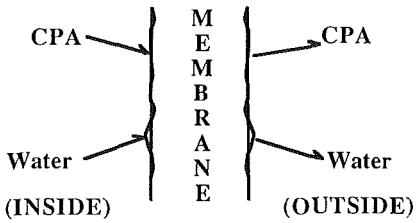


**Fig. 1 A word bond graph illustrating multicomponent transport across a cell membrane. The bond graph shows communication between the intracellular and extracellular spaces by transport of specific chemical species, such as water and a cryoprotective additive (CPA), across the plasma membrane.**

For example, the simultaneous transport of water and a CPA across a membrane may be modeled as shown in Fig. 1. In this system the intracellular and extracellular compartments communicate across the plasma membrane by the exchange of specific molecular species. The process consists of an energetic flow between two areas of differing potential, resulting in an actual flow of power. The half arrows indicate the positive direction of power flow associated with the transport process. Although the graph in Fig. 1 is easy to interpret, it is highly limited in practical application. There is no way that the governing equations that describe the system performance can be determined uniquely from it, and it does not show the energetic and the information and communication networks that exist among the system subunits. Neither is it specific in identifying the actual flows that exist within the system. Therefore, it is desirable to have a more rigorous and detailed basis for drawing graphs to represent a system.

There are a number of standard elements that are used to build up the structure of a bond graph (Paynter; 1961; Rosenberg and Karnopp, 1983). Those that are relevant to the present analysis are described as follows along with their appropriate interpretation.

In addition, it is necessary to designate the causality of a

| Element | Physical Significance |
|---|---|
| **C** | Storage |
| **R** | Dissipation |
| **T** | Cross-coupling between chemical species |
| **0** | Σ species flow at a common potential |
| **1** | Σ potential at a common species flow |

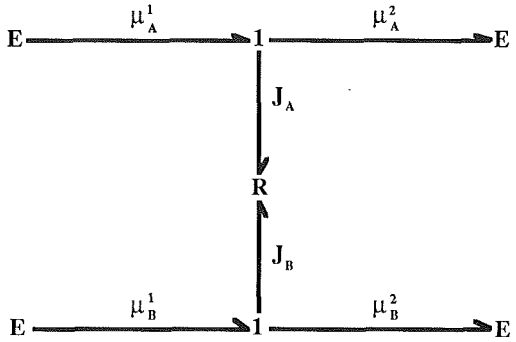


**Fig. 2 Bond graph of the steady-state transport of two species A and B across the plasma membrane. The dissipation is lumped into a single two-port resistance element that accounts for the flow of all chemical species.**

system, which identifies the cause and effect relation for the energy exchange between component elements, in order to define the governing equations fully. For a model presented in this format, not only is it possible to generate the system equations automatically, i.e., the bond graph is equivalent to the full set of system equations, but the model can be modified very easily to account for alterations in the physical system or its environmental perturbations.

The modeling elements described above can be used to build a simple model of the multicomponent membrane transport process described in Fig. 1, as indicated further in Fig. 2. In this bond graph the transport across the membrane is shown by a two-port resistance element. This model indicates the general dissipative nature of the species flow between the intracellular and extracellular regions without any specific indication of the mechanisms involved. There are two inputs to the irreversibility, one associated with the movement of each chemical species identified. The fluxes $J_A$ and $J_B$ occur in response to the differentials in chemical potentials $\Delta\mu_A$ and $\Delta\mu_B$ imposed across the membrane (as indicated by the superscripts 1 and 2) by the existence of the nonequal effort sources **E** on opposing sides of the membrane. The product of the conjugate efforts and flows has the dimensions of power; this is a common feature of all bond graph interactions that makes modeling of coupled phenomena involving energy transduction between different transport domains particularly effective and efficient.

## Nomenclature

$A$ = cell surface area, $m^2$
$B$ = cooling rate, K/s
$C$ = concentration, osmolal or osmolar, osmol/kg $H_2O$ or mol/L sol
**C** = bond graph storage element
$\Delta E$ = activation energy, J/mol
**E** = bond graph effort source
$J_i$ = mass flux of species $i$, $mol/m^2$ s
$L$ = phenomenological coefficient (see equations (2) and (9))
$L_p$ = water permeability, $m^3$/nt s)
$n_i$ = mol of species $i$, mol
$P$ = pressure, Pa
**r** = bond graph transduction scaling factor
$r$ = mass ratio of permeable solute to electrolyte
$\Re$ = universal gas constant = 8.314 J/mol K
**R** = bond graph dissipation element
$S$ = entropy, J/K
$t$ = time, s
**T** = bond graph transduction element
$T$ = temperature, K
$T_{in}$ = initial temperature, K
$T_o$ = 298.15 K or 273.15 K
$v$ = rate of volume change, $m^3$/s
$V$ = volume, $m^3$
$X$ = generalized driving force
**0** = bond graph flow summation junction
**1** = bond graph potential summation junction
$\theta$ = volume fraction
$\mu_i$ = chemical potential of $i$, J/mol
$\nu_i$ = partial molar volume of $i$, $m^3$/mol
$\sigma$ = reflection coefficient
$\phi$ = dissipation function (see equations (6) and (7))
$\omega$ = solute permeability, mol/nt s

### Subscripts

$a$ = additive
$f$ = fixed
$s$ = salt, nonpermeable solute
$w$ = water

### Superscripts

$b$ = bound
$f$ = free
$i$ = inside, intracellular
$m$ = mean
$o$ = outside, extracellular

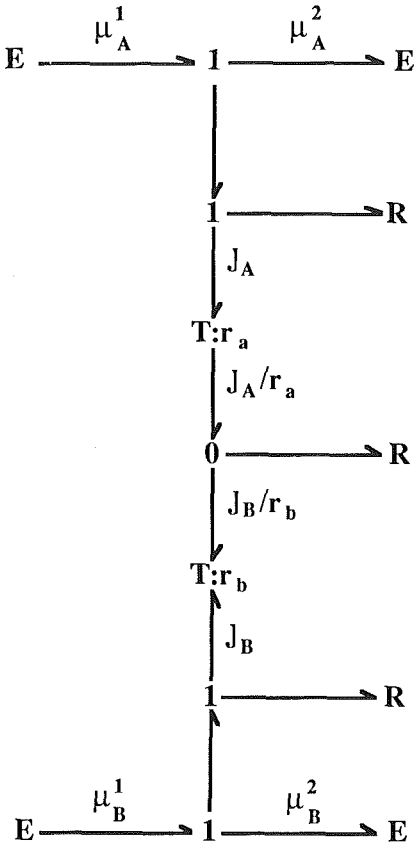


**Fig. 3 A reticulated bond graph of the stationary state hydrodynamic coupling between simultaneous diffusion of two different chemical species across the membrane depicted in Fig. 2. Details of the dissipation are indicated in the greater refinement of elements representing the membrane transport process, including the transformer elements that show the cross coupling of the two flows. The transformed energetic flows and associated components of dissipation are indicated.**

In many instances the bond graph in Fig. 2 may be adequate to describe the functioning of a system to the extent that its physical basis is understood. However, the condition may arise for which details of the transport process have been identified to a greater degree of refinement than just the realization of a general dissipative process. As in the present case in which there are experimental data that describe in more detail the nature of the species transfer across the membrane, it is useful to develop a bond graph with a higher degree of reticulation, as shown in Fig. 3 (Oster et al., 1973). This graph shows that there is a transduction interaction between the flows of the two species $A$ and $B$, as indicated by the **T** elements. The crossflow transductions are scaled by the factors $\mathbf{r}_a$ and $\mathbf{r}_b$, and dissipation is denoted by three single-port elements associated with the two species flows. This graph corresponds in principle with the K-K steady-state analysis of coupled membrane flows in which three phenomenological coefficients are required to describe two coupled fluxes (Kedem and Katchalsky, 1958). Dissipation resulting from the crossflows is indicated in the middle **R** element.

It is also possible and desirable to develop a nonsteady-state model for the membrane transport process. Since a transitory system has the capability for storage of the substance being transported, it is necessary that the bond graph include **C** elements as appropriate. In the present system the storage occurs as the positive or negative accumulation of molecular species within the cell in response to changes in the extracellular composition of components $A$ and $B$. A bond graph describing this system is shown in Fig. 4 in which the interior capacity of the cell is represented as a single three-port capacitance. The volume of the cell is altered by either changing the pressure or by exchanging moles of chemical species across the membrane. This model lumps the entire transient intracellular mass together into a single element that, in principle, represents the changing volume of the cell that could be measured under an experimentally imposed osmotic stress. The capacitor has a single port for the flow of each of the mobile chemical species, and a port for the pressure–volume interactions. The capacitor element represents a coupled storage process in which the individual chemical potentials are funtions of the numbers of moles of all species present.

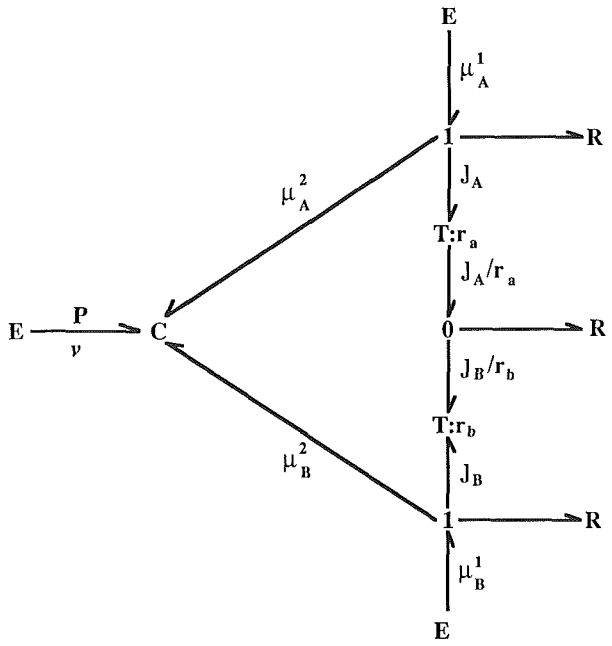


**Fig. 4 A bond graph of the transient membrane transport process showing the intracellular accumulation of the two mobile chemical species A and B in terms of a three-port capacitance element. Pressure-volume interactions on the cell are also included.**

The capacitance may be modified to describe a more idealized case, as shown in Fig. 5, for which the capacitances for each chemical species are uncoupled, corresponding to a removal of coupling in the storage process. Each of the species acts independently, and the response to pressure–volume interactions are realized through a common effort junction. The chemical potentials of individual species in this system are dependent only on the same species mole numbers. Applicability of this refinement is dependent on the elements that compose the system.

The building block approach to bond graph modeling is illustrated by the progressive development of a system simulation discussed in this section. The bond graph presented in Fig. 5 has adequate detail to describe the physical processes that govern the osmotic behavior of cells during freezing. However, most experiments are designed to measure biophysical properties of the cell that do not correspond to the elements in the model; specifically, the three **R** dissipation elements are not quantifiable by simply executed experimental protocols. Kedem and Katchalsky (1958) have identified membrane permeability parameters amenable to experimental measurement. It is thus convenient to rebuild the bond graph so that these parameters are identified. The K-K permeability parameters will be defined in the next section and the bond graph rebuilt accordingly using the building blocks already presented. Application of this technique to a specific problem involving cell cryopreservation will be addressed.

## Theoretical Model

The theoretical derivation of a thermodynamic model for

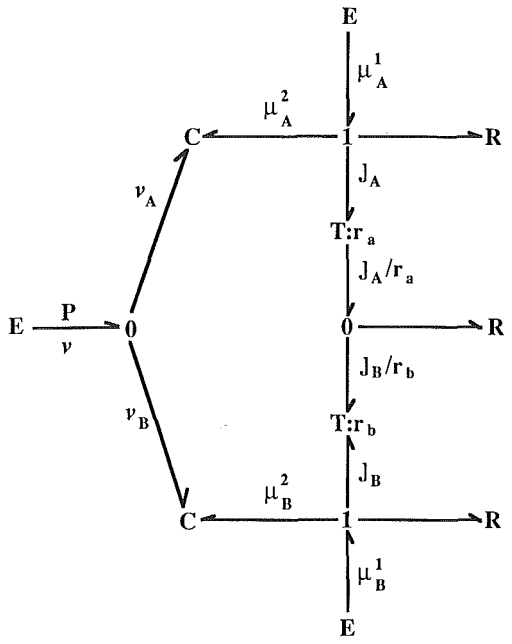


**Fig. 5 Reticulation of the bond graph in Fig. 4 to include single-port capacitance elements for the ideal case of independent intracellular accumulation of each of the mobile chemical species that can be transported across the plasma membrane**

the freezing of cells has been presented previously in detail for both binary (Mazur, 1963) and ternary (Diller and Lynch, 1983) solutions. Briefly, the model consists of an isothermal, isobaric, thermodynamic system composed of the cell and its extracellular medium divided by a semipermeable membrane. This membrane is assumed to allow the mass flux of water $J_w$ and of cryoprotectant additive $J_a$, but to be impermeable to electrolytes and other solutes. Both fluxes arise from the chemical potential differences of water and additive across the membrane $\Delta\mu_w = \mu^i_w - \mu^o_w$ and $\Delta\mu_a = \mu^i_a - \mu^o_a$, where the superscripts $i$ and $o$ stand for inside and outside of the cell, respectively. The internal entropy generation per unit area is given by (Katchalsky and Curran, 1967)

$$(dS/dt)/A = J_w \Delta\mu_w/T + J_a\ \Delta\mu_a/T \tag{1}$$

From irreversible thermodynamics the flows can be represented as a linear function of forces since the sum of the product of flows ($J_i$) and forces ($\Delta\mu_i$) is equal to the entropy generation, that is, $J_i = \Sigma_j L_{ij}\ \Delta\mu_j$, where the $L_{ij}$ are called phenomenological coefficients. Therefore, for a membrane permeable to water and additive, the flux equations can be written as

$$\begin{aligned} J_w &= L_{ww}\Delta\mu_w + L_{wa}\Delta\mu_a \\ J_a &= L_{aw}\Delta\mu_w + L_{aa}\Delta\mu_a \end{aligned} \tag{2}$$

and, according to the Onsager reciprocal relation, $L_{wa} = L_{aw}$. Therefore, three parameters are needed to characterize the membrane as relating to the water permeability $L_{ww}$, the additive permeability $L_{aa}$, and the coupling coefficient $L_{wa}$.

Kedem and Katchalsky (1958) have transformed the transport equations (2) into a new set of coupled equations in terms of three convenient membrane parameters and simply measured concentration driving forces. In the derivation of these equations it is assumed that the solutions are volume dilute, and therefore, they approximate ideal solutions for which the chemical potentials can be given as

$$\Delta\mu_w = \nu_w \Re T \Delta C_w \text{ and } \Delta\mu_a = \Re T \Delta C_a / C^m_a \tag{3}$$

$C^m_a$ is the mean additive molar concentration, $C^m_a = (C^i_a + C^o_a)/\ln(C^i_a/C^o_a)$. For a closed thermodynamic system the mass is constant; therefore, the concentration difference of water can be expressed in terms of the concentration differences of additive and nonpermeable solute (electrolyte) as $\Delta C_w = -(\Delta C_a + \Delta C_s)$, which yields

$$\Delta\mu_w = -\nu_w \Re T\ (\Delta C_a + \Delta C_s) \tag{4}$$

The transformation to the new (K–K) equations from equations (2) is produced by defining a new set of flows: the volume flux $J_V$ and a differential volume flux $J_D$

$$\begin{aligned} J_V &= J_W\ \nu_w + J_a\ \nu_a \\ J_D &= J_a/C^m_a - J_w\ \nu_w \end{aligned} \tag{5}$$

We may obtain a new set of forces related to these flows by imposing that the dissipation function, $\phi = T\ dS/dt$, be unchanged in the transformation to the new set of flows and forces: From equation (1)

$$\phi_1/A = J_w\ \Delta\mu_w + J_a\ \Delta\mu_a \tag{6}$$

and with the new set of flows

$$\phi_2/A = J_V X_V + J_D\ X_D \tag{7}$$

Setting $\phi_1 = \phi_2$ and solving for the forces we obtain

$$\begin{aligned} X_V &= \Delta\mu_w/[\nu_w\ (1+\theta)] + C^m_a\ \Delta\mu_a/(1+\theta) \\ X_D &= \{C^m_a/(1+\theta)\}[\Delta\mu_a - \nu_a\ \Delta\mu_w/\nu_w] \end{aligned} \tag{8}$$

where $\theta = \nu_a\ C^m_a$. $J_V$ and $J_D$ will also depend linearly on the forces $X_V$ and $X_D$ and a new set of phenomenological coefficients

$$\begin{aligned} J_V &= L_{11}\ X_V + L_{12}\ X_D \\ J_D &= L_{12}\ X_V + L_{22}\ X_D \end{aligned} \tag{9}$$

The coefficients $L_{11}$, $L_{22}$, and $L_{12} = L_{21}$ can be expressed in terms of the K–K permeability coefficients: the water permeability $L_p$, the solute permeability $\omega$, and the reflection coefficient $\sigma$. By eliminating the concentration driving forces between equations (8) and (9), and solving for $J_w$ and $J_a$ with equations (5), we obtain the equivalent K–K transport equations

$$dn_w/dt = (A\Re T L_p/\nu_w)\ \{\Delta C_s + \nu_a\ \omega/L_p)\ \Delta C_a\} \tag{10}$$

$$dn_a/dt = A\Re T L_p\ \{C^m_a(1-\sigma)\ \Delta C_s + [\sigma(1-\sigma)\ C^m_a - \omega/L_p]\ \Delta C_a\}$$

where the fluxes have been expressed in terms of the rate of change of moles of each species and the cell surface area, $J_w = -1/A\ (dn_w/dt)$ and $J_a = -1/A\ (dn_a/dt)$.

The transmembrane concentration differences of impermeable solute, $\Delta C_s = C^i_s - C^o_s$, and additive, $\Delta C_a = C^i_a - C^o_a$, depend on the amount of water, impermeable solute, and additive within the cell

$$\begin{aligned} \Delta C_s\ \text{(osmol/liter)} &= n_s/n_w\nu_w - C^o_s \\ \Delta C_a\ \text{(osmol/liter)} &= n_a/n_w\nu_w - C^o_a \end{aligned} \tag{11}$$

These concentration differences can be converted to molal terms (mol/kg $H_2O$) by introducing the conversion factors for dilute aproximations, 1 liter solution/kg $H_2O$. The concentrations outside the cell are fixed and set by imposed external conditions.

The total amount of water in the cell $n_w$ is composed of water that is osmotically active (free to participate in flows across the membrane), and water that is tightly bound to the nonpermeable solutes and cannot participate in the osmotic process

$$n_w = n^f_w + n^b_w \tag{12}$$

where the superscripts $f$ and $b$ stand for the free and bound water. Therefore, the water referred to in equation (10) is the water that is capable of permeating through the membrane $n^f_w$. However, to compute the intracellular solute concentrations, either the total water or the free water content may be used as in equations (11), depending on the constitutive model used (Levin et al., 1976).

The total cell volume is computed from all the constituents within the cell plus the membrane

$$V_{\text{cell}} = n_w v_w + n_a v_a + n_s v_s + V_{\text{mem}} \tag{13}$$

Since the volume of the membrane, the impermeable solute, and water tightly bound to it do not participate in the osmotic process, these may be lumped into a single "fixed" volume $V_f$. Therefore

$$V_{\text{cell}} = n_w^f \; v_w + n_a \; v_a + V_f \tag{14}$$

A value for the fixed volume may be obtained by suspending the cells in a saline solution and measuring the equilibrium volume while increasing the concentration. A Boyle–Van't Hoff curve can be produced by plotting a linear regression of the volume versus the inverse of the salt osmolality. The fixed volume is obtained by extrapolating this line to infinite concentration.

For freezing it is assumed that ice is formed only in the extracellular solution, giving rise to a transient chemical potential difference across the membrane. The composition of the remaining extracellular liquid is determined for temperatures above the eutectic point by the equilibrium ternary phase diagram and the initial concentration. Equations (10) can be transformed to a temperature basis for freezing processes by introducing the cooling rate $B = dT/dt$. Thus

$$T = Bt + T_{in} \tag{15}$$

where $T_{in}$ is the initial temperature at time $t = 0$.

The temperature dependence of the permeability parameters $L_p$ and $\omega$ can be expressed as an Arrhenius function

$$L_p = L_{pg} e^{[(-\Delta E/\Re)(1/T - 1/T_o)]} \tag{16}$$

and $L_p/\omega = \text{const}$, i.e., $L_p$ and $\omega$ have the same activation energy in lieu of specific data to the contrary, where $\Delta E$ is the activation energy and $T_o = 298.15$ K. The reflection coefficient $\sigma$ is assumed to remain constant over the temperature range of interest. The temperature-dependent coupled transport equations are obtained by substituting equations (15) and (16) into (10).

## Network Thermodynamic Model for Cell Freezing

The preceding formulation of the coupled membrane transport process can be expressed in terms of the basic bond graph elements that were presented earlier. For example, the Onsager reciprocal relations that describe the dissipative flows across a membrane can be written as

$$\begin{aligned} \Delta\mu_A &= \mathbf{R}_A \; J_A + \mathbf{R}_{AB} J_B \\ \Delta\mu_B &= \mathbf{R}_{AB} \; J_A + \mathbf{R}_B J_B \end{aligned} \tag{17}$$

where

$$\begin{aligned} \mathbf{R}_A &= (R_a + R_c/r_a^2) \\ \mathbf{R}_B &= (R_b + R_c/r_b^2) \\ \mathbf{R}_{AB} &= (R_c/r_a \; r_b) \end{aligned} \tag{18}$$

Equations (17) and (18) can be represented in matrix form as $[\Delta\mu] = [\mathbf{R}]\,[J]$. This equation transforms to equations (2) for a water plus permeable solute system, which may be written in matrix form as

$$[J] = [L]\,[\Delta\mu] \tag{19}$$

by inverting the matrix of phenomenological coefficients $[L]$ and equating it to the matrix of coefficients $[\mathbf{R}]$ where $[\mathbf{R}] = [L]^{-1}$. The resistances are expressed in terms of the phenomenological coefficients as

$$\mathbf{R}_A = L_{aa}/|L|, \; \mathbf{R}_B = L_{ww}/|L|, \text{ and } \mathbf{R}_{AB} = -L_{wa}/|L| \tag{20}$$

where $|L|$ is the determinant of the matrix $[L]$. In this transformation the flows are replaced by the fluxes, and the product of the conjugate power variables produces the dissipation function per unit area $\phi'$.

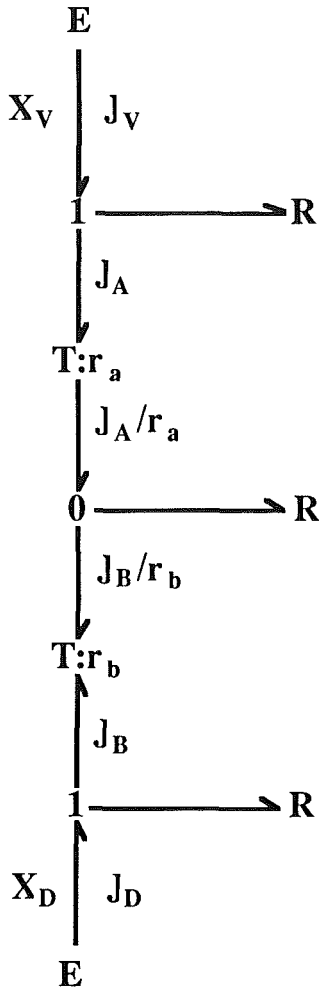


**Fig. 6 Bond graph representation of the hydrodynamic coupling between the diffusive fluxes shown in Fig. 3 in terms of alternate forces and flows defined in equation (9)**

It is noted that three resistances are required to characterize this flow: a resistance for each of the two permeable species, and a coupling resistance. This is in accord with the development by Kedem and Katchalsky (1958) discussed previously where the permeability equations for coupled flow in a membrane are expressed in terms of three coefficients.

In order to express the bond graph resistances in terms of the commonly used K-K membrane parameters, it is necessary that equations (9), as written in matrix format, have the same form as equation (19) when the forces are replaced by $X_V$ and $X_D$ and the flows by $J_V$ and $J_D$, i.e., $[J] = [L']\,[X]$. Therefore, the bond graph of Fig. 3 can be transformed to formulate equations (9) by replacing $\Delta\mu_A$ and $\Delta\mu_B$ by $X_V$ and $X_D$, and $J_V$ and $J_D$ by $J_A$ and $J_B$, respectively, as shown in Fig. 6. The conjugate sources of effort that produce the forces $X_V$ and $X_D$ must be included. For this bond graph the resistances are determined by inverting the matrix of coefficients, $[\mathbf{R}] = [L']^{-1}$. Once again the resistances are expressed in terms of the phenomenological coefficients as

$$R_A = L_{22}/|L'|, \; \mathbf{R}_B = L_{11}/|L'|, \text{ and } \mathbf{R}_{AB} = -L_{12}/|L'| \tag{21}$$

These resistances can be expressed in terms of the K-K membrane parameters $L_p$, $\sigma$, and $\omega$, by introducing the following definitions for the coefficients (Kedem and Katchalsky, 1958):

$$\begin{aligned} L_{11} &= L_p \\ L_{12} &= -\sigma L_p/[1 + \theta\,(1 - \sigma)] \end{aligned} \tag{22}$$

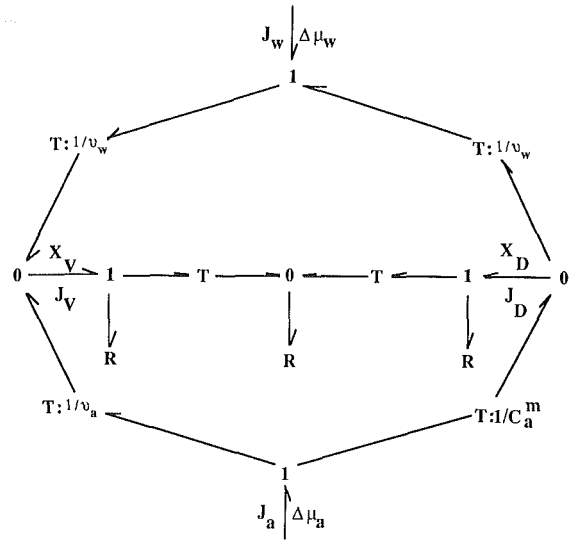


**Fig. 7 Bond graph representation of the coupling structure of additive and water fluxes across a membrane in terms of the K-K governing transport parameters**

$$L_{22} = \omega(1+\theta)^2/[C_a^m\{\theta(1-\sigma)+1\}] + \sigma^2 L_p/\{\theta(-\sigma)+1\}^2$$

From equations (18), (21), and (22) the resistances are solved for as

$$R_a = C_a^m/[\omega(1+\theta)]$$
$$R_b = 1/L_p + \sigma/[\omega(1+\theta)]^2\ [C_a^m\sigma/[\theta(1-\sigma)+1] + 1/\nu_a\} \quad (23)$$
$$R_c = -\theta\sigma C_a^m/[\omega(1+\theta)]^2$$

where the transformer moduli in equation (18) have been conveniently selected as $r_a = 1$ and $r_b = -\theta$.

The fluxes $J_V$ and $J_D$ are implemented in the bond graph as shown in Fig. 7 according to their definition in equations (5). The flows $J_w$ and $J_a$, which are multiplied by a modulating constant or variable at the transformers, add at the **0** junctions at the sides of the graph according to the power direction arrows producing $J_V$ and $J_D$ at the center portion input bonds. The forces at the top and bottom **1** junctions must be $\Delta\mu_w$ and $\Delta\mu_a$, respectively, since the dissipation function was held constant in the definition of the new set of forces $X_V$ and $X_D$ and the product of all the forces and flows in this bond graph produce $\phi'$. This is the power conservation characteristic of the junction structures; the total power entering the junction must be equal to the power leaving the junction (Paynter, 1961).

The bond graph described above is constructed to model a constant hydrodynamic coupling between water and permeable additive in a membrane with the resistances expressed in terms of the K-K membrane parameters. The transient nature of the flows in a cell are coupled with the change in mol content (or displacement variables) of each species within the cell due to the fluxes across the membrane. Therefore, the cell intracellular solution is modeled as a capacitor of water and of permeable additive, and the extracellular solution as a source of mass at a defined concentration for each species. The extracellular sources are dependent on the system temperature during freezing processes according to the ternary thermodynamic phase diagram for the mixture.

A capacitor and a source for each permeable species may also be implemented in a bond graph as shown in Fig. 8. The chemical potential differences $\Delta\mu_w$ and $\Delta\mu_a$ are produced in the top and bottom **1** junctions by the sources and capacitors since the efforts add at the **1** junctions according to the power direction arrows. Also, since the flows are the same at the **1** junctions, the respective fluxes $J_w$ and $J_a$ are the same out of the extracellular sources, into the intracellular capacitors, and into the central coupling structure.

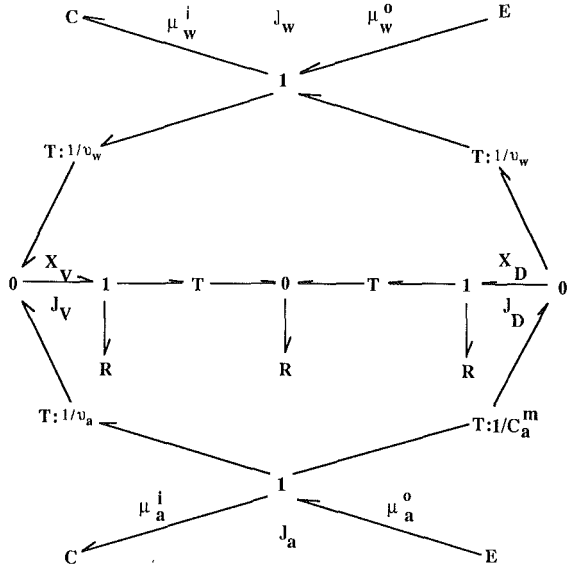


**Fig. 8 Bond graph model of the coupled membrane transport in terms of the K-K force and flow parameters. Capacitance, dissipation, and transformation components and their communication within the system are indicated clearly.**

The constitutive relation for the capacitances of the species $i$ is

$$n_i = V\exp\ [(\mu_i - \mu_i^o)/\Re T] \quad (24)$$

where $V$ is the volume of the intracelluar solution and $\mu_i^o$ is the reference chemical potential. Note that $\mu^o{}_i$ must contain a normalizing factor to allow for the units in equation (24) to be consistent. Since the flows at the top and bottom **1** junctions are known, the incremental capacitance **C** for each capacitor can be determined by the definition $\mathbf{C} = \partial q/\partial e$, where $q$ is the generalized displacement and $e$ the generalized effort. The displacements are computed by integrating over time the flow

$$q_i = \int f_i dt = -1/A\int(dn_i/dt)dt \quad (25)$$

Thus

$$q_w = -n_w/A \text{ and } q_a = -n_a/A \quad (26)$$

The respective capacitances are computed as

$$\mathbf{C}_w = -n_w/A\Re T \text{ and } \mathbf{C}_a = -n_a/A\Re T \quad (27)$$

The resistances and some transformers are modulated indirectly by $n_w$ and $n_a$, for example, by containing in their constitutive relations $C_a^m$, which is a function of $n_w$ as well as $n_a$. This "cross-modulation" makes the bond graph very nonlinear and difficult to formulate and reduce for simulation by hand. However, the model contains all the necessary information to produce automatically the governing equations. Note that the chemical potential differences $\Delta\mu_w$ and $\Delta\mu_a$ will have to be approximated by equations (3) and (4) to produce the K-K equations in the formulation process.

## Sample Simulation of Coupled Membrane Transport

The bond graph model shown in Fig. 8 was applied to simulate the process of adding a glycerol solution to a suspension of human erythrocytes in preparation for subsequent freezing. This protocol corresponds to that devised by Papanek (1978) to test the data evaluation procedure for experiments involving mixing of osmotically active agents with cell suspensions in a stopped-flow chamber. The bond graph is designed such that the effort variables are the transmembrane concentration driving forces and the flow variables are the water and additive fluxes. The reduction and formulation of this bond graph produces the governing K-K equations.

The model for the coupled transport can be represented for

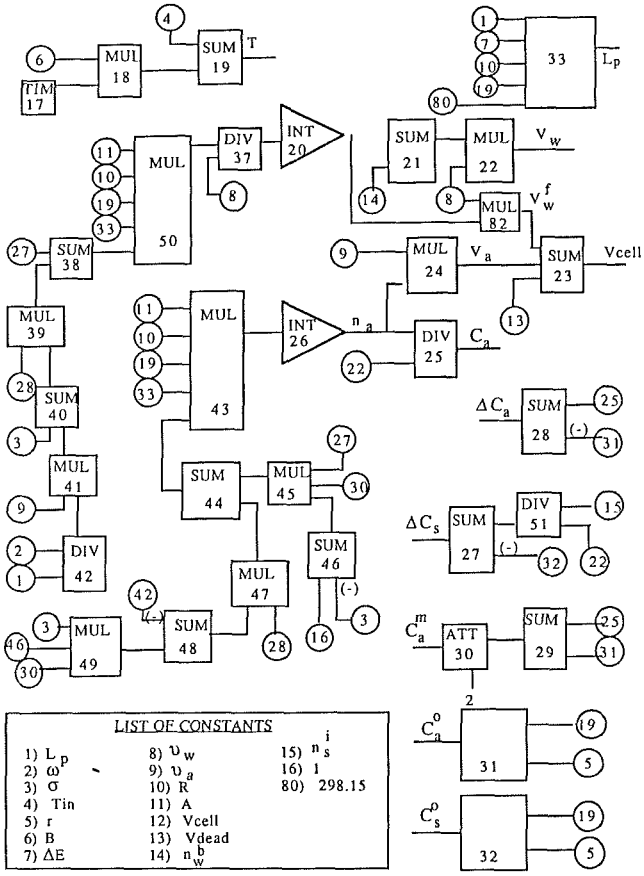


**Fig. 9 Block diagram model for implementing the K-K membrane coupled transport equations and determining the transient cell volume during a defined osmotic stress**

simulation purposes if block diagram model elements are combined with the bond graph elements. The idea behind the block diagrams is to represent the system variables as signals constrained to flow along the lines connecting the blocks, enforcing the governing equations. The advantage of using block diagram models is that they can be used with existing software to simulate the model on a computer with an approach similar to that for solving differential equations on analog computers. This also permits a simple accommodation of nonlinearities that characterize biological systems. The basic block elements are the integrator block, which integrates the rate of change of a variable to produce that variable; the arithmetic blocks, which perform the basic arithmetic operations; and the function blocks, which apply a certain function (e.g., sine, exponential, logarithmic) to the input signals.

In the study of cell osmotic response it is often desirable to be able to simulate the transient cell volume for several different processes and compare the dynamic response. For example, one may wish to compare graphically the cell response to freezing for different permeability parameters or with different nucleation temperatures. Also one may be interested in changing some parameter such as temperature or external concentration during the actual simulaton. It was found that the cell volume can be simulated in a versatile fashion using the simulating program TUTSIM[2] (Twente University of Technology Simulating Program). This is a program that simulates dynamic systems interactively, allowing flexibility of changing model parameters during the simulation. The governing equations are generated automatically and are solved by a simple Euler method. TUTSIM accepts model inputs in

[2]For further information contact Applied i, 200 California Ave., Suite 212, Palo Alto, CA 94306.

**Table 1 Cell biophysical data for human erythrocytes as implemented in the simulation (from Papanek, 1978)**

| | | |
|---|---|---|
| isotonic cell volume | $V_{cell}(iso)$ | $100 \times 10^{-12}$ cm$^3$ |
| cell surface area | A | $135 \times 10^{-8}$ cm$^2$ |
| non-perm. solute content | $n_s$ | $2.16 \times 10^{-14}$ osmol |
| free water content | $n_w^f(iso)$ | $3.33 \times 10^{-12}$ mol |
| bound water content | $n_w^b$ | $6.66 \times 10^{-13}$ mol |
| cell fixed volume | $V_f$ | $40. \times 10^{-12}$ cm$^3$ |

Permeability parameters for cells initially suspended in isotonic saline immersed in isotonic saline and 0.25M glycerol included:

$L_p = 1.23 \times 10^{-11}$ cm$^3$/dyne sec

$\omega = 2.14 \times 10^{-16}$ mol/dyne sec

$\sigma = 0.88$

the form of block diagrams, bond graphs, and combinations of both.

In the present analysis the program TUTSIM was implemented for simulation of the coupled transport process on an IBM PC/AT microcomputer. An equivalent block diagram of the coupled membrane transport system is shown in Fig. 9, and has been described in greater detail previously (Montoya et al., 1987). Nonetheless, a few brief comments are offered to indicate how the model is interpreted in this format. The membrane coupled transport, which is governed by equations (10), can be modeled completely with a block diagram. In addition to enforcing the K-K equations, this block diagram models the cell volume: Block 22 produces the total water volume in the cell computed with equation (12), and block 23 the total cell volume according to equation (14). All the blocks to the left of the integrators enforce the right-hand side of equations (10). The temperature is computed according to equation (15) and is produced by block 19. The permeability temperature dependence of equation (16) is produced by block 33. Blocks 27 and 28 output the concentration differences according to equations (11) and block 30 outputs $C_a^m$. The extracellular concentration of electrolyte and additive are produced by blocks 32 and 31 according to the ternary phase diagram for a given temperature and initial concentration. The initial concentration is expressed as the initial ratio of mass of additive to the mass of electrolyte in the solution, $r = m_a/m_e$. The structure of blocks 31 and 32 will depend on the particular cryoprotectant additive used.

This method of simulation has proven to be very versatile with regard to the flexibility of changing model elements interactively on the computer and the capability of implementing the program on a microcomputer IBM PC/AT for solving the coupled nonlinear transport equations. Although more advanced methods are being developed for direct simulation of nonlinear bond graphs, TUTSIM does afford a present illustration of the utility of this approach to modeling.

A brief Fortran subroutine was written in the standard format defined for TUTSIM to provide necessary parameter initial or constant values. The biophysical parameters supplied to the model were identical to those defined in Papanek's data, and are summarized in Table 1.

The specific protocol that was simulated consisted of the constant temperature osmotic response of erythrocytes to mixing with 0.25 M glycerol solution. Both the initial and final solutions were assumed to include isotonic saline. This type of constant-temperature osmotic stress trial was simulated because it constitutes an important class of experiments conducted in our laboratory to measure the physiological properties of living cells relevant to their response to the stress of cryopreservation (e.g., Schwartz and Diller, 1983; Diller and

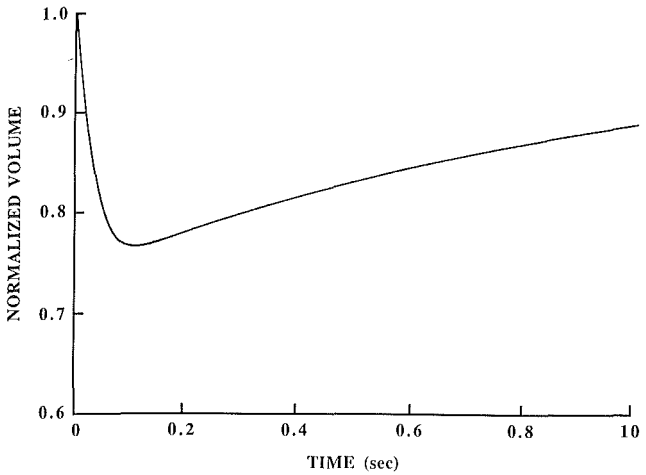


**Fig. 10 Output from a simulation showing the osmotic induced transient volume response of human erythrocytes initially suspended in isotonic saline to rapid mixing with a solution of 0.25 M glycerol in isotonic saline. The typical shrink-swell response sequence is observed.**

Bradley, 1984; Aggarwal et al., 1988; McCaa et al., 1988). These experiments are run at constant temperatures both above and below 0°C. Further application of the model to problems characterized by a transient temperature is accomplished by transforming the equations from the temporal to the thermal domain, and will be described in a subsequent paper.

In this simulation the activation energy was set to zero since the temperature was held constant; therefore the values for $L_{pg}$ and $\omega_{pg}$ were equated to the corresponding values listed in Table 1. In trials for which ice is present the extracellular medium, which causes a concentrating of solutes in the liquid phase and thereby produces an osmotic stress on the cells, the salt and glycerol concentrations are determined according to the ternary phase diagram in terms of the system temperature and initial concentration. The equations for solute concentration as a function of temperature between the melting point and the "pseudo-binary eutectic point" were those developed by Pegg (1983). In the present simulation in which the cellular environment was manipulated by a simple step change in the bathing medium chemical composition at constant temperature, the input to the effort source in the model was a change in the extracellular solute concentration to a composition of 0.29 osmol/kg and 0.25 M glycerol.

The expected shrink-swell response was observed from the output, as shown in Fig. 10. The simulation was complete after about 20 s of computer time. The integration time step size was 5 ms and the equations were integrated over a time span of 10 s. It should be noted that Papanek modified the K-K equations in order to model nondilute solutions; however, the solutions in the test example were sufficiently dilute to be modeled accurately by the original K-K equations. Indeed, comparison of the transient volume plots generated by the present model and by Papanek for the same protocol shows that the results of the two simulations are indistinguishable.

The network thermodynamic method of simulation by bond graphs is very general and is conducive to easy alteration of system parameters and boundary interactions interactively on the computer without requiring reformulation of the mathematical description of the problem. In the present application this versatility should permit the efficient prediction of optimal freezing procedures by simulating and comparing the model response for a variety of cells and freezing protocols.

## Acknowledgments

This research was sponsored by grants from the Juvenile Diabetes Foundation and the Texas Advanced Technology Research Program.

## References

Aggarwal, S. J., Diller, K. R., and Baxter, C. R., 1988, "Hydraulic Permeability and Activation Energy of Human Keratinocytes at Subzero Temperatures," *Cryobiology*, Vol. 25, pp. 203–211.

Diller, K. R., and Bradley, D. A., 1984, "Measurement of the Water Permeability of Single Human Granulocytes on a Microscopic Stopped-Flow Mixing System," ASME *Journal of Biomechanical Engineering*, Vol. 106, pp. 384–393.

Diller, K. R., and Lynch, M. E., 1983, "An Irreversible Thermodynamic Analysis of Cell Freezing in the Presence of Membrane Permeable Additives," *Cryo-Letters*, Vol. 4, pp. 295–308.

Katchalsky, A., and Curran, P. F., 1967, *Nonequilibrium Thermodynamics in Biophysics*, Harvard University Press, Cambridge, MA.

Kedem, O., and Katchalsky, A., 1958, "Thermodynamic Analysis of the Permeability of Biological Membranes to Non-electrolytes," *Biochimica et Biophysica Acta*, Vol. 27, pp. 229–246.

Levin, R. L., Cravalho, E. G., and Huggins, C. E., 1976, "Effect of Hydration on the Water Content of Human Erythrocytes," *Biophysical Journal*, Vol. 16, pp. 1411–1426.

Levin, R. L., 1979, "Water Permeability of Yeast Cells at Sub-zero Temperatures," *Journal of Membrane Biology*, Vol. 46, pp. 91–124.

Mazur, P., 1963, "Kinetics of Water Loss From Cells at Sub-zero Temperatures and the Likelihood of Intracellular Freezing," *Journal of General Physiology*, Vol. 47, pp. 347–369.

McCaa, C., Diller, K. R., Aggarwal, S. J., and Takahashi, T., 1988, "Cryomicroscopic Determination of the Membrane Osmotic Properties of Human Monocytes at Subfreezing Temperatures," *Cryobiology*, submitted.

Montoya, J. P., Diller, K. R., Beaman, J. J., and Breedfeld, P. C., 1987, "A Network Thermodynamic Model for Coupled Membrane Transport: Application to Cell Cryopreservation," *Proceedings of the 1987 ASME-JSME Thermal Engineering Joint Conference*, P. J. Marto and I. Tanasawa, eds., ASME, New York, Vol. 3, pp. 537–542.

Mikulecky, D. C., 1984, "Network Thermodynamics: A Simulation and Modeling Method Based on the Extension of Thermodynamic Thinking Into the Realm of Highly Organized Systems," *Mathematical Biosciences*, Vol. 71, pp. 1–23.

Oster, G. F., Perelson, A. S., and Kathchalsky, A., 1973, "Network Thermodynamic Modelling of Biophysical Systems," *Quarterly Reviews of Biophysics*, Vol. 6, pp. 1–134.

Paynter, H. M., 1961, *Analysis and Design of Engineering Systems*, MIT Press, Cambridge, MA.

Papanek, T. H., 1978, "The Water Permeability of Human Erythrocytes in the Temperature Range 25°C to −10°C," Ph.D. Thesis, Massachusetts Institute of Technology, Cambridge, MA.

Pegg, D. E., 1983, "Simple Equations for Obtaining Melting Points and Eutectic Temperatures for the Ternary System Glycerol/Sodium Chloride/Water," *Cryo-Letters*, Vol. 4, pp. 259–268.

Pegg, D. E., 1984, "Red Cell Volume in Glycerol/Sodium Chloride/Water Mixtures," *Cryobiology*, Vol. 21, pp. 234–239.

Rosenberg, R. C., and Karnopp, D. C., 1983, *Introduction to Physical System Dynamics*, McGraw-Hill, New York.

Schwartz, G. J., and Diller, K. R., 1983, "Analysis of the Water Permeability of Human Granulocytes in the Presence of Extracellular Ice," ASME *Journal of Biomechanical Engineering*, Vol. 105, pp. 360–366.

# Forced Convection in the Entrance Region of a Packed Channel With Asymmetric Heating

**P. Cheng**
Department of Mechanical Engineering,
University of Hawaii at Manoa,
Honolulu, HI 96822
Fellow ASME

**C. T. Hsu**
Fluid Mechanics Department
TRW Systems and Energy,
Redondo Beach, CA 90278

**A. Chowdhury**
Department of Mechanical Engineering,
University of Hawaii at Manoa,
Honolulu, HI 96822

*The problem of a thermally developing forced convective flow in a packed channel heated asymmetrically is analyzed in this paper. The flow in the packed channel is assumed to be hydrodynamically fully developed and is governed by the Brinkman–Darcy–Ergun equation with variable porosity taken into consideration. A closed-form solution based on the method of matched asymptotic expansions is obtained for the axial velocity distribution, and the wall effect on pressure drop is illustrated. The energy equation for the thermally developing flow, with transverse thermal dispersion and variable stagnant thermal conductivity taken into consideration, was solved numerically. To match the predicted temperature distributions with existing experimental data, it is found that a wall function must be introduced to model the transverse thermal dispersion process in order to account for the wall effect on the lateral mixing of fluid. The variations of the local Nusselt number along the streamwise direction in terms of the appropriate parameters are illustrated. The thermal entrance length effect on forced convection in a packed channel is discussed.*

## Introduction

In the early experimental study of forced convection in a heated packed tube, the heat transfer coefficient and the effective thermal conductivity were determined independently. The heat transfer coefficient was determined from the amount of energy absorbed by the fluid, which was obtained by measuring the inlet and outlet temperatures of the fluid (Colburn, 1931). The value of the local effective thermal conductivity was determined by a graphic differentiation of temperature data (Hall and Smith, 1949; Bunnel et al., 1949). From the early experimental data, it has been observed that steep radial temperature gradients exist near the heated and cooled walls of a packed tube (Hall and Smith, 1949; Bunnel et al., 1949; Coberly and Marshall, 1951). These steep temperature gradients, resembling a temperature discontinuity at the wall and porous medium interface, are especially pronounced at high Reynolds numbers or high particle/tube diameter ratios. It has been suggested that the steep radial temperature gradient, which implies additional thermal resistance there, is caused by the wall effects on velocity, stagnant thermal conductivity, and the transverse thermal dispersion process.

To account for the localized thermal resistance near the wall while retaining the plug flow assumption, Coberly and Marshall (1951) introduced the concept of a wall heat transfer coefficient $h_w$, which is defined as

$$q_w = h_w (T_w^* - T_{\text{ext}}^*) \tag{1}$$

where $q_w$ is the local heat flux, $T_{\text{ext}}^*$ is the temperature of the packed bed at the wall, which differs from the wall temperature $T_w^*$. It follows from equation (1) that the Nusselt number $\text{Nu}_w$ is given by

$$\text{Nu}_w = \frac{h_w d_p}{k_f^*} = \frac{q_w d_p}{k_f^* (T_w^* - T_{\text{ext}}^*)} \tag{2}$$

where $k_f^*$ is the thermal conductivity of the fluid. To be consistent with equation (1) and the plug flow model, Coberly and Marshall (1951) introduced the following thermal boundary condition for the analysis of forced convection in a packed tube:

$$-k_{er}^* \left(\frac{\partial T^*}{\partial r^*}\right)_{r^* = r_0^*} = h_w (T_w^* - T^*)_{r^* = r_0^*} \tag{3}$$

where $k_{er}^*$ is the average effective radial thermal conductivity of a cylindrical packed column with radius $r_0^*$. It is relevant to note that equations (1)–(3) have made the unrealistic assumption that a temperature discontinuity exists at the wall and porous medium interface.

If the values of $h_w$ and $k_{er}^*$ in equation (3) are assumed to be constant (i.e., independent of position), the energy equation (with the assumption of a plug flow) subject to boundary condition (3) and the entrance condition can be solved by a separation of variables. With the aid of the analytical solution and in comparison with the temperature data, the values of $k_{er}^*$ and $h_w$ can be determined simultaneously as a function of the Reynolds number $\text{Re}_d$. This method and its variations have been used for the determination of $k_{er}^*$ and $h_w$ by most of the subsequent investigators. It has been found (Beck, 1962) while the value of $k_{er}^*$ can be correlated as a linear function of $\text{Re}_d$, the exponent of $\text{Re}_d$ in the correlation equations for $\text{Nu}_w$, however, varies widely from 0.33 to 1.0 as reported by various investigators. Li and Finalyson (1977) have attributed the widely scattered data to the thermal entrance length effect, i.e., the value of $h_w$ in equation (3) is not constant but is a function of position.

Little experimental work has been done on forced convection in a packed channel. As far as the authors are aware, the only published data on forced convection in a packed bed of this geometry are from Schroeder et al. (1981), who have performed an experiment on forced convection of water in a packed bed between parallel plates separated by a distance $2H$ and heated asymmetrically. The packed channel, having a high length ($L$) to width ($2H$) ratio, was filled with glass spheres having a particle diameter ($d_p$) to half-width ($H$) ratio of 0.074 and 0.37. The temperature profiles at the location $x^*/2H = 13.5$ were measured. The correlation equations for the average effective transverse thermal conductivity and $\text{Nu}_w$ (defined in equation (2)) as a function of $\text{Re}_d$ were obtained.

In a series of papers, Cheng and co-workers (Cheng and

Contributed by the Heat Transfer Division for publication in the JOURNAL OF HEAT TRANSFER. Manuscript received by the Heat Transfer Division April 27, 1987. Keywords: Forced Convection, Packed and Fluidized Beds, Porous Media.

Vortmeyer, 1986; Cheng and Hsu, 1986a, 1986b) have performed analytical studies of a hydrodynamically and thermally fully developed flow in a rectangular or an annular packed column with asymmetric heating. In these analyses, the Brinkman–Darcy equation (Brinkman, 1947) with variable porosity was used as the momentum equation. The transverse thermal dispersion conductivity is regarded as a point function, which depends on the local axial velocity. A wall function was introduced to account for the reduction of the lateral mixing of fluid due to the presence of the wall. As a result, the unrealistic boundary condition given by equation (3) need not be imposed.

In this paper an analysis is carried out for the problem of thermal entrance length effect on forced convection in a packed channel, using an approach similar to those of the previous papers (Cheng and co-workers, 1986, 1986a, 1986b). Instead of the linear Brinkman–Darcy equation, however, the nonlinear Brinkman–Darcy–Ergun model (Vafai and Tien, 1981; Vafai 1984) is used as the momentum equation to take into consideration the inertial effect. Both the method of matched asymptotic expansions (Van Dyke, 1964) and the finite difference method are used to solve the nonlinear equation for the axial velocity distribution. The pressure drop in the packed channel as a function of the Reynolds number is obtained. The wall effects on transverse thermal dispersion and stagnant thermal conductivity are taken into consideration in the energy equation, which is solved numerically for the thermally developing flow. The constants in the expression for the transverse thermal dispersion conductivity are determined by matching the predicted temperature distributions in the packed channel with the experimental data of Schroeder et al. (1981).

## Flow Field

Consider a hydrodynamically fully developed flow through a packed bed between parallel plates located at $y^* = 0$ and $y^* = 2H$. If the porosity variation near the walls is taken into consideration, the porosity can be approximated by (Vafai, 1984; Vortmeyer and Schuster, 1983)

$$\phi^* = \phi^*_\infty [1 + C_1 \exp(-N_1 y^*/d_p)] \qquad 0 \le y^* \le H \qquad (4a)$$

$$\phi^* = \phi^*_\infty \{1 + C_1 \exp[-N_1(2H - y^*)/d_p]\}, \quad H \le y^* \le 2H \qquad (4b)$$

where $\phi^*_\infty = 0.4$ is the porosity at the core of the packed bed; $d_p$ is the particle diameter; $C_1 = 1$ and $N_1 = 2$ (Vafai, 1984; Vortmeyer and Schuster, 1983). The momentum equation based on the Brinkman–Darcy–Ergun model (Vafai and Tien, 1981; Vafai, 1984) is

$$\frac{\mu^* u^*}{K^*} + \frac{\rho^* F^*}{\sqrt{K^*}} u^{*2} = -\frac{dp^*}{dx^*} + \frac{\mu^*}{\phi^*} \frac{d^2 u^*}{dy^{*2}} \qquad (5)$$

where $u^*$ is the Darcian velocity in the $x^*$ direction (i.e., the streamwise direction). $dp^*/dx^*$ is the externally imposed pressure gradient; $\rho^*$ and $\mu^*$ are the density and viscosity of the fluid. For a packed-sphere bed, the permeability of the bed is related to the porosity by

$$K^* = \frac{\phi^{*3} d_p^2}{a(1-\phi^*)^2} \qquad (6)$$

where $a = 150$ is an empirical constant (Ergun, 1952). The quantity $F^*$ in equation (5) is a dimensionless coefficient for the inertial effect, which depends only on $\phi^*$, i.e.,

$$F^* = \frac{b}{\sqrt{a}\phi^{*3/2}} \qquad (7)$$

where $b = 1.75$ is also an empirical constant (Ergun 1952). Since the velocity profile is symmetric about the centerline at $y^* = H$, we need to consider the flow field in half of the packed bed, i.e., in the domain of $0 \le y^* \le H$. Thus, the boundary conditions for the velocity are

## Nomenclature

$A$ = constant defined in equation (40*b*)
$a$ = empirical constant in equation (6)
$B$ = constant defined in equation (40*b*)
$B_p$ = porosity function defined in equation (56)
$b$ = empirical constant in equation (7)
$C$ = constant defined in equation (40*b*)
$C_\infty$ = constant defined in equation (13)
$C_1$ = constant in equation (4)
$C_T$ = constant defined in equation (62)
$c_p^*$ = specific heat at constant pressure
$D$ = integration constant defined in equation (43)
$D_T$ = empirical constant defined in equation (57)
$d_p$ = particle diameter
$F^*, F$ = dimensional and dimensionless functions defined in equations (7) and (10), respectively
$H$ = half-width of the channel
$h_w$ = wall heat transfer coefficient defined in equation (1)
$K^*, K$ = dimensional and dimensionless permeabilities of the packed bed defined in equations (6) and (10), respectively
$k_d^*$ = stagnant thermal conductivity of the packed bed
$k_f^*$ = thermal conductivity of fluid
$k_s^*$ = thermal conductivity of particles
$k_T^*$ = thermal dispersion conductivity of the packed bed
$k_{er}^*$ = effective radial thermal conductivity of the packed bed
$k_{ey}^*, k_{ey}$ = dimensional and dimensionless effective transverse thermal conductivity of the packed bed defined in equations (54) and (63)
$l$ = wall function defined in equations (57) and (58)
$m$ = empirical constant defined in equation (57)
$N$ = inertial parameter
$N_1$ = constant defined in equation (4)
$n$ = constant associated with the inertial parameter $N$
$\mathrm{Nu_d}$ = local Nusselt number defined in equation (67*a*)
$\overline{\mathrm{Nu}}_\mathrm{d}$ = average Nusselt number defined in equation (67*b*)
$\mathrm{Nu}_w$ = Nusselt number defined in equation (2)
$p^*$ = pressure
Pr = Prandtl number of the fluid
$q_w$ = local surface heat flux
$\bar{q}_w$ = average surface heat flux
$r^*$ = radial coordinate
$r_0^*$ = radius of a cylindrical packed column

$$y^* = 0: \quad u^* = 0 \tag{8}$$

$$y^* = H: \quad u^* = u^*_\infty \tag{9}$$

where $u^*_\infty$ is the velocity in the core region.

We now define the following normalized variables:

$$u = u^*/u^*_\infty, \quad \phi = \phi^*/\phi^*_\infty, \quad K = K^*/K^*_\infty,$$
$$F = F^*/F^*_\infty, \quad y = y^*/H \tag{10}$$

where $K^*_\infty = \phi^{*3}_\infty d_p^2/a(1-\phi^*_\infty)^2$ and $F^*_\infty = b/\sqrt{a}\phi^{*3/2}_\infty$. Equations (4)–(7) in terms of the new dimensionless variables are

$$\frac{u}{K} + \frac{NF}{K^{1/2}} u^2 = \alpha_\infty + \frac{\sigma^2}{\phi} \frac{d^2u}{dy^2} \tag{11}$$

$$\phi = 1 + C_1 e^{-N_1 y/\gamma} \tag{12}$$

$$K = \frac{\phi^3}{[1 + C_\infty(1-\phi)]^2} \tag{13}$$

$$F = \phi^{-3/2} \tag{14}$$

where $\gamma = d_p/H$, $\sigma = (\sqrt{K^*_\infty/\phi^*_\infty})/H = 5.44 \times 10^{-2}\gamma$ (if $\phi^*_\infty = 0.4$), $\alpha_\infty = -(K^*_\infty/\mu^* u^*_\infty)\, dp^*/dx^*$, $C_\infty = \phi^*_\infty/(1-\phi^*_\infty) = 2/3$ (if $\phi^*_\infty = 0.4$), and $N = n\, Re_\infty$ with $n = [1/(1-\phi^*_\infty)]\, b/a = 1.94 \times 10^{-2}$ (if $\phi^*_\infty = 0.4$, $a = 150$, and $b = 1.75$) and $\mathrm{Re}_\infty = u^*_\infty d_p/\nu$ where $\nu^*$ is the kinematic viscosity of the fluid.

Boundary conditions (8) and (9) in terms of the new variables are

$$y = 0: \quad u = 0 \tag{15}$$

$$y = 1: \quad u = 1 \tag{16}$$

The relative importance of the inertial resistance to that of Darcian resistance can be examined from the momentum balance in the core region. In the core region where the boundary friction effect is negligible and $u = \phi = F = K = 1$, equation (11) becomes

$$1 + N = \alpha_\infty \tag{17}$$

where $N$ is a positive quantity. Substituting equation (17) into equation (11) yields

$$\frac{u}{K} + N\left[\frac{F}{K^{1/2}} u^2 - 1\right] = 1 + \frac{\sigma^2}{\phi} \frac{d^2u}{dy^2} \tag{18}$$

Equation (18) together with equations (12)–(16) are the governing equations and boundary conditions for the problem. We now attempt to solve the problem by the method of matched asymptotic expansions under the conditions $\sigma \ll 1$, $\gamma < 1$, and $\epsilon = \sigma/\gamma\sqrt{1+N} = 5.44 \times 10^{-2}/\sqrt{1+N} \ll 1$, where $\epsilon$ is the thickness ratio of the boundary friction layer to the variable porosity layer.

**Outer Solution.** For the variable porosity layer, we define the following outer variables

$$Y = y/\gamma \tag{19a}$$

$$U = u \tag{19b}$$

Equations (12) and (18) in terms of the outer variables are

$$\phi = 1 + C_1 e^{-N_1 Y} \tag{20}$$

$$\frac{U}{K} + N\left[\frac{F}{K^{1/2}} U^2 - 1\right] = 1 + \frac{\epsilon^2(1+N)}{\phi} \frac{d^2U}{dY^2} \tag{21a}$$

where

$$\epsilon = \sigma/\gamma\sqrt{1+N}. \tag{21b}$$

Equations (20) and (21) with $K$ and $F$ given by equations (13) and (14) are to be solved subject to the boundary condition

$$Y \to \infty: \quad U = 1 \tag{22}$$

We now assume the following series expansions for the outer variable $U$:

$$U = U_0 + 0(\epsilon) \tag{23}$$

Substituting equation (23) into equations (21) and (22) yields

## Nomenclature (cont.)

$\mathrm{Re}_d$ = Reynolds number based on the mean velocity
$\mathrm{Re}_\infty$ = Reynolds number based on the velocity in the core of the packed bed
$T^*$ = temperature
$T^*_c$ = temperature of the cold plate
$T^*_h$ = temperature of the hot plate
$T^*_i$ = inlet temperature of the fluid
$T^*_w$ = wall temperature
$T^*_{\mathrm{ext}}$ = temperature of the packed bed at the wall that is extrapolated from the interior of the bed
$u^*, u$ = dimensional and dimensionless axial velocities defined in equation (10)
$u^*_m, u_m$ = dimensional and dimensionless mean axial velocities defined in equation (51)
$U$ = outer variable defined in equation (19)
$x^*$ = streamwise coordinate
$Y$ = dimensionless outer variable defined in equation (19a)
$y^*, y$ = dimensional and dimensionless coordinate defined in equation (10)
$\hat{Y}_c$ = constant defined in equation (46b)
$\alpha_\infty$ = dimensionless pressure gradient based on $u^*_\infty$
$\alpha_m$ = dimensionless pressure gradient based on $u^*_m$ defined in equation (53)
$\gamma$ = constant in equation (12)
$\epsilon$ = perturbation parameter defined in equation (21b)
$\zeta$ = transformed coordinate in the axial direction defined in equation (62)
$\zeta_L$ = transformed coordinate defined in equation (66)
$\theta$ = dimensionless temperature defined in equation (63)
$\lambda$ = constant defined in equation (38b)
$\Lambda$ = ratio of thermal conductivity of the fluid to that of the solid
$\mu^*$ = viscosity of the fluid
$\nu^*$ = kinematic viscosity of the fluid
$\rho^*$ = density of the fluid
$\sigma$ = parameter in equation (11)
$\phi^*, \phi$ = porosity and normalized porosity defined in equation (10)
$\omega$ = empirical constant in equation (58)

**Superscript**

$\hat{}$ = quantities associated with inner variables

**Subscripts**

$\infty$ = quantities at the core
0 = first-order perturbation

$$\frac{U_0}{K}+N\left[\frac{F}{K^{1/2}}\,U_0^2-1\right]=1 \tag{24}$$

$$Y\to\infty:\quad U_0=1 \tag{25}$$

Equation (24) together with equations (13) and (14) subject to the boundary condition (25) constitutes the first-order outer problem. Since equation (24) is an algebraic equation, it can be solved for $U_0$ to give

$$U_0=\frac{-\dfrac{1}{K}+\sqrt{\dfrac{1}{K^2}+\dfrac{4N(1+N)}{K^{1/2}}F}}{\dfrac{2NF}{K^{1/2}}} \tag{26}$$

where the positive sign in front of the square root has been chosen so that the boundary condition (25) can be satisfied. It is relevant to note that at the limit of $n\to 0$, equation (24) gives

$$U_0=K \tag{27a}$$

and in the limit of $N\to\infty$, equation (24) gives

$$U_0=\frac{\sqrt[4]{K}}{\sqrt{F}} \tag{27b}$$

**Inner Solution.** With the inertial effect taken into consideration, the characteristic length of the boundary friction layer depends not only on $\sigma$ but also on $N$, which can be shown as follows. From equation (11), it is seen that the thickness of the viscous sublayer is of $0(\sigma)$ when $N \ll 1$, while the thickness of the sublayer is of $0(\sigma/\sqrt{N})$ when $N \gg 1$. In order to combine these two scales into the perturbation analysis, the following inner variables are introduced:

$$\hat{Y}=\frac{\sqrt{1+N}}{\sigma}\,y,\quad \hat{u}=u,\quad \hat{\phi}=\phi,\quad \hat{F}=F,\quad \hat{K}=K \tag{28}$$

In terms of these variables, equations (20) and (21) become

$$\hat{\phi}=1+C_1 e^{-\epsilon N_1 \hat{Y}} \tag{29}$$

$$\frac{1}{1+N}\,\frac{\hat{u}}{\hat{K}}+\frac{N}{1+N}\,\frac{\hat{F}}{\hat{K}^{1/2}}\,\hat{u}^2=1+\frac{1}{\hat{\phi}}\,\frac{d^2\hat{u}}{d\hat{Y}^2} \tag{30}$$

which is to be solved subject to the boundary condition

$$\hat{Y}=0:\quad \hat{u}=0 \tag{31}$$

and the matching condition obtained from the outer solution.

For the first-order approximation, the inner variables can be expanded as

$$\begin{aligned}\hat{u}&=\hat{u}_0+0(\epsilon)\\ \hat{\phi}&=\hat{\phi}_0+0(\epsilon)\\ \hat{K}&=\hat{K}_0+0(\epsilon)\\ \hat{F}&=\hat{F}_0+0(\epsilon)\end{aligned} \tag{32}$$

Substituting equations (32) into equations (29)–(31), (13), and (14) yields the following first-order inner problem:

$$\hat{\phi}_0=1+C_1 \tag{33}$$

$$\frac{1}{1+N}\,\frac{\hat{u}_0}{\hat{K}_0}+\frac{N}{1+N}\,\frac{\hat{F}_0\hat{u}_0^2}{\hat{K}_0^{1/2}}=1+\frac{1}{\hat{\phi}_0}\,\frac{d^2\hat{u}_0}{d\hat{Y}^2} \tag{34}$$

$$\hat{K}_0=\frac{\hat{\phi}_0^3}{[1+C_\infty(1-\hat{\phi}_0)]^2} \tag{35}$$

$$\hat{F}_0=\hat{\phi}_0^{-3/2} \tag{36}$$

subject to the boundary condition

$$\hat{u}_0(0)=0 \tag{37}$$

and the matching condition

$$\hat{u}_0(\hat{Y})=\lambda\quad\text{as}\quad \hat{Y}\to\infty \tag{38a}$$

where

$$\lambda=U_0(0)=\frac{-\dfrac{1}{\hat{K}_0}+\sqrt{\dfrac{1}{\hat{K}_0^2}+\dfrac{4N(1+N)\hat{F}_0}{\hat{K}_0^{1/2}}}}{2N\hat{F}_0/K_0^{1/2}} \tag{38b}$$

which is obtained from the outer solution given by equations (24) or (26) letting $Y\to 0$. It is relevant to note that $\lambda$ satisfies equation (24), which gives

$$\frac{\lambda}{\hat{K}_0}+\frac{N\hat{F}_0}{\hat{K}_0^{1/2}}\,\lambda^2=1+N \tag{39}$$

It will now be shown that a closed-form solution exists for the first-order inner problem given by equations (33)–(38). To this end, equation (34) will first be written as

$$\frac{d^2\hat{u}_0}{d\hat{Y}^2}=\frac{3}{2}\,A\hat{u}_0^2+B\hat{u}_0-\frac{C}{2} \tag{40a}$$

where

$$A=\frac{2}{3}\,\frac{N}{1+N}\,\frac{\hat{F}_0\hat{\phi}_0}{\hat{K}^{1/2}},\quad B=\frac{1}{1+N}\,\frac{\hat{\phi}_0}{\hat{K}_0}\quad\text{and}\quad C=2\hat{\phi}_0. \tag{40b}$$

Equation (40*a*) can be integrated once to give

$$\frac{d\hat{u}_0}{d\hat{Y}}=\sqrt{A\hat{u}_0^3+B\hat{u}_0^2-C\hat{u}_0+D} \tag{41}$$

where $D$ is an integration constant. Note that the positive sign in front of the square root in equation (41) has been chosen on the physical ground so that at $\hat{Y}=0$, $d\hat{u}_0/d\hat{Y}=\sqrt{D}\geq 0$. It follows that $D$ must be a positive number. The integration of equation (41) leads to

$$\int_0^{\hat{u}_0}\frac{d\hat{u}_0}{\sqrt{A\hat{u}_0^3+B\hat{u}_0^2-C\hat{u}_0+D}}=\hat{Y} \tag{42}$$

which is an elliptic integral (Abramowitz and Stegan, 1965). In order for equation (42) to satisfy the boundary condition (38*a*), it is required that the denominator vanish as $\hat{u}_0\to\lambda$, i.e.,

$$D=C\lambda-B\lambda^2-A\lambda^3 \tag{43}$$

Note that in terms of $A$, $B$, and $C$, equation (39) can be written as

$$C=3A\lambda^2+2B\lambda \tag{44}$$

Substituting equations (43) and (44) into equation (42), it can be shown that

$$\int_0^{\hat{u}_0}\frac{dx}{(\lambda-x)\sqrt{Ax+2A\lambda+B}}=\hat{Y} \tag{45}$$

where $x$ is a dummy variable. Equation (45) can be integrated in closed form to give

$$\hat{u}_0(\hat{Y})=\lambda-(3\lambda+B/A)\,\mathrm{sech}^2\left[\left(\frac{\hat{Y}+\hat{Y}_c}{2}\right)\sqrt{3A\lambda+B}\right] \tag{46a}$$

where

$$\hat{Y}_c=\frac{2}{\sqrt{3A\lambda+B}}\,\mathrm{sech}^{-1}\sqrt{\frac{\lambda}{3\lambda+B/A}} \tag{46b}$$

Equation (46) is similar in form to the solution given by Leibovich and Seebass (1984) for the propagation of nonlinear waves.

We now examine the inner velocity distribution in the asymptotic limits of $n\to 0$ (i.e., $b=0$) and $N\to\infty$ ($\mathrm{Re}_d\to\infty$ and $b=1.75$). At the limit of $n\to 0$, equations (40*b*), (38*b*), (27*a*), and (43) give $A=0$, $B=\hat{\phi}_0/\hat{K}_0$, $D=\hat{\phi}_0\hat{K}_0$, and $\lambda=\hat{K}_0$. It follows from the integration of equation (45) that

$$\hat{u}_0(\hat{Y})=\hat{K}_0[1-\exp(-\sqrt{B}\,\hat{Y})]\quad\text{where}\quad \hat{Y}=y/\sigma \tag{47}$$

which reduces to the equation given previously (Cheng and Vortmeyer, 1986; Cheng and Hsu, 1986b). As discussed by

Cheng and Vortmeyer (1986), equations (27*a*) and (47) are independent of the Reynolds number because the inertial effect has been neglected.

At the limit of $N \to \infty$, equations (38*b*) and (40*b*) give $\lambda = \hat{K}_0^{1/4}/(\hat{F}_0\hat{\phi}_0)^{1/2}$, $A = 2\hat{\phi}_0/3\lambda^2$, and $B = 0$. It follows from equations (46) that

$$\hat{u}_0(\hat{Y}) = \lambda - 3\lambda \operatorname{sech}^2\left[\frac{(\hat{Y}+\hat{Y}_c)}{2}\sqrt{32A\lambda}\right] \tag{48a}$$

where

$$\hat{Y}_c = \frac{2}{\sqrt{3A\lambda}}\operatorname{sech}^{-1}\left[\frac{1}{\sqrt{3}}\right] \quad \text{and} \quad \hat{Y} = \sqrt{N}y/\sigma \tag{48b,c}$$

All of the preceding discussion is also applicable to the case of a constant porosity packed bed (Cheng, 1987) where $C_1 = 0$ and $F = \phi = K = \hat{F}_0 = \hat{\phi}_0 = \hat{K}_0 = 1$. With these values the outer solution given by equations (26*a*) and (38*b*) reduces to $U_0 = \lambda = 1$, while the inner solution is given by equation (46) with $A = 2N/3(1+N)$, $B = 1/(1+N)$, $C = 2$, and $D = 1 + N/3(N+1)$.

**Results and Discussion.** A composite solution for $u$ can be constructed from the first-order inner and outer solutions based on the multiplicative rule (Van Dyke, 1964) as follows:

$$u = U_0(Y)\hat{u}_0(\hat{Y})/\lambda + 0(\epsilon) \tag{49}$$

where $\hat{u}_0(\hat{Y})$ is given by equation (46) while $U_0(Y)$ is given by equation (26) with $Y = \epsilon\hat{Y}$. Equation (49) can be computed in terms of $\mathrm{Re}_\infty$. However, it will be more meaningful to present the results in terms of $\mathrm{Re}_d$, the Reynolds number based on the average mean velocity, which is defined as

$$\mathrm{Re}_d = u_m^* d_p/\nu = \mathrm{Re}_\infty u_m \tag{50}$$

where $u_m^*$ and $u_m$ are the dimensional mean velocities defined as

$$u_m^* = \frac{1}{H}\int_0^H u^* dy^* \tag{51a}$$

and

$$u_m = \frac{u_m^*}{u^*} = \int_0^1 u\, dy = \epsilon\gamma\int_0^{\frac{1}{\epsilon\gamma}} u\, d\hat{Y} \tag{51b}$$

Equation (51*b*) shows that $u_m$ is a function of $\mathrm{Re}_d$ as well as $\gamma$.

It will be of interest to investigate the effect of $\gamma$ on the axial velocity normalized with respect to $u_m^*$. To this end, we note that

$$u^*/u_m^* = u/u_m \tag{52}$$

where $u$ is given by equation (49) and $u_m$ is given by equation (51*b*). For given values of $\gamma$ and $\mathrm{Re}_\infty$, the normalized velocity given by equation (52) can be computed with the aid of equations (49) and (51*b*). Equation (50) can then be used to convert the value of $\mathrm{Re}_\infty$ into $\mathrm{Re}_d$. The results of these computations for the normalized velocity $(u^*/u_d^*)$ versus $y\,(y = y^*/H)$ (with $C_1 = 1$, $N_1 = 2$, and $\phi_\infty^* = 0.4$) at different Reynolds numbers are presented as solid lines in Fig. 1 for $\gamma = 0.074$ and $\gamma = 0.37$, which corresponds to the experiments performed by Schroeder et al. (1981). It is shown that the velocity overshoot occurs at a distance of 0.1 $d_p$ to 0.15 $d_p$ away from the wall depending on the value of $\mathrm{Re}_d$. The peak velocity decreases as the value of $\gamma$ is increased.

To check the accuracy of the asymptotic solution, finite difference solutions to equations (11)–(16) similar to previous work (Georgiadis and Catton, 1987) were also obtained for comparison. The results of the finite difference solution are plotted as dashed lines in Fig. 1. It is shown that the finite difference solution differs only slightly from that of the asymptotic solution except at low Reynolds numbers ($\mathrm{Re}_d \ll 10$).

The dimensionless pressure gradient based on the mean velocity is defined as $\alpha_m$, which is related to $\alpha_\infty$ by

$$\alpha_m = -\frac{K_\infty^*}{\mu^* u_m^*}\frac{dp^*}{dx^*} = \frac{\alpha_\infty}{u_m} = (1+N)/u_m \tag{53}$$

Equation (53) was computed for a variable porosity bed with three values of $\gamma$ ($\gamma = 0.03$, 0.074, and 0.37) based on the analytical and finite difference solutions. The results of the computations are presented as solid lines for the analytical solution and as dashed lines for the finite difference solution in Fig. 2, which shows excellent agreement between analytical and finite difference solutions for $\mathrm{Re}_d > 10$, for which $\epsilon$ is small. At a given value of $\mathrm{Re}_d$, it is shown that the value of $\alpha_m$

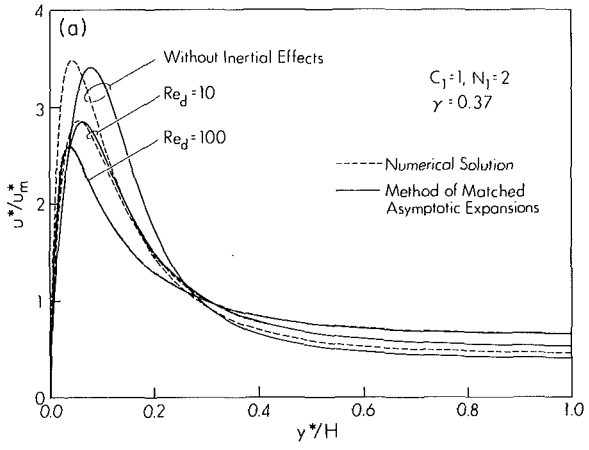


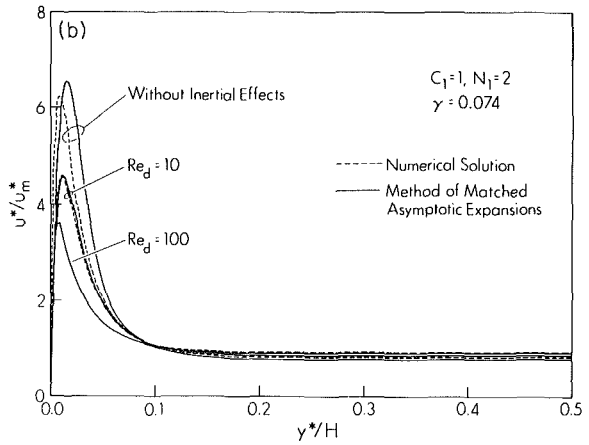


**Fig. 1 Wall effects on velocity in a variable-porosity packed channel: (*a*) $\gamma = 0.074$; (*b*) $\gamma = 0.37$**

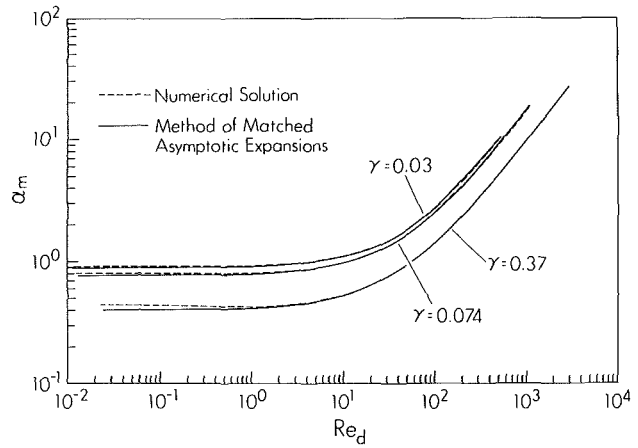


**Fig. 2 Wall effects on dimensionless pressure drop in a variable-porosity packed channel**

decreases as the value of $\gamma$ is increased. This is because the higher the value of $\gamma$, the lesser are the Darcian and inertial resistances per unit volume of the packed bed. The effect of $\gamma$ on $\alpha_m$ is shown to be more pronounced in the Darcian flow region ($\mathrm{Re}_d < 10$) and the transitional flow region ($10 \le \mathrm{Re}_d \le 10^2$) than in the Forchheimer flow region ($\mathrm{Re}_d > 10^2$). The wall channeling effect on $\alpha_m$ is negligibly small if $\gamma < 0.03$, which is consistent with experimental observations.

**Temperature Field.** The heat transfer characteristics of a thermally developing forced convective flow in a constant porosity packed channel heated symmetrically with transverse thermal dispersion neglected has been analyzed by Kaviany (1985). In the following, the effects of the thermal entrance length and transverse thermal dispersion on forced convection in a variable-porosity packed channel heated asymmetrically will be analyzed.

For a thermally developing flow in a packed channel the energy equation for the present problem is

$$(\rho^* c_p^*)_f u^* \frac{\partial T^*}{\partial x^*} = \frac{\partial}{\partial y^*}\left(k_{ey}^* \frac{\partial T^*}{\partial y^*}\right) \tag{54}$$

where $(\rho^* c_p^*)_f$ is the heat capacity of the fluid while $k_{ey}^*$ is the effective transverse thermal conductivity of the packed bed, which is given by

$$k_{ey}^* = k_d^* + k_T^* \tag{55}$$

In the above equation, $k_d^*$ is the stagnant thermal conductivity of the packed bed, which is given by (Zehner and Schluender, 1970)

$$\frac{k_d^*}{k_f^*} = 1 - \sqrt{1-\phi^*} + \frac{2\sqrt{1-\phi^*}}{1-\Lambda B_p}\left[\frac{(1-\Lambda)B_p}{(1-\Lambda B_p)^2}\ln\left(\frac{1}{\Lambda B_p}\right) - \frac{B_p+1}{2} - \frac{B_p-1}{1-\Lambda B_p}\right] \tag{56}$$

where $B_p = 1.25[(1-\phi^*)/\phi^*]^{10/9}$ is for a packed-sphere bed and $\Lambda = k_f^*/k_s^*$ is the ratio of the thermal conductivity of the fluid phase to that of the solid phase. In equation (55), $k_T^*$ is the transverse thermal dispersion conductivity, which is given by (Cheng and co-workers, 1986, 1986a, 1986b)

$$\frac{k_T^*}{k_f^*} = D_T\left[\mathrm{Pe}_d\left(\frac{u}{u_m}\right)\right]^m l \tag{57}$$

where $\mathrm{Pe}_d = \mathrm{Pr}\,\mathrm{Re}_d$ is the Peclet number with Pr denoting the Prandtl number of the fluid. In the above equation, $u$ and $u_m$ are the dimensionless velocities obtained from the previous section, $D_T$ and $m$ are empirical constants, and $l$ is the wall function for transverse thermal dispersion introduced by Cheng and co-workers (1986, 1986a, 1986b) to account for the wall effect on the reduction of lateral mixing of fluid. If the Van Driest type of wall function is introduced, the expression for $l$ is

$$l = \begin{cases} 1 - e^{-y/\omega}, & 0 \le y \le \dfrac{1}{\gamma} \qquad (58a) \\ 1 - e^{-\left(\frac{2}{\gamma} - y\right)/\omega}, & \dfrac{1}{\gamma} \le y \le \dfrac{2}{\gamma} \qquad (58b) \end{cases}$$

where $\omega$ is the empirical constant to be determined. It is pertinent to note that equation (54) has neglected the axial heat conduction effect, which is small for $\mathrm{Pe}_d > 1$ and for a relatively long channel. Equations (54)–(58) are to be solved subject to the entrance condition

$$x^* = 0: \qquad T^* = T_i^* \tag{59}$$

and the boundary conditions

$$y^* = 0: \qquad T^* = T_c^* \tag{60}$$

$$y^* = 2H: \qquad T^* = T_h^* \tag{61}$$

To solve equations (54)–(61) numerically, it is convenient to convert the semi-infinite domain ($0 < x^* < \infty$) into a finite one by a coordinate transformation in the axial direction. For this purpose, the following coordinate transformation (Wang and Longwell, 1964) will now be introduced:

$$\zeta = 1 - \frac{1}{1 + C_T x} \tag{62}$$

wher $x = x^*/H$ and $C_T$ is a dimensionless constant. Equation (54) written in dimensionless form in terms of the transformed coordinate is

$$C_T(1-\zeta)^2 \frac{\mathrm{PrRe}_d}{\gamma} u \frac{\partial \theta}{\partial \zeta} + \frac{\partial}{\partial y}\left[k_{ey}\frac{\partial \theta}{\partial y}\right] = 0 \tag{63}$$

where $\theta = (T^* - T_c^*)/(T_h^* - T_c^*)$, $k_{ey} = k_{ey}^*/k_f^*$, and $y = y^*/H$. If the finite difference approximation is applied to equation (63) with the convective term approximated by the upwind difference, the resulting linear algebraic equations becomes

$$C_T(1-\zeta_i)^2 \frac{\mathrm{PrRe}_d}{\gamma} u_j \left[\frac{\theta_{i,j} - \theta_{i-1,j}}{\Delta\zeta}\right] = \frac{1}{(\Delta y)^2}\left[k_{ey,\,j+1/2}(\theta_{i,j+1} - \theta_{i,j}) - k_{ey,\,j-1/2}(\theta_{i,j} - \theta_{i,j-1})\right] \tag{64}$$

Equation (64) subject to the entrance condition (59) and boundary conditions (60) and (61) can be solved numerically by the marching technique (Bodoia and Osterle, 1961). For a thermally fully developed flow in the packed channel, the first term in equations (54) or (64) is omitted.

The local heat flux at the wall is

$$q_w = -k_{ey,\,1/2}^* \frac{(T_h^* - T_c^*)}{H} \frac{(\theta_{i,0} - \theta_{i,1})}{\Delta y} \tag{65}$$

where $\theta_{i,0}$ is the dimensionless temperature at the wall. For the thermally developing flow, the average surface heat flux can be obtained by an integration of the local surface heat flux, i.e.,

$$\bar{q}_w = \frac{1}{L}\int_0^L q_w dx^* = -\left(\frac{H}{C_T L}\right)\int_0^{\zeta_L} \frac{q_w(\zeta)d\zeta}{(1-\zeta)^2} \tag{66}$$

where $\zeta_L = 1 - 1/(1 + C_T L/H)$. Once $q_w$ is computed from equation (65), the average $\bar{q}_w$ given by equation (66) can be integrated numerically.

For the present problem with asymmetric heating, the local and average Nusselt numbers for the thermally developing flow are given, respectively, by

$$\mathrm{Nu_d} = \frac{q_w d_p}{k_f^*(T_h^* - T_c^*)} \tag{67a}$$

and

$$\overline{\mathrm{Nu}}_\mathrm{d} = \frac{\bar{q}_w d_p}{k_f^*(T_h^* - T_c^*)} \tag{67b}$$

For prescribed values of $\mathrm{Re_d}$, Pr, $\Lambda$, $\gamma$, and $x^*/2H$, equations (64)–(67) can be used to compute the temperature profiles and the local and the average Nusselt number of the thermally developing flow in the packed channel if the values of $\omega$, $D_T$, and $m$ are known. In a previous paper (Cheng and Hsu, 1986b) the values of $\omega$, $D_T$, and $m$ were obtained by matching the predicted heat transfer characteristics with experimental data of Schroeder et al. (1981) and by assuming: (1) a thermally fully developed flow, and (2) the inertial effect is negligible. These two restrictions are relaxed in the present paper so that a more accurate determination of the values of $\omega$, $D_T$, and $m$ can be achieved. To this end, different values of $\omega$, $D_T$, and $m$ were used in equations (64)–(67), and the predicted temperature distributions at $x^*/2H = 13.5$ were compared with the data of Schroeder et al. for forced convection of

water (Pr = 5 and $k_f^*$ = W/m-K) with inlet temperature $T_i^* = (T_h^* + T_c^*)/2$ through a channel packed with glass spheres ($k_s^*$ = 1.05 W/m-K). For each computation, a coarse grid size $\Delta y$ was used initially. The grid size was gradually reduced until the local Nusselt number computed from equation (67*a*) attained an asymptotic value. The grid size for which the Nusselt number did not change more than 5 percent was considered acceptable. Experience has shown that a finer grid size is required as the Reynolds number is increased. This can be attributed to the fact that the wall temperature gradient becomes steeper as the Reynolds number is increased (see discussion below).

Computations for the heat transfer characteristics were first carried out for $\omega = 0$ (i.e., $l = 1$) with different values of $D_T$ and $m$ and with velocity profiles shown in Fig. 1, which is based on $C_1 = 1$ and $N_1 = 2$. It was found that with $\omega = 0$ and $m = 1 - 2$, it was impossible to find a value of $D_T$ such that both the predicted temperature distributions would match with experimental data. In particular, with $\omega = 0$, $m = 1 - 2$, and any value of $D_T$, the predicted temperature distribution at $x^*/2H = 13.5$ in a channel having $\gamma = 0.37$ is almost linear across the channel. This is contradictory to the data of Schroeder et al. (1981), which show steep temperature gradients at the walls (see Fig. 3). To examine the effect of porosity variations on the temperature distribution, computations for the heat transfer characteristics were also carried out with $N_1 = 5$, $\omega = 0$, and different values of $D_T$. Again, it was found that the steep temperature gradient near the walls cannot be reproduced with any value of $D_T$ and $m$. This shows that the wall effect on velocity and stagnant thermal conductivity alone cannot account for the steep temperature gradient at the walls as observed from the experiment.

After establishing that a wall function must be introduced (i.e., $\omega \neq 0$) to account for the reduction of lateral mixing of fluid, computations for the heat transfer characteristics were carried out with different values of $\omega$, $D_T$, and $m$. The predicted temperature distributions were then compared with the data of Schroeder et al. The values of $\omega$, $D_T$, and $m$ were chosen based on the best match between theory and experimental results. It was found that the values of $\omega$ and $D_T$ depend on the value of $N_1$. For $N_1 = 2$, the predicted heat transfer characteristics based on the values of $\omega = 1.5$, $D_T = 0.17$, and $m = 1$ match the best with experimental data. For $N_1 = 5$, the values of $\omega = 1.0$, $D_T = 0.12$, and $m = 1$ should be used. In fact, the value of $N_1 = 5$ appears to be closer to the experimental data for the porosity variation although the value of $N_1 = 2$ has been used in most of the previous analyses. A comparison of the experimental data and the predicted temperature distributions based on the values of $N_1 = 2$, $\omega = 1.5$, $D_T = 0.17$, and $m = 1$ is presented in Figs. 3 and 4.

The predicted temperature profiles of the thermally developing flow at three different locations in a packed channel with $\gamma = 0.37$ are presented in Fig. 3(*a*) for $Re_d$ = 321, and in Fig. 3(*b*) for $Re_d$ = 2248. The three locations are: $x^*/2H = 0$, (i.e., at the entrance), $x^*/2H$ = 13.5 (where the temperature data was taken), and $x^*/2H \to \infty$ (i.e., a thermally fully developed flow, which is represented by dashed lines). It is shown in these figures that the predicted temperature profiles at $x^*/2H$ = 13.5 and $x^*/2H \to \infty$ are indistinguishable. This confirms the observations by Schroeder et al. (1981) that

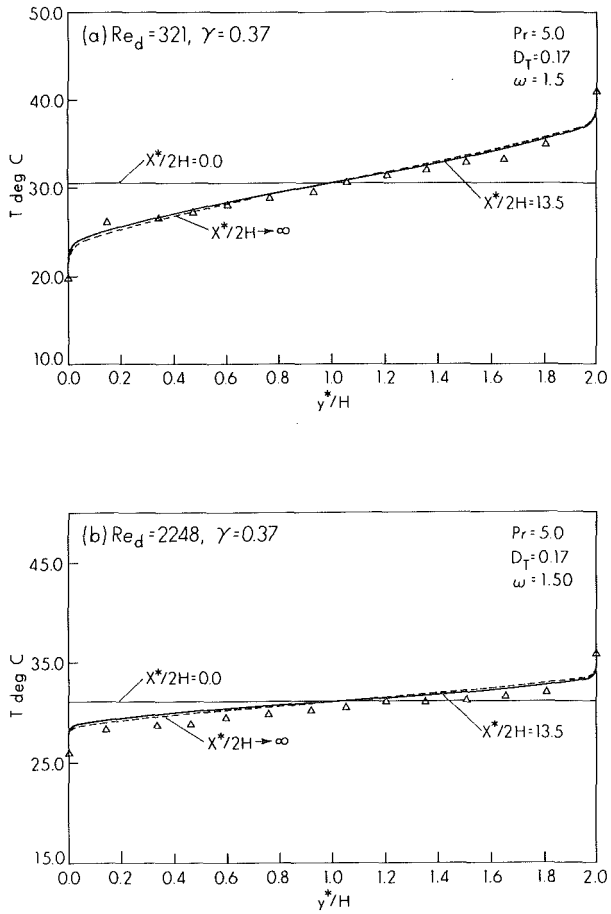


Fig. 3 Transverse temperature profiles at different locations in a variable-porosity packed channel with $\gamma$ = 0.37: (*a*) $Re_d$ = 321; (*b*) $Re_d$ = 2248

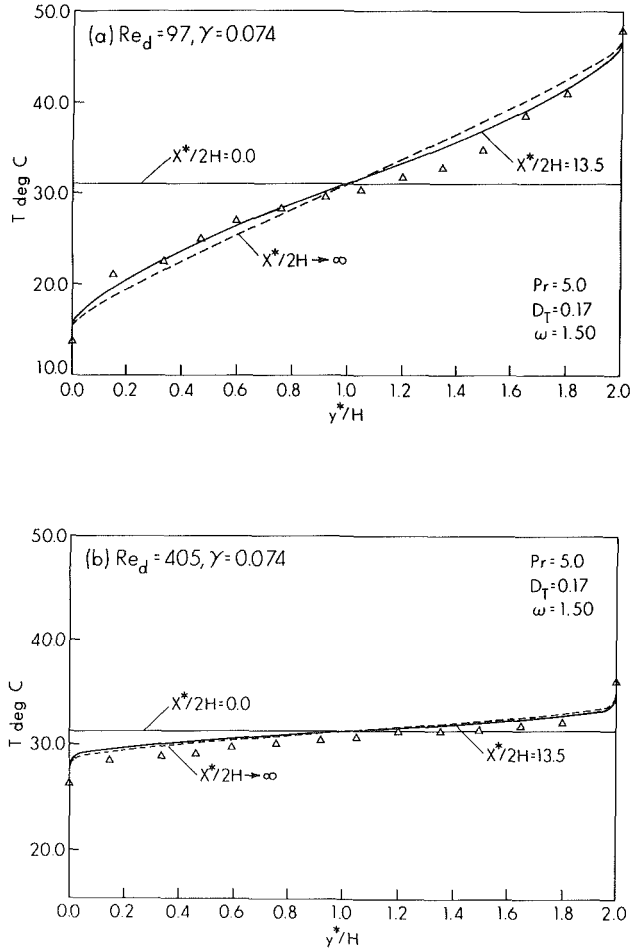


Fig. 4 Transverse temperature profiles at different locations in a variable-porosity packed channel with $\gamma$ = 0.74: (*a*) $Re_d$ = 97; (*b*) $Re_d$ = 405

the flow at $x^*/2H = 13.5$ was thermally fully developed in the packed channel with $\gamma = 0.37$. A similar plot for a packed channel with $\gamma = 0.074$ is shown in Fig. 4(*a*) for $Re_d = 97$ and in Fig. 4(*b*) for $Re_d = 405$. For a thermally fully developed flow ($x^*/2H \to \infty$), it is seen that the predicted temperature variations are linear in the core of the packed channel. On the other hand, the predicted temperature profiles at $x^*/2H = 13.5$ (which are supposed to match with the temperature data) are far from linear in the core of the packed bed. This confirms the speculation of Schroeder et al. that the flow at $x^*/2H = 13.5$ in the packed channel with $\gamma = 0.074$ was not a thermally fully developed flow. It is relevant to note while the predicted temperature profiles are asymmetric with respect to the centerline, the temperature data are not exactly asymmetric due to the temperature dependence of the viscosity. In both Figs. 3 and 4, the predicted temperature profiles (with $\omega = 1.5$, $D_T = 0.17$, and $m = 1$) match better with the temperature data in the cold region $0 \le y^*/H \le 1$.

The predicted normalized Nusselt number $Nu_d/Nu_\infty$ (with $Nu_\infty$ denoting the Nusselt number of the thermally fully developed flow at the same values of $\gamma$ and $Re_d$) as a function of the dimensionless distance from the entrance ($x^*/H$) at two values of $Re_d$ is presented in Fig. 5 for $\gamma = 0.074$ and $\gamma = 0.37$. As expected, the normalized local Nusselt number decreases from the entrance and attains an asymptotic limit of a thermally fully developed flow downstream. The thermal entrance length can be defined as the location where the local Nusselt number $Nu_d$ is within 5 percent of those of a thermally fully developed flow $Nu_\infty$. The values of $Nu_\infty$ and the dimensionless thermal entrance length ($L/H$) for the four cases shown in Fig. 5 are listed in Table 1. It is seen from Fig. 5 and Table 1 that the thermal entrance length decreases as $\gamma$ is increased or as $Re_d$ is decreased. At a high value of $\gamma$, the thermal entrance length is relatively independent of the Reynolds number.

The solid lines in Fig. 6 are the predicted average Nusselt number for a packed channel with $L/2H = 13.5$, which corresponds to the apparatus used by Schroeder et al. (1981). The dashed lines represent the predicted average Nusselt number for a thermally fully developed flow ($L/2H \to \infty$). At a given Reynolds number, the difference in value given by the solid line and dashed lines represents the thermal entrance length effect. From this figure, it can be seen that the entrance length effect is small at low Reynolds numbers. The thermal entrance length effect increases as the value of $\gamma$ is decreased. For $Re_d > 10$ the slope of the average Nusselt number ($\overline{Nu}_d$) curve changes from a value of 0.6 at $\gamma = 0.074$ and to 0.7 at $\gamma = 0.37$. Because of the different slopes for $\gamma = 0.074$ and $\gamma = 0.37$, these curves converge to each other at high Reynolds numbers.

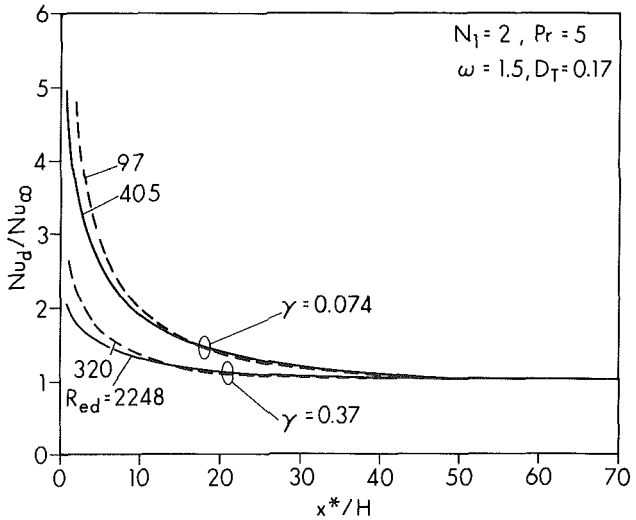


**Fig. 5 Variations of the normalized local Nusselt number in a variable-porosity packed channel**

**Table 1 Values of $Nu_\infty$ and dimensionless thermal entrance length ($L/H$)**

| $\gamma$ | $Re_d$ | $Nu_\infty$ | $L/H$ |
|---|---|---|---|
| 0.074 | 97 | 2.25 | 30.12 |
| 0.074 | 405 | 8.81 | 48.48 |
| 0.37 | 321 | 14.10 | 28.40 |
| 0.37 | 2248 | 77.83 | 28.64 |

## Concluding Remarks

The model presented in this paper depends on a large number of empirical constants: $C_1$, $N_1$, and $\phi^*_\infty$ in the porosity variation, $a$ and $b$ in the Brinkman-Darcy-Ergun equation, as well as $\omega$, $D_T$, and $m$ in the expression of the transverse thermal dispersion conductivity. The values of $\omega = 1.5$, $D_T = 0.17$, and $m = 1$ in the present paper were obtained by matching the predicted temperature distributions based on $a = 150$, $b = 1.75$, $C_1 = 1$, $N_1 = 2$, and $\phi^*_\infty = 0.4$ with the experimental data of Schroeder et al. (1981). If any one of the empirical constants $a$, $b$, $c$, $N_1$, and $\phi^*_\infty$ is changed, the values of $\omega$ and $D_T$ have to be modified slightly. For example, if the value of $N_1$ is changed to $N_1 = 5$, the values of $\omega = 1$ and $D_T = 0.12$ should be used. In both cases ($N_1 = 2$ and $N_1 = 5$), it was found that a wall function ($\omega \neq 0$) must be introduced to account for the reduction of the lateral mixing of fluid in order to match with the observed temperature behavior near the wall.

After this work had been completed, the authors received a copy of the paper from Hunt and Tien (1987) who use $N_1 = 6$ in their paper for the study of radial thermal dispersion effects in a packed tube. Their numerical results match with experimental data without introducing a wall function. This is probably due to the fact that the experiments were performed for a packed tube with small $\gamma$ ($\gamma = 0.088$) for which the wall effect on radial dispersion is negligible.


## Acknowledgments

The senior author (P.C.) would like to thank Professor D. Vortmeyer of the Technical University of Munich for helpful discussions.


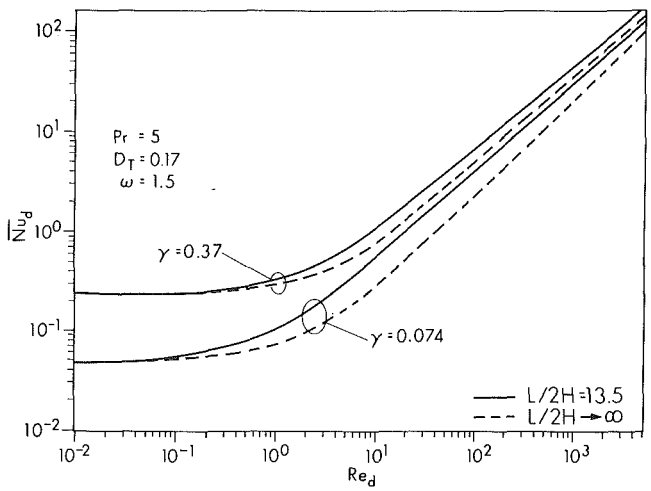


**Fig. 6 Predicted average Nusselt number as a function of the Reynolds number in a variable-porosity packed channel**

## References


Abramowitz, M., and Stegan, I. A., 1965, *Handbook of Mathematical Functions*, Dover, New York.

Beck, J., 1962, "Design of Packed Catalytic Reactors," *Adv. in Chem. Eng.*, Vol. 3, pp. 203–270.

Brinkman, H. C., 1947, "A Calculation of the Viscous Force Exerted by a Flowing Fluid on a Dense Swarm of Particles," *Applied Sci. Res.*, Vol A1, pp. 27–34.

Bodoia, J. R., and Osterle, J. F., 1961, "Finite Difference Analysis of Plane Poiseuille and Couette Flow Developments," *Applied Sci. Res.*, Vol. 10, pp. 265–276.

Bunnel, D. G., Irvin, H. B., Olson, R. W., and Smith, J. M., 1949, "Effective Thermal Conductivities in Gas-Solid Systems," *Ind. Eng. Chem.*, Vol. 41, pp. 1977–1981.

Cheng, P., 1987, "Wall Effects on Fluid Flow and Heat Transfer in Porous Media," *Proc. of 2nd ASME/JSME Thermal Engineering Joint Conference*, Vol. 2, pp. 297–304.

Cheng, P., and Vortmeyer, D., 1986, "Transverse Thermal Dispersion and Velocity Profile in a Packed Bed With Forced Convective Flow," *Chem. Eng. Sci.* (accepted for publication 1986).

Cheng, P., and Hsu, C. T., 1986a, "Fully-Developed Flow in an Annular Packed-Sphere Bed With Wall Effects," *Int. J. Heat Mass Transfer*, Vol. 29, pp. 1843–1853.

Cheng, P., and Hsu, C. T., 1986b, "Applications of Van Driest's Mixing Length Theory to Transverse Thermal Dispersion in a Packed Bed With Bounding Walls," *Int. Comm. Heat & Mass Transfer*, Vol. 13, pp. 613–625.

Coberly, C. A., and Marshall, W. R., Jr., 1951, "Temperature Gradients in Gas Streams Flowing Through Fixed Granular Beds," *Chem. Eng. Progress*, Vol. 47, pp. 141–150.

Colburn, A. P., 1931, "Heat Transfer and Pressure Drop in Empty, Baffled, and Packed Tubes," *Ind. Eng. Chem.*, Vol. 23, pp. 910–923.

Ergun, S., 1952, "Fluid Flow Through Packed Columns," *Chem. Eng. Progress*, Vol. 48, pp. 89–94.

Georgiadis, J., and Catton, I., 1987, "Transport in Pipes Filled With Uniform, Non-uniform and Random Porous Media," *Proc. of the 2nd ASME/JSME Thermal Engineering Conference*, Vol. 2, pp. 395–400.

Hall, R. E., and Smith, J. M., 1949, "Design of Gas-Solid Catalytic Reactors," *Chem. Eng. Progress*, Vol. 45, pp. 459–470.

Hunt, M. L., and Tien, C. L., 1987, "Non-Darcian Convection in Cylindrical Packed Beds," *Proc. of 2nd ASME/JSME Thermal Engineering Conference*, Honolulu, HI, pp. 433–438.

Kaviany, M., 1985, "Laminar Flow Through Porous Media Bounded by Isothermal Parallel Plates," *Int. J. Heat Mass Transfer*, Vol. 28, pp. 851–859.

Leibovich, S., and Seebass, A. R., 1974, *Nonlinear Waves*, University Press, p. 133.

Li, Chi-Hsiung, and Finalyson, B. A., 1977, "Heat Transfer in Packed Beds – A Re-evaluation," *Chem. Eng. Sci.*, Vol. 32, pp. 1055–1066.

Schroeder, K. J., Renz, V., and Elegeti, K., 1981, "Forschungsberichte des Landes Nordrhein-Westfalen," No. 3037.

Vafai, K., and Tien, C. L., 1981, "Boundary and Inertia Effects on Flow and Heat Transfer in Porous Media," *Int. J. Heat Mass Transfer*, Vol. 24, pp. 195–203.

Vafai, K., 1984, "Convective Flow and Heat Transfer in Variable-Porosity Media," *Journal of Fluid Mechanics*, Vol. 147, pp. 233–259.

Van Dyke, M. D., 1964, *Perturbation Methods in Fluid Mechanics*, Academic Press, New York.

Vortmeyer, D., and Schuster, J., 1983, "Evaluation of Steady Flow Profiles in Rectangular and Circular Packed Beds by a Variational Method," *Chem. Eng. Sci.*, Vol. 38, pp. 1691–1699.

Wang, Y. L., and Longwell, P. A., 1964, "Laminar Flow in the Inlet Section of Parallel Plates," *AIChE J.*, Vol. 10, pp. 323–329.

Zehner, P., and Schluender, E. U., 1970, "Waermeleitfahigkeit von Schuettungen bei Massigen Temperaturen," *Chem. Ing. Tech.*, Vol. 42, pp. 933–941.

# Liquid and Gas-Phase Distributions in a Jet With Phase Change

**Flavio Dobran**
New York University,
Applied Science Department,
New York, NY 10003

*A two-phase flow high-velocity jet with phase change was studied numerically. The jet is assumed to be created by the two-phase critical flow discharge through a pipe of variable length and attached to a vessel containing the saturated liquid at different stagnation pressures. The jet flow is assumed to be axisymmetric and the modeling of the two-phase flow was accomplished by a nonequilibrium model that accounts for the relative velocity and temperature difference between the phases. The numerical solution of the governing set of balance and conservation equations revealed steep gradients of flow properties in both radial and axial directions. The liquid phase in the jet is shown to remain close to the jet axis, and its velocity increases until it reaches a maximum corresponding to the gas velocity, and thereafter decreases at the same rate as the gas velocity. The effect of decreasing the pipe length is shown to produce a larger disequilibrium in the jet and a double pressure peak in the total pressure distribution. A comparison of the predicted total pressure distribution in the jet with the experimental data of steam–water at different axial locations is demonstrated to be very reasonable.*

## 1 Introduction

The discharge of a subcooled liquid at high pressure from a vessel through a pipe into an ambient atmosphere produces a rapid depressurization of the liquid and may produce two-phase critical flow at the discharge end of the pipe. Depending on the liquid stagnation conditions in the vessel and pipe geometric characteristics, the exiting two-phase mixture from the pipe may be in a considerable mechanical and thermal disequilibrium (Dobran, 1987). This disequilibrium is associated with the relative velocity and temperature difference between the phases, and may significantly affect the distribution of phases in the jet expansion region as the liquid and vapor are decelerated to the ambient conditions of the local atmosphere on the outside of the pipe. Due to the high momentum and pressure of the emerging two-phase mixture from the pipe, the expanding jet may create large forces on the surrounding objects, if they happen to be located in the vicinity of the jet discharge, and produce considerable loading on the pipe support structure and vessel to which the pipe is attached.

The purpose of this paper is to present a summary of results of the distribution of phases in the two-phase flow jet expansion region which were obtained by a nonequilibrium two-phase flow model of an axisymmetric jet with phase change. For the more extensive results of numerical simulations the reader is referred to Dobran (1985a, 1985b, 1985c, 1986). Section 2 of the paper deals with a brief description of the model, whereas in section 3 the results of a numerical study are presented and compared with data of the total pressure distribution at various positions along the jet.

## 2 Two-Phase Flow Jet Model and Solution Procedure

An axisymmetric two-phase flow configuration is illustrated in Fig. 1. The two-phase high-velocity jet exits from a pipe of diameter $D$ and, upon encountering a low-pressure region surrounding the pipe, expands in the jet expansion region. The thermohydrodynamic conditions of the liquid and gas at the pipe exit are assumed to be known and the region surrounding the pipe is modeled as an ambient atmosphere at 0.1 MPa. The boundary conditions at the pipe exit must be determined by a critical two-phase flow model of sufficient generality in order to be able to predict reliably the detailed flow conditions at the exit. In this paper these boundary conditions were determined by a nonequilibrium critical flow model as described by Dobran (1987), which has been tested with the experimental data of steam–water for different stagnation pressures and liquid subcoolings in the vessel and for variable length pipes. The critical flow rates and tube exit pressures predicted by this model are shown to be within ±10 percent of the experimental values for wide range of fluid stagnation conditions and pipe geometric characteristics.

**Governing Conservation and Balance Equations.** For an axisymmetric flow configuration as depicted in Fig. 1, the governing conservation and balance equations of two-phase flow with phase change may be written in the following *conservation* form (Dobran, 1985a, 1985b):

$$\frac{\partial r\mathbf{f}}{\partial t}+\frac{\partial r\mathbf{F}}{\partial z}+\frac{\partial r\mathbf{G}}{\partial r}=r\mathbf{S} \tag{1}$$

where the vector $(r\mathbf{f})$ consists of the dependent variables, and the vectors $(r\mathbf{F})$, $(r\mathbf{G})$, and $(r\mathbf{S})$ depend on $(r\mathbf{f})$, i.e.

$$r\mathbf{f}=\begin{bmatrix} r\bar{\rho}_L \\ r\bar{\rho}_G \\ r\bar{\rho}_L u_L \\ r\bar{\rho}_L v_L \\ r\bar{\rho}_G u_G \\ r\bar{\rho}_G v_G \\ r\bar{\rho}_L[\epsilon_L+(u_L^2+v_L^2)/2] \\ r\bar{\rho}_G[\epsilon_G+(u_G^2+v_G^2)/2] \end{bmatrix} \tag{2}$$

Contributed by the Heat Transfer Division for publication in the JOURNAL OF HEAT TRANSFER. Manuscript received by the Heat Transfer Division February 9, 1987. Keywords: Jets, Multiphase Flows, Nonequilibrium Flows.

$$r\mathbf{F} = \begin{bmatrix} r\bar{\rho}_L u_L \\ r\bar{\rho}_G u_G \\ (r\bar{\rho}_L u_L)^2/(r\bar{\rho}_L) + r(1-\alpha)P \\ (r\bar{\rho}_L u_L)(r\bar{\rho}_L v_L)/(r\bar{\rho}_L) \\ (r\bar{\rho}_G u_G)^2/(r\bar{\rho}_G) + r\alpha P \\ (r\bar{\rho}_G u_G)(r\bar{\rho}_G v_G)/(r\bar{\rho}_G) \\ (r\bar{\rho}_L u_L)[\epsilon_L + (u_L^2+v_L^2)/2 + (1-\alpha)P/\bar{\rho}_L] \\ (r\bar{\rho}_G u_G)[\epsilon_G + (u_G^2+v_G^2)/2 + \alpha P/\bar{\rho}_G] \end{bmatrix} \quad (3)$$

$$r\mathbf{G} = \begin{bmatrix} r\bar{\rho}_L v_L \\ r\bar{\rho}_G v_G \\ (r\bar{\rho}_L u_L)(r\bar{\rho}_L v_L)/(r\bar{\rho}_L) \\ (r\bar{\rho}_L v_L)^2/(r\bar{\rho}_L) + r(1-\alpha)P \\ (r\bar{\rho}_G u_G)(r\bar{\rho}_G v_G)/(r\bar{\rho}_G) \\ (r\bar{\rho}_G v_G)^2/(r\bar{\rho}_G) + r\alpha P \\ (r\bar{\rho}_L v_L)[\epsilon_L + (u_L^2+v_L^2)/2 + (1-\alpha)P/\bar{\rho}_L] \\ (r\bar{\rho}_G v_G)[\epsilon_G + (u_G^2+v_G^2)/2 + \alpha P/\bar{\rho}_G] \end{bmatrix} \quad (4)$$

$$r\mathbf{S} = (r\mathbf{S}_1, r\mathbf{S}_2, r\mathbf{S}_3, r\mathbf{S}_4, r\mathbf{S}_5, r\mathbf{S}_6, r\mathbf{S}_7, r\mathbf{S}_8)^T \quad (5)$$

In the above equations the partial densities of liquid and gas are defined by

$$\bar{\rho}_L = (1-\alpha)\rho_L \quad (6)$$

$$\bar{\rho}_G = \alpha\rho_G \quad (7)$$

where $\alpha$ is the void fraction. The components of the vector ($r\mathbf{S}$) are reported by Dobran (1985a, 1985b) will not be reproduced here. The liquid and gas velocities consist of the components along the axis of the jet, $u_L$ and $u_G$, and in the radial direction of the jet, $v_L$ and $v_G$, as illustrated in Fig. 1.

Notice that the solution of $\mathbf{f} = \mathbf{f}(t, r, z)$ from equations (1) allows for the determination of the detailed two-phase flow conditions in the jet, since the liquid and gas densities are given by the equations of state, i.e.

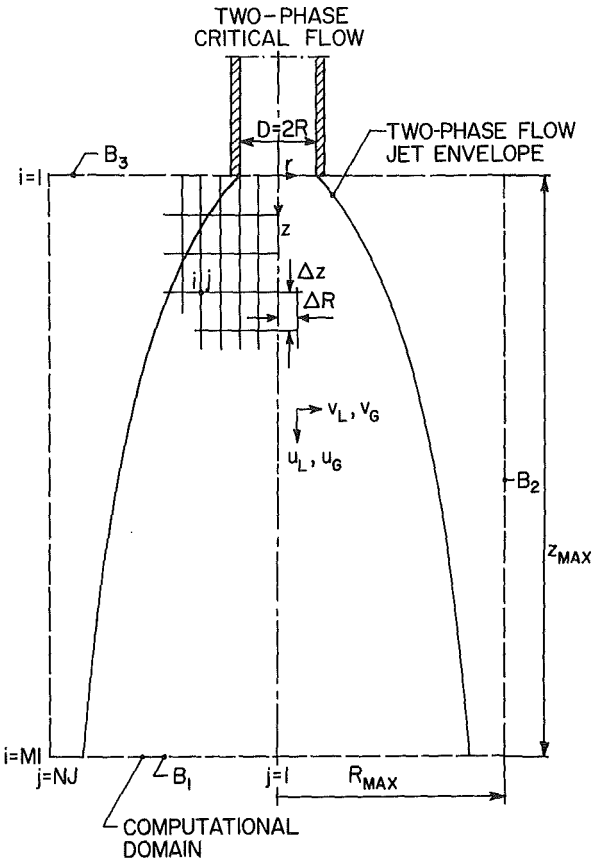


**Fig. 1 Schematic illustration of the two-phase flow jet expansion region and computational mesh structure**

$$\rho_L = \rho_L(P, \epsilon_L) \quad (8)$$

$$\rho_G = \rho_G(P, \epsilon_G) \quad (9)$$

For example, the liquid and gas velocities and internal energies may be found from the following relations:

$$u_L = \frac{(\bar{\rho}_L u_L)}{\bar{\rho}_L}, \quad v_L = \frac{(\bar{\rho}_L v_L)}{\bar{\rho}_L} \quad (10)$$

## Nomenclature

$A$ = interfacial area density, defined by equation (17)
$Cp$ = specific heat at constant pressure
$D$ = tube diameter
$\mathbf{f}$ = vector defined by equation (2)
$\mathbf{F}$ = vector defined by equation (3)
$\mathbf{G}$ = vector defined by equation (4)
$G_o'$ = critical mass flux in the tube
$i$ = computational node in the axial jet direction
$j$ = computational node in the radial jet direction
$k$ = thermal conductivity
$L$ = pipe length
$K$ = interfacial drag coefficient
$N$ = droplet density
$P$ = pressure
$P_o'$ = stagnation pressure in the vessel to which the pipe is attached
Pr = Prandtl number
$r$ = radial coordinate of the jet, Fig. 1
$r_p$ = mean droplet radius, defined by equation (23)
$\tilde{R}$ = interfacial heat transfer rate, defined by equation (18)
$R$ = pipe radius
Re = Reynolds number, defined by equation (22)
$R_u$ = gas constant
$\mathbf{S}$ = vector, defined in Dobran (1985a, 1985b)
$t$ = time
$T$ = temperature
$u$ = axial component of velocity
$\mathbf{U}$ = velocity vector
$v$ = radial component of velocity
$z$ = axial coordinate of the jet, Fig. 1
$\alpha$ = void fraction
$\Gamma$ = evaporation or condensation rate, defined by equations (15) and (16)
$\epsilon$ = internal energy
$\lambda$ = time relaxation parameter
$\mu$ = viscosity
$\rho$ = density
$\bar{\rho}$ = partial density, defined by equations (6) and (7)

**Subscripts**

$c$ = condensation
$e$ = evaporation
$G$ = denotes the gas or vapor phase
$L$ = denotes the liquid phase
$s$ = saturation condition

Table 1 Tube exit conditions computed by Dobran's (1987) critical two-phase flow model

| Tube geometry | | Stagnation conditions | | Computed pipe exit conditions | | | | | | | |
|---|---|---|---|---|---|---|---|---|---|---|---|
| $L/D$ | $D$, m | $P_o'$, MPa | $T_{sub}$, °C | $G_o'$, kg/m$^2$-s | $P$, MPa | $\alpha$ | $u_L$, m/s | $u_G$, m/s | $v_L = v_G$, m/s | $\epsilon_L$, J/kg | $\epsilon_G$, J/kg |
| 300 | 0.0125 | 2.58 | 0 | 9294 | 1.094 | 0.914 | 120.5 | 120.5 | 0 | $8.35\times10^5$ | $2.58\times10^6$ |
| 100 | 0.0125 | 3.38 | 0 | 14,845 | 1.681 | 0.846 | 111.6 | 112.9 | 0 | $9.32\times10^5$ | $2.60\times10^6$ |

$$u_G=\frac{(\bar\rho_G u_G)}{\bar\rho_G},\quad v_G=\frac{(\bar\rho_G v_G)}{\bar\rho_G} \tag{11}$$

$$\epsilon_L=\frac{\bar\rho_L[\epsilon_L+(u_L^2+v_L^2)/2]}{\bar\rho_L}-\frac{1}{2\bar\rho_L^2}[(\bar\rho_L u_L)^2+(\bar\rho_L v_L)^2] \tag{12}$$

$$\epsilon_G=\frac{\bar\rho_G[\epsilon_G+(u_G^2+v_G^2)/2]}{\bar\rho_G}-\frac{1}{2\bar\rho_G^2}[(\bar\rho_G u_G)^2+(\bar\rho_G v_G)^2] \tag{13}$$

By eliminating the void fraction $\alpha$ in equations (6) and (7) and utilizing the equations of state (8) and (9) it is then possible to solve for the pressure from the following relation:

$$\bar\rho_L\rho_L(P,\epsilon_L)+\bar\rho_G\rho_G(P,\epsilon_G)=\rho_L(P,\epsilon_L)\rho_G(P,\epsilon_G) \tag{14}$$

and subsequently to determine the void fraction from either equation (6) or equation (7).

Equations (1) apply everywhere in the jet except along the jet axis where $r=0$. To obtain a valid set of equations along the axis it is necessary to divide equations (1) by $r$ and take the limit $r\to0$ and recognize that $\mathbf{G}=\mathbf{0}$ at $r=0$.

**Constitutive Equations.** The closure of the balance equations (1) requires the specification of constitutive equations for the interfacial drag $K$, evaporation and condensation rates $\Gamma_e$ and $\Gamma_c$, respectively, and the interfacial heat transfer rate $\tilde R$ contained in the source terms $\mathbf{S}$. The results of the numerical simulation presented below were obtained by assuming that the drag $K$ is a constant and that the phase change process is controlled by the diffusion within the liquid and gas and not by the rate of energy exchange from the phase change. Under these conditions the evaporation and condensation rates are determined from the bulk liquid and vapor temperatures and may be written as (Solbrig et al., 1978):

$$\Gamma_e=\lambda_e A(1-\alpha)\rho_L\alpha(T_sR_u)^{1/2}(T_L-T_s)/T_s,\quad \text{for } T_L\ge T_s \tag{15}$$
$$=0,\ \text{otherwise}$$

$$\Gamma_c=\lambda_c A\alpha\rho_G(1-\alpha)(T_sR_u)^{1/2}(T_s-T_G)/T_s,\quad \text{for } T_G<T_s \tag{16}$$
$$=0,\ \text{otherwise}$$

where $\lambda_e=\lambda_c=0.1$ are the time relaxation parameters for evaporation and condensation with the unit of 1/s. For the equilibrium situation, the relaxation parameters are equal to one, whereas for very slow rates of phase change they would be equal to much less than one. The variable $A$ in the above equations is proportional to the area of contact between the phases; for $N$ equal size spherical droplets of radius $r_p$ per unit volume, it is given by the following expressions:

$$A=\begin{cases}\alpha^{2/3}(4\pi N/3)^{1/3}, & \text{when } \alpha\le0.5\\ (1-\alpha)^{2/3}(4\pi N/3)^{1/3}, & \text{when } \alpha>0.5\end{cases} \tag{17}$$

A better model for the evaporation and condensation rates may be the one that assumes that these rates are controlled by the diffusion of energy from the bulk phases to the interface.

The interfacial heat transfer rate $\tilde R$ models the exchange of thermal energy between the liquid and gas. Its form is taken from the work of Solbrig et al. (1978), i.e.

$$\tilde R=\alpha\tilde R_G+(1-\alpha)\tilde R_L \tag{18}$$

where

$$\tilde R_G=(1+0.37\,\mathrm{Re}^{1/2}\mathrm{Pr}_G^{0.35})/r_p \tag{19}$$

$$\tilde R_L=8.067\,k_L/r_p \tag{20}$$

$$\mathrm{Pr}_G=\mu_G Cp_G/k_G \tag{21}$$

$$\mathrm{Re}=2r_p\rho_G|\mathbf{U}_G-\mathbf{U}_L|/\mu_G \tag{22}$$

$$r_p=\begin{cases}[3\alpha/4\pi N]^{1/3}, & \text{when } \alpha\le0.5\\ [3(1-\alpha)/4\pi N]^{1/3}, & \text{when } \alpha>0.5\end{cases} \tag{23}$$

and $N=10^{10}$ droplets/m$^3$ was assumed to be constant.

**Initial and Boundary Conditions.** The system of partial differential equations represented by equation (1) was solved in the computational domain as illustrated in Fig. 1 with the initial and boundary conditions specified in this domain. The computational region includes the two-phase flow jet envelope and extends sufficiently far into the radial and axial directions such that for $r>R_{max}$ and $z>z_{max}$ the initial flow field should not be significantly disturbed upon the introduction of the jet.

The initial flow configuration, or the local flow field configuration in the computational domain prior to the introduction of the jet, was assumed to consist of steam with the temperature and pressure equal to an air atmosphere, in which ambient conditions are given by $T_L=T_G=294$ K, $P=0.1$ MPa, $\alpha=0.999$, $\rho_L=935$ kg/m$^3$, $\rho_G=0.63$ kg/m$^3$, and $\mathbf{U}_L=\mathbf{U}_G=\mathbf{0}$.

The boundary conditions are specified at the tube exit and on boundaries $B_1$, $B_2$, and $B_3$ (see Fig. 1). At the tube exit the boundary conditions are determined by utilizing a suitable two-phase critical flow model. Table 1 summarizes these conditions for two different runs obtained by the critical flow model of Dobran (1987). The reason for selecting these runs is the availability of the experimental data of Celata et al. (1984) for the total pressure distribution in the jet, which can be used to determine the suitability of the jet model for the simulation of complex thermohydrodynamic processes within the jet. At the outflow boundary $B_1$ it is assumed that the flow properties in the jet do not vary significantly and that the jet properties can be determined by means of the second-order extrapolation of jet characteristics from the upstream points in the computational domain (Lapidus and Pinder, 1982). At the side boundary $B_2$ the boundary conditions are assumed to correspond to the initial conditions, except for the radial components of liquid and gas velocities, which are set equal to the corresponding values at one node away from $B_2$, i.e., at $j=NJ-1$ in Fig. 1. At the inflow boundary $B_3$ the liquid and gas densities, internal energies, radial components of velocities, and pressure are set equal to the initial conditions. The axial components of fluid velocities are set floating in order to allow for the mass transfer across $B_3$.

**Numerical Procedure.** The governing conservation and balance equations of two-phase flow (1) together with the initial and boundary conditions discussed above were solved numerically by the extended Lax's finite difference scheme (Lapidus and Pinder, 1982) until the steady-state jet profiles were obtained. This numerical procedure is first-order accurate in time and second-order accurate in space, and it has a dissipative mechanism built into it whose coefficient of ar-

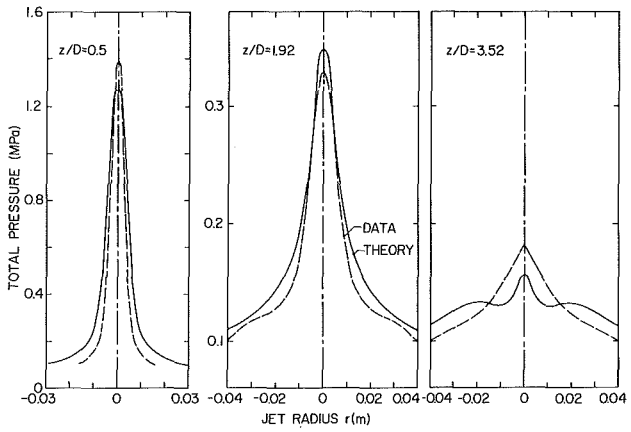


**Fig. 2 Comparison of the predicted total pressure distribution in the jet with the experimental data of steam-water at various distances from the pipe end for $L/D$ = 300, $P_o'$ = 2.58 MPa, and $\Delta T_{sub}$ = 0°C**

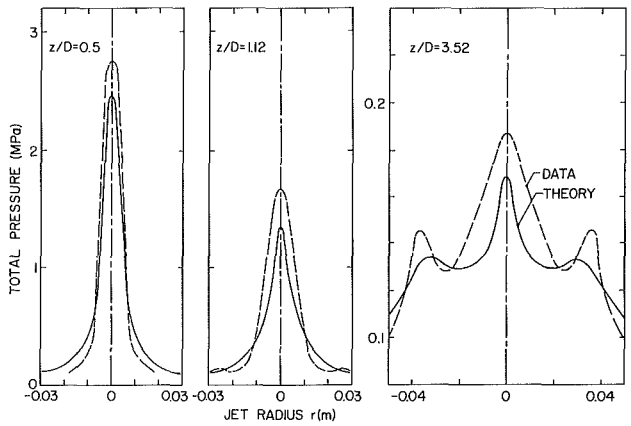


**Fig. 3 Comparison of the predicted total pressure distribution in the jet with the experimental data of steam-water at various distances from the pipe end for $L/D$ = 100, $P_o'$ = 3.38 MPa, and $\Delta T_{sub}$ = 0°C**

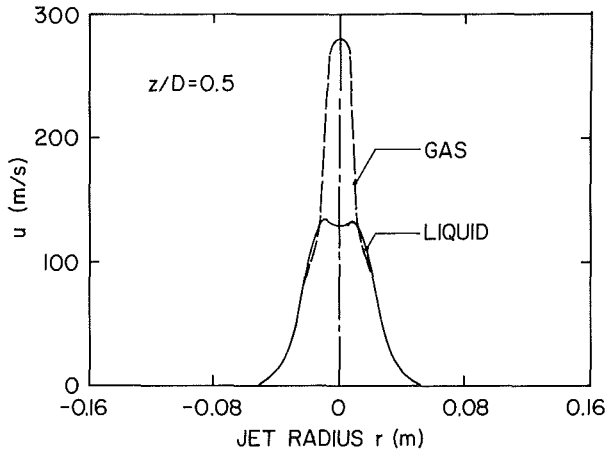


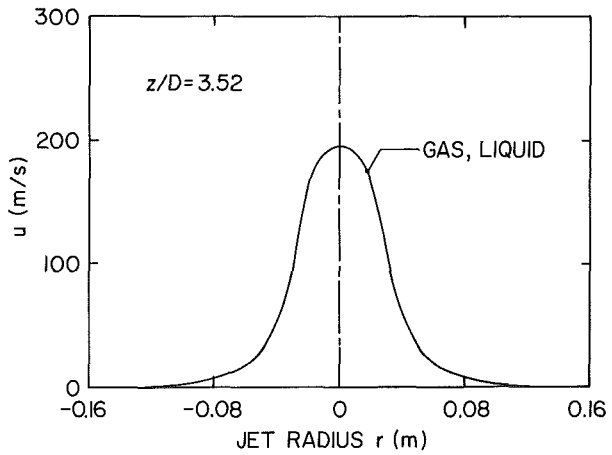


**Fig. 4 Predicted distribution of the axial components of liquid and gas velocities in the jet for $L/D$ = 300, $P_o'$ = 2.58 MPa, and $\Delta T_{sub}$ = 0°C**

tificial viscosity is proportional to $(\Delta z)^2/2\Delta t$. An accurate resolution of steep gradients in the jet, such as close to the pipe exit region, required, therefore, the use of the largest possible time step consistent with the Courant–Friedricks–Levy stability condition of the explicit finite difference methods. The discretized system of partial differential equations (1) was solved in the computational domain shown in Fig. 1, consisting of 40 radial and 60 axial nodes with nonuniform node separation as discussed in Dobran (1985b). The nonuniform node distribution was necessary in order to extend the computational domain in the radial and axial directions sufficiently far away from the steep gradients of flow properties close to the jet axis and tube exit. With this grid size specification and time step of $2 \times 10^{-6}$ s, the steady-state conditions in the jet were established in a few ms. The effect of the mesh size on the accuracy of the computed variables was validated by a run with a uniform mesh size of 1.56 mm. When the computations were carried out with a variable mesh size as noted above it was established that such a small node separation was only necessary close to the jet centerline in order for the computed variables to remain within 3 percent accuracy in the entire computational domain.

## 3 Results and Discussion

Figures 2–6 illustrate the predicted steady-state pressure, velocity, and void fraction distributions in the jet at different axial positions corresponding to the two-phase flow pipe exit conditions in Table 1. Figures 2 and 3 show the predicted total or stagnation pressure distribution and a comparison with the experimental data of Celata et al. (1984). The stagnation pressure was computed according to the following equation:

$$P_{TOT} = P + 0.5[\alpha\rho_G u_G + (1-\alpha)\rho_L u_L]^2/[\alpha\rho_G + (1-\alpha)\rho_L] \quad (24)$$

As shown in Figs. 2 and 3, the predicted pressure distribution at different axial positions in the jet compares well with the steam–water data. The centerline pressure in the jet is underpredicted, whereas the jet spreading in the radial direction is overpredicted. Larger values of the interfacial drag $K$ than the one used have the effect of producing a better comparison of the total pressure distribution in the jet with the experiment by increasing the centerline pressure and decreasing the radial jet dispersion. Nevertheless, the selected value of $K = 10^5$ kg/m$^2$-s was found to be very reasonable in predicting the radial and axial distributions of the total pressure and was used in producing all the results reported in the paper. The variation of other constants in the model ($\lambda_c$, $\lambda_e$, and $N$) by an order of magnitude from the selected values did not produce a practical change in the results reported in the paper.

At the axial position in the jet corresponding to $z/d$ = 3.52, the predicted total pressure distribution exhibits a second peak for both runs in Table 1. For the two-phase flow situation in a long pipe ($L/D$ = 300), the predicted second pressure peak is not as pronounced as for the flow through a shorter pipe ($L/D$ = 100). Shorter tubes have the effect of producing larger mechanical and thermal disequilibrium at the tube exit (Dobran, 1987) as may be seen in Table 1, and this disequilibrium appears to be responsible for the occurrence of

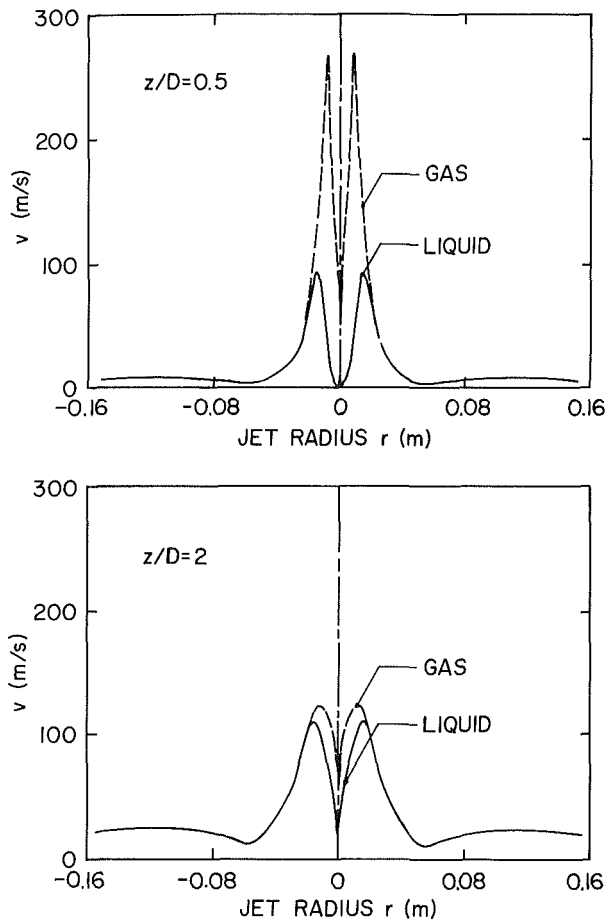


Fig. 5 Predicted distribution of the radial components of liquid and gas velocities in the jet for $L/D$ = 300, $P_o'$ = 2.58 MPa, and $\Delta T_{sub}$ = 0°C

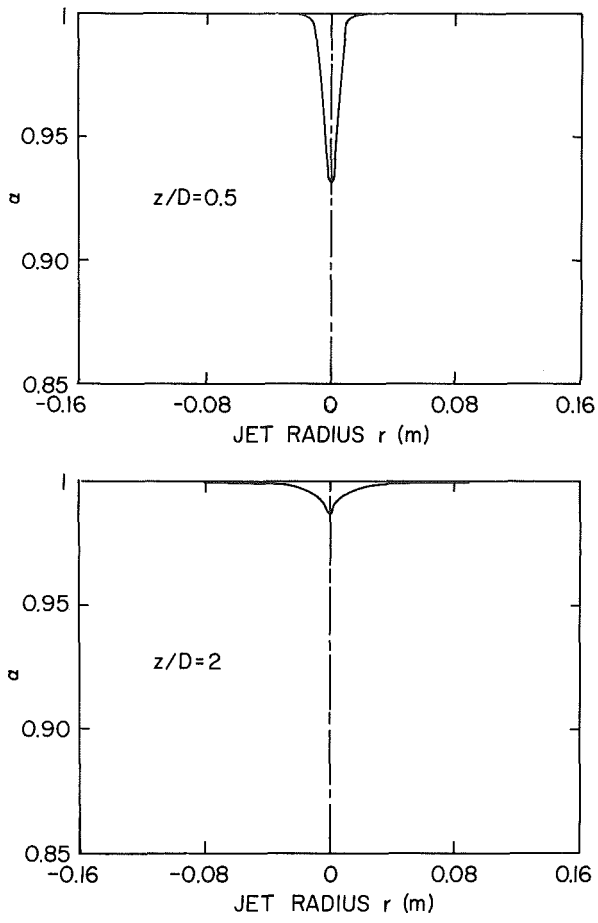


Fig. 6 Predicted void fraction distribution in the jet for $L/D$ = 300, $P_o'$ = 2.58 MPa, and $\Delta T_{sub}$ = 0°C

double pressure peaks of larger strengths. A pressure probe, such as pitot tube used to measure the total pressure distribution in the jet, may be responsible for the disturbance of the flow to such an extent that it may not yield an observation of a phenomenon such as a second pressure peak if this peak is of mild strength, as appears to be the case in Fig. 2 under the conditions of greater mechanical and thermal equilibrium. For the situation of $L/D = 100$ in Fig. 3, both the experiment and the theory show the occurrence of an off-axis pressure peak of sufficient strength.

An explanation of the foregoing observations on the total pressure distribution in the jet may be sought by examining the velocity and void fraction distributions in the jet. Figures 4 and 5 illustrate some typical distributions of the axial and radial components of velocity profiles at different positions in the jet. Close to the pipe end in the jet expansion region the gas velocity is seen to exceed substantially the liquid velocity, which may be attributed physically to the compressibility of the gas phase and to the finite value of the drag $K$. That is, as the gas and liquid exit from a pipe they encounter a zone of low pressure where only the gas phase can expand substantially. The liquid phase cannot, however, expand and its velocity can only increase as it is being dragged along by the gas. This explains why in Figs. 4 and 5 the gas-phase speeds in both axial and radial directions continue to decrease as the distance from the tube end is increased, and why at first the liquid velocity increases until it becomes equal to the gas velocity and thereafter it decreases at the rate corresponding to the gas velocity. The velocity vector plots of liquid and gas, shown in Dobran (1985b), serve to illustrate that the gas phase has a greater tendency (due to its lower inertia) than the liquid phase to move in the radial than in the axial direction. Indeed, the void fraction distributions in the jet illustrated in Fig. 6 confirm this observation, and are, furthermore, consistent with the qualitative x-ray measurements of Celata et al. (1985).

The profiles of the jet velocities illustrate that the selected computational domain discussed in the previous section is satisfactory, since the most significant changes of flow properties appear to occur well within this region. Another aspect of the numerical results is that the critical flows through shorter tubes (with the corresponding larger disequilibrium conditions at the tube exit) exhibit jet profiles of larger radial dispersion than for the longer tubes. This radial dispersion, as well as the remaining jet characteristics discussed above, are consistent with the experimental data of Celata et al. (1984) for steam–water jets discharging into an ambient air atmosphere.

## 4 Summary and Conclusions

A two-phase flow nonequilibrium model was used to study the distribution of liquid and gas in an axisymmetric jet with phase change, which is created by two-phase critical flow discharge through a pipe. The model assumes mechanical and thermal nonequilibrium between the phases, and the governing set of conservation and balance equations were solved by an explicit finite difference scheme until the steady-state jet characteristics were obtained. The numerical results predicted steep gradients of flow properties close to the pipe exit and along the jet axis, with the gas phase having the tendency to move more in the radial direction than the liquid phase. The total pressure distribution in the jet exhibits a double pressure peak: one at the jet centerline and another of lower amplitude off from the axis of the jet. The magnitude of the second

pressure peak may be associated with the degree of disequilibrium in the jet, since an increase in this disequilibrium has the effect of producing a larger radial dispersion of the gas phase and a correspondingly larger amplitude peak. A comparison of the predicted total pressure distribution in the jet with the steam–water data was shown to be very reasonable, both for the situations of radial and axial jet dispersion and the existence of double pressure peaks. The discrepancies between the numerical results and experimental data may be attributed to the uncertainties in the two-phase flow model and boundary conditions at the tube exit, as well as in simulating the ambient air atmosphere by a steam atmosphere. The numerical errors attributed to the artificial viscosity and variable grid size are judged to be minimal in view of the performed trial test with different grid sizes and time steps showing no practical changes in the results as presented in the paper.

## References


Celata, G. P., Cumo, M., Farello, G. E., and Incalcaterra, P. C., 1984, "Physical Insight in the Evaluation of Jet Forces in LOCA," *Proc. 5th Int. Meeting on Thermal Reactor Safety*, Karlsruhe, Federal Republic of Germany, Sept. 10–13.

Celata, G. P., Cumo, M., and Farello, G. E., 1985, "X-Ray Analysis in Unbounded Two-Phase Critical Flows," *Specialists Meeting on Small Break LOCA Analyses in LWR's*, Giardini Editori e Stampatori, Pisa, Italy, Vol. 1, pp. 279–298.

Dobran, F., 1985a, "Analysis and Computation of Two-Phase Flow Jets With Phase Change," SIT Report No. ME-RT85010.

Dobran, F., 1985b, "Distribution of Liquid and Gas in a Jet With Phase Change," *Int. Symp. on Jets and Cavities*, J. H. Kim et al., eds., ASME, New York, pp. 49–56.

Dobran, F., 1985c, "Numerical Study of a Two-Phase Flow Jet," *Proc. 4th Int. Conf. on Numerical Methods in Thermal Problems*, R. W. Lewis and K. Morgan, eds., Pineridge Press, United Kingdom, Part 2, pp. 807–818.

Dobran, F., 1986, "The Effect of Liquid Subcooling and Tube Length on the Two-Phase Critical Flow in Tubes and Flow in the Jet," *Proc. 8th Int. Heat Transfer Conf.*, Hemisphere, New York, Vol. 5, pp. 2301–2306.

Dobran, F., 1987, "Nonequilibrium Modeling of Two-Phase Critical Flows in Tubes," ASME JOURNAL OF HEAT TRANSFER, Vol. 109, pp. 731–738.

Lapidus, L., and Pinder, G. F., 1982, *Numerical Solution of Partial Differential Equations in Science and Engineering*, Wiley, New York.

Solbrig, C. W., McFadden, J. H., Lyczkowski, R. W., and Hughes, E. D., 1978, "Heat Transfer and Friction Correlations Required to Describe Steam–Water Behavior in Nuclear Safety Studies," *AIChE Symp. Series*, Vol. 74, pp. 100–128.

# Film Boiling Heat Transfer From a Sphere and a Horizontal Cylinder Embedded in a Liquid-Saturated Porous Medium

J. Orozco

R. Stellman

M. Gutjahr

Department of Mechanical Engineering,
University of Illinois at Chicago,
Chicago, IL 60680

*This paper analyses both theoretically and experimentally the problem of film boiling from a body embedded in a liquid-saturated porous medium. Two body geometries are investigated thoroughly: a horizontal cylinder and a sphere. The theoretical model relies on the Brinkman-extended flow model to describe the flow field inside the thin vapor layer occupying the neighborhood near the heated surface. The theoretical model also includes an improved formulation of the effective conductivity in the vicinity of the heater as a function of the vapor layer thickness and the geometry of the porous medium material. Solutions are obtained for the vapor layer thickness and the local Nusselt number as a function of angular position. Numerical solutions are also obtained for the overall heat transfer rates from the surface to the fluid for a given vapor superheat. Experimental data for a 12.70 mm stainless steel cylindrical heater embedded in a 3-mm glass particle porous medium were obtained under steady−state operation. The experimental data obtained are compared with the theoretical analysis. The comparison shows that there is a good agreement between theory and experiments. The theoretical model is also compared with the experimental data obtained by other investigators for a spherical geometry. Excellent results are obtained in such comparison.*

## Introduction

Boiling heat transfer in porous media is fundamental and has many technological applications such as in the design of heat pipes, in heat removal during the reflooding process after loss-of-coolant accidents in a nuclear reactor, and in geothermal energy utilization. In the presence of porous media the boiling process is significantly different from that in an unrestrained fluid. As suggested by Cheng (1985), the introduction of the concept of relative permeability to account for the fact that some of the pore space is partly filled with vapor and partly with liquid simplifies the modeling of two-phase flow while using the popular Darcy model. Thus, analytical solutions for two-phase flow problems, such as film boiling in porous media, can be obtained. One key assumption in the modeling process is the existence of a well-defined interface between the two phases (vapor and liquid). This assumption eliminates some of the mathematical complexities that the use of the relative permeability introduces.

Two-phase flow in porous media, unlike two-phase flow in classical fluids, has received considerably less attention. Cheng and Verma (1985) have examined the problem of film boiling from a heated isothermal vertical plate embedded in a porous media filled with a subcooled fluid. They have shown that at a given vapor Rayleigh number, the local Nusselt number is uniquely dependent on the vapor film dimensionless parameters related to the degree of superheat, the wall temperature, the extent of subcooling of the surrounding liquid, and a property ratio of the vapor and the liquid phases. Later, Ip and Minkowycz (1987) extended the analysis of Cheng and Verma to include the effect of the presence of an axial pressure gradient on the boiling process.

Experimental work on boiling heat transfer in porous media has also been reported in the literature. For example, Tsung et al. (1985) have recently investigated boiling heat transfer from a spherical heater embedded in liquid-saturated porous media. In their experiments, with Freon-113 as the working fluid, the diameter of the glass particles forming the porous layer was varied parametrically. The experimental results showed that the maximum heat flux increased monotonically with increasing particle diameter and approached an asymptotic value corresponding to the maximum heat flux obtained in a pool of liquid free of particles. However, they observed that the minimum heat flux was nearly insensitive to the particle size and that the film boiling heat transfer coefficient increased slightly with decreasing particle size.

More studies are needed to improve our understanding of boiling heat transfer in porous media. This paper presents such a study. The problem of film boiling from a sphere and from a cylinder embedded in a saturated porous medium is modeled theoretically. Since the vapor film is occupying a thin region near the heated surface, the Brinkman-modified Darcy model is used to described the flow inside the vapor film. This model has proven especially appropriate for flows near solid boundaries (see Tong and Subramanian, 1985, and Hsu and Cheng, 1985). The results obtained from this analysis, for the use of the spherical heater, are compared with the experimental data obtained by Tsung et al. (1985). Experimental data for a cylindrical heater are also obtained and compared with the theoretical model. Both comparisons shows a good agreement between theory and experiments.

## Heat Transfer Apparatus and Experimental Procedures

The heat transfer measurements made in the present study were performed using the electrically heated cylinder and the test section shown in Fig. 1. More specifically, Fig. 1(*b*) shows a cross section of the cylinder used in this experiment. The cylinder consists of a stainless steel rod of 12.70 mm outside diameters. The cylindrical rod was machined to accommodate the installation of a 6.35 mm o.d., 54.8 mm long, high-power density cartridge heater. Care was taken in reducing the cylinder thickness beyond the heated area to minimize the heat dissipation in the axial direction. Power to the heater was controlled by means of a Variac.

Contributed by the Heat Transfer Division for publication in the JOURNAL OF HEAT TRANSFER. Manuscript received by the Heat Transfer Division June, 1987.
Keywords: Augmentation and Enhancement, Boiling, Porous Media.

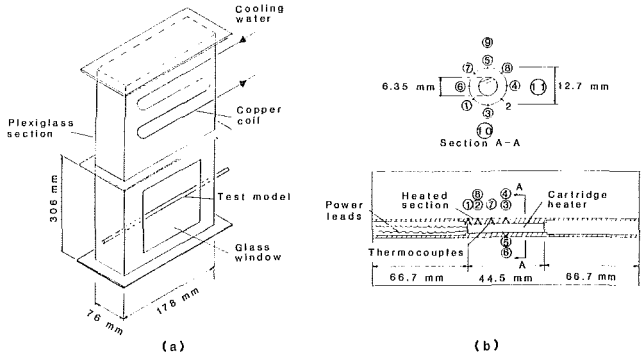


**Fig. 1 Test section and heat transfer model**

The steady-state bulk temperature of the porous medium $T_\infty$ was measured by means of three chromel-alumel thermocouples, $T_9$, $T_{10}$, and $T_{11}$, located directly above, to the side, and directly below the test specimen as shown in Fig. 1(*b*). Thermocouples were also attached at selected locations on the heated surface and at a distance of 1.59 mm below the surface. The steady-state surface temperature $T_w$, corresponding to an arbitrarily imposed overall rate of heat dissipation $Q$, was measured by averaging the readings of the surface temperatures. It was observed that during partial film boiling the heated surface would experience temperature variations as large as 50°C between the forward and backward stagnation points. During nucleate boiling, negligible surface temperature gradients were observed. The axial flows of energy were computed by means of the temperature differences $T_1 - T_2$ and $T_1 - T_8$ at the ends of the heated area.

It is worth mentioning that two types of heated surfaces were initially considered in the design of the heaters. A copper surface was first selected in order to minimize the temperature gradients in the radial direction corresponding to a given power setting. However, the high thermal conductivity of copper would also increase the flow of energy in the axial direction, consequently limiting the range of operation of the heater, since less energy would be available for the boiling process. On the other hand, the selection of a stainless steel surface would permit us to operate the heated surface at a higher surface temperature and with a higher flow of energy into the porous medium. The relatively low conductivity of stainless steel minimizes the axial conduction of energy; however, care has to be exercised in adjusting the power input to the heater. We could have instances, mainly during power adjustments, during which the electric heater would be operating very close to its burnout point while the surface registered a much lower temperature.

The prorous medium consisted of 3-mm glass beads. All properties of this medium were measured: porosity, $\phi = 0.39$; effective (liquid-saturated) thermal conductivity, $K = 0.97$ $W/m°C$, and the permeability, $K_{sol} = 2 \times 10^{-9}$ $m^{-2}$. Freon-113 was used as the working fluid.

Figure 1(*a*) shows the test section. It consists of a rectangular stainless steel box with glass windows on two sides so that visual observations of the convection and boiling process could be made. The thermocouple outputs were measured and recorded by a Hewlett-Packard computer-data acquisition system.

**Preparation of the Heated Surface.** Different sets of experiments were performed for different surface finishes. In the first set of experiments the stainless steel cylinders were polished to a mirrorlike surface finish at the beginning of each experiment. In another set, we allowed a layer of oxide to form on the heater surface by heating it in air at a temperature of 200°C for 2 h before each experiment. The purpose of the different surface conditions was to study their effects on the film boiling process in porous media.

**Theoretical Model.** Consider the problem of steady heating of an isothermal sphere or cylinder embedded in a porous medium filled with a saturated liquid, as shown in Fig. 2. In both cases, it is assumed that the boiling phenomenon is of the filmwise type and that the vapor film thickness is small compared to the body diameter.

The mathematical model for the sphere and cylinder are conceptually identical. Therefore, only the model for the cylinder will be presented in detail. Selected key results for the spherical geometry will also be outlined.

Since the vapor film is occupying a thin region near the heated surface, the Brinkman-modified Darcy model is used to described the flow field inside the vapor film. This model

## Nomenclature

$A$ = area
$C_1$ = constant defined by $C_1 = (\rho_L - \rho_v) g K / \mu_v$
$C_P$ = specific heat of the fluid
$D$ = diameter of the heater
Da = Darcy number, defined by $\mathrm{Da} = K\tilde{\mu}_v / D^2 \mu_v$
$g$ = acceleration of gravity
$h$ = heat transfer coefficient
$h_{fg}$ = latent heat of vaporization including the effects of vapor superheat
$K$ = permeability of the porous medium
$k$ = thermal conductivity
$k_{m,v}$ = effective thermal conductivity of the fluid and the porous medium
$\dot{m}$ = mass flux
$M$ = problem parameter defined by

$$M = \frac{k_{m,v}(T_w - T_s)\mu_v}{D\rho_v(\rho_L - \rho_v)h_{FG}Kg}$$

$n$ = coordinate perpendicular to the surface
$N$ = number of particles completely immersed in the vapor film
Nu = Nusselt number $= hD/k$
$\overline{\mathrm{Nu}}$ = average Nusselt number

$$= \frac{1}{A}\int_A \mathrm{Nu}\, dA$$

$q_L$ = local heat flux
$q$ = average heat flux
$Q$ = heat rate
$R$ = radius of the heater
$R_P$ = radius of the particles
$s$ = coordinate along the surface of the heater, measured from the lower stagnation point
$T$ = temperature
$s$ = velocity in $s$ direction
$\bar{u}$ = average vapor velocity in $s$ direction
$v$ = velocity in $n$ direction
$\alpha$ = equivalent thermal diffusivity
$\delta$ = boundary layer thickness
$\theta_D$ = angle of vapor detachment
$\mu$ = viscosity of the fluid
$\tilde{\mu}$ = effective viscosity of the fluid and the porous medium
$\mu$ = density of the fluid
$\phi$ = porosity

**Subscripts**

$l$ = liquid phase
$s$ = saturated condition
$v$ = vapor phase
$w$ = condition at the wall
$\infty$ = condition at infinity
$v,s$ = vapor–solid
sol = solid
$lh$ = lower half
$up$ = upper half

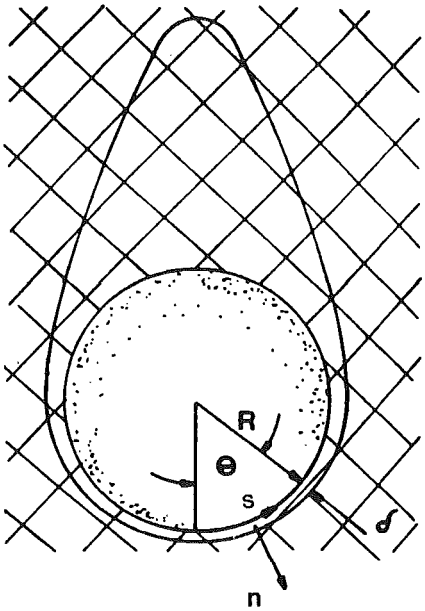


Fig. 2 Theoretical model for flow film boiling in a saturated porous medium

has proven especially appropriate for flows near solid boundaries. The following additional assumptions will now be made:

1 A distinct boundary layer between the vapor and the liquid with no mixed region in between.

2 The interface at $n=\delta_v$ is smooth and stable, and is at a constant temperature $T_s$.

3 Shear stresses at the interface are negligible, i.e.,

$$\left(\frac{\partial u_v}{\partial n}\right)_{n=\delta_v}=0 \tag{1}$$

4 A linear temperature profile exists across the vapor film.

5 The properties of the liquid, vapor, and porous medium are assumed constant, except for the effective conductivity of the vapor-porous medium, $K_{m,v}$, which will be formulated as a function of $\delta_v$, the vapor layer thickness, and $R_p$, the radius of the particles forming the porous medium.

6 The porous medium consists of spherical particles of radius $R_p$.

After the usual boundary layer assumptions are taken into account, the Brinkman–Darcy momentum equation for the vapor reads

$$-(\rho_L-\rho_v)g\sin\left(\frac{s}{R}\right)=-\frac{\mu_v}{K}u_v+\tilde{\mu}_v\frac{d^2u_v}{dn^2} \tag{2}$$

where $s$ and $n$ are the curvilinear coordinates along the surface and normal to the heated surface (Fig. 2), $u_v$ the vapor velocity component in the $s$ direction, $K$ the permeability, $\mu_v$ the vapor viscosity, $\tilde{\mu}_v$ the effective vapor viscosity, and $\rho_v$ and $\rho_L$ the vapor and liquid viscosity, respectively.

The boundary conditions at the heated surface and at the interface are:

$$\text{at } n=0\text{: } u_v=0 \tag{3}$$

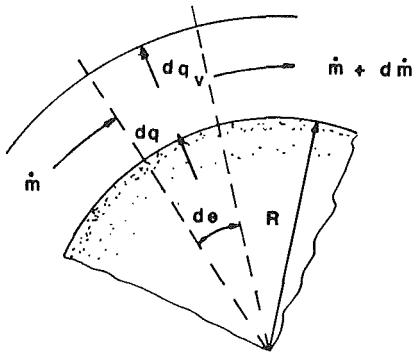


Fig. 3 Differential element for mass-energy balance

$$\text{at } n=\delta_v\text{: } \frac{\partial u_v}{\partial n}=0 \tag{4}$$

Equation (2) is now integrated analytically subject to conditions (3) and (4) to yield the vapor velocity in the $s$ direction

$$u_v=C_1\sin\left(\frac{s}{R}\right)\times\left[1-\frac{\exp\left(\mathrm{Da}^{-1/2}\frac{n}{D}\right)+\exp\left(\mathrm{Da}^{-1/2}\frac{2\delta_v-n}{D}\right)}{1+\exp\left(2\mathrm{Da}^{-1/2}\frac{n}{D}\right)}\right] \tag{5}$$

where

$$C_1=\frac{(\rho_L-\rho_v)gK}{\mu_v} \tag{6}$$

and

$$\mathrm{Da}=\frac{\tilde{\mu}_vK}{\mu_vD^2} \tag{7}$$

is the Darcy number.

The average velocity as a function of angular position can now be written as

$$\bar{u}_v=C_1\sin\left(\frac{s}{R}\right)\times\left[1-\frac{1}{\mathrm{Da}^{-1/2}\frac{\delta_v}{D}}\,\frac{\exp\left(2\mathrm{Da}^{-1/2}\frac{\delta_v}{D}\right)-1}{\exp\left(2\mathrm{Da}^{-1/2}\frac{\delta_v}{D}\right)+1}\right] \tag{8}$$

Based on the assumption of a linear temperature profile in the vapor layer and no subcooling in the liquid, a mass-energy balance on a differential element shown in Fig. 3 gives

$$k_{m,v}R\,\frac{T_w-T_s}{\delta_v}\,d\left(\frac{s}{R}\right)=d[\bar{u}_v\rho_v\delta_vh'_{fg}] \tag{9}$$

where $k_{m,v}$ is the effective thermal conductivity of the porous medium in the vapor film, and $h'_{fg}$ is the latent heat of vaporization including the effects of vapor superheat. Equation (8) can now be substituted into equation (9) to yield

$$\frac{d\left(\frac{\delta_v}{D}\right)}{d\left(\frac{s}{R}\right)}=\frac{\frac{M}{2\left(\frac{\delta_v}{D}\right)}-\cos\left(\frac{s}{R}\right)\left[\left(\frac{\delta_v}{D}\right)-\mathrm{Da}^{1/2}\,\frac{\exp\left(2\mathrm{Da}^{-1/2}\frac{\delta_v}{D}\right)-1}{\exp\left(2\mathrm{Da}^{-1/2}\frac{\delta_v}{D}\right)+1}\right]}{\sin\left(\frac{s}{R}\right)\left[\frac{\exp\left(2\mathrm{Da}^{-1/2}\frac{\delta_v}{D}\right)-1}{\exp\left(2\mathrm{Da}^{-1/2}\frac{\delta_v}{D}\right)+1}\right]} \tag{10}$$

where

$$M=\frac{k_{m,v}(T_w-T_s)\mu_v}{D\rho_v(\rho_L-\rho_v)h'_{fg}Kg} \tag{11}$$

The energy analysis for the sphere is identical. For the sake of completeness, we report only one key result: the final differential equation for $\delta_v$, which is analogous to equation (10):

$$\frac{d\left(\frac{\delta_v}{D}\right)}{d\left(\frac{s}{R}\right)}=2\left(\frac{\delta_v}{D}\right)\frac{\frac{M}{2\left(\frac{\delta_v}{D}\right)}-2\cos\left(\frac{s}{R}\right)\left[\frac{\delta_v}{D}-\mathrm{Da}^{1/2}\frac{\exp\left(2\mathrm{Da}^{-1/2}\frac{\delta_v}{D}\right)-1}{\exp\left(2\mathrm{Da}^{-1/2}\frac{\delta_v}{D}\right)+1}\right]}{\sin\left(\frac{s}{R}\right)\left[\frac{\exp\left(2\mathrm{Da}^{-1/2}\frac{\delta_v}{D}\right)-1}{\exp\left(2\mathrm{Da}^{-1/2}\frac{\delta_v}{D}\right)+1}\right]} \tag{12}$$

Equations (10) to (12) for the cylinder and sphere, respectively, need to be solved numerically to yield the thickness of the vapor film. The numerical integration is performed with the help of the fourth-order Runge-Kutta method (Ferziger, 1985). Two major points related to the numerical integration are worth clarifying. First, initial conditions ($\theta=0$) are required to start the numerical integration. To obtain the vapor thickness at $\theta=0$, one makes use of symmetry and sets the left-hand side of equations (10) and (12) equal to zero. In both cases, cylinder and sphere, the above procedure results in nonlinear algebraic equations. These equations are solved numerically each time to yield the value of the vapor thickness at $\theta=0$. This value makes it possible to start the numerical integration of equations (10) and (12).

The second point that needs clarification pertains to the upper limit of integration. We have found that just like in the case of flow film boiling from bodies embedded in porous media (Orozco et al., 1986), we do not have a critical angle $\theta_c$ at which the vapor velocity gradient at the wall is equal to zero, indicating flow reversal for values of $\theta$ larger than $\theta_c$. In the present study the existence of a negative pressure gradient along the heated surface forces the vapor velocity to remain positive for all values of $\theta$ (see Fig. 2). Therefore, our model should remain valid at all points around the circumference of the cylinder or sphere, and it is physically correct to perform the integration starting from $\theta=0$ and ending at the point of vapor detachment as long as the condition $\delta_v << D$ is not violated.

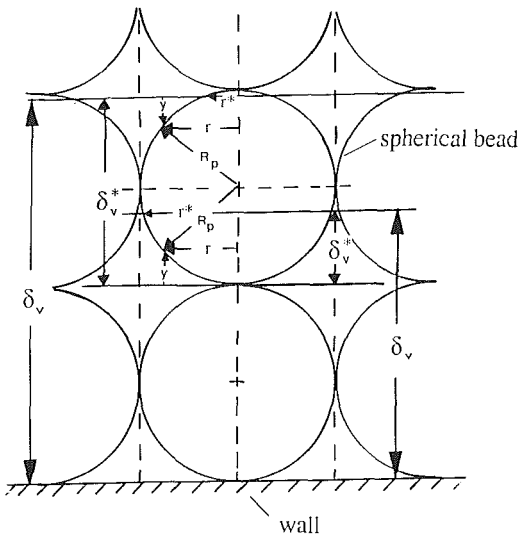


Fig. 4 Porous medium model

Once the vapor film thickness is known as a function of angular position, the velocity field can be calculated from equation (5). In addition, important heat transfer results can be obtained pertaining to both the local and overall heat transfer from the heated surface to the fluid–porous medium matrix.

The local heat transfer is given by

$$q_{w,l}=\frac{k_{m,v}(T_w-T_s)}{\delta_v} \tag{13}$$

since the temperature distribution inside the vapor layer is assumed to be linear. Based on the above equation, it is easy to verify that the local heat transfer coefficient and the local Nusselt number are

$$h=k_{m,v}/\delta_v \qquad \mathrm{Nu}(\theta)=\frac{hD}{k_{m,v}}=D/\delta_v \tag{14}$$

The overall Nusselt number is obtained in the usual manner by averaging the local Nusselt number over the heated surface. Since it is difficult to identify experimentally the point of vapor detachment, the numerical integration is performed over the surface of the cylinder or sphere up to the angular position where $\delta_v/D=0.1$. The expression for the overall Nusselt number, therefore, is

$$\overline{\mathrm{Nu}}=\begin{cases}\dfrac{1}{\pi}\displaystyle\int_0^{\theta_d}\mathrm{Nu}(\theta)\,d\theta & \text{(cylinder)} \qquad (15)\\[2ex] \dfrac{1}{2}\displaystyle\int_0^{\theta_d}\mathrm{Nu}(\theta)\sin\theta\,d\theta & \text{(sphere)} \qquad (16)\end{cases}$$

where $\theta_d$ denotes the angular position where the detachment of the vapor film occurs. The integration of equations (15) and (16) was performed numerically after the value of $\mathrm{Nu}(\theta)$ was obtained. A similar analysis has been developed for film boiling heat transfer to a pool of saturated liquid. For the sake of completeness, only the key results will be reported. For both the sphere and the cylinder the vapor velocity in the vapor film is given by

$$u_v=\frac{(\rho_l-\rho_v)g\sin(s/R)}{\mu_v}\left(\delta_v n-\frac{n^2}{2}\right) \tag{17}$$

The energy analysis for the cylinder yields

$$\frac{d\left(\frac{\delta_v}{D}\right)}{d\left(\frac{s}{R}\right)}=\left[\frac{M_1}{\left(\frac{\delta_v}{D}\right)^3}-\frac{\cos(s/R)}{3}\left(\frac{\delta_v}{D}\right)\right]\cdot\frac{1}{\sin\left(\frac{s}{R}\right)} \tag{18}$$

and for the sphere

$$\frac{d\left(\frac{\delta_v}{D}\right)}{d\left(\frac{s}{R}\right)}=\left[\frac{M_1}{\left(\frac{\delta_v}{D}\right)^3}-\frac{2\cos(s/R)}{3}\left(\frac{\delta_v}{D}\right)\right]\cdot\frac{1}{\sin\theta} \tag{19}$$

where $M_1$ is given by

$$M_1 = \frac{k_v \Delta T v \mu_v}{2\rho_v h'_{fg} g(\rho_1 - \rho_v) D^3} \tag{20}$$

**Formulation of the Vapor-Porous Medium Effective Conductivity.** The effective conductivity of a porous medium $k_{m,v}$ is generally defined as

$$k_{m,v} = \phi k_v + (1-\phi) k_{\text{sol}} \tag{21}$$

where $\phi$ stands for porosity, and $k_v$ and $k_{\text{sol}}$ represent the thermal conductivities of the vapor and porous medium material, respectively. However, in the case of film boiling, a better formulation of the effective conductivity is necessary.

Basing the effective conductivity analysis on one single spherical particle representing the porous medium and with a packing arrangement as shown in Fig. 4, we have that the porosity in the vicinity of the heated surface is a function of the thickness of the vapor layer. Figure 4 also shows that the efffective conductivity will be vapor dominant for values of $\delta_v^* \ll R_p$. However, as $\delta_v^*$ increases, the conductivity of the solid comes into play, and consequently, the effective conductivity becomes porous medium material dominant.

Under the assumption of a linear temperature profile across the vapor layer, and for the condition $\delta_v^* \leq R_p$, we have the heat transfer rate across $\delta_v^*$ given by

$$Q_T = Q_v + Q_{v,s} = k_{m_{1h}} 4R_p^2 \frac{(T_{in} - T_s)}{\delta_v^*} \tag{22}$$

where $T_{in}$ is the porous medium temperature at a distance $\delta_v - \delta_v^*$ away from the heated surface, $Q_T$ is the net energy flow across $\delta_v^*$, and $Q_v$ and $Q_{v,s}$ are the energy flows through a pure vapor and a vapor-porous medium material path, respectively. Thus, $Q_v$ and $Q_{v,s}$ are given by

$$Q_v = k_v A_v \frac{(T_{in} - T_s)}{\delta_v^*} \tag{23}$$

$$Q_{v,s} = k_{v,s} A_{v,s} \frac{(T_{in} - T_s)}{\delta_v^*} \tag{24}$$

where

$$A_v = 4R_p^2 - \pi r^{*2} \tag{25}$$

$$r^{*2} = \delta_v^{*2}\left(\frac{2R_P}{\delta_v^*} - 1\right) \tag{26}$$

$$A_{v,s} = \pi r^{*2} \tag{27}$$

and $k_{v,s}$ is the average conductivity through the vapor-porous material path.

Substituting equations (23) and (24) into equation (22), one obtains the effective conductivity across $\delta_v^*$ for values of $\delta_v^* \leq R_p$

$$km_{lh} = \frac{1}{4R_p^2}\left[k_v A_v + k_{v,s} A_{v,s}\right] \tag{28}$$

The average conductivity $k_{v,s}$ through the vapor-porous medium material path is now formulated by focusing our attention on the flow of energy from an element of area $dA$ in the porous medium at the temperature $T_{in}$. Figure 4 shows that if we take $y$ to be the vertical distance from the element of area $dA$ located at a distance $\delta_v - \delta_v^*$ away from the heated sruface to a point on the surface of a spherical particle representing the porous medium, the energy flow across $\delta_v^*$ could then be written as

$$dQ_{v,s} = \left[\frac{Y}{k_v} + \frac{\delta_v^* - y}{k_{\text{sol}}}\right]^{-1} (T_{in} - T_s) dA_{v,s} \tag{29}$$

Integrating equation (30) over $A_{v,s}$ one obtains

$$K_{v,s} = B_0 \int_0^{r^*} \frac{r\, dr}{B_1 - B_2 (R_P^2 - r^2)^{1/2}} \tag{30}$$

where

$$B_0 = 2k_v k_{\text{sol}} / (2R_p - \delta_v^*) \tag{31}$$

$$B_1 = R_p (k_{\text{sol}} - k_v) + \delta_v^* k_v \tag{32}$$

and

$$B_2 = (k_{\text{sol}} - k_v) \tag{33}$$

$$r^* = \delta_v^* (2R_p/\delta_v^* - 1)^{1/2} \tag{34}$$

Finally, the total effective conductivity $k_{m,v,}$ is given by the following equation:

$$k_{m,v} = \delta v \left[\frac{\delta_v^*}{k_{m_{lh}}} + \frac{2NR_P}{k_o}\right]^{-1} \tag{35}$$

where $N$ stands for the number of particles completely immersed in the vapor film and $k_o$ is the value of $k_{m_{lh}}$ when $\delta_v^*$ is equal to $R_p$. A similar approach is taken for the case when $\delta_v^* \geq R_p$. When such a situation exists, $k_{m,v}$ is given by

$$k_{m,v} = \delta_v \left[\frac{\delta_v^* - R_p}{k_{m_{uh}}} + \frac{2(N+1)R_P}{k_o}\right]^{-1} \tag{36}$$

where

$$k_{m_{uh}} = \frac{\delta_v^*}{A_T}\left[\frac{k_o}{R_P} A_T + \frac{k_{\text{sol}} A_{\text{sol}} + k_{v,s} A_{v,s}}{(\delta_v^* - R_p)}\right]^{-1} \tag{37}$$

$$A_{\text{sol}} = \pi (r^*)^2 \tag{38}$$

$$A_{v,s} = 4R_P^2 - \pi r^{*2} \tag{39}$$

$$A_T = 4R_P^2 \tag{40}$$

$$r^* = [(R_P^2 - (\delta_v^* - R_P))]^{1/2} \tag{41}$$

and $k_{v,s}$ is given by

$$k_{v,s} = \frac{2\pi(\delta_v^* - R_P) k_v k_{\text{sol}}}{4R_P^2 - \pi r^{*2}} \int_{R_P}^{r^*} \frac{r dr}{(\delta_v^* - R_P) k_{\text{sol}} - (k_{\text{sol}} - k_v)(R_P^2 - r^2)^{1/2}} \tag{42}$$

Therefore, one additional feature of the numerical integration of equations (10) and (12) involves the numerical computation of the effective conductivity given by equations (35) and (36) at each angular position.

**Data Reduction.** For a given power input to the heater, the cylinder heat flux was compared from

$$q_{\text{cyl}} = (VI - Q_{\text{loss}})/A_{\text{cyl}} \tag{43}$$

where $V$ is the voltage input, $I$ the ammeter reading, $Q_{\text{loss}}$ the heat losses in the axial direction, and $A_{\text{cyl}}$ the cylinder surface area, respectively.

The end losses $Q_{\text{loss}}$ were computed with the aid of temperature differences $T_2 - T_1$ and $T_8 - T_1$. Temperature measurements were made at different locations on the heater surface as previously described. However, for each power setting, additional temperature measurements were generated by rotating the cylindrical heater about its axis. The average wall temperature was found by fitting polynomial curves through the temperatures measured at various angular and axial locations, and then computing an area-weighted temperature average using

$$\overline{Tw} = \frac{1}{A} \int_A T_w(x, \theta) dA \tag{44}$$

Reproducibility between experiments performed at the same condition was quite good, with a deviation of only few percent between comparable data.

The steady-state uncertainty in the heat transfer results was due to the observer resolution in amperage readings, and in temperature recording errors. A detailed uncertainty analysis (Stellman, 1987) showed that a maximum expected error of ±6 percent would occur.

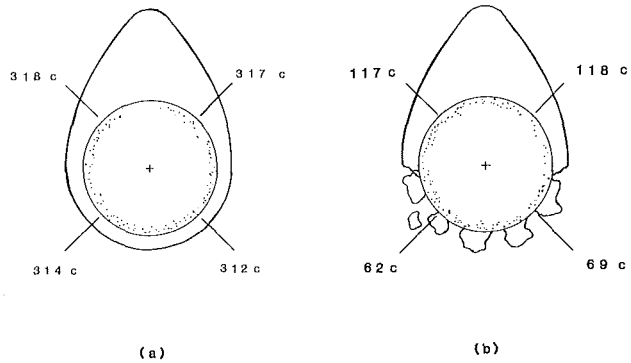


Fig. 5 Observed temperature distributions

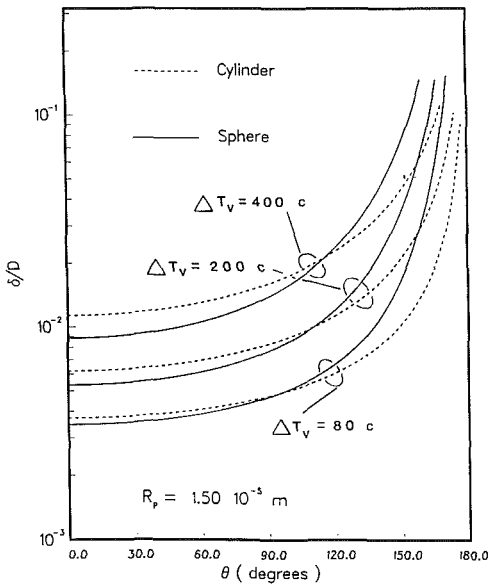


Fig. 6 Effect of vapor superheat on film thickness

**Observations.** It was observed that while the heater was operating in the stable film boiling regime, there was always a dependence of wall temperature on angular location. It was also determined that the lowest temperatures would occur at the heater lower stagnation point while the highest temperature would take place at the upper stagnation point. Figure 5(*a*) illustrates a typical temperature distribution occurring at the heater surface while its operating in stable film boiling. However, there were instances when relatively large temperature gradients were observed along the heated surface. Figure 5(*b*) is an illustration of such an occurrence. We believe that the pronounced temperature gradients were an indication that the lower half of the heated surface was operating in the nucleate boiling regime while the upper half remained in the stable film boiling regime. Another aspect of the boiling process worth mentioning is the fact that the collapse of the vapor film in the absence of the porous medium was much more precipitous than that observed with the porous medium present. The porous medium seems to stretch the occurrence of the minimum heat flux over a wider range of temperature.

It was also observed that there were instances during stable film boiling when one of the thermocouples located on the heater surface would register a temperature much lower than those registered by the other thermocouples. A simple repacking of the porous medium usually brought partly to the low reading. However, inspection of the heater with regard to the oxidation of its surface after an experimental run revealed that the low reading was caused by a nonspherical glass bead "sticking" to the heater surface. The relatively large conductivity of the porous medium in comparison to that of vapor would enhance the energy dissipation from the area covered by this nonspherical glass bead, therefore depressing the surface temperature, and minimizing the oxidation. It was also determined that the oxidation of the surface had a negligible effect on the heat transfer rates during stable film boiling.

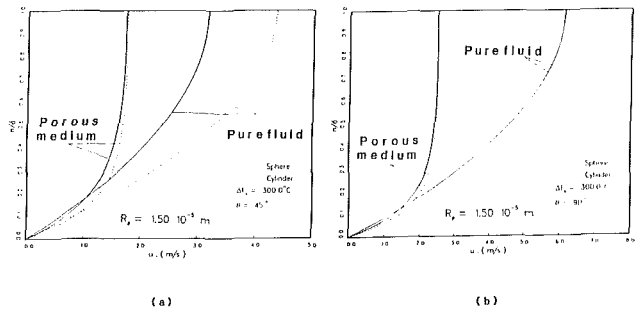


Fig. 7 Velocity profiles at two different angular locations

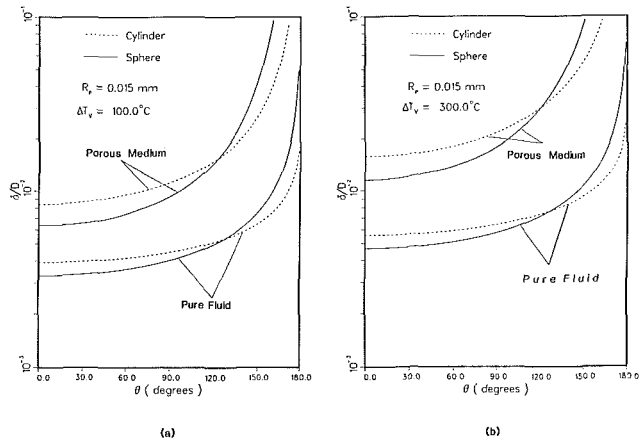


Fig. 8 Comparison of vapor layer thickness growth with and without the porous matrix

## Results and Discussion

**Theoretical Resutls.** Figure 6 illustrates the effect of the vapor superheat on the thickness of the vapor layer for both the cylinder and sphere. As expected, increasing the superheat of the vapor increases the thickness of the vapor layer. However, it is observed that the vapor film thickness for the cylinder is thicker than that for the cylinder for small values of $\theta$. As $\theta$ increases after a specific value, the sphere vapor remains the larger of the two thicknesses thereafter. The value of $\theta$ at which this "overtake" occurs increases as the vapor superheat increases.

Figure 7 compares the vapor velocity profiles at two angular locations along the surface of the heaters in the presence of a porous medium to those profiles for the pure fluid case. It is observed that lower average vapor velocities are produced for the case of the film boiling in a porous medium.

Figures 8(*a*) and 8(*b*) compare the growth of the vapor film for the pure fluid case to that in the presence of a porous medium for two different degrees of superheat. A thicker film is calculated for the heaters embedded in a porous medium; however, the pure fluid vapor film has a faster rate of growth and overtakes the porous medium vaper layer around the 90 deg mark. This overtake may be attributed to the larger pressure gradient in the *s* direction experienced by the pure fluid.

Figure 9 shows the effect of the vapor superheat on the average Nusselt number. The results for the cylinder and for the sphere exhibit the same qualitative behavior; however, the values of the average Nusselt number for the sphere are con-

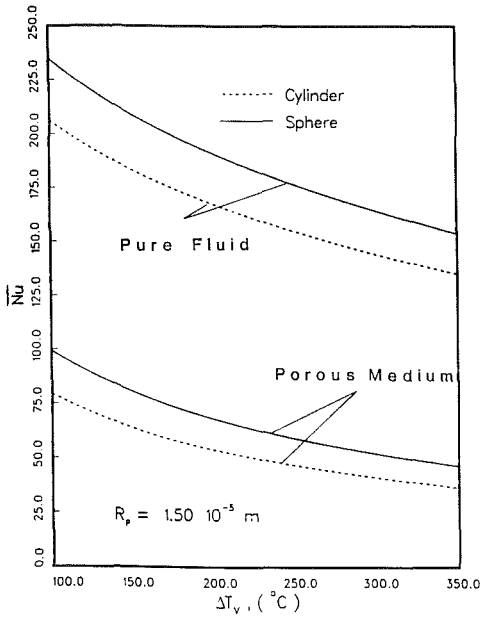


Fig. 9 Effect of vapor superheat on the average Nusselt number

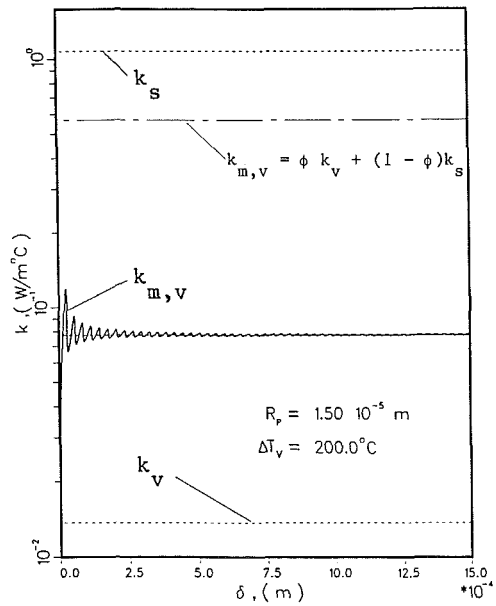


Fig. 10 Dependency of the effective conductivity on position along the surface of the heater

sistently higher than the values of $\overline{Nu}$ for the cylinder. For the two geometries, the difference in average Nusselt number between the pure fluid case and the porous medium case is a reflection of the dependence of the vapor film thickness on angular position and degree of superheat as illustrated in Figs. 8(*a*) and 8(*b*).

Figure 10 describes the dependency of the effective conductivity on the vapor film thickness as formulated by equations (39) and (36). Near the forward stagnation point, were the thickness of the vapor film reaches a minimum, the value of the effective conductivity is very close to that for pure vapor. However, as the thickness of the vapor layer increases, the effective conductivity aproaches the conductivity of the porous medium.

**Experimental Results and Comparison to Theory.** Figure 11(*a*) is a comparison of the theory developed in this investigation to the recent measurements of Tsung and Dhir (1985) for film boiling from a spherical heater embedded in a saturated

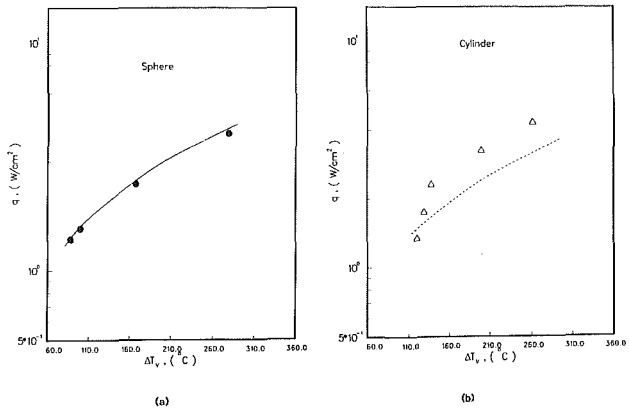


Fig. 11 Comparison of experiments and theory

porous medium. The comparison of the theory to the experimental, data for the spherical heater shows an excellent agreement between theory and experiments. For the cylindrical heater, see Fig. 11(*b*), we find that there is good agreement, however, the theory underpredicts the experimental data by a factor of 20 percent. This discrepancy may be attributed to the nonuniformity in temperature in the axial direction registered by the heater surface. Axial temperature gradients of the order of 30°C were observed while the heater was operating in the film boiling regime.

## Conclusions

The theory developed in this investigation predicts the heat flux very well for the heat transfer regime where stable film boiling exists over the entire heater area for both cylinders and spheres embedded in a liquid-saturated porous medium. Good agreement exists between the theory and the experimental data of other investigator (Tsung et al., 1985) for the spherical heater. The theory has been compared with the experimental data obtained by the authors for a cylindrical heater, and good agreement was also found. Higher heat fluxes are produced in stable film boiling when there is a porous medium present. It was also found that the oxidation of the heated surface had a negligible effect on the energy dissipation during film boiling.

## Acknowledgments

The author would like to thank the University of Illinois Research Board and Amoco Research for their support of this project.

## References

Cheng, P., 1981, "Film Condensation Along an Inclined Surface in Porous Medium," *Int. J. Heat Mass Transfer*, Vol. 24, pp. 983-990.

Cheng, P., and Verman, A. K., 1981, "The Effect of Subcooled Liquid on Film Boiling Above a Vertical Heated Surface in a Porous Medium," *Int. J. Heat Masss Transfer*, Vol. 24, pp. 1151-1160.

Ferziger, J. A., 1985, *Numerical Methods for Engineering Applications*, Wiley, New York, pp. 76-484.

Hsu, T. C., and Cheng, P., 1985, "The Brinkman Model for Natural Convection About a Semi-Infinite Vertical Flat Plate in Porous Medium," *Int. J. Heat Mass Transfer*, Vol. 28, pp. 683-697.

Ip, S.-S., and Minkowycz, W. J., "The Effect of Axial Pressure Variations on Film Boiling About a Heated Vertical Plate Embedded in a Porous Medium," *Numerical Heat Transfer*, in press.

Orozco, J., Poulikakos, D., and Gutjahr, M., "Flow Film Boiling From a Sphere and Horizontal Cylinders Embedded in Porous Medium," *Journal of Thermophysics and Heat Transfer*, in press.

Stellman, R., 1987, "Studies in Boiling Heat Transfer, M.S. Thesis, University of Illinois—Chicago.

Tong, T. W., and Subramanian, E., 1985, "A Boundary Layer Analysis for Natural Convection in Vertical Porous Encloures—Use of Brinkman-Extended Darcy Model," *Int. J. Heat Mass Transfer*, Vol. 28, pp. 563-571.

Tsung, V. X., Dhir, V. K., and Singh, S., 1985, "Experimental Study of Boiling Heat Transfer From a Shpere Embedded in Liquid Saturated Porous Media," in: *Heat Transfer in Porous Media and Particulate Flows*, L. S. Yao et al., eds., ASME HTD-Vol. 46, pp. 127-134.

A. K. Stubos

J.-M. Buchlin

von Karman Institute for Fluid Dynamics,
B-1640 Rhode-Saint-Genèse, Belgium

# Modeling of Vapor Channeling Behavior in Liquid-Saturated Debris Beds

*The formation and evolution of vapor channels in a liquid-saturated and heat-generating particulate bed is modeled. The effect of the sticking forces on the onset of channeling is considered. Simple experimental techniques are devised to support the model development. Satisfactory interpretation of the D10 in-pile test performed at Sandia Laboratories can be achieved with the present channel model.*

## 1 Introduction

A wide variety of industrial, agricultural, and energy production processes are related to the thermohydraulics of porous media saturated with multiple fluid phases. Examples include drying of porous solids, freezing of soils, geothermal applications, thermally enhanced oil recovery, heat transfer from buried pipelines, design of heat pipes, underground high-level nuclear energy disposal, and Post Accident Heat Removal (PAHR). This last application addressed to the nuclear safety analysis of Liquid Metal Fast Breeder (LMFB) and Light Water (LW) reactors is the main concern of the present paper.

The PAHR scenario describing the sequel of a hypothetical core meltdown accident forecasts the formation of a particulate debris bed in the reactor vessel. This porous medium saturated by stagnant liquid coolant is subjected to the decay heat of the fission products. The long-range coolability of this heat-generating particle bed is an important question to be solved (Joly and Le Rigoleur, 1979). Heat removal can be achieved by single-phase natural convection and by two-phase flow. Boiling is a very efficient internally cooling process, which unfortunately is also self-limiting in the case of the PAHR situation: generation of a high vapor flow rate prevents the replenishment of the porous matrix by liquid and subsequently dryout occurs.

In-pile experiments with prototypical materials (Gronager et al., 1981; Mitchell and Ottinger, 1982; Ottinger et al., 1982; Mitchell et al., 1984) and out-of-pile simulations (Gabor et al., 1972; Barleon et al., 1984; Stevens and Trenberth, 1982; Buchlin and Van Koninckxloo, 1986) outline the eventual presence of vapor channels in the bed and their effect on its coolability. This experimental ascertainment fosters the development of appropriate modeling to predict the behavior of channeled debris beds. Accordingly, the present paper deals with a theoretical and experimental investigation of the formation and evolution of vapor channels in a boiling particulate bed.

## 2 Modeling of Channeled Bed

Among the several aspects of boiling in liquid-saturated self-heated particle beds, channeling is a dominant process for which modeling uncertainties still exist. Vapor channels form in the upper part of the bed as shown in Fig. 1, where a typical visualization obtained within the O.P.E.R.A. test facility developed at the VKI (Buchlin and Van Konickxloo, 1986) is reported. The vapor phase flows upward through discrete and low resistance paths from which particles are expelled and deposited aside. The lower part of the bed continues to experience packed boiling.

The flow behavior and characteristics of the channeled region have not been explicitly and fully described. A qualitative analogy between spouting of fluidized powder and channeling has been exploited by Buchlin et al. (1982), leading to the implementation of an empirical model in the TORPEDO code (Benocci, 1981). Naik and Dhir (1982) used a pipe flow formulation for the vapor flow in the channels and obtained experimental data on the shape and number of channels. Recently, Schwalm (1985) as well as Barleon et al. (1985) suggested modeling the channeled region as a porous layer of higher permeability.

In fact, the modeling approach commonly adopted (Jones et al., 1982; Schwalm and Nijsing, 1982; Reed, 1982) is exemplified by the Lipinski model (1982). It is assumed that the vapor pressure at the bottom of a channel is sufficient to offset the weight of the overlying particles plus liquid and that the flow resistances in the channeled region are negligible. However, Lipinski's model presents certain shortcomings regarding the prediction of out-of-pile (Schwalm, 1985) as well as in-pile (Mitchell et al., 1984) channel data. This fact along with the uncertainties concerning the influence of the vapor channel formation on the coolability of the bed (Barleon et al., 1984; Schwalm, 1985) stresses the need for further refinement of the modeling of channel behavior.

In previous attempts the friction between particles as channels are formed is neglected. Lipinski (1984) introduces the idea of a sticking factor $S_f$, which means that the vapor pressure must be $S_f$ times the overlying bed pressure at the bottom of a channel. The same idea in terms of a sticking pressure is proposed by Schwalm (1985). However, it appears

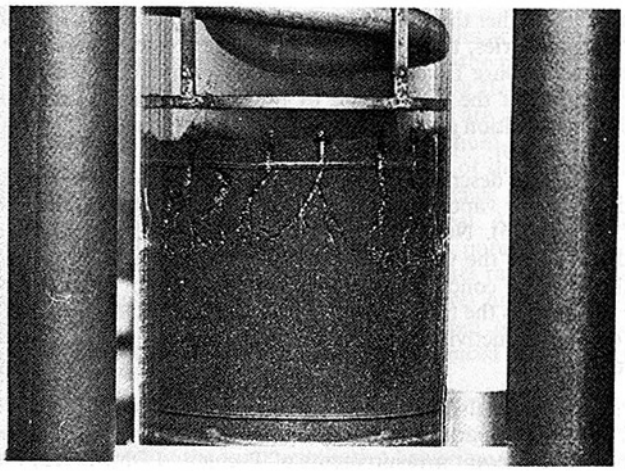

Fig. 1 Channel visualization in heated bed

Contributed by the Heat Transfer Division for publication in the JOURNAL OF HEAT TRANSFER. Manuscript received by the Heat Transfer Division January 27, 1987. Keywords: Boiling, Packed and Fluidized Beds, Porous Media.

that a nondimensionalization of this sticking pressure leads straightforwardly to the sticking factor concept.

Therefore Lipinski's model can be extended as follows: The vapour pressure $P_v$ at the bottom of a channel is expressed as

$$P_v = S_f \cdot (\rho_p \cdot (1-\epsilon) + \rho_l \cdot \epsilon) \cdot g \cdot L_c \tag{1}$$

where $L_c$ is the channel length and $\rho_p$ and $\rho_l$ are the solid and liquid density, respectively.

In the channeled region liquid flows slowly and orderly downward between the channels so that liquid pressure $P_l$ at the channel bottom is regarded as hydrostatic

$$P_l = \rho_l \cdot g \cdot L_c \tag{2}$$

Introducing the capillary pressure $P_c$ by means of the Leverett function $J(s)$, which depends on the effective saturation $s$, it turns out

$$P_c = P_v - P_l = \sigma \cdot \sqrt{\epsilon/\kappa} \cdot J(s) \tag{3}$$

where $\epsilon$ is the porosity and $\kappa$ the permeability of the bed. An expression for channel length is finally obtained

$$L_c = \frac{\sigma\sqrt{\epsilon/\kappa}}{[S_f \cdot (\rho_p \cdot (1-\epsilon) + \rho_l \cdot \epsilon) - \rho_l] \cdot g} \cdot J(s) \tag{4}$$

The saturation value at the channel bottom needed for the calculation of the Leverett function is obtained using the continuity of the pressure gradient at this point. Equation (1) gives

$$\left.\frac{dP_v}{dz}\right|_{z=L_c} = -S_f \cdot (\rho_p (1-\epsilon) + \rho_l \cdot \epsilon) \cdot g \tag{5}$$

while from the vapor momentum equation

$$\frac{dP_v}{dz} = -\rho_v \cdot g - \frac{\mu_v \cdot V_v}{\kappa \cdot \kappa_v} - \frac{\rho_v \cdot V_v^2}{\eta \cdot \eta_v} \tag{6}$$

Since the vapor velocity just below the base of a channel is a function of the heat flux at this point, which in turn is a function of the channel length $L_c$, equations (4), (5), and (6) are solved simultaneously to give both the channel length and the saturation value at the top of the packed region, provided that a value of $S_f$ is available. This fact allows for the computation of the saturation profile in the packed region and the prediction of the dryout power for a channeled bed (Lipinski, 1982).

Lipinski states that an empirical value of 1.6 for the sticking factor should be used to fit the out-of-pile channel suppression data of Barleon et al. (1985). In addition the results of the D10 in-pile test demonstrate that a sticking factor of about 7.2 must be used to explain the onset of channeling (Mitchell et al., 1984). In conclusion, an appropriate model for $S_f$ is needed. This is the purpose of the next section.

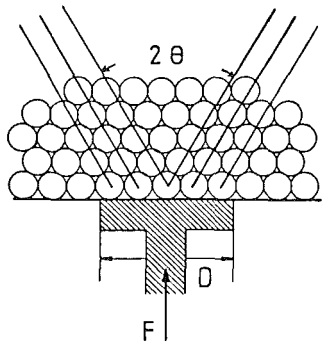


Fig. 2 Physical model for sticking factor

## 3 Development of $S_f$ Model

**3.1 Mathematical Formulation.** The sticking factor model relies upon the analysis of the motion of particles caused by the upward displacement of a piston through the bed. Such a simulation is regarded as representative of the onset of channeling. It is sketched in Fig. 2. Simple visualization tests conducted with a two-dimensional array of spherical marbles show that the upward motion of a particle located at the bottom of the packing affects only the particles whose centers lie on the two sides of the angle $2\theta$, as indicated in Fig. 2. Therefore a force balance applied to a single bottom particle includes the weight of the overlying particles and the friction force required to move the affected particles

$$F_p = N \cdot W_p + \sum_{i=1}^{N} T_i \tag{7}$$

where $W_p$ is the weight of a particle and $N$ the number of particle layers to be expelled; $N$ is related to the channel length and the particle diameter $d$

$$L_c/d = 1 + (N-1)\cos\theta/2 \tag{8}$$

$T_i$ is the friction force at each layer $i$ and is proportional to the force exerted on the moving particles normal to the direction of motion; simple mechanics considerations allow us to write

$$T_i = \frac{fi\ W_p}{(2\cos\theta)} \tag{9}$$

$f$ is defined as a friction coefficient that accounts for the solid material properties and the particle shape. From equation (7) an expression for the total force $F$ is obtained. It is combined with equations (8) and (9) and reduced by the weight $W$ of the overlying column to lead to the following equation for the sticking factor (Stubos, 1985):

## Nomenclature

$A$ = condensation coefficient
$C$ = coefficients of equation (10)
$C_p$ = specific heat
$D$ = channel or piston diameter
$d$ = particle diameter
$F$ = force
$f$ = friction coefficient
$g$ = acceleration of gravity
$J$ = Leverett function
$K_e$ = effective thermal conductivity coefficient
$L_c$ = channel length
$L_f$ = latent heat
$P$ = pressure
$P_c$ = capillary pressure
$Q_v$ = volumetric power deposition
$S_f$ = sticking factor
$s$ = effective saturation (liquid fraction)
$T$ = temperature
$V$ = superficial velocity
$W$ = weight
$z$ = bed coordinate
$\alpha$ = contact angle
$\epsilon$ = porosity
$\eta$ = passability
$\eta_l$ = relative liquid passability
$\eta_v$ = relative vapor passability
$\theta$ = angle of motion
$\kappa$ = permeability
$\kappa_l$ = relative liquid permeability
$\kappa_v$ = relative vapor permeability
$\mu$ = viscosity
$\rho$ = density
$\sigma$ = surface tension

**Subscripts**

$a$ = air
$b$ = boiling
$l$ = liquid
$p$ = particle
$v$ = vapor

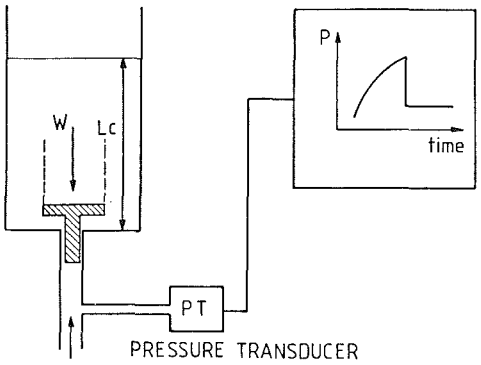


Fig. 3 Piston penetration technique

$$S_f = 1 + f \cdot (C1 \cdot L_c^* + C2 \cdot L_c^*/d^* + C3 \cdot d^* + C4) \qquad (10)$$

$L_c^*$ and $d^*$ are the channel length and the particle diameter normalized by the channel diameter $D$, which is represented by the piston plateau.

Equation (10) reveals the importance of the channel diameter as a parameter of the problem and shows that a higher sticking factor has to be expected when beds of irregular particle shape are considered. The resulting effect of the particle diameter on $S_f$ is not straightforward because it is controlled by the values of the $C$ coefficients, which depend on the actual type of particle arrangement (angle $\theta$ and porosity). They cannot be easily expressed from this simplified analytical approach and have to be determined by means of an experimental procedure. Two experimental techniques are used for this purpose. The first one refers to the penetration of a piston through a particle packing and the second one is based on the simulation of boiling by gas injection at the bottom of the bed.

### 3.2 Experimental Support

*3.2.1 The Piston Penetration Technique.* The setup sketched in Fig. 3 is mainly composed by a cylindrical water saturated particle bed through which a small brass piston with a diameter ranging from 8 to 12 mm is pushed upward by compressed air. The force required to cause the piston displacement is obtained from pressure measurement. The penetration is identified as soon as the signal displays a sharp decrease. The weight of the column is computed on the basis of the piston diameter and the height of the bed, which is equal to the channel length $L_c$ in these tests. Experiments are carried out to investigate the effect of the particle diameter $d^*$ and the solid density $\rho_p$, in the following range: $0.06 < d^* < 0.4$, $2600 < \rho_p < 7800$ kg/m$^3$.

Typical results are shown in Figs. 4 and 5. The sticking factor $S_f$ is plotted versus the reduced channel length and the normalized particle diameter, respectively. Figure 5 shows that $S_f$ tends to an asymptotic value with increasing particle diameter. On the same graphs the theoretical predictions obtained with relationship (10) are compared with success. A unique set of $C$ coefficients fits all the available data points within 15 percent, except for the 0.5-mm glass bed. The change in the solid material and the nature of particles is accommodated by the value assigned to the friction coefficient $f$ only. The presence of liquid in the bed can also be accommodated in the same way as shown by tests with dry beds (Stubos, 1985). The points shown in those figures are averages over several trials, and the observed scattering was of the order of ± 10 percent.

The table below gives the actual form of equation (10) for the case of water-saturated glass and steel beds.

*Glass Bed*

$$S_f = 1 + 1.95L_c^* + 1.185d^* - 0.05\,\frac{L_c^*}{d^*} - 1.15$$

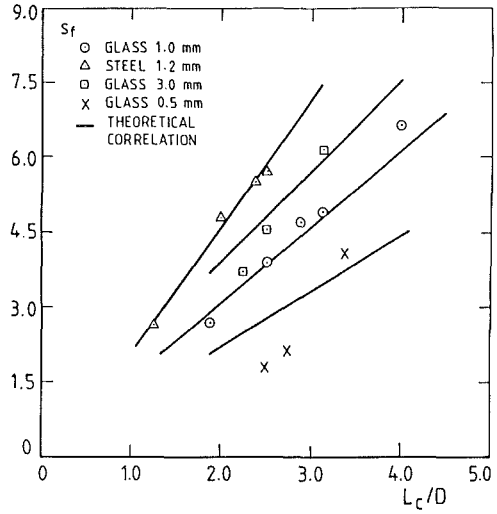


Fig. 4 Sticking factor versus channel length

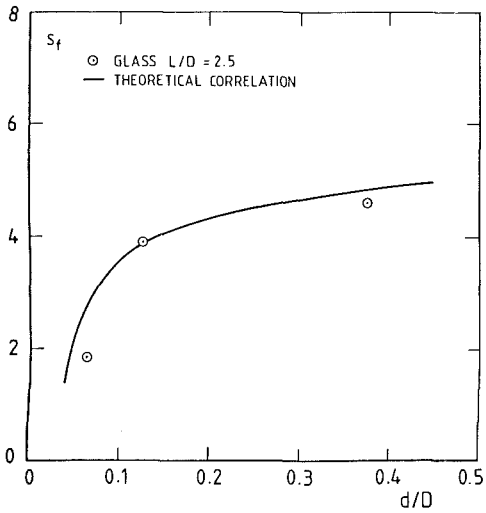


Fig. 5 Sticking factor versus particle diameter

*Steel Bed*

$$S_f = 1 + 3.12L_c^* + 1.9d^* - 0.08\,\frac{L_c^*}{d^*} - 1.84$$

*3.2.2 The Gas Injection Technique.* The piston penetration technique provides data for the channel onset phenomenon. To proceed further and analyze the evolution of channels when vapor flux is growing a more realistic simulation is required. The idea behind the gas injection method is to simulate the boiling process in the particulate bed by forcing gas flow through the packing from a porous bottom support. This experimental procedure allows us not only to observe the channel formation but also its development versus the gas velocity, i.e., the power deposition in a heat-generating debris bed. A schematic representation of the test rig used is reported in Fig. 6. A particle bed is formed in a cylindrical pyrex tube of 12 cm diameter that is specially implemented with a "fritted" glass porous plate. The gas used is dry air.The mass flow rate is measured by means of a rotameter and adjusted by the tuning of the valve. Uniform distribution of air flow in the bed is reached. In these experiments the sticking factor is given by equation (1). The length of the channel is measured from visualizations as shown by the photograph of Fig. 7. The measurement of the air pressure at the bottom of the channel is problematic because it is not known a priori where the chan-

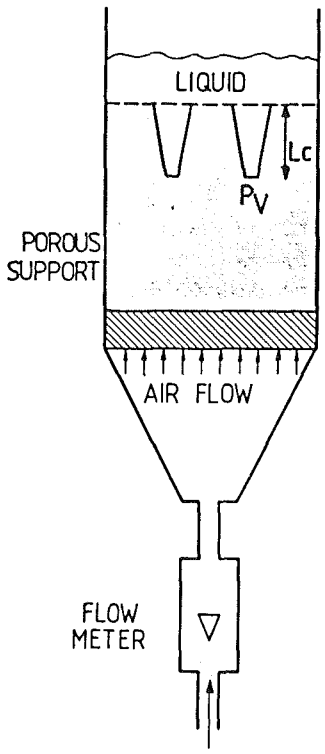


Fig. 6 Gas injection technique

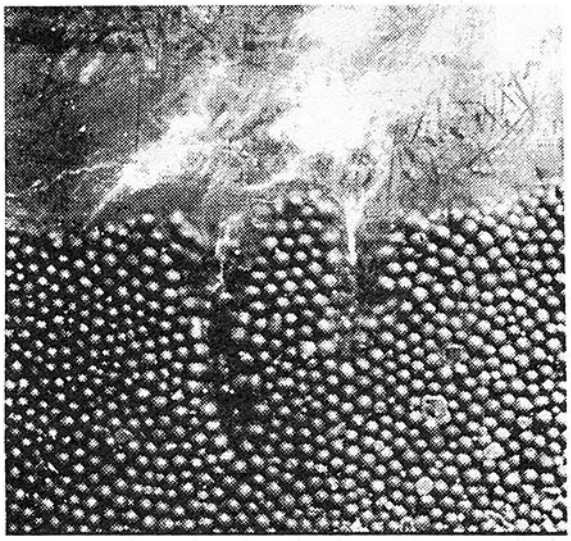

Fig. 7 Channel visualization from gas injection experiment

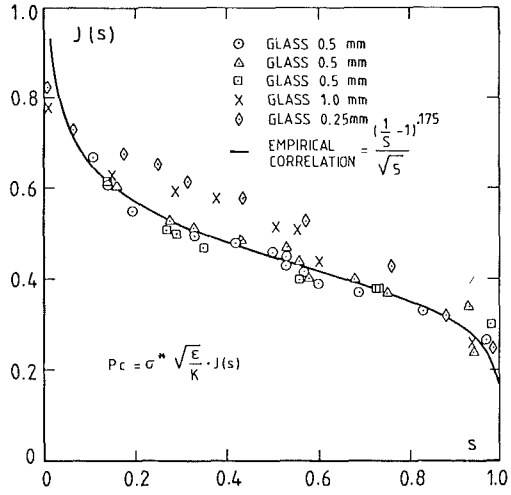


Fig. 8 Leverett's function versus liquid saturation

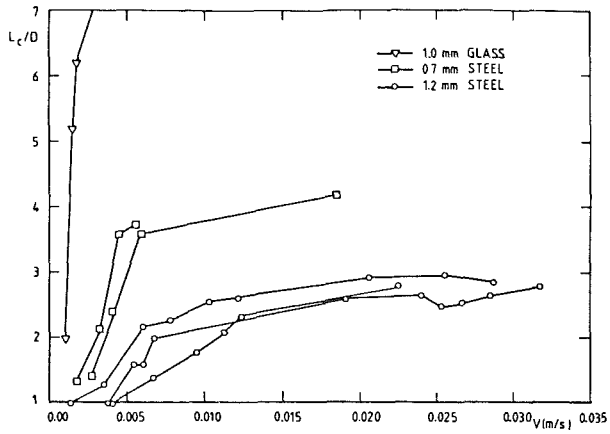


Fig. 9 Channel length versus gas velocity

nel will occur. In addition it must be noted that the presence of the air bubbly flow (no condensation process) in the overlying liquid layer prohibits the determination of the saturation by measurement of the liquid lift. Therefore the following approach is adopted: The liquid pressure is given by the hydrostatic term (equation (2)) since $V_l = 0$; it is assumed for this experimental simulation that $s$ is constant in the packed region of the bed. This approximation is acceptable as long as the air velocity is sufficiently low. If so, the gas phase momentum equation reduces to the laminar term of the Ergun equation. Therefore from equation (3) it can be written

$$\frac{dP_v}{dz} = \frac{dP_l}{dz} \tag{11}$$

and

$$\frac{\mu_a \cdot V_a}{\kappa(1-s)^3} = \rho_l \cdot g \tag{12}$$

The relative permeability is taken equal to $(1-s)^3$ (Lipinski, 1982). The saturation value at the top of the packed region is calculated from equation (12). Finally, the gas pressure $P_v$ can be calculated using the capillary pressure definition (3). The Leverett function is determined from drainage measurements performed with the same test facility (Stubos, 1985). Typical results are plotted in Fig. 8 along with the empirical correlation

$$J(s) = \frac{(s^{-1}-1)^{0.175}}{\sqrt{5}}$$

Figure 9 shows the evolution of the channel length with the air velocity in 0.7 and 1.2 mm steel and 1.0 mm glass beds. Good test repeatability is observed. It is worth noting that the values of the air velocity fall in the range of vapor velocities estimated in heated bed experiments. An average value of $D = 2.5$ mm for the channel diameter is obtained from visual observations (see Fig. 7). The measured channel diameters range from 2.0 to 2.8 mm in agreement with the channel data given by Naik and Dhir (1982) as well as with the average value reported by Reed (1982).

As expected, with decreasing particle diameter and density, channels extend; the gas velocity required to form a channel decreases and the slope of the curves steepens. For a light material such as glass the change in $L_c$ is very sharp for a small

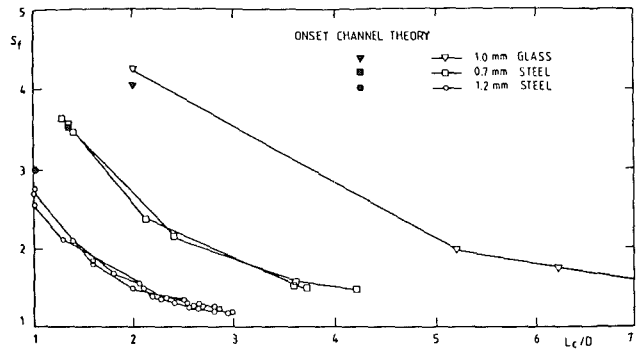


Fig. 10 Sticking factor versus channel length

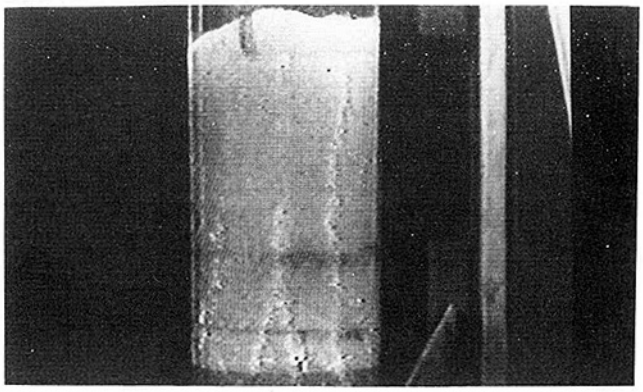

Fig. 11(*a*) Bottom-heated bed

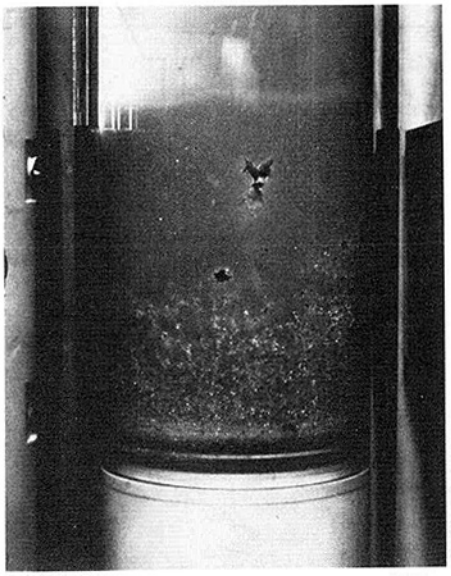

Fig. 11(*b*) Volumetrically heated bed

Fig. 11 "Channel" instabilities in particulate beds

increase in $V_a$, while for steel $L_c$ increases gradually and seems to tend toward a maximum value.

The main features of the proposed model are exemplified in Fig. 10. Making the clear distinction between onset and evolution of channels, it is pointed out that at incipient channeling (first point of each curve), the $S_f$ values found from the air injection experiments, as already described, are within 10 percent of the calculated values. In view of the average value of $D$, the scattering in $L_c$ data ($\pm 10$ percent), the fitting capability of equation (10), and the repeatability noted in Figs. 9 and 10, this agreement is more than satisfactory. Note further that the uncertainty in the experimental $S_f$ points caused by the $L_c$ scattering as well as by the estimation of the saturation value from equation (12) is not smaller than 15 percent.

Thereafter as $V_a$ increases, $S_f$ decreases rapidly and tends to an asymptotic value close to 1. Once the channels are formed, it is much easier for air to lengthen them as its velocity (i.e., power in heated beds) increases.

A review of some published channel length data from out-of-pile tests (Barleon et al., 1984; Stevens and Trenberth, 1982; Jones et al., 1982; Reed, 1986) shows that they generally refer to the extended channeling situation. Consequently, the interpretation of these data in terms of sticking factor may be misleading as could be the case in the work by Schwalm (1985).

It can be noted that the extended-channel length is well predicted by a relation of the following form as proposed by Jones et al. (1982) and Reed (1986):

$$L_c = Cst \cdot \frac{\sigma \cdot \cos \alpha}{(\rho_p - \rho_l) \cdot g \cdot \epsilon \cdot d} \tag{13}$$

where the constant ranges between 4.6 and 6. Relation (13) coincides with equation (4) when the value of the Leverett function lies between 0.38 and 0.49. These limits correspond to liquid saturation of 0.73 and 0.37, respectively, at the bottom of the channels when they have reached their final length. The average saturation value obtained in the present air injection experiment is 0.68 ($\pm 0.03$) and fits quite well the relation (13) when the Reed constant of 4.62 is used.

However, it must be mentioned that some uncertainties exist both in experiments and predictions in the case of light particle beds, such as those made by small glass beads. Most of the tests performed with such beds reveal unstable "channel" behavior, especially when the particles are smaller than about 0.6 mm in diameter and the liquid is water (Jones et al., 1982; Campos, 1983; Gladnick, 1985; Reed, 1986). There are mainly two different types of observed unstable "channeling": The first is the case of long thin twisted vapor paths characterized by a short lifetime corresponding to the time needed for a chain of bubbles to rise through them and taking place sporadically in random locations in the beds. In the second case, the bed can be occasionally disturbed by the formation of large bubbles growing until the pressure is enough for them to rise through the solid packing. Figures 11(*a*, *b*) are visualizations of such instabilities performed at the VKI within bottom and volumetric heated beds, respectively (Campos, 1983; Buchlin et al., 1983).

In the present investigation these unstable bed disturbances are not considered as channeling and only the data referred to stable channels are plotted in Fig. 9, which shows that light particle beds tend to experience early extended channel configuration.

In the situation of in-pile tests where the coolant is the highly thermally conductive liquid sodium, the presence of a large top subcooled zone prohibits early channel penetration contrary to the out-of-pile experiments. The clear distinction made by the present model between the onset ($S_f > 1$) and evolution of channels ($S_f \approx 1$) allows us to account for the nonoccurrence of channeling even at high bed power levels, while the other models predict early channel formation and large channel lengths.

For the interpretation of the channeling data from heated beds, the limitations of the experimental simulation concerning the conduction of heat through the bed and the condensation of vapor in the subcooled zone at the top of heated beds must be emphasized. More data, especially from beds with high expected incipient channel length, are of course needed to support further the use of such an experimental simulation for the study of channeling phenomena. This is under way at the VKI.

At present it can be said that recent experiments at the

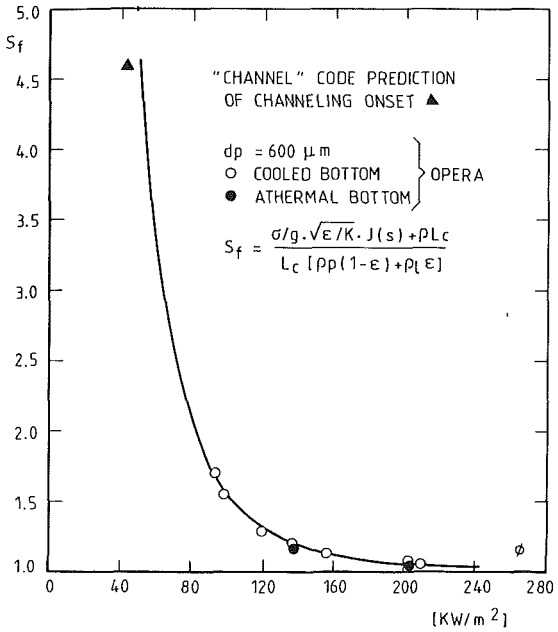


Fig. 12 Sticking factor versus top heat flux

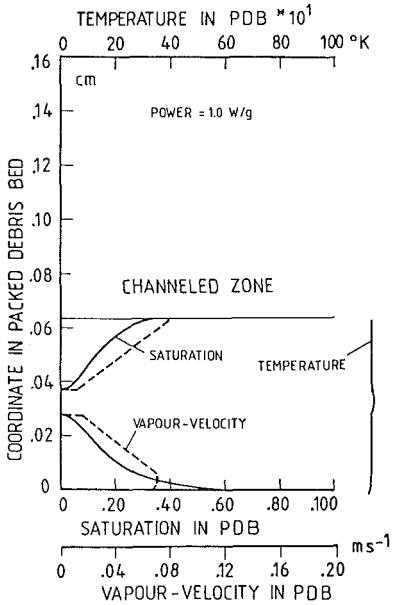


Fig. 13 Typical "channel" prediction of D10 experiment

O.P.E.R.A. facility at the VKI have also found a sticking factor decrease from the value corresponding to the onset of channeling to a final one close to unity as shown in Fig. 12 (Buchlin and Van Koninckxloo, 1986). The bed of 0.6 mm ferrite particles is heated by a dielectric process and saturated with distilled water. The average value of final channel length observed in O.P.E.R.A. experiment is 3.8 cm and agrees well with the value of 3.65 cm predicted by the present model. In addition, incipient channel lengths ranging from 5 to 9 mm were observed in top-heated beds of 0.25 mm glass particles saturated by freon-113, and are favorably compared to the predicted 8 mm length. It is worth noting that in both these cases the observed channel diameters (from 2.0 to 3.0 mm) justify the use of an average value of 2.5 mm.

Another significant observation is the irreversibility of the channeling process. Disturbances in the beds do not disappear even if the velocity is significantly reduced after the occurrence of channels. Early channel formation is then observed if the velocity is increased again.

Table 1 D10 interpretation; height of bed = 0.16 m

| | | | |
|---|---|---|---|
| PACKED BED | | | |
| DRYOUT [W/G] | 0.41 | 0.35 | 0.33 |
| ONSET OF CHANNELS [W/G] | 1.06 | 0.43 | 1.18 |
| S·F | 7.2 | 1.0 | 7.6 |
| DISTURBED BED | | | |
| CHANNELED DRYOUT [W/G] | 1.1 | 3.0 | 1.0 |
| S·F | - | 1.0 | 1.2 |
| CHANNEL LENGTH [M] | 0.08 | 0.135 | 0.095 |

D10 INTERPRETATION
HEIGHT OF THE BED = 0.16 [M]

## 4 Application of the $S_f$ Model

The present sticking factor model is implemented in the one-dimensional code "CHANNEL" developed at the VKI to simulate boiling and extended dryout in the debris bed (Evenhouse and Stubos, 1984). Basically, the phasic mass, momentum, and energy conservation equations for boiling and condensation are solved. The code includes the channel model described in Sections 2 and 3. A pure conduction approach based on effective conductivity coefficient is adopted to deal with the subcooled and dryout parts (see Appendix). The applicability of the present code version is exemplified by attempting the interpretation of the in-pile test D10 conducted at Sandia Laboratories with a bottom-cooled particulate bed (Mitchell et al., 1984). Typical predictions from CHANNEL are listed facing the experimental data and the results deduced from the Lipinski model (Lipinski, 1982) in Table 1. The comparative analysis is achieved using the $S_f$ data of steel bed experiments. The packed dryout power is underestimated by 20 percent. Such a discrepancy emphasizes the difficulty to simulate correctly all the boundary conditions of D10 tests as far as the heat losses are concerned. Their effect is more marked during the packed boiling. As reported by Mitchell et al. (1984), the incipient channeling happens at a specific power of 1.06 W/g and the subsequent channel suppression coefficient is 7.2.The code predicts a power deposition of 1.18 W/g and a $S_f$ value of 7.6 along with an initial channel length of 11 mm accompanied by an extended dry zone. It is worth noting that during the experiment the dryout zone formed at each power step above 0.42 W/g is rewetted to avoid high temperatures in the bed. In this sense it is observed that at a power of 1.06 W/g no dry zone is detected. The explanation might come from the fact that, as claimed by Mitchell et al. (1984), channel formation is followed by a major flashing disturbance in the bed, which possibly caused the rewetting of the dry zone that would normally form. This disturbance may be attributed to the high vapor overpressure, about 7.2 times the bed pressure, which is released at the moment channels are formed. It can be assumed that such a disturbance is of the same type as those observed in glass beds (Jones et al., 1982; Gladnick, 1985; Reed, 1986). The fact that a solid material like $UO_2$ is heavier than glass can be compensated for partly

by the increase of the surface tension of liquid when using sodium and the smaller size of fuel particles.

In the sequel of D10 experiments the power is reduced to low levels in an attempt to repack the bed. However, according to visual out-of-pile observations, it appears that beds that have experienced channeling are irreversibly perturbed. Hence, the second part of the present approach is more dedicated to explain the following D10 data. Prediction for channeled dryout of the disturbed debris bed is successfully completed on the basis of a sticking factor of 1.3. The corresponding state of the D10 bed is numerically simulated in Fig. 13. The axial temperature, liquid saturation, and vapor velocity of the packed region are plotted. A small dryout zone is predicted. A channeled zone of 95 mm is found that is not in contradiction with the experimental temperature distributions.

## 5 Conclusions

The formation and behavior of vapor channels in liquid saturated debris beds are modeled. The concept of the sticking factor as channel suppression criterion is exploited. The mathematical formulation of the sticking factor is supported by experimental investigation involving piston penetration and gas injection techniques.

The distinction between the onset of channeling and the evolved channel configuration is emphasized. Incipient channeling in fresh beds is predictable by the proposed $S_f$ correlation. The evolution of channel length is characterized by a rapid decrease of $S_f$, tending to a value close to unity. The irreversibility of the channeling process is noted and is included in the proposed model.

## References


Barleon, L., Thomauske, K., and Werle, H., 1984, "Cooling of Debris Beds," *Nuclear Technology*, Vol. 65, pp. 67–86.

Barleon, L., Thomauske, K., and Werle, H., 1985, "Investigation on Channel Penetration at KfK," *Meeting on Debris Bed Modeling*, Ispra, May 29–30.

Benocci, C., Buchlin, J.-M., and Joly, C., 1981, "Theoretical and Numerical Modeling of the PAHR Debris Bed Behaviour Implemented in the Torpedo Code," von Karman Institute, CR 1982-04/EA.

Buchlin, J.-M., Benocci, C., Joly, C., and Siebertz, A., 1982, "A Two-Dimensional Finite Difference Modeling of the Thermohydraulic Behaviour of the PAHR Debris Bed up to Extended Dryout," von Karman Institute, Preprint 1982-24.

Buchlin, J.-M., Simon, G., and Barth, U., 1983, "Experimental Simulation of the Post Accident Heat Removal of Liquid Saturated Debris Bed," von Karman Institute, CR 1984-05/EA.

Buchlin, J.-M., and Van Koninckxloo, T., 1986, "O.P.E.R.A. II – A Test Facility to Study the Thermohydraulics of Liquid Saturated Self Heated Porous Media," von Karman Institute, TM 41.

Campos, J. M., 1983, "Theoretical and Experimental Investigation of Channeled Boiling in Bottom Heated Particulate Beds," von Karman Institute, PR 1983-05.

Evenhouse, E., and Stubos, A. K., 1984, "An Updated Computer Code Simulating the PAHR Situation," von Karman Institute, SR 1984-09.

Gabor, J. D., Hesson, J.C., Baker, L., and Cassulo, J. C., 1972, "Simulation Experiments on Heat Transfer from Fast Reactor Fuel Debris," *Trans. ANS*, Vol. 15, No. 2, p. 836.

Gladnick, P. G., 1985, "Experimental Investigation of Channeling During Boiling in Liquid Saturated Porous Media," von Karman Institute, SR 1985-24.

Gronager, J. A., Schwarz, M., and Lipinski, R. J., 1981, "PAHR Debris Bed Experiment D-4," NUREG/CR 1809.

Joly, C., and Le Rigoleur, C., 1979, "General and Particular Aspects of the Particulate Bed Behavior in the PAHR Situation for Liquid Metal Fast Breeder Reactors," in: *von Karman Institute LS 1979-04 "Fluid Dynamics of Porous Media in Energy Applications."*

Jones, S. W., Baker, L., Bankoff, S. G., Epstein, M., and Pedersen, D. R., 1982, "A Theory for Prediction of Channel Depth in Boiling Particulate Beds," ASME JOURNAL OF HEAT TRANSFER, Vol. 104, No. 4, pp. 806–807.

Lipinski, R. J., 1982a, "A Model for Boiling and Dryout in Particle Beds," Sandia Labs., SAND 82-0765; NUREG/CR-2646.

Lipinski, R. J., 1982b, "Approximate D10 Predictions," Sandia Labs.

Lipinski, R. J., 1984, "A Coolability Model for Post Accident Nuclear Reactor Debris," *Nuclear Technology*, Vol. 65, pp. 53–66.

Mitchell, G. W., and Ottinger, C. A., 1982, "The D7 Experiment Heat Removal From a Shallow Stratified $UO_2$-Sodium Particle Bed," *Proc. 5th Post Accident Heat Removal Information Exchange Meeting*, Karlsruhe.

Mitchell, G. W., Ottinger, C. A., and Meister, H., 1984, "Coolability of $UO_2$ with Downward Heat Removal – the D10 Experiment," *Proc. 6th Information Exchange Meeting on Debris Coolability*, University of California, Los Angeles.

Naik, A. S., and Dhir, V. K., 1982, "Force Flow Evaporative Cooling of a Volumetrically Heated Porous Layer," *Int. Journal of Heat and Mass Transfer*, Vol. 25, No. 4, pp. 541–552.

Ottinger, C. A., Kelly, J.E., and Lipinski, R. J., 1982, "Preliminary Report of the D9 Debris Bed Experiment."

Reed, A. W., 1982, "The Effect of Channeling on the Dryout of Heated Particle Beds Immersed in a Liquid Pool," Ph.D. Thesis, M.I.T., Cambridge, MA.

Reed, A. W., 1986, "A Mechanistic Explanation of Channels in Debris Beds," ASME JOURNAL OF HEAT TRANSFER, Vol. 108, No. 1, pp. 125–131.

Schwalm, D., and Nijsing, R., 1982, "Influence of Subcooing on Dryout Inception in Sodium-Saturated Fuel Particle Beds With Top Cooling and Adiabatic Bottom," *Nuclear Engineering & Des.*, Vol. 70, pp. 201–208.

Schwalm, D., 1985, "Some Remarks on Channeling in Particle Beds," Ispra Joint Research Center; EUR 10.005 EN.

Stevens, G. F., and Trenberth, R., 1982, "Experimental Studies of Boiling Heat Transfer and Dryout in Heat Generating Particulate Beds in Water at 1 Bar," AEEW-R 1545.

Stubos, A. K., 1985, "Experimental and Theoretical Investigation of Boiling in Liquid Saturated Porous Media," von Karman Institute, PR 1985-25.


## APPENDIX

CHANNEL is a one-dimensional code simulating the steady-state thermohydraulic behavior of a liquid-saturated, self-heated, particulate bed. It identifies boiling, condensation, subcooled and dryout regimes in the bed and calculates the temperature, saturation, and vapor velocity profiles along it. The channel formation model already presented has been implemented into the code. The equations applying to the packed part of the bed in one dimension are:

**Conduction and Dryout Zones:** These are modeled through an effective thermal conductivity coefficient $K_e$, whose values differ from zone to zone

$$d\left(K_e \frac{dT}{dz}\right) = -Q_v \tag{A-1}$$

where $T$ is the temperature and $Q_v$ the volumetric power deposition in the bed.

**Boiling Zone:** The local mass balance gives

$$\rho_l V_l + \rho_v V_v = 0 \tag{A-2}$$

and the equation of motion for each phase

$$\frac{dP_l}{dz} = -\frac{\mu_l V_l}{\kappa \cdot \kappa_l} - \frac{\rho_l V_l^2}{\eta \cdot \eta_l} - \rho_l \cdot g \tag{A3}$$

$$\frac{dP_v}{dz} = -\frac{\mu_v V_v}{\kappa \cdot \kappa_v} - \frac{\rho_v V_v^2}{\eta \cdot \eta_v} - \rho_v \cdot g \tag{A4}$$

where the relative permeabilities and passabilities are expressed as follows (Lipinski, 1982):

$$\kappa_l = \eta_l = s^3, \qquad \kappa_v = \eta_v = (1-s)^3 \tag{A5}$$

The energy equation for this zone can be written

$$\rho_v L_f \frac{dV_v}{dz} = Q_v \tag{A-6}$$

where $L_f$ is the latent heat of the liquid. Temperature is assumed constant and equal to the boiling temperature $T_b$

$$T = T_b \tag{A7}$$

Finally, the definition of capillary pressure gives

$$P_c = P_v - P_l = \sigma \cdot \cos\alpha \cdot \sqrt{\epsilon/\kappa} \cdot J(s) \tag{A8}$$

where the Leverett function is expressed as

$$J(s) = \frac{(s^{-1}-1)^{0.175}}{\sqrt{5}} \tag{A9}$$

**Condensation Zone**: The energy equation is now changed compared to the boiling zone

$$Q_v + \frac{d}{dz}\left(K_e \frac{dT}{dz}\right) + \rho_l C_{p_l} \frac{d}{dz}\left(V_l\,(T_b - T)\right) = L_f \cdot \rho_v \frac{dV_v}{dz} \tag{A10}$$

where $C_p$ is the specific heat. The assumption is made that the rate of condensation is proportional to the degree of subcooling

$$A(T_b - T) + L_f \cdot \rho_v \frac{dV_v}{dz} = 0 \tag{A11}$$

where $A$ is a condensation coefficient.

An iterative boundary tracking procedure is adopted to solve the equations along with their interfacing and boundary conditions. The final output consists of the temperature, saturation, and vapor velocity profiles along the bed.

# A Parametric Study of Boiling Heat Transfer in a Horizontal Tube Bundle

**M. K. Jensen**
Department of Mechanical Engineering, Aeronautical Engineering and Mechanics, Rensselaer Polytechnic Institute, Troy, NY 12180-3590

**J.-T. Hsu**
Department of Mechanical Engineering, University of Wisconsin—Milwaukee, Milwaukee, WI 53201

*Boiling heat transfer outside of a section of a uniformly heated horizontal tube bundle in an upward crossflow was investigated using R-113 as the working fluid. The inline tube bundle had five columns and 27 rows with a pitch-to-diameter ratio of 1.3. Heat transfer coefficients obtained from the 14 instrumented tubes are reported for a range of fluid and flow conditions; slightly subcooled liquid inlet conditions were used. At most heat fluxes there was no significant variation in the local heat transfer coefficients throughout the tube bundle. However, at low heat fluxes and mass velocities, the heat transfer coefficient increased at positions higher in the tube bundle. As pressure and mass velocity increased so did the heat transfer coefficients. For the local heat transfer coefficient, a Chen-type correlation is compared to the data; the data tend to be overpredicted by about 20 percent. Reasons for the overprediction are suggested.*

## Introduction

Shellside boiling in horizontal tube heat exchangers is used extensively in the chemical process industries. In multitube kettle reboilers, once-through crossflow boilers, flooded evaporators, etc., the gross, *overall* effects of boiling on the shellside are established well enough that heat exchangers have been designed to perform adequately for a given set of fluid conditions and geometries. However, research interest has been growing to determine *local* (i.e., tube position within the tube bundle) heat transfer coefficients so that the heat transfer processes that are occurring throughout the tube bundle can be better understood and modeled and, thus, more efficient heat exchanger designs can be developed.

Early research on heat transfer coefficients in large, multitube bundles was performed by Palen and co-workers (1962, 1963, 1972). Only tube-bundle average heat transfer coefficients were obtained, but those coefficients were greater than those for a single tube in saturated pool boiling. Other early investigations on smaller tube bundles in pool boiling, e.g., Mednikova (1973), Meyers and Katz (1953), Nakajima (1979), Nakajima and Morimoto (1969), Nakajima and Shiozawa (1975), Robinson and Katz (1951), and Wallner (1971), obtained local heat transfer coefficients on a few of the tubes in their bundles. The results indicated that the induced circulation and turbulence around the upper tubes in the bundles caused increased heat transfer coefficients. Unfortunately, neither the mass velocity nor the quality were known in these tests, which makes the results difficult to use.

More recently, the local conditions throughout a large multitube bundle have been investigated (Leong and Cornwell, 1979). Local heat transfer coefficients have been determined in a bundle for one pitch-to-diameter ratio by Cornwell and co-workers (1979, 1980, 1982). A 241-tube bundle ($p/d = /1.33$) operating in a natural circulation mode was tested using R-113. Fluid recirculation in the shell of the similated slice of a reboiler was caused by rising vapor. Heat transfer coefficients increased with increasing height in the bundle. In a similar experiment (Grant et al., 1983) on a small steam-heated kettle reboiler (177 tubes; $p/d = 1.33$) using R-12, nucleate boiling appeared to be the primary heat transfer mechanism. The heat transfer coefficient for the entire bundle (for the region where nucleate boiling dominates) was expressed as a function of the heat flux raised to a power. It is interesting to note that whereas Leong and Cornwell (1979) obtained a variation up to a factor of about eight in the heat transfer coefficients between tubes at the bottom of the bundle compared to tubes at the top of the bundle, Grant et al. (1983) found only a small variation (10–20 percent) in their tests. The difference was attributed to the much higher heat fluxes used by Grant et al. (1983) compared to those used by Leong and Cornwell (1979). For none of these tests (Leong and Cornwell, 1979; Cornwell et al., 1980; Cornwell and Schuller, 1982; Grant et al., 1983) were local fluid conditions known. To avoid the problem of not knowing local fluid conditions Polley et al. (1980) tested a 36-tube, six-row bundle ($p/d = 1.24$) using R-113 in forced convection. Two-phase forced flow was found to enhance the heat transfer coefficient compared to pool boiling or to saturated liquid forced convective boiling, particularly at low wall superheats. The enhancement ranged up to a factor of about 2.5. A Chen-type correlation (Chen, 1963) was adapted from in-tube two-phase boiling to model the heat transfer behavior with moderate success. Hwang and Yao (1986) tested a three column, eight-row bundle ($p/d = 1.50$) using R-113 and also modified the Chen correlation to predict the heat transfer coefficients. They predicted the heat transfer coefficients to within ±20 percent.

Various attempts have been made to model either kettle reboilers (Brisbane et al., 1980; Kim, 1975; Fair and Klip, 1983; Palen and Yang, 1983; Whalley and Butterworth, 1983) or once-through submerged boilers (Payvar, 1985). Brisbane et al. (1980), in attempting to develop a prediction method for a kettle reboiler, concluded that a method of calculating the local heat transfer coefficient is essential to understanding the heat transfer behavior in reboilers.

A review of the pertinent literature has indicated that each set of tests on tube bundles has been performed at only one pressure and the quality and mass velocity ranges have been limited. Generally, the results of various investigations have shown a wide variety of trends. It is evident that more research is required to determine the effect of flow conditions on local heat transfer coefficients in tube bundles. Hence, a model of a section of a much larger tube bundle was designed, built, and tested to determine the effect of mass velocity, quality, and pressure on the heat transfer coefficient. Only heat transfer

Contributed by the Heat Transfer Division and presented at the ASME/JSME Thermal Engineering Joint Conference, Honolulu, Hawaii, March 22–27, 1987. Manuscript received by the Heat Transfer Division November 13, 1986. Keywords: Boiling, Heat Exchangers, Multiphase Flows.

results will be discussed in this paper; the pressure drop data have been discussed by Schrage et al. (1988).

## Experimental Apparatus

The tests were run in a closed-flow loop (Fig. 1), which uses R-113 as the working fluid. The liquid flow rate to and the pressure in the test section were controlled by bypassing liquid around the test section and by adjusting valves downstream of the test section. Inlet fluid conditions were set by adjusting either the power to variable-power electric preheaters or the steam flow to a steam-to-R-113 heat exchanger. Upstream of the test section was an expansion/contraction section with flow straighteners to ensure a relatively uniform velocity profile at the first row of tubes in the tube bundle. After passing through the test section, the two-phase mixture flowed into a water-cooled condenser and through a pressure control valve; the liquid R-113 then flowed through one of three calibrated rotameters. A high-accuracy ($\pm 0.69$ kPa) pressure gage was used to measure the test-section pressure. A thermocouple located near the pressure tap was used to measure the fluid temperature. Pressure drops across portions of the test section were measured with inverted, inclined, water-filled manometers. Direct-current power was supplied to the instrumented tubes by a low-ripple (<1 percent) power supply and a-c power was supplied to the noninstrumented tubes by powerstats; current was measured with calibrated shunts. All instrumented tube voltage drops, shunt voltage drops, and thermocouple voltages were measured using a high-accuracy digital voltmeter, which was part of a Hewlett-Packard data acquisition system.

The test section was as shown in Fig. 2. The in-line bundle was composed of five columns and 27 rows of heated tubes in a square array with a pitch-to-diameter ratio of $p/d = 1.3$. Fourteen of the tubes in the center column were instrumented and electrically resistance heated; the evaluation of the heat transfer coefficients was made with data obtained from these tubes. The remaining 121 tubes were heated with cartridge heaters; no heat transfer coefficient measurements were made on these tubes. The two outside columns were placed half in the wall and half in the channel to minimize wall effects on the flow through the channel. These tubes were heated with cartridge heaters. All the tubes were made of 7.94/7.62 mm stainless steel with a length of 82.6 mm. The surface was used in its "as is" condition except that the surface was manually cleaned with fresh R-113 and 400 grit emery cloth before installation into the test section to ensure consistent surface conditions. Pressure taps were placed just before the first row and after the sixth, eleventh, sixteenth, twenty-first, and twenty-seventh rows. The test section was heavily insulated to prevent heat loss.

The instrumented tubes were connected in series; brass bus bars were silver-soldered to each end of the stainless steel tubing. Voltage taps were located on each end of the instrumented tubes so that the power to each individual instrumented tube could be measured; the minor voltage drop between the voltage tap and the start of the heated section was taken into account when calculating test-section power. Thirteen of the tubes were equipped with four copper-constantan thermocouples to measure the inside wall temperature at half the length of the tubes from the channel wall; the remaining one was equipped with eight thermocouples. For both sets of tubes, the thermocouples were evenly spaced around the circumference of the tube and the tubes positioned in the test section such that the angular locations of the thermocouples with respect to the test section were known. The thermocouple beads were held firmly against the tube wall and were electrically insulated from the tube wall with a 0.05-mm-thick piece of Teflon tape.

## Experimental Procedure

Prior to any testing, the R-113 was thoroughly degassed to avoid biasing the data in any way. The flow to and the pressure in the test section were set to predetermined values. The loop preheaters were adjusted to bring the liquid R-113 to within a maximum of 1 K of the saturation temperature at the test section pressure; thus, the flow into the test section was always slightly subcooled. This ensured the accuracy of subsequent calculations of quality throughout the test section when using an energy balance between the electrical power dissipation and the enthalpy gain of the fluid. All qualities were calculated assuming equilibrium conditions. The heat flux on all of the tubes was set by adjusting the various power supplies. For all of the flow tests, a uniform wall heat flux was maintained on all of the tubes in the tube bundle. Before any data were taken, the flow loop was allowed to come to steady state. Outside tube wall temperatures were calculated using the measured inside wall temperatures, the measured power dissipation, and the tube geometry in the one-dimensional steady-state heat conduction equation for thin-wall tubes. Because of the thin walls, low thermal conductivity, and high

## Nomenclature

$A$ = $u_L^*(\rho_L\mu_L)^{1/3}/\sigma$, $(s^2/mkg)^{1/3}$
$B$ = $u_g^*(\rho_g/\rho_L)^{1/2}$, m/s
$C_1$–$C_5$ = coefficients in equation (4)
$d$ = tube diameter, m
$F$ = two-phase Reynolds number factor
$F_1$, $F_2$ = equations in Table 1
$f$ = friction factor
$G$ = mass velocity based on minimum flow area, $kg/m^2s$
$g$ = gravitational constant
$h$ = heat transfer coefficient $W/m^2K$
$i$ = enthalpy, kJ/kg
$k$ = thermal conductivity, W/mK
$m$ = Reynolds number exponent in single-phase heat transfer correlation
$n$ = Reynolds number exponent in Blasius-type friction factor correlation
$N$ = number of data points
Nu = Nusselt number = $hd/k$
$P$ = pressure, kPa
$p$ = tube pitch, m
Pr = Prandtl number = $\mu c_p/k$
$q''$ = heat flux, $W/m^2$
Re = Reynolds number = $Gd/\mu$
$S$ = suppression factor
$T$ = temperature, K
$u_g^*$ = $Gx/\rho_g$
$u_L^*$ = $G(1-x)/\rho_L$
$x$ = quality
$Y_0$ = bubble growth region, equation (5), m
$\mu$ = dynamic viscosity, kg/ms
$\rho$ = density, $kg/m^3$
$\sigma$ = surface tension, N/m
$\phi_L^2$ = liquid-only two-phase friction multiplier
$\chi_{tt}$ = Martinelli parameter

### Subscripts

conv = convective
exp = experimental
$f$ = saturated liquid
fluid = fluid
$g$ = vapor
$L$ = liquid
$NB$ = nucleate boiling
out = outlet
pred = predicted
sat = saturation
$TP$ = two-phase
$w$ = wall

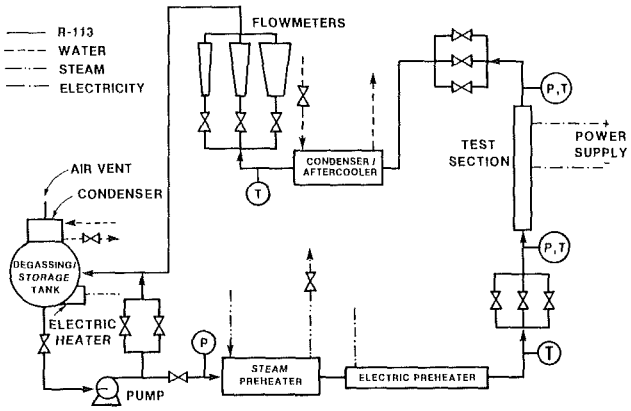


Fig. 1 Schematic of test loop

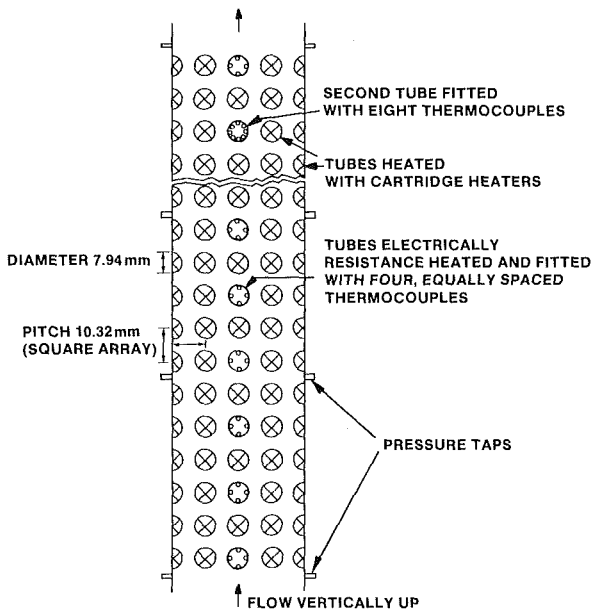


Fig. 2 Schematic of in-line test section ($p/d = 1.30$)

heat transfer coefficients, circumferential conduction was negligible (Baughn, 1978) and a uniform heat flux was assumed. Heat transfer coefficients for each instrumented tube were calculated by averaging the individual heat transfer coefficients obtained with $h = q''/(T_w - T_{\text{fluid}})$ for each thermocouple location, where $T_{\text{fluid}}$ was either the subcooled or saturated fluid temperature; $T_{\text{sat}}$ was evaluated at the local fluid pressure.

One hundred ten flow boiling tests were run with a slightly subcooled inlet. The inlet quality ranged from $-0.025$ to $-0.004$ where quality is $(i - i_f)/i_{fg}$. The nominal ranges of conditions covered by these tests were as follows:

| | |
|---|---|
| Heat flux | 1.6 to 44.1 kW/m$^2$ |
| Local quality | 0–36 percent |
| Pressure | 200, 400, 500 kPa |
| Mass velocity | 50 to 675 kg/m$^2$s |

In addition, single-phase (nonboiling) heat transfer tests were run for Reynolds numbers of 1300 to 20,700; saturated pool boiling tests were run on the eight-thermocouple tubes with no other tubes in the bundle heated. Uncertainties in the experimental data, as estimated through a propagation-of-error analysis, are suggested to be: $P$, $\pm 1.5$ kPa; $G$, $\pm 2$ percent, $x$, $\pm 3$ percent; $q''$, $\pm 1$ percent; $h \pm 11$ percent at the lowest heat flux to $\pm 2$ percent at the highest heat flux. Typical data are shown in the accompanying figures. Details of the experimental apparatus and procedure and complete data tables can be found in Hsu (1987). Note that all boiling heat transfer coefficients shown are local values; no bundle average values are shown.

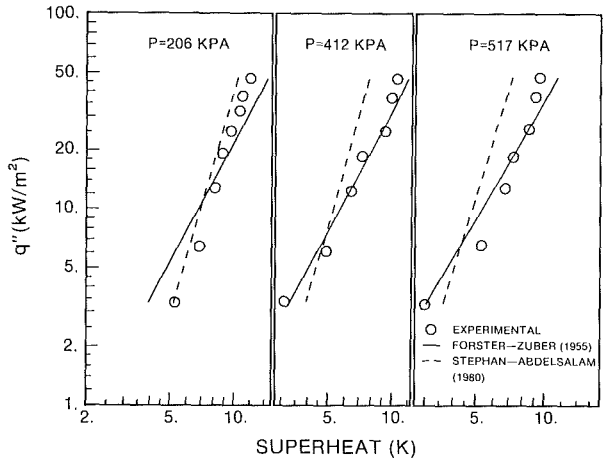


Fig. 3 Comparison of pool boiling behavior between the experimental data and the predictions

## Results and Discussion

Single-phase and saturated pool boiling heat transfer data were obtained to validate the experimental apparatus and procedure before any of the flow boiling tests were run. The single-phase heat transfer tests were run over a Reynolds number range of 1300 to 20,700. All the tubes in the bundle were heated. The heat flux was uniform throughout the bundle for all tests and was set at a level such that $(T_w - T_L)$ was always in the range of 10 K; this was done to ensure accuracy of the data. The results and trends agreed well with standard correlations (e.g., ESDU, 1973). The single-phase heat transfer coefficient was low at the first row of the bundle, increased to a maximum at about the third row, then decreased slightly and remained approximately constant over the rest of the tube bundle. Comparison of the experimental data with predictions using the correlation given in ESDU (1973) showed that the predictions were consistently high and had an average absolute deviation ($\Sigma |h_{\text{pred}}/h_{\text{exp}} - 1|/N$) between the predictions and the experimental data of 9.6 percent. The leading coefficient and the Reynolds number exponent were refit to the present data to obtain a better prediction; the following equation was obtained and

$$\text{Nu}_L = 0.137\, \text{Re}_L^{0.692} \text{Pr}_L^{0.34} \tag{1}$$

had an average absolute deviation of 2.1 percent between the predictions and the experimental data.

Saturated pool boiling data (see Fig. 3) were obtained from the tube with eight thermocouples as it was located inside the tube bundle. The tests were run at three pressures with the two outside columns of tubes heated at a low power level to maintain saturation conditions in the pool. To avoid hysteresis effects, the only data used were those data obtained for decreasing heat fluxes after the highest heat flux was reached. Generally, there was fair agreement between the data and the predictions (based on the heat flux) of two correlations from the literature. The Forster–Zuber (1955) correlation (average absolute deviation of 10.7 percent) had a lower slope than the data while the Stephan–Abdelsalam (1980) correlation (average absolute deviation of 20.9 percent) had a higher slope. A simple power curve fit of the data (one for each pressure level) gave an average absolute deviation between the predicted and experimental data of 4.9 percent.

Typical forced convective boiling data from the tube bundle

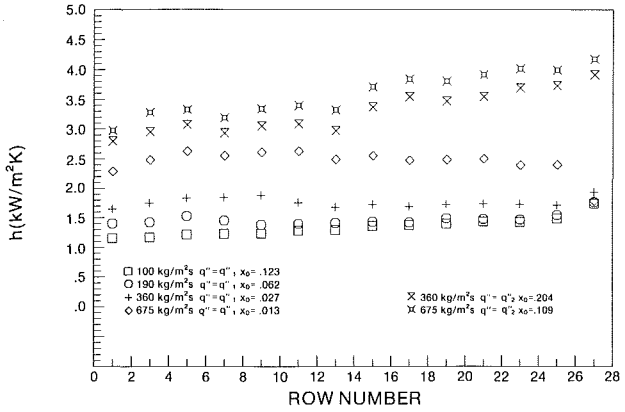


Fig. 4 Effect of mass flux on the heat transfer coefficient at $P = 206$ kPa and at $q''_1 = 6.3$ kW/m$^2$, $q''_2 = 37.8$ kW/m$^2$

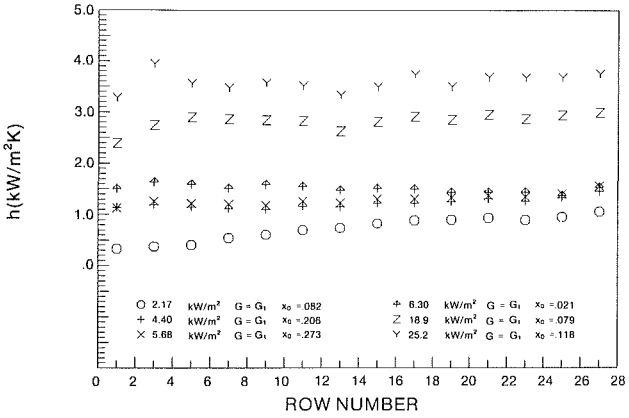


Fig. 6 Effect of heat flux on the heat transfer coefficient at $P = 517$ kPa and at $G_1 \approx 50$ kg/m$^2$, $G_2 = 460$ kg/m$^2$s

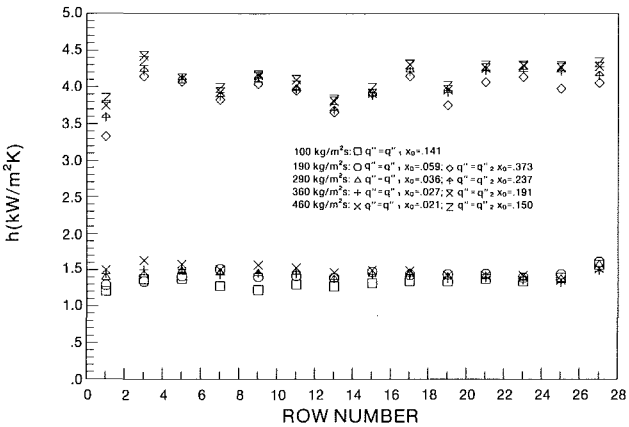


Fig. 5 Effect of mass flux on the heat transfer coefficient at $P = 517$ kPa and at $q''_1 = 6.3$ kW/m$^2$, $q''_2 = 31.5$ kW/m$^2$

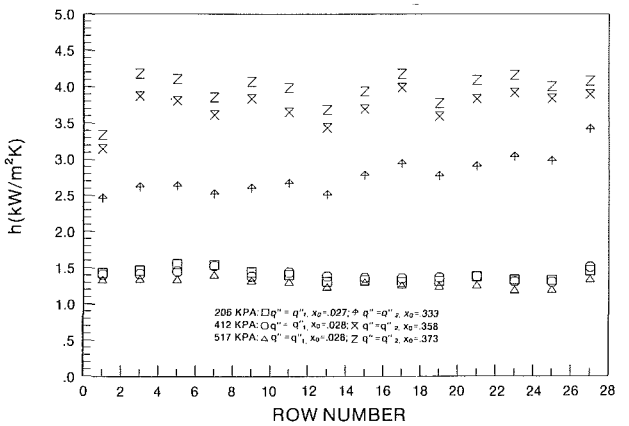


Fig. 7 Effect of pressure on the heat transfer coefficient at $G = 190$ kg/m$^2$s and $q''_1 = 3.15$ kW/m$^2$, $q''_2 = 31.5$ kW/m$^2$

are shown in Figs. 4–7. For any particular test run there was some scatter in the data. For example, on Fig. 5 the heat transfer coefficient is not a smoothly increasing curve; this is a result of usual experimental scatter in boiling experiments and tends to be more pronounced at the higher heat fluxes. (Row No. 1 was at the bottom of the tube bundle.) The trends in the data were more similar to the results of Grant et al. (1983) or Polley et al. (1980) than those of Leong and Cornwell (1979): The increase in the heat transfer coefficient from the bottom to the top of the bundle usually was small—in the order of 5–25 percent; only at low mass velocities and heat fluxes did the increase in the heat transfer coefficient at the top of the bundle approach a factor of two or three greater than that at the bottom of the bundle.

As shown in Fig. 4, the heat transfer coefficient is relatively constant across the tube bundle for the given flow conditions at the low heat flux. The effect of the mass velocity is to increase the heat transfer coefficient by a factor up to about 2.4. As the heat flux increases, changes in the mass velocity have much less effect. We can speculate that this behavior indicates a tradeoff between convective effects and nucleation effects. At the higher heat flux nucleation effects apparently dominate, thus causing a much smaller spread in the data than at the lower heat flux, even though there is a large change in mass velocity in both cases. At the higher heat flux can also be seen the minor effect quality has on the heat transfer coefficient. At $G = 290$ kg/m$^2$s and $q'' = 37.8$ kW/m$^2$, between Row 1 and Row 27, the quality increases to 28 percent, but the heat transfer coefficient increases by only 40 percent. Figure 5, which is similar to Fig. 4 but is at a higher pressure, shows that the convective effects are less important at low and high heat fluxes and that nucleation effects seemingly are dominant. Again, the effect of changing quality on the heat transfer coefficient was minor.

The effect of heat flux on the heat transfer coefficient is shown in Fig. 6. For both low and high mass velocities the heat transfer coefficient increases significantly with increasing heat flux. At the lower mass velocity and heat fluxes is noted an apparent shift from convective effects being important to nucleation effects becoming dominant. At the lower two heat fluxes, the heat transfer coefficient increases by about a factor of three from the bottom to the top of the bundle. It would appear that the convective effects due to increased quality in the higher portions of the bundle play a significant role in the enhancement of the heat transfer coefficient. However, as the heat flux increases, nucleation becomes dominant as evidenced by only modest increases in the heat transfer coefficient between the bottom and top of the bundle, and the convective effects due to increased quality (thus increasing fluid velocity) are insufficient to overcome the nucleation effects. This is further indicated by the higher mass velocity data, which show a relatively constant heat transfer coefficient across the tube bundle.

Figure 7 shows the effect of pressure on the heat transfer coefficient. As can be seen the effect of pressure becomes important at the higher heat fluxes. The trend in the higher heat flux data is the same as with pool boiling data; the heat transfer coefficient increases with increasing pressure. However, at the lower heat fluxes, the data act in a peculiar manner. For all of the data, at the lowest heat fluxes the lower pressure heat transfer coefficients were larger than the higher pressure heat transfer coefficients. As the heat flux increased,

the data reversed positions and the usual behavior was observed. Wege and Jensen (1984) noted this same phenomenon when studying a single horizontal tube in both a saturated liquid and a two-phase crossflow. They suggested that at low heat fluxes for a fixed mass velocity there appeared to be a tradeoff between an increase in the heat transfer coefficient due to increasing pressure and a decrease in the heat transfer coefficient due to the decreased flow velocity caused by the increased fluid density that accompanies the increase in pressure. Apparently a similar tradeoff is occurring in the tube bundle.

Three factors could be responsible for the qualitative differences between the present data and the data of Leong and Cornwell (1979), which were obtained in a simulated kettle reboiler. Their data showed up to a factor of eight increase in the heat transfer coefficient between the bottom and top tube rows. First, the bottom center tubes were in an area of the bundle where the flow is very restricted. Hence, the boiling behavior would be more similar to a pool boiling situation rather than one in which there is a strong flow across the bundle such as in the present experiment. Second, because of inflow from the sides, the mass velocity past the tubes in the upper center column could be increasing. As shown in this study, mass velocity can have a strong effect on the heat transfer coefficient. Third, there could be an outflow from the center column such that the remaining two-phase flow has a relatively high quality, the liquid film on the tubes is very thin, and the heat transfer behavior is similar to a thin-film evaporator with its very high heat transfer coefficients. Because the local mass velocity and quality are unknown throughout the tube bundle in Leong and Cornwell (1979), no speculation as to the effect of quality can be made.

As an initial attempt to predict the local forced convective boiling heat transfer coefficients, a Chen-type correlation was used (equation (2)):

$$h_{TP} = Fh_{conv} + Sh_{NB} \tag{2}$$

Chen (1963) showed that the two-phase Reynolds number factor $F$ could be described with a two-phase friction multiplier through the use of a momentum analogy. Using this analogy for the present case of flow through a tube bundle, the following expression for $F$ can be developed:

$$F = (\phi_L^2)^{m/(2-n)} \tag{3}$$

where $m$ is the Reynolds number exponent in the single-phase convective heat transfer correlation (equation (1)), $n$ is the Reynolds number exponent in the single-phase friction factor in a Blasius-type correlation for the tube bundle, and $\phi_L^2$ is the liquid-only two-phase friction multiplier. For this tube bundle with $f = C\mathrm{Re}^{-n}$, $n = 0.674$ for $2000 < \mathrm{Re} < 7000$ and $n = 0.191$ for $7000 < \mathrm{Re} < 20{,}000$.

From a study by Schrage et al. (1988), the void fraction and two-phase friction multiplier have been developed for this test section; in the prediction of the total pressure drop from the present tests, the average absolute deviation between the predictions and the experimental data was 9.8 percent. Hence, the Schrage et al. two-phase friction multiplier can be used with confidence in equation (3). The liquid-only two-phase friction multiplier was

$$\phi_L^2 = 1 + C/\chi_{tt} + C_5/\chi_{tt}^2$$
$$C = C_1 Fr^{C_2} \ln\chi_{tt} + C_3 Fr^{C_4} \tag{4}$$

where $\chi_{tt} = (((1-x)/x)^{1.8}\,(\rho_g/\rho_L)\,(\mu_L/\mu_g)^{0.2})^{0.5}$. The values of $C_1$ through $C_5$ are given in Table 1 and depend on the flow pattern.

The single-phase heat transfer coefficient $h_{conv}$ was calculated with equation (1). The Reynolds number was evaluated as if the liquid was flowing alone in the bundle, the mass velocity was based on the minimum flow area, and the characteristic length was the tube diameter.

**Table 1 Coefficients in two-phase friction multiplier correlation (equation (4))**

| Flow pattern | Spray | Slug | Bubble |
|---|---|---|---|
| $C_1$ | 0.253 | 2.18 | 0.036 |
| $C_2$ | −1.50 | −0.643 | 1.51 |
| $C_3$ | 12.4 | 11.6 | 7.79 |
| $C_4$ | 0.207 | 0.233 | −0.057 |
| $C_5$ | 0.205 | 1.09 | 0.774 |

if $B \geq F_1$ — Spray
if $B < F_1$ and $B < F_2$ — Slug
if $B < F_1$ and $B \geq F_2$ — Bubble

where $F_1 = 0.678A^{0.354}$
$F_2 = 1.86A^{-1.93}$
$A = u_L^*(\rho_L/\mu_L)^{1/3}/\sigma$, s²/m kg$^{1/3}$
$B = u_L^*(\rho_g/\rho_L)^{1/2}$, m/s

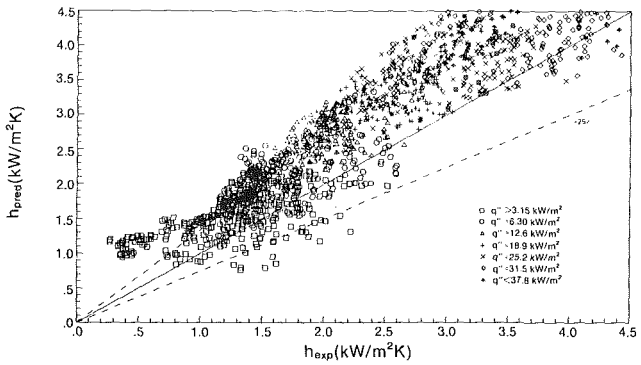


**Fig. 8 Comparison of the present local data to the local predictions using equations (1)-(5)**

The suppression factor $S$ was evaluated with an expression developed by Bennett et al. (1980) for downflow in a tube bundle during thin film evaporation

$$S = (k_L/Fh_{conv}Y_0)(1 - \exp(-Fh_{conv}Y_0/k_L)) \tag{5}$$

where $Y_0 = 0.041\ (\sigma/g(\rho_L - \rho_g)^{0.5}$. The effect of the bundle geometry on $S$ is taken into account through the use of $h_{conv}$.

The nucleate pool boiling heat transfer coefficient was evaluated through the use of a simple power curve fit ($h_{NB} = Aq''^B$) of the pool boiling data taken with the present apparatus. Each pressure was fit individually. It was felt that this procedure was more representative of this test section's characteristics than trying to use either the Forster-Zuber correlation or the Stephan-Abdelsalam correlation.

In all, 1540 data points from individual tubes covering a wide range of operating conditions were compared to the local predictions obtained with equation (2). Using the Schrage et al. (1988) model for $\phi_L^2$ the local heat transfer coefficients were predicted 23.1 percent high on the average. The scatter around this average was ±15.9 percent. A scatter plot of the data is shown in Fig. 8. Generally, the predictions were better at the higher heat fluxes. It should be noted that the range of the Martinelli parameter for this experiment was generally from 0.85 to 100 (a few data had higher and lower values). There are other two-phase friction multipliers in the literature (e.g., Ishihara et al., 1980; Chisholm, 1983), but those did not predict the present pressure drop data well. Hwang and Yao (1986) have developed a similar prediction scheme for the heat transfer coefficient and used an estimated $F$ factor, based on a suggestion by Polley et al. (1980), for use in a modified Chen correlation. Using information from these three studies, the present heat transfer coefficients were again predicted. All of the predictions were high, with results similar to those obtained with the Schrage et al. (1988) two-phase friction multiplier.

Hwang and Yao (1986) concluded that a Chen-type correlation can be used to obtain reasonable results for predictions of the two-phase heat transfer coefficient. However, even though their predictions generally were within $\pm 20$ percent of their data, there is no assurance that their predictions are an accurate test of the general applicability of a modified Chen correlation for use in tube bundles. This is because of their use of an $F$ factor that was not developed specifically for their test-section geometry. The present predictions used an $F$ factor developed specifically for the present geometry and were high. We conclude that while the basic form of the Chen-type correlation is applicable to crossflow in tube bundles, the method of determining the $F$ and $S$ factors requires more work; applying Chen's approach exactly as he did for in-tube flow does not work for crossflow.

The slightly different conclusions drawn by Hwang and Yao (1986) and the present study may be a result of the different geometries used. The present tube bundle had a $p/d = 1.30$; Hwang and Yao used $p/d = 1.5$. With smaller $p/d$ ratios, less of the tube circumference will be swept by the two-phase flow. For many flow conditions in the present experiments, the heat transfer coefficients at the two sides were 10–15 percent higher than the tube average heat transfer coefficient; the bottom of the tube had the next highest heat transfer coefficients; and the top had the lowest heat transfer coefficient. This distribution is consistent with those locations that are swept most vigorously with flowing fluid: The sides are exposed to the forced convective flow and the bottom is swept by vapor generated at the next lower tube. The Chen-type correlations are based on the assumption that the whole heated surface is swept by the flow. This is clearly not the case in tube bundles. Part of the tube is shielded from the flow. As $p/d$ increases more of the tube surface should be swept, but on the downstream side there will (probably) always be a relatively unswept area. Hence, it appears that modifying the Chen correlation as was done in this paper and in Hwang and Yao (1986) is insufficient to predict the heat transfer coefficient accurately. Account must be taken of the areas that are and are not swept by the flow.

## Conclusions

An experimental investigation has been performed to evaluate the effect of mass velocity, heat flux, quality, and pressure level on the boiling heat transfer coefficient in a tube bundle. Except at low heat fluxes and mass velocities, there was only a modest increase in the heat transfer coefficient from the bottom tube row to the top tube row. Mass velocity and heat flux had the strongest influence on the heat transfer coefficient while the effect of quality generally was minor. As in pool boiling, the heat transfer coefficient increased with pressure. It was concluded that a Chen-type correlation is applicable to crossflow in tube bundles but that better methods of evaluating the $F$ and $S$ factors are required.

## Acknowledgments

This research is based on work supported by the National Science Foundation under Grant No. MEA-8319596.

## References

Baughn, J. W., 1978, "Effect of Circumferential Wall Heat Conduction on Boundary Conditions for Heat Transfer in Circular Tubes, ASME JOURNAL OF HEAT TRANSFER, Vol. 100, pp. 537–539.

Bennett, D. L., Davis, M. W., and Hertzler, B. L., 1980, "The Suppression of Saturated Nucleate Boiling by Forced Convective Flow," *AIChE Symposium Series No. 199*, Vol. 26, pp. 91–103.

Brisbane, T. W. C., Grant, I. D. R., and Whalley, P. B., 1980, "A Prediction Method for Kettle Reboiler Performance," ASME Paper No. 80-HT-42.

Chen, J., 1966, "A Correlation for Boiling Heat Transfer to Saturated Fluids," *Industrial and Engineering Chemistry, Process Design and Development*, Vol. 5, No. 3, pp. 322–329.

Chisholm, D., 1983, *Two-Phase Flow in Pipelines and Heat Exchangers*, George Godwin, London–New York.

Cornwell, K., Duffin, N. W., and Schuller, R. B., 1980, "An Experimental Study of the Effects of Fluid Flow on Boiling Within a Kettle Reboiler Tube Bundle," ASME Paper No. 80-HT-45.

Cornwell, K., and Leong, L. S., 1979, "On the Analysis of Low Quality Flow Boiling," *International Journal of Heat and Fluid Flow*, Vol. 1, No. 2, pp. 63–69.

Cornwell, K., and Schuller, R. B., 1982, "A Study of Boiling Outside a Tube Bundle Using High Speed Photography," *International Journal of Heat and Mass Transfer*, Vol. 25, pp. 683–690.

ESDU, 1973, "Convective Heat Transfer During Crossflow of Fluids Over Plain Tube Banks," Item No. 73031, Engineering Sciences Data Unit, London.

Fair, J. R., and Klip, A., 1983, "Thermal Design of Horizontal Reboilers," *Chemical Engineering Progress*, Vol. 79, No. 8, pp. 86–95.

Forster, H. K., and Zuber, N., 1955, "Dynamics of Vapor Bubbles and Boiling Heat Transfer," *AIChE Journal*, Vol. 1, pp. 531–535.

Grant, I. D. R., Cotchin, C. D., and Henry, J. A. R., 1983, "Tests on a Small Kettle Reboiler," *Heat Exchangers for Two-Phase Applications*, ASME HTD-Vol. 27, New York, pp. 41–45.

Hsu, J.-T., 1987, "A Parametric Study of Boiling Heat Transfer in a Horizontal Tube Bundle," Ph.D. Dissertation, University of Wisconsin—Milwaukee, Milwaukee, WI.

Hwang, T. H., and Yao, S. C., 1986, "Forced Connective Boiling in Horizontal Tube Bundles," *International Journal of Heat and Mass Transfer*, Vol. 29, pp. 785–795.

Ishihara, K., Palen, J. W., and Taborek, J., 1980, "Critical Review of Correlations for Predicting Two-Phase Flow Pressure Drop Across Tube Banks," *Heat Transfer Engineering*, Vol. 1, pp. 23–32.

Kim, R. H., 1975, "Computer-Aided Design Analysis and Selection of Heat Exchanger With Phase-Changing Media," ASME Paper No. 75-WA/PID-5.

Leong, L. S., and Cornwell, K., 1979, "Heat Transfer Coefficients in a Reboiler Tube Bundle," *The Chemical Engineer*, No. 343, pp. 219–221.

Mednikova, N. M., 1973, "Concerning the Boiling of Freon-22 and 502 on a Tube Bundle at Low Temperatures," *Heat Transfer—Soviet Research*, Vol. 6, No. 2, pp. 30–37.

Myers, J. E., and Katz, D. L., 1953, "Boiling Coefficients Outside Horizontal Tubes," *Chemical Engineering Progress Symposium Series No. 5*, Vol. 49, pp. 107–114.

Nakajima, K. I., 1979, "Boiling Heat Transfer Outside Horizontal Multitube Bundles," *Heat Transfer—Japanese Research*, Vol. 7, No. 2, pp. 1–24.

Nakajima, K. I., and Morimoto, K., 1969, "Boiling Heat Transfer on Outside Wall of Horizontal Tube Bundles for Freon 11 and 12," *Refrigeration* [in Japanese], Vol. 44, No. 495, pp. 3–15.

Nakajima, K. I., and Shiozawa, A., 1975, "An Experimental Study on the Performance of a Flooded Type Evaporator," *Heat Transfer—Japanese Research*, Vol. 4, No. 4, pp. 49–66.

Palen, J. W., and Small, W. M., 1963, "New Way to Design Kettle and Internal Reboilers," *Hydrocarbon Processing*, Vol. 43, No. 11, pp. 199–208.

Palen, J. W., and Taborek, J. J., 1962, "Refinery Kettle Reboilers—Proposed Method for Design and Optimization," *Chemical Engineering Progress*, Vol. 58, No. 7, pp. 37–46.

Palen, J. W., and Yang, C. C., 1983, "Circulation Boiling Model for Analysis of Kettle and Internal Boiler Performance," *Heat Exchangers for Two-Phase Applications*, ASME HTD-Vol. 27, New York, pp. 55–61.

Palen, J. W., Yarden, A., and Taborek, J., 1972, "Characteristics of Boiling Outside Large-Scale Horizontal Multitube Bundles," *AIChE Symposium Series*, Vol. 68, No. 118, pp. 50–61.

Payvar, P., 1985, "Analysis of Performance of Full Bundle Submerged Boilers," in: *Two-Phase Heat Exchanger Symposium*, ASME HTD-Vol. 44, pp. 11–18.

Polley, G. T., Ralston, T., and Grant, I. D. R., 1980, "Forced Crossflow Boiling in an Ideal In-Line Tube Bundle," ASME Paper No. 80-HT-46.

Robinson, D. B., and Katz, D. L., 1951, "Effects of Vapor Agitation on Boiling Coefficients," *Chemical Engineering Progress*, Vol. 47, pp. 317–324.

Schrage, D. S., Hsu, J.-T., and Jensen, M. K., 1988, "Two-Phase Pressure Drop in Vertical Crossflow Across a Horizontal Tube Bundle," *AIChE Journal*, Vol. 34, pp. 107–115.

Stephan, K., and Abdelsalam, M., 1980, "Heat Transfer Correlations for Natural Convection Boiling," *International Journal of Heat and Mass Transfer*, Vol. 23, pp. 73–87.

Wallner, R., 1971, "Boiling Heat Transfer in Flooded Shell and Tube Evaporators," *Proceedings of the 13th International Congress of Refrigeration*, Paper No. 2.19, pp. 185–191.

Whalley, P. B., and Butterworth, D., 1983, "A Simple Method for Calculating the Recirculating Flow in Vertical Thermosyphon and Kettle Reboilers," *Heat Exchangers for Two-Phase Applications*, ASME HTD-Vol. 27, New York, pp. 47–54.

Wege, M. E., and Jensen, M. K., 1984, "Boiling Heat Transfer From a Horizontal Tube in an Upward Flowing Two-Phase Crossflow," ASME JOURNAL OF HEAT TRANSFER, Vol. 106, pp. 849–855.

# Forced Condensation in a Tube With Suction at the Wall for Microgravitational Applications

**A. Faghri**
Professor,
Department of Mechanical Systems Engineering,
Wright State University,
Dayton, OH

**L. C. Chow**
Professor,
Department of Mechanical Engineering,
University of Kentucky,
Lexington, KY

*The condensation of vapor within a tube is examined for a tube wall that has a constant temperature and uniform suction in a microgravitational environment. The motion of the condensate is due to the interfacial shear between the vapor and the liquid as well as the suction at the wall. The decrease in the vapor flow rate due to condensation has been taken into account. The governing boundary layer momentum and energy equations have been solved by approximating the convective and inertial terms. It is concluded that simultaneous suction and vapor shear can effectively drain the condensate to ensure the continuous operation of space condensers.*

## Introduction

Future space missions envision the need for high-performance condensers that can perform at an order of magnitude better than the present technology allows. Stringent requirements on weight, heat transfer, and compactness prevent complex designs. Four methods for removing condensate in a microgravitational environment have been recommended. These are: vapor shear (Cess, 1960; Koh, 1962; Shekriladze and Gomelauri, 1966; Chow and Parish, 1986; Faghri and Chow, 1987), suction through a porous wall (Frankel and Bankoff, 1965), centrifugal force (Sparrow and Gregg, 1959), and capillary force (McEver and Hwangbo, 1983). Both vapor shear and suction through a porous wall reduce the liquid film thickness and thereby increase the heat transfer rate significantly. The mechanics of condensation with vapor shear has been addressed analytically in the past for various geometries (Cess, 1960; Koh, 1962; Shekriladze and Gomelauri, 1966; Chow and Parish, 1986; Faghri and Chow, 1987; Dobran and Thorsen, 1980). It has been shown that vapor shear can ensure continuous condensation in the absence of a gravitational force. The removal of the liquid film in a condensation process by suction through a porous tube has also been investigated by Frankel and Bankoff (1965) for vapor flowing outside of a horizontal tube.

It is essential to have very effective condensers for space applications. It is, therefore, logical to consider the potential of using the combination of vapor shear and suction at the wall for the removal of the condensate. The purpose of the present paper is to investigate laminar film condensation inside a tube when no body force is present, the curvature of the film is neglected, and the motion of the liquid film results from the sweeping effect of the vapor and the suction at the wall of the tube.

One expects to use an annular configuration to overcome the difficulty associated with providing for the flow of condensate through a porous wall, while at the same time providing a conduction path other than the condensate removal system, whereby heat can be transferred to the coolant. In the system shown in Fig. 1, steam flows through a porous pipe and cooling water flows through the annular region between a solid outer pipe and the porous inner pipe. The steam condenses onto the inner pipe because the cooling water keeps the temperature of the inner pipe lower than the steam. The condensate is driven through the porous pipe by a pressure difference between the steam and the coolant. The condensate mixes with the cooling water in the jacket and is swept away to a heat exchanger, where it is recycled to pass through the annulus again.

The Nusselt analysis for laminar film condensation is extended for flow inside of a tube with a constant-temperature porous wall. The decrease in the shear stress due to condensation is considered. A numerical solution is derived and the results given are the film thickness and the Reynolds number of the vapor in terms of Reynolds numbers for radial suction at the wall. By changing the radial Reynolds number at the wall or by alternating the properties of the fluid, the limiting situations were attained in the prediction of the film thickness and the vapor Reynolds number. These analyses neglect the effect of ripples at the interface, about which there is no information for a microgravitational environment. This may, however, be an important factor (Faghri and Seban, 1985). The analysis, nevertheless, gives an insight into the physical phenomenon and illustrates the effects of various parameters that are considered.

## Analysis

The purpose of this analysis is to investigate the effect of suction on the condensation of a vapor flowing inside a tube in a microgravitational environment. If the properties of the fluid are assumed to be constant and the curvature of the tube is neglected by assuming the liquid layer is thin relative to the radius of the pipe, the nondimensional momentum and energy equations for invariant axial temperature and $v = v_w$ and $u\,\partial u/\partial x << v_w\,\partial u/\partial y$ within the thin boundary layer are

$$\frac{\partial u_L^*}{\partial y^*} = -\mathrm{Pr}_L \frac{\partial^2 u_L^*}{\partial y^{*2}} \tag{1}$$

$$\frac{\partial T^*}{\partial y^*} = -\frac{\partial^2 T^*}{\partial y^{*2}} \tag{2}$$

where $v$ is constant from the continuity equation and the nondimensional variables are specified as

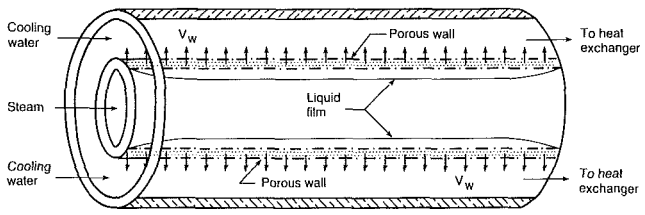


**Fig. 1 Model of the condensation process**

Contributed by the Heat Transfer Division and presented at the ASME Winter Annual Meeting, Boston, Massachusetts, December 13-18, 1987. Manuscript received by the Heat Transfer Division July 20, 1987. Keywords: Condensation, Forced Convection, Microgravity Heat Transfer.

$$y^* = \frac{-yv_w}{\alpha_L} \qquad u^* = \frac{-u_L}{v_w} \qquad T^* = \frac{T - T_w}{T_s - T_w}$$

The inertial effects and the convective effects are approximated in equations (1) and (2), and the results are the asymptotic behavior of the conservation of momentum and energy equations as $\mathrm{Pr}_L \to \infty$.

A momentum balance for the vapor indicates a relation between the pressure drop and the interfacial shear stress. As shown in the paper by Spendel (1984), the pressure drop is insignificant in comparison with the interfacial shear stress for condensation inside a wickless gravity-assisted thermosyphon. The boundary conditions for cocurrent flow, uniform wall temperature, and uniform suction at the wall are: $u^* = T^* = 0$ at the wall, while $T^* = 1$ at the interface. Two additional boundary conditions are necessary. Across the liquid–vapor interface, the interfacial shear stress is specified and an energy balance is made. The general solution of equation (1) by integration over $0 < y^* < \delta^*$, where $\delta^*$ is the dimensionless boundary layer thickness $-v_w\delta/\alpha_L$, is

$$u_L^* = -A\mathrm{Pr}_L\left\{e^{\left[\frac{-y^*}{\mathrm{Pr}_L}\right]} - 1\right\} \tag{3}$$

At the liquid–vapor interface, $y^* = \delta^*$, the dimensionless shear stress $N_2 = \tau_\delta \alpha_L/\mu_L v_w^2$ is specified and therefore the constant in equation (3) is $A = N_2 e^{[\delta^*/\mathrm{Pr}_L]}$. The temperature distribution can also be calculated by integrating equation (2) twice and applying the appropriate boundary specifications

$$T^* = \frac{e^{-y^*} - 1}{e^{-\delta^*} - 1} \tag{4}$$

Under steady-state conditions and by neglecting the vapor temperature gradient, an energy balance at the liquid–vapor interface indicates that the latent heat liberated at the interface must equal the heat conducted away from the interface on the liquid side, that is

$$\rho h_{fg}\left\{v_w - \frac{d}{dx}\int_0^\delta u_L dy\right\} = -K\frac{dT}{dy}\bigg|_{y=\delta} \tag{5}$$

Equation (5) reduces to the following dimensionless form upon letting $N_T = C_p(T_s - T_w)/h_{fg}$ and $x^* = -xv_w/\alpha_L$:

$$\frac{d}{dx^*}\int_0^{\delta^*} u_L^* dy^* = N_T\left[\frac{-e^{-\delta^*}}{e^{-\delta^*} - 1}\right] - 1 \tag{6}$$

The left-hand side of expression (6) can be calculated using equation (3). The resulting expression is

$$\frac{d\phi_1}{dx^*} = \phi_2 \tag{7}$$

where

$$\phi_1 = \frac{N_2\mathrm{Pr}_L^2}{e^{\left[-\frac{\delta^*}{\mathrm{Pr}_L}\right]}}\left\{e^{\left[\frac{-\delta^*}{\mathrm{Pr}_L}\right]} + \frac{\delta^*}{\mathrm{Pr}_L} - 1\right\} \tag{8}$$

and

$$\phi_2 = N_T\left[\frac{e^{-\delta^*}}{1 - e^{-\delta^*}}\right] - 1 \tag{9}$$

The dimensionless thickness of the liquid layer $\delta^*$ is a function of $x^*$ and the integration of equation (7) specifies this variation.

The mass flow rate of the vapor is related to the mass flow rate of the condensate, with the inclusion of the suction term. This conservation of mass yields a relationship between the Reynolds number of the liquid and the Reynolds number of the vapor along the pipe.

$$\mathrm{Re}_{v,e} - \mathrm{Re}_v = \frac{\mu_L}{\mu_v}(\mathrm{Re}_L - \mathrm{Re}_{L,e}) + 4\frac{\mu_L x^*}{\mu_v \mathrm{Pr}_L} \tag{10}$$

where $\mathrm{Re}_v = u_v D_h/\nu_v$ and $\mathrm{Re}_L = 4\int_0^\delta \rho_L u_L dy/\mu_L = 4\phi_1/\mathrm{Pr}_L$.

The above expression also indicates the availability of sufficient vapor for the condensation process.

The shear stress at the interface is due to the friction between the liquid and the vapor plus the momentum gain of the liquid from condensation of the faster-moving vapor onto the slower-moving liquid and is given in dimensionless form $N_2 = \tau_\delta \alpha_L/\mu_L v_w^2$ by the following relation:

$$N_2 = \frac{C_f}{2}\frac{\rho_v}{\rho_L}\frac{1}{\mathrm{Pr}_L}(u_v^* - u_{L,\delta}^*)^2 + \frac{N_T}{\mathrm{Pr}_L}\frac{e^{-\delta^*}}{1 - e^{-\delta^*}}(u_v^* - u_{L,\delta}^*) \tag{11}$$

where $u_v^* = -\mathrm{Re}_v\nu_v/\mathrm{Re}_w\nu_L$ with $\mathrm{Re}_w = D_h v_w/\nu_L$ as the radial Reynolds number at the wall and

$$u_{L,\delta}^* = -N_2 e^{\frac{\delta^*}{\mathrm{Pr}_L}}\mathrm{Pr}\left\{e^{\frac{-\delta^*}{\mathrm{Pr}_L}} - 1\right\}$$

specifies the dimensionless axial velocity of the liquid at the interface. It should be noted that a linear temperature distribution is assumed in the liquid and the effect of the vapor temperature variation is neglected. For laminar flow of the vapor ($\mathrm{Re}_v < 2300$) the frictional coefficient is given by

$$\frac{C_f}{2} = \frac{8}{\mathrm{Re}_v} \tag{12}$$

For horizontal, turbulent flow of the vapor ($\mathrm{Re}_v > 2300$), Henstock and Hanratty (1976) recommend that the friction factor for a smooth-walled tube be multiplied by an additional factor $F$. This factor is based on the average shear stress

## Nomenclature

$A$ = constant used in equation (3)
$C_f$ = friction coefficient = $(2\tau_\delta)(\rho_v u_v^2)$
$C_p$ = specific heat of liquid
$D$ = diameter
$h_x$ = local heat transfer coefficient
$h_{fg}$ = latent heat of vaporization
$K$ = thermal conductivity
$\dot{m}_v$ = mass flow rate of vapor
$N_T$ = Jakob number = $C_p(T_s - T_w)/h_{fg}$
$N_2$ = dimensionless shear stress = $\tau_\delta \alpha_L/\mu_L v_w^2$
Nu = Nusselt number = $h_x D/K$
Pr = Prandtl number = $\nu/\alpha$
$\mathrm{Re}_v$ = vapor Reynolds number = $u_v D_h/\nu_v$
$\mathrm{Re}_L$ = liquid Reynolds number = $4\bar{u}_L\delta/\nu_L$
$\mathrm{Re}_w$ = wall Reynolds number = $D_h v_w/\nu_L$
$T$ = temperature
$u, v$ = velocity components along $x$, $y$
$x, y$ = rectangular coordinates
$\alpha$ = thermal diffusivity
$\delta$ = film thickness
$\mu$ = dynamic viscosity
$\nu$ = kinematic viscosity
$\rho$ = density
$\tau$ = shear stress

**Subscripts**

$e$ = entrance to the pipe
$h$ = hydraulic
$L$ = liquid
$s$ = saturation
$v$ = vapor
$w$ = wall
$\delta$ = at liquid–vapor interface

**Superscripts**

* = nondimensional parameter
\+ = normalized parameter
− = mean value

around the circumference of the annular flow. The recommended correlation is

$$\frac{C_f}{2} = 0.023\ \mathrm{Re}_v^{-0.2}\{1 + 850\ F\} \tag{13}$$

where

$$F = \frac{\Psi \dfrac{\mu_L}{\mu_v}}{\left[\dfrac{\rho_L}{\rho_v}\right]^{0.5} \mathrm{Re}_v^{0.9}}$$

and

$$\Psi = \{(0.707\mathrm{Re}_L^{0.5})^{2.5} + (0.0379\mathrm{Re}_L^{0.9})^{2.5}\}^{0.4}$$

A similar specification has been used in the past for interfacial shear by Seban and Hodgson (1982) and Seban and Faghri (1984) for condensation inside vertical tubes.

The local heat transfer coefficient $h_x$ is given in terms of the Nusselt number by the following expression:

$$\mathrm{Nu} = \frac{h_x D_h}{K} = \{-e^{-\delta^*} + 1\}^{-1} \mathrm{Pr}_L \mathrm{Re}_w \tag{14}$$

With the assumption of $\delta^*/\mathrm{Pr}_L << 1$ and constant $N_2$, the variables $\phi_1$ and $\phi_2$ can be approximated by the following relationships:

$$\phi_1 = \frac{N_2 \delta^{*2}}{2} \tag{15}$$

and

$$\phi_2 = \frac{N_T}{\delta^*} - 1 \tag{16}$$

Substitution of equations (15) and (16) into equation (7) yields

$$\delta^{*2}\frac{d\delta^*}{dx^*} + \frac{\delta^*}{N_2} = \frac{N_T}{N_2} \tag{17}$$

The solution of equation (17) noting that $\delta^* = 0$ at $x^* = 0$ gives

$$x^* = -\frac{1}{2}N_2\delta^{*2} - N_2 N_T \delta^* + N_2 N_T^2 \ln\left|\frac{N_T}{N_T - \delta^*}\right| \tag{18}$$

The model approximating the analytical solution of equation (18) can be considered as condensation along a horizontal porous plate of infinite width and length such that vapor flows along the plate with the coefficient of friction being independent of length. The above problem is governed by the following parameters: $N_T$, $\mathrm{Pr}_L$, $\mu_L/\mu_v$, $\rho_L/\rho_v$, $\mathrm{Re}_w$, $\mathrm{Re}_{v,e}$.

## Calculations

Choose an initial small $\delta_0^*$ with an initial mass flow rate of vapor at the inlet, which specifies the initial value of $\mathrm{Re}_v = 4\dot{m}_v/\pi D\mu_v$. Obtain a first guess for $N_2$ by using equation (11) and neglecting the shear stress induced by mass transfer. Then solve for $\phi_1$ using equation (8). Solve again for $N_2$ using $\phi_1$ to find $\mathrm{Re}_L$ and $C_f$. Find $\phi_1$ again and continue iterating between $\phi_1$ and $N_2$ until $N_2$ converges to within 0.5 percent of the previous value. Once $\phi_1$ is obtained for the initial step, solve for $x^*$ using equation (18). From this time on the solution is made in the following way:

1. A small increment for $\delta^*$ is selected in order to define the next downstream value of $\delta^*$, which is $\delta_1^*$.
2. Using the last value obtained for $N_2$ solve for $\phi_1$. Using the last value obtained for $x^*$, solve for $\mathrm{Re}_v$ using equation (10). Now find a new value for $N_2$ in order to solve for a new $\phi_1$.
3. With the new $\phi_1$ and the $\phi_1$ for the previous converged value of $x^*$ solve for the increment $\Delta x^*$ using the following equation:

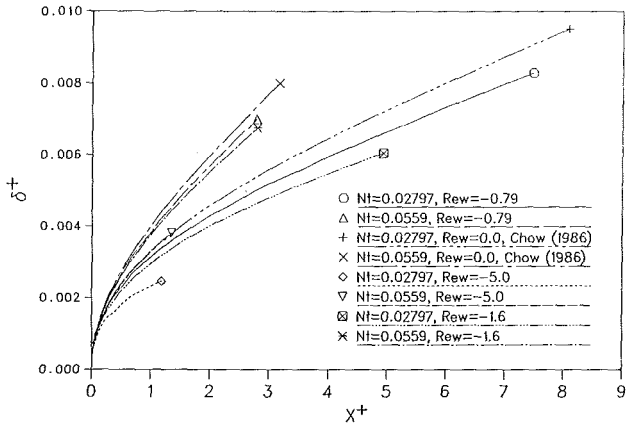


**Fig. 2 The variation of $\delta^+$ along the tube for $\mathrm{Re}_{v,e} = 5000$**

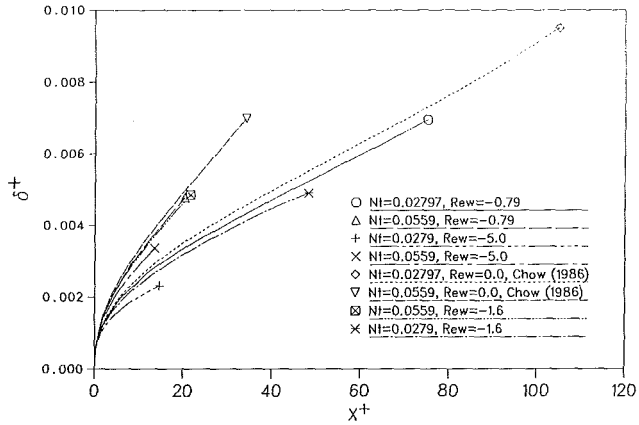


**Fig. 3 The variation of $\delta^+$ along the tube for $\mathrm{Re}_{v,e} = 50{,}000$**

$$\Delta x^* = \frac{\phi_1 \Big|_{\delta_1^*}^{\delta_2^*}}{\phi_2 \left|_{\frac{\delta_1^* + \delta_2^*}{2}}\right.} \tag{19}$$

The new value of $x^*$ along with $\phi_1$ is used to find $\mathrm{Re}_v$. This iteration procedure continues until $\Delta x^*$ is within 0.5 percent of the previous value.

4. Increase $\delta^*$ by another increment as in step (1) and in general the process is repeated until complete condensation or $d\mathrm{Re}_L/dx^* = 0$.

The accuracy of the numerical solution was checked by varying the grid spacing systematically and the results for different grid sizes were compared to the extrapolated results of an infinitesimal grid spacing. A number of different uniform incremental film thickness spacings were chosen to test the convergence of the solution. The final incremental film thickness ($\Delta\delta^*$) was 0.0005. The maximum deviation between this incremental film thickness and of 0.001 was less than 1 percent.

## Results

Calculations were carried out by the above procedure for steam condensing at one atmosphere. Wall temperatures of 85°C and 70°C were considered. The liquid properties were calculated at the film temperature using the average of the wall temperature and the vapor temperature of 100°C. These specifications were chosen to facilitate comparison of the numerical results with those obtained by Chow and Parish (1986) for no suction. The normalized film thickness $\delta^+$ =

$\delta/D = -\delta^*/\mathrm{Re}_w\mathrm{Pr}_L$ is plotted as a function of the normalized axial distance $x^+ = x/D = -x^*/\mathrm{Re}_w\mathrm{Pr}_L$ for $\mathrm{Re}_{v,e} = 5000$ and $\mathrm{Re}_{v,e} = 50{,}000$. These new normalized variables are chosen for the presentation of the results to eliminate the suction velocity from the dimensionless variables and thus reveal the effect of the Reynolds number for suction at the wall on the film thickness along the tube. Furthermore, the Nusselt number expression given by equation (14) is approximated by $1/\delta^+$, provided that $\delta^* << 1$, which is always true for the variation of the parameters in the range of practical interest.

Figures 2 and 3 show the variation of the normalized film thickness with the normalized axial distance for Reynolds numbers of the vapor at the inlet of 5000 and 50,000. The two specifications of properties $N_T = 0.02797$ and $N_T = 0.0559$ correspond to $T_s - T_w = 15°C$ and 30°C, respectively. Three Reynolds numbers for suction at the wall of $-0.79$, $-1.6$, and $-5.0$ were also specified. The numerical results for all of the cases are presented up to a point before the steam is completely condensed because of the inaccuracies of the numerical results that are due to the end effects. Therefore, it should be noted that the final $x^+$ in Figs. 2 and 3 for each case does not present the required length for the complete condensation of the steam. These numerical results show the important effect of suction in the condensation process in a microgravitational environment for a given pipe length (at a given $x^+$) by increasing the overall heat transfer coefficient.

From the plots, increased rates of heat transfer are seen to be possible by the use of suction. This is clearly due to the reduction in the film thickness. Increases are small for small values of the Reynolds number for suction at the wall but become more significant when greater amounts of the condensate are extracted from the tube. This conclusion is in agreement with the results obtained by Frankel and Bankoff (1965) for condensation onto a horizontal tube under normal gravity when the condensate is drained into the tube.

The vapor condenses much faster in pipes with suction than with no suction at the wall for the same Reynolds number of the vapor at the inlet. This translates to a much shorter condenser length if suction is used. The heat transfer coefficient is greatest for small values of $N_T$, which is in agreement with the results previously given for no suction (Chow and Parish, 1986) as well as the classical Nusselt solution. Therefore, higher heat transfer coefficients can be obtained by increasing suction or decreasing $N_T$, which corresponds to a lower $T_s - T_w$ or a higher latent heat of vaporization. It should be emphasized that these increases in heat transfer by suction can be obtained with a suction velocity $v_w$ of the order of $10^{-5}$ m/s. It is not surprising that the film thicknesses for the same axial distance and a given pipe diameter are much smaller for higher Reynolds numbers of the vapor at the inlet because of the increase in the mass flow rate of the vapor.

## Conclusions

The Nusselt analysis of film condensation was extended to condensation of a vapor flowing inside a porous tube with a uniform suction velocity at the wall when no body force is present. Simplified equations were solved numerically including the effect of the variation of the interfacial drag along the tube. It is concluded that the combination of suction and vapor shear can effectively drain the condensate to ensure the continuous operation of condensers for space applications.

## Acknowledgments

The authors are grateful for the support from the Air Force Office of Scientific Research while this research was performed.

## References

Cess, R. D., 1960, "Laminar Film Condensation on a Flat Plate in the Absence of a Body Force," *Z. Angew. Math. Phys.*, Vol. 11, pp. 426–433.

Chow, L. C., and Parish, R. C., 1986, "Condensation Heat Transfer in a Microgravity Environment," AIAA Paper No. 86-0068.

Dobran, F., and Thorsen, R. S., 1980, "Forced Flow Laminar Filmwise Condensation of a Pure Saturated Vapor in a Vertical Tube," *International Journal of Heat and Mass Transfer*, Vol. 23, pp. 161–177.

Faghri, A., and Seban, R. A., 1985, "Heat Transfer in Wavy Liquid Films," *International Journal of Heat and Mass Transfer*, Vol. 28, pp. 506–509.

Faghri, A., and Chow, L. C., 1987, "Annular Condensation Heat Transfer in a Microgravity Environment," AIAA Paper No. 87-1533.

Frankel, N. A., and Bankoff, S. G., 1965, "Laminar Film Condensation on a Porous Horizontal Tube With Uniform Suction Velocity," ASME JOURNAL OF HEAT TRANSFER, Vol. 87, pp. 95–102.

Henstock, W. H., and Hanratty, T. J., 1976, "The Interfacial Drag and the Height of the Wall Layer in Annular Flows," *AIChE Journal*, Vol. 22, pp. 990–1000.

Koh, Y. C. Y., 1962, "Film Condensation in a Forced-Convection Boundary Layer Flow," *International Journal of Heat and Mass Transfer*, Vol. 5, pp. 941–954.

McEver, W. S., and Hwangbo, H., 1983, "Surface Tension Effects in a Space Radiator Condenser With Capillary Liquid Drainage," AIAA Paper No. 83-1525.

Seban, R. A., and Hodgson, J. A., 1982, "Laminar Film Condensation in a Tube With Upward Vapor Flow," *International Journal of Heat and Mass Transfer*, Vol. 25, pp. 1291–1300.

Seban, R. A., and Faghri, A., 1984, "Film Condensation in a Tube With a Closed Top," *International Journal of Heat and Mass Transfer*, Vol. 27, pp. 944–948.

Shekriladze, I. G., and Gomelauri, V. I., 1966, "Theoretical Study of Laminar Condensation of Flowing Vapor," *International Journal of Heat and Mass Transfer*, Vol. 9, pp. 581–591.

Sparrow, E. M., and Gregg, J. L., 1959, "A Theory of Rotating Condensation," ASME JOURNAL OF HEAT TRANSFER, Vol. 81, pp. 113–120.

Spendel, Th., 1984, "Laminar Film Condensation Heat Transfer in a Closed Two-Phase Thermosyphon," *Research and Development of Heat Pipe Technology*, Vol. I, pp. 208–213.

**M. A. Anisimov**
Professor.

**S. B. Kiselev**
Associate Professor.

**I. G. Kostukova**
Researcher.

Physics Department,
Moscow Gubkin Oil and Gas Institute,
Moscow B-296, 117917, USSR

# Asymmetric Scaled Equation of State and Critical Behavior of Binary Mixtures

*An equation of state for binary mixtures, accounting for the asymmetry with respect to the critical isochore in the wide neighborhood of the liquid-gas critical line, has been obtained on the basis of the isomorphic scaled free energy of mixtures and the extended scaled equation of state for pure fluids. Universal behavior of critical binary mixtures is demonstrated. The universal function is used for the description of experimental heat capacity data for a number of binary mixtures.*

## Introduction

In recent years great success has been achieved toward describing critical phenomena in fluids. According to the scaling theory of critical behavior, the physical properties that depend upon temperature and density in the vicinity of a critical point are described by simple power laws (Wilson and Kogut, 1974; Patashinskii and Porkrovskii, 1979). Critical exponents are universal constants for all simple fluids and their mixtures. The theory, using renormalization group methods, made it possible not only to calculate the values of the critical exponents but also to obtain an equation of state. However, the scaled equation of state has been rigorously obtained only for systems with isolated points (two independent thermodynamic variables). Such a point is the liquid-gas critical point of a one-component fluid. In binary solutions, there is a line of liquid-gas critical points. The application of scaling theory to these more complex systems is being solved on the basis of the isomorphism hypothesis (Fisher, 1968; Griffiths and Wheeler, 1970; Anisimov et al., 1971; Leung and Griffiths, 1973). According to this hypothesis, the equation of state, when adding a new thermodynamic variable (a generalized "density"), conserves the universal form if a "field" conjugate to the "density" is fixed. For a binary solution in the vicinity of the liquid-gas critical points, this means that the form of the thermodynamic potential remains the same as for a pure fluid if the chemical potential of the component is fixed.

The main result of such an approach is renormalization of the critical exponents in a binary mixture if the experiment is carried out at a constant concentration. Thus, for example, the isochoric heat capacity of a mixture at the constant concentration $x = N_2/(N_1 + N_2)$ on the critical isochore does not diverge at the critical point, since the renormalization of the critical exponent of the heat capacity takes place. The isomorphism hypothesis and the scaled equation of state basically describe the critical behavior of binary mixtures. However (as recently performed calculations show (Anisimov et al., 1982)) the accuracy and the range of the description, even for one-component fluids, are greatly influenced by the asymmetry of a fluid with respect to the critical isochore. In this paper an equation of state for binary mixtures, taking into account such an asymmetry in the vicinity of the liquid-gas critical points of binary mixtures, is obtained on the basis of the isomorphous equation for mixtures (Anisimov et al., 1982) and an extended scaled equation of state for real fluids (Sengers and Levelt Sengers, 1986; Kiselev, 1986). An explicit form of the universal part of the thermodynamic potential of a binary mixture is obtained. The equations obtained have been used in describing the isochoric heat capacity of a number of binary mixtures in the critical region.

## Scaled Equation of State

The free energy per mole of a binary mixture, as a function of the chemical potential

$$\mu = \mu_2 - \mu_1 = \left(\frac{\partial F}{\partial x}\right)_{T,\rho} \tag{1}$$

($\mu_1$ and $\mu_2$ are the chemical potentials of the components) is

$$F^*(T, \rho, \mu) = F(T, \rho, x) - \mu x(T, \rho, \mu) \tag{2}$$

where $F(T, \rho, x)$ is the free energy of a mixture, which is a function of the concentration. According to the isomorphism hypothesis (Anisimov et al., 1971), $F^*(T, \rho, \mu)$ has the same dependence on temperature and density as the free energy of a one-component fluid. Incidentally, one assumes (Anisimov et al., 1973; Anisimov et al., 1982) that the critical values of temperature, density, pressure, and all the other nonuniversal constants in the free energy $F^*(T, \rho, \mu)$ are analytical functions of the chemical potential, and consequently they may be represented in a series of $\mu$. However, this does not appear to be convenient in practice since when the solution concentration $x$ changes from $x=0$ to $x=1$ the value of the chemical potential $\mu$ varies from $-\infty$ to $+\infty$, which leads to divergence of the series. To avoid these difficulties one should change the variable $\mu$ to a new one, as follows:

$$\tilde{x} = \exp(\mu/RT_0)/[1 + \exp(\mu/RT_0)] \tag{3}$$

where $R$ is the gas constant and $T_0$ is the characteristic temperature of a solution (e.g., critical temperature of a component). It can be seen from the correlation given by equation (3) that when $\mu$ changes from $-\infty$ to $+\infty$, $\tilde{x}$ varies from $\tilde{x}=0$ to $\tilde{x}=1$, similar to the mixture concentration. Incidentally, the isomorphic behavior is determined by the condition $\mu = \text{const}$ as usual. This is equivalent to the condition $\tilde{x} = \text{const}$. Therefore in the free energy equation (2), we put the value $\tilde{x}$ instead of $\mu$ everywhere.

If we assume the scaled form proposed by Kiselev (1986) for the free energy of a pure fluid, the isomorphous energy per mole of a binary solution is

$$F^*(T, \rho, \tilde{x}) = \frac{1}{\rho}\psi(r, \theta, \tilde{x}) + F_0(T, \rho, \tilde{x}) \tag{4}$$

Here the polar variables $r$ and $\theta$ are related to the dimensionless temperature $\tau(\tilde{x}) = [T - T_c(\tilde{x})]/T_c(\tilde{x})$ and density $\Delta\rho(\tilde{x}) = [\rho - \rho_c(\tilde{x})]/\rho_c(\tilde{x})$ by the correlations

$$\tau = r(1 - b^2\theta^2) \tag{5a}$$

$$\Delta\rho = kr^\beta\theta - B_3\tau \tag{5b}$$

Contributed by the Heat Transfer Division for publication in the JOURNAL OF HEAT TRANSFER. Manuscript received by the Heat Transfer Division August 10, 1987. Keywords: Phase-Change Phenomena, Supercritical Fluids, Thermophysical Properties.

The extended scaling function $\psi(r, \theta)$ has the form (Kiselev, 1986; Anisimov et al., 1985)

$$\psi(r, \theta) = \psi_{LM}(r, \theta) + \psi_{NA}(r, \theta) + \psi_{AS}(r, \theta) \tag{6}$$

where the first item can be determined by the Linear Model (*LM*) of the equation of state (see, e.g., Anisimov et al., 1985)

$$\psi_{LM}(r, \theta) = \frac{1}{2}\frac{ak}{b^2} r^{2-\alpha}\left[\frac{2\beta(b^2-1)}{2-\alpha} + \frac{2\beta(2\gamma-1)}{\gamma(1-\gamma)}(1-b^2\theta^2) - \frac{1-2\beta}{\alpha}(1-b^2\theta^2)^2\right] \tag{7a}$$

the second item is related to the scaling nonasymptotic (*NA*) terms

$$\psi_{NA}(r, \theta) = \frac{1}{2}\frac{ck}{b^2}\frac{r^{2-\alpha+\Delta}}{1-\alpha+\Delta}\left[\frac{\gamma-\Delta}{2-\alpha+\Delta} - (1-2\beta)b^2\theta^2\right] \tag{7b}$$

and the third item accounts for the asymmetry (*AS*) of a real fluid with respect to the critical isochore

$$\psi_{AS}(r, \theta) = kr^{2\gamma+3\beta-1}\theta\left\{d + \frac{1}{3}[f-2d(e-\beta)]b^2\theta^2 + \frac{1-2\beta}{5\beta-e}\left[d(e-\beta)(1-2\beta) + \frac{1}{3}[f-2d(e-\beta)](e-3\beta)\right]b^4\theta^4\right\} \tag{7c}$$

Here $\gamma$, $\alpha$, and $\beta$ are the critical exponents of the isomorphous susceptibility $K_{T,\mu}$, heat capacity $C_{v,\mu}$, and the coexistence curve in the isomorphous variables

$$\Delta\rho(\tilde{x}) = \pm B_0|\tau|^{\beta} \pm B_1|\tau|^{\beta+\Delta} + B_2|\tau|^{1-\alpha} + B_3|\tau| \tag{8}$$

where $\Delta$ is Wegner's critical exponent. According to the theory all the critical exponents are universal, in addition: $b^2 = (\gamma-2\beta)/\gamma(1-2\beta)$ and $e = 2\gamma+3\beta-1$ are also universal constants; $k = B_0(b^2-1)^{\beta}$ and the parameters $a$, $c$, $d$, $f$, $B_0$, $B_1$, $B_2$, and $B_3$ are related to the individual properties of a fluid and generally are analytical functions of $x$. The regular part of the free energy $F_0(T, \rho, \tilde{x})$ is an analytical function of temperature, density, and the chemical potential, which at $\tilde{x} = \text{const}$ has the form of the corresponding function for a pure fluid (Anisimov et al., 1985)

$$F_0(T, \rho) = \frac{1}{\rho}[-P_c + f_1\tau + f_2\tau^2] + m_0 + m_1\tau + m_2\tau^2 \tag{9}$$

For a mixture $P_c(\tilde{x})$ is a critical pressure and the parameters $f_1$, $f_2$, $m_0$, $m_1$, and $m_2$ are analytical functions of $\tilde{x}$. The system of equations (4)-(9) contains the immeasurable variable $\tilde{x}$. The real experiment in the vicinity of the gas-liquid critical points is carried out at the fixed concentration $x$ and not at constant $\tilde{x}$. To calculate the actually measured thermodynamic values (at $x = \text{const}$) equations (4)-(9) should be supplemented by the thermodynamic definition of a concentration

$$x = -\left(\frac{\partial F^*}{\partial \mu}\right)_{T,\rho} = -\tilde{x}(1-\tilde{x})\left(\frac{\partial \tilde{F}^*}{\partial \tilde{x}}\right)_{T,\rho} \tag{10}$$

where $\tilde{F}^* = F^*(T, \rho, \tilde{x})/RT_0$ is the dimensionless free energy of a solution. Equation (10), taking account of equations (7) and (9), enables us to perform a transformation from the surface $\tilde{x} = \text{const}$ ($\mu = \text{const}$) to $x = \text{const}$ at every fixed value of density and temperature. Then we can represent all the nonuniversal constants in the form of a series of $\tilde{x}$, demanding $\tilde{x} = x$ not only at $x = 0$ and $x = 1$ also everwhere on the critical line ($T = T_c(x)$, $\rho = \rho_c(x)$). These requirements put the additional restriction on the constants $m_0$ and $m_1$ in the regular part of the free energy given by equation (9).

From equation (10), incorporating equations (4)-(9), we obtain

$$m_0 = RT_0\ln(1-\tilde{x}) \tag{11}$$

$$m_1 = -RT_0\frac{\tilde{T}_c}{\tilde{\rho}_c}\left(\frac{d\tilde{T}_c}{d\tilde{x}}\right)^{-1}\frac{d\tilde{P}_c}{d\tilde{x}} - \frac{f_1}{\tilde{\rho}_c(\tilde{x})} \tag{12}$$

## Nomenclature

$a$ = parameter of Linear Model
$A$ = critical amplitude of the isomorphic isochoric heat capacity $C_{v,\mu}$
$b$ = combination of critical exponents
$B_0, B_1, B_2, B_3$ = nonuniversal parameters of equation of state
$c$ = parameter of Linear Model
$C_{v,x}$ = isochoric heat capacity of a mixture at constant $x$
$d$ = nonuniversal parameter of equation of state
$e$ = combination of critical exponents
$f$ = nonuniversal parameter of equation of state
$f_1, f_2$ = parameters of regular part of free energy
$F$ = Helmholtz free energy per mole
$F^*$ = free energy as a function of $\mu$
$F_0$ = regular part of the free energy
$k$ = parameter of the Linear Model
$m_0, m_1, m_2$ = parameters of the regular part of the free energy
$P$ = pressure
$P(n, m)$ = Pade function
$r$ = variable of the Linear Model of the equation of state
$R$ = gas constant
$T$ = temperature
$w$ = combination of critical constants
$x$ = molar concentration
$y, y_1, y_2$ = combinations of critical exponents
$\alpha, \beta, \gamma, \Delta$ = universal critical exponents
$\theta$ = variable of the Linear Model of the equation of state
$\mu_1$ = chemical potential of a solvent
$\mu_2$ = chemical potential of a second component $\mu = \mu_2 - \mu_1$
$\xi, \tilde{\xi}, \xi_1$ = combinations of critical exponents
$\rho$ = density
$\Phi_S, \Phi_{1S}$ = universal functions of the scaled equation of state for mixtures
$\psi_0, \psi, \psi_1$ = scaled variables of the equation of state for mixtures

**Subscripts**

$c$ = critical parameter of mixture

Here and further the tilde symbol above the letter means dimensionless values:

$$\tilde{\rho}_c = \rho_c(\tilde{x})/\rho_0,\ \tilde{T}_c = T_c(\tilde{x})/T_0,\ \tilde{P}_c = P_c(\tilde{x})/RT_0$$

$\tilde{\rho}_c$, $\tilde{T}_c$, and $\tilde{P}_c$ are the dimensionless critical density, temperature, and pressure, respectively, and $\rho_0$ is the characteristic density (for example, $\rho_0$ may be the critical density of the first component). Equations (11) and (12) imply that $\tilde{x}=x$ along the critical line and the functions $T_c(\tilde{x})$, $P_c(\tilde{x})$, and $\rho_c(\tilde{x})$ coincide with $T_c(x)$, $P_c(x)$, and $\rho_c(x)$. Since dependence of the critical temperature, density, and pressure on concentration is determined by independent experiments, one can consider the functions $T_c = T_c(\tilde{x})$, $\rho_c = \rho_c(\tilde{x})$, and $P_c = P_c(\tilde{x})$ to be known. Furthermore, the parameters $a$, $c$, $d$, $f$, $m_2$, $B_0$, and $B_3$ can be represented in a first approximation as linear functions of $\tilde{x}$:

$$k(\tilde{x}) = k_1(1-\tilde{x}) + k_2\tilde{x}, \text{ etc.} \tag{13}$$

where the indices "1" and "2" are related to the pure first and second components of the mixture. Since the values of all the parameters for pure fluids are known, equations (4)–(13) completely determine the equation of state for a binary mixture in the vicinity of the liquid–gas critical points. Incidentally, equations (4), (9), (10), and (11) may be rewritten in the form

$$x = \tilde{x} - \tilde{x}(1-\tilde{x})\left[\frac{1}{\rho}\left(\frac{\partial\psi}{\partial\tilde{x}}\right)_{T,\rho} + \left(\frac{\partial\tilde{F}_0}{\partial\tilde{x}}\right)_{T,\rho}\right] \tag{14}$$

where $\tilde{F}_0(T, \rho, \tilde{x}) = [F_0(T, \rho, \tilde{x}) - RT_0\ln(1-\tilde{x})](RT)^{-1}$ is the dimensionless regular part of the free energy of a mixture.

Thus we see that a transformation from the chemical potential to the variable $\tilde{x}$, and a special choice of the parameters $m_0$ and $m_1$ in the regular part of the free energy, allows us not only to simplify the equation of state for a solution, in comparison with equation (6), but also to expand its description area to the whole concentration range $0 \le x \le 1$.

## Behavior of Thermodynamic Properties

To know the behavior of the experimentally investigated properties of fluids one should obtain the equation of state in terms of $T$, $\rho$, and $x$. For this purpose let us analyze the asymptotic solution of equation (14) at the critical isochore $\Delta\rho(x)=0$, representing the value $\tilde{x}$ in the form $\tilde{x} = x + \Delta\tilde{x}$. Then, in the case of $z(\tilde{x}) = \tau(\tilde{x})/|\Delta\rho(\tilde{x})|^{1/\beta} \gg 1$, equation (14), incorporating equations (4)–(9) in the linear approximation, takes the form

$$[\tau(\tilde{x})]^{1-\alpha}[1 + [\tau(x)]^{\alpha}\xi y_2] = \tau(x)\xi y_1 \tag{15}$$

Using the condition

$$\tau(\tilde{x}) \ll |\xi y_2|^{-1/\alpha} \tag{16}$$

we obtain

$$\tau(\tilde{x}) = |\tau(x)\xi y_1|^{1/(1-\alpha)} \tag{17}$$

where

$$\xi = \frac{(1-\alpha)T_c^2}{\tilde{A}x(1-x)}\left(\frac{dT_c}{dx}\right)^{-2} \tag{18}$$

$$\tilde{A} = \frac{\tilde{a}k\gamma(\gamma-1)}{2\alpha b^2} \tag{19}$$

$$y_1 = 1 + yx(1-x)\left(\frac{1}{T_c}\frac{dT_c}{dx}\right)^2(\tilde{f}_1 + w) \tag{20}$$

$$y_2 = 1 + 2x(1-x)\left(\frac{1}{T_c}\frac{dT_c}{dx}\right)^2[y(\tilde{f}_1 + w) - (\tilde{m}_2 + \tilde{f}_2)] \tag{21}$$

$$y = \frac{T_c}{\rho_c}\frac{d\rho_c}{dx}\left(\frac{dT_c}{dx}\right)^{-1} \tag{22}$$

$$w = T_c\left(\frac{dT_c}{dx}\right)^{-1}\frac{d\tilde{P}_c}{dx} \tag{23}$$

When $\tau(x) \gg |\xi y_2|^{-1/\alpha}$ the dimensionless temperatures $\tau(\tilde{x})$ and $\tau(x)$ practically coincide

$$\tau(\tilde{x}) = \tau(x)\,|y_1 y_2^{-1}| \simeq \tau(x) \tag{24}$$

Now one can analyze the asymptotic behavior of the first and second derivatives of the free energy $F(T, \rho, x)$ with respect to temperature at the critical isochore of the binary mixture ($z(\tilde{x}) \gg 1$). For this purpose let us extract the terms related to the entropy from equation (1)

$$\left(\frac{\partial F}{\partial T}\right)_{\rho,x} = \left(\frac{\partial F^*}{\partial T}\right)_{\rho,\tilde{x}} = -S(T, \rho, x) \tag{25}$$

hence, taking account of equations (4) and (14), we have

$$\left(\frac{\partial^2 F}{\partial T^2}\right)_{\rho,x} = \frac{1}{\rho}\left(\frac{\partial^2\psi}{\partial T^2}\right)_{\rho,\tilde{x}} + \left(\frac{\partial^2 F_0}{\partial T^2}\right)_{\rho,\tilde{x}} - \frac{\dfrac{\partial^2 F^*}{\partial T\partial\tilde{x}}}{\tilde{x}(1-2\tilde{x})\left(\dfrac{\partial^2 F^*}{\partial\tilde{x}^2}\right)_{T,\rho} + (1-2\tilde{x})\left(\dfrac{\partial F^*}{\partial\tilde{x}}\right)_{T,\rho}} \tag{26}$$

One can show that when $x \neq 1$ and $x \neq 0$ the latter term on the right side of equation (26) is not equal to zero. Therefore at $\tau(x) \ll |\xi y_2|^{-1/\alpha}$, the second derivative of the singular part of the free energy $F_s(T, \rho, x)$ has the asymptotic behavior

$$\left(\frac{\partial^2 F_S}{\partial T^2}\right)_{\rho_{SOC},x} \sim [\tau(x)]^{\alpha/(1-\alpha)} - \text{const} \tag{27}$$

In the case of $x=0$ or $x=1$, and also at the condition

$$\tau(\tilde{x}) \gg |\xi y_2|^{-1/\alpha} \tag{28}$$

the derivative $(\partial^2 F_s/\partial T^2)_{\rho_c}$, $x$ behaves similar to a pure fluid (the first term in the right part of equation (26))

$$\left(\frac{\partial^2 F_S}{\partial T^2}\right)_{\rho_c,x} \sim -[\tau(x)]^{-\alpha} \tag{29}$$

The asymptotic behavior of the derivative $(\partial F_s/\partial T)_{\rho_c,x}$ is evaluated the same way. At the condition given by equation (16)

$$\left(\frac{\partial F_S}{\partial T}\right)_{\rho_c,x} \sim \tau(x)\{[\tau(x)]^{\alpha/(1-\alpha)} - \text{const}\} \tag{30}$$

but in the range of temperatures determined by the inequality (28) one can obtain

$$\left(\frac{\partial F_S}{\partial T}\right)_{\rho_c,x} \sim -[\tau(x)]^{1-\alpha} \tag{31}$$

which corresponds to the behavior of the entropy in a pure fluid.

Substitution of equations (17)–(21) into the correlations given by equations (16) and (27)–(31) shows that at the critical isochore, the critical behavior of all the binary mixtures has a universal nature. The behavior is determined by the value of the dimensionless parameter

$$\psi_0 = \tau(x)\tilde{\xi}^{1/2} \tag{32}$$

where $\tilde{\xi} = |\xi y_2|(y_1 y_2^{-1})^{\alpha}$. In the case of $\psi_0 \ll 1$ renormalization of $\tau(\tilde{x}) \simeq \tau(x)^{1/(1-\alpha)}$ takes place, the singular part of the free energy splits up into two terms, and the singular part of the heat capacity at the critical isochore has the asymptotic behavior

$$C_{v,x} \approx -A\tilde{\xi}[\tilde{\xi}(\tau\tilde{\xi})^{\frac{\alpha}{1-\alpha}} - 1] + \text{background} \tag{33}$$

One can see that the isochoric heat capacity at constant concentration does not diverge at the critical line (Fisher, 1968).

For $\psi_0 \gg 1$ the renormalization is absent ($\tau(\tilde{x}) \approx \tau(x)$) and the heat capacity behaves similar to a pure fluid

$$C_{v,x} \approx A[\tau(x)]^{-\alpha} + \text{background} \tag{34}$$

A comprehensive analysis of the asymptotic critical behavior of the isochoric heat capacity as well as other thermodynamic properties of mixtures can be found in works by Anisimov et al. (1971, 1973), Griffiths and Wheeler (1970), Sengers and Levelt Sengers (1986), and Rainwater and Williamson (1986).

## Universal Scaling Function

The results obtained show that the singular part of the free energy $F[T, \rho_c(x), x]$ of a mixture in the vicinity of the critical point can be written in the form

$$F_s(T, \rho_c(x)) = A_1[\tau(x)]^{2-\alpha} \cdot \phi_s(\psi_0) \tag{35}$$

where $\phi_s(\psi_0)$ is a universal function. $A_1(x)$ is a nonuniversal coefficient depending on the individual properties of a mixture. The universal function $\phi_s(\psi_0)$, in accordance with equations (33) and (34), can be represented by the form

$$\phi_s(\psi_0) = f_{1S}^{\kappa_1}(\psi_0) - f_S^{\kappa_2}(\psi_0) \tag{36}$$

where $\kappa_1$ and $\kappa_2$ are determined through the known critical exponents and, consequently, have universal values; $f_{1S}(\psi_0)$ and $f_S(\psi_0)$ are monotonic analytical functions. While passing to the pure components, and when $\psi_0 \gg 1$, the function $F_S$ transforms to the corresponding expression for a pure fluid and the function $\phi_S(\psi_0)$ must have a limit $\lim_{\psi_0 \to \infty} \phi_S = 1$. To satisfy this condition one should demand

$$\lim_{\psi_0 \to \infty} f_{1S}(\psi_0) = 2[\lim_{\psi_0 \to \infty} f_S(\psi_0)] = 2 \tag{37}$$

That is always satisfied if $f_{1S} = 2f_S$. Then the expression given by equation (34) can be rewritten in the form

$$\phi_S(\psi_0) = f_S^{\kappa_1}(\psi_0)[2 - f_S^{\kappa_2 - \kappa_1}(\psi_0)] \tag{38}$$

and the function $f_S(\psi_0)$, accounting for the analysis previously performed (see solutions of equations (29)-(34)), must have the following asymptotic properties:

$$\lim_{\psi_0 \to \infty} f_S(\psi_0) = 1, \qquad \lim_{\psi_0 \to 0} f_S(\psi_0) = \psi_0 \tag{39a}$$

$$\lim_{\psi_0 \to \infty} f_S'(\psi_0) = (+)0, \qquad \lim_{\psi_0 \to 0} f_S'(\psi_0) = (+)\text{const} \tag{39b}$$

$$\lim_{\psi_0 \to \infty} f_S''(\psi_0) = (-)0, \qquad \lim_{\psi_0 \to 0} f_S''(\psi_0) = (-)\text{const} \tag{39c}$$

For the exponents $\kappa_1$ and $\kappa_2$, after double differentiating the expressions given by equations (35) and (38) and incorporating equations (29)-(34), one obtains

$$\kappa_1 = \alpha, \qquad \kappa_2 = \frac{\alpha(2-\alpha)}{(1-\alpha)} \tag{40}$$

To find the form of the analytical function $f_s(\psi_0)$ one can use the Pade approximation method, i.e.,

$$f_S(\psi_0) = P(n, m) = \frac{\sum_{i=1}^{n} \alpha_i \psi_0^{i-1}}{\sum_{j=1}^{m} b_j \psi_0^{j-1}} \tag{41}$$

restricted to the third-order terms ($n=3$, $m=3$). Then the expansion coefficients $\alpha_i$ and $b_j$ can be precisely found from the rigorous correlations given by equations (39). Indeed from the condition given by equation (39*a*) one has $\alpha_1 = 0$. The condition given by equation (39) gives $\alpha_3 = b_3 = 0$. The correlations given by equations (39*b*) and (39*c*) lead to the requirements that $b_1 > 0$ and $b_2 > 0$. Since the parameters $A_1$ and $\tilde{\xi}$ depend upon the individual properties of a fluid and they are adjusted ones in a general case (as well as the parameters $a, f_1, f_2$, and $m_2$ in equations (19)-(23)) one can assume that $\alpha_2 = b_1 = b_2 = 1$. Finally the functions $f_S(\psi_0)$ and $\phi_s(\psi_0)$ take the form

$$f_s(\psi_0) = \frac{\psi_0}{1+\psi_0} \tag{42}$$

$$\phi_S(\psi_0) = f_S^{\alpha}[2 - f_S^{\alpha/(1-\alpha)}] \tag{43}$$

The conclusion about the universal behavior of a mixture in the vicinity of the liquid-gas critical points is fully in accordance with the results obtained by Anisimov et al. (1971). The main difference is that the parameter in $\psi_0$ not only depends on the singular part of the free energy but also it is determined by the regular one (see equations (19)-(23)). This enables us to extend the description given by equations (36) and (43) to the noncritical isochores. For this purpose one should replace the temperature $\tau(x)$ by $r(x)$ (a dimensionless distance from the critical point), in equations (32) and (35), and consider $\tilde{\xi}$ as an independent adjusted parameter. Then the free energy of a binary mixture in the vicinity of the liquid-gas critical points, accounting for equation (7), can be represented by the form

$$\rho F(T, \rho, x) = \phi_S(\psi)\Psi_{LM}(r, \theta, x) + \Psi_{NA}(r, \theta, x) + \Psi_{AS}(r, \theta, x) + \rho F_0(T, \rho, x) \tag{44}$$

where the parameter $\psi$ is determined by the expression

$$\psi = r(x)\tilde{\xi}^{1/\alpha} \tag{45}$$

The polar coordinates $r(x)$ and $\theta(x)$ in equations (44) and (45) are determined as usual by the correlations given by equations (5*a*) and (5*b*), taking into account the substitution of $x$ instead of $\tilde{x}$. It is easy to show that at such a determination equation (35) is a particular case of equation (44) (at $\Delta\rho(x) = 0$ and $c = d = f = 0$) and that $\psi_0$ corresponds to the value of $\psi$ at the critical isochore.

## Fit of Experiments

The possibility of a universal description of the critical behavior of a binary mixture on the basis of the free energy given by equation (44) has been verified for the isochoric heat capacity of a number of binary mixtures. The equation for the isochoric heat capacity $C_{v,x} = T(\partial^2 F/\partial T_2)_{\rho,x}$ of a binary mixture, using equations (42)–(45), takes the form

$$\frac{\rho C_{v,x}}{T} = \phi_S(\psi) r^{-\alpha} - r^{\alpha}\left(\frac{\partial^2 \Psi_{LM}}{\partial T^2}\right)_{\rho,x} - \frac{\alpha}{(1-\alpha)(1+\psi)} 2r^{\alpha-1}\left(\frac{\partial \Psi_{LM}}{\partial T}\right)_{\rho,x}\left(\frac{\partial r}{\partial T}\right)_{\rho,x}\left(2 - \alpha - \frac{2}{2 - f_S^{\alpha/(1-\alpha)}}\right) + (2-\alpha)r^{\alpha-2}\Psi_{LM}\left(\frac{\partial r}{\partial T}\right)_{\rho,x}^2\left(F_{2S} - \frac{F_{2S} + 2\alpha/(1+\psi)}{(2 - f_S^{\alpha/(1-\alpha)})(2-\alpha)}\right) - \left(\frac{\partial^2 \Psi_{NA}}{\partial T^2}\right)_{\rho,x} - \left(\frac{\partial^2 \Psi_{AS}}{\partial T^2}\right)_{\rho,x} - \left(\frac{\partial^2 F_0}{\partial T^2}\right)_{\rho,x} \tag{46}$$

where

$$F_{2S} = \left[\frac{\alpha(2-\alpha)}{(1-\alpha)} - 1\right]\frac{1}{1+\psi} - 2f_S + r\left(\frac{\partial r}{\partial T}\right)_{\rho,x}^{-2}\left(\frac{\partial^2 r}{\partial T^2}\right)_{\rho,x} \tag{47}$$

and the regular part of the free energy is determined by equation (9) using the variable $x$ instead of $\tilde{x}$.

Equation (46) was used to describe the experimental data for the isochoric heat capacity at two concentrations of an ethane–heptane mixture ($x = 0.0093$, 0.0316 heptane mol. fractions); for an ethane–carbon dioxide mixture ($x = 0.281$, 0.430 ethane mol. fractions) at the critical isochore (Shmakov, 1973) as well as the data for an argon–carbon dioxide mixture

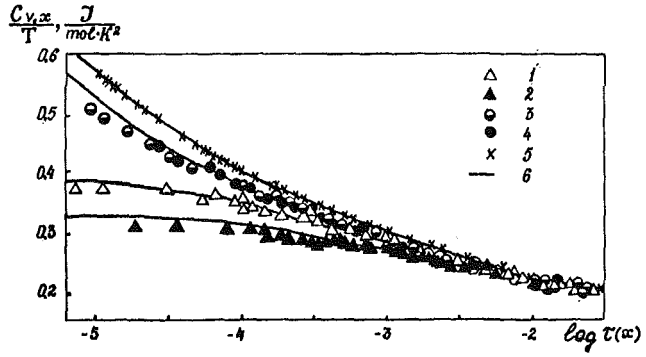


Fig. 1 Renormalization of the heat capacity in pure ethane and binary mixtures at the critical isochore: 1, 2 are ethane-heptane system $x = 0.0093$, 0.0315; 3, 4, are ethane-carbon dioxide system $x = 0.281$, 0.436; 5 is pure ethane; 6 is calculated from equation (46)

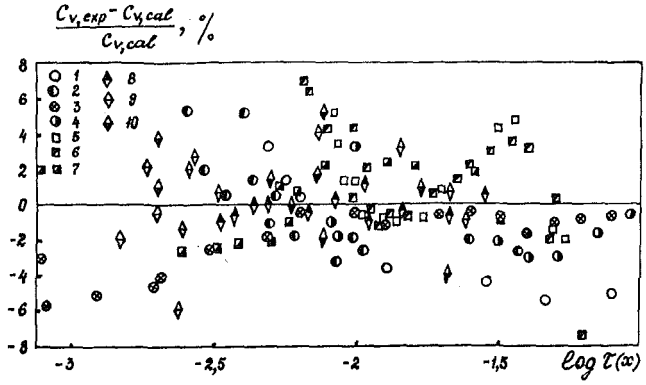


Fig. 2 Deviation of the heat capacity experimental data from the calculation results for Ar-$CO_2$ mixture at the isochores: 1, 2, 3, 4: $x = 0.1088$ ($\rho/\rho_c = 0.8$, 0.9, 1.0, 1.2); 5, 6, 7: $x = 0.182$ ($\rho/\rho_c = 0.8$, 0.9, 1.1); 8, 9, 10: $x = 0.4885$ ($\rho/\rho_c = 0.97$, 1.02, 1.07)

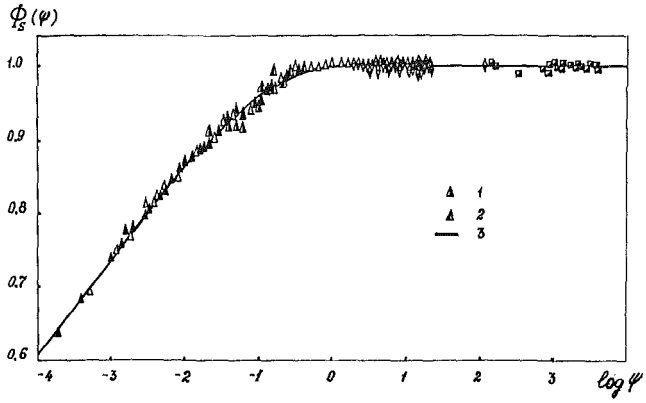


Fig. 3 Universal scaling function for binary mixtures: 1, 2 are ethane-heptane system $x = 0.0315$ ($\rho/\rho_c = 0.908$, 1.033); 3 is calculation from equation (46); the other notes are the same as in Figs. 1 and 2

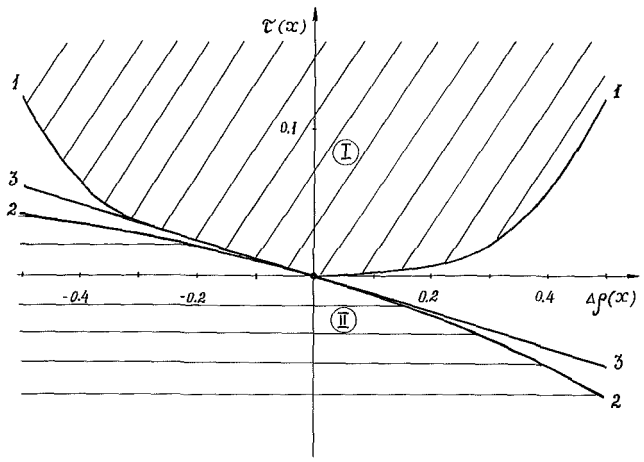


Fig. 4 Critical region of a binary mixture at $x = \text{const}$: 1 is the line $z(x) = 1$; 2 is the boundary curve; 3 is the tangent to the curve 2 at the critical point; I is justification area of equation (46); II is the two-phase region

(Adamov et al., 1981) at three concentrations ($x = 0.1088$, 0.1820, 0.4885 argon mol. fractions) for a wide range of densities and temperatures. While fitting the data, the functions $T_C(x)$ and $\rho_c(x)$ were taken from the experiment and the critical exponents were fixed using the universal theoretical values $\alpha = 0.11$, $\beta = 0.325$, $\Delta = 0.5$. The values of $a$ and $k$ for the mixtures were calculated from the additive correlations given by equation (13), in which the corresponding values for pure components were taken from Berestov and Kiselev (1979). The parameter $B_3$ in equation (6) was assumed to be equal to zero and the value of the parameter $\tilde{\xi}$ was found by trial and error to yield the best description of the experimental data. The values of $\tilde{\xi}$ thus obtained for all the mixtures coincide with the fitting accuracy of the values calculated from equations (19)-(21). The other parameters are adjusted ones and they were determined by the least squares method. The results of the fit are represented in Figs. 1-3.

One can note a qualitative difference in the divergence of $C_{v,x}$ in ethane-heptane and ethane-$CO_1$ mixtures (Fig. 1). This can be easily explained by the substantial difference in the parameter $\xi$, which is determined by equation (18), for these systems. For an ethane-heptane mixture the value of $dT_c/dx$ is one order of magnitude more than for an ethane-$CO_2$ one (Anisimov et al., 1973). This means, according to equation (32), that the characteristic temperature of the renormalization of the heat capacity for an ethane-$CO_2$ mixture is much closer to the critical temperature than for an ethane-heptane one. Therefore the complete renormalization is accessible only for ethane-heptane mixtures (if they are not too dilute).

## Discussion

The fit of the experimental data has shown the possibility of a universal description of binary mixtures in the critical region at $z(\tilde{x}) \gg 1$ (Fig. 4). However, attempting to extend equations (46) and (47) to the critical isotherm and the ($z(\tilde{x}) = 0$) by equations (43) and (44) is qualitatively wrong. To show this, consider the solution of equation (14) on the critical isotherm. In the case of $z(\tilde{x}) \ll 1$, accounting for equations (4)-(9), we have from equation (26) that when

$$|\Delta\rho(x)| \ll |\xi y_2|^{-1/\alpha} |y y_2^{-1}| \tag{48}$$

*renormalization of* $-\alpha/\beta \to \alpha/(1-x)$ *takes place and at* $\Delta\rho(x) \to 0$ the heat capacity $C_{v,x}$ tends to

$$C_{v,x} \sim \text{const} - |\Delta\rho(x)|^{\alpha/(1-\alpha)} \tag{49}$$

On the contrary, in the range of densities $|\Delta\rho(x)| \gg |y_2|^{-1/\alpha} |y y_2^{-1}|$, unusual renormalization of $-\alpha/\beta \to -\alpha/(1-\alpha)$ takes place and the heat capacity has the asymptotic behavior

$$C_{v,x} \sim |\Delta\rho(x)|^{-\alpha/(1-\alpha)} + \text{const} \tag{50}$$

This renormalization cannot be taken into account only by the substitution of $r(x)$ for $\tau(x)$ in equation (32) and $\psi$ for $\psi_0$ in equations (42) and (43). The correct behavior of $C_{v,x}$ at $z(\tilde{x}) \lesssim 1$ can be obtained (in addition to the procedure men-

tioned above) using the following form of density at constant concentration:

$$\Delta\rho(x) = \phi_{1S}(\psi_1) k r^{\beta} \theta - B_3 \tau \tag{51}$$

The universal function $\phi_{1S}(\psi_1)$ can be obtained the same way that was used for obtaining the function $\phi_S(\psi_0)$. It was obtained by Kiselev (to be published) from analysis of the behavior of the inverse isothermal compressibility at constant $x$ of the binary mixture, yielding

$$\phi_{1S}(\psi_1) = \left(\frac{\psi_1}{1+\psi_1}\right)^{\gamma/2} \tag{52}$$

$$\psi_1 = r(x)\xi_1^{1/\gamma} \tag{53}$$

where

$$\xi_1 = \tilde{a} y_2 \left[\left(\frac{d\tilde{P}_c}{dx} + f_1 \frac{dT_c}{dx}\frac{1}{T_c}\right)^2 kx(1-x)\right]^{-1}$$

It is easy to show that such a determination of the function $\phi_{1S}(\psi_1)$ also corresponds to the renormalization of the isochoric heat capacity $C_{v,x}$ on the critical isotherm. Indeed, differentiating equation (44) twice by temperature, for $\psi \ll 1$ and $\psi \ll 1$ on the critical isotherm ($\tau(x) = 0$), and using equations (6), (7), (44), and (51)-(53), we have

$$C_{v,x} \simeq \text{const} - |\Delta\rho(x)|^{\frac{\alpha}{1-\alpha}\left(\frac{2}{2-\alpha}\right)} \tag{54}$$

and when $\psi \gg 1$ and $\psi_1 \ll 1$ we have

$$C_{v,x} \simeq |\Delta\rho(x)|^{-\frac{\alpha}{1-\alpha}\left(\frac{2-2\alpha}{2-\alpha}\right)} + \text{const} \tag{55}$$

The critical exponents in equations (53)-(55) practically coincide with those in equations (49) and (50) with the accuracy of the small parameter $\alpha/2$. At $\psi \gg 1$ and $\psi \gg 1$ the behavior of a binary mixture in the critical region fully corresponds to the behavior of a one-component fluid.

Leung and Griffiths (1973) were the first to propose the approach closely related to this study. The major distinction of the present approach is the transformation from the isomorphous variables $T$, $\mu_1$, $\mu_2$ to the experimental variables $T$, $\rho$, $x$. It seems from the figures that equation (46) fully describes the behavior of the heat capacity $C_{v,x}$ of the binary mixtures for a wide range of temperatures and densities. The agreement between the experiment and the theory for mixtures appears to be similar to pure fluids (Berestov and Kiselev, 1979). Moreover, the form of the energy of binary mixtures in the vicinity of the liquid-gas critical points is universal and is accurately described by equations (43) and (44) and (51)–(53) (see Fig. 3). Incidentally equations (43) and (44) and (51)–(53) are transformed into the rigorous equations for a pure fluid at $x \to 0$. This manifests the reliability of the proposed approach and the possibility of a universal description of the critical behavior for binary mixtures.

The next problem that should be solved is the description of $P\rho Tx$ data and phase equilibrium binary mixtures, on the basis suggested in this work.

## References


Adamov, Sh. P., Anisimov, M. A., Kiselev, S. B., Rabinovich, V. A., and Smirnov, V. A., 1981, "Investigation of the Equation of State of Binary Mixtures Near the Line of the Liquid-Gas Critical Points," *Teplofiz. Vys. Temp. (High Temperature)*, Vol. 17, p. 1115.

Anisimov, M. A., Voronel, A. V., and Gorodetskii, E. E., 1971, "Isomorphism of Critical Phenomena," *Soviet Physics JETP*, Vol. 33, pp. 605–612.

Anisimov, M. A., Gorodetskii, E. E., and Shmakov, N. G., 1973, "Experimental Verification of the Isomorphism Hypothesis of Critical Phenomena," *Soviet Physics JETP*, Vol. 36, pp. 1143–1150.

Anisimov, M. A., Berestov, A. T., and Kiselev, S. B., 1982, "Isomorphous Equation of State in a Broad Vicinity of the Critical Point of a Binary Mixture," *Soviet Physics JETP*, Vol. 55, pp. 667–673.

Anisimov, M. A., Kiselev, S. B., and Kostukova, I. G., 1985, "A Scaled Equation of State for Real Fluids in the Critical Region," *International Journal of Thermophysics*, Vol. 6, pp. 465–481.

Berestov, A. T., and Kiselev, S. B., 1979, "Possibility of Joining Together the Scaled Equation of State and the Virial Expansion," *Teplofiz. Vys. Temp. (High Temperature)*, Vol. 17, pp. 1202–1209.

Fisher, M. E., 1968, "Renormalization of Critical Exponents by Hidden Variables," *Physical Review*, Vol. 176, pp. 257–272.

Griffiths, R. G., and Wheeler, J. C., 1970, *Physical Review*, A, Vol. 2, p. 1047.

Kiselev, S. B., 1986, "Asymmetric Scaled Equation and Behavior of a Real Fluid in the Critical Region Including the Metastable State," *Teplofiz. Vys. Temp. (High Temperature)*, Vol. 24, pp. 500–509.

Kiselev, S. B., "Universal Scaled Equation of State of One-Component Liquids and Binary Mixtures," *Teplofiz. Vys. Temp. (High Temperature)*, to be published.

Leung, S. S., and Griffiths, R. B., 1973, "Thermodynamic Properties Near the Liquid–Vapor Critical Line in Mixtures of $He^3$ and $He^4$," *Physical Review*, Vol. 8A, pp. 2670–2683.

Patashinskii, A. Z., and Pokrovskii, V. L., 1979, *Fluctuation Theory of Phase Transitions*, Pergamon Press, London.

Rainwater, J. C., and Williamson, R. F., 1986, "Vapor–Liquid Equilibrium of Near-Critical Binary Alkane Mixtures," *International Journal of Thermophysics*, Vol. 7, pp. 65–74.

Sengers, J. V., and Levelt Sengers, J. M. H., 1986, "Thermodynamic Behavior of Fluids Near the Critical Point," *Annual Reviews of Physical Chemistry*, Vol. 37, p. 189.

Shmakov, N. G., 1973, "Isochoric Heat Capacity of Pure Ethane and the Ethane–Carbon Dioxide and Ethane–Heptane Mixtures Near the Liquid–Gas Critical Points," in: *GSSD*, ser. Teplofizicheskie Svoistva Veshchestv i Materialov (Thermophysical Properties of Substances and Materials), No. 7, pp. 155–167.

Wilson, K. G., and Kogut, J., 1974, "The Renormalization Group and the $\epsilon$-Expansion," *Physical Reports*, Vol. 12C, p. 75.

# Thermal Conductivity of Gaseous and Liquid Ammonia

**A. A. Clifford**

**R. Tufeu**

Laboratoire des Interactions Moléculaire et des Hautes Pressions, C.N.R.S., Université Paris Nord, 93430, Villetaneuse, France

*The thermal conductivity of gaseous and liquid ammonia has been measured in the range 300–300 K and at pressures up to 50 MPa. The measurements were a necessary preliminary to a fitting of the thermal conductivity surface in the density–temperature plane, which is part of the current program of the Transport Properties Subcommittee of the I.U.P.A.C. Results were obtained that are believed to be accurate to 2 percent. It is difficult to make a good comparison of these results with previous data until a full correlation of the thermal conductivity of ammonia is carried out. A preliminary assessment for the liquid phase indicates that agreement is reasonable over much of the range with differences up to around 5 percent under certain conditions. For the gas phase an approximate extrapolation to atmospheric pressure can be made and the results compared with some recent recommended values. Differences of ±3 percent are observed.*

## Introduction

Ammonia is an important industrial fluid, both as a refrigerant and in other respects, and the International Union of Pure and Applied Chemistry (I.U.P.A.C.) has been concerned with producing recommended values of some of its important properties. Variations of its properties with pressure are accentuated by molecular association. The Subcommittee on Transport Properties has adopted, as part of its program, the fitting of both the viscosity and thermal conductivity of ammonia in the density–temperature plane. The viscosity project has been completed and the results will be published separately (Watson, 1988).

Experimental work on the thermal conductivity of ammonia has been reviewed up to 1977 by Golubev et al. (1978) and by Vargaftik et al. (1978), who have evaluated the data and produced some recommended values. Both reviews refer to data from a large number of authors over restricted ranges of temperature and pressure and also data from three groups over much wider ranges, i.e., Needham and Ziebland (1964) (294-450 K, 0.1-48.1 MPa), Golubev and Sokolova (1964) (208-668 K, 0.1-39.5 MPa), and Richter and Sage (1964) (278-478 K, 0.1-36.5 MPa). There are wide discrepancies in the data; at atmospheric pressure the values cover a range of 20 percent. However, the data of Needham and Ziebland and Golbubev and Sokolova agree over much of the temperature–pressure plane. Nevertheless there are some important differences, particularly in the critical region, where there are rapid variations in the thermal conductivity, and also in the liquid region. Differences of up to 5 percent are present in the liquid data, as can be seen, for example, in Fig. 2(*a*) below.

Since 1977 the only major experimental publication on the thermal conductivity of ammonia (Tufeu et al., 1984) has come from this laboratory. Measurements were made over a wide temperature and pressure range (381-578 K and 1-80 MPa). This included a substantial number of measurements in the critical region. These were fitted to recent expressions for the critical-region anomaly in thermal conductivity and help to solve the difficulties experienced with the previous data in this region. However, no measurements were made at lower temperatures in the liquid region where there are also discrepancies with the previous data. The present study extends the measurements to these lower temperatures.

Contributed by the Heat Transfer Division and presented at the ASME Winter Annual Meeting, Anaheim, California, December 7–12, 1986. Manuscript received by the Heat Transfer Division April 3, 1987. Keywords: Conduction, Refrigeration, Thermophysical Properties.

The measurements of Needham and Ziebland (1965) were made using a cell constructed of coaxial cylinders with guard rings. Those of Golubev and Sokolova (1964) were made with a "cylindrical bicalorimeter," which has the same geometry. With guard rings there is always the risk of axial heat flow, particularly at high thermal conductivities, and so measurements with a different type of apparatus are desirable. The most obvious candidate is the transient hot-wire apparatus (Haarman, 1969; Nieto de Castro, 1977; Kestin et al., 1980), as this also avoids (or makes obvious) the convection problem. However, there are problems in electrically insulating the wire from the conducting liquid ammonia. In the basic theory of this experiment the wire is infinitely thin, and to make accurate measurements, minimizing the corrections for the wire of such thickness is obviously a problem, and although attempts are being made at Imperial College, London, UK, to coat thin tantalum wires with an insulating oxide, this technique is still being developed (Wakeham, 1987). Attempts to make measurements on ammonia in the gas phase at the UK National Engineering Laboratory with a noninsulated wire have also proved to be unsuccessful because of electrical effects (Clifford, 1987). Under the circumstances, therefore, measurements using the coaxial cylinder apparatus without guard rings at L.I.M.H.P. seemed the most worthwhile course to check the data for liquid ammonia.

## Experimental

The apparatus used has been described in detail previously (Le Neindre et al., 1976). Briefly it consists of vertical coaxial cylinders constructed of silver, without guard rings. The inner cylinder is 100 mm long and 15 mm in diameter. It is centered in a cavity of the same shape by means of five sapphire centering pins, such that the gap all around is 0.26 mm. The method is in principle absolute, although the small corrections made necessary because of conduction by the centering pins and electrical leads were obtained by calibration with gases of known thermal conductivity. The calibration gases were Ar at 1 MPa, Ne at 2 MPa, and He at 5 MPa, and the calibration values were those obtained by the transient hot-wire method (Kestin et al., 1980; Clifford et al., 1981; Johns et al., 1983). The temperature difference between the cylinders during an experiment was less than 1 K. Temperature measurements both of temperature differences and absolute temperature were made using Pt–Pt/Rh thermocouples and the pressure was measured with calibrated Heise Bourdon gages. Ammonia of 99.96 percent purity was supplied by Air Liquide.

Table 1 Measured values of the thermal conductivity of ammonia, λ, at temperature *T*, pressure *P*, and density ρ

| T (K) | P (MPa) | ρ (kg m$^{-3}$) | λ (mW m$^{-1}$ K$^{-1}$) |
|---|---|---|---|
| 297.5 | 0.97 | 7.5 | 27.6 |
| 303.7 | 1.5 | 595 | 459 |
| 302.9 | 5.0 | 600 | 465 |
| 302.4 | 10.2 | 605 | 471 |
| 300.9 | 20.1 | 616 | 489 |
| 295.6 | 30.0 | 630 | 512 |
| 299.9 | 40.0 | 632 | 515 |
| 297.9 | 50.2 | 641 | 533 |
| 327.2 | 1.02 | 6.9 | 29.5 |
| 328.9 | 2.24 | 17.2 | 34.2 |
| 334.7 | 2.9 | 543 | 396 |
| 334.6 | 5.0 | 546 | 398 |
| 327.0 | 10.0 | 567 | 425 |
| 332.4 | 20.3 | 571 | 429 |
| 332.3 | 30.1 | 581 | 445 |
| 332.9 | 40.5 | 590 | 462 |
| 326.4 | 50.5 | 607 | 485 |
| 354.0 | 0.94 | 5.7 | 33.1 |
| 354.3 | 1.99 | 13.0 | 35.3 |
| 354.8 | 3.02 | 21.5 | 38.6 |
| 355.7 | 4.00 | 31.3 | 43.6 |
| 360.2 | 5.6 | 492 | 343 |
| 365.3 | 10.0 | 493 | 340 |
| 360.4 | 20.5 | 525 | 373 |
| 361.0 | 30.2 | 539 | 391 |
| 362.6 | 40.5 | 550 | 411 |
| 360.0 | 50.8 | 565 | 427 |
| 381.9 | 1.00 | 5.6 | 37.0 |
| 381.9 | 2.02 | 11.8 | 39.0 |
| 382.0 | 3.00 | 18.6 | 41.2 |
| 382.0 | 4.00 | 26.4 | 44.2 |
| 382.1 | 5.01 | 35.6 | 48.4 |
| 382.4 | 6.06 | 47.4 | 55.0 |
| 382.2 | 7.07 | 63.3 | 66.7 |
| 384.7 | 8.4 | 426 | 287 |
| 387.1 | 10.0 | 427 | 279 |
| 386.9 | 20.0 | 471 | 319 |
| 385.9 | 30.4 | 498 | 347 |
| 385.0 | 40.2 | 516 | 369 |
| 384.7 | 50.2 | 531 | 387 |

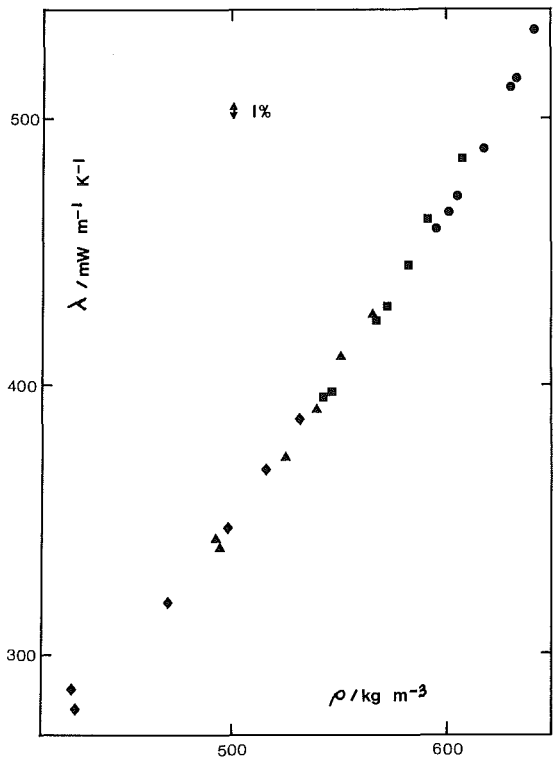


Fig. 1 Measured values of the thermal conductivity λ of liquid ammonia at various temperatures shown as a function of density ρ: ●, 296-304 K; ■, 326-335 K; ▲, 360-365 K; ◆, 385-387 K

Although it was not examined after use, it is believed that corrosion of the silver surfaces by ammonia was negligible as the cell did not noticeably change its characteristics after the measurements. Most of the electrical leads were isolated from ammonia by using a two-gas system. The cell, which is gas-tight but not pressurizable, is filled with ammonia and surrounded by helium. The two gases are kept at the same pressure by means of a flexible bellows within the pressure system. Helium was used as the pressurizing gas, because of its high thermal conductivity, to keep the cell as uniformly close to the thermostat temperature as possible. This is important for materials of high thermal conductivity such as liquid ammonia where high heat inputs are used.

## Results and Discussion

Measurements were made at four temperatures and at 1 MPa intervals until the liquefaction point, just above this point, and then at 10 MPa intervals up to 50 MPa. The results for both gas and liquid are given in Table 1. They are believed to have an absolute accuracy of 2 percent.

The results for the liquid at 385 K supersede those previously published from this laboratory. The use of argon as a pressurizing gas in the earlier measurements is now thought to have introduced a systematic error for the reasons discussed in the experimental section. This effect is only important for high values of the thermal conductivity at lower temperatures up to about 400 K. Differences of up to 6 percent occur with the data at 385 K, well outside the experimental error. Of the previously published data (Tufeu et al., 1984), most of the results at 385 K and perhaps the highest density point at 412.4 K are now thought to be in error. Data for the gas phase at this temperature agree, however, and the two sets are felt to be equivalent.

Densities for ammonia are also shown in Table 1; these were calculated from the equation of state proposed by Haar and

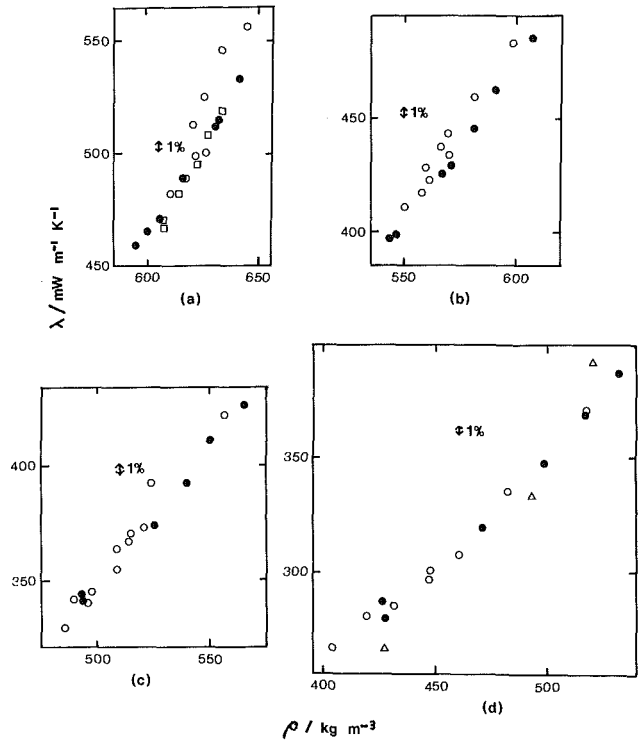


**Fig. 2 Measured values of the thermal conductivity λ of liquid ammonia shown as a function of density compared with previous data: (*a*) ~ 300 K; (*b*) ~ 330 K; (*c*) ~ 360 K; (*d*) ~ 390 K; •, present results; ○, Needham and Ziebland (1965); □, Golubev and Sokolova (1964); △, Richter and Sage (1964)**

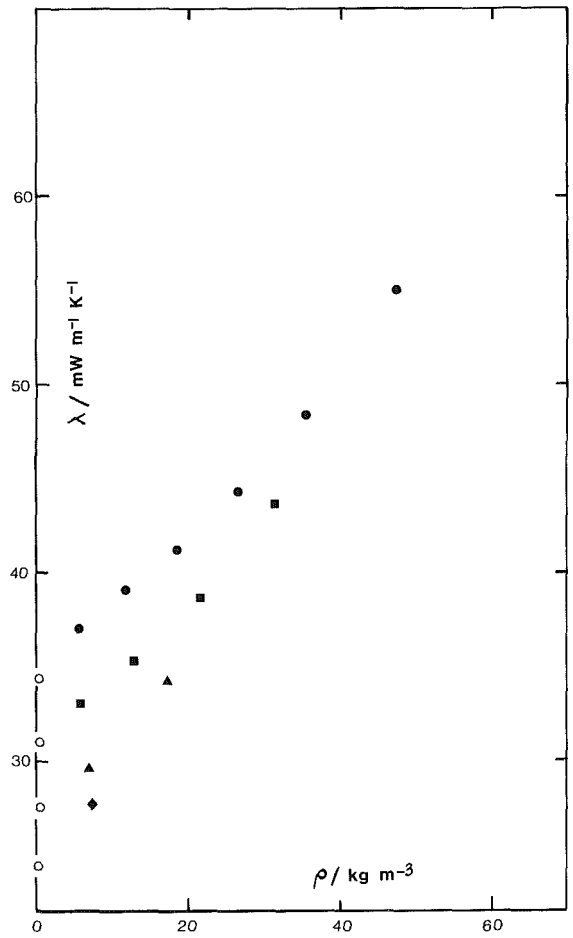


**Fig. 3 Values of the thermal conductivity λ of gaseous ammonia as a function of density ρ: present results: ◆, 298 K; ▲, 328 K; ■, 355 K; ●, 382 K; ○, Golubev's recommended values at 1 atm pressure (1978)**

Gallagher (1978). The data for liquid ammonia are then plotted against density on Fig. 1. This shows that, while the data given for the liquid depend strongly on density, they are only feebly dependent on temperature, as all points lie on the same curve to within experimental error. Closer examination shows, however, that the curves for each group of points for a small temperature range are shifted relative to each other by small amounts (of the same order of magnitude as the differences for the gas).

The lowest density points at the two highest temperatures are anomalously above the next value at higher density. As these high points are close to the saturation line, this may be due to an experimental problem. However, as these points agree to within experimental error, and as there is no objective reason for removing any of the them, all are included. Whether these points are included or not, the points for each small temperature range appear to be on a **J**-shaped curve.

The data presented here are under different conditions from those of previous measurements, and so an accurate comparison can only be made after fitting all the data (present and previous) to an appropriate function of temperature and density. For the liquid, however, an approximate comparison can be made, as the thermal conductivity appears to be only weakly dependent on temperature. This is done in Fig. 2. Differences of up to 5 percent are observed with Richter and Sage (1984) and also with Needham and Ziebland (1965) at lower temperatures and higher densities, but elsewhere agreement is good. The data of Needham and Ziebland, especially if all their data are examined, appear to fall into two groups, different by 3-4 percent. Our data seem to agree with their group of lower values.

For the gas phase comparison is more difficult. Our data are plotted in Fig. 3 along with the recommendations of Golubev et al. (1978) at 1 atm. It can be seen that an approximate extrapolation of our data would give differences of ±3 percent with the recommendations of Golubev et al. (1978). In view of the fact that the latter were obtained from experimental data covering a range of 10 percent, agreement seems reasonable.

## Acknowledgments

We would like to thank M. B. Le Neindre and Mr. J. T. R. Watson for useful discussions. The latter also provided a computer program for calculating ammonia densities. One of us (A.A.C.) is grateful for financial support under the European Science Exchange Programme.

## References

Clifford, A. A., Gray, P., Johns, A. I., Scott, A. C., and Watson, J.T.R., 1981, "Thermal Conductivity of Argon, Nitrogen and Hydrogen Between 300 and 400 K and up to 25 MPa," *Journal of the Chemical Society Faraday Transactions I*, Vol. 77, pp. 2679-2691.

Clifford, A. A., 1987, University of Leeds, Leeds, UK, Private Communication.

Golubev, I. F., and Solokova, V. P., 1964, "The Thermal Conductivity of Ammonia at Different Temperatures and Pressures," *Teploenergetika*, Vol. 9, pp. 64-67.

Golubev, I. F., Kyashova, V. P., Perel'schtein, I. I., and Parushin, E. B., 1978, "Thermophysical Properties of Ammonia," *Izdatel'stvo Standartov*, Moscow, Chap. 5.

Haar, L., and Gallaher, J. S., 1978, "Thermodynamic Properties of Ammonia," *Journal of Physical and Chemical Reference Data*, Vol. 7, pp. 635-792.

Haarman, J. W., 1969, "An Accurate Method for the Determination of the Thermal Conductivity Coefficients of Gases (Non-stationary Wire Method)," Ph.D. Thesis, Technische Hochschule, Delft, Holland.

Johns, A. I., Scott, A. C., Watson, J. T. R., Ferguson, D., and Clifford, A.

A., 1983, "An Apparatus for Measuring the Thermal Conductivity of Gases by the Transient Hot-Wire Method," N.E.L. Report No. 685, Department of Trade and Industry, UK, pp. 58–59.

Kestin, J., Paul, R., Clifford, A. A., and Wakeham, W. A., 1980, "Absolute Determination of the Thermal Conductivity of the Noble Gases at Room Temperature up to 35 MPa," *Physica*, Vol. 100A, pp. 349–369.

Le Neindre, B., Bury, P., Tufeu, R., and Vodar, B., 1976, "Thermal Conductivity Coefficients of Water and Heavy Water in the Liquid State up to 370°C," *J. Chem. Eng. Data*, Vol. 21, pp. 265–274.

Needham, D. P., and Ziebland, H., 1965, "The Thermal Conductivity of Liquid and Gaseous Ammonia, and Its Anomalous Behaviour in the Vicinity of the Critical Point," *International Journal of Heat and Mass Transfer*, Vol. 8, pp. 1387–1414.

Nieto de Castro, C. A., 1977, "Thermal Conductivity Measurement of Liquid Hydrocarbons by the Hot-Wire Method," Ph.D. Thesis, Instituto Superior Technico, Lisbon, Portugal.

Richter, G. N., and Sage, B. H., 1964, "Thermal Conductivity of Fluids," *Journal of Chemical and Engineering Data*, Vol. 9, pp. 75–78.

Tufeu, R., Ivanov, D. Y., Garrabos, Y., and Le Neindre, B., 1984, "Thermal Conductivity of Ammonia in a Large Temperature Range Including the Critical Region," *Berichte der Bunsen-Gesellschaft für physikalische Chemie*, Vol. 88, pp. 422–427.

Vargaftik, N. B., Filippov, L. P., Tarzimanov, A. A., and Tolskiy, E. E., 1978, "Thermal Conductivity of Liquids and Gases," *Izdatel'stvo Standartov*, Moscow, pp. 103–109.

Wakeham, 1987, Imperial College, Private Communication, London, UK.

Watson, J. T. R., 1988, "The Dynamic Viscosity of Ammonia," *Journal of Physical and Chemical Reference Data*, in press.

Journal of Heat Transfer

# Technical Notes

This section contains shorter technical papers. These shorter papers will be subjected to the same review process as that for full papers.

## Evaluation of Thermal Contact Conductance Between Mold Compound and Heat Spreader Materials

G. P. Peterson[1] and L. S. Fletcher[2]

### Nomenclature

$C_c$ = dimensionless conductance $= \sigma h/mk_m$
$c_1$ = Vickers hardness parameter, MPa
$c_2$ = Vickers hardness parameter
$h$ = contact conductance, W/m$^2$-K
$H_c$ = Vickers surface microhardness, MPa
$K$ = thermal conductivity, W/m-K
$k_m$ = harmonic mean thermal conductivity $= 2k_ak_b/(k_a + k_b)$, W/m-K
$m$ = combined absolute asperity slope $= \sqrt{m_a^2 + m_b^2}$
$P$ = apparent contact pressure, MPa
$\sigma$ = combined rms surface roughness $= \sqrt{\sigma_a^2 + \sigma_b^2}$, m

### Subscripts

$a$ = mold compound material
$b$ = substrate material

### Introduction

The need to develop microelectronic devices capable of operating at increased performance levels with high reliability requires a better understanding of the factors that govern the thermal performance of semiconductor packages. With the recent trend toward increased miniaturization and component density, thermal management within these packages has become the primary factor that limits the physical size of both individual components and multichip modules.

In a wide variety of electronic packages, the construction techniques utilized involve a silicon wafer that has been bonded to a heat spreader using an organic glue loaded with metallic particles; a hard solder, such as eutectics or gold/tin alloys; or a soft solder comprised of large percentages of lead, tin, or indium (Yerman, 1983). Once the chip has been bonded to the heat spreader, the entire device is encased in a silica mold compound. As a result, the heat generated in the chip is transferred from the chip through the bonding material, to the substrate, and in turn to the mold compound.

In a review of thermal management in electronic packages, Antonetti and Yovanovich (1984) have presented and discussed specific factors that contribute to the high internal resistances encountered in semiconductor devices. Several previous experimental investigations have studied some of these factors, including those of Yerman et al. (1983) and Mahalingham et al. (1984), which were directed toward determining the effect of voids or cracks on the thermal conductivity of the bonded interface, and that of Peterson and Fletcher (1987), which investigated the thermal contact conductance occurring at the chip/diebond and diebond/substrate interfaces.

Although extensive testing and analysis of the thermal conductivity of various mold compound materials have been performed by several different manufacturers, presently no experimental information is available on the contact conductance occurring at the interface between mold compounds and substrate or heat spreader materials.

From a modeling perspective, numerous standard thermal modeling techniques, which have been modified to accommodate electronic packages, are currently in use. In addition, a number of numerical models have been developed specifically for electronic packages by Pogson and Franklin (1973), Buchanan and Reeber (1973), Andrews et al. (1981), and Chyu and Aghazadeh (1987). Most of these latter techniques utilize either finite difference or finite element schemes to predict the temperature distribution in the package as a function of the boundary conditions and the physical properties of the package components. However, none of these existing models incorporates the effects of the contact conductance present at the mold compound and heat spreader interface.

For similar metal-to-metal interfaces, Yovanovich et al. (1983) have developed an expression for predicting the contact conductance as a function of the pressure and the surface microhardness, defined by Song and Yovanovich (1987) as

$$\frac{P}{H_c} = \left[ \frac{P}{c_1 \left( \frac{1.62 \times 10^6 \, \sigma}{m} \right)^{c_2}} \right]^{\frac{1}{1 + 0.071 c_2}} \tag{1}$$

This expression

$$C_c = 1.25 \left( \frac{P}{H_c} \right)^{0.95} \tag{2}$$

has been shown to agree within $\pm 1.5$ percent of the exact

[1]Assistant Professor of Mechanical Engineering, Mechanical Engineering Department, Texas A&M University, College Station, TX 77843; Mem. ASME.
[2]Associate Dean of Engineering and Professor of Mechanical Engineering, Mechanical Engineering Department, Texas A&M University, College Station, TX 77843; Fellow ASME.
Contributed by the Heat Transfer Division and presented at the National Heat Transfer Conference, Pittsburgh, Pennsylvania, August 1987. Manuscript received by the Heat Transfer Division April 27, 1987. Keywords: Conduction, Electronic Equipment, Thermal Packaging.

**Table 1 Test specimen characteristics and properties**

| Sample Number | Mold Compound Material | k(W/m -°C) | σ(μm) | m(rad) | Heat Spreader Material | k(W/m -°C) | σ(μm) | m(rad) |
|---|---|---|---|---|---|---|---|---|
| 1 | MG25F-LMP* | 0.816 | 0.0762 | 0.021 | Invar+ | 10.47 | 0.0279 | 0.007 |
| 2 | MG25F-LMP | 0.816 | 0.0508 | 0.021 | Alloy 42+ | 15.92 | 0.0102 | 0.006 |
| 3 | MG25F-LMP | 0.816 | 0.0635 | 0.017 | Kovar+ | 17.30 | 0.0305 | 0.010 |
| 4 | MG45F-04* | 1.670 | 0.0624 | 0.020 | Invar | 10.47 | 0.0235 | 0.006 |
| 5 | MG45F-04 | 1.670 | 0.0596 | 0.027 | Alloy 42 | 15.92 | 0.0194 | 0.009 |
| 6 | MG45F-04 | 1.670 | 0.0762 | 0.032 | Kovar | 17.30 | 0.0330 | 0.008 |
| 7 | Polyset 410B** | 0.628 | 0.0509 | 0.017 | Invar | 10.47 | 0.0152 | 0.006 |
| 8 | Polyset 410B | 0.628 | 0.0633 | 0.027 | Alloy 42 | 15.92 | 0.0254 | 0.007 |
| 9 | Polyset 410B | 0.628 | 0.0648 | 0.019 | Kovar | 17.30 | 0.0584 | 0.008 |
| 10 | Polyset 410C** | 1.420 | 0.0634 | 0.017 | Invar | 10.47 | 0.0203 | 0.006 |
| 11 | Polyset 410C | 1.420 | 0.0765 | 0.024 | Alloy 42 | 15.92 | 0.0330 | 0.011 |
| 12 | Polyset 410C | 1.420 | 0.0508 | 0.033 | Kovar | 17.30 | 0.0432 | 0.015 |

* Manufactured by Dynachem Corporation
** Manufactured by The Dexter Corporation
\+ Manufactured by A. D. Mackay Inc.

theoretical results for a range of $10^{-6} \leq P/H_c \leq 10^{-2}$. Investigations by Antonetti (1983), Yovanovich et al. (1983), and Hegazy (1985) have all verified the accuracy of this expression for contacting metal-to-metal surfaces. A subsequent investigation by Eid and Antonetti (1986), in which the thermal contact resistance at the interface between 2 mm × 2 mm aluminum test sections and similarly sized silicon samples was investigated, indicated that this expression could also be used to predict the contact conductances for bare metal-to-silicon junctions of the size encountered in semiconductor devices.

Therefore, in order better to understand the contact conductance occurring at the interface between mold compounds and heat spreader materials, an experimental investigation was conducted. The objective of this investigation was to determine whether any of the models previously developed for metal-to-metal contacts could be used to predict accurately the thermal contact conductance occurring at the interface between mold compounds and the heat spreader materials used in the assembly of semiconductor devices.

To accomplish this objective, the interfaces between three different types of substrate materials, Invar, Kovar, and Alloy 42, and four types of mold compounds, including both novalaks and anhydrides, were studied. These materials, which are typical of the types used in semiconductor packages, were selected in order to provide a wide range of thermophysical and mechanical properties. Using the materials listed in Table 1, measurements of the thermal contact conductance occurring at the interface formed between the mold compounds and the heat spreader materials were made over an interface temperature range of 20°C to 70°C and an interface pressure range of 0.5 to 5.0 MPa.

## Experimental Investigation

The experimental facilities used in this investigation, along with the details of the facility construction, operation, and accuracy, have been reported previously by Duncan (1987). The test apparatus consisted of a vertical column comprised of an electrical resistance heater around the lower test fixture, the mold compound test specimen, the heat spreader specimen, and a liquid-cooled heat sink attached to the upper test fixture. The interface pressure was varied through the use of a bellows vessel and measured using a load cell. The test specimens were arranged so that a vertical stack was formed and "sandwiched" between the two metal test fixtures. Radial heat losses were monitored by a thermocouple on the surface of each of the test fixtures, and these losses were minimized by placing radiation shields (made of sheet aluminum and asbestos) around the test column.

The tests were conducted at a vacuum pressure less than $1.33 \times 10^{-3}$ Pa to eliminate the conduction and convection losses to the surrounding air and also to eliminate the effects of any interstitial fluids on the thermal contact conductance

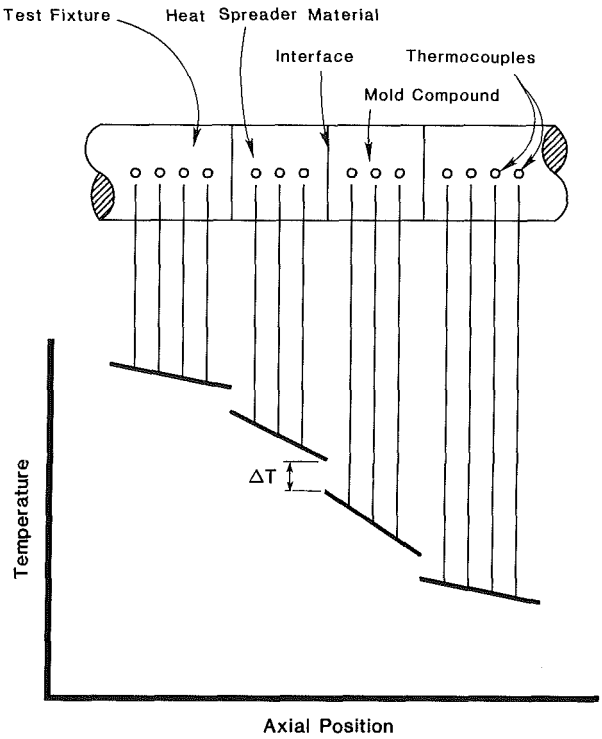


**Fig. 1 Determination of the contact conductance**

measurements. To determine the thermal contact conductance at the mold/spreader interface, a series of thermocouples was located along the centerline of the fixtures, the mold compound, and the heat spreader. The temperatures at the contact surfaces were determined by extrapolating the measured centerline temperatures in the mold compound and the heat spreader materials to the contact surface, as shown in Fig. 1. The heat flux was determined using the known thermal conductivity of the fixtures.

The experimental procedure followed for all of the thermal contact conductance tests was as follows: The substrate materials were machined into segments 2.54 cm long. After machining, the interface surfaces were ground and polished. Once the surfaces had been thoroughly cleaned with acetone, the mold compound material was thermally molded onto the metallic sample in a mold press specifically designed for this purpose. The thermocouples were installed, and the test specimens were placed between the test fixtures. A thin layer of Dow Corning 340 heat sink compound was placed at the interface between the test fixtures and at each end of the test specimen to reduce the thermal resistance at those interfaces. Special care was taken throughout this procedure to prevent the test interface from breaking, since it was desirable to test the interface in an "as-molded condition."

The temperature and pressure conditions were set by adjusting the heater voltages and pressurizing the gas bellows. The test procedure followed was first to vary the pressure in increments of approximately 0.5 MPa, maintaining the mean interface temperature at 38°C ± 2°C until an upper limit of 5.0 MPa was reached. At this point, a constant pressure was maintained and the heat flux was varied. In this manner, the contact conductance could be measured as a function of the mean interface temperature. Data were taken when the temperatures of the test specimen did not vary more than 0.5°C over a 45-min period.

Upon completion of the tests, each of the thermal test specimens was removed from the test facility and the interface was broken apart. After separation, the interface surfaces of both the mold compound and the heat spreader samples were

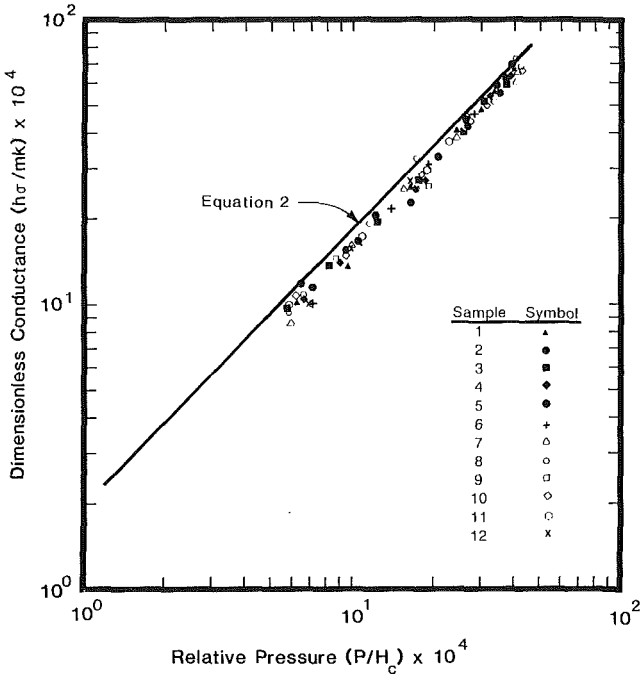


**Fig. 2 Comparison of predicted and experimental values for the mold compound and heat spreader interfaces**

characterized by measuring the average surface roughness, average asperity slope, rms surface roughness, rms asperity slope, and flatness deviation. Upon completion of the measurement of the surface characteristics, which are listed in Table 1, measurements of the Vickers microhardness were made using the procedure outlined by Hegazy (1986). These hardness measurements were made subsequent to the measurement of the contact conductance, since determination of the Vickers hardness was a destructive test requiring five measurements at each of six loads with a diamond indenter. Using this information, the dimensionless contact pressure $P/H_c$ and the dimensionless conductance were determined using equations (1) and (2), respectively.

## Results and Discussion

In the experimental investigation described here, the gaseous contribution to the joint conductance was assumed to be zero, since all of the tests were conducted in a vacuum. The radiation effects were also assumed to be negligible due to the relatively low temperature range of the experimental tests. By combining the sources of error, most notably the location and accuracy of the thermocouples and the resolution of the loading mechanism, the experimental uncertainty was determined to be ±9 percent. Since the axial heat flux through the samples was determined from the temperature distributions in the fixtures, the accuracy of the thermal conductivity of the mold compound, as specified by the manufacturer, was not a factor. However, the mold compound thermal conductivity data were used to indicate whether the mold compound had been properly cured.

Based upon the results of this investigation it is apparent that variations in the mean interface temperature have little effect on the thermal contact conductance over the temperature range investigated, with all of the data falling within ±9 percent of a horizontal line. The measured interface resistance values were found to be significant and equivalent to the thermal resistance resulting from 0.2 to 2.0 mm of the mold compound material, depending upon the thermal conductivity of the mold compound and the interfacial pressure.

Figure 2 compares the relationship that exists between the dimensionless contact pressure and the dimensionless contact conductance. As shown, the correlation between the experimental values obtained in this investigation and the predicted values as determined from equation (2) are quite good. Further analysis of the data indicates that although the expression presented in equation (2) was developed for metal-to-metal contacts that experienced work hardening due to the surface preparation, all of the experimental data fall within 19 percent of the predicted values.

The hardness measurements conducted on the metallic surfaces indicate that work hardening did occur and resulted in a slight increase in the hardness near the surface. A similar hardness layer, although extremely thin, was also apparent in the mold compound. The presence of these hardness layers in both the mold compound and the metal specimens may account for the unexpected accuracy of the expression developed by Yovanovich et al. (1983).

## Conclusions

This study provides experimental data that can be used not only to determine the contact conductance at the interface between different mold compounds and heat spreader materials, but also to provide additional information for use in expanding the existing analytical and numerical models.

The results indicate that the thermal contact conductance occurring at the mold compound/heat spreader interface in electronic packages is significant and although relatively constant with respect to the mean interface temperature, it is strongly dependent upon the interfacial pressure. In addition and perhaps more important, the experimental data suggest that the correlation given by equation (2) for metal-to-metal surfaces in contact can be used to predict the contact conductance accurately at the interface between metallic surfaces and plastic mold compounds, such as those used in electronic packaging, over a fairly broad range of temperatures and pressures.

## References

Andrews, J. A., 1981, "Thermal Characteristics of 16 and 40 Pin Plastic DIPs," *IEEE Transactions on Components, Hybrids, and Manufacturing Technology*, pp. 455–451.

Antonetti, V. M., 1983, "On the Use of Metallic Coatings to Enhance Thermal Contact Conductance," Ph.D. Thesis, University of Waterloo, Waterloo, Ontario, Canada.

Antonetti, V. M., and Yovanovich, M. M., 1984, "Thermal Contact Resistance in Microelectronic Equipment," *Thermal Management Concepts in Microelectronics Packaging*, ISHM Technical Monograph Series, No. 6984-003, pp. 135–151.

Buchanan, R. C., and Reeber, M. D., 1973, "Thermal Considerations in the Design of Hybrid Microelectronic Packages," *Solid State Technology*, Feb., pp. 39–43.

Chyu, M. K., and Aghazadeh, M., 1987, "Modeling and Measurements of Heatspreader Thermal Performance in Molded Plastic Packages," *Proceedings of the International Symposium on Cooling Technology for Electronic Equipment*, Honolulu, Hawaii, pp. 187–199.

Duncan, A. B., 1987, "Effective Thermal Conductivity of Packed Beds of Spheres," M. S. Thesis, Mechanical Engineering Department, Texas A&M University, College Station, TX.

Eid, J. C., and Antonetti, V. W., 1986, "Small Scale Thermal Contact Resistance of Aluminum Against Silicon," *Proceedings of the 8th International Heat Transfer Conference*, pp. 659–664.

Hegazy, A. A., 1985, "Thermal Joint Conductance of Conforming Rough Surfaces: Effects of Surface Microhardness Variation," Ph.D. Dissertation, University of Waterloo, Waterloo, Ontario, Canada.

Mahalingham, M., Nadhuker, M., Lofgran, L., Andrews, J., Olsen, D. R., and Berg, H. M., 1984, "Thermal Effects of Die Bond Voids in Metal, Ceramic and Plastic Packages," *Semiconductor International*, Sept., pp. 71–79.

Peterson, G. P., and Fletcher, L. S., 1987, "Thermal Contact Resistance of Silicon Chip Bonding Materials," *Proceedings of the International Symposium on Cooling Technology for Electronic Equipment*, Honolulu, Hawaii, pp. 438–449.

Pogson, J. T., and Franklin, J. L., 1973, "Analysis and Temperature Control of Hybrid Microcircuits," ASME Paper No. 73-ENAS-6.

Song, S., and Yovanovich, M. M., 1987, "Explicit Relative Contact Pressure Expression: Dependence Upon Surface Roughness Parameters and Vickers Microhardness Coefficients," presented at the AIAA 25th Aerospace Sciences Meeting, Paper No. AIAA-87-0152.

Yerman, A. J., Burgess, J. F., Carlson, R. O., and Neugebauer, C. A., 1983, "Hot Spots Caused by Voids and Cracks in the Chip Mountdown Medium in

Power Semiconductor Packaging," *IEEE Transactions on Components, Hybrids, and Manufacturing Technology*, Vol. 6, No. 4, pp. 455-461.

Yovanovich, M. M., Hegazy, A., and Antonetti, V. M., 1983, "Experimental Verification of Contact Conductance Models Based Upon Distributed Surface Microhardness," AIAA 21st Aerospace Sciences Meeting, Paper No. AIAA-83-0532.

## Modeling and Simulation of a Heat Regenerator in Cyclic Equilibrium With Radiation

**M. P. Di Marco[1] and F. F. Pironti[1]**

### Nomenclature

$a$ = specific surface area, $m^2/m^3$
$A'$ = absorption constant, $m^{-1}$
$B'$ = back-scattering absorption constant
$C_f$ = fluid heat capacity, J/kgK
$C_s$ = solid heat capacity, J/kgK
$h$ = fluid–solid heat transfer coefficient, $W/m^2K$
$I'$ = radiant heat flux density, forward direction, $W/m^2$
$J'$ = radiant heat flux density, backward direction, $W/m^2$
$L$ = regenerator length, m
$P$ = period length, s
$r$ = reflectivity, $r_0$ at $x' = 0$ and $r_L$ at $x' = L$
$t$ = time, s
$T'$ = solid temperature, K
$v$ = fluid average velocity in the axial direction, m/s
$x'$ = bed axial position, m
$\epsilon$ = emissivity, $\epsilon_0$ at $x' = 0$ and $\epsilon_L$ at $x' = L$
$\eta$ = regenerator thermal ratio
$\theta'$ = fluid temperature, K
$\xi$ = mean bed porosity
$\rho$ = density, $kg/m^3$
$\sigma$ = Stefan–Boltzmann constant, $W/m^2K^4$

### Introduction

Heat exchangers containing a heat storing mass are called "regenerators." The heat storing mass, usually formed of porous packing material, offers a large heat transfer surface to the fluids passing through it. Regenerators are reversed at fixed, usually regular, time intervals. The thermal storing mass removes heat from the hot fluid passing through it and after the reversal releases it to the cold fluid. The passages of the fluids, between which heat is exchanged, are separated in time but not spatially. Regenerators are clearly distinguished from recuperators by the fact that their operation depends not only on position but also on time, and an exact calculation is considerably more involved for regenerators than it is for recuperators. A comprehensive review article by Shah (1983) encompasses all aspects of regenerator theory. However, one finds that the radiation mechanism has not been directly considered, except as a part of the heat exchange coefficient (Razelos and Benjamin, 1978) or by including an apparent thermal solid conductivity involving a solid–solid–fluid contact radiation effect (Olalde et al., 1980). With a high fluid temperature, it would seem appropriate to consider radiation energy transfer directly into the model equations, as is done in this work. Furthermore, in view of the attention focused in the last few years on the use of a porous bed as a solid matrix for energy storage in solar applications, this work also considers the effect of void fraction on the various heat transfer mechanisms.

[1]Departamento de Termodinamica, Universidad Simon Bolivar, Caracas, Venezuela.

Contributed by the Heat Transfer Division for publication in the JOURNAL OF HEAT TRANSFER. Manuscript received by the Heat Transfer Division October 15, 1986. Keywords: Heat Exchangers, Heat Recovery, Radiation.

### Governing Equations

To represent the physical phenomena inside the regenerator, a heterogeneous system is considered and energy balances are taken around a differential volume of packed bed for the fluid and solid phases. The following simplifying assumptions are used in this work.

(*a*) No losses to the surroundings.
(*b*) Constant fluid and solid physical properties.
(*c*) The solid bed may be characterized by a constant bulk porosity.
(*d*) There are not internal temperature gradients in solid particles.
(*e*) No fluid phase axial dispersion or conduction takes place.
(*f*) Solid packing heat conduction in the direction of fluid flow is neglected.
(*g*) The effects of residual fluid during the reversal period are not considered.
(*h*) Constant fluid mass fluxes at each period and in plug flow.
(*i*) The convective heat transfer coefficient does not include radiation and it varies only with bed porosity.
(*j*) Fluids are transparent to radiation. The radiant heat transfer in the porous bed is carried out by transmission through the void space, by reflection, by absorption, and by reradiation. The medium is treated as an isotropic continuous material, and the radiant energy transfer through it is described by the two-flux model (Hamaker, 1947; Chen and Churchill, 1963), where the dispersed and reradiated energy is propagated only in the positive and negative axial directions.

Then, the governing equations are in dimensionless form

$$\partial T/\partial \tau = A(I+J) - ACT^4 - T + D + (1-D)\theta \quad (1)$$

$$R\partial\theta/\partial\tau = (T-D)/(1-D) - \theta - (1/\Lambda)\partial\theta/\partial x \quad (2)$$

$$\partial I/\partial x = -(A+B)I + BJ + CAT^4/2 \quad (3)$$

$$\partial J/\partial x = (A+B)J - BI - CAT^4/2 \quad (4)$$

where $T = T'/\theta'_{hi}$ and $\theta = (\theta' - \theta'_{ci})/(\theta'_{hi} - \theta'_{ci})$ are the dimensionless solid and fluid temperatures, respectively; $I = I'/haL\theta'_{hi}$ and $J = J'/haL\theta'_{hi}$ are the dimensionless forward and backward radiant heat fluxes, respectively; $A = A'L$ and $B = B'L$ are dimensionless absorption and back-scattering constants; $C = 2\sigma\theta'^3_{hi}/haL$ is reduced emission coefficient, $D = \theta'_{ci}/\theta'_{hi}$ is the ratio of cold to hot inlet fluid temperatures; $R = \rho_f C_f \xi/\rho_s C_s(1-\xi)$ is a ratio of volume heat capacities, $\tau = hat/(1-\xi)\rho_s C_s$ and $x = x'/L$ are the dimensionless time and position, respectively; and $\Lambda = hLa/\xi\rho_f C_f$ is the reduced bed length.

Associated boundary conditions are constant fluid inlet temperatures, and cyclic steady state is reached when the solid and fluid temperature profiles along the regenerator at any time during the cycle are repeated during the next and subsequent cycles; then

$$\theta = 1, \quad x = 0, \quad N \le \tau \le N + \Pi_h \quad (5)$$

$$\theta = 0, \quad x = 1, \quad N + \Pi_h \le \tau \le N + \Pi_h + \Pi_c \quad (6)$$

$$I = C\epsilon_0 T^4/2 + r_0 J, \quad x = 0, \quad N \le \tau \le N + \Pi_h + \Pi_c \quad (7)$$

$$J = C\epsilon_L T^4/2 + r_L I, \quad x = 1, \quad N \le \tau \le N + \Pi_h + \Pi_c \quad (8)$$

Power Semiconductor Packaging," *IEEE Transactions on Components, Hybrids, and Manufacturing Technology*, Vol. 6, No. 4, pp. 455-461.

Yovanovich, M. M., Hegazy, A., and Antonetti, V. M., 1983, "Experimental Verification of Contact Conductance Models Based Upon Distributed Surface Microhardness," AIAA 21st Aerospace Sciences Meeting, Paper No. AIAA-83-0532.

## Modeling and Simulation of a Heat Regenerator in Cyclic Equilibrium With Radiation

**M. P. Di Marco[1] and F. F. Pironti[1]**

### Nomenclature

$a$ = specific surface area, $m^2/m^3$
$A'$ = absorption constant, $m^{-1}$
$B'$ = back-scattering absorption constant
$C_f$ = fluid heat capacity, J/kgK
$C_s$ = solid heat capacity, J/kgK
$h$ = fluid–solid heat transfer coefficient, $W/m^2K$
$I'$ = radiant heat flux density, forward direction, $W/m^2$
$J'$ = radiant heat flux density, backward direction, $W/m^2$
$L$ = regenerator length, m
$P$ = period length, s
$r$ = reflectivity, $r_0$ at $x' = 0$ and $r_L$ at $x' = L$
$t$ = time, s
$T'$ = solid temperature, K
$v$ = fluid average velocity in the axial direction, m/s
$x'$ = bed axial position, m
$\epsilon$ = emissivity, $\epsilon_0$ at $x' = 0$ and $\epsilon_L$ at $x' = L$
$\eta$ = regenerator thermal ratio
$\theta'$ = fluid temperature, K
$\xi$ = mean bed porosity
$\rho$ = density, $kg/m^3$
$\sigma$ = Stefan–Boltzmann constant, $W/m^2K^4$

### Introduction

Heat exchangers containing a heat storing mass are called "regenerators." The heat storing mass, usually formed of porous packing material, offers a large heat transfer surface to the fluids passing through it. Regenerators are reversed at fixed, usually regular, time intervals. The thermal storing mass removes heat from the hot fluid passing through it and after the reversal releases it to the cold fluid. The passages of the fluids, between which heat is exchanged, are separated in time but not spatially. Regenerators are clearly distinguished from recuperators by the fact that their operation depends not only on position but also on time, and an exact calculation is considerably more involved for regenerators than it is for recuperators. A comprehensive review article by Shah (1983) encompasses all aspects of regenerator theory. However, one finds that the radiation mechanism has not been directly considered, except as a part of the heat exchange coefficient (Razelos and Benjamin, 1978) or by including an apparent thermal solid conductivity involving a solid–solid–fluid contact radiation effect (Olalde et al., 1980). With a high fluid temperature, it would seem appropriate to consider radiation energy transfer directly into the model equations, as is done in this work. Furthermore, in view of the attention focused in the last few years on the use of a porous bed as a solid matrix for energy storage in solar applications, this work also considers the effect of void fraction on the various heat transfer mechanisms.

[1]Departamento de Termodinamica, Universidad Simon Bolivar, Caracas, Venezuela.

Contributed by the Heat Transfer Division for publication in the JOURNAL OF HEAT TRANSFER. Manuscript received by the Heat Transfer Division October 15, 1986. Keywords: Heat Exchangers, Heat Recovery, Radiation.

### Governing Equations

To represent the physical phenomena inside the regenerator, a heterogeneous system is considered and energy balances are taken around a differential volume of packed bed for the fluid and solid phases. The following simplifying assumptions are used in this work.

(*a*) No losses to the surroundings.
(*b*) Constant fluid and solid physical properties.
(*c*) The solid bed may be characterized by a constant bulk porosity.
(*d*) There are not internal temperature gradients in solid particles.
(*e*) No fluid phase axial dispersion or conduction takes place.
(*f*) Solid packing heat conduction in the direction of fluid flow is neglected.
(*g*) The effects of residual fluid during the reversal period are not considered.
(*h*) Constant fluid mass fluxes at each period and in plug flow.
(*i*) The convective heat transfer coefficient does not include radiation and it varies only with bed porosity.
(*j*) Fluids are transparent to radiation. The radiant heat transfer in the porous bed is carried out by transmission through the void space, by reflection, by absorption, and by reradiation. The medium is treated as an isotropic continuous material, and the radiant energy transfer through it is described by the two-flux model (Hamaker, 1947; Chen and Churchill, 1963), where the dispersed and reradiated energy is propagated only in the positive and negative axial directions.

Then, the governing equations are in dimensionless form

$$\partial T/\partial \tau = A(I+J) - ACT^4 - T + D + (1-D)\theta \tag{1}$$

$$R\partial\theta/\partial\tau = (T-D)/(1-D) - \theta - (1/\Lambda)\partial\theta/\partial x \tag{2}$$

$$\partial I/\partial x = -(A+B)I + BJ + CAT^4/2 \tag{3}$$

$$\partial J/\partial x = (A+B)J - BI - CAT^4/2 \tag{4}$$

where $T = T'/\theta'_{hi}$ and $\theta = (\theta' - \theta'_{ci})/(\theta'_{hi} - \theta'_{ci})$ are the dimensionless solid and fluid temperatures, respectively; $I = I'/haL\theta'_{hi}$ and $J = J'/haL\theta'_{hi}$ are the dimensionless forward and backward radiant heat fluxes, respectively; $A = A'L$ and $B = B'L$ are dimensionless absorption and back-scattering constants; $C = 2\sigma\theta'^3_{hi}/haL$ is reduced emission coefficient, $D = \theta'_{ci}/\theta'_{hi}$ is the ratio of cold to hot inlet fluid temperatures; $R = \rho_f C_f \xi/\rho_s C_s(1-\xi)$ is a ratio of volume heat capacities, $\tau = hat/(1-\xi)\rho_s C_s$ and $x = x'/L$ are the dimensionless time and position, respectively; and $\Lambda = hLa/\xi\rho_f C_f$ is the reduced bed length.

Associated boundary conditions are constant fluid inlet temperatures, and cyclic steady state is reached when the solid and fluid temperature profiles along the regenerator at any time during the cycle are repeated during the next and subsequent cycles; then

$$\theta = 1, \quad x = 0, \quad N \le \tau \le N + \Pi_h \tag{5}$$

$$\theta = 0, \quad x = 1, \quad N + \Pi_h \le \tau \le N + \Pi_h + \Pi_c \tag{6}$$

$$I = C\epsilon_0 T^4/2 + r_0 J, \quad x = 0, \quad N \le \tau \le N + \Pi_h + \Pi_c \tag{7}$$

$$J = C\epsilon_L T^4/2 + r_L I, \quad x = 1, \quad N \le \tau \le N + \Pi_h + \Pi_c \tag{8}$$

where $\Pi = haP/(1 - \xi)\rho sCs$ is the reduced period and $N = n(\Pi_h + \Pi_C)$, $n$ being an integer.

## Numerical Procedure

The orthogonal collocation method was applied to equations (1)–(8) in order to convert the above system of partial differential equations into an initial value problem. The method assumes as solution a series of orthogonal Jacobi polynomials where the collocation points are the roots of these polynomials and the dependent variables are the solution values precisely at these points. Convergency trials indicated that six collocation points were sufficient for this problem. The numerical procedure was implemented in a Basic language written program, run on an HP-87 microcomputer and consisting of the following steps:

(*a*) Initial profiles were assumed for the solid and fluid phases.

(*b*) The Gauss elimination method was applied to solve the reduced algebraic system.

(*c*) Temperature values were calculated by a Gear's predictor-corrector method.

(*d*) It was checked, after a cycle, whether final temperature profiles obtained for the solid and fluid are equal to values assumed in (*a*). A maximum error of 0.1 percent was allowed; otherwise the cycle was restarted with the last calculated values.

The values fixed for the dimensionless parameters defined above needed for the model simulation are given in Table 1 for five cases. Typical values for the absorption and dispersion coefficients, per unit of packed bed volume, were taken from the experimental work of Chen and Churchill (1963). Remaining values were estimated by assuming spherical particles of 3 mm in diameter with an initial bed porosity of 0.35 and a bed length of 5 m. Time-averaged fluid outlet temperatures, $\theta'_{hm}$ for the hot and $\theta'_{cm}$ for the cold periods, were calculated by numerical integration and used for the computation of thermal effectiveness or ratio, $\eta_h = (\theta'_{hi} - \theta'_{hm})/(\theta'_{hi} - \theta'_{ci})$ and $\eta_c = (\theta'_{cm} - \theta'_{ci})/(\theta'_{hi} - \theta'_{ci})$.

## Results and Discussion

Hausen (1983) proposed that the thermal ratio of a regenerator be represented only by two parameters, reduced length $\Delta$ and reduced period $\Pi$. The first one is a measure of size of the regenerator relative to the thermal load imposed by the mass flow rate of the heating or cooling fluids, while the latter is a measure of period length relative to the heat capacity of the packing and the available surface area. In general terms, the larger the reduced length and the smaller the reduced period, the greater the effectiveness of the regenerator. Hausen (1983) has produced a chart for $\eta = \eta_h = \eta_c$ over the range $0 \leq \Lambda \leq 50$, valid for symmetric balanced systems, where $\Lambda_h = \Lambda_c = \Delta$ and $\Pi_h = \Pi_c = \Pi$. When $\Lambda_h/\Pi_h \neq \Lambda_c/\Pi_c$, then the regenerator is said to be unbalanced and the thermal ratios are not equal. Hausen (1983) considers the use of "harmonic means" defined as $1/\Pi_{\text{harmonic}} = (1/\Pi_h + 1/\Pi_c)/2$ and $1/\Lambda_{\text{harmonic}} = (\Pi_h/\Lambda_h + \Pi_c/\Lambda_c)/2\Pi_{\text{harmonic}}$ to characterize the equilibrium condition in terms of a symmetric system. Analytical solutions can be found for balanced systems; however, for unbalanced systems most of the published results are numerical, the main reason for this study being to analyze five cases for an unbalanced regenerator.

**Table 1 Parameter values for model simulation**

| Case | $\Delta_h$ | $\Delta_c$ | $\Pi_h$ | $\Pi_c$ | $A$ | $B$ | $C$ | $D$ |
|---|---|---|---|---|---|---|---|---|
| 1 | 45 | 35 | 1.2 | 1.9 | 6.1 | 7054 | 0.49 | 3.4 |
| 2 | 45 | 89 | 1.2 | 1.9 | 6.1 | 7054 | 0.49 | 3.4 |
| 3 | 45 | 55 | 1.2 | 1.9 | 6.1 | 7054 | 0.49 | 3.4 |
| 4 | 45 | 89 | 1.2 | 1.9 | 11.3 | 3609 | 0.91 | 1.65 |
| 5 | 45 | 89 | 1.2 | 1.9 | 3.9 | 11319 | 0.14 | 2.05 |

### (*a*) Numerical Results Without Radiation

(*a1*) *Unbalanced Systems and a Very Low Value for the Fluid-Solid Heat Capacity Ratio* ($R = 0.001$). If one integrates in space and time equations (1) and (2) (excluding radiation and neglecting the fluid heat capacity), and takes into account the cyclic equilibrium conditions, then an expression relating the thermal ratios is obtained: $(\Pi_h/\Lambda_h)\eta_h = (\Pi_c/\Lambda_c)\eta_c$. One may further apply the approximate method described by Shah (1985) in order to obtain the unbalanced thermal ratios from a balanced one by using the above defined harmonic means. This is done as shown in Table 2, where corresponding approximate values are compared with numerical results obtained in this work for cases 1, 2, and 3 of Table 1 and for $R = 0.001$. In general, all values obtained are in agreement.

(*a2*) *Unbalanced Systems and High Values for the Fluid-Solid Heat Capacity Ratio* ($0.3 \leq R \leq 0.86$). In Hausen's approach to the theory of thermal regenerators, the $R$ parameter does not appear since for a gas-solid system it would be very small. The number $R$ represents the fluid to solid heat capacity or relaxation time ratio and it can be significant for different kind of packed beds. For instance, $R$ values may vary from 1 for water, to 0.3 for iron-sodium, to 0.001 for air packed beds. Because of the importance of new systems for solar energy storage (particularly packed beds of iron spheres with liquid sodium coolant for solar central receiver power plants, and also packed beds with water as a fluid for storage in adsorbent materials), a range of $R$ values between 0.3 and 0.86 was also used for the simulation. Thermal ratios for these cases are also shown in Table 2, where now differences are observed when compared with the corresponding low heat capacity ratio.

(*b*) *Numerical Results With Radiation. Influence of Radiation Parameters and Bed Porosity.* Numerical simulations were done for cases 2, 4, and 5 of Table 1, whereby radiation parameters were the only values changed while others were kept constant and equal to case 2, and compared with results obtained for same runs but solving without radiation. Little difference in temperature profiles and thermal ratios was observed. It seems that for this range of values used the radiation process does not constitute the predominant mechanism for heat transfer. The effect of bed porosity was also considered, taking into account that changes in $\xi$ will affect simultaneously radiation and convection processes. It was

**Table 2 Comparison of model predictions for an unbalanced system without radiation**

| | Case 1 | | Case 2 | | Case 3 | |
|---|---|---|---|---|---|---|
| $\Lambda_{\text{harmonic}}$ | 36.32 | | 61.23 | | 48.03 | |
| $\Pi_{\text{harmonic}}$ | 1.47 | | 1.47 | | 1.47 | |
| $R_h$ | 0.001 | 0.30 | 0.001 | 0.45 | 0.001 | 0.40 |
| $R_c$ | 0.001 | 0.86 | 0.001 | 0.30 | 0.001 | 0.50 |
| $\eta_h$ | 0.991 | 0.999* 0.997 | 0.796 | 0.789* 0.995 | 0.999 | 0.999* 0.999 |
| $\eta_c$ | 0.504 | 0.496* 0.952 | 0.999 | 0.999* 0.984 | 0.786 | 0.780* 0.931 |

*Calculated by the approximate method.

**Table 3 Variation of regenerator thermal ratio with bed porosity**

| | Without radiation | With radiation |
|---|---|---|
| $\xi = 0.35$ | 0.976 | 0.983 |
| $\xi = 0.40$ | 0.900 | 0.920 |
| $\xi = 0.60$ | 0.897 | 0.967 |
| $\xi = 0.80$ | 0.825 | 0.974 |

assumed that the heat transfer coefficient for a porous bed varied proportional to $((1 - \xi)/\xi^2)^{1.6}$ according to Olalde et al. (1980). Also, the dispersion coefficient $B$ was assumed to be proportional to the solid fraction in the bed $(1 - \xi)$, following Flamant (1982); and making use of Chen and Churchill (1963) work, a relation for $A$ and $C$ parameters was deduced such that $C$ was found to be proportional to $\xi^{3.2}A/(1 - \xi)^{2.6}$. The specific surface area $a$ was supposed to vary with $(1 - \xi)$ since the characteristic length of the particle would be unchanged. From the above analysis, one would expect the following variations for the reduced length and period:

$$\Lambda \propto (1-\xi)^{2.6}/\xi^{4.2} \text{ and } \Pi \propto ((1-\xi)/\xi^2)^{1.6} \quad (9)$$

In Table 3, thermal ratios are shown for four different values of bed porosity with and without radiation. An apparent minimum is observed on the thermal ratio for $\xi = 0.4$, wheres no minimum is present when radiation is not accounted for. It seems from these results that the convection-conduction mechanism is predominant at low bed porosity while radiation overtakes at higher porosity.

### References


Chen, J. C., and Churchill, S. W., 1963, "Radiant Heat Transfer in Packed Beds," *AIChE Journal*, Vol. 9, pp. 35-41.

Flamant, G., 1982, "Theoretical and Experimental Study of Radiant Heat Transfer in a Solar Fluidized-Bed Receiver," *AIChE Journal*, Vol. 28, pp. 529-535.

Hamaker, H. C., 1947, "Radiation and Heat Conduction in Light-Scattering Material," *Philips Res. Rep.*, Vol. 2, pp. 55-67.

Hausen, H., 1983, *Heat Transfer in Counterflow, Parallel Flow and Cross Flow*, McGraw-Hill, New York, pp. 291-463.

Olalde, G., Peube, J. L., and Daguenet, M., 1980, "Theoretical Study of Gas Heated in a Porous Material Subjected to a Concentrated Solar Radiation," *Revue de Physique Appliquee*, Vol. 15, pp. 423-426.

Razelos, P., and Benjamin, M. K., 1978, "Computer Model of Thermal Regenerators," *Int. J. Heat Mass Transfer*, Vol. 21, pp. 735-743.

Shah, R. K., 1985, "Heat Exchangers, Part 3," in: *Handbook of Heat Transfer Applications*, 2nd ed., W. N. Rohsenow, J. P. Hartnett, and E. N. Ganic, eds., McGraw-Hill, New York, pp. 4-188.


## The Effect of Heat Generation on the Convective Heat Transfer in a Tube of Elliptical Cross Section Maintained Under Constant Wall Temperature


**M. A. Ebadian,[1] H. C. Topakoglu,[2] and O. A. Arnas[3]**


### Introduction

The analysis of convective heat transfer within a pipe of elliptical cross section from Ebadian et al. (1985) is extended to the case of a heat-generating fluid. Using the method of successive approximations, the temperature distribution in any section of the pipe is obtained. On the basis of this temperature field, the Nusselt number is obtained as a function of the ellipticity $m$ of the cross section of the pipe, and the dimensionless heat generation number $\gamma$.

For the dimensionless heat generation number $\gamma = 3.01$ (Arnas et al., 1985), the variation of Nusselt number with the ellipticity of the cross section is plotted and compared with the case of no heat generation. A further comparison is made between the ratio of Nusselt number for the case with heat generation ($\gamma = 3.01$) to the Nusselt number for the case of no heat generation ($\gamma = 0.0$).

### Energy Equation

The steady-state energy equation where viscous dissipation and axial heat conduction are negligible is given by Ebadian et al. (1986) as

$$\left(\frac{T_0 - T}{T_0 - T_m}\right) W \frac{dT_m}{dZ} = \alpha\left(\frac{\partial^2 \bar{T}}{\partial X^2} + \frac{\partial^2 \bar{T}}{\partial Y^2} + \frac{H}{k}\right) \quad (1)$$

where

$X$, $Y$ are the rectangular coordinates in the cross section of the pipe, m
$Z$ is the coordinate along the pipe, m
$\bar{T}$ is the temperature under constant wall temperature condition, K
$T$ is the temperature under constant wall heat flux condition, K
$T_0$ is the wall temperature, K
$T_m$ is the mixed mean temperature, K
$\alpha$ is the thermal diffusivity, $m^2/s$
$k$ is the thermal conductivity W/m-K
$W$ is the velocity along the pipe, m/s
$H$ is the heat generation volume density, $W/m^3$

The semi-major and semi-minor axes of the elliptic section are denoted by A and B, respectively, and the mean semi-axis

$$L = \frac{1}{2}(A + B) \quad (2)$$

is chosen as the reference length; the following dimensionless variables, lower case letters, are introduced

$$X = Lx, \quad Y = Ly, \quad Z = Lz, \quad W = \frac{\nu}{L}w, \quad H = \frac{F}{L}h \quad (3)$$

where $F$ denotes an arbitrary reference heat flux and $\nu$ is the kinematic viscosity of the fluid.

The dimensionless velocity in an elliptic pipe expressed in elliptic coordinates is (Ebadian et al., 1986)

$$w = (\mathrm{Re})(w_0 - w_2 \cos 2\eta) \quad (4)$$

with

$$w_0 = 1 + m^4 - \xi^2 - \frac{m^4}{\xi^2}, \quad w_2 = \frac{2m^2}{1 + m^4} w_0 \quad (5)$$

where $m$ is the ellipticity of the section given as

$$m = \left[\left(1 - \frac{B}{A}\right) \Big/ \left(1 + \frac{B}{A}\right)\right]^{1/2} \quad (6)$$

and $\xi$ and $\eta$ are nondimensional elliptic coordinates.

The Reynolds number Re involved in equation (4) is equivalent to that Reynolds number which would occur in a circular pipe of radius $L$ maintained under the same pressure gradient as that of the elliptic pipe (Topakoglu and Arnas, 1974).

### Temperature Distribution for Constant Wall Heat Flux Condition

The energy equation to be satisfied by $e$ in elliptic coordinates is (Topakoglu and Arnas, 1974)


[1]Department of Mechanical Engineering, Florida International University, The State University of Florida at Miami, Miami, FL 33199; Mem. ASME.

[2]Department of Mechanical Engineering, Southern University, Baton Rouge, LA 70813.

[3]Department of Mechanical Engineering, California State University, Sacramento, CA 95819; Fellow ASME.



Contributed by the Heat Transfer Division and presented at the ASME Winter Annual Meeting, Miami Beach, Florida, November 17-21, 1985. Manuscript received by the Heat Transfer Division January 2, 1986. Keywords: Enclosure Flows, Forced Convection, Nucleonics.

**Table 3 Variation of regenerator thermal ratio with bed porosity**

| | Without radiation | With radiation |
|---|---|---|
| $\xi = 0.35$ | 0.976 | 0.983 |
| $\xi = 0.40$ | 0.900 | 0.920 |
| $\xi = 0.60$ | 0.897 | 0.967 |
| $\xi = 0.80$ | 0.825 | 0.974 |

assumed that the heat transfer coefficient for a porous bed varied proportional to $((1 - \xi)/\xi^2)^{1.6}$ according to Olalde et al. (1980). Also, the dispersion coefficient $B$ was assumed to be proportional to the solid fraction in the bed $(1 - \xi)$, following Flamant (1982); and making use of Chen and Churchill (1963) work, a relation for $A$ and $C$ parameters was deduced such that $C$ was found to be proportional to $\xi^{3.2}A/(1 - \xi)^{2.6}$. The specific surface area $a$ was supposed to vary with $(1 - \xi)$ since the characteristic length of the particle would be unchanged. From the above analysis, one would expect the following variations for the reduced length and period:

$$\Lambda \propto (1-\xi)^{2.6}/\xi^{4.2} \text{ and } \Pi \propto ((1-\xi)/\xi^2)^{1.6} \quad (9)$$

In Table 3, thermal ratios are shown for four different values of bed porosity with and without radiation. An apparent minimum is observed on the thermal ratio for $\xi = 0.4$, wheres no minimum is present when radiation is not accounted for. It seems from these results that the convection-conduction mechanism is predominant at low bed porosity while radiation overtakes at higher porosity.

### References


Chen, J. C., and Churchill, S. W., 1963, "Radiant Heat Transfer in Packed Beds," *AIChE Journal*, Vol. 9, pp. 35-41.

Flamant, G., 1982, "Theoretical and Experimental Study of Radiant Heat Transfer in a Solar Fluidized-Bed Receiver," *AIChE Journal*, Vol. 28, pp. 529-535.

Hamaker, H. C., 1947, "Radiation and Heat Conduction in Light-Scattering Material," *Philips Res. Rep.*, Vol. 2, pp. 55-67.

Hausen, H., 1983, *Heat Transfer in Counterflow, Parallel Flow and Cross Flow*, McGraw-Hill, New York, pp. 291-463.

Olalde, G., Peube, J. L., and Daguenet, M., 1980, "Theoretical Study of Gas Heated in a Porous Material Subjected to a Concentrated Solar Radiation," *Revue de Physique Appliquee*, Vol. 15, pp. 423-426.

Razelos, P., and Benjamin, M. K., 1978, "Computer Model of Thermal Regenerators," *Int. J. Heat Mass Transfer*, Vol. 21, pp. 735-743.

Shah, R. K., 1985, "Heat Exchangers, Part 3," in: *Handbook of Heat Transfer Applications*, 2nd ed., W. N. Rohsenow, J. P. Hartnett, and E. N. Ganic, eds., McGraw-Hill, New York, pp. 4-188.


## The Effect of Heat Generation on the Convective Heat Transfer in a Tube of Elliptical Cross Section Maintained Under Constant Wall Temperature


**M. A. Ebadian,[1] H. C. Topakoglu,[2] and O. A. Arnas[3]**


### Introduction

The analysis of convective heat transfer within a pipe of elliptical cross section from Ebadian et al. (1985) is extended to the case of a heat-generating fluid. Using the method of successive approximations, the temperature distribution in any section of the pipe is obtained. On the basis of this temperature field, the Nusselt number is obtained as a function of the ellipticity $m$ of the cross section of the pipe, and the dimensionless heat generation number $\gamma$.

For the dimensionless heat generation number $\gamma = 3.01$ (Arnas et al., 1985), the variation of Nusselt number with the ellipticity of the cross section is plotted and compared with the case of no heat generation. A further comparison is made between the ratio of Nusselt number for the case with heat generation ($\gamma = 3.01$) to the Nusselt number for the case of no heat generation ($\gamma = 0.0$).

### Energy Equation

The steady-state energy equation where viscous dissipation and axial heat conduction are negligible is given by Ebadian et al. (1986) as

$$\left(\frac{T_0 - T}{T_0 - T_m}\right) W \frac{dT_m}{dZ} = \alpha\left(\frac{\partial^2 \bar{T}}{\partial X^2} + \frac{\partial^2 \bar{T}}{\partial Y^2} + \frac{H}{k}\right) \quad (1)$$

where

$X$, $Y$ are the rectangular coordinates in the cross section of the pipe, m
$Z$ is the coordinate along the pipe, m
$\bar{T}$ is the temperature under constant wall temperature condition, K
$T$ is the temperature under constant wall heat flux condition, K
$T_0$ is the wall temperature, K
$T_m$ is the mixed mean temperature, K
$\alpha$ is the thermal diffusivity, $m^2/s$
$k$ is the thermal conductivity W/m-K
$W$ is the velocity along the pipe, m/s
$H$ is the heat generation volume density, $W/m^3$

The semi-major and semi-minor axes of the elliptic section are denoted by A and B, respectively, and the mean semi-axis

$$L = \frac{1}{2}(A + B) \quad (2)$$

is chosen as the reference length; the following dimensionless variables, lower case letters, are introduced

$$X = Lx, \quad Y = Ly, \quad Z = Lz, \quad W = \frac{\nu}{L}w, \quad H = \frac{F}{L}h \quad (3)$$

where $F$ denotes an arbitrary reference heat flux and $\nu$ is the kinematic viscosity of the fluid.

The dimensionless velocity in an elliptic pipe expressed in elliptic coordinates is (Ebadian et al., 1986)

$$w = (\mathrm{Re})(w_0 - w_2 \cos 2\eta) \quad (4)$$

with

$$w_0 = 1 + m^4 - \xi^2 - \frac{m^4}{\xi^2}, \quad w_2 = \frac{2m^2}{1 + m^4} w_0 \quad (5)$$

where $m$ is the ellipticity of the section given as

$$m = \left[\left(1 - \frac{B}{A}\right) \Big/ \left(1 + \frac{B}{A}\right)\right]^{1/2} \quad (6)$$

and $\xi$ and $\eta$ are nondimensional elliptic coordinates.

The Reynolds number Re involved in equation (4) is equivalent to that Reynolds number which would occur in a circular pipe of radius $L$ maintained under the same pressure gradient as that of the elliptic pipe (Topakoglu and Arnas, 1974).

### Temperature Distribution for Constant Wall Heat Flux Condition

The energy equation to be satisfied by $e$ in elliptic coordinates is (Topakoglu and Arnas, 1974)


[1] Department of Mechanical Engineering, Florida International University, The State University of Florida at Miami, Miami, FL 33199; Mem. ASME.

[2] Department of Mechanical Engineering, Southern University, Baton Rouge, LA 70813.

[3] Department of Mechanical Engineering, California State University, Sacramento, CA 95819; Fellow ASME.



Contributed by the Heat Transfer Division and presented at the ASME Winter Annual Meeting, Miami Beach, Florida, November 17-21, 1985. Manuscript received by the Heat Transfer Division January 2, 1986. Keywords: Enclosure Flows, Forced Convection, Nucleonics.

$$\left(\frac{\partial^2}{\partial t^2}+\frac{\partial^2}{\partial \eta^2}\right)e=-h(x_2-2m^2\cos 2\eta)$$
$$+G(E_0-E_2\cos 2\eta+E_4\cos 4\eta) \quad (7)$$

with

$$G=c\mathrm{Pe}$$
$$E_0=x_2w_0+m^2w_2$$
$$E_2=2m^2w_0+x_2w_2 \quad (8)$$
$$E_4=m^2w_2$$
$$x_2=\xi^2+\frac{m^4}{\xi^2}$$

where $c$ is the dimensionless temperature gradient in the longitudinal direction and Pe is the Peclet number.

The solution of the differential equation (7) using the boundary condition $e=0$ for $\xi=1$ is

$$e=h(f_0+f_2\cos 2\eta)+G(e_0+e_2\cos 2\eta+e_4\cos 4\eta) \quad (9)$$

where

$$f_0=\frac{1}{4}(1+m^4-x_2)$$
$$f_2=-\frac{1}{2}m^2\left(1-\frac{1}{1+m^4}x_2\right)$$
$$e_0=-\frac{1}{16}\left[3(1+m^8)-4\frac{1+m^8}{1+m^4}x_2+x_4\right] \quad (10)$$
$$e_2=\frac{1}{6}\frac{m^2}{1+m^4}\left[3(1+m^8)-4\frac{1+m^8}{1+m^4}x_2+x_4\right]$$
$$e_4=-\frac{1}{24}\frac{m^4}{1+m^8}\left[x_4+3(1+m^8)-4\frac{1+m^8}{1+m^4}x_2\right]$$

and

$$x_4=\xi^4+\frac{m^8}{\xi^4}$$

The mixed mean excess temperature $E_m$ for the temperature distribution, equation (9), is obtained from

$$E_m=T_m-T_0=\frac{\rho}{Q}\int_s W\,E\,dS \quad (11)$$

where $\rho$ is the density, $S$ and $dS$ are the full and elemental cross-sectional areas, respectively, and $Q$ is the mass rate of flow and is given as

$$Q=2\pi(\mu u)\,L\,\mathrm{Re}\,I_{oo} \quad (12)$$

where $\mu u$ is the coefficient of viscosity.

After some algebra, one obtains

$$E_m=-\frac{FL}{k}\frac{J}{I_{oo}} \quad (13)$$

where

$$I_{oo}=\frac{1}{4}\frac{(1-m^4)^3}{1+m^4}$$
$$J=h(J_6+J_8)+G(J_0+J_2+J_4) \quad (14)$$

and

$$J_0=\frac{1}{32}\frac{1-m^4}{1+m^4}(1+m^8)^2+\frac{5}{96}\frac{1-m^4}{1+m^4}(1+m^8)(1$$
$$+4m^4+m^8)-\frac{7}{128}(1-m^{16})$$
$$J_2=\frac{m^4}{(1+m^4)^2}\left[-\frac{1}{3}\frac{1-m^4}{1+m^4}(1+m^8)^2-\frac{5}{48}(1-m^{16})\right.$$
$$\left.+\frac{1}{9}\frac{1+m^8}{1+m^4}(1-3m^8+3m^4-m^{12})\right] \quad (15)$$

$$J_4=-\frac{7}{48}\frac{1-m^4}{1+m^4}m^8+\frac{1}{96}\frac{1-m^8}{1+m^8}m^8$$
$$+\frac{1}{24}\frac{1-m^8}{(1+m^4)^2}m^8-\frac{1}{144}\frac{1-m^4}{1+m^4}\frac{m^8}{1+m^8}(1+4m^4+m^8)$$
$$J_6=-\frac{1}{24}(1-m^4)(1+m^4+m^8)$$
$$J_8=-\frac{1}{6}m^4\frac{(1-m^4)^3}{(1+m^4)^2}-\frac{1}{8}\frac{m^4}{1+m^4}(1-m^8)$$

**Temperature Distribution for Constant Wall Temperature Condition**

Defining the dimensionless temperatures as

$$\bar{t}=\frac{k}{LF}\bar{T} \quad \text{and} \quad e_m=\frac{k}{LF}E_m \quad (16)$$

equation (1) combines with equation (9) to give

$$\left(\frac{\partial^2}{\partial t^2}+\frac{\partial^2}{\partial \eta^2}\right)\bar{t}=\frac{G^2}{e_m}\left\{E_0e_0-\frac{1}{2}E_2e_2+\frac{1}{2}E_4e_4\right.$$
$$+\frac{h}{G}\left(E_0f_0-\frac{1}{2}f_2\right)-\frac{e_m}{G}\frac{h}{G}x_2+\left[E_0e_2-E_2e_0-\frac{1}{2}E_2e_4\right.$$
$$\left.+\frac{1}{2}E_4e_2-\frac{h}{G}(E_2f_0-E_0f_2)+\frac{1}{4}E_4f_2+2\frac{e_m}{G}\frac{h}{G}m^2\right]\cos 2\eta$$
$$+\left[E_0e_4-\frac{1}{2}E_2e_2+E_4e_0+\frac{h}{G}\left(E_4f_0-\frac{1}{2}E_2f_2\right)\right]\cos 4\eta$$
$$\left.+\left[\frac{1}{2}E_4e_2-\frac{1}{2}E_2e_4+\frac{1}{2}\frac{h}{G}E_4f_2\right]\cos 6\eta+\frac{1}{2}E_4e_4\cos 8\eta\right\} \quad (17)$$

The solution satisfying the boundary condition

$$\bar{t}=0 \text{ for } \xi=1 \quad (18)$$

is obtained as

$$\bar{t}=\frac{G^2}{e_m}(a_0+a_2\cos 2\eta+a_4\cos 4\eta$$
$$+a_6\cos 6\eta+a_8\cos 8\eta) \quad (19)$$

where $a_0$, $a_2$, $a_4$, $a_6$, $a_8$ are given by Ebadian et al. (1985). These coefficients depend on the ellipticity $m$ and on the dimensionless number

$$\gamma=\frac{h}{G}=\frac{LH}{kc\mathrm{Pe}} \quad (20)$$

which will be called the heat generation number (Arnas et al., 1985).

The mixed mean temperature for $\bar{T}$ is

$$\bar{T}_m=\frac{\rho}{Q}\int_s W\bar{T}dS \quad (21)$$

After substituting equations (3), (16), and (19) into equation (21), equation (21) becomes

$$\bar{T}_m=-\frac{FL}{k}\frac{\bar{J}}{I_{oo}} \quad (22)$$

where

$$\bar{J}=-\frac{1}{2\pi(\mathrm{Re})}\int_0^{2\pi}\int_m^1 \xi j^2 w\bar{t}d\xi d\eta$$
$$j^2=\frac{1}{\xi^2}(x_2-2m^2\cos 2\eta) \quad (23)$$

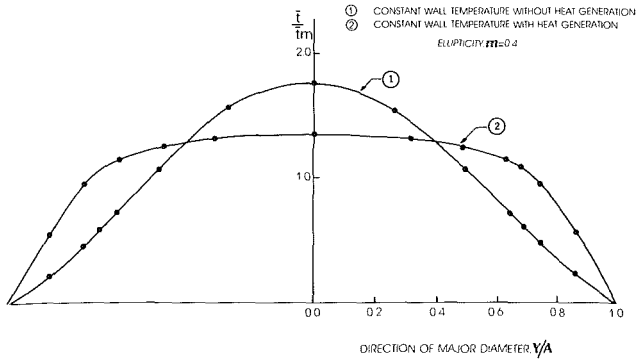


**Fig. 1 Temperature ratio distribution along major diameter**

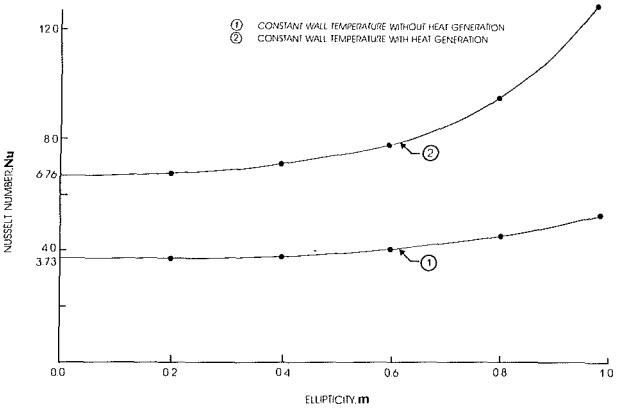


**Fig. 2 Nusselt number variation versus ellipticity factor**

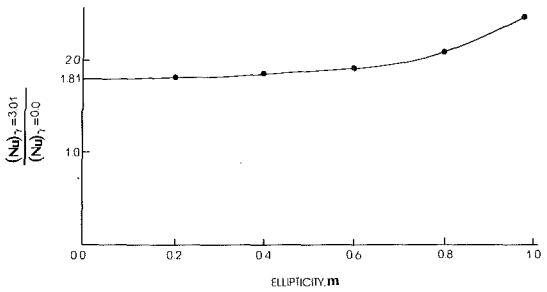


**Fig. 3 Nusselt number ratio versus ellipticity factor**

After some calculations and then grouping similar terms together, one obtains

$$\frac{\bar{J}}{G}=\frac{G}{e_m}(J_{01}+J_{21}+J_{41}) \tag{24}$$

in which the factors $J_{01}$, $J_{21}$, $J_{41}$ are expressions depending only on the ellipticity of the cross section and the heat generation number and are given by Ebadian et al. (1985).

Defining a dimensionless mixed mean temperature for $\bar{T}_m$ by

$$\bar{t}_m=\frac{k}{LF}\bar{T}_m \tag{25}$$

the dimensionless temperatures can now be expressed by

$$\left(\frac{\bar{T}-T_0}{\bar{T}_m-T_0}\right) \text{ for constant wall temperature } = \frac{\bar{t}}{\bar{t}_m} \tag{26}$$

In Fig. 1, we have plotted equation (26) when the heat generation number is $\gamma=3.01$ and the ellipticity is $m=0.4$. This corresponds to many practical nuclear engineering applications (Arnas et al., 1985).

The Nusselt number expression based on the hydraulic diameter of the elliptic section is obtained as

$$\mathrm{Nu}=\frac{D}{L}\frac{a_0'(1)}{J_{01}+J_{21}+J_{41}}I_{oo} \tag{27}$$

where

$$\frac{D}{L}=\frac{\pi^2(1-m^2)}{2(1+m^2)E_1^2} \tag{28}$$

The quantity $E_1$ in equation (28) is the complete elliptic integral of the second kind which is a function of the eccentricity, $2m(1+m^2)$, of the elliptic periphery.

The other factor in equation (27) is

$$a_0'(1)=\frac{1}{8}[2\bar{A}_{10}+\bar{B}_{10}(1+m^8)+2\bar{E}_{10}](1-m^8)$$

$$-\frac{1}{2}(m^4\bar{C}_{10}+\bar{D}_{10})(1-m^4)-\frac{1}{6}\bar{C}_{10}(1-m^{12})$$

$$+\gamma\left[\frac{1}{2}(\bar{B}_{100}+m^4\bar{D}_{100})(1-m^4)-\frac{1}{4}(\bar{A}_{100}+\bar{C}_{100})(1-m^8)\right.$$

$$\left.+\frac{1}{6}\bar{D}_{100}(1-m^{12})-\frac{1}{2}\frac{(e_m)_{\mathrm{CHF}}}{G}(1-m^4)\right] \tag{29}$$

where $(e_m)_{\mathrm{CHF}}$ refers to the constant heat flux and the factors $\bar{A}_{10}$, $\bar{B}_{10}$, $\bar{C}_{10}$, $\bar{D}_{10}$, $\bar{E}_{10}$, $\bar{A}_{100}$, $\bar{B}_{100}$, $\bar{C}_{100}$, $\bar{D}_{100}$ are given by Ebadian et al. (1985).

The Nusselt number given in equation (27) is the result of the first successive approximation of the convective heat transfer problem for constant wall temperature condition. Further successive approximation will make the result more accurate. A check of Nusselt number for the almost circular case is found as 3.7288. If $m$ is taken as zero, this will approach the well-known value of 3.6568. Also, it was observed by Ebadian et al. (1986) that in the case of no heat generation, the first iteration produces a very satisfactory solution. It is assumed that this is still true for the problem with heat generation.

## Discussion and Remarks

It is found that the temperature distribution over the cross section and the Nusselt number at the wall depend on two parameters:

(*i*) the ellipticity of the cross section $m$; and
(*ii*) the heat generation number $\gamma$.

In Fig. 1, representative curves for the temperature profiles plotted along the major diameter of the cross section of the pipe illustrate the temperature distributions with no heat generation. When heat generation is included, the temperature varies less over the cross section of the pipe than the case of no heat generation. It must be noted that the temperature ratio for each curve is in reference to its own bulk temperature. Therefore, the two curves in each figure cannot be compared to each other directly.

Figure 2, which shows the variation of the Nusselt number with the ellipticity of the section for $\gamma=3.01$, includes another curve corresponding to the case of no heat generation. The quantitative increase of Nusselt number with the selected heat generation number can be obtained from Fig. 2 for any value of ellipticity $m$.

The effect of heat generation on the Nusselt number when $\gamma=3.01$ is presented in Fig. 3. It is found that the increase of Nusselt number for $\gamma=3.01$ is not very sensitive to the shape of the cross section. However, it increases slightly with ellipticity of the section. Figure 3 also shows that the Nusselt number with $\gamma=3.01$ is about two times larger than the Nusselt number with no heat generation. In the particular case of a circular section, $m=0$, the presence of heat generation causes an 81 percent increase in the Nusselt number for $\gamma=3.01$.

Table 1 Nusselt number with heat/generation ($\gamma = 0.0, 0.5, 1.0, 1.5, 2.0, 2.5, 3.01, 3.5, 4.0, 5.0$)

| Ellipticity m | Nusselt Number $\gamma = 0$ | $\gamma = 0.5$ | $\gamma = 1.0$ | $\gamma = 1.5$ | $\gamma = 2.0$ | $\gamma = 2.5$ | $\gamma = 3.01$ | $\gamma = 3.5$ | $\gamma = 4.0$ | $\gamma = 5.0$ | Pipe Flatness A/B |
|---|---|---|---|---|---|---|---|---|---|---|---|
| 0.00005 | 3.728805 | 5.038157 | 6.612230 | 6.820794 | 6.736606 | 6.632177 | 6.543418 | 6.475880 | 6.376955 | 6.310929 | 1.0000 |
| 0.20000 | 3.732506 | 5.099242 | 6.695199 | 6.898531 | 6.811865 | 6.706161 | 6.616561 | 6.548429 | 6.448641 | 6.382024 | 1.0833 |
| 0.40000 | 3.785217 | 5.769099 | 7.151921 | 7.242018 | 7.156838 | 7.069104 | 6.996649 | 6.941772 | 6.861138 | 6.806921 | 1.3810 |
| 0.60000 | 4.000550 | 7.635196 | 7.914338 | 7.877586 | 7.834785 | 7.801848 | 7.776612 | 7.757991 | 7.730933 | 7.712766 | 2.1250 |
| 0.80000 | 4.502069 | 9.431917 | 9.421855 | 9.416569 | 9.413567 | 9.411651 | 9.410304 | 9.409357 | 9.408034 | 9.407175 | 4.5556 |
| 0.98000 | 5.221236 | 12.834570 | 12.81456 | 12.80486 | 12.80126 | 12.80026 | 12.80025 | 12.80011 | 12.80009 | 12.80008 | 49.5051 |

Although Figs. 1, 2, and 3 use only $\gamma = 3.01$, the results are nevertheless conclusive, showing the effect of heat generation. Other values of $\gamma$ may be used for given situations, as given in Table 1.


### Acknowledgments

The results presented in this paper were obtained in the course of research sponsored by the National Science Foundation, Washington, DC under Grant No. R11-8305297.


### References


Arnas, O. A., Ebadian, M. A., and Topakoglu, H. C., 1985, "Convective Heat Transfer in Annular Tubes Carrying Radioactive Slurry," *Journal of Heat and Technology*, Vol. 3, No. 2, pp. 47-63.

Ebadian, M. A., Topakoglu, H. C., and Arnas, O. A., 1985, "The Effect of Heat Generation on the Convective Heat Transfer Within a Tube Having a Constant Wall Temperature and an Elliptic Cross Section," ASME Paper No. 85-WA/HT-57.

Ebadian, M. A., Topakoglu, H. C., and Arnas, O. A., 1986, "On the Convection Heat Transfer in a Tube of Elliptic Cross Section Maintained Under Constant Wall Temperature," ASME JOURNAL OF HEAT TRANSFER, Vol. 108, pp. 33-39.

Topakoglu, H. C., and Arnas, O. A., 1974, "Convective Heat Transfer for Steady Laminar Flow Between Two Confocal Elliptic Pipes With Longitudinal Uniform Wall Temperature Gradient," *Int. J. Heat Mass Transfer*, Vol. 17, pp. 1487-1498.


## Natural Convection Heat Transfer From a Discrete Thermal Source on a Channel Wall


**T. L. Ravine[1] and D. E. Richards[2]**


### Introduction

This paper presents the results of an experimental study of natural convection heat transfer from a discrete thermal source located on the wall of a vertical channel. This configuration has both an unheated inlet and outlet region and produces a confined wall plume, which rises between the parallel plates that form the channel walls.

In the present study, a thermal source of length $l$ was placed on one wall of a vertical channel formed by two plates of length $L$ separated a distance $b$ (Fig. 1). The thermal source was located a distance $d$ downstream of the channel inlet. The local distance $x$ along the plate was measured from the leading edge of the source. A dimensional analysis for this problem indicates that the local Nusselt number $Nu_x$ can be correlated in terms of the local Rayleigh number $Ra_x$, the Prandtl number Pr, a dimensionless distance $x/l$, and three geometric ratios, $L/l$, $d/l$, and $b/l$.

Most studies of natural convection in vertical channels have only considered cases with uniform thermal boundary conditions that extend over the entire surface, i.e., $L/l = 1$ and $d/l = 0$. A recent contribution in this area is the paper by Wirtz and Stutzman (1982).

Few studies have considered natural convection heat transfer from discrete thermal sources located on the wall of a vertical channel. Aung et al. (1973) measured the heat transfer from a uniform distribution of discrete thermal sources using vertical channels formed by printed circuit boards. Oosthuizen (1984) solved the governing equations for natural convection in a vertical channel with symmetric heating, $d/l = 0$, and an adiabatic extension at the channel exit, $L/l > 1$. Haaland and Sparrow (1983) obtained similar results in a numerical study of a channel plume and a parallel-walled chimney. Recently Wirtz and Haag (1985) examined the effect of an unheated entry length, $d/l > 0$, on natural convection between isothermal parallel plates. However, no studies are available that consider the effect of both an unheated inlet and an unheated outlet region.

### Experimental Apparatus

For the experiments, a channel was formed from two plates. The plate with the thermal source was 3.2 mm thick and measured $114.3 \times 304.8$ mm ($L \times w$). The thermal source consisted of a resistance heater, one-mil stainless steel shim stock, $12.7 \times 304.8$ mm ($l \times w$), mounted on a phenolic substrate. Upstream and downstream sections of the plate were constructed of balsa wood and epoxied to the phenolic. Unfortunately, this design did not give well-controlled boundary conditions because of conduction from the heater into the balsa wood sections. The other plate, also of balsa wood, was 6.4 mm thick and measured $114.3 \times 304.8$ mm. The total


[1]Graduate Research Associate, Department of Mechanical Engineering, The Ohio State University, Columbus, OH 43210; current address: Mechanical Engineer, M/A-COM Omni Spectra, Inc., Chandler, AZ 85226; Assoc. Mem. ASME.

[2]Assistant Professor, Department of Mechanical Engineering, The Ohio State University, Columbus, OH 43210; Assoc. Mem. ASME.



Contributed by the Heat Transfer Division and presented at the ASME Winter Annual Meeting, New Orleans, Louisiana, December 9-13, 1984. Manuscript received by the Heat Transfer Division August 28, 1985. Paper No. 84-WA/HT-90. Keywords: Electronic Equipment, Natural Convection, Plumes.

Table 1 Nusselt number with heat/generation ($\gamma = 0.0, 0.5, 1.0, 1.5, 2.0, 2.5, 3.01, 3.5, 4.0, 5.0$)

| Ellipticity m | Nusselt Number | | | | | | | | | | Pipe Flatness |
|---|---|---|---|---|---|---|---|---|---|---|---|
| | $\gamma = 0$ | $\gamma = 0.5$ | $\gamma = 1.0$ | $\gamma = 1.5$ | $\gamma = 2.0$ | $\gamma = 2.5$ | $\gamma = 3.01$ | $\gamma = 3.5$ | $\gamma = 4.0$ | $\gamma = 5.0$ | A/B |
| 0.00005 | 3.728805 | 5.038157 | 6.612230 | 6.820794 | 6.736606 | 6.632177 | 6.543418 | 6.475880 | 6.376955 | 6.310929 | 1.0000 |
| 0.20000 | 3.732506 | 5.099242 | 6.695199 | 6.898531 | 6.811865 | 6.706161 | 6.616561 | 6.548429 | 6.448641 | 6.382024 | 1.0833 |
| 0.40000 | 3.785217 | 5.769099 | 7.151921 | 7.242018 | 7.156838 | 7.069104 | 6.996649 | 6.941772 | 6.861138 | 6.806921 | 1.3810 |
| 0.60000 | 4.000550 | 7.635196 | 7.914338 | 7.877586 | 7.834785 | 7.801848 | 7.776612 | 7.757991 | 7.730933 | 7.712766 | 2.1250 |
| 0.80000 | 4.502069 | 9.431917 | 9.421855 | 9.416569 | 9.413567 | 9.411651 | 9.410304 | 9.409357 | 9.408034 | 9.407175 | 4.5556 |
| 0.98000 | 5.221236 | 12.834570 | 12.81456 | 12.80486 | 12.80126 | 12.80026 | 12.80025 | 12.80011 | 12.80009 | 12.80008 | 49.5051 |

Although Figs. 1, 2, and 3 use only $\gamma = 3.01$, the results are nevertheless conclusive, showing the effect of heat generation. Other values of $\gamma$ may be used for given situations, as given in Table 1.


### Acknowledgments

The results presented in this paper were obtained in the course of research sponsored by the National Science Foundation, Washington, DC under Grant No. R11-8305297.


### References


Arnas, O. A., Ebadian, M. A., and Topakoglu, H. C., 1985, "Convective Heat Transfer in Annular Tubes Carrying Radioactive Slurry," *Journal of Heat and Technology*, Vol. 3, No. 2, pp. 47-63.

Ebadian, M. A., Topakoglu, H. C., and Arnas, O. A., 1985, "The Effect of Heat Generation on the Convective Heat Transfer Within a Tube Having a Constant Wall Temperature and an Elliptic Cross Section," ASME Paper No. 85-WA/HT-57.

Ebadian, M. A., Topakoglu, H. C., and Arnas, O. A., 1986, "On the Convection Heat Transfer in a Tube of Elliptic Cross Section Maintained Under Constant Wall Temperature," ASME JOURNAL OF HEAT TRANSFER, Vol. 108, pp. 33-39.

Topakoglu, H. C., and Arnas, O. A., 1974, "Convective Heat Transfer for Steady Laminar Flow Between Two Confocal Elliptic Pipes With Longitudinal Uniform Wall Temperature Gradient," *Int. J. Heat Mass Transfer*, Vol. 17, pp. 1487-1498.


## Natural Convection Heat Transfer From a Discrete Thermal Source on a Channel Wall


**T. L. Ravine[1] and D. E. Richards[2]**


### Introduction

This paper presents the results of an experimental study of natural convection heat transfer from a discrete thermal source located on the wall of a vertical channel. This configuration has both an unheated inlet and outlet region and produces a confined wall plume, which rises between the parallel plates that form the channel walls.

In the present study, a thermal source of length $l$ was placed on one wall of a vertical channel formed by two plates of length $L$ separated a distance $b$ (Fig. 1). The thermal source was located a distance $d$ downstream of the channel inlet. The local distance $x$ along the plate was measured from the leading edge of the source. A dimensional analysis for this problem indicates that the local Nusselt number $Nu_x$ can be correlated in terms of the local Rayleigh number $Ra_x$, the Prandtl number Pr, a dimensionless distance $x/l$, and three geometric ratios, $L/l$, $d/l$, and $b/l$.

Most studies of natural convection in vertical channels have only considered cases with uniform thermal boundary conditions that extend over the entire surface, i.e., $L/l = 1$ and $d/l = 0$. A recent contribution in this area is the paper by Wirtz and Stutzman (1982).

Few studies have considered natural convection heat transfer from discrete thermal sources located on the wall of a vertical channel. Aung et al. (1973) measured the heat transfer from a uniform distribution of discrete thermal sources using vertical channels formed by printed circuit boards. Oosthuizen (1984) solved the governing equations for natural convection in a vertical channel with symmetric heating, $d/l = 0$, and an adiabatic extension at the channel exit, $L/l > 1$. Haaland and Sparrow (1983) obtained similar results in a numerical study of a channel plume and a parallel-walled chimney. Recently Wirtz and Haag (1985) examined the effect of an unheated entry length, $d/l > 0$, on natural convection between isothermal parallel plates. However, no studies are available that consider the effect of both an unheated inlet and an unheated outlet region.

### Experimental Apparatus

For the experiments, a channel was formed from two plates. The plate with the thermal source was 3.2 mm thick and measured $114.3 \times 304.8$ mm ($L \times w$). The thermal source consisted of a resistance heater, one-mil stainless steel shim stock, $12.7 \times 304.8$ mm ($l \times w$), mounted on a phenolic substrate. Upstream and downstream sections of the plate were constructed of balsa wood and epoxied to the phenolic. Unfortunately, this design did not give well-controlled boundary conditions because of conduction from the heater into the balsa wood sections. The other plate, also of balsa wood, was 6.4 mm thick and measured $114.3 \times 304.8$ mm. The total


[1]Graduate Research Associate, Department of Mechanical Engineering, The Ohio State University, Columbus, OH 43210; current address: Mechanical Engineer, M/A-COM Omni Spectra, Inc., Chandler, AZ 85226; Assoc. Mem. ASME.

[2]Assistant Professor, Department of Mechanical Engineering, The Ohio State University, Columbus, OH 43210; Assoc. Mem. ASME.



Contributed by the Heat Transfer Division and presented at the ASME Winter Annual Meeting, New Orleans, Louisiana, December 9-13, 1984. Manuscript received by the Heat Transfer Division August 28, 1985. Paper No. 84-WA/HT-90. Keywords: Electronic Equipment, Natural Convection, Plumes.

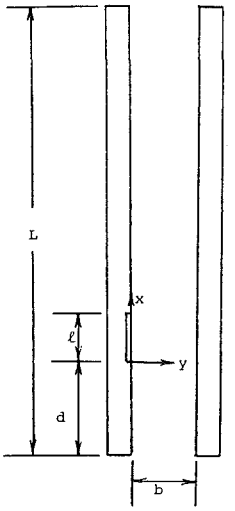


$$Pr = \frac{\nu}{\alpha}$$

$$Gr_x = \frac{g\beta}{\nu^2}(T_w - T_\infty)x^3$$

$$Ra_x = Gr_x Pr$$

Fig. 1 Vertical channel geometry

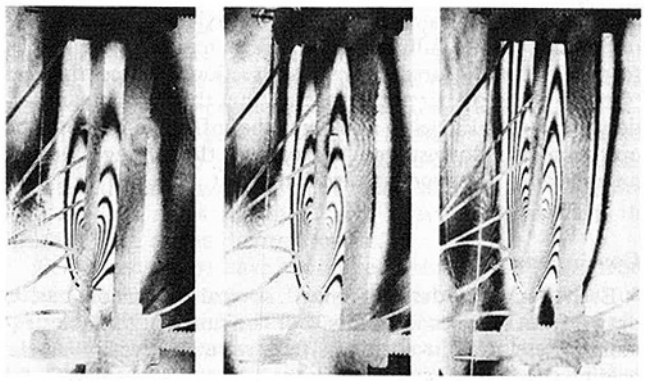

Fig. 2 Interferograms of a vertical channel with a finite-sized thermal source ($b/l = 0.508$, $L/l = 9.0$, $d/l = 2.0$): (a) $Ra_l = 2090$, (b) $Ra_l = 3583$, (c) $Ra_l = 6430$

length of the channel was $L = 114.3$ mm. To form the channel, holes were drilled at the four corners of each plate and the plates were bolted together. Channel spacing was maintained by gage blocks at each corner. The spacers and bolts obstructed approximately 6 percent of the inlet flow area at either end of the length traversed by the $z$ axis.

The channel was suspended from an overhead frame in the test beam of a Mach-Zehnder interferometer to insure that the inlet and outlet regions were unobstructed. Local temperatures and heat fluxes were obtained from infinite-fringe interferograms using standard techniques to reduce the data. Complete details of the experiments are presented in Ravine (1984). The uncertainty in the local and average Nusselt and Rayleigh numbers is ±8 percent with 95 percent confidence.

## Results

A series of runs were made with $b/l = 0.272$, 0.508, and 0.962 and $Ra_x < 7100$ to investigate the influence of plate spacing on heat transfer. The local Rayleigh number $Ra_x$ was defined in terms of the local wall-to-ambient temperature difference. In all of these runs $L/l = 9.00$ and $d/l = 2.00$. As discussed by Ravine and Richards (1988), the heat transfer from the heater when the channel spacing is very large, $b/l \gg 1$, can be predicted very accurately by assuming the heater is a vertical flat plate of length $l$ and using the local wall-to-ambient temperature difference.

Figure 2 shows a series of three interferograms with a constant channel spacing, $b/l = 0.508$, and increasing values of

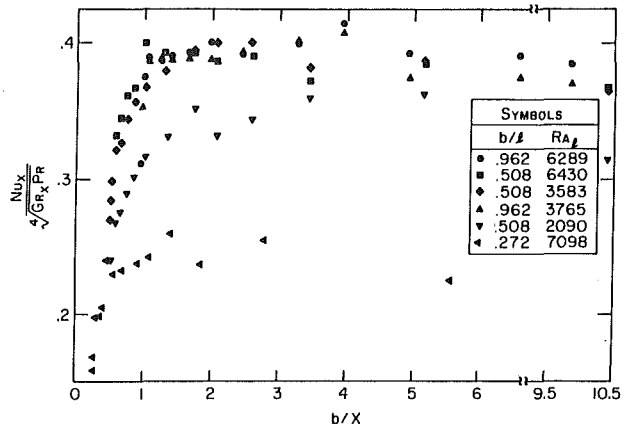


Fig. 3 Influence of channel width on local Nusselt numbers

$Ra_l$, the average Rayleigh number based on the area-averaged wall-to-ambient temperature difference and length $l$. Because the infinite-fringe setting was used for the interferometer, the fringes can be interpreted as isotherms. The temperature increases above the ambient value as the heater is approached. In Fig. 2, the plate with the heater forms the left wall of the channel. Because the heater plate was of a symmetric design, an external wall plume on the left side of the photographs is clearly visible. The channel inlet located at the bottom of the photograph is partially obstructed by the plate supports; however, the temperature in the inlet region is clearly the same as the ambient. The interferograms show that the channel walls are not truly adiabatic. Comparing Figs. 2(*a*), 2(*b*), and 2(*c*), it appears that beyond some value of $x/l$, which appears to increase with increasing $Ra_l$, the temperature profile across the channel is symmetric. If the walls were truly adiabatic and the channel were extended far enough, the symmetric profile would gradually decay until the fluid temperature in the channel was uniform at any $x$ position.

To quantify the effect of channel spacing, the measured values of $Nu_x Ra_x^{-1/4}$ for finite values of $b/l$ were plotted against the ratio $b/x$ in Fig. 3. The quantity $Nu_x Ra_x^{-1/4}$ is a constant for natural convection on a vertical flat plate, and the ratio $b/x$ represents the ratio of hydraulic diameter, i.e., channel spacing, to the distance measured from the leading edge of the source. This approach was used by Keutsch (1949) to examine the channel effect for natural convection between two symmetrically heated vertical, parallel plates.

For $b/x > 2$, the quantity $Nu_x Ra_x^{-1/4}$ approaches a limiting value for all the runs; however the limiting values all fall below the value of 0.412 for an isolated flat plate. This behavior supports the conclusion that near the leading edge of the heater a boundary-layer-type flow exists. The magnitude of the constant of proportionality between $Nu_x$ and $Ra_x^{-1/4}$ appears to be function of both $b/l$ and $Ra_l$. For $b/l = 0.962$ and 0.508, all the data follow similar trends and approach the same limiting value except for the case with the lowest Rayleigh number, $Ra_l = 2090$. For $b/l = 0.272$, the data fall significantly below the other cases. Comparing these results with the results for $b/l = 0.962$ at approximately the same Rayleigh number, it appears that the reduction is primarily due to decreased channel spacing. One possible explanation for this reduction is the increase in viscous drag that results when the channel spacing is decreased.

For $b/x < 2$, the values of $Nu_x Ra_x^{-1/4}$ decrease with decreasing $b/x$. At the smallest values of $b/x$ all of the data points appear to fall on a line with a slope of approximately 0.5. This type of behavior clearly demonstrates that as $b/x$ decreases the local heat transfer coefficient dependence on $x$ changes from an $x^{-1/4}$ relation characteristic of a boundary-layer to an $x^{-5/4}$

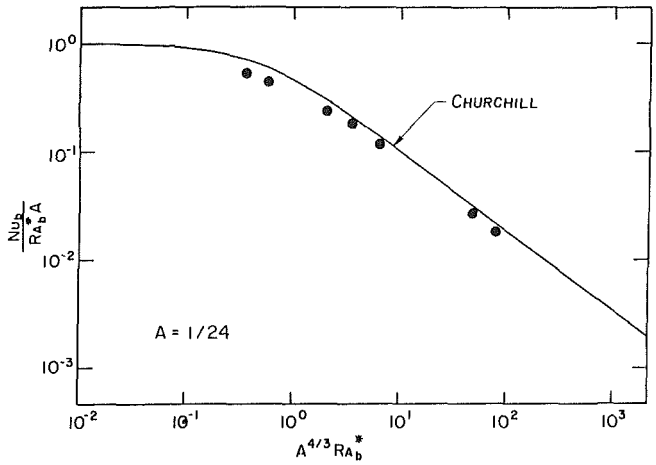


**Fig. 4 Comparison of measured average channel Nusselt numbers with Churchill's (1967) correlation**

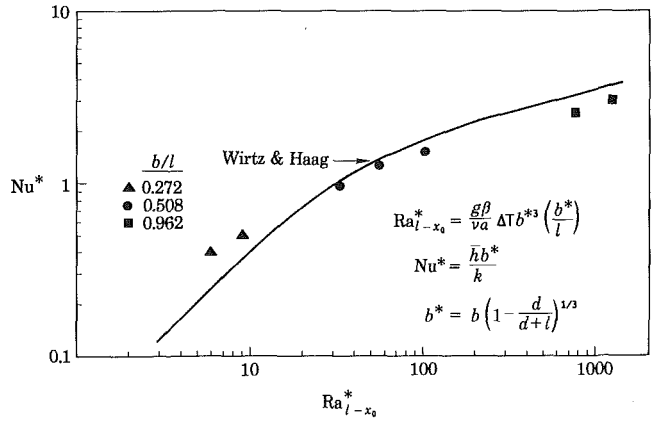


**Fig. 5 Comparison of measured average channel Nusselt numbers with Wirtz and Haag's (1985) correlation**

relation. This is another clear indication of the influence of channel spacing. Careful study of Fig. 3 also reveals that the value of $b/x$ where this transition begins to occur is approximately 1.5 and, for these experiments, is independent of $b/l$. Because $d/l$ and $L/l$ were constant for all the experiments, the dependence on these parameters is unknown.

In an attempt to come up with a predictive technique for this problem, the experimental data were compared with the correlation developed by Churchill (1967), which covers the complete range of flow regimes with isothermal boundary conditions

$$\frac{\mathrm{Nu}_b}{A\,\mathrm{Ra}_b^*} = \left\{1 + \left(\frac{4}{3}A\right)^{3/2}\left[1 + \left(\frac{0.492}{\mathrm{Pr}}\right)^{9/16}\right]^{2/3}\mathrm{Ra}_b^{*9/8}\right\}^{-2/3}$$

where $A = 1/24$; $\mathrm{Nu}_b = hb/k$; $\mathrm{Ra}_b^* = (g\beta/\nu\alpha)(T_w - T_\infty)b^3$ $(b/L_c)$; and $L_c$ is a characteristic channel length, usually evaluated as the total channel height when the channel has uniform thermal boundary conditions. For the present data, when $L_c$ was set equal to the total channel length $L$, the agreement was poor; however, when $L_c$ was set equal to the heater length $l$, the data agreed favorably with Churchill's correlation. The comparison is shown in Fig. 4. For values of $\mathrm{Ra}_b^* > 100$, the measured values fell approximately 10 percent below the predicted values; for $\mathrm{Ra}_b^* < 100$, the deviation increased to as much as 30 percent. Because the Churchill correlation does not account for any unheated sections, the increased deviation with decreasing values of $\mathrm{Ra}_b^*$ may be the result of the unheated inlet and outlet sections in the present study.

Only two previous studies, Oosthuizen (1984) and Wirtz and Haag (1985), consider the effects of unheated inlet and outlet regions. Oosthuizen predicted that an adiabatic outlet section augments the heat transfer process, placing his predictions above Churchill's correlation shown in Fig. 4. The data of the present study fall 35 to 60 percent below the values predicted by Oosthuizen. This deviation may be due to the presence of the unheated inlet section and the inability to maintain adiabatic conditions in the outlet section.

The present data agree much more favorably with the results of Wirtz and Haag (1985) even though they only considered an unheated inlet section. This comparison is shown in Fig. 5 using their notation. To use their correlations, the total length of the plate was assumed to equal the sum of the unheated inlet and the heater length, thus neglecting the outlet section.

For the smallest channel spacings, which correspond to the smallest Rayleigh numbers, Wirtz and Haag underpredict the Nusselt number while Churchill overpredicts. At larger values of Rayleigh number, both correlations overpredict the Nusselt number. This indicates that at small Rayleigh numbers corresponding to the fully developed flow region, the chimney formed by the unheated downstream section enhances the heat transfer when compared to a case without the downstream section. At larger Rayleigh numbers, the influence of both the upstream and downstream sections on the average Nusselt number does not appear to be significant.

## Conclusions

Even though the data are limited, several conclusions can be drawn from these experiments. For the range of variables examined here, definite channel effects were observed. Near the leading edge of the heater, the local Nusselt number exhibited a typical boundary-layer-like dependence on local Rayleigh number, however the proportionality constant was reduced below that of an isolated, vertical plate. Farther downstream on the heater surface, the local Nusselt number loses its boundary-layer-like characteristics and exhibited a stronger dependence on $x$. The average Nusselt numbers measured in the experiments were predicted fairly well using either Churchill's correlation for isothermal channels or Wirtz and Haag's correlation, which only accounts for the influence of the unheated inlet section. In either case, the channel length must be modified appropriately. The data do show that in the fully developed flow region, the unheated downstream section does enhance the natural convection heat transfer.

## References


Aung, W., Kessler, T., and Beitin, K., 1973, "Free Convection Cooling of Electronic Systems," *Transactions on Parts, Hybrids and Packaging*, IEEE, Vol. PHP-9, No. 2, pp. 75-86.

Churchill, S., 1967, "A Comprehensive Correlating Equation for Buoyancy Induced Flow in Channels," *Lett. Heat Mass Transfer*, Vol. 4, pp. 193-199.

Haaland, S. E., and Sparrow, E. M., 1983, "Solutions for the Channel Plume and the Parallel-Walled Chimney," *Numerical Heat Transfer*, Vol. 6, pp. 155-172.

Keustch, R., 1949, "Interferometric Investigation of the Heat Transfer Coefficient in Free Convection Between Two Vertical Heated Flat Plates," M. S. Thesis, The Ohio State University, Columbus, OH.

Oosthuizen, P. H., 1984, "A Numerical Study of Laminar Free Convective Flow Through a Vertical Open Partially Heated Plane Duct," *Fundamentals of Natural Convection/Electronic Equipment Cooling*, 22nd ASME/AIChE National Heat Transfer Conference, ASME Heat Transfer Division, Vol. HTD-32.

Ravine, T. L., 1984, "Natural Convection Cooling of a Finite-Sized Thermal Source on the Wall of a Vertical, Adiabatic Channel," M. S. Thesis, Department of Mechanical Engineering, The Ohio State University, Columbus, OH.

Ravine, T. L., and Richards, D. E., 1988, "Natural Convection Heat Transfer From a Discrete Thermal Source on a Vertical Surface," ASME JOURNAL OF HEAT TRANSFER, Vol. 110, this issue.

Wirtz, R. A., and Haag, T., 1985, "Effect of an Unheated Entry on Natural Convection Between Vertical Parallel Plates," presented at the ASME Winter Annual Meeting, Miami Beach, FL, Paper No. 85-WA/HT-14.

Wirtz, R., and Stutzman, R., 1982, "Experiments on Free Convection Between Vertical Plates With Symmetric Heating," ASME JOURNAL OF HEAT TRANSFER, Vol. 104, pp. 501-507.

# Natural Convection Heat Transfer From a Discrete Thermal Source on a Vertical Surface

**T. L. Ravine[1] and D. E. Richards[2]**

## Introduction

This paper presents results of an experimental study of natural convection heat transfer from a discrete thermal source located on a vertical plate. The object of the paper is to present empirical evidence to support the use of laminar boundary-layer assumptions to model natural convection heat transfer from discrete thermal sources.

In the present study, a discrete thermal source of length $l$ was located on a vertical plate of length $L$. The thermal source, as shown in Fig. 1, was placed a distance $d$ downstream of the plate leading edge, and produced a wall plume, which rose vertically along the plate. A dimensional analysis for this problem indicates that the local Nusselt number $Nu_x$ can be correlated in terms of a local Grashof number $Gr_x$, two geometric ratios $L/l$ and $d/l$, a dimensionless distance $x/l$, and the Prandtl number Pr. Note that the distance $x$, as shown in Fig. 1, is measured from the leading edge of the thermal source.

Few investigators have considered natural convection from discrete thermal sources, and even fewer have done so experimentally. Jaluria and Gebhart (1977) studied the case of a line source at the leading edge of a vertical plate; later Sparrow et al. (1978) considered a similar case with a finite-length thermal source. Jaluria (1982, 1984) also examined the case of multiple, discrete thermal sources on a vertical plate. These studies, which have been either analytical or numerical, have assumed that the laminar boundary-layer equations apply. In addition they have assumed that the leading edge of the plate and the thermal source coincide, i.e., $d=0$. None of the studies have considered the full set of governing equations and investigated what if any impact moving the thermal source downstream of the plate leading edge has upon the heat transfer.

Zinnes (1970), Carey and Mollendorf (1977), and Baker (1972) experimentally studied the buoyancy-induced flow produced by a discrete thermal source on a vertical plate. Most recently Park and Bergles (1985) have investigated natural convection heat transfer from small thermal sources (5 mm × 5 mm) that produce a three-dimensional plume. Only Baker (1972) and Park and Bergles (1985) report values for the local heat transfer coefficients.

## Experimental Apparatus

For the experiments, a composite plate 3.2 mm thick was constructed, which measured 114.3 × 304.8 mm ($L \times w$) (Fig. 1). The thermal source consisted of a resistance heater, one-mil stainless steel shim stock, which measured 12.7 × 304.8 mm ($l \times w$), mounted on a phenolic substrate. The upstream and downstream sections of the plate were made of balsa wood and epoxied to the phenolic section. This provided an unheated section ($d=25.4$ mm) upstream of the heater. Unfortunately, this design did not produce a well-controlled constant heat flux or isothermal boundary condition at the heater surface. Conduction from the heater into the balsa sections also produced nonadiabatic boundary conditions immediately upstream and downstream of the heater. A similar problem has plagued other experimenters who have studied discrete thermal sources experimentally using air as the working fluid.

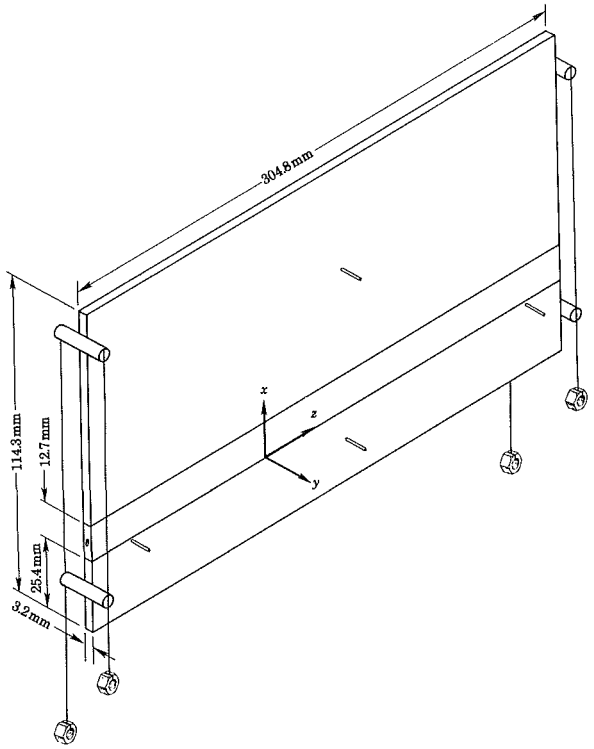


**Fig. 1 Single-plate test apparatus**

For the experiments, the plate was suspended from an overhead frame and placed in the test beam of a Mach-Zehnder interferometer. The test fluid for all conditions was atmospheric air. Local fluid temperatures and local heat fluxes at the wall were obtained from infinite-fringe interferograms using standard technqiues to reduce the data. Complete details of the experiments and the data reduction are discussed by Ravine (1984). The estimated uncertainty in the local and average Nusselt and Rayleigh numbers is ± 8 percent with 95 percent confidence.

## Results

Figure 2 shows an interferogram for the case where $Ra_l = 5774$, $L/l = 9.00$, and $d/l = 2.00$. The average Rayleigh number $Ra_l$ is based on the source length and the area-averaged wall-to-ambient temperature difference. Because the infinite-fringe setting was used for the interferometer, the fringes can be interpreted as isotherms. The temperature increases above the ambient value as the heater is approached. The vertical strings and horizontal pins used for alignment are clearly visible in Fig. 2 and can be identified by comparing it with Fig. 1. The numerous horizontal shadows that cross the field of view were produced by thermocouple wires and the heater connections. None of these wires intersected the flow field.

As shown in Fig. 2, all of the isotherms grow out from the thermal source. Upstream of the heater, the isotherms intersect the plate at an angle indicating that the surface is not

[1]Graduate Research Associate, Department of Mechanical Engineering, The Ohio State University, Columbus, OH 43210; current address: Mechanical Engineer, M/A-COM Omni Spectra, Inc., Chandler, AZ 85226; Assoc. Mem. ASME.

[2]Assistant Professor, Department of Mechanical Engineering, The Ohio State University, Columbus, OH 43210; Assoc. Mem. ASME.

Contributed by the Heat Transfer Division and presented at the ASME Winter Meeting, New Orleans, Louisiana, December 9-13, 1984. Manuscript received by the Heat Transfer Division August 28, 1985. Paper No. 84-WA/HT-90. Keywords: Electronic Equipment, Natural Convection, Plumes.

Wirtz, R. A., and Haag, T., 1985, "Effect of an Unheated Entry on Natural Convection Between Vertical Parallel Plates," presented at the ASME Winter Annual Meeting, Miami Beach, FL, Paper No. 85-WA/HT-14.
Wirtz, R., and Stutzman, R., 1982, "Experiments on Free Convection Between Vertical Plates With Symmetric Heating," ASME JOURNAL OF HEAT TRANSFER, Vol. 104, pp. 501-507.

# Natural Convection Heat Transfer From a Discrete Thermal Source on a Vertical Surface

**T. L. Ravine[1] and D. E. Richards[2]**

## Introduction

This paper presents results of an experimental study of natural convection heat transfer from a discrete thermal source located on a vertical plate. The object of the paper is to present empirical evidence to support the use of laminar boundary-layer assumptions to model natural convection heat transfer from discrete thermal sources.

In the present study, a discrete thermal source of length $l$ was located on a vertical plate of length $L$. The thermal source, as shown in Fig. 1, was placed a distance $d$ downstream of the plate leading edge, and produced a wall plume, which rose vertically along the plate. A dimensional analysis for this problem indicates that the local Nusselt number $Nu_x$ can be correlated in terms of a local Grashof number $Gr_x$, two geometric ratios $L/l$ and $d/l$, a dimensionless distance $x/l$, and the Prandtl number Pr. Note that the distance $x$, as shown in Fig. 1, is measured from the leading edge of the thermal source.

Few investigators have considered natural convection from discrete thermal sources, and even fewer have done so experimentally. Jaluria and Gebhart (1977) studied the case of a line source at the leading edge of a vertical plate; later Sparrow et al. (1978) considered a similar case with a finite-length thermal source. Jaluria (1982, 1984) also examined the case of multiple, discrete thermal sources on a vertical plate. These studies, which have been either analytical or numerical, have assumed that the laminar boundary-layer equations apply. In addition they have assumed that the leading edge of the plate and the thermal source coincide, i.e., $d=0$. None of the studies have considered the full set of governing equations and investigated what if any impact moving the thermal source downstream of the plate leading edge has upon the heat transfer.

Zinnes (1970), Carey and Mollendorf (1977), and Baker (1972) experimentally studied the buoyancy-induced flow produced by a discrete thermal source on a vertical plate. Most recently Park and Bergles (1985) have investigated natural convection heat transfer from small thermal sources (5 mm × 5 mm) that produce a three-dimensional plume. Only Baker (1972) and Park and Bergles (1985) report values for the local heat transfer coefficients.

## Experimental Apparatus

For the experiments, a composite plate 3.2 mm thick was constructed, which measured 114.3 × 304.8 mm ($L \times w$) (Fig. 1). The thermal source consisted of a resistance heater, one-

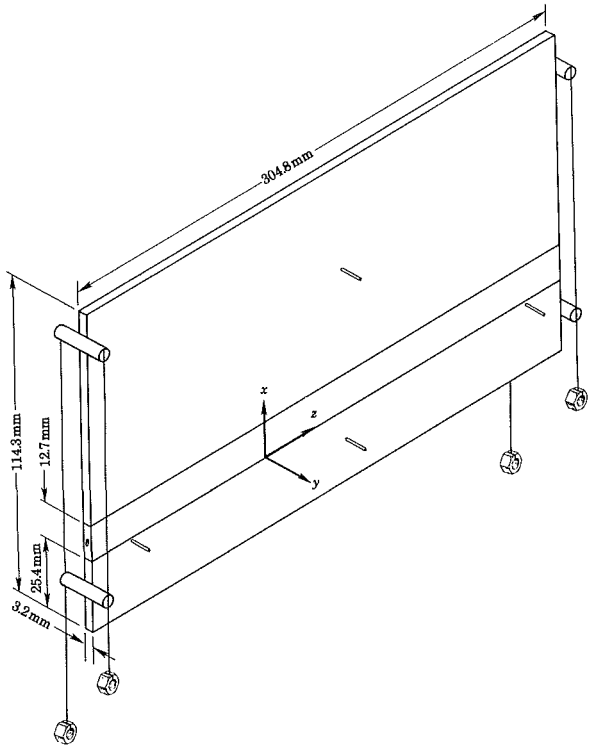


**Fig. 1 Single-plate test apparatus**

mil stainless steel shim stock, which measured 12.7 × 304.8 mm ($l \times w$), mounted on a phenolic substrate. The upstream and downstream sections of the plate were made of balsa wood and epoxied to the phenolic section. This provided an unheated section ($d=25.4$ mm) upstream of the heater. Unfortunately, this design did not produce a well-controlled constant heat flux or isothermal boundary condition at the heater surface. Conduction from the heater into the balsa sections also produced nonadiabatic boundary conditions immediately upstream and downstream of the heater. A similar problem has plagued other experimenters who have studied discrete thermal sources experimentally using air as the working fluid.

For the experiments, the plate was suspended from an overhead frame and placed in the test beam of a Mach-Zehnder interferometer. The test fluid for all conditions was atmospheric air. Local fluid temperatures and local heat fluxes at the wall were obtained from infinite-fringe interferograms using standard technqiues to reduce the data. Complete details of the experiments and the data reduction are discussed by Ravine (1984). The estimated uncertainty in the local and average Nusselt and Rayleigh numbers is ± 8 percent with 95 percent confidence.

## Results

Figure 2 shows an interferogram for the case where $Ra_l=5774$, $L/l=9.00$, and $d/l=2.00$. The average Rayleigh number $Ra_l$ is based on the source length and the area-averaged wall-to-ambient temperature difference. Because the infinite-fringe setting was used for the interferometer, the fringes can be interpreted as isotherms. The temperature increases above the ambient value as the heater is approached. The vertical strings and horizontal pins used for alignment are clearly visible in Fig. 2 and can be identified by comparing it with Fig. 1. The numerous horizontal shadows that cross the field of view were produced by thermocouple wires and the heater connections. None of these wires intersected the flow field.

As shown in Fig. 2, all of the isotherms grow out from the thermal source. Upstream of the heater, the isotherms intersect the plate at an angle indicating that the surface is not

[1]Graduate Research Associate, Department of Mechanical Engineering, The Ohio State University, Columbus, OH 43210; current address: Mechanical Engineer, M/A-COM Omni Spectra, Inc., Chandler, AZ 85226; Assoc. Mem. ASME.
[2]Assistant Professor, Department of Mechanical Engineering, The Ohio State University, Columbus, OH 43210; Assoc. Mem. ASME.
Contributed by the Heat Transfer Division and presented at the ASME Winter Meeting, New Orleans, Louisiana, December 9-13, 1984. Manuscript received by the Heat Transfer Division August 28, 1985. Paper No. 84-WA/HT-90. Keywords: Electronic Equipment, Natural Convection, Plumes.

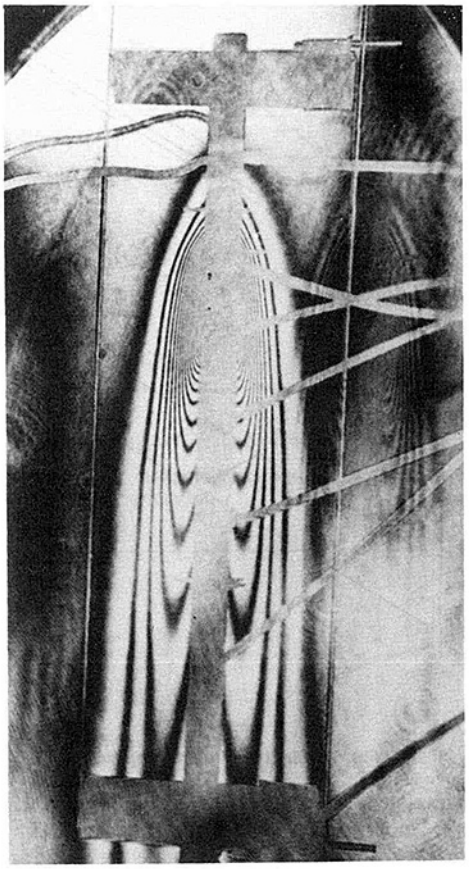

Fig. 2 Interferograms of a vertical flat plate with a discrete thermal source ($Ra_l = 5774$, $d/l = 2.00$, and $L/l = 9.00$)

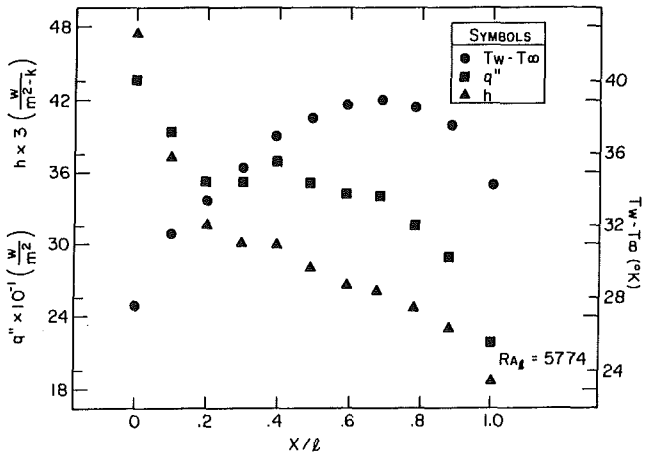


Fig. 3 Measured local heat flux, surface temperature, and heat transfer coefficient along the thermal source ($Ra_l = 5774$, $d/l = 2.00$, and $L/l = 9.00$)

adiabatic. This region extends upstream of the heater approximately 1/2 heater length for $Ra_l = 5774$. Experiments at lower values of $Ra_l$ showed that as $Ra_l$ decreased, this nonadiabatic region extended farther upstream. This can be explained by recognizing that as $Ra_l$ is decreased, the buoyancy flow decreases and conduction in the wall can extend further upstream from the heater. Note, however, that the temperature gradient, which is proportional to local heat flux, is significantly smaller in this region than on the heater surface. Downstream of the heater, the wall plume is clearly visible. Again in this region, the isotherms intersect the wall at an angle. Immediately downstream of the heater, the wall appears to be relatively adiabatic, and as the plume rises it loses energy back to the plate.

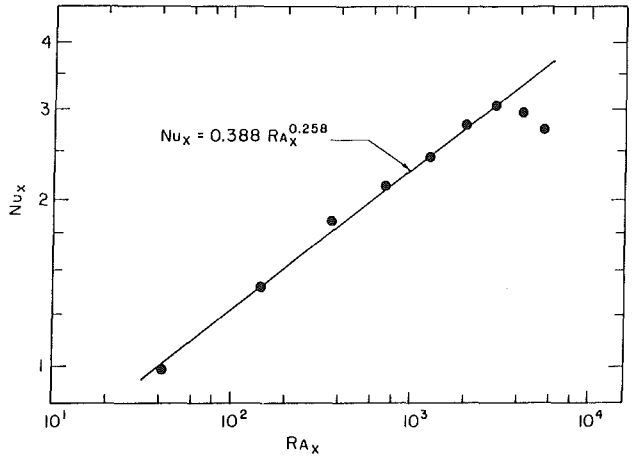


Fig. 4 Local Grashof number along the thermal source ($Ra_l = 5774$, $d/l = 2.00$, and $L/l = 9.00$)

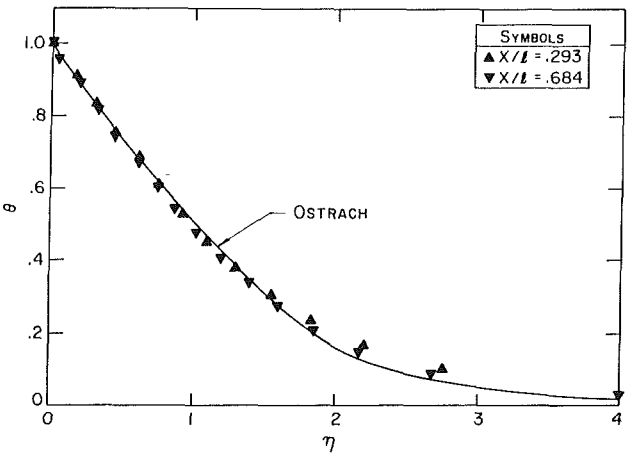


Fig. 5 Boundary-layer temperature profiles measured along the thermal source ($Ra_l = 5774$, $d/l = 2.00$, and $L/l = 9.00$)

Dimensional heat transfer data for the case with $Ra_l = 5774$ are presented in Fig. 3. It is clear from these results that the thermal boundary condition provided by the heater was neither a uniform heat flux nor an isothermal surface. The local wall-to-ambient temperature difference was a minimum at the heater leading edge and increased until it reached a maximum value near $x/l = 0.7$. The existence of a maximum in the surface temperature of the heater was attributed to the conduction losses into the downstream balsa wood section. When normalized to the area-averaged wall-to-ambient temperature difference, the maximum deviation in local temperature difference is $-22$ percent and the average deviation is $\pm$ 8 percent. The local heat flux was a maximum at the heater leading edge, was fairly uniform over the central portion of the heater, $0.2 < x/l < 0.65$, and then decreased with increasing $x/l$. The local heat transfer coefficient is also shown for comparison. As expected, it decreased monotonically with increasing $x/l$.

Figure 4 shows local Nusselt number plotted versus local Rayleigh number. The local Nusselt number and local Rayleigh number are both based on the local wall-to-ambient temperature difference. The nine data points shown correspond to the points in Fig. 3 with $0.2 < x/l < 1$. Using only those data points in Fig. 3 with $0.098 < x/l < 0.8$, a correlation for local Nusselt number was developed: $Nu_x = 0.388\ Ra_x^{0.258}$. When compared with a published correlation for an isothermal, vertical flat plate in air, $Nu_x = 0.412\ Ra_x^{0.25}$, the

scatter was within ± 5 percent. Using the area-averaged wall-to-ambient temperature difference, the average Nusselt number $Nu_l$ for $Ra_l = 5774$ was 5 percent below the predicted value for an isothermal plate of length $l$.

The measured temperature profiles in the fluid adjacent to the heater at $x/l = 0.293$ and 0.684, i.e., $Ra_x = 145$ and 1848, are presented in Fig. 5. The local temperature difference is plotted using similarity variables for a natural convection boundary layer on an isothermal surface. For comparison, the boundary-layer temperature profile for an isothermal flat plate (Ostrach, 1953) is also presented. The agreement between the measured profiles and the theoretical profile is excellent. Note that the distance for boundary-layer growth was measured from the leading edge of the heater, although the interferograms clearly show that the plate upstream of the heater is not adiabatic.

## Conclusions

Even though the data are limited, several conclusions can be drawn from this study. First, even though the boundary conditions obtained in these experiments differed from the classical uniform heat flux or uniform temperature conditions and unheated sections were located upstream and downstream of the heater, the local and average Nusselt numbers measured on the heater surface compared very favorably with those predicted for an isothermal flat plate of length $l$. Second, the temperature profiles measured in the fluid adjacent to the heater surface showed excellent agreement with the profiles predicted for natural convection boundary layers. Third, the unheated sections upstream and downstream of the heater did not appear to influence the thermal boundary-layer growth on the heater because the data correlates well with traditional flat plate correlations for a plate of length $l$, the heater length; thus, the results are independent of $d/l$ and $L/l$. Finally, these experiments demonstrate that the laminar boundary-layer equations should be valid for predicting heat transfer for this type of flow as long as $Ra_x > 145$.

## References


Baker, E., 1972, "Liquid Cooling of Microelectronic Devices by Free and Forced Convection," *Microelectronics and Reliability*, Vol. 11, pp. 213–222.

Carey, V., and Mollendorf, J., 1977, "The Temperature Field Above a Concentrated Heat Source on a Vertical Adiabatic Surface," *International Journal of Heat and Mass Transfer*, Vol. 20, pp. 1059–1067.

Jaluria, Y., 1982, "Buoyancy-Induced Flow Due to Isolated Thermal Source on a Vertical Surface," ASME JOURNAL OF HEAT TRANSFER, Vol. 104, pp. 223–227.

Jaluria, Y., 1984, "Interaction of Natural Convection Wakes Arising From Thermal Sources on a Vertical Surface," in: *Fundamentals of Natural Convection/Electronic Equipment Cooling*, L. C. Witte and L. S. Saxena, eds., American Society of Mechanical Engineers, New York, HTD-Vol. 32, pp. 67–76.

Jaluria, Y., and Gebhart, B., 1977, "Buoyancy-Induced Flow Arising From a Line Thermal Source on an Adiabatic Vertical Surface," *International Journal of Heat and Mass Transfer*, Vol. 20, pp. 153–157.

Ostrach, S., 1953, "An Analysis of Laminar Free Convection Flow and Heat Transfer About a Flat Plate Parallel to the Direction of the Generating Force," NACA Technical Report TR 1111.

Park, K. A., and Bergles, A. E., 1985, "Natural Convection Heat Transfer Characteristics of Simulated Microelectronic Chips," in: *Heat Transfer in Electronic Equipment—1985*, S. Oktay and R. J. Moffat, eds., American Society of Mechanical Engineers, New York, HTD-Vol. 48, pp. 29–37.

Ravine, T. L., 1984, "Natural Convection Cooling of a Finite-Sized Thermal Source on the Wall of a Vertical, Adiabatic Channel," M. S. Thesis, Department of Mechanical Engineering, The Ohio State University, Columbus, OH.

Sparrow, E., Patankar, S., and Abdel-Wahed, R., 1978, "Development of Wall and Free Plumes Above a Heated Vertical Plate," ASME JOURNAL OF HEAT TRANSFER, Vol. 100, pp. 184–190.

Zinnes, A., 1970, "The Coupling of Conduction With Laminar Natural Convection From a Vertical Flat Plate With Arbitrary Surface Heating," ASME JOURNAL OF HEAT TRANSFER, Vol. 92, pp. 528–535.


# Two-Dimensional Transient Temperature Distribution Within a Metal Undergoing Multiple Phase Changes Caused by Laser Irradiation at the Surface


**A. Minardi[1] and P. J. Bishop[2]**


## Nomenclature

- $a$ = laser beam radius, cm
- $c_p$ = specific heat capacity, J/g-K
- $D$ = depth, cm
- $f, F$ = fraction of element transformed: $f$—in present interval, $F$—in all previous time intervals
- $H$ = latent heat, J/g
- $k$ = thermal conductivity, J/cm-s-K
- $Q$ = absorbed laser intensity, W/cm
- $r$ = radial coordinate, cm
- $T$ = element temperature, K
- $T_0$ = ambient temperature, K
- $z$ = coordinate in laser beam direction, cm
- $\alpha$ = absorptivity
- $\varphi$ = density, g/cm$^3$

### Subscripts

- $m$ = melt
- $v$ = vapor

## Introduction

Metal-laser interactions have become increasingly important due to advances in laser-machining processes, laser weaponry, and rocket propulsion using laser beams.

An interesting physical phenomenon that is not well understood is the interaction of the metal plasma above a surface with a laser beam. This phenomenon, called thermal coupling, has been experimentally observed by Maher and Hall (1980) when a metal surface's ability to absorb energy increases dramatically. This study is the first step in understanding the physical aspects of laser-metal interactions. It deals exclusively with the sensible heating and phase transformations within the metal. Several one-dimensional models have been developed previously (Harrach, 1977) that deal specifically with laser-metal interactions. Other multidimensional models have been developed (Shamsundar and Sparrow, 1975) that are more general and demonstrate a solution technique for Stefan problems. Most studies that deal with the laser irradiation of metal assume that the laser beam power density is spatially constant, that the thermophysical properties are constant even as the metal is changing phase, and in papers by Bar-Isaac and Korn (1973) and Paek and Gagliano (1972) that the liquid phase can be neglected because the heat of fusion is small when compared to the latent heat of vaporization.

Although most models neglect the natural convection, other papers, such as by Sparrow et al., (1977), have considered this effect and found it to be of importance at low energy fluxes.

This study assumes that the laser beam has a spatial variation, and thus a two-dimensional model for the temperature distribution within the substrate is required. Further, it was assumed at first that the thermophysical properties are constant, but modifications were made to allow for different ther-


[1]Assistant Professor, University of Central Florida, Orlando, FL 32816.

[2]Associate Professor, University of Central Florida, Orlando, FL 32816.



Contributed by the Heat Transfer Division for publication in the JOURNAL OF HEAT TRANSFER. Manuscript received by the Heat Transfer Division December 9, 1986. Keywords: Laser Processing, Numerical Methods, Phase-Change Phenomena.

scatter was within ± 5 percent. Using the area-averaged wall-to-ambient temperature difference, the average Nusselt number $Nu_l$ for $Ra_l = 5774$ was 5 percent below the predicted value for an isothermal plate of length $l$.

The measured temperature profiles in the fluid adjacent to the heater at $x/l = 0.293$ and 0.684, i.e., $Ra_x = 145$ and 1848, are presented in Fig. 5. The local temperature difference is plotted using similarity variables for a natural convection boundary layer on an isothermal surface. For comparison, the boundary-layer temperature profile for an isothermal flat plate (Ostrach, 1953) is also presented. The agreement between the measured profiles and the theoretical profile is excellent. Note that the distance for boundary-layer growth was measured from the leading edge of the heater, although the interferograms clearly show that the plate upstream of the heater is not adiabatic.

## Conclusions

Even though the data are limited, several conclusions can be drawn from this study. First, even though the boundary conditions obtained in these experiments differed from the classical uniform heat flux or uniform temperature conditions and unheated sections were located upstream and downstream of the heater, the local and average Nusselt numbers measured on the heater surface compared very favorably with those predicted for an isothermal flat plate of length $l$. Second, the temperature profiles measured in the fluid adjacent to the heater surface showed excellent agreement with the profiles predicted for natural convection boundary layers. Third, the unheated sections upstream and downstream of the heater did not appear to influence the thermal boundary-layer growth on the heater because the data correlates well with traditional flat plate correlations for a plate of length $l$, the heater length; thus, the results are independent of $d/l$ and $L/l$. Finally, these experiments demonstrate that the laminar boundary-layer equations should be valid for predicting heat transfer for this type of flow as long as $Ra_x > 145$.

## References


Baker, E., 1972, "Liquid Cooling of Microelectronic Devices by Free and Forced Convection," *Microelectronics and Reliability*, Vol. 11, pp. 213–222.

Carey, V., and Mollendorf, J., 1977, "The Temperature Field Above a Concentrated Heat Source on a Vertical Adiabatic Surface," *International Journal of Heat and Mass Transfer*, Vol. 20, pp. 1059–1067.

Jaluria, Y., 1982, "Buoyancy-Induced Flow Due to Isolated Thermal Source on a Vertical Surface," ASME JOURNAL OF HEAT TRANSFER, Vol. 104, pp. 223–227.

Jaluria, Y., 1984, "Interaction of Natural Convection Wakes Arising From Thermal Sources on a Vertical Surface," in: *Fundamentals of Natural Convection/Electronic Equipment Cooling*, L. C. Witte and L. S. Saxena, eds., American Society of Mechanical Engineers, New York, HTD-Vol. 32, pp. 67–76.

Jaluria, Y., and Gebhart, B., 1977, "Buoyancy-Induced Flow Arising From a Line Thermal Source on an Adiabatic Vertical Surface," *International Journal of Heat and Mass Transfer*, Vol. 20, pp. 153–157.

Ostrach, S., 1953, "An Analysis of Laminar Free Convection Flow and Heat Transfer About a Flat Plate Parallel to the Direction of the Generating Force," NACA Technical Report TR 1111.

Park, K. A., and Bergles, A. E., 1985, "Natural Convection Heat Transfer Characteristics of Simulated Microelectronic Chips," in: *Heat Transfer in Electronic Equipment—1985*, S. Oktay and R. J. Moffat, eds., American Society of Mechanical Engineers, New York, HTD-Vol. 48, pp. 29–37.

Ravine, T. L., 1984, "Natural Convection Cooling of a Finite-Sized Thermal Source on the Wall of a Vertical, Adiabatic Channel," M. S. Thesis, Department of Mechanical Engineering, The Ohio State University, Columbus, OH.

Sparrow, E., Patankar, S., and Abdel-Wahed, R., 1978, "Development of Wall and Free Plumes Above a Heated Vertical Plate," ASME JOURNAL OF HEAT TRANSFER, Vol. 100, pp. 184–190.

Zinnes, A., 1970, "The Coupling of Conduction With Laminar Natural Convection From a Vertical Flat Plate With Arbitrary Surface Heating," ASME JOURNAL OF HEAT TRANSFER, Vol. 92, pp. 528–535.


# Two-Dimensional Transient Temperature Distribution Within a Metal Undergoing Multiple Phase Changes Caused by Laser Irradiation at the Surface


**A. Minardi[1] and P. J. Bishop[2]**


## Nomenclature

- $a$ = laser beam radius, cm
- $c_p$ = specific heat capacity, J/g-K
- $D$ = depth, cm
- $f, F$ = fraction of element transformed: $f$—in present interval, $F$—in all previous time intervals
- $H$ = latent heat, J/g
- $k$ = thermal conductivity, J/cm-s-K
- $Q$ = absorbed laser intensity, W/cm
- $r$ = radial coordinate, cm
- $T$ = element temperature, K
- $T_0$ = ambient temperature, K
- $z$ = coordinate in laser beam direction, cm
- $\alpha$ = absorptivity
- $\varphi$ = density, g/cm$^3$

### Subscripts

- $m$ = melt
- $v$ = vapor

## Introduction

Metal-laser interactions have become increasingly important due to advances in laser-machining processes, laser weaponry, and rocket propulsion using laser beams.

An interesting physical phenomenon that is not well understood is the interaction of the metal plasma above a surface with a laser beam. This phenomenon, called thermal coupling, has been experimentally observed by Maher and Hall (1980) when a metal surface's ability to absorb energy increases dramatically. This study is the first step in understanding the physical aspects of laser-metal interactions. It deals exclusively with the sensible heating and phase transformations within the metal. Several one-dimensional models have been developed previously (Harrach, 1977) that deal specifically with laser-metal interactions. Other multidimensional models have been developed (Shamsundar and Sparrow, 1975) that are more general and demonstrate a solution technique for Stefan problems. Most studies that deal with the laser irradiation of metal assume that the laser beam power density is spatially constant, that the thermophysical properties are constant even as the metal is changing phase, and in papers by Bar-Isaac and Korn (1973) and Paek and Gagliano (1972) that the liquid phase can be neglected because the heat of fusion is small when compared to the latent heat of vaporization.

Although most models neglect the natural convection, other papers, such as by Sparrow et al., (1977), have considered this effect and found it to be of importance at low energy fluxes.

This study assumes that the laser beam has a spatial variation, and thus a two-dimensional model for the temperature distribution within the substrate is required. Further, it was assumed at first that the thermophysical properties are constant, but modifications were made to allow for different ther-


[1]Assistant Professor, University of Central Florida, Orlando, FL 32816.

[2]Associate Professor, University of Central Florida, Orlando, FL 32816.



Contributed by the Heat Transfer Division for publication in the JOURNAL OF HEAT TRANSFER. Manuscript received by the Heat Transfer Division December 9, 1986. Keywords: Laser Processing, Numerical Methods, Phase-Change Phenomena.

mal conductivities of the liquid and solid phases. The model was developed to describe the physical processes until the vapor just forms, so that movement of the vapor away from the surface will not be considered. Natural convection will be neglected in the liquid pool, and radiation losses from the surface will be neglected since these are very small in comparison to the energy absorbed from the high intensity laser beam. Similar assumptions have been made by Ready (1965) and Bar-Isaac and Korn (1973).

### Mathematical and Numerical Description

The temperature distribution within a metal irradiated by a laser beam is a function of both radius and depth. Physically, as the metal is heated by the laser beam, radial and axial conduction are important energy transfer mechanisms. As the metal melts and then vaporizes, latent energy becomes important.

The conservation of energy equation written in dimensionless form is

$$T'_{r'r'} + (1/r')T'_{r'} + T'_{z'z'} - H'(t') = T'_{t'} \tag{1}$$

where $T' = (T - T_0)/T_0$, $r' = r/a$, $z' = z/a$, $t' = kt/a^2\varphi c_p$, and $H'(t') = [H_m f_m + H_v f_v]/T_0 c_p$.

The boundary and initial conditions in dimensionless form are:

$$\partial T'/\partial z' = aQ/T_0 k \text{ at } r' < 1,\ \partial T'/\partial z' = 0 \text{ at } r' \geq 1$$

at the surface $[z' = 0]$

$$\partial T'/\partial z' = 0 \text{ as } z' \to \infty,\ \partial T'/\partial r' = 0 \text{ as } r' \to \infty$$

$$\partial T'/\partial r' = 0 \text{ at } r' = 0,\ T'(r', z', 0) = 0$$

A finite difference scheme with relaxation was used to transform equation (1) and the initial and boundary conditions, and a modified Gauss-Seidel procedure was used to solve for temperature.

The computer model initially determines element temperatures assuming no latent effects ($H' = 0$). A comparison is made to the phase transformation temperatures. If the element temperature is greater than the melt or vaporization temperature, the solution procedure is repeated but for this iteration accounting for the latent effects. The element undergoing phase change will be held at the transformation temperature. Using this post-iterative method, the latent energy required for the phase changes and the phase boundary positions were determined for each time interval

Equation (2) determines the fraction of melt and vapor formed during a specific time interval

$$f_m = [T' - T'_m]/[H_m/(T_0 * c_p)]$$
$$f_v = [T' - T'_v]/\{[H_v/(T_0 * c_p)] - (H_m/H_v) * [1 - F_m]\} \tag{2}$$

where $F_m$ is the summation of the fraction melted in all previous time intervals.

### Results and Discussion

Computer results were compared to available experimental and analytical solutions in an effort to verify the model. Von Allmen (1976) has predicted spot center temperatures for copper where surface temperatures as a function of time are given for two laser intensities. Good agreement between this model and Von Allmen exists during the initial heating and melting phases. The time required to complete vaporization is very close for both models, about 0.9 $\mu$s for this model and 1.0 $\mu$s from Von Allmen for an intensity of 180 MW/cm$^2$.

A comparison was also made between results obtained by Abrams and Viskanta (1974) using fluorite with conduction only and different thermal conductivities for each phase, solid and liquid; the analytical solution for different thermal conductivities by Carslaw and Jaeger (1959); and the results obtained using this model. The results of this model fall between

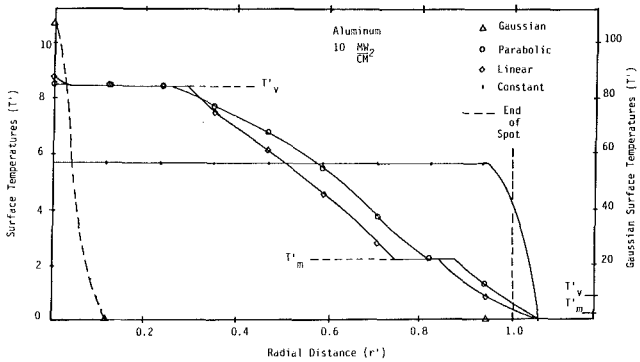


Fig. 1 Surface radial temperature distribution after 10 $\mu$s

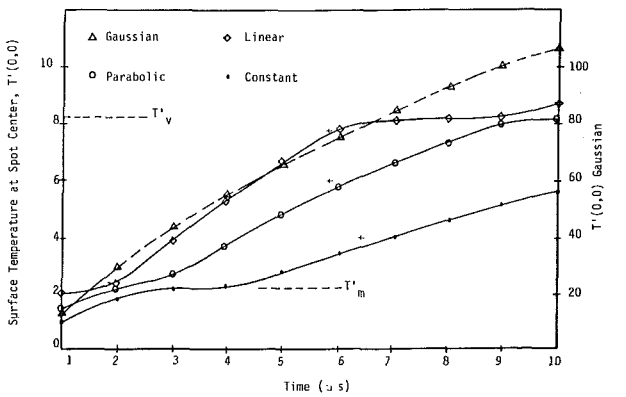


Fig. 2 Spot center temperatures for different laser profiles at various times

the analytical solution and temperatures calculated by Abrams and Viskanta.

After verification, the model was used to predict transient temperature distributions in aluminum for high-intensity laser irradiation. Using different laser heat flux distributions at the surface, metal temperatures were predicted as a function of radius, depth, and time. All laser profiles examined (constant, linear, parabolic, and Gaussian) had the same energy fluence based upon a constant intensity of 10 MW/cm$^2$. As laser profiles are made flatter, the radial distribution will approach a constant. Realistically, most laser profiles have a modified Gaussian distribution.

There is a wide variation in the temperature distribution predicted for the various laser profiles. For a constant laser intensity the radial temperature distribution is virtually constant except near the laser beam edge where temperatures decrease sharply as shown in Fig. 1. A constant laser intensity would result in a one-dimensional temperature profile; several investigators have made this assumption including Ready (1965).

Other laser beam profiles produce a variable radial temperature distribution, as shown in Fig. 1. The Gaussian distribution, due to its exponential behavior, exhibits much higher temperatures at the spot center while temperatures fall off drastically beyond this point. Similar results have been reported by Paek and Gagliano (1972) for radial distributions outside of the hole produced by laser drilling using an analytical approach.

Figure 2 further illustrates this as a function of time at the laser beam center. As time increases the metal temperature increases so that melting and eventually vaporization occur to different extents for various profiles. The Gaussian profile vaporizes within 1 $\mu$s and this is consistent with that reported

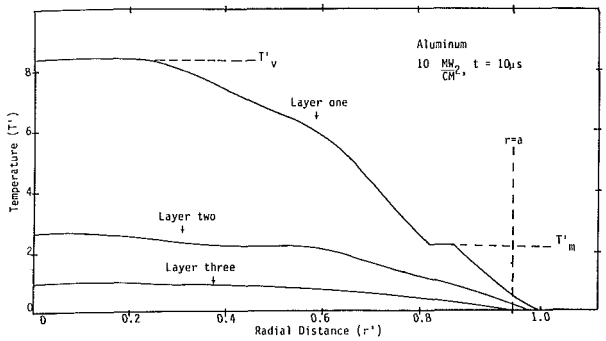


**Fig. 3 Radial temperature distributions for the parabolic intensity profile for various depths (layer thickness $\Delta z = 21.8$ $\mu$m)**

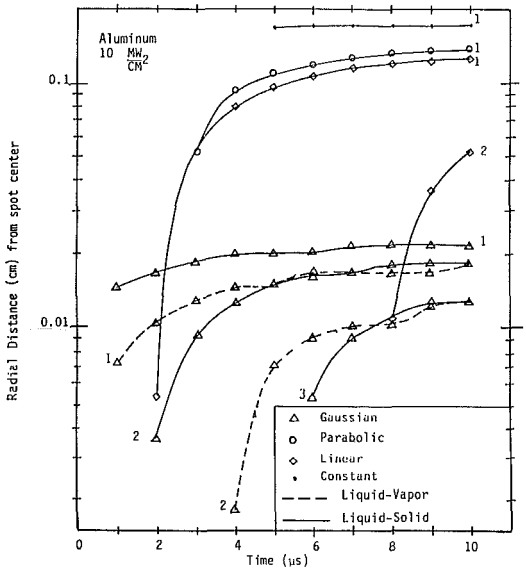


**Fig. 4 Radial location of liquid-solid and liquid-vapor phase boundaries (layer thickness $\Delta z = 21.8$ $\mu$m; layers are numbered; laser beam radius, $a = 0.2$ cm)**

experimentally by Ready (1965) and Von Allmen (1976),while the constant laser profile does not vaporize within 10 $\mu$s.

Figure 3 shows the radial temperature distribution for various depths at a fixed time (10 $\mu$s) using a parabolic laser profile. Similar trends were exhibited by the different laser profiles and the results of the parabolic are presented and discussed as representative results for all profiles. Due to the large incident energy flux absorbed at the surface, the surface layer exhibits a wide variation in temperature from vaporization to ambient. This layer has metal that has melted and vaporized. The layer just below the surface ($\Delta z = 21.8$ $\mu$s) where conduction dominates has some metal (40 percent) that has melted, while no vaporization has occurred. Beyond this depth, no phase transformation has taken place and only sensible heating of the metal by conduction has caused the material to heat up. The motion of the phase boundary is illustrated in Fig. 4.

The laser profile has a large effect on the phase boundary location. The constant profile melts farther radially but takes the longest time to do so, and only melts at the surface layer. The Gaussian profile does not melt as far radially but does melt to a greater depth and exhibits melting in the third layer as shown in Fig. 4. Vaporizaiton also occurs with the Gaussian profile in both the first and second layers.

## Conclusions

1 A two-dimensional cylindrical model using finite differencing was developed to determine transient temperature distributions with phase changes in materials irradiated by a laser beam.

2 The radial intensity profile of the laser beam is a critical parameter in determining temperature distributions.

3 A Gaussian intensity profile results in high spot center temperatures, which decrease rapidly in the radial direction.

4 The Gaussian profile does not melt/vaporize as far radially but does melt/vaporize to a greater depth than the other intensity profiles.

## References


Abrams, M., and Viskanta, R., 1974, "The Effects of Radiative Heat Transfer Upon the Melting and Solidification of Semitransparent Crystals," ASME JOURNAL OF HEAT TRANSFER, Vol. 96, pp. 184-190.

Bar-Isaac, C., and Korn, U., 1973, "Moving Heat Source Dynamics in Laser Drilling Processes," *Applied Physics*, Vol. 3, pp. 45-54.

Carslaw, H. S., and Jaeger, J. C., 1959, *Conduction of Heat in Solids*, 2nd ed., Oxford University Press, London.

Harrach, R. J., 1977, "Analytical Solutions for Laser Heating and Burnthrough of Opaque Solid Slabs," *Journal of Applied Physics*, Vol. 48, No. 6, pp. 2370-2383.

Maher, W. E., and Hall, R. B., 1980, "Pulsed Laser Heating Profile Width and Changes in Total Coupling With Pulse Length and Pressure," *Journal of Applied Physics*, Vol. 51, No. 3, pp. 1338-1344.

Paek, U., and Gagliano, F. P., 1972, "Thermal Analysis of Laser Drilling Processes," *IEEE Journal of Quantum Electronics*, Vol. QE-8, No. 2, pp. 112-119.

Ready, J. F., 1965, "Effects Due to Absorption of Laser Radiation," *Journal of Applied Physics*, Vol. 36, No. 2, pp. 462-468.

Shamsundar, N., and Sparrow, E. M., 1975, "Analysis of Multidimensional Conduction Phase Change Via the Enthalpy Method," ASME JOURNAL OF HEAT TRANSFER, Vol. 97, pp. 333-340.

Sparrow, E. M., Patankar, S. V, and Ramadhyani, S., 1977, "Analysis of Melting in the Presence of Natural Convection in the Melt Region," ASME JOURNAL OF HEAT TRANSFER, Vol. 99, pp. 520-526.

Von Allmen, M., 1976, "Laser Drilling Velocity in Metals," *Journal of Applied Physics*, Vol. 47, No. 12, pp. 5460-5463.


# Analysis of the Radiative and Conductive Heat Transfer Characteristics of a Waste Package Canister


**K. Vafai[1] and J. Ettefagh[1]**


## 1 Introduction

This paper presents an investigation on the effects of stabilizers on the heat transfer characteristics and the temperature distribution inside a waste package canister. Figure 1 depicts the stabilizers and the canister, which is filled up with hundreds of smaller diameter (relative to the canister) rods. Due to the large number of rods inside the canister, a full experimental simulation of the canister as shown in Fig. 1 is not practical.

The numerical simulation will take advantage of the symmetry of the problem and is therefore based on the wedge shown in Fig. 2. The numerical experiments were done for three cases. The first two cases were either conduction or radiation dominated. In the third case both radiation and conduction mechanisms were considered. Because of the compact packing of the rods the diffusion approximation was used for the cases where radiation was considered. In all the cases the natural convection contribution was considered to be negligible compared to the radiative and conductive contributions. This is a reasonable assumption due to the compact packing of the fuel rods in the canister. Furthermore, the neglect of natural convection provides a conservative basis for investigating the maximum allowable temperature inside the waste canister.

The numerical simulation is based on solving the governing two-dimensional energy equations in two separate domains us-


[1]Department of Mechanical Engineering, Ohio State University, Columbus, OH 43210.



Contributed by the Heat Transfer Division for publication in the JOURNAL OF HEAT TRANSFER. Manuscript received by the Heat Transfer Division June 1, 1987. Keywords: Porous Media, Radiation, Radiation Interactions.

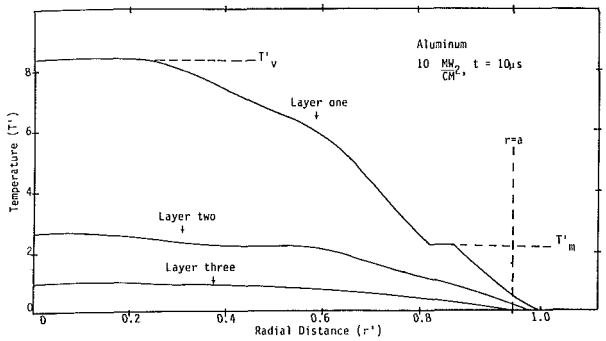


**Fig. 3 Radial temperature distributions for the parabolic intensity profile for various depths (layer thickness $\Delta z = 21.8$ $\mu$m)**

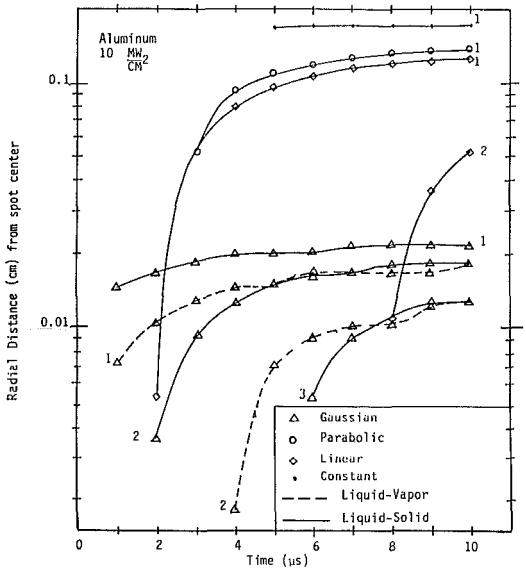


**Fig. 4 Radial location of liquid-solid and liquid-vapor phase boundaries (layer thickness $\Delta z = 21.8$ $\mu$m; layers are numbered; laser beam radius, $a = 0.2$ cm)**

experimentally by Ready (1965) and Von Allmen (1976),while the constant laser profile does not vaporize within 10 $\mu$s.

Figure 3 shows the radial temperature distribution for various depths at a fixed time (10 $\mu$s) using a parabolic laser profile. Similar trends were exhibited by the different laser profiles and the results of the parabolic are presented and discussed as representative results for all profiles. Due to the large incident energy flux absorbed at the surface, the surface layer exhibits a wide variation in temperature from vaporization to ambient. This layer has metal that has melted and vaporized. The layer just below the surface ($\Delta z = 21.8$ $\mu$s) where conduction dominates has some metal (40 percent) that has melted, while no vaporization has occurred. Beyond this depth, no phase transformation has taken place and only sensible heating of the metal by conduction has caused the material to heat up. The motion of the phase boundary is illustrated in Fig. 4.

The laser profile has a large effect on the phase boundary location. The constant profile melts farther radially but takes the longest time to do so, and only melts at the surface layer. The Gaussian profile does not melt as far radially but does melt to a greater depth and exhibits melting in the third layer as shown in Fig. 4. Vaporizaiton also occurs with the Gaussian profile in both the first and second layers.

## Conclusions

1 A two-dimensional cylindrical model using finite differencing was developed to determine transient temperature distributions with phase changes in materials irradiated by a laser beam.

2 The radial intensity profile of the laser beam is a critical parameter in determining temperature distributions.

3 A Gaussian intensity profile results in high spot center temperatures, which decrease rapidly in the radial direction.

4 The Gaussian profile does not melt/vaporize as far radially but does melt/vaporize to a greater depth than the other intensity profiles.

## References


Abrams, M., and Viskanta, R., 1974, "The Effects of Radiative Heat Transfer Upon the Melting and Solidification of Semitransparent Crystals," ASME JOURNAL OF HEAT TRANSFER, Vol. 96, pp. 184-190.

Bar-Isaac, C., and Korn, U., 1973, "Moving Heat Source Dynamics in Laser Drilling Processes," *Applied Physics*, Vol. 3, pp. 45-54.

Carslaw, H. S., and Jaeger, J. C., 1959, *Conduction of Heat in Solids*, 2nd ed., Oxford University Press, London.

Harrach, R. J., 1977, "Analytical Solutions for Laser Heating and Burnthrough of Opaque Solid Slabs," *Journal of Applied Physics*, Vol. 48, No. 6, pp. 2370-2383.

Maher, W. E., and Hall, R. B., 1980, "Pulsed Laser Heating Profile Width and Changes in Total Coupling With Pulse Length and Pressure," *Journal of Applied Physics*, Vol. 51, No. 3, pp. 1338-1344.

Paek, U., and Gagliano, F. P., 1972, "Thermal Analysis of Laser Drilling Processes," *IEEE Journal of Quantum Electronics*, Vol. QE-8, No. 2, pp. 112-119.

Ready, J. F., 1965, "Effects Due to Absorption of Laser Radiation," *Journal of Applied Physics*, Vol. 36, No. 2, pp. 462-468.

Shamsundar, N., and Sparrow, E. M., 1975, "Analysis of Multidimensional Conduction Phase Change Via the Enthalpy Method," ASME JOURNAL OF HEAT TRANSFER, Vol. 97, pp. 333-340.

Sparrow, E. M., Patankar, S. V, and Ramadhyani, S., 1977, "Analysis of Melting in the Presence of Natural Convection in the Melt Region," ASME JOURNAL OF HEAT TRANSFER, Vol. 99, pp. 520-526.

Von Allmen, M., 1976, "Laser Drilling Velocity in Metals," *Journal of Applied Physics*, Vol. 47, No. 12, pp. 5460-5463.


# Analysis of the Radiative and Conductive Heat Transfer Characteristics of a Waste Package Canister


**K. Vafai[1] and J. Ettefagh[1]**


## 1 Introduction

This paper presents an investigation on the effects of stabilizers on the heat transfer characteristics and the temperature distribution inside a waste package canister. Figure 1 depicts the stabilizers and the canister, which is filled up with hundreds of smaller diameter (relative to the canister) rods. Due to the large number of rods inside the canister, a full experimental simulation of the canister as shown in Fig. 1 is not practical.

The numerical simulation will take advantage of the symmetry of the problem and is therefore based on the wedge shown in Fig. 2. The numerical experiments were done for three cases. The first two cases were either conduction or radiation dominated. In the third case both radiation and conduction mechanisms were considered. Because of the compact packing of the rods the diffusion approximation was used for the cases where radiation was considered. In all the cases the natural convection contribution was considered to be negligible compared to the radiative and conductive contributions. This is a reasonable assumption due to the compact packing of the fuel rods in the canister. Furthermore, the neglect of natural convection provides a conservative basis for investigating the maximum allowable temperature inside the waste canister.

The numerical simulation is based on solving the governing two-dimensional energy equations in two separate domains us-


[1]Department of Mechanical Engineering, Ohio State University, Columbus, OH 43210.



Contributed by the Heat Transfer Division for publication in the JOURNAL OF HEAT TRANSFER. Manuscript received by the Heat Transfer Division June 1, 1987. Keywords: Porous Media, Radiation, Radiation Interactions.

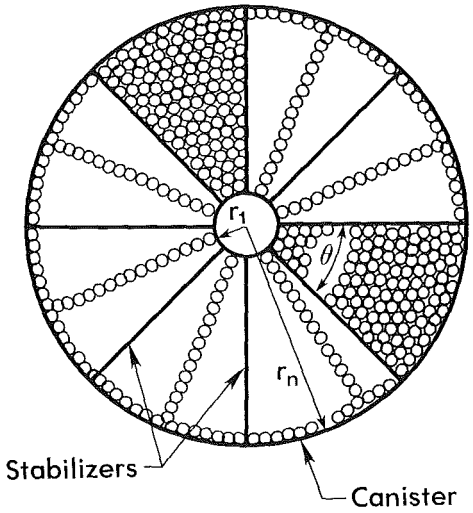


**Fig. 1 Schematic of the waste package canister and the position of the fuel rods and the stabilizers**

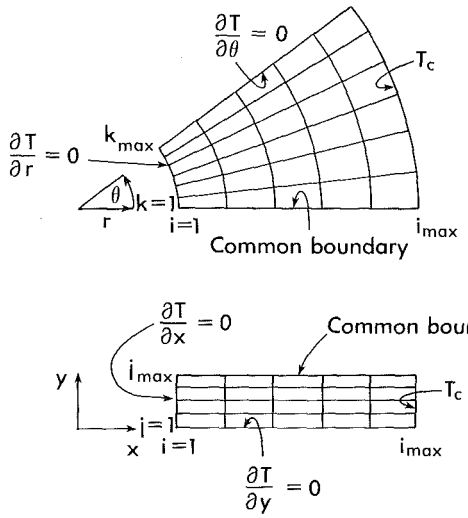


**Fig. 2 Numerical grid system used for the wedge and the stabilizer**

ing the ADI technique. A Cartesian mesh size of (31 × 6) is used for the stabilizer and a polar mesh size of (31 × 7) is used for the wedge. The two domains are solved simultaneously and are then integrated together through the numerical scheme. It has been found that this procedure gives very accurate and stable results. The effects of variations of the thickness of the stabilizer and the variations of the surface temperature of the canister on the temperature distribution and the hot spots inside the canister were analyzed. For each case the full transient temperature distribution inside the canister with and without the stabilizer is investigated. It is found that the stabilizers are quite effective for reducing the overall temperature of the waste canister for typical design conditions. It is also found that the stabilizers shift the location of the hot spots inside the canister.

## 2 Analysis and Computational Scheme

The problem is modeled as a transient two-dimensional heat transfer in two domains: a porous medium (comprised of fuel rods) and the stabilizer. As shown in Fig. 2(*b*), a polar coordinate system is used for the wedge and a Cartesian coordinate system is used for the stabilizer. The governing equations for the transient two-dimensional heat transfer in the wedge and the stabilizer, which are based on a diffusion approximation for radiative transfer, are:

$$\frac{\partial T}{\partial t}=\alpha_s\left(\frac{\partial^2 T}{\partial x^2}+\frac{\partial^2 T}{\partial y^2}\right) \tag{1}$$

$$[(1-E)\rho_s c_s+E\rho_f c_f]\frac{\partial T}{\partial t}=k_e\left[\frac{1}{r}\frac{\partial}{\partial r}\left(r\frac{\partial T}{\partial r}\right)+\frac{1}{r^2}\frac{\partial^2 T}{\partial \theta^2}\right]$$

$$+\frac{16\sigma}{3a_R}\left[\frac{1}{r}\frac{\partial}{\partial r}\left(rT^3\frac{\partial T}{\partial r}\right)+\frac{1}{r^2}\frac{\partial}{\partial \theta}\left(T^3\frac{\partial T}{\partial \theta}\right)\right]+(1-E)q_S \tag{2}$$

where $T$ is the temperature, $t$ the time, $E$ the porosity, $\rho_f$ the fluid (air) density, $\rho_s$ the solid density, $c_f$ the fluid heat capacity, $c_s$ the solid heat capacity, $q_s$ the heat generation per unit volume, $\alpha_s$ the thermal diffusivity of the stabilizer, $k_e$ the effective conduction thermal conductivity of the wedge, $a_R$ the Rosseland mean absorption coefficient, $\sigma$ the Stefan-Boltzmann constant, and $[x, y]$ and $[r, \theta]$ are the corresponding Cartesian and polar coordinate systems for the stabilizer and the wedge, respectively.

To solve equations (1) and (2) there is a need to estimate the values of $k_e$ and $a_R$. The conductive effective thermal conductivity $k_e$ was calculated by obtaining the average of two statistical bounds as described in Tien and Vafai (1979). It should be noted that the above procedure provides an estimate of the thermal conductivity and not an exact value. An estimate for the Rosseland mean absorption coefficient is more complicated. To obtain an estimate for $a_R$ the governing radiative equations are analyzed from two different approaches. These are the net-radiation method and the diffusion approximation. The combination of these two methods provides an interesting way for estimating the value of $a_R$ as described below.

The general steady-state equations for determining radiation exchange in a gray, diffuse enclosure of $n$ surfaces by the net-radiation method is given by (Siegel and Howell, 1981)

$$\sum_{j=1}^{n}(F_{ij}-\delta_{ij})\sigma(T_j^4-T_n^4)$$

$$=\sum_{j=1}^{n}\left(F_{ij}\frac{1-\epsilon_j}{\epsilon_j}-\frac{\delta_{ij}}{\epsilon_j}\right)\frac{Q_j}{A_j}, \qquad i=1, 2, 3, \ldots, n \tag{3}$$

where $T_n$ is the canister temperature, $T_j$ is the temperature of the surface $j$, and $Q_j$ is the net heat transfer from the surface $j$. Considering the surface $k$ ($Q_k \neq 0$) as the reference surface, and the fact that the energy absorbed by the canister from fuel rods within is equal to sum of the heat losses from these rods, and also realizing that in most practical applications the heat generation from each rod is approximately the same, and the emissivity of each rod is the same as the emissivity of the canister, equation (3) can be rearranged as (Cox 1977)

$$\sum_{j=1}^{m}(F_{ij}-\delta_{ij})Z_j=-1, \qquad i=1, 2, 3, \ldots, m \tag{4}$$

$$Z_j=R_j-\left(\frac{1-\epsilon}{\epsilon}\right)\left(1+\frac{mA_1}{A_n}\right) \tag{5}$$

$$R_j=\frac{\sigma(T_j^4-T_n^4)}{Q_k/A_k} \tag{6}$$

where $m$ is the number of rods in the canister, $A_1$ the surface area of a single rod, and $A_n$ is the surface area of the canister. Therefore the total heat transfer out of the canister is given by

$$Q_{\text{total}}=\sum_{j=1}^{m}Q_j=mQ_1$$

or

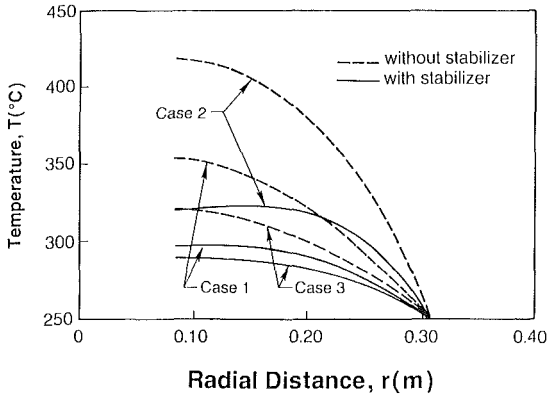


Fig. 3 Temperature distribution in the wedge region at steady state

$$Q = mR_1^{-1}\sigma(T_1^4 - T_n^4) \tag{7}$$

Alternatively, the radial radiative heat transfer based on the diffusion approximation is given by (Siegel and Howell, 1981)

$$Q_r = -\frac{4\sigma}{3a_R}\frac{dT^4}{dr} \tag{8}$$

where the quantity $k_r = 16\sigma T^3/3a_R$ is considered as an effective radiative conductivity. Comparison between the total heat transfer obtained by the net radiation method, equation (7), and the radiative diffusion method, equation (8), yields the estimated value for the Rosseland mean absorption coefficient $a_R$. To evaluate $a_R$ two quantities are needed: $R_1$ and $T_1$. From equation (5) $R_1$ can be obtained in terms of $Z_1$ and the value of $Z_1$ is in turn obtained by the numerical solution of equation (4) for all $Z_j$. These equations are solved by Cox (1977) and the values of $Z_j$ are all tabulated. This tabulation is done in terms of different shape factors, which are based on different pitch-to-diameter ratios. In the waste package problem, due to the compactness of the packing, the ratio of pitch to diameter is very close to 1. Using this ratio the value of $Z_1$ could then be found from Cox (1977). However, the universal connector temperature $T_1$ is an unknown quantity at this point. Therefore, a short iteration loop is required in the numerical scheme to come up with the correct estimate of $a_R$. Another and more direct way of obtaining the value of $a_R$ is by using equations (5), (7), and (8) to obtain $a_R$ in terms of $Z_1$ and $dT^4/dr|_{r_n}$. Then using an iteration procedure $dT^4/dr|_{r_n}$ and hence $a_R$ can be obtained from the numerical results. In this work the latter approach, which is considered to be more accurate, is used to come up with an estimate of the Rosseland mean absorption coefficient (170 $m^{-1}$). It should be mentioned that the iteration procedure converges quite rapidly.

Equations (1) and (2) are solved by finite difference approximation. The ADI method is used for the numerical solution of the governing equations. The region between the stabilizer and the wedge requires special consideration. This is because the temperature at the common boundary between the wedge and the stabilizer is an unknown. To overcome this difficulty a numerical scheme is devised based on satisfying two physical constraints at the common boundary between the wedge and the stabilizer. The first physical constraint is the equality of the temperature for both the stabilizer and the wedge at their common boundary. The second physical constraint is the equality of the heat fluxes at the boundary between the wedge and the stabilizer. The criteria for the convergence have been based on the relative heat flux difference and the relative temperature difference in both domains using a tolerance of $1.0 \times 10^{-7}$.

## 3 Boundary Condition for the Canister

In performing the numerical investigations there is a need for a reasonable estimate for the canister surface temperature.

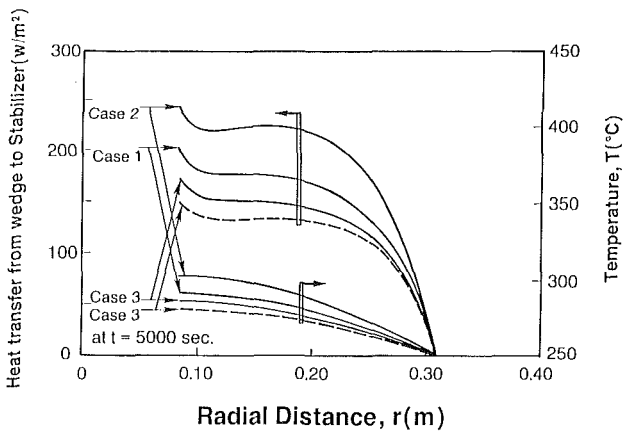


Fig. 4 Heat flux distribution from the wedge to the stabilizer and temperature distribution in the stabilizer

This is done by noting that at steady state the total heat generated within the canister must be equal to the amount of heat transferred from the canister to the surrounding host rock. This heat transfer occurs by a combination of convection and radiation through the air gap, and conduction through the overpack material. Assuming one-dimensional conduction through the overpack the total heat transfer from the canister can be written as

$$Q = Q_{\text{conv}} + Q_{\text{rad}} = Q_{\text{cond}}$$

where

$$Q_{\text{cond}} = \frac{2\pi k(T_B - T_A)}{\ln(r_A/r_B)}$$

$$Q_{\text{rad}} = \frac{\sigma A_r(T_C^4 - T_B^4)}{\frac{1}{\epsilon_1} + \frac{1-\epsilon_2}{\epsilon_2}\left(\frac{r_c}{r_B}\right)}$$

$$Q_{\text{conv}} = \frac{2\pi k_{\text{eff}}(T_C - T_B)}{\ln(D_B/D_C)}$$

The temperatures $T_C$, $T_B$, and $T_A$ are the canister, interface of the overpack material and the air gap, and interface of the overpack material and the geological media, respectively. The expression for $k_{\text{eff}}$ is taken from the work of Raithby and Hollands (1975) for two concentric cylinders. Using the above equations and $T_c = 175°C$ (based on some empirical data) the estimated canister surface temperature was found to be 250°C. It should be noted that our transient solution is obtained on the basis of obtaining the canister surface temperature at steady state. This is a good approximation, since our main interest is in the steady-state results and the transient solution is used only to obtain an estimate of the time required to reach steady state.

## 4 Results and Conclusions

The results for the steady-state temperature distribution in the canister with and without the stabilizer for all three cases are shown in Fig. 3. The temperature distribution in the wedge is presented at $\theta = 30$ deg. The heat flux from the fuel rods to the stabilizer as a function of the distance along the stabilizer and the temperature distribution in the stabilizer are shown in Fig. 4. All the results presented here are based on actual physical dimensions and thermophysical data, which are planned for the waste package canister (Table 1) (Westinghouse Report, 1983). Although the temperature distribution in the stabilizer was considered to be two dimensional, the computational results indicated that the temperature distribution in the stabilizer is almost one dimen-

**Table 1 Characteristics of a spent fuel package**

| Canister | Characteristics |
|---|---|
| Outside diameter | 62 cm |
| Length | 400 cm |
| Weight, gross | 8390 kg |
| Initial heat load | 6600 W |
| Material of construction | carbon steel |
| Quantity of spent fuel assemblies | 12 pressurized-water reactor (PWR) |
| Quantity of spent fuel pins/assemblies | 264 |
| Quantity of spent fuel assemblies/wedge | 2 (PWR) |
| Container | |
| Outside diameter | 84.5 cm |
| Inside diameter | 64.5 cm |
| Length | 446.5 cm |
| Material of construction | carbon steel |
| Maximum surface temperature | 175°C |
| Rosseland mean absorption coefficient | 170 $m^{-1}$ |

Source: Westinghouse Electric Corporation, 1983.

sional as can be seen in Fig. 5. Even though this was found to be true for all cases investigated, nevertheless the stabilizer computations must be carried out in two dimensions. This is because of the need for computing the heat flux at the common boundary in both the stabilizer and the wedge sections. The maximum allowable temperature inside of the canister for all cases is $T_{crit} = 375°C$ (Westinghouse Report, 1983). As can be seen in Fig. 3, the maximum temperature criteria are met for the conduction case with or without the stabilizers. However, since the criteria are barely met for the case without the stabilizer, the stabilizer does provide a needed margin of safety. Also seen in Fig. 3 is the shift of the hot spots from the inner core (without the stabilizer) to a location inside the fuel rod region (with the stabilizer). This shift was observed in all the cases investigated; however the shift can hardly be seen from Fig. 3 for the first and third cases, whereas in the radiation case it is more pronounced. The reason for this shift can be traced back to heat flux distribution along the stabilizer. As seen in Fig. 4 the heat flux distribution along the stabilizer goes through an S shape behavior. This is due to the wedge geometry, which produces two opposing effects. Due to the wedge geometry of the fuel rods the amount of heat generated at each circular strip increases in the radial direction. On the other hand as $r$ increases the circular strips become closer to the host rock, which has the lowest temperature in the wedge region. Therefore, these two opposing effects produce the heat flux distribution, which in turn creates the shift in the hot spots. This shift in the location of the hot spots, which is observed in all cases, is especially valuable since it causes a distance between the highest temperature in the canister and the universal connector, which is the most crucial component of the waste package canister. As can be seen in Fig. 3, based on radiative heat transfer only, the maximum temperature criteria are not met for the case without the stabilizer. Therefore, if the radiation is the dominant heat transfer mechanism, the stabilizers are required to meet the maximum temperature criteria. Figure 3 also indicates that for the case when both the conductive and radiative mechanisms are present the maximum temperature criteria are met with or without the stabilizer. However, the stabilizer again provides a margin of safety for the canister. It should be noted that for all cases the steady-state conditions were reached in less than two days. In the process of analyzing the three cases, i.e., conduction only, radiation only, and combined conduction and radiation, we have in effect also analyzed the effects of variations of the total effective thermal conductivity on the performance of the stabilizers.

To investigate the effects of an increase in the thickness of the stabilizer on the temperature distribution inside the canister, the thickness of the stabilizer was doubled. From the numerical experiments it was found that the increase in thickness of the stabilizers did not provide any significant reduction (about 8 percent) in the temperature distribution or the hot spots inside of the canister. This was found to be true for all situations studied in this work. The effects of temperature variations at the surface of the canister were also investigated. The outside surface temperature of the canister around the periphery was varied from its constant value by as much as ±10 percent. It was found that this surface temperature variation does not impose any significant changes on any of our conclusions.


### Acknowledgments

*This research was supported by Battelle Memorial Institute and the Department of Energy under contract No. DE-AC02-83-CH10140.*


### References


Carslaw, H. S., and Jaeger, J. C., 1973, *Conduction of Heat in Solids*, 2nd ed., Oxford Press, United Kingdom.

Cox, R. L., 1977, *Radiative Heat Transfer in Arrays of Parallel Cylinders*, ORNL-5239, Oak Ridge, TN.

Raithby, G. D., and Hollands, K. G., 1975, "A General Method of Obtaining Approximate Solutions to Laminar and Turbulent Free Convection Problems," *Advances in Heat Transfer*, Vol. 11, pp. 265–315.

Siegel, R., and Howell, J. R., 1981, *Thermal Radiation Heat Transfer*, 2nd ed., McGraw-Hill, New York.

Tien, C. L., and Vafai, K., 1979, "Statistical Bounds for the Effective Thermal Conductivity of Microsphere and Fibrous Insulation," *AIAA Progress Series*, Vol. 65, pp. 135–148.

Westinghouse Electric Corporation, 1983, "Waste Package Reference Conceptual Designs for a Repository in Salt," WSTD-TIME-001.


## A Note on the Solutions of Thermal Radiant Energy Interchange Problems


**R. M. Saldanha da Gama**[1]


### 1 Introduction

The interchange of radiant energy among diffusely emitting and diffusely reflecting opaque surfaces, separated by radiatively nonparticipating media, is a phenomenon governed by systems of integral equations. If it is assumed that temperature fields are known, these systems are linear and may have, as unknown, the local radiosities over each surface considered.

We shall develop our discussion for an enclosure composed of $M$ diffusely emitting and diffusely reflecting opaque surfaces. If we assume that the medium is radiatively nonparticipating, all the energy that leaves a region of a given surface will reach one (or more) of the other $(M-1)$ surfaces and/or itself.

This principle enables us to write the energy balance for the enclosure in the following way (Saldanha da Gama, 1985):

$$B_i(\lambda, r_i) = \epsilon_i(\lambda, r_i) e_b(\lambda, T_i(r_i)) + \rho_i(\lambda, r_i) \sum_{j=1}^{M} \int_{A_j} B_j(\lambda, s_j) K(r_i, s_j) dA \quad i = 1, 2, \ldots, M \tag{1}$$

in which $\lambda$ is the wavelength, $r_i$ is the position over the surface $i$, $s_j$ is also the position over the surface $i$ (the character $s$ is employed for integration variables), $\epsilon_i$ $(\lambda, r_i)$ is the mono-


[1]Laboratório Nacional de Computação Científica, 22290, Rio de Janeiro, Brazil.



Contributed by the Heat Transfer Division for publication in the JOURNAL OF HEAT TRANSFER. Manuscript received by the Heat Transfer Division April 20, 1987. Keywords: Radiation.

**Table 1 Characteristics of a spent fuel package**

| Canister | Characteristics |
|---|---|
| Outside diameter | 62 cm |
| Length | 400 cm |
| Weight, gross | 8390 kg |
| Initial heat load | 6600 W |
| Material of construction | carbon steel |
| Quantity of spent fuel assemblies | 12 pressurized-water reactor (PWR) |
| Quantity of spent fuel pins/assemblies | 264 |
| Quantity of spent fuel assemblies/wedge | 2 (PWR) |
| Container | |
| Outside diameter | 84.5 cm |
| Inside diameter | 64.5 cm |
| Length | 446.5 cm |
| Material of construction | carbon steel |
| Maximum surface temperature | 175°C |
| Rosseland mean absorption coefficient | 170 $m^{-1}$ |

Source: Westinghouse Electric Corporation, 1983.

sional as can be seen in Fig. 5. Even though this was found to be true for all cases investigated, nevertheless the stabilizer computations must be carried out in two dimensions. This is because of the need for computing the heat flux at the common boundary in both the stabilizer and the wedge sections. The maximum allowable temperature inside of the canister for all cases is $T_{crit} = 375°C$ (Westinghouse Report, 1983). As can be seen in Fig. 3, the maximum temperature criteria are met for the conduction case with or without the stabilizers. However, since the criteria are barely met for the case without the stabilizer, the stabilizer does provide a needed margin of safety. Also seen in Fig. 3 is the shift of the hot spots from the inner core (without the stabilizer) to a location inside the fuel rod region (with the stabilizer). This shift was observed in all the cases investigated; however the shift can hardly be seen from Fig. 3 for the first and third cases, whereas in the radiation case it is more pronounced. The reason for this shift can be traced back to heat flux distribution along the stabilizer. As seen in Fig. 4 the heat flux distribution along the stabilizer goes through an S shape behavior. This is due to the wedge geometry, which produces two opposing effects. Due to the wedge geometry of the fuel rods the amount of heat generated at each circular strip increases in the radial direction. On the other hand as $r$ increases the circular strips become closer to the host rock, which has the lowest temperature in the wedge region. Therefore, these two opposing effects produce the heat flux distribution, which in turn creates the shift in the hot spots. This shift in the location of the hot spots, which is observed in all cases, is especially valuable since it causes a distance between the highest temperature in the canister and the universal connector, which is the most crucial component of the waste package canister. As can be seen in Fig. 3, based on radiative heat transfer only, the maximum temperature criteria are not met for the case without the stabilizer. Therefore, if the radiation is the dominant heat transfer mechanism, the stabilizers are required to meet the maximum temperature criteria. Figure 3 also indicates that for the case when both the conductive and radiative mechanisms are present the maximum temperature criteria are met with or without the stabilizer. However, the stabilizer again provides a margin of safety for the canister. It should be noted that for all cases the steady-state conditions were reached in less than two days. In the process of analyzing the three cases, i.e., conduction only, radiation only, and combined conduction and radiation, we have in effect also analyzed the effects of variations of the total effective thermal conductivity on the performance of the stabilizers.

To investigate the effects of an increase in the thickness of the stabilizer on the temperature distribution inside the canister, the thickness of the stabilizer was doubled. From the numerical experiments it was found that the increase in thickness of the stabilizers did not provide any significant reduction (about 8 percent) in the temperature distribution or the hot spots inside of the canister. This was found to be true for all situations studied in this work. The effects of temperature variations at the surface of the canister were also investigated. The outside surface temperature of the canister around the periphery was varied from its constant value by as much as ±10 percent. It was found that this surface temperature variation does not impose any significant changes on any of our conclusions.


### Acknowledgments

*This research was supported by Battelle Memorial Institute and the Department of Energy under contract No. DE-AC02-83-CH10140.*


### References


Carslaw, H. S., and Jaeger, J. C., 1973, *Conduction of Heat in Solids*, 2nd ed., Oxford Press, United Kingdom.

Cox, R. L., 1977, *Radiative Heat Transfer in Arrays of Parallel Cylinders*, ORNL-5239, Oak Ridge, TN.

Raithby, G. D., and Hollands, K. G., 1975, "A General Method of Obtaining Approximate Solutions to Laminar and Turbulent Free Convection Problems," *Advances in Heat Transfer*, Vol. 11, pp. 265–315.

Siegel, R., and Howell, J. R., 1981, *Thermal Radiation Heat Transfer*, 2nd ed., McGraw-Hill, New York.

Tien, C. L., and Vafai, K., 1979, "Statistical Bounds for the Effective Thermal Conductivity of Microsphere and Fibrous Insulation," *AIAA Progress Series*, Vol. 65, pp. 135–148.

Westinghouse Electric Corporation, 1983, "Waste Package Reference Conceptual Designs for a Repository in Salt," WSTD-TIME-001.


## A Note on the Solutions of Thermal Radiant Energy Interchange Problems


**R. M. Saldanha da Gama**[1]


### 1 Introduction

The interchange of radiant energy among diffusely emitting and diffusely reflecting opaque surfaces, separated by radiatively nonparticipating media, is a phenomenon governed by systems of integral equations. If it is assumed that temperature fields are known, these systems are linear and may have, as unknown, the local radiosities over each surface considered.

We shall develop our discussion for an enclosure composed of $M$ diffusely emitting and diffusely reflecting opaque surfaces. If we assume that the medium is radiatively nonparticipating, all the energy that leaves a region of a given surface will reach one (or more) of the other $(M-1)$ surfaces and/or itself.

This principle enables us to write the energy balance for the enclosure in the following way (Saldanha da Gama, 1985):

$$B_i(\lambda, r_i) = \epsilon_i(\lambda, r_i) e_b(\lambda, T_i(r_i)) + \rho_i(\lambda, r_i) \sum_{j=1}^{M} \int_{A_j} B_j(\lambda, s_j) K(r_i, s_j) dA \quad i = 1, 2, \ldots, M \tag{1}$$

in which $\lambda$ is the wavelength, $r_i$ is the position over the surface $i$, $s_j$ is also the position over the surface $i$ (the character $s$ is employed for integration variables), $\epsilon_i$ $(\lambda, r_i)$ is the mono-


[1]Laboratório Nacional de Computação Científica, 22290, Rio de Janeiro, Brazil.



Contributed by the Heat Transfer Division for publication in the JOURNAL OF HEAT TRANSFER. Manuscript received by the Heat Transfer Division April 20, 1987. Keywords: Radiation.

chromatic emittance, and $\rho_i\ (\lambda,\ r_i)$ is the monochromatic reflectance at the point $r_i$.

The monochromatic radiosity will be denoted here by $B_i(\lambda, r_i)$ for the wavelength $\lambda$ and position $r_i$ (over the surface $i$).

The kernel $K(r_i, s_j)$ has the following properties:

(*a*) $K(r_i, s_j) = 0$ if the points $r_i$ and $s_j$ cannot exchange energy directly.

(*b*) $$K(r_i, s_j) = K(s_j, r_i) \tag{2}$$

(*c*) $$\sum_{j=1}^{M} \int_{A_j} K(r_i, s_j)\, dA = 1$$

$$\text{for all } r_i, \quad 1 \le i \le M \tag{3}$$

All real surfaces reflect a finite amount of the incident energy, in each wavelength range. This fact is sufficiently strong in order to assure existence and uniqueness of the solutions $B_i(\lambda, r_i)$ for equation (1). However, in this paper, we shall show that this sufficient condition is not necessary. Actually we may assume that, over some surfaces, the monochromatic reflectance is equal to one (perfectly reflecting surface), if some conditions are satisfied.

Equation (1) may be rewritten in the following way

$$\underline{\underline{T}}\,\underline{B} = \underline{f} \tag{4}$$

in which $\underline{B}$ is the vector field with components $B_i\ (\lambda, r_i)$ and the vectors field $\underline{\underline{T}}\,\underline{B}$ and $\underline{f}$ have their $i$ component given as

$$(\underline{\underline{T}}\,\underline{B})_i = B_i(\lambda, r_i) - \rho_i(\lambda, r_i) \sum_{j=1}^{M} \int_{A_j} B_j(\lambda, s_j) K(r_i, s_j)\, dA \tag{5}$$

$$f_i = \epsilon_i(\lambda, r_i) e_b(\lambda, T_i(r_i)) \tag{6}$$

In engineering calculations we generally look for the local heat flux, which is the amount of heat transfer per unit time and unit area, which is given, at the point $r_i$, by

$$q_i(r_i) = \int_0^{\infty} \left( B_i(\lambda, r_i) - \sum_{j=1}^{M} \int_{A_j} B_j(\lambda, s_j) K(r_i, s_j)\, dA \right) d\lambda \tag{7}$$

that represents the difference between all thermal radiant energy that leaves the surface $i$, at the point $r_i$, and all the incident thermal energy at the same point.

## 2 Existence and Uniqueness of Solution

In order to show that equation (1) (or equation (4)) has a solution it is sufficient to show that the linear operator $\underline{\underline{T}}$ has an inverse. This inverse exists if and only if (Kreyszig, 1978)

$$\underline{\underline{T}}\,\underline{B} = \underline{0} \Rightarrow \underline{B} = \underline{0} \tag{8}$$

In order to show that assertion (8) holds, we look for the solutions of the homogeneous system

$$B_i(\lambda, r_i) = \rho_i(\lambda, r_i) \sum_{j=1}^{M} \int_{A_j} B_j(\lambda, s_j) K(r_i, s_j)\, dA, \quad i = 1, 2, \ldots, M \tag{9}$$

If equation (9) admits only the trivial solution then the assertion (8) holds.

From equation (9) we may write the following inequality (Kreyszig, 1978):

$$|B_i(\lambda, r_i)| \le \rho_i(\lambda, r_i) \sum_{j=1}^{M} \int_{A_j} |B_j(\lambda, s_j)|\, K(r_i, s_j)\, dA, \quad i = 1, 2, \ldots, M \tag{10}$$

since $\rho_i(\lambda, r_i)$ and $K(r_i, s_j)$ are positively valued functions.

Aiming to show that the solution of equation (9) must be the trivial solution, let us integrate the inequality (10) over all considered $A_i\ (1 \le i \le M)$ which, taking into account equation (2), gives us

$$\sum_{i=1}^{M} \int_{A_i} |B_i(\lambda, r_i)|\, dA \le \sum_{i=1}^{M} \int_{A_i} \left( |B_i(\lambda, r_i)| \left( \sum_{j=1}^{M} \int_{A_j} \rho_j(\lambda, s_j) K(r_i, s_j)\, dA \right) dA \right) \tag{11}$$

In order to prove the existence of $\underline{\underline{T}}^{-1}$, it is necessary and sufficient to show that

$$\sum_{j=1}^{M} \int_{A_j} \rho_j(\lambda, s_j) K(r_i, s_j)\, dA < 1$$

$$\text{for all } 1 \le i \le M \tag{12}$$

Aiming to satisfy the above inequality it is sufficient (because of equation (3)) to show the existence of a region $A_k$ such that

$$\int_{A_k} (1 - \rho_k(\lambda, s_k)) K(r_i, s_k)\, dA > 0$$

$$\text{for all } 1 \le i \le M \tag{13}$$

and this implies that

$$\sum_{i=1}^{M} \int_{A_i} |B_i(\lambda, r_i)|\, dA = 0 \tag{14}$$

Physically the sufficient condition (13) says that the existence of a certain region $A_k$ that can exchange radiant energy directly with all the points in the enclosure (composed by the $M$ surfaces) and that has reflectance $\rho_k\ (\lambda, s_k)$ lower than one is sufficient for the existence of $\underline{\underline{T}}^{-1}$. It is important to notice that the quantity $M$ of considered surfaces is arbitrary, being chosen in a convenient way.

In real problems the sufficient condition (13) is always satisfied because all surfaces have reflectance lower than one, and this fact is sufficient for inequality (12) to hold.

Uniqueness may be shown taking into account the fact that $\underline{\underline{T}}$ is a linear operator. This enables us to write that

$$\text{if } \underline{\underline{T}}\,\underline{B}^* = \underline{f} \text{ and } \underline{\underline{T}}\,\underline{B}^{**} = \underline{f} \quad \text{then } \underline{\underline{T}}(\underline{B}^* - \underline{B}^{**}) = \underline{0} \tag{15}$$

The existence of $\underline{\underline{T}}^{-1}$ assures that $\underline{B}^* = \underline{B}^{**}$, which means uniqueness.

## 3 Upper and Lower Bounds for the Solution

Considering equation (3) we may prove that there are always two points $r_k$ and $r_n$, in each wavelength, that satisfy the following inequality for all $r_i$:

$$B_k(\lambda, r_k) \ge \sum_{j=1}^{M} \int_{A_j} B_j(\lambda, s_j) K(r_i, s_j)\, dA \ge B_n(\lambda, r_n) \tag{16}$$

Aiming to establish an upper bound for the solution, let us take equation (1), combined with inequality (16), at the point $r_k$

$$B_k(\lambda, r_k) \le \epsilon_k(\lambda, r_k) e_b(\lambda, T_k(r_k)) + \rho_k(\lambda, r_k) B_k(\lambda, r_k) \tag{17}$$

Since the surfaces are opaque and it is assumed that the radiation is not polarized we may write (Sparrow and Cess, 1978)

$$\epsilon_k(\lambda, r_k) = 1 - \rho_k(\lambda, r_k) \tag{18}$$

which, associated with inequality (17), allows us to conclude that

$$B_k(\lambda, r_k) \le e_b(\lambda, T_k(r_k)) \tag{19}$$

By a procedure analogous to the one previously used we may write the following inequality:

$$B_n(\lambda, r_n) \ge \epsilon_n(\lambda, r_n) e_b(\lambda, T_n(r_n)) + \rho_n(\lambda, r_n) B_n(\lambda, r_n) \tag{20}$$

which, because of equation (18), allows us to conclude that

$$B_n(\lambda, r_n) \ge e_b(\lambda, T_n(r_n)) \tag{21}$$

The inequalities (19) and (21) provide us an upper bound and a lower bound to monochromatic local radiosity in a radiation heat transfer problem.

With these bounds we can, from the knowledge of temperature fields, establish a priori the maximum and the minimum values that can be assumed by the monochromatic radiosity. This assertion may be expressed as

$$\mathrm{MAX}[e_b(\lambda, T)] \ge B_i(\lambda, r_i) \ge \mathrm{MIN}[e_b(\lambda, T)] \tag{22}$$

for all $\lambda$ and $r_i$, where MAX[ ] and MIN [ ] are the maximum and the minimum values assumed (for each wavelength) by the black-body emissive power in the considered enclosure.

These bounds may be obtained a priori, through Planck's law (Planck, 1959), because the temperature fields are known.

## 4 Solution Through Neumann Series

All diffuse radiation heat transfer problems, through non-participating media, may have their solution expressed in Neumann series.

Let us take equation (1) in the following form:

$$\underline{B} - \underline{\underline{S}}\,\underline{B} = \underline{f} \tag{23}$$

in which the $i$ component of vector $\underline{\underline{S}}\,\underline{B}$ is given as

$$(\underline{\underline{S}}\,\underline{B})_i = \rho_i(\lambda, r_i) \sum_{j=1}^{M} \int_{A_j} B_j(\lambda, s_j) K(r_i, s_j) dA \tag{24}$$

Now, we define the metric $d(\underline{u}, \underline{v})$ as

$$d(\underline{u}, \underline{v}) = \sup | u_i(\lambda, r_i) - v_i(\lambda, r_i) | \tag{25}$$

for each $\lambda$, in which the considered fields are bounded as the monochromatic radiosity. The supremum is taken over all points $r_i$, over all surfaces $i$, with $1 \le i \le M$.

In order to show that $\underline{\underline{S}}$ is a contraction, we have

$$d(\underline{\underline{S}}\,\underline{u}, \underline{\underline{S}}\,\underline{v}) \le \sup | u_i(\lambda, r_i) - v_i(\lambda, r_i) | \sup | \rho_i(\lambda, r_i) \sum_{j=1}^{M} \int_{A_j} K(r_i, s_j) dA | \tag{26}$$

From equation (3) we conclude that

$$d(\underline{\underline{S}}\,\underline{u}, \underline{\underline{S}}\,\underline{v}) \le \sup[\rho_i(\lambda, r_i)] d(\underline{u}, \underline{v}) \tag{27}$$

In a real problem we always have

$$\sup[\rho_i(\lambda, r_i)] < 1 \tag{28}$$

which assures that the operator $\underline{\underline{S}}$ is a contraction.

The solution of equation (1) (or equation (23)) may be evaluated, because $\underline{\underline{S}}$ is a contraction, by the following convergent Series:

$$\underline{B} = \underline{f} + \sum_{p=1}^{\infty} \underline{\underline{S}}^p \underline{f} \tag{29}$$

called the "Neumann Series."

## 5 A Variational Principle

We may rewrite equation (1) by using only self-adjoint operators (Helmberg, 1969). In this way we have

$$\underline{\underline{R}}\,\underline{B} - \underline{\underline{Q}}\,\underline{B} = \underline{g} \tag{30}$$

in which the $i$ components of vectors $\underline{\underline{R}}\,\underline{B}$, $\underline{\underline{Q}}\,\underline{B}$, and $\underline{g}$ are

$$(\underline{\underline{R}}\,\underline{B})_i = \frac{1}{\rho_i(\lambda, r_i)} B_i(\lambda, r_i) \tag{31}$$

$$(\underline{\underline{Q}}\,\underline{B})_i = \sum_{j=1}^{M} \int_{A_j} B_j(\lambda, s_j) K(r_i, s_j) dA \tag{32}$$

$$g_i = \frac{\epsilon_i(\lambda, r_i)}{\rho_i(\lambda, r_i)} e_b(\lambda, T_i(r_i)) \tag{33}$$

The vector field $\underline{B}$ that satisfies equation (30) (or equation (1)) is the vector field that makes the extremum the functional $I[\underline{B}]$, given as (Saldanha da Gama, 1985)

$$I[\underline{B}] = \langle \underline{\underline{Q}}\,\underline{B} | \underline{B} \rangle - \langle \underline{\underline{R}}\,\underline{B} | \underline{B} \rangle + 2\langle \underline{g} | \underline{B} \rangle \tag{34}$$

in which the inner product "$\langle\ |\ \rangle$" is defined as

$$\langle \underline{u} | \underline{v} \rangle = \sum_{i=1}^{M} \int_{A_i} u_i(\lambda, r_i) v_i(\lambda, r_i) dA \tag{35}$$

and the admissible vector fields need to satisfy $\langle \underline{B} | \underline{B} \rangle < \infty$.

## References


Helmberg, G., 1969, *Introduction to Spectral Theory in Hilbert Space*, North-Holland Series in Applied Mathematics and Mechanics, Vol. 6, Amsterdam.

Kreyszig, E., 1978, *Introductory Functional Analysis With Applications*, Wiley, New York.

Planck, M., 1959, *The Theory of Heat Radiation*, Dover Publications, New York.

Saldanha da Gama, R. M., 1985, "Uma Formulação Variacional Geral para Problemas de Troca de Calor por Radiação Difusa," *Revista Brasileira de Ciências Mecânicas*, Vol. 7, pp. 163-179.

Sparrow, E. M., and Cess, R. D., 1978, *Radiation Heat Transfer*, McGraw-Hill, Washington.


# Characteristic of Heat Transfer Enhancement Due to Bubbles Passing Through a Narrow Vertical Channel


**M. Monde**[1]


## Nomenclature

- $a$ = thermal diffusivity of liquid = $\lambda/\rho c$
- $B_1$ = dimensionless parameter $= q_{wo}\sqrt{a_l T_o}/\lambda_l (T_{wo} - T_l)$
- $B_2$ = dimensionless parameter $= (\rho c \lambda)_s \delta_s / (\rho c \lambda)_l \sqrt{a_s T_o}$
- $\bar{h}$ = time-averaged heat transfer coefficient
- $q_w(t)$ = instantaneous heat flux at the heated surface
- $q_{wo}$ = initial heat flux of the heated surface
- $T$ = temperature
- $T_0$ = period of passing bubble
- $T_w(t)$ = temperature of heated surface
- $T_{wo}$ = initial temperature of the heated surface


[1]Department of Mechanical Engineering, Saga University, 1 Honjo Saga, 840 Japan.



Contributed by the Heat Transfer Division for publication in the JOURNAL OF HEAT TRANSFER. Manuscript received by the Heat Transfer Division July 6, 1987. Keywords: Augmentation and Enhancement, Heat Exchangers, Transient and Unsteady Heat Transfer.

which, associated with inequality (17), allows us to conclude that

$$B_k(\lambda, r_k) \le e_b(\lambda, T_k(r_k)) \tag{19}$$

By a procedure analogous to the one previously used we may write the following inequality:

$$B_n(\lambda, r_n) \ge \epsilon_n(\lambda, r_n) e_b(\lambda, T_n(r_n)) + \rho_n(\lambda, r_n) B_n(\lambda, r_n) \tag{20}$$

which, because of equation (18), allows us to conclude that

$$B_n(\lambda, r_n) \ge e_b(\lambda, T_n(r_n)) \tag{21}$$

The inequalities (19) and (21) provide us an upper bound and a lower bound to monochromatic local radiosity in a radiation heat transfer problem.

With these bounds we can, from the knowledge of temperature fields, establish a priori the maximum and the minimum values that can be assumed by the monochromatic radiosity. This assertion may be expressed as

$$\mathrm{MAX}[e_b(\lambda, T)] \ge B_i(\lambda, r_i) \ge \mathrm{MIN}[e_b(\lambda, T)] \tag{22}$$

for all $\lambda$ and $r_i$, where MAX[ ] and MIN [ ] are the maximum and the minimum values assumed (for each wavelength) by the black-body emissive power in the considered enclosure.

These bounds may be obtained a priori, through Planck's law (Planck, 1959), because the temperature fields are known.

## 4 Solution Through Neumann Series

All diffuse radiation heat transfer problems, through non-participating media, may have their solution expressed in Neumann series.

Let us take equation (1) in the following form:

$$\underline{\underline{B}} - \underline{\underline{S}}\,\underline{B} = \underline{f} \tag{23}$$

in which the $i$ component of vector $\underline{\underline{S}}\,\underline{B}$ is given as

$$(\underline{\underline{S}}\,\underline{B})_i = \rho_i(\lambda, r_i) \sum_{j=1}^{M} \int_{A_j} B_j(\lambda, s_j) K(r_i, s_j) dA \tag{24}$$

Now, we define the metric $d(\underline{u}, \underline{v})$ as

$$d(\underline{u}, \underline{v}) = \sup | u_i(\lambda, r_i) - v_i(\lambda, r_i) | \tag{25}$$

for each $\lambda$, in which the considered fields are bounded as the monochromatic radiosity. The supremum is taken over all points $r_i$, over all surfaces $i$, with $1 \le i \le M$.

In order to show that $\underline{\underline{S}}$ is a contraction, we have

$$d(\underline{\underline{S}}\,\underline{u}, \underline{\underline{S}}\,\underline{v}) \le \sup | u_i(\lambda, r_i) - v_i(\lambda, r_i) | \sup | \rho_i(\lambda, r_i) \sum_{j=1}^{M} \int_{A_j} K(r_i, s_j) dA | \tag{26}$$

From equation (3) we conclude that

$$d(\underline{\underline{S}}\,\underline{u}, \underline{\underline{S}}\,\underline{v}) \le \sup[\rho_i(\lambda, r_i)] d(\underline{u}, \underline{v}) \tag{27}$$

In a real problem we always have

$$\sup[\rho_i(\lambda, r_i)] < 1 \tag{28}$$

which assures that the operator $\underline{\underline{S}}$ is a contraction.

The solution of equation (1) (or equation (23)) may be evaluated, because $\underline{\underline{S}}$ is a contraction, by the following convergent Series:

$$\underline{\underline{B}} = \underline{f} + \sum_{p=1}^{\infty} \underline{\underline{S}}^p \underline{f} \tag{29}$$

called the "Neumann Series."

## 5 A Variational Principle

We may rewrite equation (1) by using only self-adjoint operators (Helmberg, 1969). In this way we have

$$\underline{\underline{R}}\,\underline{B} - \underline{\underline{Q}}\,\underline{B} = \underline{g} \tag{30}$$

in which the $i$ components of vectors $\underline{\underline{R}}\,\underline{B}$, $\underline{\underline{Q}}\,\underline{B}$, and $\underline{g}$ are

$$(\underline{\underline{R}}\,\underline{B})_i = \frac{1}{\rho_i(\lambda, r_i)} B_i(\lambda, r_i) \tag{31}$$

$$(\underline{\underline{Q}}\,\underline{B})_i = \sum_{j=1}^{M} \int_{A_j} B_j(\lambda, s_j) K(r_i, s_j) dA \tag{32}$$

$$g_i = \frac{\epsilon_i(\lambda, r_i)}{\rho_i(\lambda, r_i)} e_b(\lambda, T_i(r_i)) \tag{33}$$

The vector field $\underline{B}$ that satisfies equation (30) (or equation (1)) is the vector field that makes the extremum the functional $I[\underline{B}]$, given as (Saldanha da Gama, 1985)

$$I[\underline{B}] = \langle \underline{\underline{Q}}\,\underline{B} \,|\, \underline{B} \rangle - \langle \underline{\underline{R}}\,\underline{B} \,|\, \underline{B} \rangle + 2\langle \underline{g} \,|\, \underline{B} \rangle \tag{34}$$

in which the inner product "$\langle\ |\ \rangle$" is defined as

$$\langle \underline{u} \,|\, \underline{v} \rangle = \sum_{i=1}^{M} \int_{A_i} u_i(\lambda, r_i) v_i(\lambda, r_i) dA \tag{35}$$

and the admissible vector fields need to satisfy $\langle \underline{B} \,|\, \underline{B} \rangle < \infty$.

## References


Helmberg, G., 1969, *Introduction to Spectral Theory in Hilbert Space*, North-Holland Series in Applied Mathematics and Mechanics, Vol. 6, Amsterdam.

Kreyszig, E., 1978, *Introductory Functional Analysis With Applications*, Wiley, New York.

Planck, M., 1959, *The Theory of Heat Radiation*, Dover Publications, New York.

Saldanha da Gama, R. M., 1985, "Uma Formulação Variacional Geral para Problemas de Troca de Calor por Radiação Difusa," *Revista Brasileira de Ciências Mecânicas*, Vol. 7, pp. 163–179.

Sparrow, E. M., and Cess, R. D., 1978, *Radiation Heat Transfer*, McGraw-Hill, Washington.


# Characteristic of Heat Transfer Enhancement Due to Bubbles Passing Through a Narrow Vertical Channel


**M. Monde**[1]


## Nomenclature

- $a$ = thermal diffusivity of liquid = $\lambda/\rho c$
- $B_1$ = dimensionless parameter $= q_{wo}\sqrt{a_l T_o}/\lambda_l (T_{wo} - T_l)$
- $B_2$ = dimensionless parameter $= (\rho c \lambda)_s \delta_s / (\rho c \lambda)_l \sqrt{a_s T_o}$
- $\bar{h}$ = time-averaged heat transfer coefficient
- $q_w(t)$ = instantaneous heat flux at the heated surface
- $q_{wo}$ = initial heat flux of the heated surface
- $T$ = temperature
- $T_0$ = period of passing bubble
- $T_w(t)$ = temperature of heated surface
- $T_{wo}$ = initial temperature of the heated surface


[1] Department of Mechanical Engineering, Saga University, 1 Honjo Saga, 840 Japan.



Contributed by the Heat Transfer Division for publication in the JOURNAL OF HEAT TRANSFER. Manuscript received by the Heat Transfer Division July 6, 1987. Keywords: Augmentation and Enhancement, Heat Exchangers, Transient and Unsteady Heat Transfer.

$t$ = time
$x$ = distance from the heated surface
$x^*$ = thickness of liquid film
$\delta$ = dimensionless thickness of liquid film
$= x^*/\sqrt{a_l T_o}$
$\theta$ = dimensionless temperature = $(T-T_l)/(T_{wo}-T_l)$
$\lambda$ = thermal conductivity
$\xi$ = dimensionless distance
$= x^*/\sqrt{a_l T_o}$
$\rho$ = density
$\tau$ = dimensionless time = $t/T_o$

**Subscripts**

$l$ = liquid
$s$ = solid

## Introduction

Heat transfer is markedly enhanced when bubbles generated on a heated surface in a narrow space pass through the narrow space under the conditions of bubble or slug flow. Ishibashi and Nishikawa (1969) explained the mechanism of enhancement by means of a transient thermal conduction model in which 70 percent of the total heat transfer was transported by convection and the remainder by latent heat. However, it was assumed that the surface temperature remained constant in spite of disturbances caused by passing bubbles. In addition, the analysis differs from the actual phenomenon since evaporation of the liquid film on the surface when a bubble passes by depends on the heat flux and the period of the rising bubbles. These effects should cause differences between theoretical and experimental results.

Kusuda et al. (1981) measured the temperature change of the heated surface due to the passing bubbles by using an electrically heated stainless steel foil as the heated surface. They proposed a model for the enhancement of heat transfer based on the relationship between the change of the surface temperature and period of the passing bubble. However, comparison of theoretical and experimental results was made over an experimental range that was not sufficient to elucidate the mechanism of the enhancement of the heat transfer due to the passing bubble.

The present study will discuss characteristics of the enhancement by applying the model proposed by Kusuda et al. (1981) to constant temperature and constant heat flux without evaporation at the interface.

## Theoretical Analysis and Its Solution

The model of Kusuda et al. (1981) for heat transfer enhancement will be explained briefly. This model is based on the following assumptions: Most of the superheated liquid is swept away by the bubble passing along the heated surface; a thin liquid film always remains between the heated surface and the passing bubble, but evaporation from its surface can be ignored; and liquid at the bulk temperature again covers the heated surface immediately after the bubble passes. Based on their assumptions, a model of heat conduction for a semi-infinite solid, as shown in Fig. 1, allows the problem to be treated since the thickness of the remaining liquid film is very thin compared with the width of the narrow space; that is, the ratio of its thickness to its width would be less than 1/10 and the value of $\sqrt{a_l T_o}$ is the order of $10^{-4}$ m. The existence of this liquid film has been pointed out by many studies (for example, Bretherton, 1959) but its thickness remains uncertain.

The basic equation for the model shown in Fig. 1 is as follows:

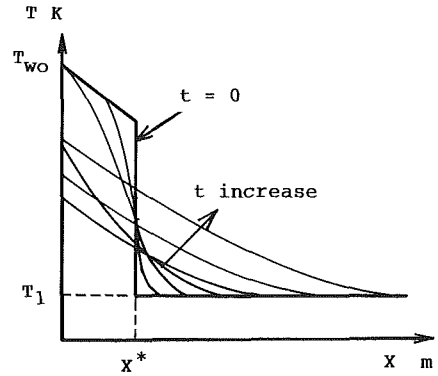


**Fig. 1 Physical model of heat transfer enhancement**

$$\frac{\partial T}{\partial t} = a_l \frac{\partial^2 T}{\partial x^2} \tag{1}$$

[Initial conditions]

$$T = T_{wo} - (q_{wo}/\lambda_l)x \qquad 0 < x < x^* \tag{2}$$

$$T = T_l \qquad x^* < x \tag{3}$$

[Boundary condition]

$$\lambda_l \frac{\partial T}{\partial x} = -q_{wo} + (\rho c \delta)_s \frac{dT_w}{dt} \qquad x = 0 \tag{4}$$

The exact solution of equations (1)-(4) is given by equation (5). From equation (5), the temperature of the heated surface is immediately given by equation (6) and the periodic solution by equation (7).

$$\vartheta(\xi, \tau) = (1 - B_1\xi) - \frac{1}{2}\left[(1 + B_1\xi + 2B_1B_2)\mathrm{erfc}\left(\frac{\delta+\xi}{2\sqrt{\tau}}\right) + (1 - B_1\xi) \times \mathrm{erfc}\left(\frac{\delta-\xi}{2\sqrt{\tau}}\right)\right] + B_1\sqrt{\frac{\tau}{\pi}}\left(e^{-(\delta+\xi)^2/4\tau} + e^{-(\delta-\xi)^2/4}\right) + (B_1B_2 - B_1\delta + 1)e^{((\delta+\xi)/B_2 + \tau/B_2^2)}\mathrm{erfc}\left(\frac{\delta+\xi}{2\sqrt{\tau}} + \frac{\sqrt{\tau}}{B_2}\right) \tag{5}$$

$$\vartheta_w(0, \tau) = 1 - (1 + B_1B_2)\mathrm{erfc}\left(\frac{\delta}{2\sqrt{\tau}}\right) + 2B_1\sqrt{\frac{\tau}{\pi}}\, e^{-\delta^2/4\tau} + (B_1B_2 - B_1\delta + 1)e^{(\delta/B_2 + \tau/B_2^2)}\mathrm{erfc}\left(\frac{\delta}{2\sqrt{\tau}} + \frac{\sqrt{\tau}}{B_2}\right) \tag{6}$$

$$(1 + B_1B_2)\mathrm{erfc}(\delta/2) - \frac{2}{\sqrt{\pi}} B_1 e^{-\delta^2/4} - (B_1B_2 - B_1\delta + 1) \times e^{(\delta/B_2 + 1/B_2^2)}\mathrm{erfc}(\delta/2 + 1/B_2) = 0 \tag{7}$$

In this study, the characteristics of solutions for two special cases of heated surfaces with a constant heat flux and a constant temperature will be developed including two limiting states of $\delta = 0$ and $\infty$.

The exact solution for a constant heat flux can be easily derived by substituting $B_2 = 0$ into equation (5)

$$\vartheta(\xi, \tau) = 1 - B_1\xi - \frac{1}{2}\left[(1 + B_1\xi)\mathrm{erfc}\left(\frac{\delta+\xi}{2\sqrt{\tau}}\right) + (1 - B_1\xi) \times \mathrm{erfc}\left(\frac{\delta-\xi}{2\sqrt{\tau}}\right)\right] + B_1\sqrt{\frac{\tau}{\pi}}\left(e^{-(\delta+\xi)^2/4\tau} + e^{-(\delta-\xi)^2/4\tau}\right) \tag{8}$$

From equation (8), the temperature of the heated surface becomes

$$\vartheta_w(\tau) = \mathrm{erf}(\delta/2\sqrt{\tau}) + 2B_1\sqrt{\frac{\tau}{\pi}}\, e^{-\delta^2/4\tau} \tag{9}$$

and the periodic condition becomes

$$B_1 = \sqrt{\pi}/2e^{\delta^2/4}\mathrm{erfc}(\delta/2) \tag{10}$$

Figure 2 shows the change in the heated surface temperature calculated from equation (9) during one period.

The exact solution for the constant temperature heated surface cannot be derived by letting $B_2 \to \infty$ in equation (5). Accordingly, we solve equations (1)–(3) again, but with $T_w$ = const to give the constant temperature solution as follows:

$$\vartheta(\xi, \tau) = \frac{1}{2}\left[(1-B_1\xi)\mathrm{erfc}\left(\frac{\xi-\delta}{2\sqrt{\tau}}\right) + (1+B_1\xi)\mathrm{erfc}\left(\frac{\xi+\delta}{2\sqrt{\tau}}\right)\right]$$

$$-B_1\sqrt{\frac{\tau}{\pi}}\left(e^{-(\xi+\delta)^2/4\tau} - e^{-(\xi-\delta)^2/4\tau}\right) \tag{11}$$

From equation (11), the wall heat flux becomes

$$q_w(\tau)/q_{wo} = \mathrm{erf}(\delta/2\sqrt{\tau}) + \frac{1}{\sqrt{\pi\tau}}(1/B_1 - \delta)e^{-\delta^2/4\tau} \tag{12}$$

and the periodic solution becomes

$$B_1 = 1/[\delta + \sqrt{\pi}e^{\delta^2/4}\mathrm{erfc}(\delta/2)] \tag{13}$$

Figure 3 shows the change in the heat flux at the wall calculated from equation (12) during one period.

### Relationship Between Heat Transfer Coefficient and Period of Passing Bubbles

The time-averaged heat transfer coefficient is defined as follows:

$$\bar{h} = \frac{1}{T_o}\int_0^{T_o} \frac{q_w(t)}{T_w(t) - T_l}\, dt \tag{14}$$

The resulting heat transfer coefficient for the constant heat flux case is:

$$\frac{\bar{h}\sqrt{a_l T_o}}{\lambda_l} = B_1\int_0^1 \frac{1}{\mathrm{erf}(\delta/2\sqrt{\tau}) + 2B_1\sqrt{\tau/\pi}\, e^{-\delta^2/4\tau}}\, d\tau \tag{15}$$

and for the constant temperature case is:

$$\frac{\bar{h}\sqrt{a_l T_o}}{\lambda_l} = B_1\mathrm{erf}(\delta/2) + \frac{2-B_1\delta}{\sqrt{\pi}}\, e^{-\delta^2/4}$$

$$-\delta(1 + B_1/2 - B_1\delta)\mathrm{erfc}(\delta/2) \tag{16}$$

Figure 4 shows the relationship between $\bar{h}\sqrt{a_l T_o}/\lambda_l$ and $\delta = x^*/\sqrt{a_l T_o}$, which can be calculated from equations (15) and (16), and the periodic solutions calculated from equations (10) and (13). A broken line in Fig. 4 shows the relationship when $\bar{h}$ is independent of $T_o$. The data for water and $q_{wo}$ = 4500 W/m$^2$ from the experiment of Kusuda et al. (1981) are all shown in the figure (the thickness $x^*$ cannot be measured and the results are based by assuming that $x^*$ = 50 $\mu$m). In addition, the theoretical result of Ishibashi and Nishikawa (1969) cannot be exactly placed in the form as shown in Fig. 4, because the thickness $x^*$ is not known and the period $T_o$ is related to the heat flux and clearance of a channel. Their result can be rearranged for $\bar{h}$ and $T_o$ as follows:

$$\bar{h}\sqrt{a_l T_o}/\lambda_l = C(a_l T_o)^{1/9}$$

It is seen from Fig. 4 that as the value of $\delta = x^*/\sqrt{a_l T_o}$ becomes large, the value of $\bar{h}$ approaches the broken line and ultimately becomes independent of $T_o$ for $\delta > 7$. Under the limiting condition that $\delta > 7$, the enhancement of heat transfer due to the passing bubble becomes saturated and more enhancement cannot be expected. The upper limits of the heat transfer coefficients for the constant heat flux and

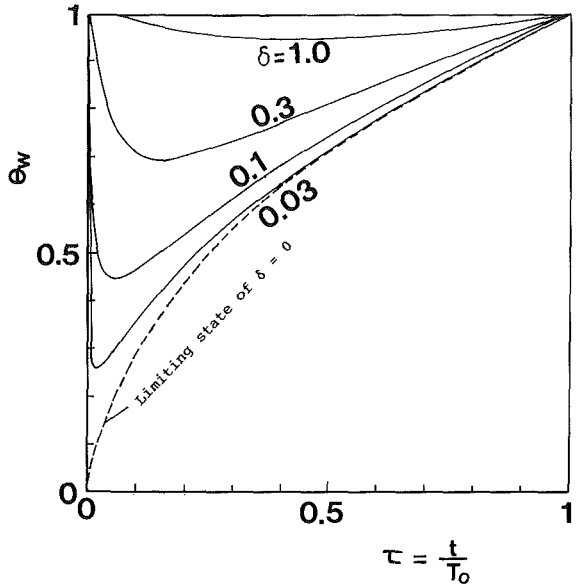


Fig. 2 Variation of heated surface temperature for constant heat flux

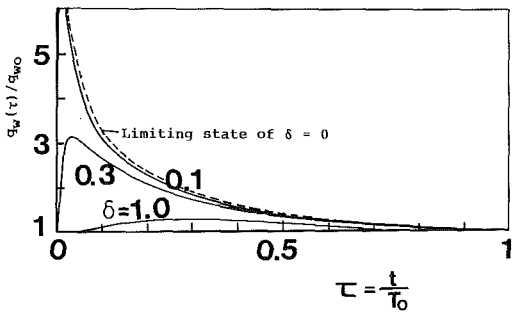


Fig. 3 Variation of heat flux of heated surface held at constant temperature

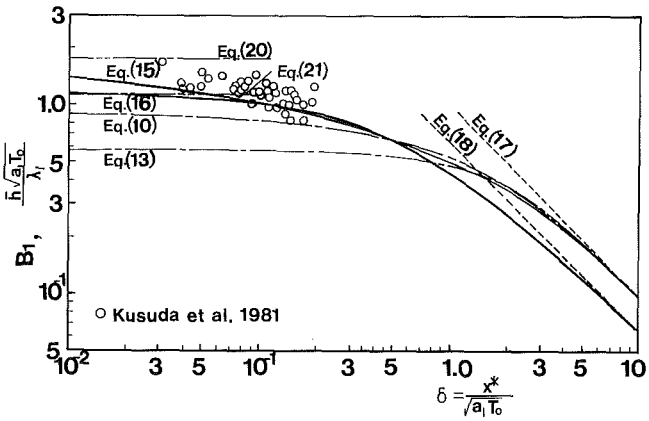


Fig. 4 $\bar{h}\sqrt{a_l T_o}/\lambda_l$ versus $\delta\,(= x^*/\sqrt{a_l T_o})$

temperature cases are given by equations (17) and (18), respectively,

$$\bar{h}(T_{wo} - T_l)/q_{wo} = \bar{h}x^*/\lambda_l = \begin{cases} 1 & (17) \\ 2/3 & (18) \end{cases}$$

It should be noted that neither an initial temperature $T_{wo}$ in the constant heat flux solution nor an initial heat flux $q_{wo}$ in the constant temperature solution can be determined by the present analysis, so two initial values must be determined by an alternative method such as an experiment. In addition, it

may be of importance to give the temperature profiles in the liquid on the heated surfaces with the constant heat flux and the constant temperature in the limiting case of $\delta > 7$. Each temperature profile for $\delta > 7$ derived from equations (8) and (11) becomes the same

$$\theta(\xi, \tau) = 1 - B_1 \xi$$
$$= 1 - q_{wo} x/\lambda_1 (T_{wo} - T_l) = 1 - x/x^* \quad (19)$$

Equation (19) shows that the temperature profile in the liquid is independent of time.

On the other hand, as $\delta = x^*/\sqrt{a_l T_o}$ becomes small, the value of $\bar{h}\sqrt{a_l T_o}/\lambda_l$ approaches constant values as follows:

$$\bar{h}\sqrt{a_l T_o}/\lambda_l = \sqrt{\pi} \text{ for the constant-heat-flux case} \quad (20)$$
$$= 2/\sqrt{\pi} \text{ for the constant-temperature case} \quad (21)$$

Although the thickness $x^*$ was not measured, the condition $\delta \ll 1$ appears when $T_o \gg 1$. Under such conditions, the temperature and heat flux of the heated surface completely recover to the initial state, corresponding to the steady-state temperature and the heat flux without passing bubbles. Defining the heat transfer coefficient as $h_o$ for the steady state without passing bubbles, we have $\bar{h}/h_o = 2$ for both cases under the condition of $\delta \ll 1$.

### Conclusion

The enhancement of heat transfer from bubbles passing has been studied theoretically. The enhancement of the heat transfer due to the passing bubble becomes saturated for $\delta > 7$, yielding its upper limits for constant-heat-flux and constant-temperature conditions predicted by equations (17) and (18). Analogous heat transfer coefficients for $\delta \ll 1$ are given by equations (20) and (21).

### References


Bretherton, F. P., 1961, "The Motion of Long Bubbles in Tubes," *J. Fluid Mechanics*, Vol. 10, pp. 166–188.

Ishibashi, E., and Nishikawa, K., 1969, "Saturated Boiling Heat Transfer in Narrow Space," *Int. J. Heat Mass Transfer*, Vol. 12, pp. 863–894.

Kusuda, H., Monde, M., Uehara, H., and Otsubo, K., 1981, "Bubble Influence on Boiling Heat Transfer in a Narrow Space," *Heat Transfer—Japanese Research*, Vol. 9, No. 2, pp. 49–60.


## Condensation of Ethylene Glycol on Horizontal Integral-Fin Tubes


**H. Masuda[1] and J. W. Rose[2]**


### Nomenclature

- $B$ = constant, see equation (3)
- $b$ = spacing between fins
- $c_{P_c}$ = isobaric specific heat capacity (coolant)
- $d$ = diameter at fin root; outside diameter of plain tube
- $d_i$ = inside diameter
- $g$ = specific force of gravity
- $h$ = fin height
- $h_{fg}$ = specific enthalpy of evaporation (condensing fluid)
- $h_{fg_c}$ = specific enthalpy of evaporation (coolant)
- $k$ = thermal conductivity (condensing fluid)
- $k_c$ = thermal conductivity (coolant)
- $l$ = length of condenser tube exposed to vapor
- Nu = vapor-side Nusselt number $= Qd/\Delta T k$
- $\mathrm{Nu}_c$ = coolant-side Nusselt number $= Q_l d_i/\Delta T_c k_c$
- $\mathrm{Pr}_c$ = coolant Prandtl number $= \mu_c c_{P_c}/k_c$
- $Q$ = heat flux $= Q_T/\pi dl$
- $Q_l$ = heat flux $= Q_T/\pi d_i l$
- $Q_T$ = heat transfer rate to coolant
- $R$ = radius to fin tip
- $\mathrm{Re}_c$ = coolant Reynolds number $= u_c \rho_c d_i/\mu_c$
- $T_b$ = inside wall temperature for local boiling of coolant, see equation (2)
- $T_c$ = mean coolant temperature $= (T_{in} + T_{out})/2$
- $T_o$ = effective surface temperature at fin-root diameter
- $T_{\mathrm{sat}_c}$ = saturation temperature (coolant)
- $T_v$ = vapor temperature
- $T_w$ = inside wall temperature
- $T_{in}$ = inlet coolant temperature
- $T_{out}$ = outlet coolant temperature
- $t$ = fin thickness
- $U$ = overall heat transfer coefficient $= Q/\Delta T_{lm}$
- $u_c$ = coolant velocity
- $v_{g_c}$ = specific volume of saturated vapor (coolant)
- $\alpha$ = vapor-side heat transfer coefficient $= Q/\Delta T$
- $\Delta T$ = vapor-side temperature difference $= T_v - T_o$
- $\Delta T_c$ = coolant-side temperature difference $= T_w - T_c$
- $\Delta T_{lm}$ = vapor-to-coolant logarithmic mean temperature difference $= (T_{out} - T_{in})/\ln\{(T_v - T_{in})/(T_v - T_{out})\}$
- $\epsilon_A$ = area enhancement $= \{(d+2h)t + bd + 2h(d+h)\}/d(b+t)$
- $\epsilon_{\Delta T}$ = $\alpha_{\text{finned tube}}/\alpha_{\text{plain tube}}$ for same $\Delta T$, see also equation (4)
- $\epsilon_Q$ = $\alpha_{\text{finned tube}}/\alpha_{\text{plain tube}}$ for same $Q$, see also equation (5)
- $\mu_c$ = viscosity of coolant at $T_c$
- $\mu_w$ = viscosity of coolant at $T_w$
- $\rho$ = density (condensate)
- $\rho_c$ = density (coolant)
- $\sigma$ = surface tension
- $\phi$ = angle from top of tube at which fin flanks become wholly "flooded" with retained condensate

### Introduction

The problem of heat transfer during consensation on horizontal finned tubes is extremely complex. The difficulty arises from the essentially three-dimensional character of the


[1]Mitsubishi Electric Corp., Itami Works, 1-1, Tsukaguchi-Honmachi, 8 Chome, Amagasaki City, Hyogo Pref., Japan 661.

[2]Department of Mechanical Engineering, Queen Mary College, University of London, London, E1 4NS, United Kingdom.



Contributed by the Heat Transfer Division and based on a paper presented at the ASME-JSME Thermal Engineering Conference, Honolulu, Hawaii, March 22–27, 1987. Manuscript received by the Heat Transfer Division July 8, 1987. Keywords: Condensation, Multiphase Flows.

may be of importance to give the temperature profiles in the liquid on the heated surfaces with the constant heat flux and the constant temperature in the limiting case of $\delta > 7$. Each temperature profile for $\delta > 7$ derived from equations (8) and (11) becomes the same

$$\theta(\xi, \tau) = 1 - B_1 \xi$$
$$= 1 - q_{wo} x/\lambda_l (T_{wo} - T_l) = 1 - x/x^* \quad (19)$$

Equation (19) shows that the temperature profile in the liquid is independent of time.

On the other hand, as $\delta = x^*/\sqrt{a_l T_o}$ becomes small, the value of $\bar{h}\sqrt{a_l T_o}/\lambda_l$ approaches constant values as follows:

$$\bar{h}\sqrt{a_l T_o}/\lambda_l = \sqrt{\pi} \text{ for the constant-heat-flux case} \quad (20)$$
$$= 2/\sqrt{\pi} \text{ for the constant-temperature case} \quad (21)$$

Although the thickness $x^*$ was not measured, the condition $\delta \ll 1$ appears when $T_o \gg 1$. Under such conditions, the temperature and heat flux of the heated surface completely recover to the initial state, corresponding to the steady-state temperature and the heat flux without passing bubbles. Defining the heat transfer coefficient as $h_o$ for the steady state without passing bubbles, we have $\bar{h}/h_o = 2$ for both cases under the condition of $\delta \ll 1$.

### Conclusion

The enhancement of heat transfer from bubbles passing has been studied theoretically. The enhancement of the heat transfer due to the passing bubble becomes saturated for $\delta > 7$, yielding its upper limits for constant-heat-flux and constant-temperature conditions predicted by equations (17) and (18). Analogous heat transfer coefficients for $\delta \ll 1$ are given by equations (20) and (21).

### References


Bretherton, F. P., 1961, "The Motion of Long Bubbles in Tubes," *J. Fluid Mechanics*, Vol. 10, pp. 166–188.

Ishibashi, E., and Nishikawa, K., 1969, "Saturated Boiling Heat Transfer in Narrow Space," *Int. J. Heat Mass Transfer*, Vol. 12, pp. 863–894.

Kusuda, H., Monde, M., Uehara, H., and Otsubo, K., 1981, "Bubble Influence on Boiling Heat Transfer in a Narrow Space," *Heat Transfer—Japanese Research*, Vol. 9, No. 2, pp. 49–60.


## Condensation of Ethylene Glycol on Horizontal Integral-Fin Tubes


**H. Masuda[1] and J. W. Rose[2]**


### Nomenclature

- $B$ = constant, see equation (3)
- $b$ = spacing between fins
- $c_{P_c}$ = isobaric specific heat capacity (coolant)
- $d$ = diameter at fin root; outside diameter of plain tube
- $d_i$ = inside diameter
- $g$ = specific force of gravity
- $h$ = fin height
- $h_{fg}$ = specific enthalpy of evaporation (condensing fluid)
- $h_{fg_c}$ = specific enthalpy of evaporation (coolant)
- $k$ = thermal conductivity (condensing fluid)
- $k_c$ = thermal conductivity (coolant)
- $l$ = length of condenser tube exposed to vapor
- Nu = vapor-side Nusselt number $= Qd/\Delta T k$
- $\mathrm{Nu}_c$ = coolant-side Nusselt number $= Q_l d_i/\Delta T_c k_c$
- $\mathrm{Pr}_c$ = coolant Prandtl number $= \mu_c c_{P_c}/k_c$
- $Q$ = heat flux $= Q_T/\pi dl$
- $Q_l$ = heat flux $= Q_T/\pi d_i l$
- $Q_T$ = heat transfer rate to coolant
- $R$ = radius to fin tip
- $\mathrm{Re}_c$ = coolant Reynolds number $= u_c \rho_c d_i/\mu_c$
- $T_b$ = inside wall temperature for local boiling of coolant, see equation (2)
- $T_c$ = mean coolant temperature $= (T_{in} + T_{out})/2$
- $T_o$ = effective surface temperature at fin-root diameter
- $T_{\mathrm{sat}_c}$ = saturation temperature (coolant)
- $T_v$ = vapor temperature
- $T_w$ = inside wall temperature
- $T_{in}$ = inlet coolant temperature
- $T_{out}$ = outlet coolant temperature
- $t$ = fin thickness
- $U$ = overall heat transfer coefficient $= Q/\Delta T_{lm}$
- $u_c$ = coolant velocity
- $v_{g_c}$ = specific volume of saturated vapor (coolant)
- $\alpha$ = vapor-side heat transfer coefficient $= Q/\Delta T$
- $\Delta T$ = vapor-side temperature difference $= T_v - T_o$
- $\Delta T_c$ = coolant-side temperature difference $= T_w - T_c$
- $\Delta T_{lm}$ = vapor-to-coolant logarithmic mean temperature difference $= (T_{out} - T_{in})/\ln\{(T_v - T_{in})/(T_v - T_{out})\}$
- $\epsilon_A$ = area enhancement $= \{(d+2h)t + bd + 2h(d+h)\}/d(b+t)$
- $\epsilon_{\Delta T}$ = $\alpha_{\text{finned tube}}/\alpha_{\text{plain tube}}$ for same $\Delta T$, see also equation (4)
- $\epsilon_Q$ = $\alpha_{\text{finned tube}}/\alpha_{\text{plain tube}}$ for same $Q$, see also equation (5)
- $\mu_c$ = viscosity of coolant at $T_c$
- $\mu_w$ = viscosity of coolant at $T_w$
- $\rho$ = density (condensate)
- $\rho_c$ = density (coolant)
- $\sigma$ = surface tension
- $\phi$ = angle from top of tube at which fin flanks become wholly "flooded" with retained condensate

### Introduction

The problem of heat transfer during consensation on horizontal finned tubes is extremely complex. The difficulty arises from the essentially three-dimensional character of the


[1]Mitsubishi Electric Corp., Itami Works, 1-1, Tsukaguchi-Honmachi, 8 Chome, Amagasaki City, Hyogo Pref., Japan 661.

[2]Department of Mechanical Engineering, Queen Mary College, University of London, London, E1 4NS, United Kingdom.



Contributed by the Heat Transfer Division and based on a paper presented at the ASME-JSME Thermal Engineering Conference, Honolulu, Hawaii, March 22–27, 1987. Manuscript received by the Heat Transfer Division July 8, 1987. Keywords: Condensation, Multiphase Flows.

condensate flow, together with significant surface tension effects. The fact that the heat transfer enhancement can significantly exceed the surface area augamentation may be attributable in part to the small "effective plate heights" associated with the fin flanks and also to the effects of surface tension in locally thinning the condensate film. Progress has been made toward the theoretical understanding of the heat transfer problem (see for instance Beatty and Katz, 1948; Honda and Nozu, 1984; and Webb et al., 1985), and for the related phenomenon of static liquid retention on horizontal finned tubes (see for instance Honda et al., 1983; Rudy and Webb, 1985; and Masuda and Rose, 1987). Experimentally, the problem is made difficult by the requirement for high accuracy in measuring the relatively high vapor-side heat transfer coefficient and the need to avoid errors that can result from the presence of noncondensing gas or from the occurrence of dropwise condensation. The large number of variables involved also presents significant difficulty.

The present note reports the continuation of a systematic experimental study. For fins of rectangular cross section, the effect of fin spacing on the vapor-side heat transfer coefficient has been observed for different condensing fluids. Work on steam and refrigerant 113 has been reported by Yau et al. (1985, 1986) and Masuda and Rose (1985). New data for ethylene glycol are given here.

## Apparatus and Procedure

The apparatus was the same as that used earlier and has been described in detail by Masuda and Rose (1985). Vapor, generated in a stainless steel boiler, flowed vertically downward over the horizontal condenser tube. Cooling water was passed through the condenser tube via a float-type flow meter. The condenser tube and the inlet and outlet ducts were well insulated from the body of the test section and from the environment with nylon and ptfe components. Condensate from the tube and uncondensed vapor were led to an auxiliary condenser and all of the condensate was returned by gravity to the boiler. The boiler, vapor supply duct, and the test section were thermally well insulated from the surroundings. The temperatures at the test section, condensate return, and cooling water inlet and outlet were measured using thermocouples, which fitted tightly in closed metal tubes. In all cases care was taken to ensure adequate isothermal immersion of the thermocouple leads. An essentially adiabatic mixing section was located at the coolant outlet. The test-section gage pressure was measured with an ethylene glycol manometer.

The test condenser tubes were of copper with 9.78 mm i.d. and length exposed to vapor 102 mm. The outside diameter at the root of fins was 12.7 mm, and the fin height and thickness were 1.59 mm and 0.5 mm, respectively. Fin spacings of 0.25, 0.5, 1, 1.5, 2, and 4 mm were used. All tests were conducted at near-atmospheric pressure. The apparatus was first run for around an hour to expel air and to achieve steady operating conditions. The condenser tube was viewed through a pyrex glass window and complete film condensation verified in all cases. For each tube in turn measurements were made on at least two separate occasions.

## Results

The heat transfer rate to the condenser tube was found from the mass flow rate and temperature rise of the cooling water. The vapor mass flow rate and hence velocity were obtained from a steady-flow energy balance between the boiler inlet and the test section. A small correction for the thermal losses from the apparatus was incoporated as indicated by Masuda and Rose (1985). The noncondensing gas (taken to be air) content was estimated from the test section temperature and pressure using the ideal-gas mixture laws and assuming saturation conditions. This was in all cases found to be less than the accuracy with which this quantity could be determined, i.e., the mass fraction of noncondensing gas was less than about 0.003. All tests were carried out using the same boiler heater power, which gave a vapor velocity, at approach to the test condenser tube, of 0.36 m/s.

**Overall Heat Transfer Coefficients.** Figure 1 shows the dependence of overall heat transfer coefficient on coolant velocity for the tubes tested. The fact that the coefficient does not increase monotonically with coolant velocity is due to local boiling of the coolant at the tube wall at low coolant velocity. The broken line XX in Fig. 1 indicates coolant velocities below which boiling occurs, calculated as outlined below.

As indicated by Masuda and Rose (1985), the coolant-side heat transfer coefficient, when condensing steam, was well represented by

$$\mathrm{Nu}_c = 0.03\ \mathrm{Re}_c^{0.8}\ \mathrm{Pr}_c^{1/3}(\mu_c/\mu_w)^{0.14} \tag{1}$$

For each tube in turn, and for each data point, the measured heat flux and coolant temperatures were used with equation (1) to determine the tube wall temperature. This was compared with the temperature for onset of local nucleate boiling

$$T_b = T_{\mathrm{sat}_c} + \left(\frac{8\sigma T_{\mathrm{sat}_c} v_{g_c} Q_i}{k_c h_{fg_c}}\right)^{1/2} \tag{2}$$

given by Sato and Matsumura (1964) and Davis and Anderson (1966). The lowest coolant velocity for which boiling would not occur, according to equation (2), was thus established. The line XX in Fig. 1 divides the boiling and nonboiling regions. The position of XX is clearly consistant with the general behavior of the curves. For coolant velocities sufficiently high to prevent boiling, i.e., to the right of XX, the overall heat transfer coefficient increases with increasing coolant velocity as expected for single-phase forced-convection coolant flow. To the left of XX coolant boiling, increasing in intensity with decreasing coolant velocity, leads to the behavior observed. The fact that the overall heat transfer coeffficient for the plain tube is virtually independent of coolant velocity, over the range used, indicates that the vapor-side resistance is controlling in this case.

**Vapor-Side Coefficients.** The data to the left of XX in Fig. 1 were discarded since the coolant-side, and hence the vapor-side, coefficient cannot be accurately evaluated. Vapor-side coefficients were then determined from the overall measurements using equation (1) for the coolant-side resistance and uniform radial conduction for the tube wall. A "modified Wilson Plot" was also used to evaluate vapor-side coefficients. In this method suitable equations are used for the inside and outside heat transfer coefficients, which involve unknown (disposable) constants found by minimizing the sum of squares of differences between calculated and measured overall quantities for a set of tests where the coolant velocity is varied. Equation (1) (with a disposable constant in place of the coefficient 0.03) was used for the coolant side and a "Nusselt-type" equation

$$\mathrm{Nu} = B\left(\frac{\rho^2 g h_{fg} d^3}{\mu k \Delta T}\right)^{1/4} \tag{3}$$

was used for the vapor side, where $B$ is a disposable constant. For a given tube and given vapor temperature and velocity, tests, covering a range of coolant velocity, were used in a curve fitting ("least squares") procedure to determine the unknown constants, i.e., $B$ and the coefficient in the coolant-side equation. The tube wall was treated on the basis of uniform radial conduction.

In both methods the tube wall was considered to extend from the inside surface to the fin roots, so that the vapor-side

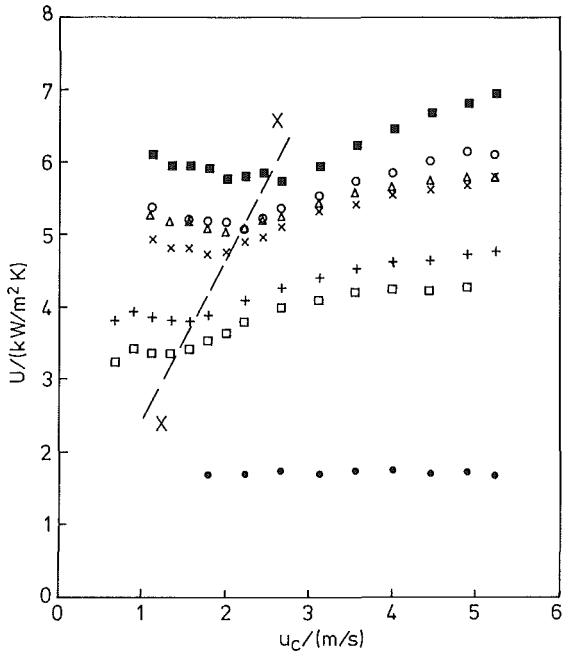


**Fig. 1 Dependance of overall heat transfer coefficient on coolant velocity:**
□ $b = 0.25$ mm
▵ $b = 0.5$ mm
■ $b = 1.0$ mm
○ $b = 1.5$ mm
× $b = 2.0$ mm
+ $b = 4.0$ mm
• plain tube

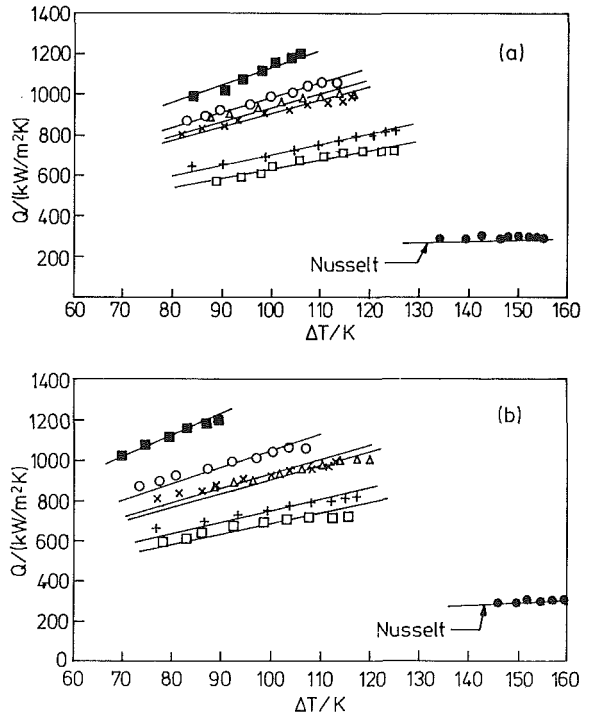


**Fig. 2 Dependence of heat flux (based on plain tube area with fin root diameter) on vapor-side temperature difference (symbols defined in Fig. 1): (a) calculated using coolant-side equation (1); (b) calculated using "modified Wilson Plot"**

temperature difference and heat transfer coefficient include the effects of both fins and condensate. Details are given by Masuda and Rose (1985).

As seen in Fig. 2, the two calculation methods give somewhat different vapor-side results but are broadly in agreement. Both show that the best-performing tube was that with a fin spacing of 1.0 mm, while the tubes with higher and

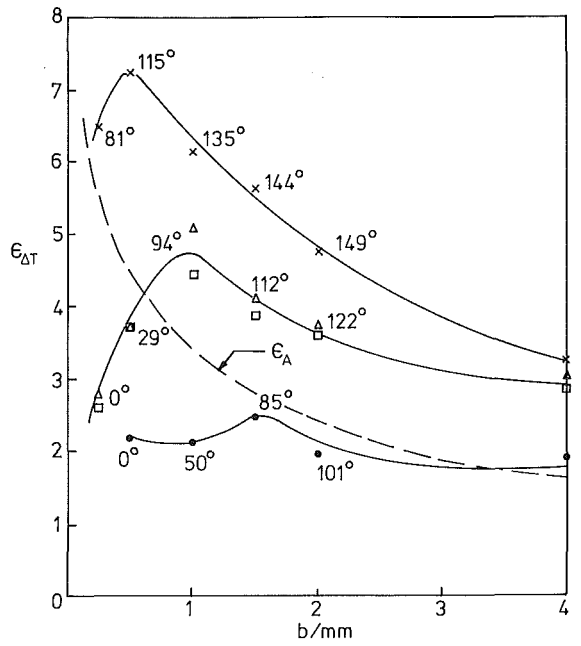


**Fig. 3 Vapor-side enhancement ratios:**
▽ **ethylene glycol, present work: vapor-side coefficient from "modified Wilson Plot**
□ **ethylene glycol, present work: vapor-side coefficient found using equation (1) for coolant side**
× **refrigerant 113 (Masuda and Rose, 1985)**
• **steam (Yau et al., 1985, 1986)**
**The angles marked at the data points are values of $\phi$ given by equation (7).**

lower fin spacing performed less well. The lines drawn through the points for the finned tubes in Fig. 2 are curve fits of $Q = \text{constant} \times \Delta T^{3/4}$ in accordance, apart from secondary effects of property variation, with equation (3).

As noted by Masuda and Rose (1985), the fact that vapor-side data for finned tubes can be represented approximately by equation (3) indicates that the vapor-side enhancement is essentially independent of $\Delta T$ and $Q$, i.e.,

$$\epsilon_{\Delta T} = B_{\text{finned tube}}/B_{\text{plain tube}} \tag{4}$$

$$\epsilon_Q = \{B_{\text{finned tube}}/B_{\text{plain tube}}\}^{4/3} \tag{5}$$

$$\epsilon_Q = \epsilon_{\Delta T}^{4/3} \tag{6}$$

$\epsilon_{\Delta T}$ is the "effective" vapor-side heat transfer coefficient for the finned tube divided by that for a plain tube having diameter equal to that at the fin root, for the same $\Delta T$. By "effective" is meant that the area used in defining the heat transfer coefficient is that of a plain tube with the fin root diameter. Thus, in design calculations the finned tube could be treated as a plain tube with the fin root diameter but with a surface heat transfer coefficient $\epsilon_{\Delta T}$ times that of the plain tube. The same statements may be made with regard to $\epsilon_Q$ except that the coefficients are then considered for the same heat transfer rate (i.e., same heat flux based on plain tube area). As seen from equation (6) the enhancement for the same heat flux is larger than for the same temperature difference.

Such limited data as exist for steam at relatively low velocity (Yau et al. 1985, 1986) suggest that $\epsilon_{\Delta T}$ and $\epsilon_Q$ do not depend strongly on vapor velocity; i.e., vapor velocity affects fined and plain tube coefficients approximately in the same proportion.

Values of $\epsilon_{\Delta T}$ were obtained from the values of $B$ determined by the two methods. Both are given in Fig. 3, together with vapor-side enhancement ratios, for the same tubes, for steam and refrigerant 113 from Yau et al. (1985, 1986) and Masuda and Rose (1985), respectively. It is seen that the

enhancement ratios for ethylene glycol are intermediate between those for steam and refrigerant 113 and that, for ethylene glycol, a maximum occurs at a fin spacing of 1 mm.

Also indicated in Fig. 3, for all the fluids, are "flooding angles," i.e., the angle measured from the top of the tube to be position at which the fin flanks are completely covered by retained condensate, according to Honda et al. (1983) and Rudy and Webb (1985), i.e.,

$$\phi = \cos^{-1}\left\{\frac{2\sigma}{\rho g b R} - 1\right\} \tag{7}$$

It is of interest to note that in all cases maximum enhancement occurs when the tubes are approximately half "flooded" ($\phi \simeq \pi/2$). Also it is seen for both ethylene glycol and steam that significant enhancement is obtained even when the tubes are fully "flooded" ($\phi = 0$). This presumably indicates significant enhancement at the fin tip or, conceivably, that secondary flow effects enhance heat transfer in the "flooded" interfin space.

## References


Beatty, K. O., and Katz, D. L., 1948, "Condensation of Vapors on Outside of Finned Tubes," *Chem. Eng. Prog.*, Vol. 44, No. 1, pp. 55–70.

Davis, E. J., and Anderson, G. H., 1966, "The Incipience of Nucleate Boiling in Forced Convection Flow," *AIChE Journal*, Vol. 12, No. 4, pp. 774–780.

Honda, H., and Nozu, S., 1984, "A Prediction Method for Heat Transfer During Film Condensation on Horizontal Intergal-Fin Tubes," *Fundamentals of Phase Change: Boiling and Condensation*, Proc. ASME Winter Annual Meeting, New Orleans, HTD-Vol. 38, pp. 107–114.

Honda, H., Nozu, S., and Mitsumori, K., 1983, "Augmentation of Condensation on Horizontal Finned Tubes by Attaching a Porous Drainage Plate," *Proc. ASME-JSME Thermal Engineering Joint Conference*, Honolulu, HI, Vol. 3, pp. 289–296.

Masuda, H., and Rose, J. W., 1987, "Static Configuration of Liquid Films on Horizontal Tubes With Low Radial Fins: Implications for Condensation Heat Transfer," *Proc. R. Soc.*, 1987, A 410, pp. 125–139.

Masuda, H., and Rose, J. W., 1985, "An Experimental Study of Condensation of Refrigerant 113 on Low Intergal-Fin Tubes," *Proc. Int. Symp. on Heat Transfer*, Beijing, China, Tsinghua Univ. Press, Vol. 2, paper 32; also in *Heat Transfer Science and Technology*, Bu-Xuan Wang, ed., Hemisphere, 1987, pp. 480–487.

Rudy, T. M., and Webb, R. L., 1985, "An Analytical Model to Predict Condensate Retention on Horizontal Integral-Fin Tubes," ASME JOURNAL OF HEAT TRANSFER, Vol. 107, pp. 361–368.

Sato, T., and Matsumura, H., 1964, "On the Conditions of Incipient Subcooled Boiling With Forced Convection," *Bull. JSME*, Vol. 7, pp. 392–398.

Webb, R. L., Rudy, T. M., and Kedzierski, M. A., 1985, "Prediction of the Condensation Coefficient on Horizontal Integral-Fin Tubes," ASME JOURNAL OF HEAT TRANSFER, Vol. 107, pp. 369–376.

Yau, K. K.,. Cooper, J. R., and Rose, J. W., 1985, "Effect of Fin Spacing on the Performance of Horizontal Integral-Fin Condenser Tubes, ASME JOURNAL OF HEAT TRANSFER, Vol. 107, pp. 377–383.

Yau, K. K., Cooper, J. R., and Rose, J. W., 1986, "Horizontal Plain and Low-Finned Condenser Tubes—Effect of Fin Spacing and Drainage Strips on Heat-Transfer and Condensate Retention," ASME JOURNAL OF HEAT TRANSFER, Vol. 108, pp. 946–950.